# STUDIA UNIVERSITATIS BABEȘ-BOLYAI CHEMIA

# S T U D I A

# UNIVERSITATIS BABEŞ–BOLYAI CHEMIA

**1**

## CUPRINS – CONTENT – SOMMAIRE – INHALT

# Professor Petru Ilea on his 65th Anniversary



Professor Petru Ilea was born on the 23rd of April 1953. In 1977 he graduated from Technical University of Timisoara as a chemical engineer. He received his PhD degree in chemical engineering in 1994, under the supervision of the distinguished Professor Liviu Oniciu.

As Teaching Assistant (1987), Assistant Professor (1990), Associate Professor (2000) and Professor (2005) at the Faculty of Chemistry and Chemical Engineering Cluj-Napoca, Petru Ilea introduced and developed the electrochemical engineering and electrochemical technology programs in the undergraduate and graduate curricula at our faculty. His courses were appreciated by both undergraduate and graduate students. He focused his research efforts in the domains of electrochemical engineering and technology. At the same time, the environmental applications of electrochemistry were among the most fruitful scientific preoccupations of Professor Petru Ilea.

In addition to over 80 scientific papers, Professor Petru Ilea also co-authored 3 books and managed numerous grants and research projects. He counts more than 110 participations to scientific conferences with lectures, posters and oral communications. The research grants he coordinated, substantially contributed to the development of electrochemical engineering and technology at "Babeş-Bolyai" University.

It is worth mentioning, that starting with 2006 Professor Petru Ilea is the head of the Physical-Chemical Analysis Center at the Institute of Interdisciplinary Research in Bio-Nano-Sciences of University "Babes-Bolyai" Cluj-Napoca.

Professor Petru Ilea was one of the founders of the Doctoral School of Chemical Engineering at our faculty and he was its head starting with 2017.

Professor Petru Ilea was a very active member of the academic community. He has served as Chancellor of Faculty of Chemistry and Chemical Engineering (2000-2009). During several years (2000-2016) he was an active member of the Faculty Council. Since 2007 he is an active member of CNADTCU/Engineering Sciences (Division of Chemical engineering, medical engineering, material and nanomaterials science).

This issue of Studia Universitas Babeş-Bolyai, Seria Chemia wishes to honor Professor Petru Ilea and to recognize his achievements within the academic community. The intention of the editors was to bring together contributions from his co-workers, scientists that have close professional contact with him and those working intensively in the field of chemical engineering and technology.

Now, at this anniversary moment, we – the colleagues of the Electrochemistry group, as well as all the colleagues and researchers of the Faculty of Chemistry and Chemical Engineering of the "Babeş-Bolyai" University, express Professor Petru Ilea their appreciation for his entire activity, along with the best wishes for a long life of successful future achievements!

Prof. dr. Ionel Catalin POPESCU
Prof. dr. Liana Maria MURESAN
Prof. habil. dr. ing. Graziella Liana TURDEAN

Cluj-Napoca, March 2020

# CYCLIC VOLTAMMETRY AND SHORT-TIME SCALE CHRONOAMPEROMETRY AT LAYER-BY-LAYER SELF-ASSEMBLED Au MODIFIED ELECTRODES. FRUCTOSE BIOSENSOR

**IONEL CĂTĂLIN POPESCU[a,*]**

**ABSTRACT.** Cyclic voltammetry (CV) and short-time scale chronoamperometry measurements were performed aiming to investigate the layer-by-layer self-assembled multilayer structures built on Au electrodes. The attractive electrostatic interactions exerted between the successively deposited layers of charged polymers were exploited in order to immobilize a cationic Os redox polymer onto the surface of Au modified electrodes. CV responses observed at the resulted Au modified electrodes proved the efficiency of the proposed design. The chronoamperometric responses were fitted by using a three-phase exponential decay function. The fitting parameters allowed comparing the ability of charge transfer of the investigated modified electrodes. The most efficient structure was used as an amperometric transducer for electrical communication between fructose dehydrogenase and the Au electrode. In order to validate the new approach as a proof of concept for obtaining reagentless biosensors, a functional amperometric biosensor for D-fructose was successfully built.

**Keywords.** *Self-assembled multilayer architecture, electrostatic interactions, Au modified electrodes, reagentless amperometric biosensors, Os redox polymer.*

## INTRODUCTION

Various approaches were proposed to obtain modified electrodes such as: chemisorption, covalent bonding, polymer film coating, and entrapment in a

---

[a] *Babeş-Bolyai University, Faculty of Chemistry and Chemical Engineering, 11 Arany Janos str., RO-400028, Cluj-Napoca, Romania,*
* *Corresponding author: cpopescu@chem.ubbcluj.ro*

conductive material [1]. Among these, a simple way exploited the spontaneous formation of the self-assembled structures immobilized on the surface of a conducting material [2, 3]. Conveniently handled, this approach yields modified electrodes covered by multilayer architectures, exhibiting high electrocatalytic activity and good selectivity and sensitivity [4, 5].

Recently, the electrostatic interaction exerted between oppositely charged monolayers was successfully used for the construction of biosensors incorporating self-assembled multilayer structures [6-12]. Thus, it was clearly demonstrated that multilayer architectures based on the alternation of a positively charged redox polymer and adequately charged polyelectrolytes yield, by simple successive self-deposition, electrochemical active platforms able to act as amperometric transducers for various biosensors used to detect: glucose [7, 10-12], hydrogen peroxide, methanol and D-fructose [12, 13].

In the present paper, a two-step method consisting in cyclic voltammetry coupled with short-time scale chronoamperometric measurements was used to examine the electrochemical behavior of the modified electrodes, built up by successive self-deposition of electrically charged layers. The CV responses were used to confirm the functionality of the modified electrodes preparation. The recorded chronoamperograms, were best fitted by using a three-phase exponential decay function [14, 15], and served to identify the most efficient structure. Finally, a reagentless amperometric biosensor for D-fructose amperometric detection was described.

## RESULTS AND DISCUSSION

The typical voltammetric behavior of a clean Au surface was confirmed by the comparing the cyclic voltammogram recorded at cleaned Au wire electrodes in contact with 0.1N $H_2SO_4$ (Figure 1) with that published in the literature [16]. It is important to notice that the potential window located between 100 and 500 mV versus Ag/AgCl,KCl$_{sat}$ is well placed in the domain of the relative electrochemical inactivity of the Au surface.

The voltammetric responses observed at bare Au electrode as well as at Au modified electrodes based on various self-assembled architectures built up by using layer-by-layer deposition technique are shown in figure 2. The scanned potential domain was selected such as it corresponds to the electrochemical activity of the $Os^{+2/+3}$ redox centers, incorporated in the Os-RP structure [17].
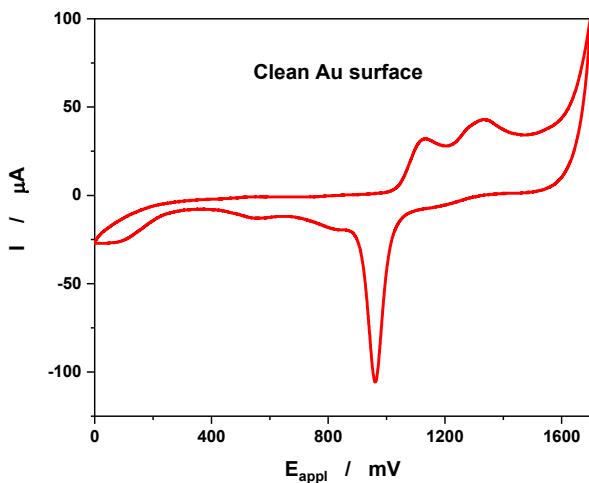
**Figure 1.** The voltammetric response recorded at clean Au electrodes. Experimental conditions: potential scan rate, 50 mv/s; initial potential, 0 mV versus Ag/AgCl,KCl$_{sat}$; supporting electrolyte, 0.1 M H$_2$SO$_4$.
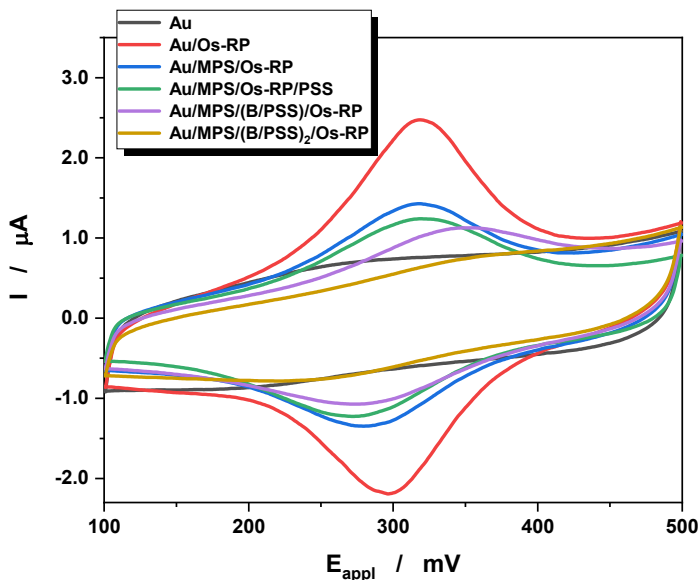


**Figure 2.** Cyclic voltammograms recorded at Au electrodes modified with different self-assembled monolayers based on self-deposited layers of **Os-RP, MPS, PSS,** and **B**. Experimental conditions: initial potential, 100 mV versus Ag/AgCl,KCl$_{sat}$; potential scan rate, 50 mV/s; supporting electrolyte, 0.1M acetate buffer (pH 5.0) containing 0.15M NaCl.

9

As can clearly be seen in figure 2, the successive interposition of one or more nonconductive layers (such as MPS, B and PSS) between the Os redox centers and the Au electrode surface induce a gradual decrease of the voltammeytric response of the investigated electrodes. Obviously, this behavior is due to an increase of the distance between the redox partners generating the observed voltammetric response: the Au electrode and the $Os^{+2/+3}$ redox centers. At the same time, this peculiar comportment is an indirect proof, validating the reliability of the layer-by-layer self-assembling technique for obtaining modified electrodes based on complex multilayer structures [12]. It is worth mentioning that the layer-by-layer self-assembling technique, based on electrostatic interactions existing between oppositely charged polymers, offers a simple and direct possibility for fine-tuning of the sensitivity as well as the selectivity of the modified electrodes [7, 10].

Figures 3A and 3B depict the short-time scale chronoamperometric responses recorded at the investigated Au modified electrodes, immersed in the supporting electrolyte.
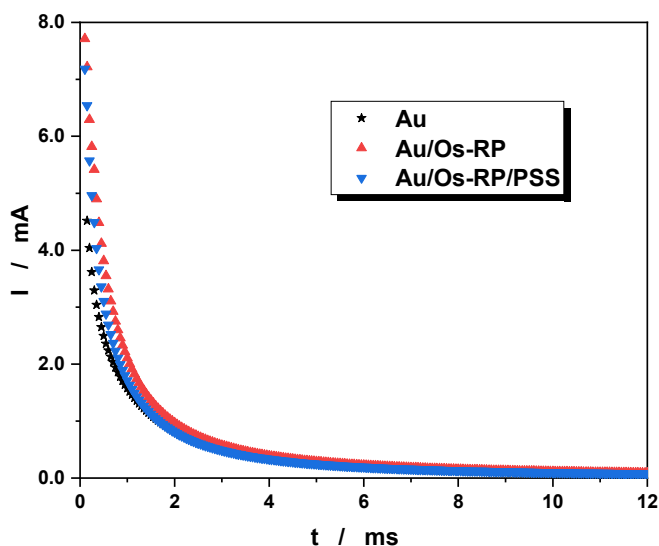


**Figure 3A.** Single potential step chronoamperograms recorded for cationic Os-redox polymer adsorbed on bare Au electrodes. Experimental conditions: initial potential, 100 mV versus Ag/AgCl,KClsat; final potential, 100 mV versus Ag/AgCl,KClsat; supporting electrolyte, 0.1M acetate buffer (pH 5.0) containing 0.15M NaCl. Each experimental point represents the average of 10 consecutive measurements carried out at the same modified electrode.
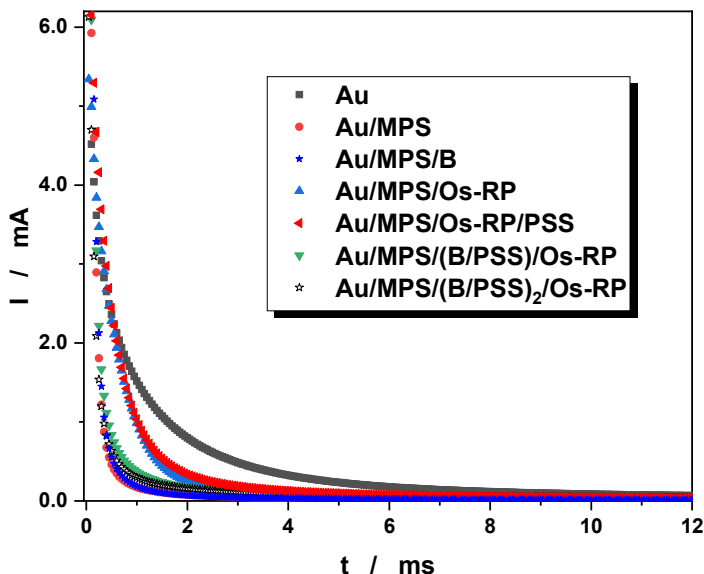
**Figure 3B.** Single potential step chronoamperograms recorded at different self-assembled Au/MPS electrodes. Experimental conditions: initial potential, 100 mV versus Ag/AgCl,KCl$_{sat}$; final potential, 100 mV versus Ag/AgCl,KCl$_{sat}$; supporting electrolyte, 0.1M acetate buffer (pH 5.0) containing 0.15M NaCl. Each experimental point represents the average of 10 consecutive measurements carried out at the same modified electrode.

As a general conclusion, it can be stated that for all investigated electrodes a meaningful correlation between the intensities of the voltammetric and chronoamperometric responses occurs. Thus, the amplitude of the transient currents follows straightly the same pattern observed for cyclic voltammetry measurements.

At the same time, qualitatively, the increasing order of the global decay rates, noticed for the chronoamperometric responses of the investigated modified electrodes, listed in the following sequence:

**Au/Os-RP < Au/Os-RP/PSS < Au < Au/MPS/Os-RP ≈ Au/MPS/Os-RP/PSS < Au/MPS/(B/PSS)/Os-RP ≈ Au/MPS/(B/PSS)₂/Os-RP< Au/MPS/B < Au/MPS**

is in a good agreement with the voltammetric data shown in Figures 3A and 3B.

Aiming to obtain more information about the electrochemical behavior of the investigated modified electrodes, the recorded short-time scale chronoamperometric responses were fitted to a three-phase exponential decay function:

$$Y = \Sigma A_i{*}exp(-x/t_i) \text{ (i = 1 - 3)}$$

This approach offers a simple way to split the global amperometric response recorded after a single potential step in its main components: capacitive, faradaic and diffusive [14, 15]. The values of the (A, t) parameter pairs were calculated by using a nonlinear fitting software (Origin 8.0) and are listed in Table 1.

Some interesting information was revealed when the variation of the $t_1$ parameter value was examined in correlation with the structural changes involved in the multilayer architecture existing on the Au electrode surface. Thus, within the limits of experimental error, the values of the $t_1$ parameter were found almost identical for **Au/MPS/B, Au/MPS, Au/MPS/(B/PSS)/Os-RP,** and **Au/MPS/(B/PSS)₂/Os-RP** modified electrodes, suggesting that in all these cases the charge transfer is the strongly hindered by the presence of nonconductive layers within the structure of the electrochemical interface.

Moreover, the **Au/MPS/Os-RP**, **Au/Os-RP/PSS**, and **Au/MPS/Os-RP/PSS** electrodes, due to their high values of the $t_1$ parameter, can be considered as the most active among the investigated redox interfaces. Consequently, these electrodes are recommended to be used as electrochemical platforms for sensors/biosensors construction.

That is why, in a final step, **FDH** was immobilized on **Au/MPS/Os-RP** by using the electrostatic attraction exerted between the positively charged surface of the **Au/MPS/Os-RP** modified electrode and the negatively charged enzyme. The bioelectrocatalytic responses recorded at the resulted **Au/MPS/Os-RP/FDH** bioelectrodes for increasing concentrations of D-fructose are shown in figure 4. The very well-shaped electrocatalytic responses, recorded at **Au/MPS/Os-RP/FDH** biosensor in presence of different D-fructose concentrations (Figure 4), doubtless confirm the efficient electrical communication established between **FDH** and the Au electrode surface, mediated by the presence of cationic Os-redox polymer.

Based on the experimental data shown in figure 4, the analytical parameters of the D-fructose biosensor were estimated as follows: linear range, up to 20 mM; sensitivity, (0.185 mA/M); detection limit, 0.4 mM D-fructose; reproducibility, better than 95%; low susceptibility to electrochemical interferences, due to the low applied potential, and an acceptable stability (better than one month).
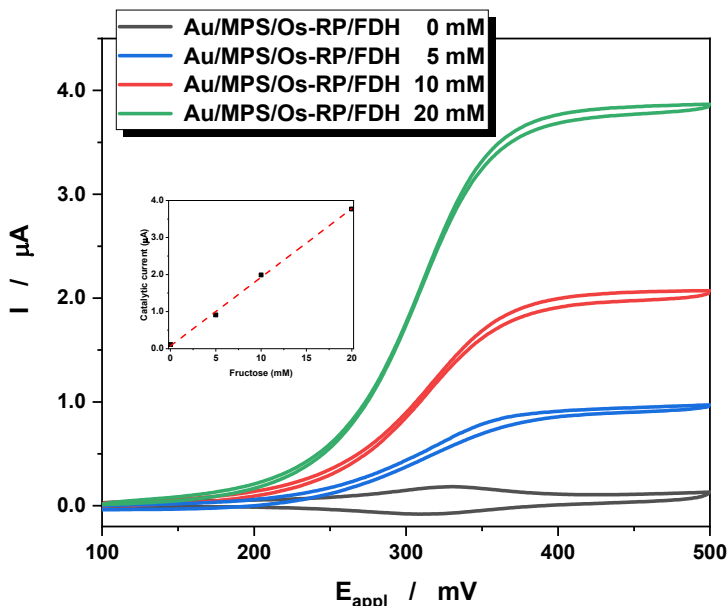
**Figure 4.** Cyclic voltammetry recorded at **Au/MPS/Os-RP/FDH** modified electrodes in presence of different concentrations of D-fructose. Experimental conditions: initial potential, 100 mV versus Ag/AgCl,KCl$_{sat}$; scan rate, 2 mV/s; supporting electrolyte, 0.1M acetate buffer (pH 5.0) containing 0.15M NaCl.

This design can be considered as a promising proof of concept for a simple way to obtain reagentless amperometric biosensors.

## CONCLUSIONS

Aiming to develop a simple and reliable method to monitor the self-assembled amperometric biosensors construction, cyclic voltammetry was coupled with short-time scale chronoampeometric measurements performed at modified electrodes based on multilayer architectures built up on attractive electrostatic interactions. A three-phase exponential decay function was used to fit the short-time scale chronoamperograms.

Finally, the applicability of the proposed method was demonstrated by the construction of a fully functional reagentless amperometric biosensor for D-fructose detection.

**Table 1.** The fitting parameters corresponding to the chronoamperograms recorded at self-assembled Au modified electrodes. The experimental curves (Figures 2A and 2B) were fitted to a three-phase exponential decay function: $Y = \Sigma A_i * \exp(-x/t_i)$, where **i=1, 2, 3**.

| Electrode type | Fitting parameters | | | | | |
|---|---|---|---|---|---|---|
| | $A_1$ (A) | $t_1$ (s) | $A_2$ (A) | $t_2$ (s) | $A_3$ (A) | $t_3$ (s) |
| Au | 3.0E-3 ± 1E-4 | 2.9E-4 ± 6E-6 | 2.4E-3 ± 7E-5 | 1.4E-3 ± 1E-4 | 2.7E-4 ± 4E-5 | 7.5E-3 ± 1E-4 |
| Au/MPS | 1.1E-2 ± 2E-3 | 1.2E-4 ± 2E-5 | 5.9E-4 ± 3E-4 | 1.2E-3 ± E-4 | 7.4E-5 ± 5E-5 | 1.4E-2 ± 3E-3 |
| Au/MPS/B | 1.3E-2 ± 1E-3 | 1.3E-4 ±1E-5 | 3.4E-4 ± 2E-4 | 1.1E-3 ± 2E-4 | 2.6E-5 ± 1E-5 | 1.7E-2 ± 5E-3 |
| Au/Os-RP | 6.4E-3 ± 3E-4 | 3.6E-4 ± 1E-5 | 2.8E-3 ± 3E-4 | 1.50E-3 ± 5E-5 | 2.7E-4 ± 2E-5 | 1.12E-2 ± 7E-4 |
| Au/Os-RP/PSS | 6.4E-3 ± 2E-4 | 2.6E-4 ± 1E-5 | 2.2E-3 ± 1E-4 | 2.4E-3 ± 2E-3 | 8.1E-4 ± 1E-4 | 9.6E-3 ± 1E-4 |
| Au/MPS/Os-RP | 5.8E-3 ± 6E-4 | 4.7E-4 ± 2E-5 | 6.0E-4 ± 4E-4 | 1.8E-3 ± 6E-4 | 4.3E-5 ± 1E-5 | 1.7E-2 ± 2E-3 |
| Au/MPS/Os-RP/PSS | 7.6E-3 ± 1E-3 | 3.4E-4 ± 3E-5 | 1.4E-3 ± 5E-4 | 1.3E-3 ± 2E-3 | 9.2E-5 ± 2E-5 | 1.3E-2 ± 1E-3 |
| Au/MPS/B/PSS/ Os-RP | 1.2E-2 ± 1E-3 | 1.3E-4 ± 1E-5 | 7.9E-4 ± 1E-4 | 9.9E-4 ± 9E-5 | 8.9E-5 ± 5E-6 | 1.4E-2 ± 6E-4 |
| Au/MPS/(B/PSS)$_2$/ Os-RP | 1.3E-2 ± 2E-3 | 1.2E-4 ± 1E-5 | 5.7E-4 ± 9E-5 | 1.0E-3 ± 1E-4 | 7.9E-5 ± 8E-6 | 2.0E-2 ± 2E-3 |

## EXPERIMENTAL SECTION

### Reagents

**Au** wires (0.5 min diameter, geometrical area ca. 0.16 cm2, 99.99% purity) were obtained from Goodfellow Cambridge (England). Sodium salt of 3-mercapto-1-propane sulfonic acid (**MPS**) and was purchased from Aldrich. The poly(styrene sulfonic acid) (MW 70,000; **PSS**) was used as received from Polyscience (Warrington, PA, USA). The cationic poly[(vinylpyridine)Os-(bpy)2Cl] redox polymer partially quaternised with bromoethylamine (**Os-RP**) was synthesized as described elsewhere [18].

The positively charged polyelectrolyte, called binder (**B**), has the same structure as Os-RP except that no Os redox centers are present. Fructose dehydrogenase (**FDH**), from *Gluconobacter* sp., (EC 1.1.99.11, 34 U/mg solid), was supplied by Sigma. D-Fructose was obtained from Fluka. All other chemicals used were of analytical grade. Water was obtained by means of a Millipore Milli-Q system.

### Equipment

Cyclic voltammetry and chronoamperometry measurements were performed using a conventional three electrode electrochemical cell connected to a computer-controlled BAS CV-50W voltammetric analyzer (Bioanalytical Systems, West Lafayette, USA). All electrode potentials were measured against a potassium chloride saturated silver-silver chloride electrode (Ag/AgCl,KCl$_{sat}$). A coiled Pt wire served as counter electrode.

### Preparation of Au modified electrodes [12]

Au wires, used as working electrodes, were successively polished by using fine, wet emery paper and 0.3–0.05 mm alumina (Buehler Inc.). Then, they were treated with freshly prepared '*piranha*' (7:3 mixture of concentrated $H_2SO_4$ and 30% $H_2O_2$) [*Caution*, *piranha reacts* v*iolently with organic compounds*!] for 30 min. Finally, the Au wires were immersed for 2 h in a boiling saturated KOH solution. The cleaned Au wire electrodes were stored in concentrated $H_2SO_4$.

The **Au/MPS** modified electrodes were obtained by immersing the cleaned gold wire into a 1 mM methanolic solution of MPS for 12 h and rinsing with pure ethanol.

The Au electrodes modified with multilayer supramolecular architectures (**Au/Os-RP, Au/MPS/B, Au/Os-RP/PSS, Au/MPS/Os-RP, Au/MPS/Os-RP/PSS; Au/MPS/B/PSS/Os-RP; Au/MPS/(B/PSS)$_2$/Os-RP**) were prepared by sequential deposition of the adequate polyelectrolytes [6-9]. The alternate immersion of the Au/MPS modified electrodes in the corresponding aqueous polyelectrolyte solutions was carried out at room temperature while stirring vigorously by using the following aqueous solutions:

-20 mg of Os-RP/ml for Os-RP deposition (2 h);
-25 mg of PSS/ml for PSS deposition (1 h);
-10 mg of B for B deposition (2 h).

The fructose bioelectrodes, Au/MPS/Os-RP/FDH were prepared by FDH deposition on the surface of the multilayer modified electrode (**Au/MPS/Os-RP**) by simple adsorption (2 h at 4°C, without stirring) from a 1 mg/ml **FDH** solution, dissolved in 0.1 M acetate buffer (pH 5.0).

## ACKNOWLEDGMENTS

# REFERENCES

1. G. A. Edwards, A. J. Bergren, M. D. Porter, "*Chemically Modified Electrodes*", p. *295–327*, in *Handbook of Electrochemistry,* Zoski, C. (ed), Elsevier Science, Amsterdam, The Netherlands, **2006**
2. A. Ulman, *Chem. Rev.*, **1996**, *96*, 1533-1554
3. A. L. Eckermann, D. J. Feld, J. A. Shaw, T. J. Meade, *Coord. Chem. Rev.,* **2010**, *254*, 1769–1802
4. D. Schlereth, *Compr. Anal. Chem.*, **2005**, *44*, 1-63
5. R. S. Freire, Ch. A. Pessoa, L. T. Kubota, *Quim. Nova*, **2003**, *26*, 381-389
6. G. Decher, J. D. Hong, *Makromol. Chem. Macromol. Symp.*, **1991**, *46*, 321–327
7. Y. Lvov, K. Anga, I. Ichinose, T. Kunitake, *J. Am. Chem. Soc.*, **1995**, *117*, 6117–6123
8. D. Laurent, J.B. Schlenoff, **1997**, *13*, 1552–1557
9. F. Caruso, K. Nlikura, D. N. Furlong, Y. Okahata, *Langmuir,* **1997**, 13, 3422–3426
10. J. Hodak, R. Etchenique, E. J. Calvo, K. Singhal, P. N. Bartlett, *Langmuir*, **1997**, *13*, 2708–2716
11. H. Shi-Feng, Y. Ke-Sheng, F. Hui-Qun, Ch. Hong-Yuan, *Talanta*, **1998**, *47*, 561–567
12. A. Nárvaez, G. Suarez, I. C. Popescu, I. Katakis, E. Domínguez, *Biosens. Bioelectron*., **2000**, *15*, 43-52
13. U. B. Trivedi, D. Lakshminarayana, I. L. Kothari, P. B. Patel, C. J. Panchal, *Sens. Actuators B Chem*., **2009**, *136*, 45-51
14. R. J. Forster, *Analyst*, **1996**, *121*, 733-741
15. R. J. Forster, *Anal. Chem.*, **1995**, *67*, 1232-1239
16. L. D. Burke, P. F. Nugent, *Gold Bull.*, **1997**, **30**, 43-53
17. I. Katakis, "Development and analysis of operation of enzyme electrodes based on electrochemically 'wired' oxidoreductases". *PhD Thesis*, **1994**, University of Texas at Austin, USA
18. I. Katakis, A. Heller, *Anal. Chem.*, **1992**, *64*, 1008–1013

# INHIBITION EFFECT OF SOME COMMERCIAL CORROSION INHIBITORS ON MILD STEEL IN 7.0 M PHOSPHORIC ACID

**JULIETA DANIELA CHELARU[a], MIHAELA CIOBRA[a] AND
LIANA MARIA MUREŞAN[a,*]**

**ABSTRACT.** Corrosion tests were carried out in order to find the best inhibitor for the protection of steel pipelines used in $H_3PO_4$ and fertilizers industry. The corrosion inhibition efficiency of five commercial inhibitors was investigated on mild steel by using electrochemical methods (EIS and polarization curves) in a 7M $H_3PO_4$ solution (pH 0.5). The efficiency of best corrosion inhibitors was tested at different concentrations.

*Key words: mild steel, corrosion inhibitors, electrochemical impedance spectroscopy, polarization curves, inhibitor efficiency, phosphoric acid.*

## INTRODUCTION

Phosphoric acid is widely used in the production of fertilizers and surface treatment of steel such as surface cleaning, chemical and electrolytic polishing, coloring, etching, removal of oxide film, phosphating and passivating [1]. Most of the acid is produced from phosphate rocks by the so-called dihydrate wet process, equivalent to 7.0 M $H_3PO_4$ (about 35% $H_3PO_4$) [2]. Most of the industrial equipment is made of steel that can be damaged by the contact with this acidic solution; this is why it is imperative to protect the steel materials used in the phosphoric acid industry.

The use of inhibitors is one of the most practical methods for protecting metals or alloys from corrosion [3]. There is a wide variety of organic compounds used as corrosion inhibitors for steel in $H_3PO_4$ media: thiosemicarbazones [4], hydroxyquinoline derivatives [5], triazole derivatives [6 - 8], imidazoles [9], tetraalkylammonium salts [10], "green compounds" such as plant extracts [11 - 13], guar gum [14] etc., but to find new efficient corrosion inhibitors remains of major interest.

---

[a] *"Babeş-Bolyai" University, Faculty of Chemistry and Chemical Engineering, Department of Chemical Engineering, 11 Arany Janos St., 400028 Cluj-Napoca, Romania*
\* *Corresponding author: limur@chem.ubbcluj.ro*

In this context, the aim of this paper is to investigate the corrosion of mild steel in 7.0 M $H_3PO_4$ solution (pH 0.5) in the absence and in the presence of three commercial products from Nalco Products, USA, (3DT177, 3DT179, Nalco 73413). The effect of these inhibitors was compared with that of Galoryl IC20 (produced by ArrMazz Chemicals SAS, USA) and Corrogard (Able Westchem, Australia). The protective effect of inhibitors at different concentrations was investigated by electrochemical methods (polarization measurements and electrochemical impedance spectroscopy).

## RESULTS AND DISCUSSION

### Open circuit potential

In order to determine the corrosion behavior of carbon steel in corrosive media 7M $H_3PO_4$ (pH = 0.5) in the absence and in the presence of corrosion inhibitors, the experiments were started by recording the open circuit potential (OCP) of the samples in time. The OCP values were situated between -0.370 V and -0.410 V vs. Ag/AgCl/KCl$_{sat}$ and become relatively constant after 1h.

### Electrochemical impedance spectroscopy

Nyquist impedance spectra were recorded immediatly after OCP monitoring in the corrosive solution (pH 0.5) in the presence of inhibitors and the obtained results were compared with those without inhibitors (Figure 1). In all cases, a pure capacitive behavior of the systems was noticed. The electrical equivalent circuit used to fit the experimental spectra was $R_e(QR_p)$, where $R_e$ is the corrosion solution resistance and the couple Q-$R_p$, represents the constant phase element corresponding to the double layer capacity and the polarization resistance, respectively. The polarization resistance corresponds to the corrosion reaction at the metal substrate / solution interface, which contains charge transfer resistance, double layer resistance, film resistance and other accumulations at the metal / solution interface [15]. As the main contribution is that of the charge transfer resistance, we assumed that $R_p$ in our case can be practically assimilated to the charge transfer resistance, $R_{ct}$. The values of $C_{dl}$ were calculated using the equation $C_{dl} = (R^{1-n}Q)^{1/n}$, where $n$ reflects the depressed feature of the capacitive loop in Nyquist diagram $(0 < n \leq 1)$ which is generally attributed to the frequency dispersion, as well as to inhomogeneities, roughness of metal surface and mass transport process [16]. The obtained results for all the analysed samples are presented in Table 1. The chi squared $(\chi^2)$ values were of order $10^{-4}$.

Analyzing the Table 1 data it can observed that in the case of using 0.2 mL/L of inhibitors, an increase of the charge transfer resistance, $R_{ct}$, can be noticed, but this increase is not significant. Best results were obtained in the case of Corrogard and Nalco 73413.
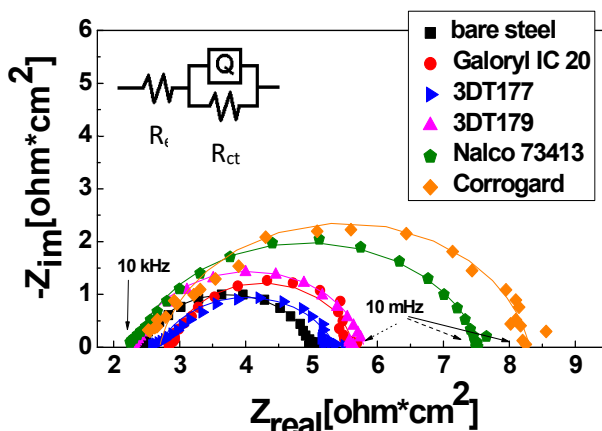


**Figure 1.** Nyquist impedance diagrams for the steel electrodes recorded in 7M $H_3PO_4$ solution (pH 0.5), in the absence and in the presence of corrosion inhibitors (c = 0.2 mL/L) after 1h at OCP; the lines represent fitted data

**Table 1.** The electrochemical impedance parameters estimated by fitting the experimental impedance data from Figure 1.

| Inhibitors | $R_e$ [$\Omega*cm^2$] | $R_{ct}$[a] [$\Omega*cm^2$] | $C_{dl}$[b] [$mF/cm^2$] | $n_{dl}$[c] |
|---|---|---|---|---|
| No inhibitors | 2.42 | 2.596 | 1.211 | 0.836 |
| 3DT177 | 2.25 | 3.387 | 0.790 | 0.878 |
| 3DT179 | 2.88 | 2.742 | 0.946 | 0.924 |
| Galoryl IC20 | 2.67 | 2.686 | 1.033 | 0.781 |
| Corrogard | 2.69 | 5.612 | 0.591 | 0.888 |
| Nalco 73413 | 2.29 | 5.267 | 0.679 | 0.821 |

[a]The standard error for $R_{ct}$ values was between 0.77% - 2.16%; [b]The standard error for Q values was between 2.34% - 5.42%; [c]The standard error for $n_{dl}$ values was between 1.02% - 2.27%

Next, in an attempt to optimize the results, the inhibitors with the best inhibition efficiencies (Corrogard and Nalco 73413) were tested at different concentrations. As before, the experiments started with the measurement of the open-circuit potential (OCP) of the steel electrodes for a period of 1 hour, followed by the recording of EIS spectra.

Figure 2 shows the Nyquist plots obtained for all analyzed steel samples, in the presence of Corrogard and Nalco 73413 at concentrations of 0.2 mL / L, 0.4mL / L, 0.6 mL / L and 0.8 mL / L. All the plots contain depressed semicircles reflecting a pure capacitive behavior. The results obtained both in the absence and in the presence of inhibitors can be suitably represented by using only one time constant circuit and the parameters obtained for all samples are shown in Table 2.
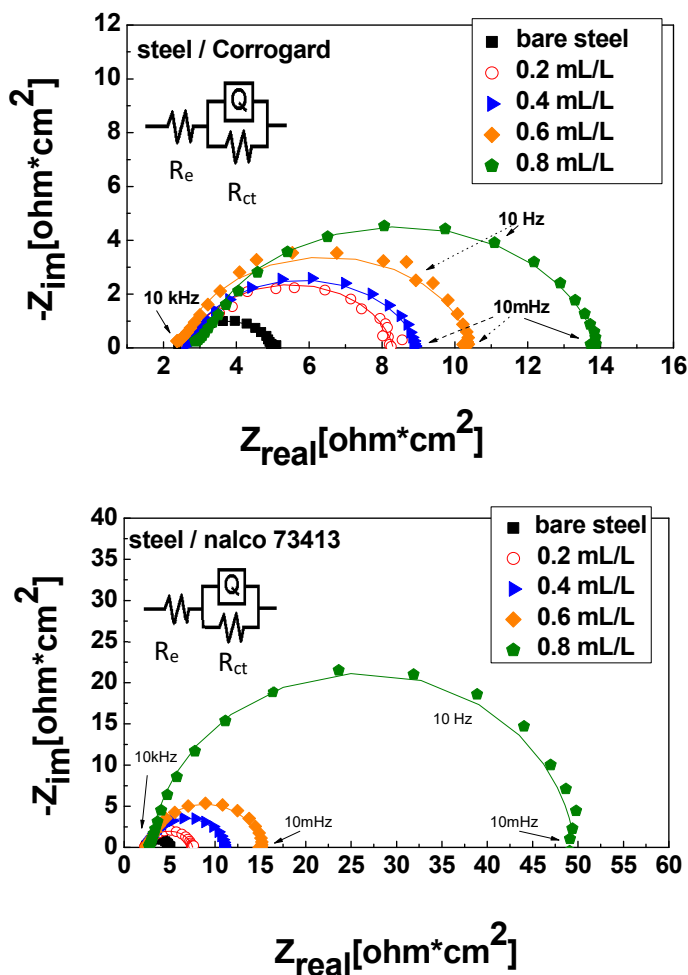


**Figure 2**. Nyquist impedance diagrams for the steel electrodes in 7M $H_3PO_4$ solution (pH 0.5), in the presence of the corrosion inhibitors Corrogard and Nalco 73413 at different concentrations; the lines represent fitted data

**Table 2.** The electrochemical impedance parameters estimated
by fitting the experimental impedance data from Figure 2.

| Inhibitors | $C_{inh}$ [mL / L] | $R_e$ [$\Omega \cdot cm^2$] | $R_{ct}$ [$\Omega \cdot cm^2$] | $C_{dl}$ [mF/cm$^2$] | $n_{dl}$ |
|---|---|---|---|---|---|
| - | 0 | 2.42 | 2.596 | 1.211 | 0.837 |
| **Corrogard** | 0.2 | 2.69 | 5.612 | 0.591 | 0.889 |
| | 0.4 | 2.63 | 6.345 | 0.588 | 0.855 |
| | 0.6 | 2.48 | 7.937 | 0.565 | 0.899 |
| | 0.8 | 2.99 | 10.92 | 0.544 | 0.878 |
| **Nalco 73413** | 0.2 | 2.29 | 5.267 | 0.717 | 0.872 |
| | 0.4 | 2.50 | 8.524 | 0.679 | 0.886 |
| | 0.6 | 2.47 | 12.85 | 0.576 | 0.864 |
| | 0.8 | 2.86 | 49.36 | 0.515 | 0.885 |

[a]The standard error for $R_{ct}$ values was between 1.41% - 2.75%; [b]The standard error for Q values was between 3.39% - 5.61%; [c]The standard error for $n_{dl}$ values was between 0.97% - 1.53%

From the data presented in Table 2, it can be concluded that, as expected, the protective effect of the inhibitors depends on their concentration and generally, the corrosion resistance slightly improved as their concentration increased.

### Polarization measurements

To determine the polarization resistance of the electrodes, linear polarization curves were recorded, in the potential domain of ± 20 mV *vs*. OCP. The polarization resistance ($R_p$) values, for each electrode, was calculated with the formula: $R_{p(\Delta E \to 0)} = \dfrac{\Delta E}{\Delta i}$ , (1), and are shown in Table 4. The protection efficiency of the inhibitors on steel was determined either with the formula: $IE[\%] = \dfrac{R_p^{inh} - R_p^0}{R_p^{inh}} \cdot 100$ , (2), where $R_p^{inh}$ and $R_p^0$ are the polarization resistances in presence and in the absence of inhibitors, respectively, or with the formula , $IE[\%] = \dfrac{i^0 - i^{inh}}{i^0} \cdot 100$ (3), where $i^{inh}$ and $i^0$ are the corrosion current densities in presence and in the absence of inhibitors, respectively.

In order to determine the kinetic parameters of the corrosion process, potentiodynamic polarization curves were recorded in the potential range of ± 200 mV vs. OCP (Figure 3), after OCP recording during 1h. The Tafel interpretation of the polarization curves provided the results presented in Table 3.
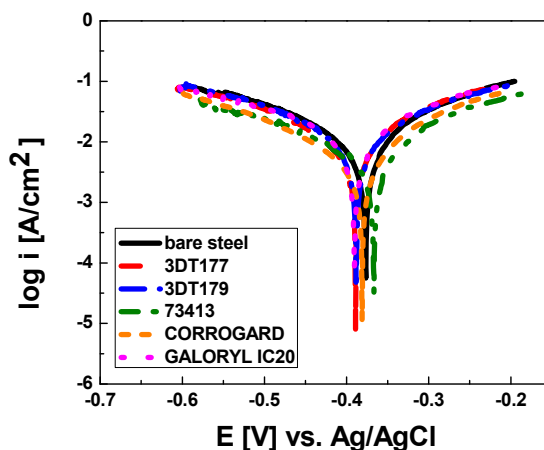
**Figure 3.** The polarization curves (± 200 mV *vs.* OCP) for the steel immersed in 7M $H_3PO_4$ (pH = 0.5) at 0.2 mL/L concentration of inhibitors; scan rate, 10 mV / min.

**Table 3.** Corrosion process parameters in the absence and in the presence of the examined inhibitors at 0.2 mL/L concentration.

| Inhibitors | OCP [mV *vs* RE] | $E_{cor}$ [mV *vs* RE] | $i_{cor}$ [mA/cm$^2$] | $\beta_a$ [mV/dec] | $\beta_c$ [mV/dec] | IE [%] |
|---|---|---|---|---|---|---|
| Bare steel | -396 | -393 | 17.62 | 236 | 344 | - |
| 3DT177 | -408 | -395 | 12.82 | 156 | 192 | 27.22 |
| 3DT179 | -410 | -381 | 14.72 | 323 | 372 | 16.44 |
| Galoryl IC20 | -439 | -391 | 15.74 | 217 | 201 | 10.66 |
| Corrogard | -402 | -384 | 12.05 | 178 | 255 | 31.60 |
| Nalco 73413 | -378 | -373 | 12.58 | 232 | 302 | 28.55 |

$\beta_a$ and $\beta_c$ are the Tafel coefficients

The analysis of the data led to the conclusion that in the case of all tested corrosion inhibitors, a slight decrease of the corrosion current densities can be noticed, even if the inhibition efficiency (IE) was not satisfactory.

In an attempt to see if responsible for this situation was the concentration of the additives, the inhibitors with the highest inhibition efficiency (Corrogard and Nalco 73413) were tested at different concentrations: 0.2 mL / L, 0.4mL / L, 0.6 mL / L and 0.8 mL / L and the corresponding polarization curves are presented in Figure 4.
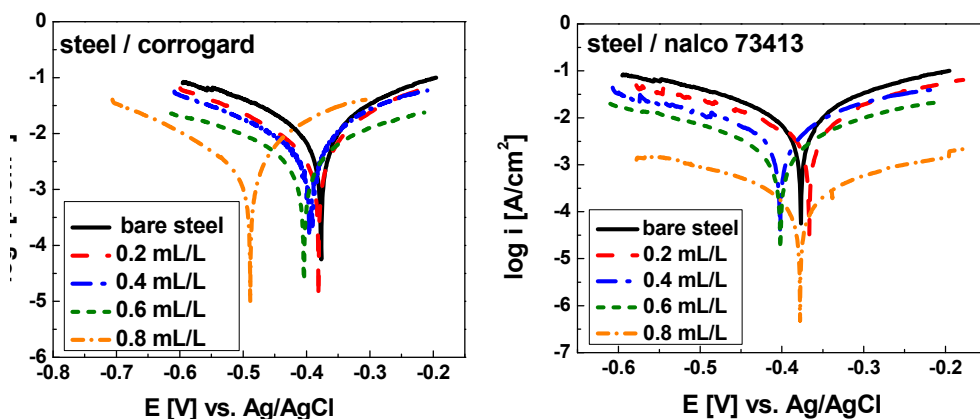
**Figure 4.** The polarization curves (± 200 mV vs. OCP) for the S235 steel immersed in 7M H3PO4 (pH = 0.5) at different concentrations of inhibitors; scan rate, 10 mV / min.

Both branches of the polarization curves are influenced by the inhibitors, proving that they act as mixed-type inhibitors. The Tafel interpretation of the polarization curves led to the results presented in Table 4.

**Table 4.** Kinetic parameters of the corrosion process in 7M $H_3PO_4$ at different concentrations of inhibitors Corrogard (1) and Nalco 73413 (2)

| Inh | $C_{inh}$ [mL/L] | OCP [mV vs RE] | $E_{cor}$ [mV vs RE] | $i_{cor}$ [mA/cm²] | $\beta_a$ [mV/dec] | - $\beta_c$ [mV/dec] | $R_p$ [Ωcm²] | IE [%] | |
|---|---|---|---|---|---|---|---|---|---|
| | | | | | | | | $i_{cor}$ | Rp |
| - | 0 | -396 | -393 | 17.62 | 236 | 344 | 6.73 | - | - |
| 1 | 0.2 | -402 | -384 | 12.05 | 177 | 255 | 10.86 | 32.09 | 38.02 |
| | 0.4 | -410 | -414 | 10.16 | 205 | 283 | 10.51 | 42.32 | 36.01 |
| | 0.6 | -415 | -416 | 5.57 | 472 | 930 | 21.27 | 68.37 | 68.36 |
| | 0.8 | -508 | -501 | 4.57 | 159 | 247 | 17.57 | 74.06 | 61.70 |
| 2 | 0.2 | -378 | -373 | 12.58 | 232 | 302 | 11.11 | 28.55 | 38.77 |
| | 0.4 | -408 | -404 | 10.14 | 351 | 628 | 13.51 | 42.46 | 49.66 |
| | 0.6 | -409 | -408 | 4.21 | 281 | 380 | 25.25 | 76.07 | 73.47 |
| | 0.8 | -378 | -375 | 0.44 | 424 | 420 | 284.09 | 97.45 | 97.63 |

It can be observed, especially in the case of Nalco 73413, a significant increase of the inhibition efficiency in parallel with the inhibitors' concentration. The highest efficiency was noticed at 0.8 mL/L, when a decrease of the

corrosion current density with two orders of magnitude was observed in comparison with the absence of the additive. The same trend was observed in the case of Corrogard, but its effect was not so important.

Both inhibitors act as mixed-type inhibitors. The inhibition effect comes from the reduction of the reaction area on the surface of the corroding metal after inhibitor adsorption [17]. The surface coverage $\theta$ of the electrode surface at different inhibitor concentrations, calculated from the equation $\theta = IE/100$, suggests an incomplete coverage of the electrode surface with inhibitor molecules, which explains their moderate effect.

The beneficial effect of inhibitors was put in evidence also by visual inspection of the corroded surfaces of the electrodes (Figure 5). It can be observed that in case of bare steel, the corrosion products layer is not uniform, with severely corroded areas, while in the case of using corrosion inhibitors, the aspect of the samples is uniform and the presence of rust is not visible.


Bare steel


Corrogard


Nalco 37413
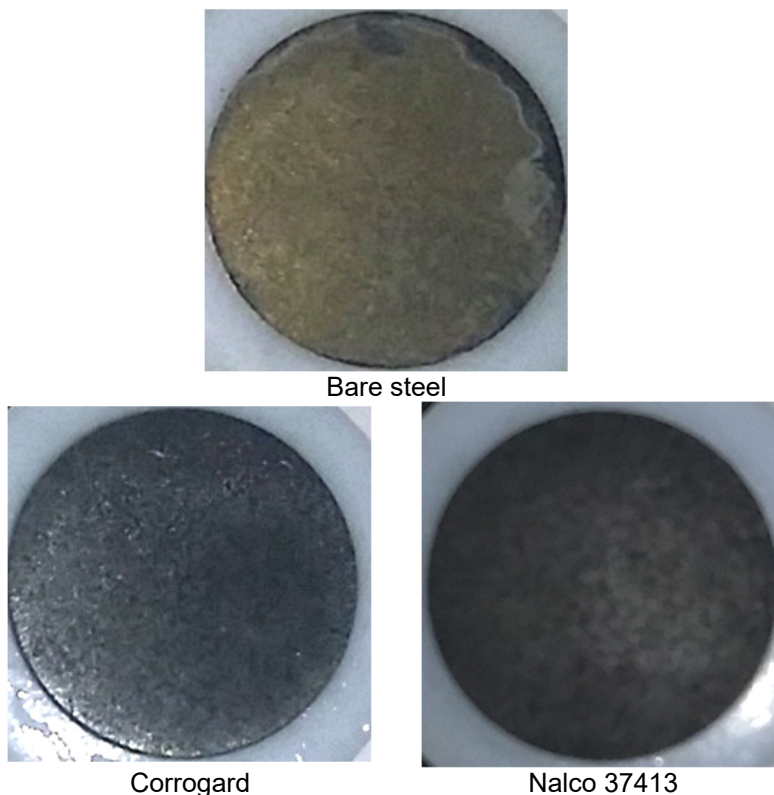
**Figure 5.** Influence of the inhibitors (c = 0.2 mL/L) on the aspect of the steel electrodes immersed in 7M $H_3PO_4$ solution after corrosion tests

## CONCLUSIONS

In terms of practical use, based on electrochemical investigations, all inhibitors tested in the present work can be used as inhibitors against steel corrosion in concentrated phosphoric acid. The best was Nalco 37413.

The protective effect of the inhibitors is moderate, depends on their concentration and generally, the corrosion resistance improved as their concentration increased.

All investigated compounds act as a mixed-type inhibitor, and the inhibition is caused by geometric blocking effect of the surface. EIS spectra exhibit only one capacitive loop which indicates that the corrosion reaction is controlled by the charge transfer process.

Further investigations to assess the corrosion morphology and to elucidate the mechanism for the inhibition of mild steel corrosion in 7M $H_3PO_4$ acidic media are required.

## EXPERIMENTAL

### Materials and solutions

The commercial inhibitors used in the experiments were Nalco 73413, two phosphino succinic oligomer derivatives (3DT177, 3DT179) from Nalco Products USA, and two other products, namely Galoryl IC20 (ArrMazz Chemicals SAS, USA) and Corrogard (Able Westchem, Australia). The inhibitors were dissolved in the corrosive solution at different concentrations: 0.2 mL / L, 0.4mL / L, 0.6 mL / L, 0.8 mL / L.

Mild steel samples (0.22% C, 0.85% Mn, 0.055% P, 0.055% S and Fe balance) were used in the experiments. The working electrodes - WE were cut from a steel bar (S = 0.5 cm$^2$) mounted in Teflon; a copper rod was attached for electrical contact.

Prior to electrochemical tests, the steel samples were ground using different emery papers up to 2000 grade, washed with distilled water and degreased with acetone, after that were dried at room temperature.

### Experimental methods

The electrochemical corrosion measurements were performed on a PC – controlled electrochemical analyzer PAR 2273 (Princeton Applied Research, USA) using a three electrodes cell containing a working electrode (steel), a saturated Ag/AgCl/KCl electrode as reference electrode, and a

platinum counter electrode. The electrolyte solution for corrosion measurements was acidic 7M $H_3PO_4$ (pH = 0.5).

The open circuit potential for steel immersed in the corrosive solution was monitored during 1 hour. Then, electrochemical impedance spectroscopy spectra (EIS) were recorded in the frequency ranging from 10 kHz – 10 mHz with a disturbance voltage of ± 10 mV at 30 points/decade. The impedance data were fitted with a R(QR) equivalent electrical circuit, using the ZSimpWin V3.21 software.

After the EIS measurement was finished, polarization curves were recorded immediately by scanning in a potential range of ± 20 mV (for polarization resistance determination) and of ± 200 mV *vs.* open circuit potential, (for Tafel interpretation) with a scan rate of 10 mV / min. The testing temperature was kept at 20 °C.

# REFERENCES

1. X. Li, S. Deng, X. Xie, *Arab. J. Chem*., **2017**, *10*, 3715-3724.
2. Y. Jianguo, W. Lin, V. Otieno-Alego, D.P. Schweinsberg, *Corros. Sci*., **1995**, *37*, 975-985.
3. M. Finšgar, J. Jackson, *Corros. Sci*., **2014**, *86*, 17-41.
4. T. Poornima, J. Nayak, A. N. Shetty, *Corros. Sci.,* **2011**, *53*, 3688–3696.
5. M. El Faydy, B. Lakhrissi, C. Jama, A. Zarrouk, L. O. Olasunkanmi, E.E. Ebenso, F. Bentiss, *J. Mat. Res. Technol*., **2020**; *9*(1), 727–748
6. Lin Wang, *Corros. Sci.,* **2006**, *48*, 608-616.
7. M.E. Belghiti, Y. Karzazi, A. Dafali, I.B. Obot, E.E. Ebenso, K.M. Emrane, I. Bahadur, B. Hammouti, F. Bentiss, *J. Mol. Liq*., **2016**, *216*, 874-886.
8. M.A. Hegazy, J. Mol. Liq., **2015**, *208*, 227-236.
9. A. Ghanbari, M.M. Attar, M. Mahdavian, *Mater. Chem. Phys*., **2010**, *124*, 1205-1209.
10. X. Li, S. Deng, H. Fu, *Corros. Sci*., **2011**, *53*, 664-670.
11. M.S. Al-Otaibi, A.M. Al-Mayouf, M. Khan, A.A. Mousa, S.A. Al-Mazroa, H.Z. Alkhathlan, *Arab. J. Chem*., **2014***, 7*, 340-346.
12. M. Boudalia, R.M. Fernández-Domene, M. Tabyaoui, A. Bellaouchou, A. Guenbour, J. García-Antón, *J. Mater. Res. Technol*. **2019**, *8*(6), 5763-5773.
13. A. S. Yaro, A. A. Khadom, R. K. Wael, *Alex. Eng. J*., **2013**, *52*, 129-135.
14. M. Messali, H. Lgaz, R. Dassanayake, R. Salghi, S. Jodeh, N. Abidi, O. Hamed, *J. Mol. Struct*., **2017**, *1145*, 43-54.
15. M. Özcan, İ. Dehri, M. Erbil, *Appl. Surf. Sci*., **2004**, *236*, 155-164.
16. E. Barsoukov, J.R. Macdonald*, Impedance spectroscopy: Theory, Experiment, and Applications, second ed. John Wiley & Sons, New Jersey, **2005**.
17. C. Cao, *Corros. Sci.*, **1996**, *38*, 2073-2082.

# PARACETAMOL DETECTION AT A GRAPHITE PASTE MODIFIED ELECTRODE BASED ON PLATINUM NANOPARTICLES IMMOBILISED ON Al-SBA-15 COMPOSITE MATERIAL

**THI THANH HIEN NGO[a], IOANA CARMEN FORT[b],
THANH HUYEN PHAM[a,\*], GRAZIELLA LIANA TURDEAN[b,\*]**

**ABSTRACT.** A composite material was obtained by immobilizing platinum nanoparticles (Pt-NPs) within an ordered mesoporous structure Al-SBA15 (having improved acidity due to the presence of Al). This was used for preparing a graphite paste modified electrode (Pt/Al-SBA-15-GPE), which was applied for paracetamol (PA) detection. The obtained electrode was investigated by electrochemical methods (*e.g.* cyclic voltammetry, CV and electrochemical impedance spectroscopy, EIS), in order to estimate the electrochemical parameters, which were compared with those of GPE unmodified electrode. Square-wave voltammetry (SWV) was used to obtain the analytical parameters of Pt/Al-SBA-15-GPE for PA detection. The good analytical parameters recommend the composite mesoporous material (Pt/Al-SBA-15) to be used for preparing modified electrodes for PA detection in real samples.

*Keywords: Pt nanoparticles, ordered mesoporous structure, graphite paste modified electrode, paracetamol*

## INTRODUCTION

Paracetamol (N-acetyl-para-aminophenol, abbreviated PA) is a substance used for medical treatment of pain and fever because of its analgesic and antipyretic properties. The determination of PA in pharmaceutical formulation use optical [1], chromatographic, capillary electrophoretic and electroanalytical

---

[a] *HaNoi University of Science and Technology, School of Chemical Engineering, 1 Dai Co Viet, Hanoi, Vietnam*
[b] *"Babes Bolyai" University, Faculty of Chemistry and Chemical Engineering, Department of Chemical Engineering, Center of Electrochemistry and Non-Conventional Materials, 11, Arany Janos, 400198 -Cluj-Napoca, Romania*
\* *Corresponding authors: gturdean@chem.ubbcluj.ro and huyen.phamthanh@hust.edu.vn*

methods [2]. Electroanalytical methods based on chemically modified electrode have more advantages over the other conventional standardized methods due to relatively low cost, high sensitivity, fast response, miniaturization/portability and instrumental simplicity. Thus, the PA detection was realized using different chemically modified electrodes, containing conducting polymers [3-6], carbon nanotubes [3, 7-8], graphenes [9] and noble metal nanoparticles (NPs) [10].

SBA-15 (Santa Barbara Amorphous No. 15), developed in 1998 by Zhao et al. [11], is a relatively new mesoporous material intensively studied because of its inert and non-toxic hexagonal structure, which possesses a high degree of structural ordering, larger pore size, thicker pore walls, ease of synthesis, and higher hydrothermal/thermal stability. The application of this material in catalysis is hindered because of its poor acidity, consequently the incorporation of Al in the framework of SBA-15 has been reported (Al-SBA-15) [12]. Also, the strategy to prepare a composite material by immobilizing metal NPs (here Pt-NPs) within the porous structure of Al-SBA-15, could be adopted in order to exploit both the advantages offered by NPs, as well as of the high surface area and ordered structure from the mesoporous silica [13-14].

From the best of our knowledge is the first time when a Pt immobilized on a mesoporous compound SBA-15 (Pt/Al-SBA-15) was used as electrode material for PA detection. In this context, a modified electrode (Pt/Al-SBA-15-GPE) was prepared by including the composite material into a graphite paste matrix. The electrochemical parameters were obtained by investigating the modified electrode by cyclic voltammetry (CV) and electrochemical impedance spectroscopy (EIS). In order to estimate the analytic parameters, either *in vitro* or in real samples, square wave voltammetry (SWV) investigation method was used.


**RESULTS AND DISCUSSION**

**Electrochemical behavior of Pt/Al-SBA-15-GPE electrode material**

In Fig. 1 are presented the cyclic voltammograms in the presence of PA at Pt/Al-SBA-15-GPE and at unmodified GPE electrode (Fig. 1 inset), recorded with a scan rate of 50 mV s$^{-1}$. The peak pairs (A1/C1) placed at $E_{pa}$ = +0.425 V *vs.* Ag|AgCl,KCl$_{sat}$ and at $E_{pc}$ = +0.312 V *vs.* Ag|AgCl,KCl$_{sat}$ potentials, respectively are attributed to the PA redox behavior. An analogous behavior was recorded at MCPE-PtMWCNTs–TX100 modified electrode (*i.e.:* $E_{pa}$ = 0.362 V and $E_{pc}$ = 0.311 V [15], where MCPE = modified carbon paste electrode, MWCNTs = multi-walled carbon nanotubes). The estimated electrochemical parameters values were: peak-to-peak separations (computed $\Delta E = E_{pa} - E_{pc}$) of +0.113 V

at Pt/Al-SBA-15-GPE and +0.238 V at GPE and the formal potentials (computed $E^{0'} = (E_{pa} + E_{pc})/2$) of +0.369 V at Pt/Al-SBA-15-GPE and +0.377 V at GPE, respectively. Also, the anodic to cathodic peak currents ratio (computed $I_{pa}/I_{pc}$) were 1.99 at Pt/Al-SBA-15-GPE and 3.55 at GPE, respectively, proving that the oxidation process of PA is predominant, comparing with the reduction one. The decrease of the $I_{pa}/I_{pc}$ ratio value in the presence of Pt-NPs in the sensing matrix (Pt/Al-SBA-15-GPE) indicates the diminution of the irreversible character of the studied electron transfer reaction encountered at the unmodified electrode (GPE).
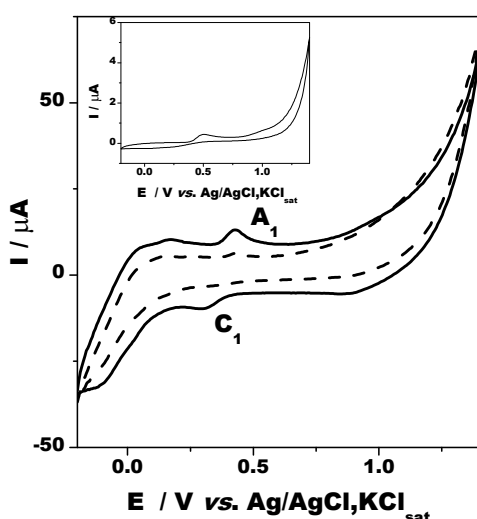


**Figure 1.** Cyclic voltammograms recorded at Pt/Al-SBA-15-GPE in absence (dot line) and in presence of $7 \times 10^{-6}$ M PA (solid line). Inset: CV at unmodified GPE in presence of $7 \times 10^{-6}$ M PA. Experimental conditions: electrolyte, 0.1 M phosphate buffer (pH 7); scan rate, 50 mV s$^{-1}$; starting potential, -0.2 V *vs.* Ag/AgCl, KCl$_{sat}$.

The full width at half of the peak maximum height (FWHM) is 107 mV and 83 mV for Pt/Al-SBA-15-GPE modified electrode and GPE unmodified electrode, respectively. Generally, values of FWHM that are different than the theoretical one (*i.e.,* 90.6/n [mV]) have been attributed to electrostatic effects due to the presence of adjacent charged species [16].

The calculation of the number of electrons involved in the PA electrooxidation process is based on Eq. 1 [17, 18, 19]:

$$E_{p,a} - E_{p,a/2} = 47.7/ \alpha n_a \text{ (mV at 25 °C)} \qquad (1)$$

where: $E_{p,a/2}$ is the half-peak oxidation potential, $\alpha$ is the electron transfer coefficient, $n_a$ is the number of transferred electrons in the oxidation reaction.

At 0.05 V s$^{-1}$, the $E_p - E_{p/2}$ values are +37 mV and -52 mV for anodic and cathodic peak (A1/C1), respectively. Consequently, for an electron transfer coefficient ($\alpha$) assumed as 0.5, the number of transferred electrons is 2. The obtained value is in accordance with the mechanism presented in literature, where PA is involved into a redox reaction transferring two electrons and two protons to form N-acetyl-p-quinone imine [15, 20, 21] (Scheme 1):



PA                N-acetyl-p-quinone imine
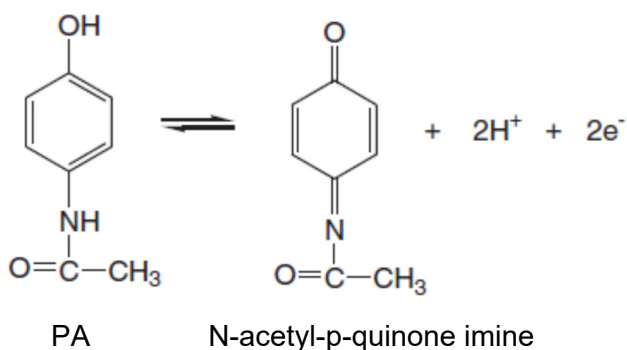
**Scheme 1**

As expected, the influence of the increase of potential scan rate on the voltammograms shape, recorded in the presence of PA at Pt/Al-SBA-15-GPE (Fig. 2), shows a shift towards positive and negative direction of the anodic and cathodic potential peak (A1/C1), respectively. The values of the slopes of the log I - log v dependencies (Fig. 2 inset) for the oxidation/reduction peaks presented in Table 1 are close to the theoretical value from equation 2 (*i.e.,* 0.5).

$$I_p = (2.99 \ 10^5) \ n(\alpha n)^{1/2} \ A \ C_o \ D^{1/2} \ v^{1/2} \qquad (2)$$

where: n is the number of electrons, $\alpha$ is the electron transfer coefficient, A is the active surface area (cm$^2$), $C_o$ is the concentration in bulk solution (mol/cm$^3$), D is the diffusion coefficient (cm$^2$/s) and v is the scan rate (V/s) [18, 19].
This behavior indicates a diffusion-controlled redox process of PA oxidation occurring to the Pt/Al-SBA-15-GPE modified electrode [18, 19, 22].
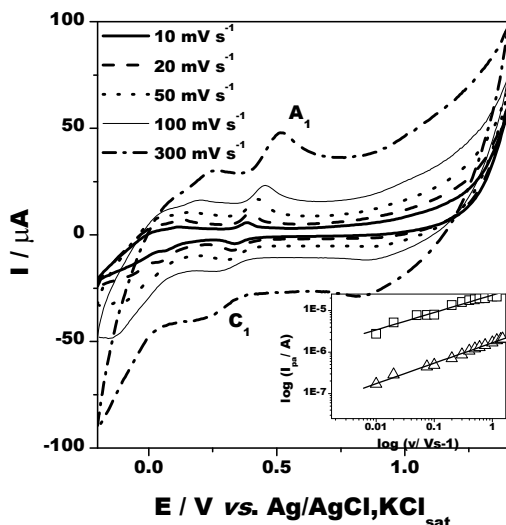
**Figure 2.** Cyclic voltammograms recorded at Pt/Al-SBA-15-GPE in the presence of $7 \cdot 10^{-6}$ M PA at different scan rate. Inset: the influence of scan rate on anodic peak currents intensities at Pt/Al-SBA-15-GPE ($\square$) and GPE ($\triangle$) electrodes. Experimental conditions: electrolyte, 0.1 M phosphate buffer (pH 7); starting potential, -0.2 V *vs.* Ag/AgCl, KCl$_{sat}$.

**Table 1.** Slope of log I *versus* log v dependency. Experimental conditions: see Fig 2.

| Electrode type | Slope R / n | |
|---|---|---|
| | anodic | cathodic |
| **GPE** | 0.491 ± 0.011 0.9969 / 14 | 0. 405 ± 0.015 0.9919 / 14 |
| **Pt/Al-SBA-15-GPE** | 0.418 ± 0.024 0.9823 / 13 | - |

## Stability of Pt/Al-SBA-15-GPE modified electrode

The short-time stability was tested by continuous cycling (20 cycles) the Pt/Al-SBA-15-GPE modified electrode potential, immersed in phosphate buffer (pH 7), with a scan rate of 50 mV s$^{-1}$. The mean value of the absolute current intensities was 31.5 ± 0.02 µA (RSD 1.98 %, for anodic process) and of 19.5 ± 0.01 µA (RSD 0.52%, cathodic process) respectively.

The long-term stability was tested by recording cyclic voltammograms in the presence of $7 \cdot 10^{-6}$ M PA, at the Pt/Al-SBA-15-GPE modified electrode with a scan rate of 50 mV s$^{-1}$, in several days after their preparation. The results revealed that after 7 days of storage in water saturated atmosphere (at 4 °C), the oxidation/reduction current intensities of PA have had a relative decrease from their original responses with 41.5% and 16.6%, respectively (estimated as: $(I_{day1} - I_{day7})*100/I_{day7}$). This behaviour demonstrates that the Pt/Al-SBA-15-GPE modified electrode possessed an acceptable reusability capacity [23].

## Electrochemical impedance spectroscopy measurements at Pt/Al-SBA-15-GPE electrode

The Nyquist plots recorded in a redox probe of 1 mM $K_3[Fe(CN)]_6/K_4[Fe(CN)]_6$ at Pt/Al-SBA-15-GPE and GPE electrodes, respectively, are shown in Fig. 3. The depressed semicircle observed at Pt/Al-SBA-15-GPE interface is characteristic to porous materials [24], indicating low interfacial electron transfer resistance and good conductivity. Contrarily, at GCE electrode a remarkable capacitive loop is present.
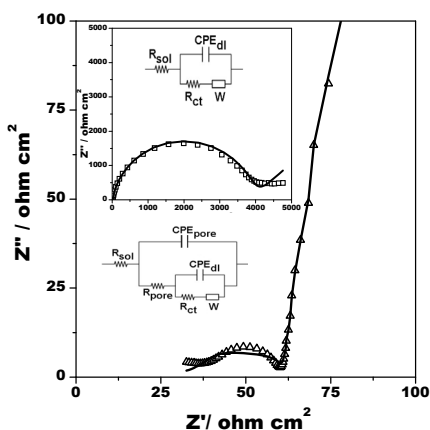


**Figure 3**. Nyquist plots recorded at Pt/Al-SBA-15-GPE modified electrode ($\Delta$) and GPE unmodified electrode ($\square$) (inset) into a solution containing 1 mM $K_4[Fe(CN)_6]/K_3[Fe(CN)_6]$ + 0.1 M phosphate buffer (pH 7). Experimental conditions: frequency, $10^{-2} - 10^4$ Hz; amplitude, 10 mV; time for OCP, 60 s; experimental data (symbol), fitted data (solid line).

Both equivalent electric circuit used for fitting the obtained experimental data (see inset Fig. 3, Table 2) consists from parallel and serially connected resistors ($R_{sol}$, $R_{ct}$ $R_{pore}$), constant phase elements ($CPE_{dl}$, $CPE_{pore}$) and Warburg impedance element (W), respectively. The $R_{sol}$ represents the resistance of the electrolyte at the interface of the mesoporous material, $R_{ct}$ is the charge transfer resistance, and $R_{pore}$ is the intrinsic material resistance [25]. The $CPE_{dl}$ is the constant phase element corresponding to the double layer capacitance, $CPE_{pore}$ is the constant phase element corresponding to the pore capacitance, and W is an element representing the restricted diffusion of ions through the multiple layers of non-homogenous distributed pores through the internal mesoporous network of the material.

As expected, at GPE the great $R_{ct}$ value indicates a hindering of the electron transfer process, while in the case of Pt/Al-SBA-15-GPE modified electrode a 10 times decrease of the $R_{ct}$ (Table 2) point out an easy electron transfer occurring at electrode interface, probably due to the presence of Pt-NPs on the mesoporous structure of the Al-SBA-15 material.

**Table 2.** EIS fitting parameters for Pt/Al-SBA-15-GPE modified electrodes.
Experimental conditions: see Fig 3.

| EIS parameters | GPE * | Pt/Al-SBA-15-GPE ** |
|---|---|---|
| $R_{sol}$ ($\Omega$ cm$^2$) | 13.36 ± 1.24 | 31.24 ± 2.77 |
| $CPE_{pore}$ (S s$^n$/cm$^2$) | - | 142.6 10$^{-5}$ ± 2.41 |
| $n_1$ | - | 0.496 |
| $R_{pore}$ ($\Omega$ cm$^2$) | - | 33.12 ± 6.61 |
| $CPE_{dl}$(S s$^n$/cm$^2$) | 1.127 10$^{-5}$ ± 1.71 | 7049.0 10$^{-5}$ ± 10 |
| $n_2$ | 0.905 | 1 |
| $R_{ct}$ ($\Omega$ cm$^2$) | 3917 ± 0.76 | 273 ± 8 |
| W (S s$^{1/2}$ / cm$^2$) | 337.4 10$^{-5}$ ± 6.98 | 529.6 ±10$^{-5}$ + 3.4 |
| chi$^2$ | 0.629 10$^{-3}$ | 0.964 10$^{-3}$ |

± values are relative standard errors expressed as %; * fitted by $R_{sol}(CPE_{dl}(R_{ct}W))$ electric circuit [26, 27]; ** fitted by $R_{sol}(CPE_{pore}(R_{pore}(CPE_{dl}(R_{ct}W))))$ electric circuit.

## Analytical characterization of Pt/Al-SBA-15-GPE electrode material Calibration curve

The quantitative analysis of PA was carried out investigating the Pt/Al-SBA-15-GPE modified electrode by square wave voltammetry (Fig 4A). The calibration curve shows excellent linearity in a concentration range between $10^{-6}$ – $10^{-5}$ M PA. The linear regression equations are: I/A = (-8.36 10$^{-7}$ ± 2.66 10$^{-7}$) + (1.68 ± 0.04) [PA]/M (R = 0.9968, n = 11 points) and I/A = (2.8 10$^{-9}$ ± 3.07 10$^{-9}$) + (29.9 10$^{-3}$ ± 0.5 10$^{-3}$) [PA]/M (R = 0.9986, n = 11 points) at Pt/Al-SBA-15-GPE modified electrode and GPE, respectively (Fig 4B). The increase of approximatively 60 times of the sensitivity of the Pt/Al-SBA-15-GPE modified electrode, compared with the unmodified GPE electrode, is due to the presence of Pt-NPs in the Pt/Al-SBA-15-GPE composite material of the electrode matrix.

The detection limit estimated for a signal-to-noise ratio (S/N) of 3 were of 0.85 10$^{-6}$ M at Pt/Al-SBA-15-GPE modified electrode. The obtained values are lower comparatively with some reported in the literature 1.1 10$^{-6}$ M at CPE-CNT-poly(3-aminophenol) [4], 2.3 10$^{-6}$ M at C-Ni/GCE [28], 1.39 10$^{-6}$ M at PEDOT/SPE [29], and 6 10$^{-6}$ M at graphene oxide-GCE [30].
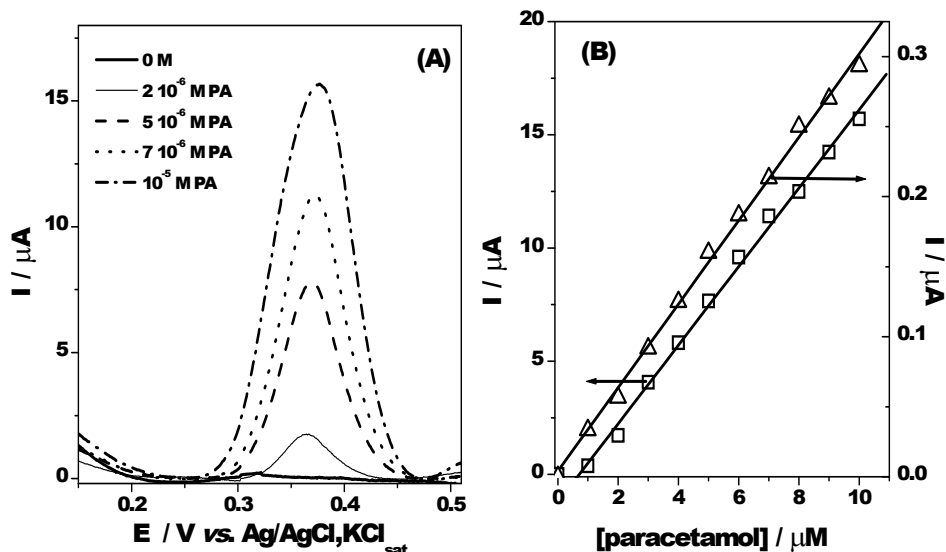
**Figure 4.** Square wave voltammograms recorded in the presence of different concentration of PA (see inset) at Pt/Al-SBA-15-GPE modified graphite paste electrode (**A**) and calibration curve of Pt/Al-SBA-15-GPE modified graphite paste electrode ($\triangle$) and GPE ($\square$) for PA (**B**). Experimental conditions: electrolyte, 0.1 M phosphate buffer (pH 7); frequency, 25 Hz; amplitude, 10 mV; step potential, 0.75 mV; starting potential, -0.2 V *vs.* Ag/AgCl, KCl$_{sat}$.

### Interferences

The possible interference for the determination of PA was also studied, under the same experimental conditions. Thus, the oxidation peak for a concentration of $7 \cdot 10^{-6}$ M PA was individually measured in the presence of different concentrations of the most common interfering compounds, like: 0.9 mM ascorbic acid and $1 \cdot 10^{-6}$ M uric acid. Their concentrations were chosen in the therapeutic concentration window. From Fig. 5, it can be seen that there is almost no influence on the detection of PA, because the peaks corresponding to the interfering compounds appear completely separated from the oxidation peak of PA.
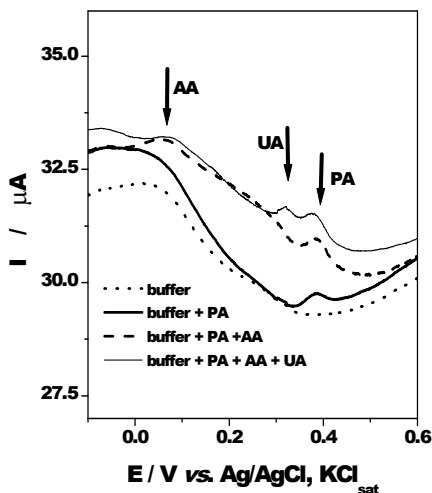
**Figure 5**. Square wave voltammograms recorded at Pt/Al-SBA-15-GPE modified electrode in the presence of a mixture of $7 \cdot 10^{-6}$ M paracetamol, $0.9 \cdot 10^{-3}$ M ascorbic acid and $1 \cdot 10^{-6}$ M uric acid. Experimental conditions: electrolyte, 0.1 M phosphate buffer (pH 7); frequency, 25 Hz; amplitude, 10 mV; step potential, 0.75 mV; starting potential, -0.2 V *vs*. Ag/AgCl, KCl$_{sat}$.

### Real sample analysis

The Pt/Al-SBA-15-GPE modified electrode was used to estimate the PA concentration in different commercial tablets, using the standard addition method, appropriate when the samples have complex matrices. The SWV measurements were performed using three different Pt/Al-SBA-15-GPE electrodes and the obtained data were used to calculate the average value of the PA concentration for the analyzed samples (Table 3). The results obtained in similar experimental conditions as for the electrode calibration against PA, were found in very good agreement with those declared by the pharmaceutical tablets producer (Table 3). It was found that the recovery of PA was in the range of 96.99 – 102.21 %. The relative standard deviation (RSD) was smaller than 3 %. The excellent average recoveries for the real samples suggest that the studied electrode material (Pt/Al-SBA-15-GPE) is able to be used for PA detection from pharmaceutical tablets.

**Table 3.** Determination of PA from pharmaceutical tablets
using Pt/Al-SBA-15-GPE modified electrode.

| Sample | Added/ μM | Found/ μM | Recovery % | RSD % |
|---|---|---|---|---|
| PA (500 mg/tablet) | 5 | 4.95 ± 0.13 | 99.6 ± 2.61 | 2.63 |

* Mean values obtained using 3 different electrodes

## CONCLUSIONS

A composite material (Pt/Al-SBA-15) based on the immobilization of Pt-NPs on a high ordered mesoporous compound (Al-SBA-15) was used to develop an electrode for electrochemical detection of paracetamol. The characterization consisted in using electrochemical methods of investigation like: cyclic voltammetry, electrochemical impedance spectroscopy and square-wave voltammetry.

The comparison of electrochemical parameters obtained in the case of Pt/Al-SBA-15-GPE modified electrode and GPE unmodified electrode suggest that the presence of Pt-NPs in the high ordered structure of the mesoporous material Al-SBA-15 enhanced the electrochemical and analytical parameters.

The very good analytical parameters (high sensibility, low limit of detection, good stability, no interference) recommend the studied compound Pt/Al-SBA-15, for the use as electrode material for paracetamol detection in real samples.

## EXPERIMENTAL SECTION

### Chemicals

As described previously, the 1% Pt/Al-SBA-15 material was prepared by a wet impregnation methodology [31]. Graphite powder and paraffin oil (Sigma-Aldrich) were used for preparing graphite paste electrode (GPE). A 0.1 M phosphate buffer solution was prepared from $KH_2PO_4$ and $K_2HPO_4$ (Merck, Darmstadt, Germany) salts. The pH of the buffer solutions was adjusted to the desired value by adding $H_3PO_4$ or KOH solutions (Merck, Darmstadt, Germany). A 1 mM $K_3[Fe(CN)]_6/K_4[Fe(CN)]_6$ solution was prepared by dissolving the appropriate weights of salts obtained from Sigma-Aldrich in phosphate buffer (pH 7). Synthetic paracetamol (PA) was purchased from Terapia-Rambaxy, (Cluj-Napoca, Romania) and used for preparing the standard solutions (1 mM). Distilled water was used for preparing all solutions. All reagents were of analytical degree and were used without further purification.

Drugs containing 500 mg PA/tablet ("Paracetamol" from EuroPharm SA) were bought from local pharmacies. Three tablets were weighed and grounded in a mortar. A quantity of the obtained homogeneous powder equivalent to the average weight of one tablet was dissolved in 0.1 M phosphate buffer solution (pH 7). After sonication for 10 min, the fresh prepared solution was analyzed, applying the standard addition method.

### Preparation of Pt/Al-SBA-15-GPE modified electrode

The Pt/Al-SBA-15-GPE modified electrode was prepared by thoroughly mixing 20 mg of graphite powder and 20 mg Pt/Al-SBA-15 powder with 15 mL of paraffin oil. The obtained paste was put into the cavity of a Teflon holder. The obtained electrode surface was smoothed using paper. When necessary, a new electrode surface was obtained by removing 2 mm of the outer paste layer, and adding freshly modified paste.

### Electrochemical measurements

All electrochemical measurements (cyclic voltammetry, electrochemical impedance spectroscopy and square wave voltammetry) were performed using a PC controlled electrochemical analyzer (AUTOLAB). A conventional three-electrodes cell equipped with a working electrode (Pt/Al-SBA-15-GPE modified electrode or GPE unmodified electrode, with a geometrical area of 0.07 cm$^2$), a counter electrode (Pt wire), and a reference electrode (Ag|AgCl,KCl$_{sat}$) was used. The experimental conditions are presented in the capture of each figure.

## REFERENCES

1. X. Liu, W. Na, H. Liu, X. Su, *Biosens. Bioelectron.*, **2017**, *98*, 222-226.
2. M. Espinosa Bosch, A.J. Ruiz Sanchez, F. Sanchez Rojas, C. Bosch Ojeda, *J. Pharm. Biomed. Anal.*, **2006**, *42*, 291-321.
3. E. Bayram, E. Akyilmaz, *Sensor. Actuat. B*, **2016**, *233*, 409-418.
4. I. Noviandri, R. Rakhmana, *Int. J. Electrochem. Sci.*, **2012**, *7*, 4479-4487.
5. J. Luo, J. Sun, J. Huang, X. Liu, *Chem. Eng.*, **2016**, *283*, 1118-1126.
6. Y. Teng, L. Fan, Y. Dai, M. Zhong, X. Lu, X. Kan, *Biosens. Bioelectron.*, **2015**, *71*, 137-142.
7. P. K. Kalambate, A. K. Srivastava, *Sensor. Actuat. B*, **2016**, *233*, 237-248.
8. A. Kutluay, M. Aslanoglu, *Sensor. Actuat. B*, **2013**, *185*, 398-404.
9. X. Kang, J. Wang, H. Wu, J. Liu, I. A. Aksay, Y. Lin, *Talanta*, **2010**, *81*, 754-759.
10. P. K. Kalambate, B. J. Sanghavi, S. P. Karna, A. K. Srivastava, *Sensor. Actuat. B*, **2015**, *213*, 285-294.

11. D. Zhao, J. Feng, Q. Huo, N. Melosh, G. H. Fredrickson, B. F. Chmelka, G. D. Stucky, *Science*, **1998**, *279*, 548-552.
12. Y. Yue, A. Gédéon, J.-L. Bonardet, N. Melosh, J.-B. D'Espinose, J. Fraissard, *Chem. Commun.*, **1999**, *19*, 1967-1968.
13. H.-C. Wu, T.-C. Chen, N.-C. Lai, C.-M. Yang, J.-H. Wu, Y.-C. Chen, J.-F. Lee, C.-S. Chen, *Nanoscale*, **2015**, *7*, 16848-16859.
14. S. Hazra, H. Joshi, B. K. Ghosh, A. Ahmed, T. Gibson, P. Millner, N. N. Ghosh, *RSC Adv.*, **2015**, *5*, 34390-34397.
15. O. J. D'Souza, R. J. Mascarenhas, T. Thomas, B. M. Basavaraja, A. Kumar Saxena, K. Mukhopadhyay, D. Roy, *J. Electroanal. Chem.*, **2015**, *739*, 49-57.
16. A. L. Eckermann, D. J. Feld, J. A. Shaw, T. J. Meade, *Coord. Chem. Rev.*, **2010**, *254*, 1769–1802.
17. P. K. Kalambate, A. K. Srivastava, *Sensor. Actuat. B*, **2016**, *233*, 237–248.
18. A. J. Bard, L. R. Faulkner, "Electrochemical Methods: Fundamentals and Applications", VCH-Wiley, **2011**.
19. C. M. A. Brett, A. M. O. Brett, "Electrochemistry. Principles, methods, and applications", Oxford University Press, New York, NY, USA, **1994**.
20. B. J. Sanghavi, A. K. Srivastava, *Electrochim. Acta*, **2010**, *55*, 8638-8648.
21. M. Zheng, F. Gao, Q. Wang, X. Cai, S. Jiang, L. Huang, F. Gao, *Mater. Sci. Eng. C*, **2013**, *33*, 1514-1520.
22. S. Kavian, S. N. Azizi, S. Ghasemi, *J. Electroanal. Chem.*, **2017**, *799*, 308-314.
23. R. Gupta, V. Ganesan, *Sensor. Actuat. B*, **2015**, *219*, 139-145.
24. F. J. Burpo, E. A. Nagelli, L. A. Morris, J. P. McClure, M. Y. Ryu, J. L. Palmer, *J. Mater. Res.*, **2017**, *32*, 4153-4165.
25. I. C. Fort, G. L. Turdean, R. Barabas, D. Popa, A. Ispas, M. Constantiniuc, *Studia UBB Chemia*, **2019**, *64*, 125-133.
26. G.L. Turdean, C.I. Fort, V. Simon, *Electrochim Acta* **2015**, *182*, 707-714.
27. M. M. Rusu, C. I. Fort, L. C. Cotet, A. Vulpoi, M. Todea, G. L. Turdean, V. Danciu, I. C. Popescu, L. Baia, *Sensor. Actuat. B*, **2018**, *268*, 398-410.
28. S. Wang, F. Xie, R. Hu, *Sensor. Actuat. B*, **2007**, *123*, 495-500.
29. W. Su, S. Cheng, *Electroanal.*, **2010**, *22*, 707-714.
30. J. Song, J. Yang, J. Zeng, J. Tan, L. Zhang, *Sensor Actuat. B*, **2011**, *155*, 220–225.
31. C. Rizescu, B. Cojocaru, N. T. Thanh Hien, P. T. Huyen, V. I. Parvulescu, *Micropor. Mesopor. Mat.*, **2019**, *281*, 142-147.

# SYNTHESIS OF NOVEL *N*-SUBSTITUTED AMPHIONIC MELAMINES WITH THE TANDEM 4-(1-CARBOXY-*n*-ALKOXY)PHENYL / 4-(*n*-OCTYLOXY)PHENYL UNITS AS POTENTIAL DENDRITIC BUILDING-BLOCKS

**STEFANIA IONESCU-ZINCA[a], PEDRO LAMEIRAS[b], DAN PORUMB[a], EMESE GÁL[c] AND MIRCEA DARABANTU[a*]**

**ABSTRACT.** Starting from etheric type derivatives of 4-aminophenol, namely (4-aminophenoxy)acetic acid or 4-(4-aminophenoxy)butyric acid and 4-(*n*-octyloxy)aniline, we report herein two routes of access to two novel *N*-substituted amphionic melamines with the tandem 4-(1-carboxy-*n*-alkoxy) phenyl/4-(*n*-octyloxy)phenyl units against the piperazin-1-yl group, as a basic site. The successful $S_N2$-Ar aminations of cyanuric chloride performed with these amine-nucleophiles are discussed in terms of chemoselectivity, mainly in the third step of the synthesis, implying piperazine as such or its *N*-Boc-mono-protected form. The amphionic nature of the targeted melamines was fully confirmed both in solution (VT-NMR) and in the solid state (IR).

*Keywords: (4-aminophenoxy)acetic acid, 4-(4-aminophenoxy)butyric acid, amphionic melamines, N-Boc-piperazine, 4-(n-octyloxy)aniline*

## INTRODUCTION

The inclusion of (4-aminophenoxy)alkanoic acid motifs, acetic or butyric, in the structure of bioactive compounds such as antisickling agents [1], anti-*Helicobacter pylori* agents [2], inhibitors of the cellular checkpoint kinase [3], antimalarial [4], analgesic, antipyretic and anti-inflammatory agents [5] is already well-documented.

[a] *Babeş-Bolyai University, Department of Chemistry, 11 Arany Janos str., RO-400028, Cluj-Napoca, Romania*
[b] *University of Reims Champagne-Ardenne, ICMR, UMR 7312, BP 1039, 51687 Reims, France*
[c] *Babeş-Bolyai University, Department of Chemistry and Chemical Engineering, Hungarian Line of Study, 11 Arany János St., 400028 Cluj-Napoca, Romania*
* *Corresponding author: darab@chem.ubbcluj.ro*

STEFANIA IONESCU-ZINCA, PEDRO LAMEIRAS, DAN PORUMB,
EMESE GÁL, MIRCEA DARABANTU

It was our Laboratory the first who reported, recently, the use of these aryl-amino acids in organic materials chemistry as well [6] (Chart1): primary, as precursors of novel *N*-substituted melamines (2,4,6-triamino-1,3,5-triazines) [6a] and then the propensity of the tripodands thus obtained to act, by simple acid-base neutralization, as anionic *meta*-trivalent central building-blocks in G-2 dendritic melamines' elaboration [6b]. This type of ionic macromolecules exhibited a noticeably supramolecular behaviour tailoring a "shell-to-shell" pre-organisation in solution, able to endorse subsequent self-assembly into large homogeneously packed spherical nano-aggregates [6, 7].
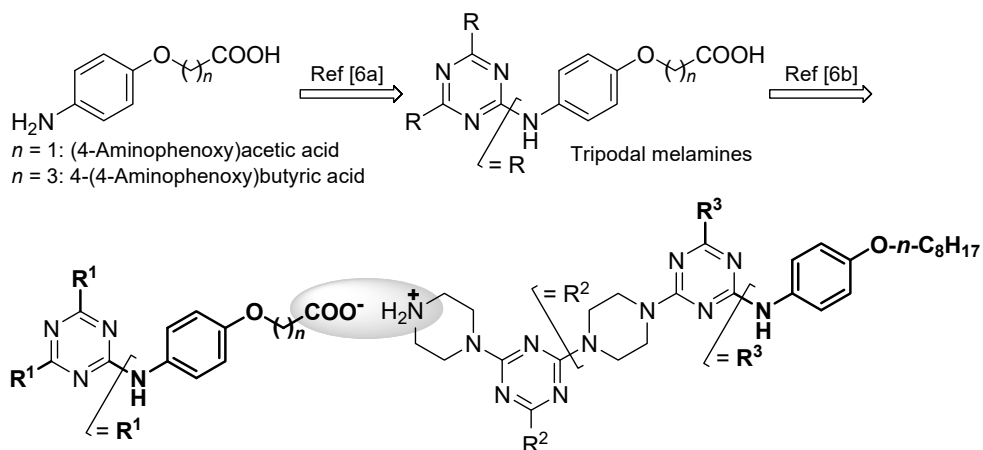


**Chart 1.** Previous use of (4-aminophenoxy)alkanoic acids and 4-(*n*-octyloxy)aniline in G-2 ionic construction of dendritic melamines

In the above context (Chart 1), so far, we utilised merely 4-(*n*-octyloxy)aniline (a "traditional" starting material for mesogenic *N*-substituted Schiff-bases [8]) playing the role of unique dendritic peripheral unit. In fact, later reports focused on organic materials area evidenced this "fatty" *p*-alkoxyaniline becoming, along the years, a well-recognised component for macromolecules fabrication [9], for example mesogenic supramolecular perylene bisimide assemblies with a number of 2-amino-4,6-bis[(4-*n*-alkoxy)phenylamino]-*s*-triazines [9a], amphiphilic azobenzene-containing linear-dendritic block copolymers [9b] and G-0 monomeric or dimeric dendritic liquid crystals with photochromic azobenzene mesogens [9c].

Accordingly, in continuation of our previous findings [6, 7], we envisaged to enlarge this topic by investigating the synthesis of novel *N*-substituted melamines with the tandem 4-(1-carboxy-*n*-alkoxy)phenyl/4-(*n*-octyloxy)phenyl units, seen as prospective G-0 dendrons.

## RESULTS AND DISCUSSION

### 1. Synthesis (Scheme 1)

Chlorodiamino-*s*-triazines **2a** and **2b** were prepared in two clean-chemoselective S$_N$2-Ar consecutive aryl aminations of cyanuric chloride by applying a one-pot mild conditions manipulation (**I+II**). In our hands, 4-(*n*-octyloxy)aniline **1c** had to be the first amine-nucleophile (**I**, Eq. 1) because this commercial compound appeared to us sensitive to light and UV irradiation during TLC control (λ=254 nm), i.e, the dichloroamino-*s*-triazine intermediate (not depicted in Scheme 1) was even not isolated.



$$\text{I } R^1\text{-NH}_2 \text{ (1c)} + C_3N_3Cl_3 + NaHCO_3 \rightarrow R^1\text{-NH-}C_3N_3Cl_2 + NaCl + CO_2 + H_2O \tag{1}$$

$$\text{II HOOC-}R^2\text{-NH}_3^+Cl^- \text{ (1a or 1b)} + K_2CO_3 \rightarrow KOOC\text{-}R^2\text{-NH}_2 + KCl + CO_2 + H_2O \tag{2}$$

$$KOOC\text{-}R^2\text{-NH}_2 + R^1\text{-NH-}C_3N_3Cl_2 + AcONa \rightarrow R^1\text{-NH-}C_3N_3Cl\text{-NH-}R^2\text{-COONa} + AcOH + KCl \tag{3}$$

$$R^1\text{-NH-}C_3N_3Cl\text{-NH-}R^2\text{-COONa} + AcOH \rightarrow R^1\text{-NH-}C_3N_3Cl\text{-NH-}R^2\text{-COOH (2a or 2b)} + AcONa \tag{4}$$
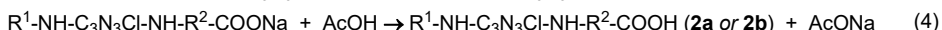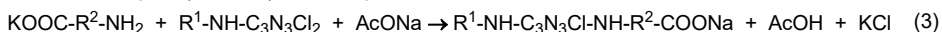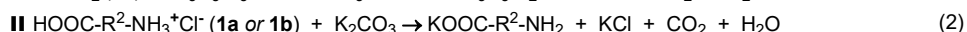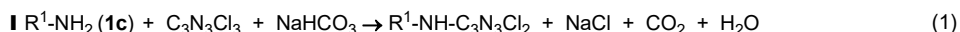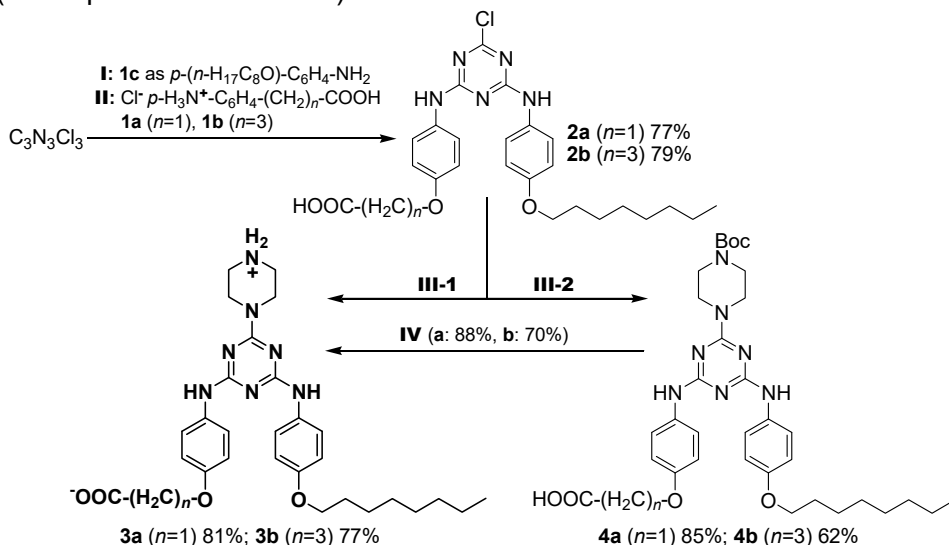
| Step | Products | Conditions |
|---|---|---|
| **I** | *not isolated* | 1.0 equiv **1c**, acetone, 0-5 °C (2 h) / 1.0 equiv NaHCO$_3$, H$_2$O, 0-5 °C / rt (24 h) / N$_2$ |
| **II** | **2a**, **2b** | 1.0 equiv **1a** (or **1b**), 1.0 equiv K$_2$CO$_3$, H$_2$O, 0-5 °C / 1.0 equiv AcONa, H$_2$O, 0-5 °C (0.5 h) / rt (24 h) / N$_2$ |
| **III-1** | **3a**, **3b** | 6.00 equiv piperazine, 6×(0.16 equiv **2a** or **2b** added every 2 h), THF / rt (24 h) / 1.0 equiv K$_2$CO$_3$ / AcOH, pH=6-6.5 |
| **III-2** | **4a**, **4b** | 2.25 equiv Boc-piperazine, 1.00 equiv K$_2$CO$_3$,THF / rt (24 h) / 55-60 °C (48 h) / AcOH, pH~6 / N$_2$ |
| **IV** | **3a**, **3b** | 3M aq HCl, 1,4-dioxane, rt (48 h) / 50-55 °C (5 h) / 25% aq NH$_3$, pH=6-6.5 |

Scheme 1

STEFANIA IONESCU-ZINCA, PEDRO LAMEIRAS, DAN PORUMB,
EMESE GÁL, MIRCEA DARABANTU

Furthermore, (4-aminophenoxy)alkanoic acids, as free bases, were released *in situ* from their hydrochlorides **1a** (*n*=1) and **1b** (*n*=3) (**II**, Eq. 2). The need to isolate the crude products, **2a** and **2b**, in neutral form by adding, in this purpose, sodium acetate, we discussed earlier (**II**, Eq. 3, 4 [6a]). Finally, the global (**I+II**) yields in the synthesis of **2a** (77%) and **2b** (79%), as pure analytical products, refer rather to their expeditious purification by simple crystallization from boiling isopropanol, than the intimate evolution of the reactions (TLC survey).

The mono-attachment of piperazine to **2a** and **2b** (**III-1**) was more problematic than we expected. Thus, inspired from our previous expertise (6b, 10), the portionwise addition of **2a** or **2b** to a 300% molar excess of piperazine, at room temperature, yielded the targeted melamines, **3a** and **3b**, with excellent NMR appearance. Only careful inspection of their HRMS spectra divulged very discrete peaks assigned to the symmetrically di-substituted piperazine-1,4-diyl byproduct. In similar attempts, reported by Simanek and co-workers [11], the use of larger piperazine molar excesses, 400 [11a] or even 500% [11b], were mentioned. Indeed, in our present cases (Scheme 1), only a 500% molar surplus of piperazine ensured a 100% chemoselectivity of the non-symmetric $S_N2$-Ar amination processes, **2a→3a** and **2b→3b**. In spite of this improvement, compounds **3a** and **3b** could be isolated, in pure analytical state, only if column chromatography on de-activated silica-gel followed by crystallization from boiling isopropanol were applied (see EXPERIMENTAL SECTION).

Therefore, we also considered a two steps alternative strategy, by employing *N*-Boc-piperazine (**III-2**) with subsequent deprotection (**IV**). To our surprise, ^{1}H NMR (rather than TLC) monitoring of the reactions between equimolar amounts of **2a** (or **2b**) and *N*-Boc-piperazine revealed, in each case, even after 48 h (at rt), still the incidence of unconsumed starting materials, **2a** (14%) or **2b** (42%). As shown in Scheme 1, a 125 % molar excess of *N*-Boc-piperazine was required for both aminations, **2a→4a** and **2b→4b**, reached completion upon long time of heating (55-60 °C, 48 h) with discrepant yields, 85% (**4a**) and 62% (**4b**). A plausible explanation for this unexpected low reactivity of Boc-piperazine in comparison with piperazine itself in our conditions might arise from i) manifestation of a transannular effect occurring in EWG-*N*-substituted piperazines (previously noticed by Lai and co-workers [12a, 12b], then by our Laboratory [10a]) against ii) a reduced aptitude as leaving-group of the remaining *s*-triazine chlorine in compounds **2a** and **2b** in $S_N2$-Ar amination conditions. Despite of all above, we note *N*-Boc-piperazine being reported [13] as a useful $S_N$ complete amination reagent versus highly *C*-electrophilic halo-compounds, cyanuric chloride [13a] and 2,4,6-tris (bromomethyl)-benzene [13b].

The successful removal of Boc-*N*-protecting group from **4a** and **4b**
(**IV**) was also mandatory to a long time reaction and heating, with satisfactory
(70%, **3b**) to good yields (85%, **3a**). To resume, the global yields were
**1a**→**3a** 62% (57% via **4a**) and **1b**→**3b** 61% (34% via **4b**).
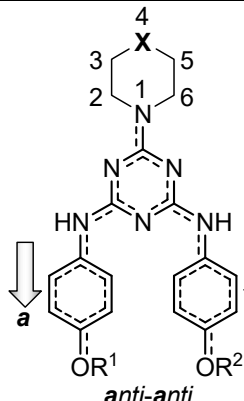
All new compounds **2**-**4a**(**b**) provided analytical and spectral data in
full agreement with the proposed structures.

## 2. Structural assignments

### 2.1. *In solution* (Table 1)

The amphionic nature of melamines **3a** and **3b** in solution was established
with the help of NMR data. However, their relevance could be evaluated by
comparison with those of precursors **2a**, **2b** and known melamine analogs **3c**

**Table 1.** Comparative 1D-$^1$H and 2D-$^1$H-DOSY NMR data of compounds **3a** and
**3b** against their 4-aminophenol (**3c**) and 4-(*n*-octyloxy)aniline (**3d**) based
analogs on $^1$H 500 MHz timescale in DMSO-$d_6$



3a-d

**X = $^+$NH$_2$**

**a**: R$^1$ = CH$_2$-COO$^-$, R$^2$ = *n*-C$_8$H$_{17}$
**b**: R$^1$ = (CH$_2$)$_3$-COO$^-$, R$^2$ = *n*-C$_8$H$_{17}$

**X = NH**

**c**: R$^1$ = R$^2$ = H (our Ref [10c])
**d**: R$^1$ = R$^2$ = *n*-C$_8$H$_{17}$ (our Ref [6b])

*anti-anti*

| No. | T (K) | 1D-$^1$H NMR: $\delta_H$ (ppm)[a] | | | M (g mol$^{-1}$) | 2D-$^1$H-DOSY NMR[a] | |
| | | Piperazin-1-yl -4-ium | | -C*H*$_2$-COO$^-$ | | | |
| | | H-2, -6 | H-3, -5 | | | D(µm$^2$ s$^{-1}$) | $d_H$ (nm) |
| **3a** | 298 | 3.80 | 2.94 | 4.47 (4.65 in **2a**)[b] | 549.66 | 164.4 | 1.33 |
| | 363 | 3.74 | 2.85 | 4.56 (4.60 in **2a**) | | - | - |
| **3b** | 298 | 3.87 | 3.08 | 2.38 (2.38 in **2b**) | 577.72 | 162.2 | 1.35 |
| | 363 | 3.90 | 3.09 | 2.38 (2.39 in **2b**) | | - | - |
| | | Piperazin-1-yl | | | | | |
| **3c** | 298 | 3.63 | 2.69 | - | 379.42 | 152.0 | 1.44 |
| | 363 | 3.65 | 2.73 | | | - | - |
| **3d** | 298 | 3.66 | 2.70 | - | 603.84 | 191.0 | 1.14 |
| | 363 | 3.67 | 2.74 | | | - | - |

[a]As 5 mM solutions; [b]As 28 mM solution

(based on 4-aminophenol, [10c]) and **3d** (based on 4-(*n*-octyloxy)aniline, [6b]) only. One must observe that all four melamines **3a-d** belong to the same family of extended p→π delocalised systems, inducing the well-known rotational diastereomerism of type *a* (*anti*)/*s* (*syn*) about the partial double bonds >N(exocyclic)═══C(*s*-triazine) [14].\* On the ^{1}H NMR 500 MHz timescale, this stereo-dynamism was exposed by the spectral shape defined as "slow exchange status between unequally populated sites" [15].

At room temperature, the existence of a protonated, at N-4, piperazine-1-yl ligand (>$NH_2^+$ as EWG) determined a noticeable deshielding ($\Delta\delta_H$~+0.30 ppm, downfield resonances) of the adjacent methylenes, H-3, -5, in **3a** and **3b** vs. **3c** and **3d**. An identical but weaker influence was observed for protons H-2, -6 ($\Delta\delta_H$~+0.20 ppm). On heating at 90 °C, the magnetic environment did not changed significantly, the shifting to lower fields being $\Delta\delta_H$~+0.23 ppm (H-3, -5) and $\Delta\delta_H$~+0.16 ppm (H-2, -6) in **3a**, **3b** vs. **3c**, **3d**, to prove, in addition, the cationic stability of the piperazin-1-yl-4-ium ligand.

The presence of the carboxylate ($COO^-$) counterpart could be indirectly attributed as well. Thus, in the case of melamine **3a** only, a shielding (upfield resonances) of the α-located –$CH_2$–(C=O)– protons was observed as the result of the COOH (EWG in **2a**)→$COO^-$ (EDG, ERG in **3a**) deprotonation. A related diagnosis, issued from an aliphatic carboxyl group ionisation thus promoting ^{1}H higher field absorptions of proximal (α and β) methylene protons, was earlier reported by Sierra and co-workers [16] in the case of some G-2 PAMAM ionic dendrimers (–$COO^-$ $H_3N^+$–) obtained by direct –COOH + $H_2N$– neutralisation in $CDCl_3$.

No fluctuation as ±$\Delta\delta_C$ (COOH vs. $COO^-$) was detectable in the whole series **2-4a**(**b**) on the 125 MHz ^{13}C NMR timescale.

Somehow predictably, DOSY charts of compounds **3a-d** did not allowed a direct correlation between *D* values by means of hydrodynamic diameters ($d_H$) (Table 1) and the molecular size [6b, 7, 17]. Hydrodynamic diameters $d_H$ were calculated from the hydrodynamic radii ($r_H$) by applying the Stokes-Einstein equation (Eq. 1).

$$\text{(Eq. 1)} \quad D = \frac{k\,T}{6\,\pi\,\eta\,r_H} \times 10^{-9}$$

where *k* is the Boltzmann's constant ($1.38\times10^{-23}$ j $K^{-1}$), $\eta$ is the dynamic viscosity ($2.00\times10^{-3}$ kg $m^{-1}$ $s^{-1}$) of DMSO at *T* (298 K) and $r_H$ (nm) is the hydrodynamic radius.

---

\*In Table 1, solely the (*a-a*) rotamer is illustrated (as the more stable type of stereoisomer, according to preceding DFT calculation of our Laboratory [6b, 7, 10c]).

DOSY data disclosed that, although the biggest in size, melamine **3d** displaced a minimum volume of solvent ($d_H$ 1.14 nm) due, most likely, to its isolated as independent molecular species in solution. By contrast, aggregation through multiple H-bonding interactions (compound **3c**, $d_H$ 1.44 nm) or by simple electrostatic attractions (compounds **3a**, **3b**, $d_H$ 1.33 and 1.35 nm respectively) suggested incipient supramolecular aptitudes, as we reported previously for other melamines based on 4-aminophenol derivatives [6b, 7, 10c, 18].

### 2.2. *In the solid state* (Figure 1)

IR spectra (KBr) completed the above attributions, limited, this time, to the carboxyl group's behavior (Figure 1). Thus, the bands located at 1712 (**2a**) and 1702 cm$^{-1}$ (**2b**) we ascribed to the $\nu_{C=O}$ stretch in the carboxylic (COOH) groups, classically associated as dimers [19]. These absorptions were significantly shifted
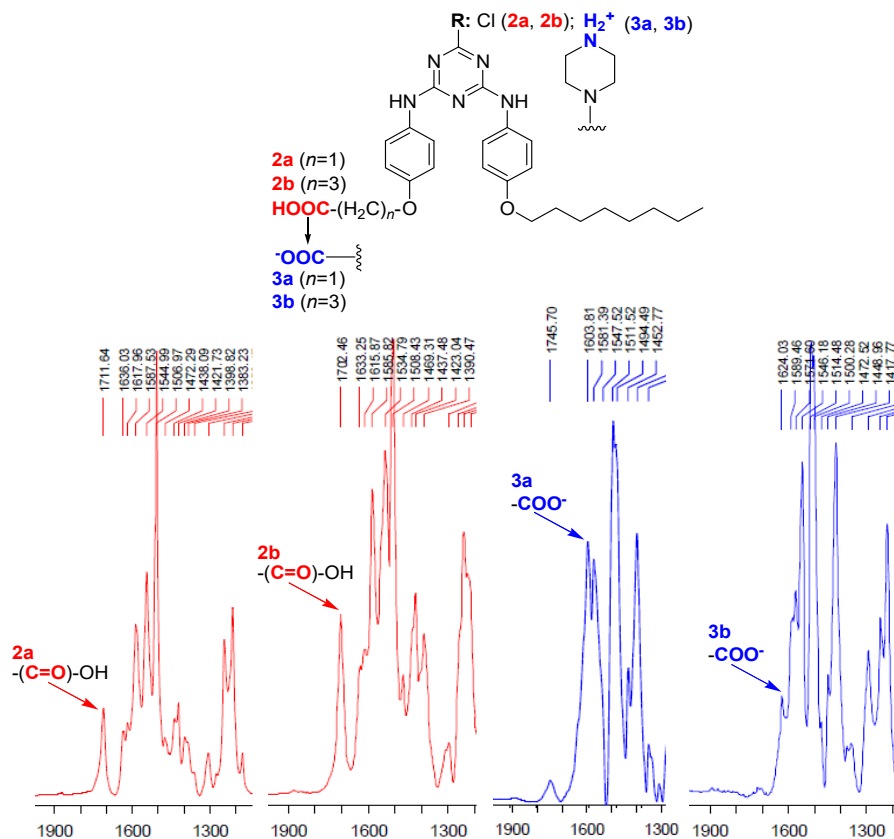


**Figure 1.** Comparative details from IR spectra (KBr) of chlorodiamino-*s*-triazines **2a** and **2b** versus amphionic melamines **3a** and **3b**

downfield, →1604 (in **3a**) and →1624 cm$^{-1}$ (in **3b**) consistent with their carboxylate (COO$^-$) environment. Other relevant bands denoting polymeric H-bonding intermolecular associations of compounds **2a** (1636, 1618 cm$^{-1}$) and **2b** (1633, 1617 cm$^{-1}$) were completely absent in the IR spectra of amphionic melamines **3a** and **3b**. Nonetheless, the stretching ($\nu_{NH}$, 3000-2700 cm$^{-1}$) or deformation ($\delta_{NH}$, 1620-1560 cm$^{-1}$) bands of the protonated >NH$_2^+$ group of the piperazin-1-yl-4-ium ligand [20] could not be definitely identified due to the overlapping in the above regions between the absorptions of the piperazine methylenes ($\nu_{CH2}$), carbonyl bonds ($\nu_{C=O}$) in the COO$^-$ groups, aryl ($\nu_{C=C}$) and *s*-triazine ($\nu_{C=N}$) bonds.

## CONCLUSIONS

In summary, two novel amphionic *N,N',N''*-substituted melamines with 4-(1-carboxylate-*n*-alkoxy)phenyl, 4-(*n*-octyloxy)phenyl and piperazin-1-yl-4-ium ligands were obtained by S$_N$2-Ar chemoselective aminations of cyanuric chloride. The chemoselective non-symmetric attachment of the piperazine ligand was achieved by using a large molar excess (500%) of this diamine-nucleophile, rather than its *N*-Boc mono-protected form. NMR and IR data had to complement each other in supporting the amphionic structure of the above melamines. (VT)-$^1$H NMR chemical shifts proved the piperazin-1-yl-4-ium cationic nature of this ligand together with its thermal stability as such in solution meanwhile IR (KBr) $\nu$-stretch bands evidenced the existence, in the solid state, of carboxylate groups.

## EXPERIMENTAL SECTION

All reagents and solvents were of commercial quality and required no purification prior to use.

Melting points were carried out on a KSP1N instrument and are not corrected.

Microanalyses were performed on a Carlo Erba CHNOS 1160 apparatus.

TLC monitoring was performed by using aluminium sheets with silica gel 60 F254. (Merck) (visualisation under UV at λ=254 nm, optionally on an I$_2$ bath).

Column chromatography was conducted on silica gel Si 60 (0.063-0.200 mm, Merck).

IR spectra were recorded on a JASCO FT-IR 6100 Spectrometer. Only relevant absorption maxima (in cm$^{-1}$) are listed throughout as being s (strong), m (medium) or w (weak).

NMR spectra were recorded on a Bruker AM 500 instrument operating at 500 or 125 MHz for $^1$H and $^{13}$C nuclei, respectively. All chemical shifts ($\delta$ values) are given in parts per million (ppm); all homocoupling patterns ($^nJ_{H,H}$ values) are given in

Hertz (Hz). No TMS was added: chemical shifts were measured against the solvent peak, taken as reference signal. In the NMR descriptions, some specific abbreviations were used: tt (triplet of triplets), qu (quartet), qui (quintet), sx (sextet), sept (septet), oct (octet), td (triplet of doublets), T (*s*-Triazine), PZ (piperazin-1-yl). In the NMR assignment of nuclei as "α", "β" and "γ" refers to their increased vicinity with respect to the carboxyl (COOH) group on the *n*-butanoic chain. Designation of topologic equivalent positions of $^1$H and $^{13}$C nuclei as ('), ('') etc. was omitted for reasons of simplicity

HRMS spectra were obtained on an LTQ ORBITRAP XL (Thermo Scientific) instrument which was externally calibrated using the manufacturer's ESI(+) calibration mix. The samples were introduced into the spectrometer by direct infusion.

*Typical procedure for the synthesis of compounds* **2a** *and* **2b**; *preparation of compound* **2a** (**I+II**, *Scheme 1*)

Under inert atmosphere, to cyanuric chloride (1.304 g 99%, 1.291 g 100%, 7.00 mmol) suspended in acetone (20 mL), a solution obtained by dissolving (4-*n*-octyloxy)aniline (1.581 g 98%, 1.549 g 100%, 7.00 mmol) in acetone (40 mL) was slowly (2 h) added at 0-5 °C with vigorous stirring to provide, in the end, a deep purple solution. At this moment, a solution obtained by dissolving anhyd NaHCO₃ (0.588 g, 7.00 mmol) in distilled water (10 mL) was injected dropwise during 15 min, keeping the temperature between 0-5 °C. The reaction mixture was let to reach the room temperature for the next 24 h. During this time, an abundant crystallisation temporarily occurred. The re-formed solution was again cooled at 0-5 °C when a solution obtained by dissolving (4-amino)phenoxyacetic acid hydrochloride (1.425 g, 7.00 mmol) in distilled water (6 mL) was added dropwise followed, immediately, by anhyd K₂CO₃ (0.967 g, 7.00 mmol) dissolved in distilled water (3.5 mL). After 30 min, anhyd AcONa (0.574 g, 7.00 mmol) dissolved in distilled water (1.50 mL) was injected dropwise. After that, the reaction mixture was let to reach again the room temperature and was stirred for additional 24 h when a second rich crystallization was observed. TLC control (eluent *n*-hexane/EtOH 1:1 v/v) indicated formation of compound **2a** as a single spot. The suspension, having pH=6-6.5, was poured on ice (150 g), stirred 2 h, then kept at 0 °C for 24 h and, finally, filtered off. The crude washed and dried material (3.400 g) was crystallized from boiling *i*-PrOH (30 mL) to give pure compound **2a** (2.695 g, 77% yield with respect to cyanuric chloride).

*2-Chloro-4-[4-(carboxymethoxy)phenyl]amino-6-[(4-n-octyloxy)phenyl]amino-s-triazine* **2a**. White solid. Mp 179.5-180 °C (*i*-PrOH). $R_f$ (*n*-hexane/EtOH 1:1 v/v)=0.50. Elemental analysis calcd. (%) for $C_{25}H_{30}ClN_5O_4$: C 60.05, H 6.05, N 14.01; found: C 60.38, H 5.91, N 13.88. IR (KBr) $\nu_{max}$ 3295 (w), 2957 (w), 2937 (m), 2922 (m), 2853 (w), 1712 (m), 1588 (s), 1545 (m), 1507 (s), 1438 (m), 1422 (m), 1245 (m), 1212 (m), 1081 (w), 999 (w), 824 (w), 795 (w) cm⁻¹. $^1$H and 2D-$^1$H,$^1$H-COSY NMR (500 MHz, 28 mM in DMSO-$d_6$, 298 K) $\delta_H$ 0.86 (3H, t, $^3J_{H,H}$=7.0 Hz, Me), 1.26-1.33 (8H, m, 4×CH₂, *n*-octyl), 1.40 (2H, tt app. qui, $^3J_{H,H}$=7.3 Hz, CH₂, *n*-octyl), 1.69 (2H, tt app. qui, $^3J_{H,H}$=7.0 Hz, OCH₂C*H*₂, *n*-octyl), 3.93 (2H, t, $^3J_{H,H}$=6.0 Hz, OCH₂, *n*-octyl), 4.65 (2H, s, OCH₂), 6.88 (4H, d, $^3J_{H,H}$=8.5 Hz, H-3, -5, Ph), 7.48, 7.49 and 7.65 (4H, d, $^3J_{H,H}$=7.0 Hz;

d, $^3J_{H,H}$=7.0 Hz; bs, H-2, -6, Ph), 9.88, 9.98, 10.06 and 10.08 (2H, 2×bs, 2×s, NH), 12.99 (1H, bs, COOH) ppm. $^1$H and 2D-$^1$H,$^1$H-COSY NMR (500 MHz, 28 mM in DMSO-$d_6$, 363 K) $\delta_H$ 0.88 (3H, t, $^3J_{H,H}$=7.0 Hz, Me), 1.28-1.36 (8H, m, 4×CH$_2$, $n$-octyl), 1.44 (2H, tt app. qui, $^3J_{H,H}$=7.3 Hz, CH$_2$, $n$-octyl), 1.72 (2H, tt app. qui, $^3J_{H,H}$=7.0 Hz, OCH$_2$C$H_2$, $n$-octyl), 3.97 (2H, t,$^3J_{H,H}$=6.5 Hz, OCH$_2$, $n$-octyl), 4.60 (2H, s, OCH$_2$), 6.87 (2H, d, $^3J_{H,H}$=9.0 Hz, H-3, -5, Ph), 6.89 (2H, d, $^3J_{H,H}$=8.5 Hz, H-3, -5, Ph), 7.50 (2H, d, $^3J_{H,H}$=8.5 Hz, H-2, -6, Ph), 7.52 (2H, d, $^3J_{H,H}$=9.0 Hz, H-2, -6, Ph), 9.62 and 9.64 (2H, 2×s, NH) ppm. 2D-$^1$H-DOSY NMR (500 MHz, 5 mM in DMSO-$d_6$, 298 K) $D$ 185.8 μm$^2$ s$^{-1}$. DEPT-$^{13}$C NMR (125 MHz, 28 mM in DMSO-$d_6$, 298 K) $\delta_C$ 14.5 (Me), 22.6, 26.1, 29.17, 29.23 and 29.3 (5×CH$_2$, $n$-octyl), 31.7 (OCH$_2$CH$_2$, $n$-octyl), 65.2 (OCH$_2$, $n$-octyl), 68.1 (OCH$_2$), 114.6 (C-3, -5, Ph), 122.7, 123.02, 123.04, 123.08, 123.09 and 123.3 (C-2, -6, Ph), 131.6 and 132.2 (C-1, Ph), 154.6 and 155.6 (C-4, Ph), 164.19, 164.21, 164.24, 164.4, 164.46,164.47,164.49 and 164.50 (C-4, -6, T), 168.3, 168.7 and 168.8 (C-2, T), 170.7 (COOH) ppm. HRMS (APCI) (rel. int. %) $m/z$: 500.2058 (100) [M+H]$^+$. [M+H]$^+$ calcd. for C$_{25}$H$_{31}$ClN$_5$O$_4$: 500.2065.

**2-Chloro-4-[4-(3-carboxypropoxy)phenyl]amino-6-[(4-n-octyloxy)phenyl]amino-s-triazine 2b**. 2.280 g (79% yield starting from 1.018 g 99%, 1.008 g 100% cyanuric chloride).White solid. Mp 164.9-165.0 ºC ($i$-PrOH). $R_f$ ($n$-hexane/EtOH 3:1 v/v)=0.60. Elemental analysis calcd. (%) for C$_{27}$H$_{34}$ClN$_5$O$_4$: C 61.41, H 6.49, N 13.26; found: C 61.18, H 6.71, N 12.89. IR (KBr) $\nu_{max}$ 3369 (w), 3280 (w), 3112 (m), 2259 (m), 2924 (m), 2853 (m), 1702 (m), 1616 (m), 1535 (s), 1508 (s), 1437 (m), 1390 (m), 1296 (s), 1261 (s), 1041 (m), 1015 (m), 998 (m), 828 (m), 793 (m), 598 (w), 520 (w) cm$^{-1}$. $^1$H and 2D-$^1$H,$^1$H-COSY NMR (500 MHz, 5 mM in DMSO-$d_6$, 298 K) $\delta_H$ 0.85 (3H, t, $^3J_{H,H}$=6.8 Hz, Me), 1.25-1.34 (8H, m, 4×CH$_2$, $n$-octyl), 1.40 (2H, tt app. qui, $^3J_{H,H}$=7.3 Hz, CH$_2$, $n$-octyl), 1.68 (2H, tt app. qui, $^3J_{H,H}$=7.0 Hz, OCH$_2$C$H_2$, $n$-octyl), 1.93 (2H, tt app. qui, $^3J_{H,H}$=6.9 Hz, H-β), 2.38 (2H, t, $^3J_{H,H}$=7.3 Hz, H-α), 3.93 (2H, t,$^3J_{H,H}$=6.5 Hz, OCH$_2$, $n$-octyl), 3.96 (2H, t, $^3J_{H,H}$=6.5 Hz, H-γ), 6.88 (4H, d, $^3J_{H,H}$=7.5 Hz, H-3, -5, Ph), 7.31, 7.47, 7.48 and 7.66 (4H, bs; d, $^3J_{H,H}$=7.5 Hz; d, $^3J_{H,H}$=5.5 Hz; bs, H-2, -6, Ph), 9.86, 9.97 and 10.05 (2H, 2×bs, s, NH), 12.13 (1H, bs, COOH) ppm. $^1$H and 2D-$^1$H,$^1$H-COSY NMR (500 MHz, 5 mM in DMSO-$d_6$, 363 K) $\delta_H$ 0.88 (3H, t, $^3J_{H,H}$=7.0 Hz, Me), 1.28-1.38 (8H, m, 4×CH$_2$, $n$-octyl), 1.44 (2H, tt app. qui, $^3J_{H,H}$=7.1 Hz, CH$_2$, $n$-octyl), 1.72 (2H, tt app. qui, $^3J_{H,H}$=7.0 Hz, OCH$_2$C$H_2$, $n$-octyl), 1.97 (2H, tt app. qui, $^3J_{H,H}$=6.9 Hz, H-β), 2.39 (2H, t, $^3J_{H,H}$=7.3 Hz, H-α), 3.97 (2H, t,$^3J_{H,H}$=6.5 Hz, OCH$_2$, $n$-octyl), 4.00 (2H, t, $^3J_{H,H}$=6.5 Hz, H-γ), 6.87 (2H, d, $^3J_{H,H}$=9.0 Hz, H-3, -5, Ph), 6.88 (2H, d, $^3J_{H,H}$=9.5 Hz, H-3, -5, Ph), 7.50 (2H, d, $^3J_{H,H}$=8.5 Hz, H-2, -6, Ph), 7.51 (2H, d, $^3J_{H,H}$=8.5 Hz, H-2, -6, Ph), 9.62 (2H, s, NH) ppm. 2D-$^1$H-DOSY NMR (500 MHz, 5 mM in DMSO-$d_6$, 298 K) $D$ 171.0 μm$^2$ s$^{-1}$. DEPT-$^{13}$C NMR (125 MHz, 5 mM in DMSO-$d_6$, 298 K) $\delta_C$ 14.4 (Me), 22.6 (CH$_2$, $n$-octyl), 24.8 (C-β), 26.0, 29.17, 29.21 and 29.3 (4×CH$_2$, $n$-octyl), 30.6 (C-α), 31.7 (OCH$_2$CH$_2$, $n$-octyl), 67.2 and 67.3 (OCH$_2$, $n$-octyl), 68.1 and 68.2 (C-γ), 114.8 and 115.0 (C-3, -5, Ph), 122.5, 123.1, 123.2 and 123.4 (C-2, -6, Ph), 131.6, 131.8 and 132.1 (C-1, Ph),155.3 and 155.6 (C-4, Ph), 163.7, 164.2 and 164.5 (C-4, -6, T), 168.2 and 168.7 (C-2, T), 174.6 (COOH) ppm. HRMS (APCI) (rel. int. %) $m/z$: 528.2407 (100) [M+H]$^+$. [M+H]$^+$ calcd. for C$_{27}$H$_{35}$ClN$_5$O$_4$: 528.2378.

*Typical procedure for the synthesis of compounds* **3a** *and* **3b***; preparation of compound* **3b** (**III-1**, Scheme 1)

Under inert atmosphere, at room temperature and with vigorous stirring, to a THF (25 mL) solution containing anhyd piperazine (0.987 g 99%, 0.977 g 100%, 11.34 mmol), solid compound **2b** (1.000 g, 1.89 mmol) was added as six equal portions every 2 h. After each of these periods, TLC monitoring indicated the complete consumption of the starting material **2b** (eluent *n*-hexane/EtOH 3:1 v/v) and formation of the desired melamine **3b** as a major spot (eluent EtOH/25% aq NH$_3$ 9:0.3 v/v). The reaction mixture was treated with solid anhyd K$_2$CO$_3$ (0.261 g, 1.89 mmol) and then evaporated, under vacuum, to dryness. At room temperature, the solid residue was taken with distilled water (25 mL) and then AcOH was added dropwise to the resulted solution to adjust its pH to 6-6.5 when crude compound **3b** precipitated. After cooling the resulted suspension at 0 ºC for 12 h, the crude product **3b** (0.990 g) was isolated by filtration. This material was purified by column chromatography on silica gel (eluent EtOH/25% aq NH$_3$ 9:0.3 v/v) to give a single fraction (0.920 g). Supplementary recrystallization of the last one from boiling *i*-PrOH (10 mL) afforded pure compound **3b** (0.840 g, 77% yield with respect to **2b**).

*1-{4-[4-(Carboxymethoxy)phenyl]amino-6-[(4-n-octyloxy)phenyl]amino-s-triazin-2-yl}-piperazine* **3a**. 1.157 g (81% yield starting from 1.300 g **2a**). White solid. Mp 252-253 ºC (*i*-PrOH). $R_f$ (EtOH/25% aq NH$_3$ 9:1 v/v)=0.70. Elemental analysis calcd. (%) for C$_{29}$H$_{39}$N$_7$O$_4$: C 63.37, H 7.15, N 17.84; found: C 62.98, H 7.22, N 17.79. IR (KBr) $\nu_{max}$ 3190 (m), 2956 (s), 2925 (s), 2854 (m), 2620 (w), 1745 (w), 1604 (s), 1581 (s), 1494 (s), 1453 (m), 1418 (s), 1335 (m), 1306 (m), 1245 (s), 1223 (s), 1045 (w), 828 (m), 802 (m) cm$^{-1}$. $^1$H and 2D-$^1$H,$^1$H-COSY NMR (500 MHz, 5 mM in DMSO-*d*$_6$, 298 K) $\delta_H$ 0.86 (3H, t, $^3J_{H,H}$=7.0 Hz, Me), 1.26-1.34 (8H, m, 4×CH$_2$, *n*-octyl), 1.40 (2H, tt app. qui, $^3J_{H,H}$=7.3 Hz, CH$_2$, *n*-octyl), 1.68 (2H, tt app. qui, $^3J_{H,H}$=6.9 Hz, OCH$_2$C*H*$_2$, *n*-octyl), 2.94 (4H, bs, H-3, -5, PZ), 3.80 (4H, bs, H-2, -6, PZ), 3.91 (2H, t, $^3J_{H,H}$=6.5 Hz, OCH$_2$, *n*-octyl), 4.47 (2H, s, OCH$_2$), 6.79 (2H, d, $^3J_{H,H}$=9.0 Hz, H-3, -5, Ph), 6.83 (2H, d, $^3J_{H,H}$=9.0 Hz, H-3, -5, Ph), 7.56 (4H, bs, H-2, -6, Ph), 8.97 (2H, bs, NH) ppm. $^1$H and 2D-$^1$H,$^1$H-COSY NMR (500 MHz, 5 mM in DMSO-*d*$_6$, 363 K) $\delta_H$ 0.88 (3H, t, $^3J_{H,H}$=6.8 Hz, Me), 1.27-1.38 (8H, m, 4×CH$_2$, *n*-octyl), 1.43 (2H, tt app. qui, $^3J_{H,H}$=7.1 Hz, CH$_2$, *n*-octyl), 1.71 (2H, tt app. qui, $^3J_{H,H}$=6.9 Hz, OCH$_2$C*H*$_2$, *n*-octyl), 2.85 (4H, t, $^3J_{H,H}$=4.8 Hz, H-3, -5, PZ), 3.74 (4H, t, $^3J_{H,H}$=5.0 Hz, H-2, -6, PZ), 3.95 (2H, t, $^3J_{H,H}$=6.5 Hz, OCH$_2$, *n*-octyl), 4.56 (2H, s, OCH$_2$), 6.83 (2H, d, $^3J_{H,H}$=9.0 Hz, H-3, -5, Ph), 6.84 (2H, d, $^3J_{H,H}$=9.0 Hz, H-3, -5, Ph), 7.55 (2H, d, $^3J_{H,H}$=10.0 Hz, H-2, -6, Ph), 7.57 (2H, d, $^3J_{H,H}$=9.5 Hz, H-2, -6, Ph), 8.56 and 8.58 (2H, 2×s, NH) ppm. 2D-$^1$H-DOSY NMR (500 MHz, 5 mM in DMSO-*d*$_6$, 298 K) *D* 164.4 µm$^2$ s$^{-1}$. DEPT-$^{13}$C NMR (125 MHz, 20 mM in DMSO-*d*$_6$, 298 K) $\delta_C$ 14.5 (Me), 22.6, 26.1, 29.2 and 29.3 (4×CH$_2$, *n*-octyl), 31.7 (OCH$_2$C*H*$_2$, *n*-octyl), 41.6 (C-2, -6, PZ), 43.7 (C-3, -5, PZ), 66.5 (OCH$_2$, *n*-octyl), 68.0 (OCH$_2$), 114.6 (C-3, -5, Ph), 122.1 and 123.0 (C-2, -6, Ph), 133.6 (C-1, Ph), 154.0 and 154.4 (C-4, Ph), 164.5 and 165.1 (C-2, -4, -6, T), 171.7 (COO$^-$) ppm. HRMS (ESI) (rel. int. %) *m/z*: 572.2991 [M+Na]$^+$ (5), 550.3176 (100) [M+H]$^+$. [M+Na]$^+$ calcd. for C$_{29}$H$_{39}$N$_7$NaO$_4$: 572.2961; [M+H]$^+$ calcd. for C$_{29}$H$_{40}$N$_7$O$_4$: 550.3142.

*1-{4-[4-(3-Carboxypropoxy)phenyl]amino-6-[(4-n-octyloxy)phenyl]amino-s-triazin-2-yl}-piperazine* **3b**. White solid. Mp 178.1-179.0 $^{o}$C (*i*-PrOH). $R_f$ (EtOH/25% aq. NH$_3$ 9:0.3 v/v)=0.75. Elemental analysis calcd. (%) for C$_{31}$H$_{43}$N$_7$O$_4$: C 64.45, H 7.50, N 16.97; found: C 64.77, H 7.81, N 17.11. IR (KBr) ν$_{max}$ 3392 (m), 2928 (m), 2851 (w), 1624 (w), 1572 (s), 1514 (s), 1418 (s), 1294 (m), 1248 (m), 1222 (s), 1130 (w), 957 (w), 827 (w), 804 (w), 594 (w) cm$^{-1}$. $^1$H and 2D-$^1$H,$^1$H-COSY NMR (500 MHz, 5 mM in DMSO-$d_6$, 298 K) $\delta_H$ 0.86 (3H, t, $^3J_{H,H}$=7.0 Hz, Me), 1.26-1.33 (8H, m, 4×CH$_2$, *n*-octyl), 1.40 (2H, tt app. sx, $^3J_{H,H}$=6.9 Hz, CH$_2$, *n*-octyl), 1.67 (2H, tt app. qui, $^3J_{H,H}$=6.9 Hz, OCH$_2$C*H$_2$*, *n*-octyl), 1.92 (2H, tt app. qui, $^3J_{H,H}$=6.9 Hz, H-β), 2.38 (2H, t, $^3J_{H,H}$=7.3 Hz, H-α), 3.08 (4H, bs, H-3, -5, PZ), 3.87 (4H, bs, H-2, -6, PZ), 3.91 (2H, t,$^3J_{H,H}$=6.8 Hz, OCH$_2$, *n*-octyl), 3.94 (2H, t, $^3J_{H,H}$=6.8 Hz, H-γ), 6.835 (2H, d, $^3J_{H,H}$=9.0 Hz, H-3, -5, Ph), 6.842 (2H, d, $^3J_{H,H}$=8.5 Hz, H-3, -5, Ph), 7.56 (4H, bs, H-2, -6, Ph), 9.01 (2H, 2×bs, NH) ppm. $^1$H and 2D-$^1$H,$^1$H-COSY NMR (500 MHz, 5 mM in DMSO-$d_6$, 363 K) $\delta_H$ 0.88 (3H, t, $^3J_{H,H}$=6.8 Hz, Me), 1.29-1.38 (8H, m, 4×CH$_2$, *n*-octyl), 1.43 (2H, tt app. qui, $^3J_{H,H}$=7.0 Hz, CH$_2$, *n*-octyl), 1.71 (2H, tt app. qui, $^3J_{H,H}$=6.9 Hz, OCH$_2$C*H$_2$*, *n*-octyl), 1.96 (2H, tt app. qui, $^3J_{H,H}$=6.8 Hz, H-β), 2.38 (2H, t, $^3J_{H,H}$=7.3 Hz, H-α), 3.09 (4H, t, $^3J_{H,H}$=5.0 Hz, H-3, -5, PZ), 3.90 (4H, t, $^3J_{H,H}$=5. 0 Hz, H-2, -6, PZ), 3.95 (2H, t,$^3J_{H,H}$=6.5 Hz, OCH$_2$, *n*-octyl), 3.98 (2H, t, $^3J_{H,H}$=6.5 Hz, H-γ), 6.83 (2H, d, $^3J_{H,H}$=9.0 Hz, H-3, -5, Ph), 6.84 (2H, d, $^3J_{H,H}$=9.0 Hz, H-3, -5, Ph), 7.536 (2H, d, $^3J_{H,H}$=9.0 Hz, H-2, -6, Ph), 7.544 (2H, d, $^3J_{H,H}$=9.0 Hz, H-2, -6, Ph), 8.64 (2H, 2×bs, NH) ppm. 2D-$^1$H-DOSY NMR (500 MHz, 5 mM in DMSO-$d_6$, 298 K) *D* 162.2 μm$^2$ s$^{-1}$. DEPT-$^{13}$C NMR (125 MHz, 20 mM in DMSO-$d_6$, 298 K) $\delta_C$ 14.6 (Me), 22.7 (CH$_2$, *n*-octyl), 24.9 (C-β), 26.1, 29.25 and 29.33 (3×CH$_2$, *n*-octyl), 30.7 (C-α), 31.8 (OCH$_2$C*H$_2$*, *n*-octyl), 40.6 (C-2, -6, PZ), 43.2 (C-3, -5, PZ), 67.3 (OCH$_2$, *n*-octyl), 68.1 (C-γ), 114.77 and 114.82 (C-3, -5, Ph), 122.4(C-2, -6, Ph), 133.4 and 133.6 (C-1, Ph),154.3, 154.5 and 154.6 (C-4, Ph), 164.6 and 165.2 (C-2, -4, -6, T), 174.8 (COO$^-$) ppm. HRMS (ESI) (rel. int. %) *m/z*: 600.3301 (7) [M+Na]$^+$, 578.3486 (100) [M+H]$^+$. [M+Na]$^+$ calcd. for C$_{31}$H$_{43}$N$_7$NaO$_4$: 600.3274; [M+H]$^+$ calcd. for C$_{31}$H$_{44}$N$_7$O$_4$: 578.3455.

*Typical procedure for the synthesis of Boc-N-protected forms of compounds* **3a** *and* **3b***; preparation of compound* **4a** *(***III-2***,* Scheme 1)

At room temperature, under inert atmosphere and with vigorous stirring, in a THF (25 mL) solution containing compound **2a** (1.000 g, 2.00 mmol), anhyd K$_2$CO$_3$ (0.276 g, 2.00 mmol) was suspended. To this suspension, Boc-piperazine (0.855 g 98%, 0.838 g 100%, 4.50 mmol) as THF (3 mL) solution was injected and the reaction mixture was stirred at room temperature for 24 h. Since after this period TLC monitoring still revealed the presence of the unreacted starting material **2a** (eluent *n*-hexane/EtOH 1:1 v/v), the reaction mixture was heated at 55-60 $^{o}$C for additional 48 h, then evaporated, under vacuum, to dryness. The solid residue was taken with distilled water (20 mL) and the pH of the resulted solution was adjusted to pH~6 with AcOH when crude compound **4a** precipitated. After complete crystallization at 0 $^{o}$C for 24 h, filtering off and drying, the crude material (1.125 g) was purified by crystallization from boiling *i*-PrOH (2.5 mL) to provide pure compound **4a** (1.100 g, 85% yield with respect to **2a**).

*{1-{4-[4-(Carboxymethoxy)phenyl]amino-6-[(4-n-octyloxy)phenyl]amino-s-triazin-2-yl}-4-tertbutoxycarbonyl}-piperazine* **4a**. White solid. Mp 240.6-241.0 ºC (*i*-PrOH). $R_f$ (*n*-hexane/EtOH 1:1.5 v/v)=0.75. Elemental analysis calcd. (%) for $C_{34}H_{47}N_7O_6$: C 62.85, H 7.29, N 15.09; found: C 63.02, H 7.41, N 14.93. IR (KBr) $\nu_{max}$ 3328 (w), 2930 (m), 2855 (m), 1700 (m), 1623 (m), 1602 (m), 1544 (s), 1513 (s), 1500 (s), 1420 (s), 1238 (m), 1173 (m), 1009 (w), 829 (m), 801 (w), 598 (w), 515 (w) cm$^{-1}$. $^1$H and 2D-$^1$H,$^1$H-COSY NMR (500 MHz, 32 mM in DMSO-$d_6$, 298 K) $\delta_H$ 0.86 (3H, t, $^3J_{H,H}$=6.8 Hz, Me, *n*-octyl), 1.26-1.32 (8H, m, 4×CH$_2$, *n*-octyl), 1.39-1.43 (2H, m, CH$_2$, *n*-octyl), 1.43 (9H, s, Me, Boc),1.68 (2H, tt app. qui, $^3J_{H,H}$=6.9 Hz, OCH$_2$C*H*$_2$, *n*-octyl), 3.39 (4H, s, H-3, -5, PZ), 3.71 (4H, s, H-2, -6, PZ), 3.91 (2H, t,$^3J_{H,H}$=6.5 Hz, OCH$_2$, *n*-octyl), 4.39 and 4.40 (2H, s, OCH$_2$), 6.79 (2H, d, $^3J_{H,H}$=9.0 Hz, H-3, -5, Ph), 6.83 (2H, d, $^3J_{H,H}$=8.5 Hz, H-3, -5, Ph), 7.57 (4H, bs, H-2, -6, Ph), 8.96 (2H, bs, s, NH), ppm. $^1$H and 2D-$^1$H,$^1$H-COSY NMR (500 MHz, 32 mM in DMSO-$d_6$, 363 K) $\delta_H$ 0.89 (3H, t, $^3J_{H,H}$=7.0 Hz, Me, *n*-octyl), 1.29-1.38 (8H, m, 4×CH$_2$, *n*-octyl), 1.40-1.45 (2H, m, CH$_2$, *n*-octyl), 1.45 (9H, s, Me, Boc), 1.71 (2H, tt app. qui, $^3J_{H,H}$=6.9 Hz, OCH$_2$C*H*$_2$, *n*-octyl), 3.42 (4H, dd, $^3J_{H,H}$=4.5 Hz, H-3, -5, PZ), 3.73 (4H, t, $^3J_{H,H}$=5.3 Hz, H-2, -6, PZ), 3.95 (2H, t,$^3J_{H,H}$=6.5 Hz, OCH$_2$, *n*-octyl), 4.37 and 4.38 (2H, s, OCH$_2$), 6.81 (2H, ddd app. dt, $^3J_{H,H}$=9.5 Hz, $^4J_{H,H}$~$^5J_{H,H}$=2.4 Hz, H-3, -5, Ph), 6.83 (2H, ddd app. dt, $^3J_{H,H}$=9.5 Hz, $^3J_{H,H}$~$^4J_{H,H}$=2.4 Hz, H-3, -5, Ph), 7.53 (2H, d, $^3J_{H,H}$=9.0 Hz, H-2, -6, Ph), 7.56 (2H, dd, $^3J_{H,H}$=7.0 Hz, $^4J_{H,H}$=2.0 Hz, H-2, -6, Ph), 8.54 and 8.59 (2H, 2×s, NH) ppm. 2D-$^1$H-DOSY NMR (500 MHz, 5 mM in DMSO-$d_6$, 298 K) $D$ 153.1 µm$^2$ s$^{-1}$. DEPT-$^{13}$C NMR (125 MHz, 32 mM in DMSO-$d_6$, 298 K) $\delta_C$ 14.5 (Me, *n*-octyl), 22.6, 26.1, (2×CH$_2$, *n*-octyl), 28.5 and 28.6 (Me, Boc), 29.2, 29.26 and 29.27 (3×CH$_2$, *n*-octyl), 31.7 (OCH$_2$C*H*$_2$, *n*-octyl), 43.1 (C-3, -5, PZ), 44.1 and 44.4 (C-2, -6, PZ), 66.8 (OCH$_2$, *n*-octyl), 68.0 (OCH$_2$), 79.6 (Cq, Boc), 114.62 and 114.64 (C-3, -5, Ph), 122.0 and 123.0 (C-2, -6, Ph), 133.5 and 133.6 (C-1, Ph), 154.1 and 154.3 (C-4, Ph), 154.4 (>CO-N<, carbamate), 164.5 and 165.1 (C-2, -4, -6, T), 171.5 and 171.6 (COOH) ppm. HRMS (ESI) (rel. int. %) *m/z*: 726.2779 [M-H+2K]$^+$ (100), 688.3220 [M+K]$^+$ (98), 650.3660 [M+H]$^+$ (72), 626.2251 [(M+K)-CH$_4$-H$_2$-CO$_2$]$^+$ (19). [M-H+2K]$^+$ calcd. for $C_{34}H_{46}K_2N_7O_6$: 726.2784; [M+K]$^+$ calcd. for $C_{34}H_{47}KN_7O_6$: 688.3225; [M+H]$^+$ calcd. for $C_{34}H_{48}N_7O_6$: 650.3666; [(M+K)-CH$_4$-H$_2$-CO$_2$]$^+$ calcd. for $C_{32}H_{41}KN_7O_4$: 626.2857.

*{1-{4-[4-(3-Carboxypropoxy)phenyl]amino-6-[(4-n-octyloxy)phenyl]amino-s-triazin-2-yl}-4-tertbutoxycarbonyl}-piperazine* **4b**. 0.800 g (62% yield starting from 1.000 g **2b**). White solid. Mp 196.5-197.0 ºC (MeOH). $R_f$ (*n*-hexane/EtOH 1:1.5 v/v) = 0.80. Elemental analysis calcd. (%) for $C_{36}H_{51}N_7O_6$: C 63.79, H 7.58, N 14.46; found: C 64.02, H 7.73, N 14.29. IR (KBr) $\nu_{max}$ 3399 (m), 3250 (m), 2929 (m), 2854 (m), 1736 (m), 1701 (m), 1678 (m), 1572 (s), 1514 (s), 1496 (s), 1431 (s), 1420 (s), 1240 (s), 1172 (m), 1011 (w), 829 (w), 738 (w) cm$^{-1}$. $^1$H and 2D-$^1$H,$^1$H-COSY NMR (500 MHz, 28 mM in DMSO-$d_6$, 298 K) $\delta_H$ 0.86 (3H, t, $^3J_{H,H}$=6.8 Hz, Me, *n*-octyl), 1.26-1.34 (8H, m, 4×CH$_2$, *n*-octyl), 1.37-1.42 (2H, m, CH$_2$, *n*-octyl), 1.42 (9H, s, Me, Boc), 1.68 (2H, tt app. qui, $^3J_{H,H}$=6.9 Hz, OCH$_2$C*H*$_2$, *n*-octyl), 1.92 (2H, tt app. qui, $^3J_{H,H}$=6.9 Hz, H-β), 2.37 (2H, t, $^3J_{H,H}$=7.3 Hz, H-α), 3.38 (4H, bs, H-3, -5, PZ), 3.71 (4H, bs, H-2, -6, PZ), 3.91 (2H, t,$^3J_{H,H}$=6.8 Hz, OCH$_2$, *n*-octyl), 3.94 (2H, t, $^3J_{H,H}$=6.5 Hz, H-γ), 6.83 (2H, d,

STEFANIA IONESCU-ZINCA, PEDRO LAMEIRAS, DAN PORUMB,
EMESE GÁL, MIRCEA DARABANTU

$^3J_{H,H}$=9.0 Hz, H-3, -5, Ph), 6.84 (2H, d, $^3J_{H,H}$=8.5 Hz, H-3, -5, Ph), 7.57 (4H, bs, H-2, -6, Ph), 8.96 (2H, bs, NH) ppm. $^1$H and 2D-$^1$H,$^1$H-COSY NMR (500 MHz, 28 mM in DMSO-$d_6$, 363 K) $\delta_H$ 0.88 (3H, t, $^3J_{H,H}$=6.8 Hz, Me, *n*-octyl), 1.29-1.36 (8H, m, 4×CH$_2$, *n*-octyl), 1.38-.45 (2H, m, CH$_2$, *n*-octyl), 1.45 (9H, s, Me, Boc), 1.71 (2H, tt app. qui, $^3J_{H,H}$=6.9 Hz, OCH$_2$C*H$_2$, *n*-octyl), 1.96 (2H, tt app. qui, $^3J_{H,H}$=6.8 Hz, H-$\beta$), 2.36 (2H, t, $^3J_{H,H}$=7.3 Hz, H-$\alpha$), 3.42 (4H, t, $^3J_{H,H}$=5.3 Hz, H-3, -5, PZ), 3.73 (4H, t, $^3J_{H,H}$=5.3 Hz, H-2, -6, PZ), 3.95 (2H, t,$^3J_{H,H}$=6.5 Hz, OCH$_2$, *n*-octyl), 3.99 (2H, t, $^3J_{H,H}$=6.5 Hz, H-$\gamma$), 6.84 (2H, d, $^3J_{H,H}$=9.0 Hz, H-3, -5, Ph), 6.85 (2H, d, $^3J_{H,H}$=9.0 Hz, H-3, -5, Ph), 7.55 (2H, d, $^3J_{H,H}$=8.5 Hz, H-2, -6, Ph), 7.56 (2H, d, $^3J_{H,H}$=9.0 Hz, H-2, -6, Ph), 8.58 (2H, s, NH) ppm. 2D-$^1$H-DOSY NMR (500 MHz, 5 mM in DMSO-$d_6$, 298 K) *D* 169.4 µm$^2$ s$^{-1}$. DEPT-$^{13}$C NMR (125 MHz, 28 mM in DMSO-$d_6$, 298 K) $\delta_C$ 14.5 (Me, *n*-octyl), 22.6 (CH$_2$, *n*-octyl), 24.9 (C-$\beta$), 26.1 (CH$_2$, *n*-octyl), 28.5 and 28.6 (Me, Boc), 29.2 and 29.3 (2×CH$_2$, *n*-octyl), 30.7 (C-$\alpha$), 31.7 (OCH$_2$C*H$_2$, *n*-octyl), 43.1 (C-3, -5, PZ), 44.0 and 44.1 (C-2, -6, PZ), 67.2 (OCH$_2$, *n*-octyl), 68.0 (C-$\gamma$), 79.6 (Cq, Boc), 114.65 and 114.71 (C-3, -5, Ph), 122.1 (C-2, -6, Ph), 133.55, 133.58 and 133.7 (C-1, Ph),154.1 and 154.3 (C-4, Ph), 154.4 (>CO-N<, carbamate), 164.5 and 165.1 (C-2, -4, -6, T), 174.7 (COOH) ppm. HRMS (ESI) (rel. int. %) *m/z*: 722.3607 (19) [M-H+2Na]$^+$, 700.3789 (56) [M+Na]$^+$, 678.3973 (100) [M+H]$^+$, 600.3265 [M+H-CH$_4$-H$_2$O-CO$_2$]$^+$ (18). [M-H+2Na]$^+$ calcd. for C$_{36}$H$_{50}$N$_7$Na$_2$O$_6$: 722.3618; [M+Na]$^+$ calcd. for C$_{36}$H$_{51}$N$_7$NaO$_6$: 700.3799; [M+H]$^+$ calcd. for C$_{36}$H$_{52}$N$_7$O$_6$ 678.3979; [M+H-CH$_4$-H$_2$O-CO$_2$]$^+$ calcd. for C$_{34}$H$_{46}$N$_7$O$_3$: 600.3662.

*Typical procedure for Boc N-protecting group removal from compounds* **4a** *and* **4b**; *alternative route towards compounds* **3a** *and* **3b** (**IV**, Scheme 1)

At room temperature, to a 1,4-dioxane (5 mL) solution containing Boc-derivative **4b** (0.715 g, 1.055 mmol), 3M aq HCl (2.5 mL) was added and then the reaction mixture was stirred in these conditions for 48 h. Since after this period TLC still revealed the presence of the unreacted starting material **4b** (eluent *n*-hexane/EtOH 1:1.5 v/v) together with the desired **3b** (eluent EtOH/25% aq NH$_3$ 9:0.3 v/v), the reaction mixture was heated at 50-55 °C for 5 h. After that, at room temperature, the pH of the solution was adjusted to 6-6.5 with 25% aq NH$_3$. Evaporation under vacuum to dryness of the resulted suspension provided a solid residue which was taken with distilled water (25 mL). After complete crystallization at 0 °C for 24 h, filtering off and drying, the crude compound **3b** (0.540 g) was purified by crystallization from boiling *i*-PrOH (5 mL) to give the pure melamine (0.426 g, 70% yield with respect to **4b**). Following the same protocol, starting from Boc-derivative **4a** (0.700 g, 1.077 mmol), melamine **3a** was obtained (0.520 g, 88% yield with respect to **4a**).

## ACKNOWLEDGMENTS

## REFERENCES

1. D. Abraham; P. E. Kennedy; A. S. Mehanna; D. C. Patwa; F. L. Williams; *J. Med. Chem.*, **1984**, *27*, 967-978
2. Y. Katsura; T. Tomishi; Y. Inoue; K. Sakane; Y. Matsumoto; C. Morinaga; H. Ishikawa; H. Takasugi; *J. Med. Chem.*, **2000**, *43*, 3315-3321
3. B. D. Palmer; J. B. Smaill; G. W. Rewcastle; E. M. Dobrusin; A. Kraker; C. V. Moore; R. W. Steinkampf; W. Dennya; *Bioorg. Med. Chem. Lett.*, **2005**, *15*, 1931-1935
4. K. Hidaka; T. Kimura; A. J. Ruben; T. Uemura; M. Kamiya; A. Kiso; T. Okamoto; Y. Tsuchiya; Y. Hayashi; E. Freire; Y. Kiso; *Bioorg. Med. Chem.*, **2008**, *16*, 10049-10060
5. R. Kumar; S. Jain; N. Jain; *Der Pharma Chem.*, **2013**, *5*, 73-78
6. a) C. Morar; L. Cost; P. Lameiras; C. Antheaume; M. Darabantu; *Synthetic Commun.*, **2015**, *45*, 1688-1695; b) C. Morar; P. Lameiras; A. Bende; G. Katona; E. Gál; M. Darabantu; *Beilstein J. Org. Chem.*, **2018**, *14*, 1704-1722
7. C. Sacalis; C. Morar; P. Lameiras; A. Lupan; R. Silaghi-Dumitrescu; A. Bende; G. Katona; D. Porumb; D. Harakat; E. Gál; M. Darabantu; *Tetrahedron*, **2019**, *75*, 1-18
8. a) T. Okuno; A. Izuoka; T. Ito; S. Kubo; T. Sugawara; N. Sato; Y. Sugawara; *J. Chem. Soc., Perkin Trans. 2*, **1998**, *4*, 889-896; b) D. De Murillas Lopez; R. Pinol; M. B. Ros; J. L. Serrano; T. Sierra; M. R. De La Fuente; *J. Mat. Chem.*, **2004**, *14*, 1117-1127; c) W. Li; W. Bu; H. Li; L. Wu; M. Lib; *Chem. Commun.*, **2005**, *30*, 3785-3787; d) M. J. Jeong; J. H. Park; C. Lee; J. Y. Chang; *Org. Lett.*, **2006**, *8*, 2221-2224
9. a) S. Yagai; M. Usui; T. Seki; H. Murayama; Y. Kikkawa; S. Uemura; T. Karatsu; A. Kitamura; A. Asano; S. Seki; *J. Am. Chem. Soc.*, **2012**, *134*, 7983-7994; b) Z. Shi; H. Lu; Z. Chen; R. Cheng; D. Chen; *Polymer*, **2012**, *53*, 359-369; c) D. -Y Kim; S. -A. Lee; Y. -J. Choi; S. -H. Hwang; S. -W. Kuo; C. Nah; M. -H. Lee; K. -U. Jeong; *Chem. Eur. J.*, **2014**, *20*, 5689-5695
10. See, for example: a) F. Popa; P. Lameiras; O. Moldovan; M. Tomoaia-Cotisel; E. Hénon; A. Martinez; C. Sacalis; A. Mocanu; Y. Ramondenc; M. Darabantu; *Tetrahedron*, **2012**, *68*, 8945-8967; b) O. Moldovan; I. Nagy; P. Lameiras; C. Antheaume; C. Sacalis; M. Darabantu; *Tetrahedron: Asymmetry*, **2015**, *26*, 683-701; c) C. Morar; G. Turdean; A. Bende; P. Lameiras; C. Antheaume; L. M. Muresan; M. Darabantu; *C. R. Chimie*, **2017**, *20*, 402-414
11. a) A. P. Umali; H. L. Crampton; E. E. Simanek; *J. Org. Chem.*, **2007**, *72*, 9866-987; b) S. A. Bell; M. E. McLean; S. -K. Oh; S. E. Tichy; W. Zhang; R. M. Corn; R. M. Crooks; E. E. Simanek; *Bioconjugate Chem.*, **2003**, *14*, 488-493
12. a) L. L. Lai; L. Y. Wang; C. H. Lee; Y. C. Lin; K. L. Cheng; *Org. Lett.*, **2006**, *8*, 1541-1544; b) L. L. Lai; C. H. Lee; L. Y. Wang; K. L. Cheng; H. F. Hsu; *J. Org. Chem.*, **2008**, *73*, 485-490
13. a) A. Chouai; V. J. Venditto; E. E. Simanek; *Org. Synth.*, **2009**, *86*, 141-150; b) S. Ricken; P. W. Osinski; P. Eilbracht; R. Haag; *J. Mol. Catal. A: Chem.*, **2006**, *257*, 78-88

14. a) T. Drakenberg; S. Forsen; *Chem. Commun*., **1971**, *21*, 1404-1405; b) S. S. Mirvish; P. Gannett; D. M. Babcook; D. Williamson; S. C. Chen; D. D. Weisenburger; *J. Agric. Food Chem.*, **1991**, *39*, 1205-1210; c) A. R. Katritzky; I. Ghiviriga; D. C. Oniciu; A. J. Barkock; *J. Chem. Soc. Perkin Trans. 2*, **1994**, *4*, 785-792; d) A. R. Katritzky; I. Ghiviriga; P. G. Steel; D. C. Oniciu; *J. Chem. Soc. Perkin Trans. 2*, **1996**, *3*, 443-447; e) I. Ghiviriga; D. C. Oniciu; *Chem. Commun.*, **2002**, *22*, 2718-2719

15. a) H. Friebolin in *Basic One- and Two Dimensional NMR Spectroscopy*; VCH Verlagsgesellschaft: Weinheim, New York, **1991**; pp 147-165, 263-291; b) E. L. Eliel; H. S. Wilen in *Stereochemistry of the Organic Compounds*; John Wiley & Sons, New York, **1994**; pp. 642

16. E. Fedeli; S. Hernández-Aínsa; A. Lancelot; R. González-Pastor; P. Calvo; T. Sierra; J. L. Serrano; *Soft Matter* **2015**, *11*, 6009-6017

17. M. A. van Dongen; B. G. Orr; M. M. Banaszak; *J. Phys. Chem. B*, **2014**, *118*, 7195-7202

18. A. R. Deac; C. Morar; G. L. Turdean; M. Darabantu; E. Gál; A. Bende; L. M. Muresan; *J. Solid State Electrochem.*, **2016**, *20*, 3071-3081

19. a) F. S. Parker in *Applications of Infrared Spectroscopy in Biochemistry, Biology and Medicine*; Plenum Press, New-York, **1971**; pp. 35; b) R. M. Silverstein; F. X. Webster; D. J. Kiemle in *Identification Spectrométrique de Composés Organiques*; De Boeck & Larcier s.a., **2007**; pp. 95, 96, 101

20. R. A. Heacock; L. Marion; *Can. J. Chem.*; **1956**, *34*, 1782-1995

# COPPER(II) COMPLEXES WITH NEW *N*-SUBSTITUTED SULFONAMIDES – SYNTHESIS, CRYSTAL STRUCTURE AND EVALUATION OF THE NUCLEASE ACTIVITY

**ANDREEA BODOKI[a,\*], GLORIA ALZUET-PIÑA[b],
JOAQUÍN BORRÁS[b], TAMARA TOPALĂ[a], ADRIANA HANGAN[a],
GHEORGHE BORODI[c], LUMINIȚA OPREAN[a]**

**ABSTRACT.** Binary Cu(II) complexes of two new N-substituted sulfonamides, N-(pyridin-2-yl-methyl)biphenyl-4-sulfonamide (HL1) and N-bis-(pyridin-2-yl-methyl)biphenyl-4-4'-sulfonamide (H$_2$L2), have been synthesized and characterized by X-ray diffraction, spectroscopic and electrochemical techniques. The structure of complex [Cu(L1)$_2$] consists of a discrete monomeric Cu(II) species stabilized by π-π stacking interactions involving the pyridyl and phenyl rings of the coordinated ligands. In contrast, in the case of complex [Cu(L2)]$_n$, each symmetrical sulfonamide structure coordinates two Cu(II) ions, giving rise to a polymeric chain. Upon coordination, CuN$_4$ chromophores with the N-pyrydil atoms in trans position are generated, and the coordination geometry of both complexes can be best described as highly distorted square-planar. The ability of complex [Cu(L1)$_2$] to promote DNA cleavage with ascorbate activation was also evaluated; the complex has a moderate nuclease activity, being able to partially cleave supercoiled DNA to nicked circular and linear DNA. We herein also report the evaluation of the nuclease activity of complex Cu$_2$(N-(pyridin-2-yl)biphenyl-4-sulfonamidate)$_4$, previously characterized in terms of structure by our group.

*Keywords: Cu(II) complexes, N-substituted sulfonamides, X-ray diffraction, nuclease activity*

---

[a] *Department of General and Inorganic Chemistry, Faculty of Pharmacy, UMF Iuliu Hatieganu, 400010 Ion Creanga, Cluj-Napoca, Romania*
[b] *Department of Inorganic Chemistry, Faculty of Pharmacy, University of Valencia, 46100 Burjassot, Valencia, Spain*
[c] *Department of Molecular and Biomolecular Service, National Institute for Research and Development for Isotopic and Molecular Technologies, 67-103 Donat, Cluj-Napoca, Romania*
\* *Corresponding author: abota@umfcluj.ro*

ANDREEA BODOKI, GLORIA ALZUET-PIÑA, JOAQUÍN BORRÁS, TAMARA TOPALĂ, ADRIANA HANGAN, GHEORGHE BORODI, LUMINIȚA OPREAN

## INTRODUCTION

In recent years there has been an increasing interest in the rational design of first row transition metal complexes with interesting features as biochemical tools and therapeutics. Substantial effort has been made during the last decades towards the development of metal complexes with a wide variety of ligand structures able to promote the degradation of nucleic acids via a hydrolytic or an oxidative mechanism [1]. To date, these synthetic nucleases are mainly employed as valuable tools for the *in vitro* investigation of a variety of biochemical processes, such as the investigation of the protein-DNA/RNA interactions, or of the structure of nucleic acids [2,3]. Metal complexes that target nucleic acids can also be developed as therapeutics since an effective interaction with DNA or RNA and the subsequent cleavage of nucleic acids are essential steps in the cascade of processes associated with the antitumor, antibiotic or antiviral action [1,4]. Although promising, the *in vivo* applications are without a doubt an area that needs further investigation. Issues such as low solubility, kinetic and thermodynamic liability, low substrate selectivity and efficiency, or deficient cellular delivery still need to be addressed [1,5].

Cu(II), an essential metal ion, has been extensively employed as coordination center for structures with a nucleolytic potential [1,6-9] on the assumption that, in general, endogenous metals may be less toxic to normal cells and tissues. Cu(II) is versatile in terms of coordination numbers and geometries, it exhibits biologically accessible redox potentials, relatively high affinity towards nucleobases, and interesting intrinsic properties [9,10].

Widely studied for their antibacterial, antidiabetic, anticancer or diuretic activity [11-14], sulfonamides are also suitable candidates for metal-ion coordination primarily due to the presence of N and O donor atoms in the sulfonamide moiety. N-substitution may include functional groups with additional donor atoms; moreover, the sulfonamide structure may be designed to exhibit particular features that allow for a certain coordination pattern or that are correlated with particular desired functions of the metal complex, e.g. the inclusion of planar aromatic rings that facilitate the intercalation of the complex between the DNA base pairs. During the past decade, the remarkable oxidative nuclease activity and the antitumor properties for several Cu(II) complexes with N-substituted sulfonamides have been reported [15-17].

With the aforementioned considerations in mind and as a continuation of our research [15-23], we herein report the synthesis and characterization of two new sulfonamide derivatives, N-(pyridin-2-yl-methyl)biphenyl-4-sulfonamide (HL1) and N-bis-(pyridin-2-yl-methyl)biphenyl-4-4'-sulfonamide ($H_2L2$) (Scheme 1). The Cu(II) complexes of these ligands, [Cu(L1)$_2$] and [Cu(L2)]$_n$ were structurally

characterized and the nuclease potential of complex [Cu(L1)$_2$] was evaluated. The nuclease activity of the dinuclear complex Cu$_2$(N-(pyridin-2-yl)biphenyl-4-sulfonamidate)$_4$, structurally characterized in our previous work [24], is also herein reported and compared with that of [Cu(L1)$_2$].

## RESULTS AND DISCUSSION

The HL1 and H$_2$L2 ligands were prepared according to Scheme 1.
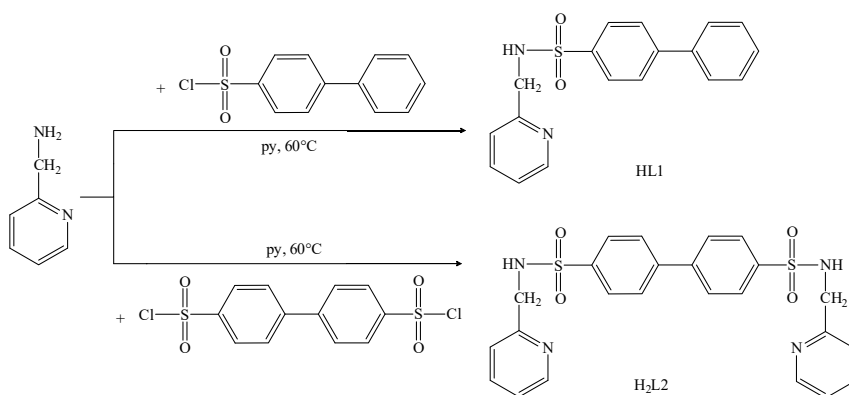


**Scheme 1.** Synthesis of ligands N-(pyridin-2-yl-methyl)biphenyl-4-sulfonamide (HL1) and N-bis-(pyridin-2-yl-methyl)biphenyl-4-4'-sulfonamide (H$_2$L2)

Complex [Cu(L1)$_2$] is readily soluble in N,N-dimethylformamide (DMF) and showed low solubility in aqueous media. Complex [Cu(L2)]$_n$ however showed very low solubility in all solvents compatible with biological media.

### X-ray crystallography

The molecular structures of complexes [Cu(L1)$_2$] and [Cu(L2)]$_n$ together with the atomic labeling scheme are shown in Figures 1 and 2. The relevant structural parameters for the complexes are listed in Table 1.

The monodeprotonated structure L1$^-$ and the double deprotonated symmetric ligand L2$^{2-}$ both coordinate the Cu(II) ions through the pyridyl and the sulfonamide nitrogen atoms.

Upon coordination, CuN$_4$ chromophores with the N-pyrdil atoms in trans position are generated for both binary complexes. Tetrahedrality estimated from the angle subtended by two planes, each encompassing Cu(II) and two donor atoms [25], is of 33.81° for complex [Cu(L1)$_2$] and of 46.63° for complex [Cu(L2)]$_n$. The calculated tetrahedrality suggest an important distortion from the strict square-planar geometry for complex [Cu(L1)$_2$], while for complex

ANDREEA BODOKI, GLORIA ALZUET-PIÑA, JOAQUÍN BORRÁS, TAMARA TOPALĂ,
ADRIANA HANGAN, GHEORGHE BORODI, LUMINIȚA OPREAN

$[Cu(L2)]_n$ it indicates that the local environment around the Cu(II) ion is mid-way between tetrahedral and square-planar. For four-coordinate Cu(II) complexes the distortion from ideal square-planar or tetrahedral geometries can be evaluated by the index $\tau_4$ ranging from 1, for perfect tetrahedral, to zero, for perfect square-planar geometry [26]. The $\tau_4$ value of 0.36 for complex $[Cu(L1)_2]$ and 0.42 for complex $[Cu(L2)]_n$ indicate highly distorted square-planar geometries.

The coordination polyhedron of complex $[Cu(L1)_2]$ exhibits features similar to those reported for other Cu(II) complexes with 2-aminomethylpyridine derivatives as ligands [27-29]. The $Cu-N_{sulfonamido}$ bond lengths, of 1.930(2)Å and 1.965(2)Å, are slightly shorter than the $Cu-N_{pyridyl}$ ones (1.988(2)Å and 1.992(2)Å). The bond angles formed by the central ion and the nitrogen atoms belonging to the same ligand structure (close to 83°) are smaller than those formed by the Cu(II) ion with the nitrogen atoms from the two distinct ligands in the coordination environment, especially with the nitrogen atoms adjacent to the sulfonyl group, probably because of the steric hindrance between these moieties [27].

For the polymeric complex $[Cu(L2)]_n$, the Cu-N bond lengths are of 1.992(7)Å for the $Cu-N_{pyridyl}$ bonds and of 1.916(8)Å for the $Cu-N_{sufonamido}$ bonds, within the expected range for Cu(II) complexes with similar ligands [23, 24, 27, 30-32]. The N-Cu-N angles that describe the coordination polyhedron, of 82.7(4)° and 103.8(4)°, deviate significantly from 90°. As it is to be expected, the smaller angles, of 82.7(4)°, correspond to those formed by Cu(II) and two nitrogen atoms belonging to the same ligand structure, because of strains induced by the sulfonamide molecule itself. The $Cu-N_{pyridyl}$ bond distances are very similar in the two complexes, while the $Cu-N_{sulfonamido}$ distances in complex $[Cu(L2)]_n$ are slightly shorter than the analogous ones in complex $[Cu(L1)_2]$. Also, the bond angles $N_{sulfonamido}-Cu-N_{pyridyl}$ are of close values in the case of both complexes.

**Table 1.** Selected bond lengths (Å) and angles (º) for complexes $[Cu(L1)_2]$ and $[Cu(L2)]_n$

| $[Cu(L1)_2]$ | | $[Cu(L2)]_n$ | |
|---|---|---|---|
| Cu(1)-N(2) | 1.930(2) | Cu(1)-N(3) | 1.916(8) |
| Cu(1)-N(4) | 1.965(2) | Cu(1)-N(3)[1] | 1.916(8) |
| Cu(1)-N(3) | 1.988(2) | Cu(1)-N(4) | 1.992(7) |
| Cu(1)-N(1) | 1.992(2) | Cu(1)-N(4)[1] | 1.992(7) |
| N(2)-Cu(1)-N(4) | 157.87(10) | N(3)-Cu(1)-N(3)[1] | 159.4(6) |
| N(2)-Cu(1)-N(3) | 102.04(9) | N(3)-Cu(1)-N(4) | 82.7(4) |
| N(4)-Cu(1)-N(3) | 83.48(9) | N(3)[1]-Cu(1)-N(4) | 103.8(4) |
| N(2)-Cu(1)-N(1) | 83.23(9) | N(3)-Cu(1)-N(4)[1] | 103.8(4) |
| N(4)-Cu(1)-N(1) | 102.59(9) | N(3)[1]-Cu(1)-N(4)[1] | 82.7(4) |
| N(3)-Cu(1)-N(1) | 150.52(9) | N(4)-Cu(1)-N(4)[1] | 144.1(5) |

Symmetry transformations used to generate equivalent atoms: [1] 1-X, +Y, 1/2-Z

The structure of complex $[Cu(L1)_2]$ consists of a discrete monomeric Cu(II) species stabilized by π-π stacking interactions involving the aromatic rings of the coordinated ligands (Figure 3). Interestingly, the monomeric nature of complex $[Cu(L1)_2]$ contrasts with the dimeric one exhibited by the previously reported complex $Cu_2$(N-(pyridin-2-yl)biphenyl-4-sulfonamidate)$_4$ [24] obtained with a ligand similar to HL1. As a tentative, this different nature could be attributed to the presence in HL1 of a CH$_2$ group linking the pyridine ring and the sulfonamide group that prevents in $[Cu(L1)]_n$ the formation of a NCN bridge found in other stable dinuclear and tetranuclear Cu(II) compounds with sulfonamide derivatives as ligands [33, 34]. A polymeric chain is generated in the case of complex $[Cu(L2)]_n$ (Figure 4), where two adjacent Cu(II) ions are separated by a distance of 13.48 Å; one $N_{pyrydil}$ (N4 and N4#1) and one $N_{sulfonamido}$ (N3 and N3#1) atoms coordinate one metallic center, while the other two nitrogen atoms of the symmetric ligand structure coordinates a second Cu(II) ion.
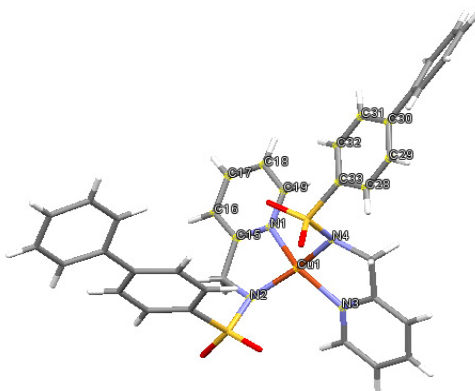


**Figure 1.** Molecular structure of complex $[Cu(L1)_2]$
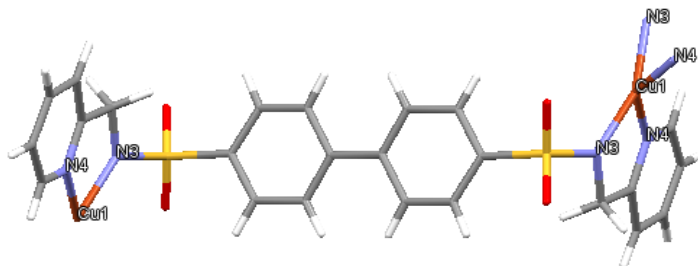


**Figure 2.** Molecular structure of complex $[Cu(L2)]_n$

ANDREEA BODOKI, GLORIA ALZUET-PIÑA, JOAQUÍN BORRÁS, TAMARA TOPALĂ,
ADRIANA HANGAN, GHEORGHE BORODI, LUMINIȚA OPREAN

The structure of complex [Cu(L1)$_2$] is stabilized by two types of moderate strength π-π interactions determined by the pyridyl-pyridyl and phenyl-pyridyl parallel stacking of the rings belonging to adjacent complex molecules. The structural parameters defining these interactions are listed in Table 2. Interactions that implied centroid-centroid distances, d($\perp$C(J)-C(I)), of less than 6Å and β<60° were investigated. The distances between the interacting centroids is approximately 3.8Å, close to the maximum at which π-π interactions occur [35]. The value of 0.02° of the dihedral angle α characterizing the pyridyl-phenyl interactions indicates a close parallelism between these interacting rings. An accentuated deviation from parallelism occurs for the pyridyl-pyridyl interaction (α = 11.97°), suggesting a rather pronounced slipping of the interacting centroids, similar to that reported for the dimeric complex Cu$_2$(N-(pyridine-2-yl)biphenyl-4-sulfonamidate)$_4$ [24]. A representation of the crystal packing of complex [Cu(L1)$_2$] showing the pyridyl-phenyl π-π interactions is shown in Figure 3.

**Table 2.** Geometric parameters for π-π stacking [Å/°] in complex [Cu(L1)$_2$]

| π-π stacking | d$_{C-C}$ | α | β | γ | d$_\perp$[Cg(I)-P(J)] | d$_\perp$[Cg(J)-P(I)] |
|---|---|---|---|---|---|---|
| Pyridyl-pyridyl | | | | | | |
| Cg(3)-Cg(3)[a] | 3.842 | 0.02 | 20.12 | 20.12 | 3.608 | 3.608 |
| Pyridyl-phenyl | | | | | | |
| Cg(3)-Cg(7)[b] | 3.841 | 11.97 | 23.19 | 13.15 | 3.741 | 3.531 |

d$_{C-C}$: distance between ring centroids; α: dihedral angle between the rings; β, γ: slipping angles; d$_\perp$[Cg(I)-P(J)] and d$_\perp$[Cg(J)-P(I)]: centroid Cg(I) to plane J distance and the opposite. [a] -x,1-y,-z [b] x,1+y,z. Cg(3): N1-C15-C16-C17-C18-C19; Cg(7): C28-C29-C30-C31-C32-C33
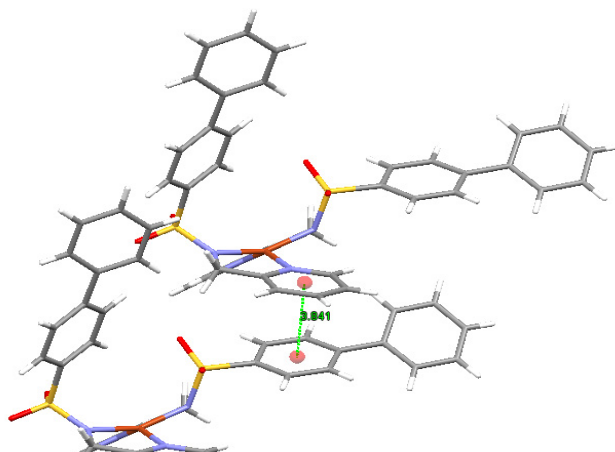


**Figure 3.** Crystal packing of complex [Cu(L1)$_2$] showing the pyridyl-phenyl stacking interactions
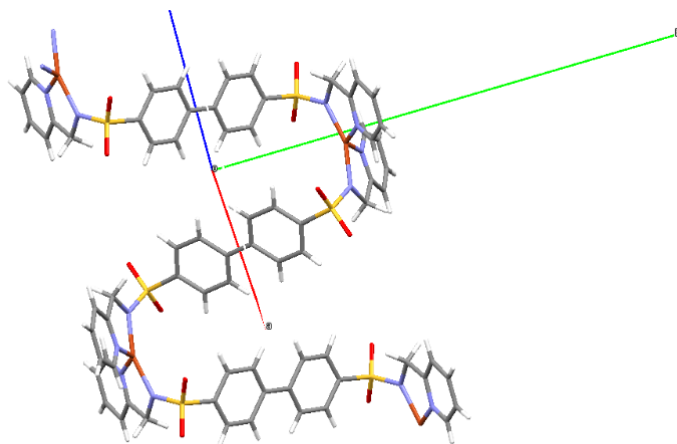
**Figure 4.** Polymer chain formation for complex [Cu(L2)]$_n$
along the crystallographic c axis

## Spectroscopic properties

Complexes [Cu(L1)$_2$] and [Cu(L2)]$_n$ exhibit the same infrared spectrum pattern, similar to that observed for other Cu(II) complexes with N-substituted sulfonamides [15, 23, 24, 28, 36]. As a consequence of the involvement of the sulfonamide moiety in the coordination of the metal center and its deprotonation, the band assigned to the N-H stretching vibration disappears, and the bands assigned to $v_{sym}(SO_2)$, $v_{asym}(SO_2)$ and $v(S-N)$ appear shifted in the IR spectra of both complexes. Thus, the band assigned to the $v_{asym}(SO_2)$ is shifted towards lower frequencies, while the $v_{sym}(SO_2)$ is shifted towards higher frequencies for [Cu(L1)$_2$] and towards lower frequencies for [Cu(L2)]$_n$. The band assigned to the vibrations of the S-N bond appears shifted towards higher frequencies in both cases. The bands corresponding to the stretching vibrations of the pyridyl ring ($v(C=N)$ and $v(C=C)$) are also slightly shifted as a result of metal ion coordination.

The diffuse reflectance spectra of both complexes exhibit a broad asymmetric band centred at 615 nm for [Cu(L1)$_2$] and at 595 nm for [Cu(L2)]$_n$. These bands correspond to the ligand field transitions characteristic of distorted square-planar complexes with CuN$_4$ chromophores [29]. The d-d band in the spectrum of complex [Cu(L1)$_2$] recorded in DMF solution appears centred at 625 nm; this shift is most likely a consequence of the intervention of the solvent. The results are in agreement with the data from the ESI experiments which reveal that a Cu(II) and two sulfonamide ligands exist as an entity in DMF solution.

The EPR spectrum of complex [Cu(L1)$_2$] is slightly rhombic. The simulated EPR parameters [37] are $g_x = 2.04$, $g_y = 2.052$ and $g_z = 2.228$. The ratio $R = (g_y - g_x) / (g_z - g_y)$, calculated for rhombic systems with $g_z > g_y > g_x$, has a value of 0.07 indicating that the unpaired electron of Cu(II) is placed mainly in the $d_{x2-y2}$ orbital [38]. Complex [Cu(L2)]$_n$ exhibits an axial EPR spectrum with the following simulated parameters: $g_{||} = 2.230$ and $g_\perp = 2.062$. The values $g_{||} > g_\perp$ are indicative of a mainly Cu(II) $d_{x2-y2}$ ground state.

## Cyclic voltammetry experiments

The electrochemical profile of complex [Cu(L1)$_2$] was studied in DMF by cyclic voltammetry in the range 1.0 to -1.0 V. The voltammogram shows one cathodic peak at -0.212 V, indicating an irreversible redox process suggesting that the Cu(II) species decomposes at higher potential.

## DNA cleavage

The ability of complex [Cu(L1)$_2$] to cleave double-stranded DNA was evaluated by gel electrophoresis on supercoiled plasmid DNA (pUC18), in 0.05 M borate buffer (pH = 8.0) using sodium ascorbate as activating agent and complex concentration in the range 3 – 12 µM. A sample containing pUC18 plasmid DNA in the presence of 12 µM Cu(II) ions was also run as control experiment. For comparison reasons, and on the premises that multiple metal centres may exhibit synergistic effects in DNA recognition and cleavage [39, 40], we have also examined the nuclease activity of the related dimeric compound Cu$_2$(N-(pyridin-2-yl)biphenyl-4-sulfonamidate)$_4$ [24], under the same experimental conditions.

The electrophoresis (Figure 5) shows that most of the pUC18 plasmid DNA remains in the supercoiled conformation in the entire range of the assayed complexes concentrations (Figure 5, lanes 4 – 7 for complex [Cu(L1)$_2$] and lanes 8 – 11 for complex Cu$_2$(N-(pyridin-2-yl)biphenyl-4-sulfonamidate)$_4$). The maximum assayed concentration of complex [Cu(L1)$_2$] (12 µM) induces however the partial transformation of supercoiled DNA into nicked and linear forms (Figure 5, lane 7), suggesting that complex [Cu(L1)$_2$] is a moderate chemical nuclease. Unfortunately, despite the presence of two Cu(II) ions per complex unit, Cu$_2$(N-(pyridin-2-yl)biphenyl-4-sulfonamidate)$_4$ was not able to induce DNA cleavage (Figure 5, lanes 8 – 11). The lack of nuclease activity of this dinuclear compound could be attributed to its high redox stability that avoids the formation of Cu(I) species (24).
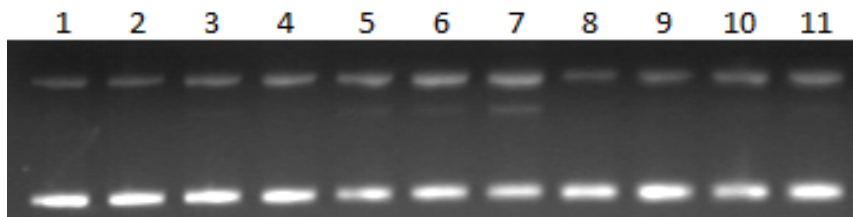
**Figure 5.** Agarose gel electrophoresis of pUC18 DNA in the presence of complex [Cu(L1)$_2$] with ascorbate activation. Incubation time: 1h (37ºC). Lane 1: pUC18; lane 2: pUC18 + 12mM ascorbate; lane 3: 12µM CuCl$_2$ + 12 mM ascorbate; lanes 4 – 7: 3, 6, 9 12 µM [Cu(L1)$_2$] + 3, 6, 9, 12 mM ascorbate, respectively; lanes 8 – 11: 3, 6, 9, 12 µM Cu$_2$(N-(pyridin-2-yl)biphenyl-4-sulfonamidate)$_4$ + 3, 6, 9, 12 mM ascorbate, respectively

The polymeric [Cu(L2)]$_n$ is poorly soluble in solvent systems that are compatible with biological media, and therefore its nucleolytic potential was not evaluated at this stage. However, surface adhesion in micelles or entrapment of Cu(II) complexes into polymeric nanoparticles are proven to address the solubility and the stability problems related to numerous Cu(II) complexes [1, 41]. A similar approach is envisaged for the complex reported herein as a way to evaluate its nucleolytic potential.

**CONCLUSIONS**

Two new N-substituted sulfonamides, N-(pyridin-2-yl-methyl)biphenyl-4-sulfonamide (HL1) and N-bis-(pyridin-2-yl-methyl)biphenyl-4-4'-sulfonamide (H$_2$L2) and their binary Cu(II) complexes, [Cu(L1)$_2$] and [Cu(L2)]$_n$, have been synthesized and structurally and physicochemically characterized. Both ligands coordinate the Cu(II) ions through the pyridyl and the sulfonamide nitrogen atoms, but the monodeprotonated L1$^-$ ligand gives rise to a discrete monomeric Cu(II) species [Cu(L1)$_2$], while the symmetrical L2$^{2-}$ coordinates Cu(II) ions to create a polymeric chain. Complex [Cu(L1)$_2$] exhibits a nuclease activity of moderate intensity upon ascorbate activation and at concentration of 12 µM. The related dinuclear Cu$_2$(N-(pyridin-2-yl)biphenyl-4-sulfonamidate)$_4$ is not able to cleave DNA, a fact that could be related to the high redox stability of the compound. The nuclease activity of complex [Cu(L2)]$_n$ could not be evaluated at this stage, due to its low solubility.

ANDREEA BODOKI, GLORIA ALZUET-PIÑA, JOAQUÍN BORRÁS, TAMARA TOPALĂ,
ADRIANA HANGAN, GHEORGHE BORODI, LUMINIȚA OPREAN

## EXPERIMENTAL SECTION

### Materials and physical measurements

All reagents and solvents were commercially available and were used without further purification.

Elemental analyses were performed on a Carlo Erba AAS instrument. NMR spectra ($^1$H, $^{13}$C, HSQC and COSY) were recorded on an Advancer DRX 300 Bruker (500 MHz) instrument. The solvent used was deuterated dimethylsulfoxide (DMSO). Chemical shifts are reported relative to the residual $d_6$-DMSO ($\delta_H$ 2.50 ppm and $\delta_C$ 39.43 ppm). IR spectra were recorded using a Jasco FT-IR 4100 instrument equipped with a ZnSe ATR crystal, in the 4000-650 cm$^{-1}$ spectral range. UV-Vis spectra in solution and diffuse reflectance electronic spectra were recorded on a Jasco V-550 spectrophotometer in the range 200-800 nm. Electrospray ionization mass spectra (positive mode) analyses were performed on a Bruker Esquire 3000 plus Ion Trap Spectrometer coupled with an Agilent 1100 Chemstation liquid chromatography-mass spectrometry system. Electronic Paramagnetic Resonance (EPR) spectra were collected with a Bruker ELEXSYS spectrometer. Cyclic voltammetry experiments were performed in a single compartment cell with a three-electrode system on a PAR 273A potentiostat/galvanostat. The working and auxiliary electrode were platinum, and the reference electrode was Ag/AgCl. The supporting electrolyte was tetrabutylammonium perchlorate.

### Synthesis of N-(pyridin-2-yl-methyl)biphenyl-4-sulfonamide (HL1) and N-bis-(pyridin-2-yl-methyl)biphenyl-4-4'-sulfonamide (H₂L2)

Solutions containing 2 g (7.9 mmol) of biphenyl-4-sulfonyl chloride (for HL1) or 2 g (5.7 mmol) of biphenyl-4,4'-disulfonyl chloride (for H$_2$L2) and the corresponding quantity of 2-aminomethylpyridine, 0.85 g (7.9 mmol) for HL1 and 1.23 g (11.4 mmol) for H$_2$L2, in 6 mL of pyridine were heated at 60°C for 4 h. By quenching with 50 mL of cold water, white-cream solids formed in the reaction mixtures and the suspensions were further stirred for additional 30 min at 0°C. The resulting solids were washed with cold water and ethanol at 60°C.

Data for **HL1** - C$_{18}$H$_{16}$N$_2$SO$_2$ (MW = 324.40): calculated (found) C, 66.65 (67.08); H, 4.97 (5.04); N, 8.64 (8.45); S, 9.88 (9.68) %. $^1$H NMR (300 MHz) (DMSO-d$_6$, δ/ppm): 8.44 [1H, d, J = 4.3, H pyridine]; 8.37 [1H, t, J = 6.3, NH]; 7.85 [4H, s, H- biphenyl]; 7.7 [3H, m, H biphenyl, H pyridine], 7.5 [2H, pseudo-t, H biphenyl]; 7.45 [1H, d, J = 6.9, H biphenyl]; 7.4 [1H, d, J = 7.8, H pyridine]; 7.25 [1H, t, J = 6.3, H pyridine]; 4.1 (2H, d, J =6.3, CH$_2$]. $^{13}$C NMR

(300 MHz) (d$_6$-DMSO, δ/ppm): 156.9, 148.4, 138.5, 122.4, 121.7 (C pyridine); 143.8, 139.2, 136.9, 129.1, 128.4, 127.2, 127.1, 127.0 (C phenyl); 47.8 (CH$_2$). IR (ATR) ($v_{max}$/cm$^{-1}$): 3066 v(N-H); 1333 $v_{asym}$(SO$_2$); 1166 $v_{sym}$(SO$_2$), 944 v(S-N). ESI$^+$ (DMF): *m/z*$^+$ 325.

Data for **H$_2$L2** - C$_{24}$H$_{22}$N$_4$S$_2$O$_4$ (MW = 494.59): calculated (found) C, 58.28 (58.13); H, 4.48 (4.53); N, 11.33 (11.05); S, 12.96 (13.11) %. $^1$H NMR (300 MHz) (d$_6$-DMSO, δ/ppm): 8.4 [2H, t, NH, H pyridine]; 7.9 [4H, s, phenyl]; 7.8 [1H, dt, H pyridine]; 7.4 [1H, d, J=7.9Hz, H pyridine]; 7.3 [1H, t, J=5.8, H pyridine]; 4.2 [2H, d, J=6.3, CH$_2$]. $^{13}$C NMR (300 MHz) (d$_6$-DMSO, δ/ppm): 156.7, 142.2, 140.1 (C phenyl, C pyridine); 148.2, 137.3, 122.6, 121.9 (C pyridine); 127.8, 127.3 (C phenyl); 47.6 (CH$_2$). IR (ATR) ($v_{max}$/cm-1): 3030 v(N-H); 1333 $v_{asym}$(SO$_2$); 1155 $v_{sym}$(SO$_2$), 944 v(S-N). ESI$^+$ (DMF): m/z$^+$ 495.

## Synthesis of complex [Cu(L1)$_2$]

A solution of 0.5 mmol HL1 (162.2 mg) in 10 mL of a pyridine: H$_2$O mixture (1 : 1 v/v) was added dropwise to a solution of 0.5 mmol CuSO$_4$·5H$_2$O (124.85 mg) in 10 mL of the same solvent mixture. The resulting dark-blue solution was stirred for 1 h and left to stand at room temperature. Within several days, blue plate Cu(II) complex monocrystals suitable for X-ray diffraction formed in the solution. The crystals were separated by means of filtration, washed with methanol and dried under vacuum.

Data for [Cu(L1)$_2$] Anal. for CuC$_{36}$H$_{30}$N$_4$S$_2$O$_4$ (MW = 710.30): calculated (found) C, 60.87 (61.32); H, 4.25 (4.24); N, 7.88 (7.93); S, 9.02 (9.88). IR (ATR) ($v_{max}$/cm$^{-1}$): 1611 v(C=C)$_{py}$ + v(C=N)$_{py}$; 1288 $v_{asym}$(SO$_2$); 1144 $v_{sym}$(SO$_2$); 966 v(S-N). ESI$^+$ (DMF): *m/z*$^+$ 732.1 [Cu(L1)$_2$ + Na]$^+$; 748.1 [Cu(L1)$_2$ + K]$^+$. Solid UV-Vis (λ$_{max}$/nm): 400; 595. UV-Vis (DMF) (λ$_{max}$/nm): 625.

## Synthesis of complex [Cu(L2)]$_n$

1 mmol (199.65 mg) of solid Cu(CH$_3$COO)$_2$·H$_2$O was added to a solution of 1 mmol (494.59 mg) H$_2$L2 in 30 mL DMF. The resulting dark-green solution was stirred for 1 h and left to stand at room temperature. Green plate monocrystals suitable for X-ray diffraction formed in the reaction mixture after 24 h. The crystals were isolated by means of filtration, washed with methanol and dried under vacuum.

Data for [Cu(L2)]$_n$ - Anal. for CuC$_{24}$H$_{20}$N$_4$S$_2$O$_4$ (MW = 556.10): calculated (found) C, 51.83 (51.34); H, 3.62 (3.97); N, 10.07 (10.99); S, 11.53 (10.40). IR (ATR) ($v_{max}$/cm$^{-1}$): 1666 v(C=C)$_{py}$ + v(C=N)$_{py}$; 1277 $v_{asym}$(SO$_2$); 1144 $v_{sym}$(SO$_2$); 966 v(S-N). Solid UV-Vis (λ$_{max}$/nm): 400; 615.

ANDREEA BODOKI, GLORIA ALZUET-PIÑA, JOAQUÍN BORRÁS, TAMARA TOPALĂ,
ADRIANA HANGAN, GHEORGHE BORODI, LUMINIŢA OPREAN

## X–ray data collection and structure refinement

Crystal data, experimental details and refinement results are listed in Table 3 Crystal data were collected at room temperature, using a dual microsource SuperNova diffractometer (50 kV and 0.8mA) equipped with Eos CCD detector using CuKα radiation. The data were processed with OLEX2 [42] and the structures were solved with SHELXS [43] using direct methods and refined with SHELXL [44] refinement package using Least Square minimization. Molecular graphics were made with program MERCURY [45].

**Table 3.** Crystal data and structure refinement
for complexes $[Cu(L1)_2]$ and $[Cu(L2)]_n$

| Complex | $[Cu(L1)_2]$ | $[Cu(L2)]_n$ |
|---|---|---|
| Empirical formula | $C_{36}H_{30}CuN_4O_4S_2$ | $C_{24}H_{20}CuN_4O_4S_2$ |
| Formula weight | 710.30 | 556.11 |
| Temperature (K) | 293(2) K | 293(2) K |
| Wavelength (Å) | 1.54184 | 1.54184 |
| Crystal system, space group | Monoclinic, P21/n (No. 14) | Monoclinic, C 2/c (No. 15) |
| a [Å] | 13.9874(2) | 10.7500(8) |
| b [Å] | 7.85430(10) | 20.734(8) |
| c [Å] | 29.1957(4) | 15.0045(7) |
| α [º] | 90 | 90 |
| β [º] | 90.0060(10) | 98.467(7) |
| γ [º] | 90 | 90 |
| Volume [Å$^3$] | 3207.48(8) | 3307.8(5) |
| Z, calculated density [mg m$^{-3}$] | 4,  1.471 | 8,  1.149 |
| Absorption coefficient [mm$^{-1}$] | 2.566 | 2.393 |
| F(000) | 1468 | 1172 |
| Crystal size [mm] | 0.40 x 0.20 x 0.01 | 0.08 x 0.08 x 0.02 |
| θ range for data collection [º] | 6.054 to 141.252 | 8.53 to 140.2 |
| Limiting indices | -16 ≤ h ≤ 17, -6 ≤ k ≤ 9, -33≤ l ≤ 35 | -11 ≤ h ≤ 12, -18 ≤ k ≤ 25, -13 ≤ l ≤ 18 |
| Reflections collected/unique | 22555 / 6084 [R(int) = 0.0429] | 6108 / 2498 [R(int) = 0.0343] |
| Data/restraints/parameters | 6084 / 0 / 424 | 2498 / 0 / 164 |
| Final $R$ indices [$I > 2\sigma(I)$] | R1 = 0.0427, wR2 = 0.1152 | R1 = 0.1231, wR2 = 0.3097 |
| R indices (all data) | R1 = 0.0526, wR2 = 0.1261 | R1 = 0.1804, wR2 = 0.3762 |

## pUC18 DNA cleavage

The nuclease activity of complex $[Cu(L1)_2]$ and $Cu_2$(N-(pyridin-2-yl)biphenyl-4-sulfonamidate)$_4$ was evaluated by means of gel electrophoresis in the presence of a sodium ascorbate as activating agent. Reactions were performed by mixing 7 $\mu$L of 0.05 M borate buffer (pH 8.0), 0.5 $\mu$L of pUC18 (0.5µg/µL, Thermo Scientific), 6 $\mu$L of a solution of the tested complex at increasing final concentrations between 3 $\mu$M and 12 $\mu$M, and 6 $\mu$L of ascorbate. All final mixtures employed for DNA cleavage evaluation contained 5% DMF. The mixtures were allowed to stand for 1 h at 37ºC. After that, 3 $\mu$L of a quench buffer solution consisting of 0.25% bromophenole blue, 0.25% xylene cyanole, and 30% glycerol was added. The solution was then subjected to electrophoresis on a 0.8 % agarose gel in 0.5 $\times$ TBE buffer (0.045 M tris, 0.045 M boric acid, and 1 mM EDTA) containing 2 $\mu$L/100 mL of a solution of ethidium bromide (10 mg/mL) at 80V for 2 h. The gel was photographed on a capturing gel printer plus TDI.

## Supplementary data

The crystals have been deposited at The Cambridge Crystallographic Data Centre and have been assigned the following deposition numbers: CCDC 1973146 for $[Cu(L1)_2]$ and CCDC 1973145 for $[Cu(L2)]_n$.

## ACKNOWLEDGEMENTS

## REFERENCES

1. Z. Yu; J. A. Cowan; *Curr. Opin. in Chem. Biol.,* **2018***, 43*, 37-42
2. B. Dey; S. Thukral; S. Krishnan; M. Chakrobarty; S. Gupta; C. Manghani; V. Rani; *Mol. Cell. Biochem.,* **2012**, *365*, 279-299
3. Z. Yang; N. E. Price; K. M. Johnson; Y. Wang; K. S. Gates; *Nucleic Acids Res.,* **2017**, *45*, 6275-6283
4. K. Mjos; C. Orvig; *Chem Rev.,* **2014**, *114*, 4540-4563
5. Z. Yu; J. A. Cowan; *Angew. Chem. Int. Ed.*, **2017,** *56*, 2763-2766
6. R. Salvio; S. Volpi; R. Cacciapaglia; F. Sansone; L. Mandolini; A. Casnati; *The Journal of Organic Chemistry*, **2016**, *81*, 4728-4735

7.  M. Soler; E. Figueras; J. Serrano-Plana; M. González-Bártulos; A. Massaguer; A. Company; M. A. Martínez; J. Malina; V. Brabec; L. Feliu; M. Planas; X. Ribas, M. Costas; *Inorg. Chem.*, **2015**, *54*,10542-10558
8.  A. M. Pisoschi; A. Pop; *Eur. J. Med. Chem.*, **2015**, *97*, 55-74
9.  C. Santini; M. Pellei; V. Gandin; M. Porchia; F. Tisato; C. Marzano; *Chem Rev*., **2014**, *114*:815-862
10. N. Hadjiliadis; E. Sletten; *Metal Complex–DNA Interactions*. John Wiley & Sons, New York, **2009**
11. T. H. Maren; C.W. Conroy; *J. Biol. Chem.,* **1993**, *268*, 26233-26239
12. A. K. Ghosh; L. M. Swanson; H. Cho; S. Leshchenko; K. A. Hussain; S. Kay; D. E. Walters; Y. Koh; H. Mitsuya; *J. Med. Chem.*, **2005**, *48*, 3576-3585
13. A. Scozzafava; T. Owa; A. Mastrolorenzo; C. Supuran; *Curr. Med. Chem*., **2003**, *10*, 925-953
14. F. Zhong; G. Geng; B. Chen; T. Pan; Q. Li; H. Zhang; C. Bai; *Org. Biomol. Chem.,* **2015,** *13*, 1792-1799
15. J. L. Garcia-Gimenez; J. Hernandez-Gil; A. Martinez-Ruiz; A. Castineiras; M. Liu-Gonzalez; F. V. Pallardo; J. Borras; G. Alzuet Pina; *J. Inorg. Biochem.*, **2013**, *121*, 167-178
16. M. González-Álvarez; A. Pascual-Álvarez; L. del Castillo Agudo; A. Castiñeiras; M. Liu-González; J. Borrás; G. Alzuet-Piña; *Dalton Trans.,* **2013**, *42*, 10244-10259
17. J. L. García-Giménez, M. González-Álvarez; M. Liu-González, B. Macías; J. Borrás, G. Alzuet; *J. Inorg. Biochem.,* **2009**, *103*, 923-934
18. A. Bodoki; A. Hangan; L. Oprean; G. Alzuet; A. Castiñeiras; J. Borrás J; *Polyhedron,* **2009**, *28*, 2537-2544
19. A. Bodoki; A. Hangan; L. Oprean; A. Castiñeiras; J. Borrás; M. Bojita; *Farmacia*, **2008**, *6*, 607-614
20. A. Pascual-Álvarez; T. Topala; F. Estevan; F. Sanz; G. Alzuet-Piña; *Eur. J. Inorg. Chem.*, **2016**, *2016*, 982-994
21. A. Hangan; R. Stan; A. Turza; L. Oprean, E. Pall, S. Gherorghe-Cetean; B. Sevastre; *Trans. Met. Chem.*, **2017**, *42*, 153-164
22. A. Hangan; A. Turza; R. Stan; B. Sevastre, E. Pall; S. Cetean; L. Oprean; *J. Chem. Sci.,* **2016**, *128*, 815-824
23. T. Topala; A. Pascual–Álvarez; M.A. Moldes–Tolosa; A. Bodoki A; A. Castiñeiras; J. Torres; C. del Pozo, J. Borrás; G. Alzuet–Piña; *J. Inorg. Biochem*., **2020**, *202*, 110823. doi:https://doi.org/10.1016/j.jinorgbio.2019.110823
24. A. Bodoki; G. Alzuet, A. Hangan; L. Oprean; F. Estevan, A. Castiñeiras; J. Borrás; *Inorg. Chim. Acta,* **2010**, *363*, 3139-3144
25. L. P. Battaglia; A. B. Corradi; G. Marcotrigiano; L. Menabue; G. C. Pellacani; *Inorg. Chem.,* **1979**, *18*, 148-152
26. L Yang; D. Powell; R. Houser; *Dalton Trans.*, **2007**, *9*, 955-964
27. B. Macias; M. V. Villa; M. Salgado; J. Borras; M. Gonzalez-Alvarez; F. Sanz; *Inorg. Chim. Acta,* **2006**, *359*, 1465-1472
28. M. Barquín; M. J. González Garmendia; L. Larrínaga; E. Pinilla; M.R. Torres; *Inorg. Chim. Acta,* **2009**, *362*, 2334-2340

29.  L. Gutierrez; G Alzuet; J. Borrás; M. Liu-González; F. Sanz; A. Castiñeiras; *Polyhedron* **2001**, *20*, 703-709

30.  J. Casanova; G. Alzuet; J. Latorre; J. Borras; *Inorg. Chem.*, **1997**, *36*, 2052-2058

31.  J. Casanova; G. Alzuet; S. Ferrer; J. Latorre, J. A. Ramirez; J. Borras; *Inorg. Chim. Acta,* **2000**, *304,*170-177

32.  S. T. Frey; H. H. J. Sun; N. N. Murthy; K. D. Karlin; *Inorg. Chim. Acta*, **1996**, *242*, 329-338

33.  J. L. García-Giménez; G. Alzuet; M. González-Álvarez; A. Castiñeiras; M. Liu-González; J. Borrás; *Inorg. Chem.*, **2007**, *46*, 7178-7188

34.  G. Alzuet, J. A. Real; J. Borrás' R. Santiago-García; S. García-Granda; *Inorg. Chem.,* **2001**, *40*, 2420-2423

35.  C. Janiak;  *J. Chem. Soc., Dalton Trans.,* 2000, *21*, 3885-3896

36.  B. Macias, M. Villa; M. Salgado; J. Borras; M. Gonzalez-Alvarez; F. Sanz; *Inorg. Chim. Acta*, **2006**, *359*, 1465-1472

37.  WINEPR Simfonia 1.25, Bruker Analytik GmbH, Karlsruhe, FRG, **1994**

38.  M. F. El-Shazly; A. El-Dissowky; T. Salem; M. Osman; *Inorg. Chim. Acta,* **1980**, *40*, 1-6

39.  Y. Zhao; J. Zhu; W. He; Z. Yang; Y. Zhu; Y. Li; J. Zhang; Z. Guo; *Chem.: Eur. J.*, **2006**, *12*, 6621-6629

40.  K. J. Humphreys; K. D. Karlin; S. E. Rokita; *J. Am. Chem. Soc.*, **2002**, *124*, 8055-8066

41.  A. Eskandari; J. N. Boodram; P. B. Cressey; C. Lu; P. M. Bruno; M. T. Hemann; K. Suntharalingam; *Dalton Trans.,* **2016**, *45*, 17867-17873

42.  O. Dolomanov; L. Bourhis; R. Gildea; J. Howard; H. Puschmann; *J. Appl. Crystallogr.*, **2009**, *42*, 339-341

43.  G. Sheldrick; *Acta Crystallogr.*, **2008**, *A64*, 112-122

44.  G. Sheldrick; *Acta Crystallogr.*, **2015**, *C71*, 3-8

45.  C. F. Macrae; I. J. Bruno; J. A. Chisholm; P. R. Edgington; P. McCabe, E.Pidcock; L. Rodriguez-Monge, R.Taylor; J. van de Streek; P. A. Wood; *J. Appl. Crystallogr.,* **2008**, *41*, 466-470

# CHARACTERIZATION AND CLASSIFICATION OF MEDICINAL PLANT EXTRACTS ACCORDING TO THEIR ANTIOXIDANT ACTIVITY USING HIGH-PERFORMANCE LIQUID CHROMATOGRAPHY AND MULTIVARIATE ANALYSIS

## ILEANA M. SIMION[a], AUGUSTIN C. MOȚ[a], RADU D. GĂCEANU[b], HORIA F. POP[b], COSTEL SÂRBU[a*]

**ABSTRACT**. Fuzzy divisive hierarchical clustering (FDHC) alongside with principal component analysis, hierarchical cluster analysis and linear discriminant analysis are efficiently employed for the characterization and clustering of some medicinal plants according to their antioxidant capacity. These methods are applied to the numerical data obtained from the chromatographic profiles monitored at 242, 260, 280, 320, 340 and 380 nm by high-performance liquid chromatography with a multistep isocratic and gradient elution system and diode array detection (HPLC-DAD). The samples were successfully classified according to the antioxidant activity determined using the DPPH assay. A correct classification rate of 100% was obtained when the samples were divided into two groups corresponding to high antioxidant activity and low antioxidant activity. Moreover, it is suggested to use the scores obtained applying principal component analysis and unprocessed data (the processed data by scaling and normalization did not improve the results), the analysis being faster with the same results. The proposed methodology could be considered as a promising tool with future applications in plant material investigations and other analytical fields.

*Keywords: Fuzzy clustering, chemometrics, high-performance liquid chromatography, antioxidant capacity, medicinal plants*

## INTRODUCTION

Nature has always involved in human development providing the necessary means in order to live a healthy and careless live through natural resource such as fruits, vegetables or medicinal plants. Herbal medicine, as

---

[a] *Babeş-Bolyai University, Faculty of Chemistry and Chemical Engineering, 11 Arany Janos str., RO-400028, Cluj-Napoca, Romania*
[b] *Babeş-Bolyai University, Department of Computer Science, str. Mihail Kogalniceanu nr. 1, 400084, Cluj-Napoca, Romania*
\* *Corresponding author: csarbu@chem.ubbcluj.ro*

the name suggests, uses plants as a replacement for chemically synthesized drugs, because they are cheaper, less toxic and have no side effects. The medicinal plant's therapeutic properties are sustained by the bioactive compounds that are produced through different processes that take place in the plant's cells called secondary metabolites. Thanks to the so-called secondary metabolites represented by alkaloids, sterols, terpenes, flavonoids, tannins, glycosides, resins, volatile oils, etc., the alternative medicine started to play an important role in the treatment of diseases all over the world, mostly because the medicinal system in many underdeveloped countries is still inexistent. Due to the above-mentioned considerations, the World Health Organization (WHO) has developed a strategic plan to promote alternative medicine by publishing four volumes containing 118 monographs regarding medicinal plants. The main purpose of WHO is to train people to develop their monographs due to the diversity of the flora that is characteristic from one territory to another [1-12].

It is also well known that the medicinal plants act as radical scavengers of free radicals that appear in the human body through metabolism, pollution, contaminants and different medical treatments, factors that lead to the appearance of some serious diseases such as diabetes, cancer or neurological disorders. The composition and antioxidant activity of plant extracts has been determined using various spectrophotometric or chromatographic methods [3, 8, 13, 14]. However, high-performance liquid chromatography (HPLC) is recommended by WHO and European Medicine Agency (EMA) for analysis of plant-based samples (additives, toxins, residues or food adulteration) [15-21]. Using these methodologies, a large volume of data may result leading to a difficult or even impossible interpretation of the obtained results, therefore chemometric methods like principal component analysis (PCA), hierarchical cluster analysis (HCA) or linear discriminant analysis (LDA) are successfully employed [22-26].

Considering all the above, the aim of this study is to characterize and classify 42 hydroalcoholic extracts prepared from medicinal plants using the chromatographic profile obtained at 242, 260, 280, 320, 340 and 380 nm according to the antioxidant capacity obtained using the 2,2-diphenyl-1-picrylhydrazyl (DPPH•) procedure.


## RESULTS AND DISCUSSION

The 42 samples of the commercially available plant extracts from the Romanian flora subjected to a comprehensive holistic characterization and classification according to their antioxidant activity estimated by radical scavenging assay using the 2,2-diphenyl-1-picrylhydrazyl (DPPH•) procedure and chromatographic profiles are presented in Table 1.

**Table 1.** Name and total radical scavenging capacity (RSC %) determined by
DPPH$^{\bullet}$ assay of the investigated hydroalcoholic extracts

| No. | Name | Scientific name | RSC$^*$ % | Antioxidant activity |
|---|---|---|---|---|
| 1 | Blueberry | *Vaccinium myrtillus* | 46.71 | High |
| 2 | Lingon berry | *Vaccinium vitis-idaea* | 36.58 | High |
| 3 | Rosemary | *Rosmarinus officinalis* | 31.01 | High |
| 4 | Hoary willowherb | *Epilobium parviflorum* | 29.82 | High |
| 5 | Lady's mantel | *Alchemilla vulgaris* | 29.61 | High |
| 6 | Quaking aspen | *Plopus nigra* | 27.97 | High |
| 7 | Lemon balm | *Melissa officinalis* | 27.36 | High |
| 8 | Sage | *Salvia officinalis* | 27.36 | High |
| 9 | Silver brich | *Betula pendula* | 26.27 | High |
| 10 | Saint John's wort | *Hypericum perforatum* | 21.12 | Moderate |
| 11 | Hawthorn | *Crataegus monogyma* | 18.74 | Moderate |
| 12 | Breckland thyme | *Thymus serpyllum* | 15.48 | Moderate |
| 13 | Burdock | *Arctium lappa* | 13.98 | Moderate |
| 14 | Great celandine | *Chelidonium majus* | 12.86 | Moderate |
| 15 | Lady's bedstraw | *Galium verum* | 11.16 | Moderate |
| 16 | Common juniper | *Juniperus communis* | 10.13 | Moderate |
| 17 | Yarrow | *Achillea millefolium* | 9.45 | Moderate |
| 18 | Spinycockle-bur | *Xanthium spinosum* | 9.44 | Moderate |
| 19 | Lavender | *Lavandula augustifolia* | 8.93 | Moderate |
| 20 | Artichoke | *Cynara scolymus* | 7.42 | Moderate |
| 21 | Liquorice | *Glycyrrhiza glabra* | 4.93 | Low |
| 22 | Gentian | *Gentiana asclepiadea* | 4.46 | Low |
| 23 | Echinacea | *Echinacea purpurea* | 4.38 | Low |
| 24 | Comfrey | *Symphytum officinale* | 4.32 | Low |
| 25 | Milk thistle | *Silybum marianum* | 3.75 | Low |
| 26 | Nettle | *Urtica dioica* | 3.69 | Low |
| 27 | Heart's ease | *Viola tricolor* | 3.06 | Low |
| 28 | Motherwort | *Leonurus cardiaca* | 2.78 | Low |
| 29 | Ginger | *Zingiber officinale* | 2.26 | Low |
| 30 | Valerian | *Valeriana officinalis* | 2.09 | Low |
| 31 | Shepherd's purse | *Capsella bursa-pastoris* | 1.78 | Low |
| 32 | Horsetail | *Equisetum arvense* | 1.70 | Low |
| 33 | Dill | *Anethum graveolens* | 1.62 | Low |
| 34 | Garlic | *Allium sativum* | 1.45 | Low |
| 35 | Mistletoe | *Viscum album* | 1.20 | Low |
| 36 | Elder | *Sambuctus nigra* | 1.19 | Low |
| 37 | Chili pepper | *Capsicum annuum* | 1.05 | Low |
| 38 | Sweet flag | *Acorus calamus* | 1.00 | Low |
| 39 | Hogweed | *Heracleum sphondylium* | 0.68 | Low |
| 40 | Wolf's-foot clubmoss | *Lycopodium clavatum* | 0.37 | Low |
| 41 | Celery | *Apium graveolens* | 0.25 | Low |
| 42 | Ramson | *Allium ursinum* | 0.22 | Low |

The visual examination of the profile of antioxidant activities highlights two
or three groups: high antioxidant activity (26.27-46.71%), group of samples 1-9,
moderate antioxidant activity (7.42-21.12%), group of samples 10-20, and low
antioxidant activity (0.22-4.93%), last group of samples 21-42.

### Fuzzy divisive hierarchical clustering

The partitions obtained applying fuzzy divisive hierarchical clustering (FDHC), using the chromatographic data (without any preprocessing), are presented in Table 2. This fuzzy algorithm provides only two classes in the majority of cases: the first one includes the plant extracts with high and moderate antioxidant activity and the second one the plant samples with low antioxidant activity. In addition, the 2D-representation of the degrees of membership (DOMs) corresponding to the two fuzzy partitions (242 nm) presented in Fig. 1 shows that there are some "anomalies": samples 21 and 22 which belong to the class with low antioxidant activity are classified in the group with high antioxidant activity and samples 14, 16, 18 and 20 are classified wrong as well.

**Table 2.** The fuzzy clustering results obtained applying
fuzzy divisive hierarchical clustering

| Fuzzy partition history | 242 nm | | 260 nm | | 280 nm | | 320 nm | | 340 nm | | 380 nm | |
|---|---|---|---|---|---|---|---|---|---|---|---|---|
| | Sample | DOM (range) | Sample | DOM (range) | Sample | DOM (range) | Sample | DOM (range) | Sample | DOM (range) | Sample | DOM (range) |
| A1 | 13, 19, 21, 6, 17, 4, 10, 5, 15, 11, 8, 2, 3, 1, 22, 9, 12, 7 | 0.503 - 0.714 | 11, 27, 21, 6, 19, 2, 15, 4, 9, 22, 5, 1, 8, 3, 12, 7 | 0.506 – 0.707 | 19, 6, 17, 13, 9, 4, 5, 1, 3, 8, 12, 7 | 0.524 – 0.740 | 15, 6, 1, 13, 17, 3, 8, 12, 7 | 0.509 – 0.745 | 11, 9, 27, 15, 6, 17, 1, 13, 3, 12, 8, 7 | 0.506 – 0.732 | 21, 3, 15, 2, 27, 1, 9, 5 | 0.514 – 0.663 |
| A2 | 33, 39, 14, 27, 16, 24, 23, 35, 32, 38, 26, 25, 29, 18, 41, 42, 40, 34, 37, 36, 30, 20, 31, 28 | 0.510 – 0.943 | 14, 39, 17, 13, 24, 33, 38, 35, 23, 26, 16, 10, 25, 29, 41, 32, 42, 34, 36, 37, 18, 40, 30, 20, 31, 28 | 0.505 – 0.945 | 14, 11, 21, 15, 2, 27, 22, 39, 23, 24, 18, 25, 26, 16, 29, 41, 10, 42, 35, 34, 37, 38, 40, 36, 30, 20, 33, 32, 31, 28 | 0.519 – 0.970 | 11, 39, 27, 9, 19, 21, 2, 23, 24, 5, 18, 26, 22, 14, 20, 4, 40, 16, 29, 30, 41, 42, 38, 34, 25, 10, 37, 36, 35, 33, 28, 32, 31 | 0.526 – 0.981 | 39, 2, 21, 22, 19, 23, 24, 5, 26, 18, 16, 14, 20, 29, 33, 30, 40, 41, 42, 34, 25, 36, 10, 35, 38, 4, 37, 28, 32, 31 | 0.574 – 0.971 | 6, 11, 8, 16, 25, 22, 17, 19, 12, 7, 14, 35, 4, 33, 39, 30, 10, 36, 13, 29, 41, 42, 34, 24, 38, 23, 37, 40, 20, 32, 18, 31, 26, 28 | 0.503 – 0.986 |
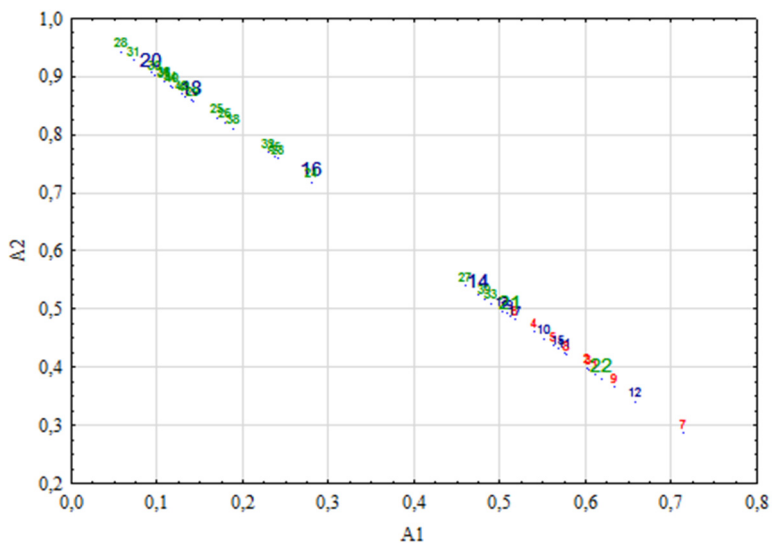
**Figure 1.** 2-D scatterplot of DOMs corresponding
to the two hierarchical fuzzy partitions (A1 and A2)

## Principal component analysis

The results obtained from PCA analysis using again the raw data
matrix indicate a significant reduction in the number of variables (Fig. 2).
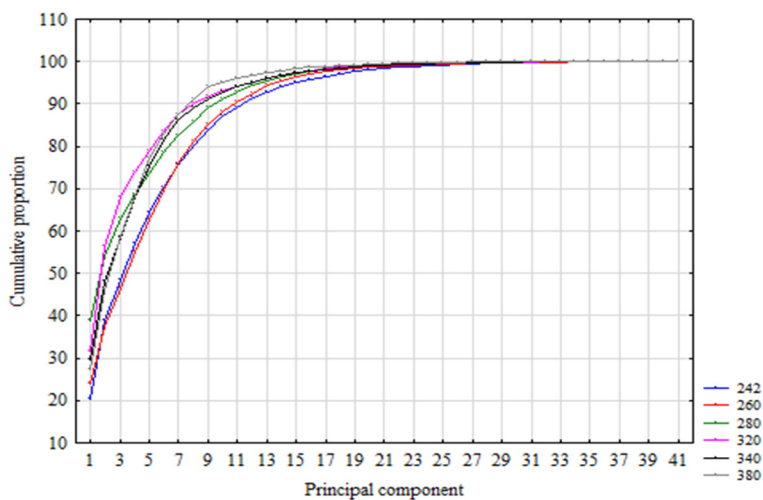


**Figure 2**. Cumulative proportion profile

In all cases, the first 41 PCs explain the total variance (100%) of the data. The variance corresponding to each PC1 is not so different, accounting, for example, more than 38% (the highest proportion) in the case of data corresponding to 280 nm detection wavelength and only 20% (the smallest proportion) for 242 nm (Table 3). However, surprisingly, the graphical representation of the samples using the first two components corresponding to data obtained at 242 nm, for example, indicates a satisfactory separation of samples according to the antioxidant activity (Fig. 3) in good agreement with the fuzzy clustering results discussed above.

**Table 3.** Proportion of the first five PC's obtained after PCA method
was applied on the data obtained at 242, 260, 280, 320, 340, and 380 nm.

| PC's | Proportion % | | | | | |
| --- | --- | --- | --- | --- | --- | --- |
| | 242 nm | 260 nm | 280 nm | 320 nm | 340 nm | 380 nm |
| PC1 | 20.33 | 23.81 | 38.72 | 31.45 | 29.67 | 27.33 |
| PC2 | 18.50 | 13.59 | 15.40 | 24.87 | 18.28 | 18.66 |
| PC3 | 9.58 | 9.07 | 8.96 | 11.54 | 10.50 | 12.62 |
| PC4 | 8.73 | 8.55 | 5.63 | 5.94 | 9.52 | 9.58 |
| PC5 | 7.16 | 7.76 | 4.93 | 5.11 | 7.25 | 8.89 |

The PC1 profile shows a similar contribution to the separation of the samples according to the antioxidant activity for 242, 260, 280 and 320 nm. It also can be seen a high contribution of PC1 to the separation of sample number 6 (quaking aspen) sample that in a PC1 vs PC2 representation appears as an outlier (Fig. 3). Besides, all the results obtained by applying PCA supports the idea of using the orthogonal and clean scores corresponding to the first 41 PCs in HCA and LDA classification of medicinal plant extracts according to their antioxidant activity.
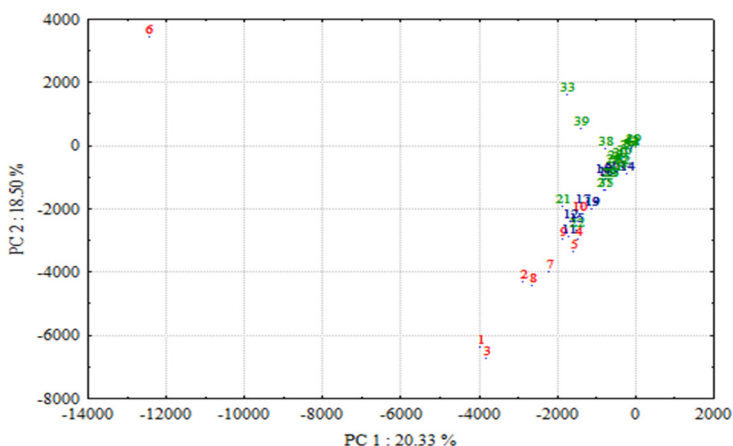


**Figure 3.** PC1-PC2 scatterplot for the score obtained at 242 nm

### Hierarchical cluster analysis

The dendrogram (Fig. 4) was obtained applying the hierarchical cluster analysis (the Ward method as linkage method and Manhattan distance as a measure of similarity) to the data corresponding to the 41 PCs (242 nm), highlighting well defined groups of plant extracts in good agreement to all the results obtained by using fuzzy clustering method and also PCA. As it can be seen in Fig. 4 there are 2 major clusters: one contains the samples with high and moderate antioxidant capacity with few exceptions (samples 21 and 22), and the group of samples with low antioxidant capacity including the following exceptions, namely 6, 10, 16, 18, 19 and 20 samples. HCA shows samples that are the most similar, that is are the closest in the sense of having the lowest dissimilarity, the group with low antioxidant capacity containing more similar plants regarding the characteristic taken into consideration (antioxidant capacity).
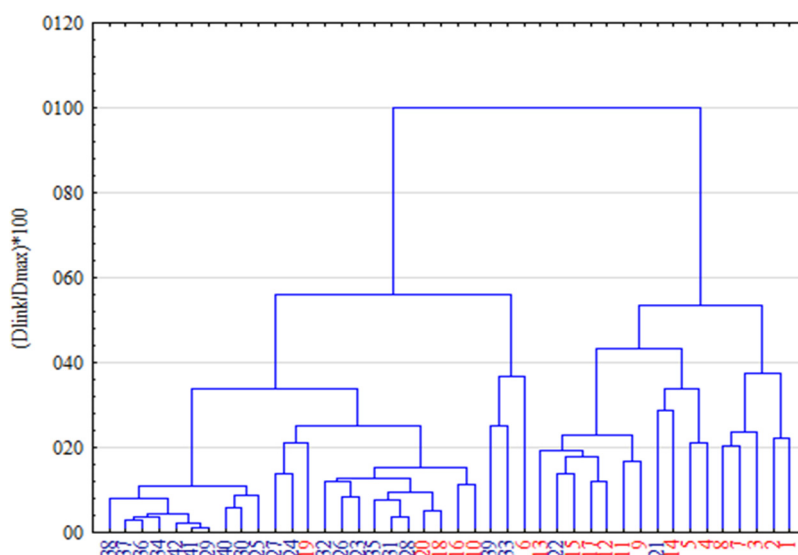


**Figure 4.** Dendrogram corresponding to the medicinal plant extracts obtained using the Ward method as linkage method and Manhattan distance as a measure of similarity

### Linear discriminant analysis

The combination of PCA with LDA led to the most efficient discrimination of the investigated medicinal plants in two classes. The results obtained applying forward stepwise LDA to the first 41 PCs indicate a very good separation of the samples in almost all cases according to the correct classification rate of original

PC score data (Table 4): the highest value (100%) was obtained for raw data in the majority of cases (242, 260, 280, 320 and 340 nm) and the lowest value (78.6%) for the score data corresponding to the 380 nm. All of the above statements concerning the efficiency of this methodology are well supported by the values of quality performance features obtained by applying the leave-one-out (LOO) cross-validation approach. The results of the cross-validation presented also in Table 4 pointed out a correct classification rate in good agreement to the results obtained for the classification of the original PC score data: the highest value (100%) was obtained again for the PC score data corresponding to 254 nm and the lowest value (76.2%) for the score data obtained at 380 nm.

**Table 4.** Values of quality performance features from PCA-LDA approach applied to each wavelength (242, 260, 280, 320, 340, 380 nm) for medicinal plants classification according to their antioxidant capacity

| Data | DAD wavelength detection | | | | | | | | | | | |
|---|---|---|---|---|---|---|---|---|---|---|---|---|
| | 242 nm | | 260 nm | | 280 nm | | 320 nm | | 340 nm | | 380 nm | |
| | Original % | *LOO % | Original % | LOO % | Original % | LOO % | Original % | LOO % | Original % | LOO % | Original % | LOO % |
| [2]Raw data | 100.0 | 100.0 | 100.0 | 95.2 | 100.0 | 95.2 | 100.0 | 97.6 | 100.0 | 92.9 | 78.6 | 76.2 |
| [2]Normalized | 88.1 | 85.7 | 100.0 | 97.6 | 100.0 | 97.6 | 95.2 | 90.5 | 85.7 | 78.6 | 92.9 | 85.7 |
| [2]Autoscaled | 100.0 | 97.6 | 100.0 | 90.5 | 100.0 | 95.2 | 95.2 | 90.5 | 100.0 | 100.0 | 85.7 | 85.7 |
| [3]Raw data | 92.9 | 90.5 | 85.7 | 81.0 | 83.3 | 76.2 | 85.7 | 78.6 | 85.7 | 76.2 | 69.0 | 64.3 |
| [3]Normalized | 71.4 | 57.1 | 88.1 | 81.0 | 78.6 | 66.7 | 85.7 | 73.8 | 72.9 | 60.3 | 73.8 | 73.8 |
| [3]Autoscaled | 88.1 | 81.0 | 92.9 | 81.0 | 83.3 | 76.2 | 76.2 | 64.3 | 85.7 | 76.2 | 90.5 | 78.6 |

*Leave-one-out validation; [2]two predefined classes; [3]three predefined classes

## CONCLUSION

This study used the chromatographic data collected at different wavelengths (242, 260, 280, 320, 340, 380 nm) for characterization and classification of medicinal plants according to their antioxidant capacity. The best results, according to the multivariate methods employed are those obtained at 242 nm detection wavelength (wavelength where the majority of the antioxidant compounds present in the samples are detected). The FDHC including classical methods PCA, HCA and LDA separated the samples into well defined groups with few exceptions: *Glycyrrhiza glabra, Gentiana Asclepiades, Chelidonium majus, Juniperus communis*, *Xanthium spinosum*, and *Cynara scolymus.* The presence of these samples in the wrong class is made according to the concentration

and not by the type of compounds (compounds that are more or less similar) found in the medicinal plant extracts that have antioxidant activity. The leave-one-out cross-validation also suggested that the samples are divided into two main classes with a correct classification rate of 100% compared with 90.5% for three classes. Moreover, this study highlights that the data can be utilized without any preprocessing: the normalization and autoscaling didn't bring any improvements of the clustering results. Another important conclusion of this study is that the scores corresponding to the principal components that explained 100% of the variance (41 PCs) can be used instead of the initial variables (4501 variables), the same results being obtained, minimizing the speed and time of the analysis.

## EXPERIMENTAL SECTION

### Chemicals and plant samples

The reagents used in this study were of analytical grade, the HPLC grade ammonium acetate and acetonitrile were from Merck (Darmstadt, Germany) and the plant samples belong to Dacia Plant manufacturer (Brașov, România) (Table 1). A number of 42 plant samples commercially available were obtained, according to the manufacturer using different parts of plants and different water: ethanol ratios comprised within the range 35-80% ethanol. The label that accompanies the alcoholic extracts offers the necessary information regarding the quality of the vegetal material, used to obtain the final products, namely, the plants meet the highest standards of quality, and are procured from their own cultures or partner producers.

### The HPLC protocol

The commercialized extracts were analyzed in order to separate the phytoconstituents using an HPLC-DAD approach. The device used to perform the separation is an Agilent 1200 HPLC system (Waldbronn, Germany) which is equipped with an on-line vacuum degasser, quaternary pump, temperature-controlled sample tray, automatic injector, a column thermostat compartment, and a DAD detector. The chromatographic column used to perform the separations was a Zorbax SB-C18 column (250 mm × 4.6 mm, 5 µm particle size) also from Agilent. The parameters used were: an injection volume of 30 µL (0.22 µm filtered extract), a column temperature of 30 °C and the flow rate of 1 mL/min. In order to optimize the method, several preliminary tests were employed using different experimental conditions. The final results were

obtained (maximum number of compounds separated and maximum resolution) using a multistep isocratic and gradient elution system: solvent A, 10 mM ammonium acetate pH 5 and as solvent B acetonitrile. The steps were as follows: 0-2 min isocratic at 5% B, 2-10 min from 5 to 35% B, 10-20 min from 35% to 45% B, 20-25 min from 45% to 95% B, 25-28 min from 95% to 100% B, 28-32 min isocratic at 100% B and 32-32.1 min back to 5% B where was kept until 35 min. The detection of the compounds in the UV-Vis range was performed using the DAD detector that measured the entire spectrum in 240-750 nm region (2 nm resolution), every 2 seconds and the chromatograms were monitored at 242, 260, 280, 320, 340 and 380 nm. The chromatograms and the mean spectra of the main chromatographic peaks were exported and analyzed using advanced chemometrics.

### Antioxidant activity assay

The antioxidant capacity of the investigated samples was determined using the 2,2-diphenyl-1-picrylhydrazyl (DPPH$^\bullet$) method. In order to perform the analysis, the extracts needed to be diluted at a dilution rate of 1:50 with a mixture of ethanol-water (60:40). The total radical scavenging capacity (RSC parameter expressed as a percent of consumed DPPH$^\bullet$ radical) of the hydroalcoholic extracts was measured at 518 nm (absorbance of DPPH$^\bullet$ solution) after 30 minutes, the required amount of time for the reaction between DPPH and samples to take place. The ratio between the investigated samples and the DPPH$^\bullet$ solution (150 µmol L$^{-1}$ prepared in ethanol) was 0.1 mL: 3 mL. The DPPH$^\bullet$ solution was daily prepared and protected from light throughout the analysis time in order to minimize the free radical decomposition.

### Chemometrics

Cluster analysis is a large field, both within fuzzy sets theory and beyond it. Clustering and classification are useful since they allow meaningful generalizations to be made about large quantities of data by recognizing among them a few basic patterns. In classical cluster analysis, each object must be assigned to exactly one cluster. This is a source of ambiguity and error in cases of outliers or overlapping clusters and allows a loss of information. This kind of vagueness and uncertainty can, however, be taken into account by using the *theory of fuzzy sets* introduced by Zadeh in 1965 [27, 28]. A *fuzzy set* or a fuzzy subset is a collection of ill-defined and not-distinct objects with un-sharp boundaries in which the transition from membership to non-membership in a subset of a reference set is gradual rather than abrupt. The theory of fuzzy set is basically a theory of graded concepts. A central concept in the fuzzy set theory is that it is permissible for an element to belong partly to a fuzzy set (partition). It provides

an adequate conceptual framework as well as a mathematical tool to model the real-world problems which are often obscure and indistinct, namely fuzzy [29-32].

HCA was extensively used to group experimental variables or samples into clusters, based on similarity within a class and dissimilarity between different classes, according to a predefined criterion. The most common clustering procedure is known to be Ward's method with Euclidean distance as a similarity measure.

LDA is a classification procedure (supervised technique), which needs an initial sample classification into predefined classes. The LDA model contains linear discriminant functions that can classify data, after a predefined criterion. The model is usually validated through leave-one-out classification, which means that each sample is tested, using the model, as an unknown sample. The higher the percentage of correct classification rate by cross-validation, the better the model is. Unlike the other two classical methods, which are clustering/ classification methods, PCA aims to transform the original variables to a new set of variables, uncorrelated and cleaned of noise, called principal components. The high variance of the data set is explained in many cases by the first principal components.

All the graphs and some chemometric methods were performed using Statistica 8.0 (StatSoft, Inc. 1984–2007, Tulsa, USA) software and leave-one-out cross-validation with IBM SPSS Statistics (International Business Machines Corp., New York, USA).

## ACKNOWLEDGMENTS

## REFERENCES

1. M. Yan; M. Chen; F. Zhou; D. Cai; H. Bai; P. Wang; H. Lei; Q. Ma; *J. Pharm. Biomed. Anal.*, **2019**, *164*, 734–741.
2. R. A. Dar; M. Shahnawaz; P. H. Qazi; *J. Phytopharmacol.*, **2017**, *6*, 349-351.
3. WHO monographs on selected medicinal plants, Volume 4, **2009.**
4. M. Al-Fatimi; *J. Ethnopharmacol.,* **2019**, *241*, 111973. doi:https://doi.org/10.1016/j.jep.2019.111973.
5. B. A. R. Hassan; *Pharmaceut. Anal. Acta.,* **2012**, *3*, DOI: 10.4172/2153-2435.1000e139

6.  M. A. Motaleb; Selected medicinal plants of Chittagong hill tracts, IUCN, Dhaka, **2011**.
7.  F. Jamshidi-Kia; Z. Lorigooini; H. Amini-Khoei; *J. Herbmed. Pharmacol*., **2018**, *7*, 1-7.
8.  M. Rafieian-Kopaei; *J. Herb. Med. Pharmacol*., **2012**, *1*, 1–2.
9.  S. Guo; X. Cui; M. Jiang; L. Bai; X. Tian; T. Guo; Q. Liu; L. Zhang; C.-Tang Ho; N. Bai; *J. Food. Drug. Anal*., **2016**, *30*, 1-8.
10. R. Singh; *J. Plant. Sci*., **2015**, *3*, 50-55.
11. F. Jamshidi-Kia; Z. Lorigooini; H. Amini-Khoei; *J. Herbmed. Pharmacol*., **2018**, *7*, 1-7.
12. M. Esteki; Z. Shahsavari; J. Simal-Gandara; *Food Res. Int*., **2019**, *122*, 303-317.
13. T. O. Obafemi; A. C. Akinmoladun; M. T. Olaleye; A. Onasanya; K. C. Komolafe; J. A. Falode; A. A. Boligon; M. L. Athayde; *J. Appl. Pharm. Sci*., **2017**, *7*, 10-118.
14. Z. Akar; N. A. Burnaz; *Food Sci. Technol.,* 2019, doi:https://doi.org/10.1016/j.lwt.2019.05.110
15. A. A. Boligon; M. L. Athayde; *Austin Chromatogr*., **2014**, *1*, 1-2.
16. S. M. Dhole; P. B. Khedekar; N. D. Amnerkar; *Pharm. Methods*, **2012**, *3*, 68-72.
17. Y. Zhao; X.-Min Youb; H. Jiang; G.-Xin Zoub; B. Wanga; *J. Chromatogr. B*, **2019**, *1104*, 11–17.
18. A. S. Rathore; S. Joshi; Process Analysis: High Performance Liquid Chromatography, Elsevier, New Delhi, **2018**.
19. O. Deveoglu; E. Torgan; R. Karadag; *Color. Technol*., **2012**, *128*, 133-138.
20. J. Lozano-Sanchez; I. Borras-Linares; A. Sass-Kiss; A. Segura-Carretero; Chromatographic Technique: High-Performance Liquid Chromatography (HPLC), Modern Techniques for Food Authentication, Elsevier, **2018.**
21. Q. Nie; S. Nie; High-performance liquid chromatography for food quality evaluation, Evaluation Technologies for Food Quality, Elsevier, **2019**.
22. I. A. Sima; C. Sârbu; R. D. Nașcu-Briciu; *Chromatographia*, **2015**, *78*, 13-14.
23. S. P. Mishra; U. Sarkar; S. Taraphder; S. Datta; D. P. Swain; R. Saikhom; S. Panda; M. Laishram; *Int. J. Lives. Res*., **2017**, *5*, 60-78.
24. R. G. Brereton; Applied Chemometrics for Scientists, John Wiley & Sons: Ltd. Chichester, **2007**.
25. I. A. Sima; M. Andrási; C. Sârbu; *J. Chromatogr. Sci*., **2018**, *56*, 49–55.
26. C. Sârbu; R. D. Nașcu-Briciu; A. Kot-Wasik; S. Gorinstein; A. Wasik; J. Namieśnik; *Food Chem*., **2012**, *130*, 994-1002.
27. L. A. Zadeh; *Inf. Control*., **1965**, *8*, 338-353.
28. F. Hoppner; R. K. Klawonn; T. Runkler; Fuzzy Cluster Analysis, John Wiley &Sons, Ltd. Chichester, **1999**.
29. H. Pop; D. Dumitrescu; C. Sârbu; *Anal. Chim. Acta*, **1995**, *310*, 269-279.
30. H. Pop; C. Sârbu; O. Horovitz; D. Dumitrescu; *J. Chem. Inf. Comput. Sci*., **1996**, *36*, 465-482.
31. C. Sârbu; K. Zehl; J. W. Einax; *Chemom. Intell. Lab. Syst*., **2007**, *86*, 121-129.
32. C. Sârbu; H. F. Pop; Fuzzy Soft-Computing Methods and Their Applications in Chemistry in Reviews in Computational Chemistry, K.B. Lipkowitz, R. Larter and T. R. Cundari (eds.), Wiley-VCH, **2004**, Chapt. 5, 249-332.

# EFFECT OF SOME ANTIOXIDANT FOOD ADDITIVES ON THE DEGRADATION OF CORNELIAN CHERRY ANTHOCYANINS

**BIANCA MOLDOVAN[a], LUMINIŢA DAVID[a*]**

**ABSTRACT.** Anthocyanin rich fruits present a great potential as source of natural food colorants. Their use in the food industry is limited by their low stability. The influence of storage media and addition of three widely used antioxidant food additives, such as citric acid, ascorbic acid and butylated hydroxyanisole, on the stability of Cornelian cherry anthocyanins, was investigated at room temperature. In aqueous solutions, the degradation of these valuable pigments occurred slower compared to alcoholic solution. Addition of ascorbic acid significantly enhanced anthocyanins degradation in ethanolic or aqueous solutions, while citric acid and BHA had a positive effect on the anthocyanins' stability in ethanol. The Cornelian cherry anthocyanins' degradation followed first-order reaction kinetics. The obtained kinetic parameters (reaction rate constants k and half-lifes $t_{1/2}$) clearly indicated that Cornelian cherry anthocyanins stored in ethanol in presence of citric acid present the highest stability, the degradation rate constant being $0.74 \cdot 10^{-3}$ h$^{-1}$.

*Keywords: Cornus mas L., antioxidant food additives, anthocyanins, degradation kinetics*

## INTRODUCTION

Consumers food choices are strongly influenced by sensory parameters of foods among which colour plays an important role. The slightest changes of this characteristic, which can occur during processing or storage, can affect the people's perception on the quality of food products, the loss of the colour being an important factor in assessing the food quality. The compounds used in the food industry in order to confer vivid colours to products are synthetic dyes which generally imply negative effects on the human health due to their high toxicity. As a consequence, there is a high concern in using synthetic dyes as food colorants and an increased tendency to replace these compounds

---

[a] *Babeş-Bolyai University, Faculty of Chemistry and Chemical Engineering, 11 Arany Janos str., RO-400028, Cluj-Napoca, Romania*
*\* Corresponding author: muntean@chem.ubbcluj.ro*

with natural pigments. One of the most valuable class of water soluble natural coloured compounds are anthocyanins which can be successfully replace synthetic dyes as a safe alternative. Adding these natural phytocomponents to foods will not only impart vivid colours ranging from red to purple and blue but will also confer functional characteristics to foods due to their wide range of healthy beneficial effects. They can be used as bioactive ingredients in a large number of functional foods as a consequence of their high antioxidant capacity which confer them the potential of reducing the risk of chronic diseases such as cancer, neurodegenerative and cardiovascular diseases. They are also known to possess antimicrobial, anti-diabetic and anti-inflammatory properties [1, 2]. Anthocyanin can be used as versatile tools for material engineering and surface functionalization [3-5]. However, their utilisation as natural food pigments is restricted due to their vulnerability to degradation during processing or storage of food products which mostly leads to an undesirable loss of colour. The anthocyanins' degradation is a complex process which is strongly influenced by many factors such as chemical structure of the pigment, temperature, pH value, light, oxygen, enzymes and presence of metals [6]. Hence, there is a growing need in finding new sources, plants rich in anthocyanic pigments and investigating their stability in various processing and storage conditions in order to use these compounds as healthy natural colorants in the food industry.

Cornelian cherries are the edible fruits of *Cornus mas* L. plant original from Middle East and South-Eastern Europe. They are less consumed fresh due to their astringency but are traditionally used as ingredients of jams, marmalades, compotes, vinegars and liquors [7]. The Cornelian cherry fruits are recognised as a rich source of health promoting compounds such as vitamin C and polyphenols among which anthocyanins are present in significant amount [8-10]. All these compounds are linked with a high range of biological activities reported for *Cornus mas* fruits such as antioxidant, anti-inflammatory, anticancer and have been traditionally used in the treatment of diarrhea, fever, urinary tract infections, malaria and kidney stones [11-14]. Due to all these biological properties, the chemical composition of Cornelian cherry fruits was intensively investigated. Their anthocyanic profile was established, and various results were reported, depending on cultivars and environmental factors. The 3-glycosylated cyanidin, pelargonidin and delphinidin derivatives were found to be the most common red pigments of Cornelian cherries. Milenckovic Andelkovic and co-workers identified three major anthocyanins: cyanidin-3-galactoside, pelargonidin-3-glucoside and delphinidin-3-galactoside [15] while Moldovan et al. reported the identification and quantification of cyanidin-3-galactoside, pelargonidin-3-glucoside and delphinidin-3-galactoside [16], results in agreement with those of Pawlowska et al. [17]. Using HPLC/DAD and UPLC-ESI/MS techniques, Sozanski et al. identified seven anthocyanins in Cornelian cherry fruits, cyanidin-3-galactoside being the major one [18].

Food products regularly contain antioxidant additives responsible for their protection against oxidation, used to increase their shelf life. Among these, the most frequently used antioxidants in food industry are ascorbic acid (AA), phenolic compounds such as tocopherols, butylated hydroxytoluene (BHT) and butylated hydroxyanisole (BHA), which act as free radical scavengers or singlet oxygen quenchers, and citric acid (CA) or EDTA which exert their antioxidant effect by chelating pro oxidative metals [19]. Apart its antioxidant activity, ascorbic acid is also added to food products, especially fruit juices, to increase their nutritional value.

The aim of the present study was to evaluate the influence of some antioxidant food additives, such as AA, BHA and CA on the stability of Cornelian cherries' anthocyanins by storage at room temperature in aqueous and alcoholic media and to determine the kinetic parameters of the degradation process of these compounds in various conditions, in order to use Cornelian cherry fruits anthocyanins as healthy food colorants in fruit derived products and alcoholic beverages.


## RESULTS AND DISCUSSION

Cornelian cherries are red fruits, colour due to the presence of anthocyanins, therefore they can be exploited as a valuable source of anthocyanin pigments. Anthocyanins are known to be degraded or decolorized during food processing and storage. Their stability are influenced by some factors such as chemical structure of the pigment, pH value, temperature, solvents, oxygen, and presence of ascorbic acid, metal ions and sugars. The presence of a glycosyl moiety and of acyl groups linked to the sugars attached to the pigment molecule positively affects the stability and colour of anthocyanins. The position of these substituents on the anthocyanin skeleton was proved to be important for the stabilisation effect. The loss of attached sugars results in a rapid decomposition and irreversible loss of colour, due to a higher reactivity of non-glycosylated compounds. Although at room temperature anthocyanins are quite stable at acidic pH, they rapidly degrade at elevated temperatures or alkaline media. The reaction of *orto*-diphenolic groups with metal ions (iron, copper, aluminium, tin) leads to the formation of stable red, blue and violet metal chelates, but the use of these metal complexes in the food industry is still limited [20]. Ascorbic acid was found to significantly enhance anthocyanins' degradation, especially at elevated temperatures, possible as a result of condensation reaction between ascorbic acid and anthocyanins. A free radical mechanism for this deterioration process was also proposed, involving an oxidative cleavage reaction of the pyrylium ring. However, the chemical structures of the degradation products of anthocyanins in the presence of ascorbic acid have not yet been determined [20, 21].

In order to isolate these pigments from the fruits, these were subjected to a solid-liquid conventional extraction, using ethanol as solvent. In order to investigate the combined effect of storage solvent and presence of the antioxidant food additives on the stability of anthocyanins isolated from *Cornus mas* fruits, the variation of the total anthocyanin content (TAC) of the extracts was monitored daily over a period of 8 days of storage in water and ethanol, in the presence of commonly used additives such as AA, CA and BHA, at room temperature. The quantitative evaluation of anthocyanins was accomplished by using a widely applied method developed by Giusti and Wrolstad [22], known as the pH differential method. This method exploits the structural, and hence the colour, dependence of anthocyanins on pH value. At pH=1, the anthocyanins are present as a red coloured flavylium cation while raising the pH to 4.5 will lead to structure change into a colourless carbinol. By using UV-Vis spectroscopy, measuring the absorbance of an anthocyanin solution at these two pH values, allows the determination of anthocyanins' concentration. The total monomeric anthocyanin content (TAC) of the Cornelian cherry fruits extract was assessed by applying this method using equations (1, 2) :

$$TAC = \frac{A \cdot MW \cdot DF \cdot 1000}{\varepsilon \cdot l}$$

(1)

where: A = absorbance, calculated as: (equation 2)

$$A = (A_{pH\ 1.0} - A_{pH\ 4.5})\ _{517\ nm} - (A_{pH\ 1.0} - A_{pH\ 4.5})\ _{700\ nm}$$

(2)

MW = 449.2 g/mol (molecular weight of Cy-3-Glu)
DF = dilution factor
l = path length (1 cm)
ε = 26900 L/mol/cm (molar extinction coefficient of Cy-3-Glu)
1000 = conversion factor from gram to milligram

The average concentration of monomeric anthocyanins in the Cornelian cherry extract was 23.54±1.12 mg/L.

The changes of total monomeric anthocyanin concentration were monitored during storage of Cornelian cherry anthocyanins in water and ethanol in the presence of AA, CA and BHA. After 192 hours of storage, the anthocyanin concentration decreased to 77.78% for the untreated sample stored in ethanol while adding ascorbic acid resulted in a concentration decrease to 73.96%. A more dramatic concentration decrease was observed for the anthocyanins stored in water in the presence of AA, only 41.75% of the initial TAC being determined after the same time interval. The deleterious effect of

AA on the anthocyanin stability was already mentioned in other studies [23-26]. The presence of AA accelerates anthocyanins' degradation leading to a significant loss of colour during storage due to either the direct condensation of anthocyanins with ascorbic acid or to formation of hydrogen peroxide which cleaves the pyrylium ring by a free radical mechanism [25, 27]. Our results are in agreement with those obtained in studies investigating anthocyanins' degradation from various sources such as blackcurrant, elderberry, purple sweet potato, pomegranate [23, 26, 28].

The addition of other food antioxidants such as CA or BHA did not present a similar destabilizing effect on the Cornelian cherry anthocyanins as AA. CA addition resulted in a slight increase of the anthocyanin stability, compared to sample stored without any antioxidant additive, by storage in ethanol while storage in water resulted in no significant influence of CA on anthocyanin stability. Butylated hydroxyanisole (BHA) enhanced the anthocyanin stability when these pigments were stored in alcohol, while a slight negative effect of this antioxidant additive was observed at water storage, in line with findings of Cata et al. [29] by storage of mulberry anthocyanins.

Anthocyanin degradation is known to follow a first order reaction kinetics [30-33]. Determining the kinetic parameters of this process such as degradation rate constant (k) and half-life value ($t_{1/2}$) is very important to compare the combined influence of the added food additives and storage solvent on the stability of the anthocyanic pigments. In order to determine these parameters the variation of concentration during storage was fitted to a first order kinetic model. The kinetic plots of anthocyanins storage degradation process in the investigated conditions are given in Figure 1 (storage in water) and Figure 2 (storage in ethanol).

The high values of the determination coefficients ($R^2 > 0.95$, Table 1) for all treatments confirm the fact that the first order kinetic model is the most suitable for predicting the Cornelian cherries anthocyanin degradation process. The kinetic rate constants k for each degradation reaction was calculated using equation (3):

$$C = C_0 \, exp(-kt) \tag{3}$$

where: C and $C_0$ are the total anthocyanin content (mg/L) at time t and t=0, respectively
t = time (h)
k = rate constant ($h^{-1}$)
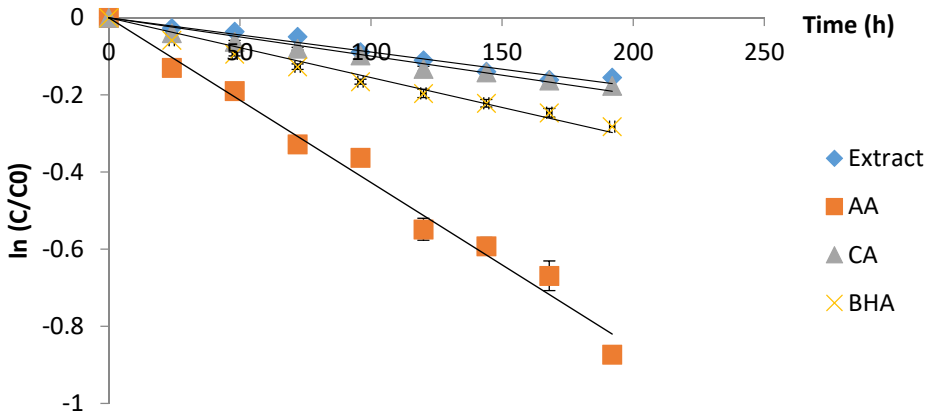
**Figure 1.** The degradation process of Cornelian cherries anthocyanins stored in water. Error bars represent standard deviation (n = 3). In the some cases they are smaller than the symbol.
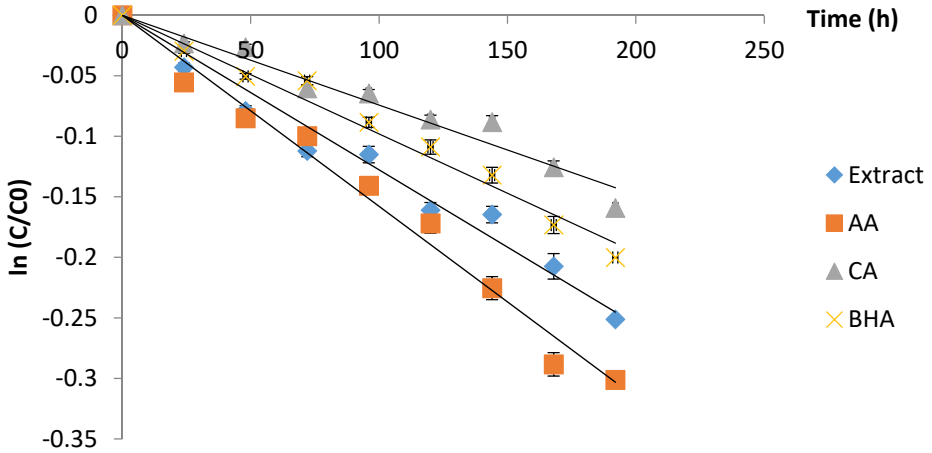


**Figure 2.** The degradation process of Cornelian cherries anthocyanins stored in ethanol. Error bars represent standard deviation (n = 3). In the some cases they are smaller than the symbol.

The half-life values $t_{1/2}$ were calculated by the equation:

$$t_{1/2} = \frac{-\ln 0.5}{k} \qquad (4)$$

The obtained values of the kinetic parameters are summarized in Table 1.

**Table 1.** Kinetic parameters of the degradation process
of anthocyanins from Cornelian cherries

| Solvent/Sample | $k \cdot 10^{-3}$ ($h^{-1}$) | $t_{1/2}$ (h) | $R^2$ |
|---|---|---|---|
| **Water** | | | |
| Fruit extract | 0.89 | 778.65 | 0.971 |
| Ascorbic acid | 4.21 | 164.61 | 0.974 |
| Citric acid | 0.99 | 700 | 0.965 |
| BHA | 1.55 | 447.09 | 0.972 |
| **Ethanol** | | | |
| Fruit extract | 1.28 | 541.41 | 0.971 |
| Ascorbic acid | 1.62 | 427.78 | 0.984 |
| Citric acid | 0.74 | 936.48 | 0.959 |
| BHA | 0.98 | 707.14 | 0.979 |

The kinetic rate constant was found to be higher by ethanol storage compared to water storage of anthocyanins without any added food additive. The same results were observed by investigating the degradation of grape anthocyanins which also degraded faster in alcohol than in aqueous solution [34]. Adding citric acid or BHA to the ethanolic solution of Cornelian cherry anthocyanins, resulted in a rate constant decrease to $0.74 \cdot 10^{-3}$ $h^{-1}$ and $0.98 \cdot 10^{-3}$ $h^{-1}$ respectively, proving the stabilizing effect of these two antioxidant additives, while AA addition resulted in a accelerate degradation process. This finding may suggest that adding BHA and CA to alcoholic beverages obtained from anthocyanin rich fruits may contribute to colour preservation of these products during storage. Regarding the Cornelian cherry anthocyanins storage in aqueous solutions, the degradation process was accelerated by the presence of BHA and AA, while CA slightly influenced the degradation rate constant, proving that this organic acid could be the most suitable antioxidant additive to be used in juices, marmalades or compotes obtained from these fruits.

## CONCLUSIONS

The present work studied the influence of storage solvent and presence of common food antioxidant additives on the degradation process of Cornelian cherry anthocyanins at room temperature. The anthocyanins' degradation process followed a first order reaction kinetics and the rate constants ranged from $0.74 \cdot 10^{-3}$ to $4.21 \cdot 10^{-3}$ $h^{-1}$. The results revealed that degradation in ethanol occurred ~1.5 fold faster than in water, while adding ascorbic acid dramatically destabilized the anthocyanic pigments, especially in water, where the process occurred ~4.7 fold faster in the presence of AA than in the crude extract. The addition of citric acid and BHA had a positive effect on the anthocyanins' stability in ethanol, while in water BHA accelerated the degradation process.

## EXPERIMENTAL SECTION

### Chemicals and reagents

All chemicals and reagents were purchased from Merck (Darmstadt, Germany), were of analytical grade and were used without further purification. A TYPDP1500 Water distiller (Techosklo LTD, Držkov, Czech Republic) was used to obtain the distilled water.

### Plant material

Cornelian cherries were purchased from a local market in August 2019 in Cluj-Napoca, Romania.

### Extract preparation

The extraction of the anthocyanins was carried out in acidified ethylic alcohol 96% (0.1% HCl). To this end, 50 grams of fresh fruits were grinded to obtain a fruit puree and 200 mL of solvent were added. The mixture was stirred for 2 hours at room temperature (22°C) and then vacuum filtered. The obtained solution was concentrated by solvent evaporation under reduced pressure using a rotary evaporator (Buchi R114 Rotovap) to 83° Brix. The total soluble solids expressed as ° Brix were determined using a digital Bellingham + Stanley RFM refractometer. In order to investigate the anthocyanin stability the obtained concentrated extract was divided in two parts.

### Degradation studies

Each part of the obtained solutions was quantitatively transferred into a 250 mL volumetric flask and made up to 250 mL with distilled water and 96% ethanol, respectively. From the obtained solutions, samples were

prepared to investigate the influence of food additives as follows: 30 mL anthocyanin solution (in water or ethanol) was mixed with butylated hydroxy anisole, ascorbic acid or citric acid in order to obtain a 0.1% (w/v). final concentration of the additive in the solution, concentration usually used in the beverages and food products.

The degradation of anthocyanins in the investigated conditions was studied during 8 days by keeping samples at room temperature in the dark. All the samples were introduced in amber vials which were well capped to avoid evaporation. Immediately after preparation (t = 0) and after 24, 48, 72, 96, 120, 144, 168 and 192 hours respectively, samples were collected and used to determine the total monomeric anthocyanin content. Changes in this content during storage were used to determine the degradation reaction kinetics.

### Determination of anthocyanin content

Total monomeric anthocyanin content was measured according to the pH differential method. The samples were 8 fold diluted with acidic buffer solutions (0.025 M KCl, pH = 1 and 0.4 M $CH_3COONa$ solution, pH = 4.5) and allowed to equilibrate for 15 minutes in the dark. An UV-VIS Perkin Elmer Lambda 25 double beam spectrophotometer was used to measure the absorbance of each sample at 506 and 700 nm. From the obtained values, the total monomeric anthocyanins content was calculated and expressed as mg/L extract in cyanidin-3-glucoside equivalents. All experiments were done in triplicate.

## REFERENCES

1. E. Pojer; F. Mattivi; D. Johnson; C.S. Stockley; *Compr. Rev. Food Sci. Food Saf.*, **2013**, *12*, 483-508.
2. S. Zafra-Stone; T. Yasmin; M. Bagchi; A. Chatterjee; J.A. Vinson; D. Bagchi; *Mol. Nutr. Food Res*., **2007**, *51*, 675-683.
3. A. Ben Lagha; S. Dudonne; Y. Desjardins; D. Grenier; *J. Agric. Food Chem*., **2015**, *63*, 6999-7008.
4. C. Xu; Y. Wang; H. Yu; H. Tian; X. Chen; *ACS Nano*, **2018**, *12*, 8255-8265.
5. O. Danila; A. Berghian Sevastre; V. Dionisie; D. Gheban; D. Olteanu; F. Tabaran; I. Baldea; G. Katona; B. Moldovan; S. Clichici; L. David; G. A. Filip; *Nanomedicine (Lond.)*, **2017**, *12*, 1455-1473
6. A. Castaneda-Ovando; M.L. de Pacheco-Hernandez; M.E. Paez-Hernandez; J.A. Rodriguez; C.A. Galan-Vidal; *Food Chem*., **2009**, *113*, 859-871.
7. O. Rop; J.Mlcek; D.Kramarova; T.Jurikova; *Afr. J. Biotechnol*., **2010**, *9*, 1205-1210.
8. M. De Biaggi; D. Donno; M.G. Mellano; I. Riondato; E.N. Rakotoniaina; G.L. Beccaro*; Plant Foods Hum. Nutr.,* **2018**, *73*, 89-94.
9. B. Moldovan; A. Popa; L. David; *J. Appl. Bot. Food Qual.*, **2016**, 89, 208-211

10. L. David; V. Danciu; B. Moldovan; A. Filip; *Antioxidants*, **2019**, *8*, 114.
11. G. A. Filip; B. Moldovan; I. Baldea; D. Olteanu; R. Suharoschi; N. Decea; C. M. Cismaru; E. Gal; M. Cenariu; S. Clichici; L. David; *J. Photochem. Photobiol. B,* **2019**, *191*, 26-37.
12. I. Baldea; A. Florea; D. Olteanu; S. Clichici; L. David; B. Moldovan; M. Cenariu; M. Achim; R. Suharoschi; S. Danescu; G. A. Filip; *Nanomedicine*, **2020**, 15, 55-75.
13. S. Asgary; R. Kelishadi; M. Rafieian-Kopaei; S. Najafi; M. Najafi; A. Sahebkar; *Pediatr. Cardiol*., **2013**, *34*, 1729-1735.
14. B. Dinda; A.M. Kyriakopoulos; S. Dinda; V. Zoumpourlis; N.S. Thomaidis; A. Velegraki; C. Markopoulos; M. Dinda; *J. Ethnopharmacol*., **2016**, *193*, 670-690.
15. A. Milenkovic Andelkovic; B. Radovanovic; M. Andelkovic; A. Radovanovic; V. Nikolic; V. Randelovic; *Adv. Technol*., **2015**, *4*, 26-31.
16. B. Moldovan; A. Filip; S. Clichici; R. Suharovschi; P. Bolfa; L. David; *J. Funct. Food*s, **2016**, 26, 77-87.
17. M. Pawlowska; F. Camangi; A. Braca; *Food Chem*., **2010**, *119*, 1257-1261.
18. T. Sozanski; A.Z. Kucharska; A. Rapak; D. Szumny; M. Trocha; A. Merwid-Lad; S. Dzimira; T. Piasecki; N. Piorecki; Jan Magdalan; A. Szelag; *Atherosclerosis*, **2016**, *254*, 151-160.
19. E. Choe; D. B. Min; *Compr. Rev. Food Sci. Food Saf*., **2009**, *8*, 345-358.
20. R. Jackman; R.Y. Yada; M.A. Tung; R.A. Speers; *J. Food Biochem*., **1987**, *11*, 201-247.
21. R. Levy; Z. Okun; A. Shpigelman; *Foods*, **2019**, *8*, 207
22. M. M. Giusti; R. E. Wrolstad; *Current Protocols in Food Analytical Chemistry*, Wiley, New York, **2001**, pp. 1–13.
23. N. Marti; A. Perez-Vicente; C. Garcia-Viguera; *J. Sci. Food Agric*., **2002**, *82*, 217-221.
24. M. Evest; L. J. Mauer; *J. Agric. Food Chem*., **2013**, *61*, 4169-4179.
25. R. Levy; Z. Okun; A. Shpiegelman; *Foods*, **2019**, *8*, 207.
26. J. Li; H. Song; N. Dong; G. Zhao; *Food Sci. Biotechnol*., **2014**, *23*, 89-96.
27. C. Garcia-Viguera; P. Bridle; *Food Chem*., **1999**, *64*, 21-26.
28. E. M. Hubbermann; A. Heins; H. Stockmann; K. Schwarz; *Eur. Food Res. Technol*., **2006**, *223*, 83-90.
29. A. Cata; I. M. C. Ienascu; C. Tanasie; M. N. Stefanut; *Rev. Roum. Chim*., **2019**, *64*, 893-899.
30. A. Wojdylo; P. Nowicka; M. Teleszko, *Processes*, **2019**, *7*, 367.
31. A. Bozdogan; K. Yasar; *Turkish J. Agric. Food Sci. Technol*., **2019**, *7*, 282-285.
32. M. M. Pragalyaashree; D. Tiroutchelvame; S. Sashikumar; *J. Appl. Pharm. Sci*., **2018**, *8*, 057-063.
33. C. C. Chen; C. Lin; M. H. Chen; P. Y. Chyang; *Foods*, **2019**, *8*, 393.
34. K. C. Tseng; H. M. Chang; J. S. B. Wu; *J. Food Process Preserv*., **2006**, *30*, 503-514.

# VIRGIN OLIVE OIL PHENOLS-SPECTROSCOPIC EVALUATION IN BASIC MEDIUM: ANALYSIS OF TOTAL CONTENT OF HYDROXYTYROSOL

## MUSTAFA CITTAN[a*]

**ABSTRACT.** Here a spectrophotometric technique in the visible region combined with an environmental friendly ultra-pure water based liquid-liquid extraction procedure has been described for the determination of total hydroxytyrosol in virgin olive oils regardless of whether it is free or combined. Determination of total hydroxytyrosol was carried out where the absorption peak of the colored compounds formed with autopolymerization of quinones that occured following the oxidation of hydroxytyrosol and its secoiridoid derivatives in a basic medium was measured as an analytical signal. The method was linear in a concentration range of 0.2-15.0 mg L$^{-1}$ with a correlation coefficient of 0.9990. Detection and quantification limits were 0.05 and 0.18 mg L$^{-1}$, respectively. Intra-day and inter-day precision studies indicated that the proposed method was repeatable. In addition, the liquid-liquid extraction procedure was quite efficient with recovery values between 108 and 117%. Finally, the proposed method was successfully applied to the analysis of total hydroxytyrosol in a virgin olive oil and the results were compared with those obtained by a method existing in the literature for the determination of total hydroxytyrosol based on acid hydrolysis of secoiridoid aglycons followed by liquid chromatography-tandem mass spectrometry.

*Keywords:* hydroxytyrosol; virgin olive oil; phenolic compounds; visible spectroscopy; liquid-liquid extraction.

## INTRODUCTION

It is well established that the Mediterranean diet (MD) is very effective against: cancer [1], cardiovascular disease [2], inflammation [3], diabetes [4], and aging [5]. Many of the benefits associated with the MD are the result of

---

[a] *Manisa Celal Bayar University, Faculty of Science and Letters, Department of Chemistry, 45140, Manisa, Turkey*
\* *Corresponding author: mustafa.cittan@cbu.edu.tr*

a high intake of antioxidants and anti-inflammatory elements present in several components of this diet [6]. Virgin olive oil (VOO) is an essential component of the MD and is directly obtained from ripe olive fruits using only mechanical extraction. The beneficial effects of VOO can be attributed to the high relationship between unsaturated and saturated fatty acids and also to the antioxidant properties of its phenolic composition [7].

The VOO phenolic fraction is mainly comprised by phenyl ethyl alcohols (hydroxytyrosol, tyrosol) and their secoiridoids derivates [8,9], linked to the aldehydic and dialdehydic forms of elenolic acid (such as oleuropein, the dialdehydic form of decarboxymethyl elenolic acid linked to hydroxytyrosol (3,4-DHPEA-EDA), 4-(acetoxyethyl)-1,2-dihydroxybenzene (3,4-DHPEA-AC), dialdehydic form of the decarboxymethyl elenolic acid linked to tyrosol (p-HPEA-EDA), p-4-hydroxyphenylethanol-elenolic acid, an isomer of ligstroside aglycone (p-HPEA-EA), 3,4-dihydroxyphenylethanol-elenolic acid, an isomer of oleuropein aglycone (3,4-DHPEA-EA) and its methylated form (methyl 3,4-DHPEA-EA)) [10]. Some other minor components are also commonly present, like: phenolic acids (such as ferulic, p-coumaric, vanillic, caffeic, hydroxyphenylacetic, gentisic, gallic, homovanillic and cinnamic acid) [8,11], lignans (pinoresinol and 1-acetoxypinoresinol) [12], flavonoids (luteolin and apigenin) [13], and aldehydes (vanillin) [14].

The origin of hydroxytyrosol (HT) is the hydrolysis of oleuropein which happens during the ripening of the olives, and during the storage and elaboration of table olives [15]. Among olive oil phenolic compounds, HT has been the most investigated compound, primarily for its bioavailability [16] and is the most potent as antioxidant [17] and the oxygen radical absorbance capacity (ORAC) of HT is twice that observed for oleuropein, three and ten times more than for epicatechin and ascorbic acid, respectively [18]. HT also leads to apoptosis and growth arrest in vitro [19], including melanoma cells [20], HL60 leukaemia cells [21], and colon cancer cell lines [22].

Numerous techniques have been applied for the extraction of phenolic compounds from VOO. A simple and fast methanol–n-hexane-based liquid–liquid extraction (LLE) was usually carried out to extract the polar fraction of VOO, especially the phenolic compounds [23]. On the other hand, solid phase extraction (SPE) [24,25], ultrasound-assisted extraction (UAE) [26], and liquid-liquid micro extraction techniques (LLME) [10,26] have all been followed for this purpose. Further, the extraction of phenolic compounds from VOO by deep eutectic solvents (DESs) has been recently reported [27].

The determination of HT in VOO was usually carried out using chromatographic techniques. High performance liquid chromatography (HPLC) technique by ultraviolet (UV) detection [28], fluorescence (FL) detection [29],

and mass spectrometric (MS) detection [30,31] were followed for this purpose. Gas chromatography-mass spectroscopy (GC-MS) [32] and capillary zone electrophoresis (CZE) equipped with diode array detector (DAD) [33] techniques were also used to determine HT in VOO.

Most of the beneficial properties of VOO have been attributed to HT and, to a lesser extent, to tyrosol (Tyr). However, the analysis of the total content of HT in VOOs fails to provide reliable data because of the unreliable quantification of secoiridoid derivatives. As there are no commercial standards available regarding these secoiridoid aglycons, it is difficult to define the derivatives and determine the accurate total amount of HT in VOO. On the other hand, a method has been described to determine the total content of HT and Tyr via acid hydrolysis process of aglycons with 2 M HCl in extraction step followed by HPLC-DAD analysis [12].

In this work, a spectrophotometric technique in the visible region combined with a simple environmental friendly ultra-pure water based LLE is proposed for the determination of total HT as HT equivalent in VOOs regardless of whether it is free or combined. The approach to determining total HT in this paper exploits the oxidation of diphenols in a basic medium (0.1 M NaOH solution) to the corresponding quinones and then absorbance measurement of the colored compounds formed by autopolymerization of the quinones [34]. This is the first report that provides the mass spectrum of the resulting colored compounds that proves the autopolymerization of diphenols in basic medium. A diagrammed illustration of the complete method was depicted in Scheme 1. The paper also provides a detailed investigation of the interference effects of the other potential VOO phenolics to the methodology by using the individual standards of 34 phenolic compounds. Consequently, the paper is quite original since it suggests a simple analytical technique combined with an environmental friendly ultra-pure water based liquid-liquid extraction procedure to determine the total contents of HT in VOOs without the interference of other predominant phenolic compounds, Tyr and its derivatives (monophenol derivatives in VOOs). The proposed method was applied for the determination of total HT in a VOO and the obtained result was compared with those obtained via the extraction process of acid hydrolysis of the aglycons proposed in the literature followed by liquid chromatography-electrospray tandem mass spectrometry (LC-ESI-MS/MS) technique [12]. The method would be a simple, cheap and rapid alternative to determine the total HT in VOOs.
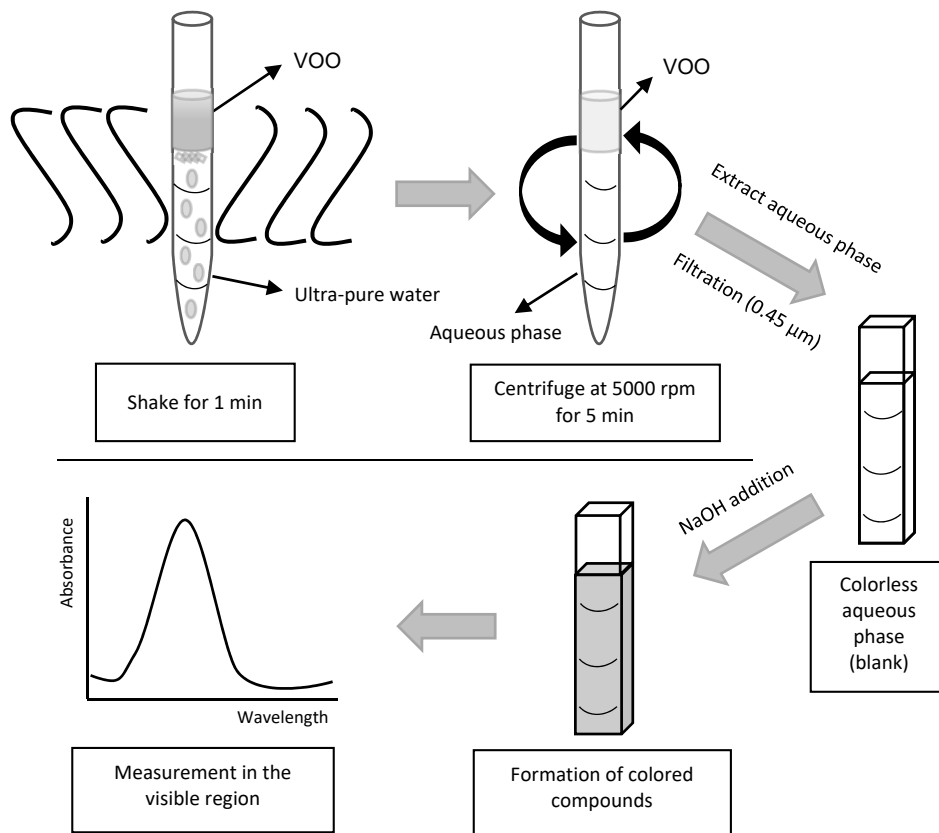
**Scheme 1.** The diagrammed illustration of total hydroxytyrosol analysis in virgin olive oil.

## RESULTS AND DISCUSSION

### Optimization of NaOH concentration

The NaOH concentration of the medium was increased from 0.01 to 1 M in order to obtain high absorption intensity. Figure 1 shows the effect of the NaOH concentration on the response of 5 mg $L^{-1}$ HT at 530 nm. The determination was performed quadruplicate for each concentration point. The results clearly demonstrated that the sensitivity increased up to 0.1 M NaOH concentration. On the other hand, higher NaOH concentrations not only reduced the sensitivity of the method, but also caused higher relative standard deviations in the analyte response. Therefore, the medium was 0.1 M NaOH.
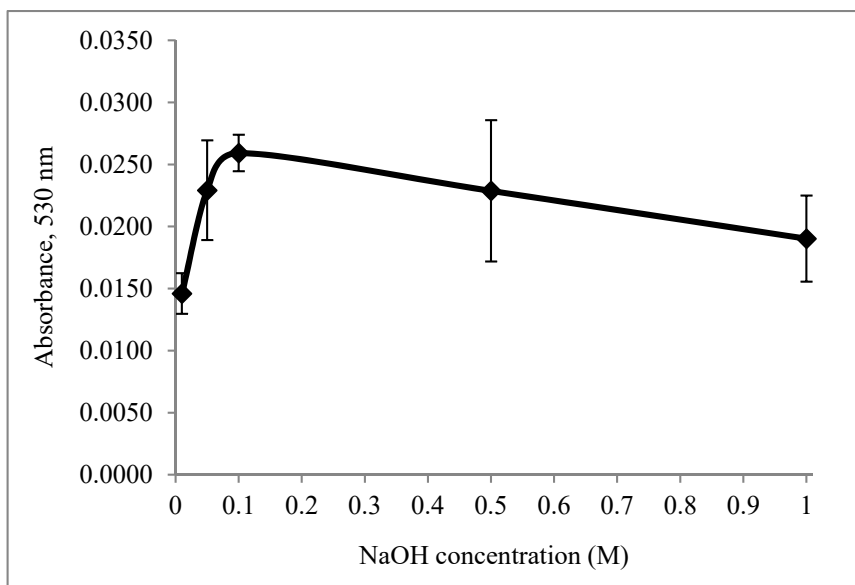
**Figure 1.** Effect of NaOH concentration on the analytical signal of hydroxytyrosol.


## Selectivity of the proposed analysis method

34 different phenolic compounds (homovanillic acid, trans-cinnamic acid, taxifolin, (+)-catechin, pyrocatechol, (−)-epicatechin, ferulic acid, chlorogenic acid, caffeic acid, gentisic acid, 3-hydroxybenzoic acid, 4-hydroxybenzoic acid, *p*-coumaric acid, sinapic acid, gallic acid, syringic acid, vanillin, rosmarinic acid, protocatechuic acid, 2-hydroxycinnamic acid, 3,4-dihydroxyphenylacetic acid, vanillic acid, apigenin, luteolin, apigenin 7-glucoside, luteolin 7-glucoside, eriodictyol, pinoresinol, tyrosol, verbascoside, kaempferol, hyperoside, hesperidin and quercetin) were used to evaluate the selectivity of the proposed analytical method for the determination of total HT. To this end, the behavior of the phenolic compounds in a concentration of 50 mg $L^{-1}$ in 0.1 M NaOH medium was observed in 350 to 800 nm wavelength range using the individual commercial analytical standards of the compounds one by one.

The approach to the proposed analysis method exploits the oxidation of diphenols in a basic medium (0.1 M NaOH solution) to the corresponding quinones and absorbance measurement of the colored compounds formed by autopolymerization of the quinones. Since the method was specific only to the compounds containing more than one hydroxyl group in the phenolic rings, monophenols such as Tyr, 3-hydroxybenzoic acid, 4-hydroxybenzoic acid,

sinapic acid, vanillic acid, ferulic acid, syringic acid, vanillin, 2-hydroxycinnamic acid, *p*-coumaric acid, pinoresinol, hesperidin, trans-cinnamic acid and homovanillic acid, as expected, did not react with NaOH to form colored compounds. Thus, Tyr and its secoiridoid derivatives, the other major components of the VOO, did not interfere with the determination of HT by the proposed method. In addition, quercetin, kaempferol, chlorogenic acid, hyperoside, luteolin, apigenin, luteolin 7-glucoside, and apigenin 7-glucoside exhibited considerable absorbance at a wavelength range of 380 - 430 nm in 0.1 M NaOH medium. Nevertheless, they did not significantly interfere with the determination of HT, as the absorbance of HT was recorded at 530 nm wavelength.

Protocatechuic acid, gentisic acid, 3,4-dihydroxyphenylacetic acid, gallic acid, (+)-catechin, (−)-epicatechin, pyrocatechol, caffeic acid, rosmarinic acid, eriodictyol, taxifolin, and verbascoside absorbed similar wavelengths with HT in 0.1 M NaOH medium which resulted significant interferences to the methodology. The phenolic content of VOO has been described numerous times in the literature and, no study has been reported that VOO contains (+)-catechin, (−)-epicatechin, pyrocatechol, verbascoside, rosmarinic acid and eriodictyol. On the other hand, gallic acid [11,35], protocatechuic acid [35], 3,4-dihydroxyphenylacetic acid [29,35], gentisic acid [11,29,35], caffeic acid [26,30,36] and taxifolin [35] have been reported in VOO. However, the reported results prove that these compounds are present at only trace levels in VOO compared to hydroxytyrosol, tyrosol and their secoiridoid derivatives [10,29,30]. As a result, when the matrix is VOO, it is considered that the proposed method is quite reliable for total HT determination without the interference of the other VOO phenolics, especially Tyr and its secoiridoid derivatives.

### Linearity, limit of detection and quantification

The linearity was examined by establishing the external standard calibration curves in a concentration range of 0.2-15.0 mg L⁻¹. All calibration curves were generated from the stock standard solution of HT with three replicates per level at 7 different concentrations (0.2, 0.5, 1.0, 3.0, 5.0, 10.0 and 15.0 mg L⁻¹) in 0.1 M NaOH solution. Well defined absorption peaks were observed (maximum absorbance at approximately 495 nm wavelength) in Figure 2A. But the absorbance of HT was recorded at 530 nm throughout the study to prevent possible interference of the phenolic compounds that exhibited considerable absorbance at a wavelength range of 380 - 430 nm in 0.1 M NaOH medium (see section selectivity of the proposed analysis method). The plot of the calibration curve (Figure 2B) was found to be linear with a 0.9990 correlation coefficient.
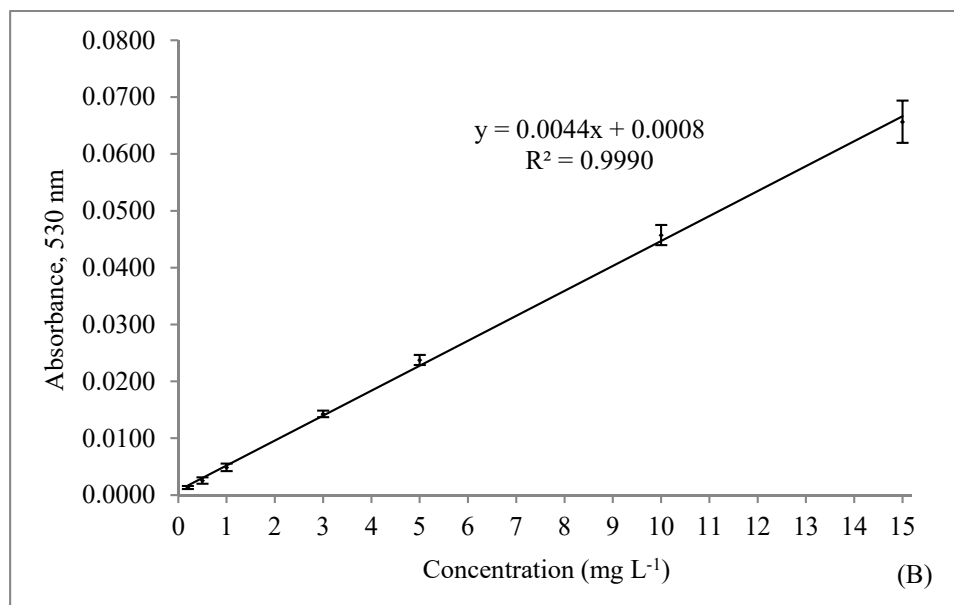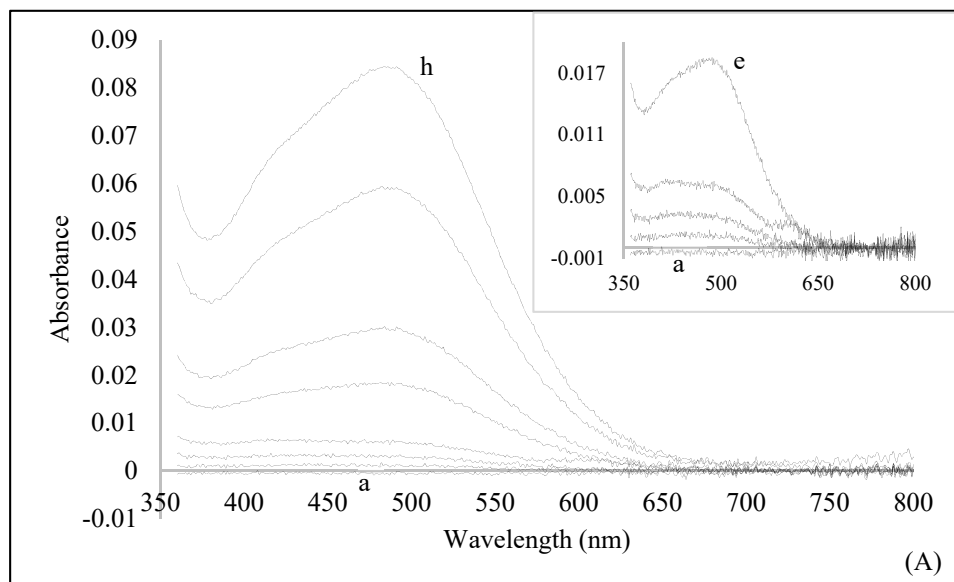
**Figure 2.** (A) Visible absorption spectrums of various concentrations of hydroxytyrosol; (a-h): blank, 0.2, 0.5, 1.0, 3.0, 5.0, 10.0 and 15.0 mg L$^{-1}$. Inset showed visible absorption spectrums of low concentrations; (a-e): blank, 0.2, 0.5, 1.0 and 3.0 mg L$^{-1}$. (B) The calibration curve for hydroxytyrosol.

The limit of detection (LOD) and limit of quantification (LOQ) were calculated using the formula LOD=3SD/b and LOQ=10SD/b, respectively, where SD is the standard deviation of ten reagent blank determinations and b is the slope of the calibration curve. The LOD and LOQ were 0.05 and 0.18 mg L$^{-1}$, respectively.

## Repeatability and precision

Calibration standards at three different concentrations of 1.0, 3.0 and 10.0 mg L$^{-1}$ were used to determine the intra-day (three repetitions of each concentration) and inter-day (three repetitions of each concentration and three days) repeatability of proposed method. The results are shown in Table 1. As expected, the intra-day precision was higher than the inter-day precision in all cases and the method showed a good overall repeatability (the intra-day relative standard deviations (RSDs) were lower than 2.1% and lower than 13.5% for inter-day assays) when the HT concentration was above 1.0 mg L$^{-1}$.

**Table 1.** Intra-day and inter-day precision of the method

| Concentration (mg L$^{-1}$) | RSD (%) | |
|---|---|---|
| | Intra-day (n=3) | Inter-day (n=9) |
| 1.0 | 2.1 | 13.5 |
| 3.0 | 1.6 | 4.0 |
| 10.0 | 0.8 | 3.9 |

RSD, relative standard deviation.

## Recovery of the proposed liquid-liquid extraction procedure

UAE technique using methanol-water mixture as extractant is one of the most effective aid to extract the phenolic compounds from foodstuffs [37–39]. To this end, proposed LLE technique using only ultra-pure water only and UAE method were followed comparatively to determine the efficiency of the proposed extraction technique for the extraction of HT from VOO. Both extracts obtained with LLE and UAE techniques were scanned for the phenolic contents by a modified LC-ESI-MS/MS method described previously [40] (include: HT and the other phenolics used in the selectivity studies except Tyr, homovanillic acid and trans-cinnamic acid, due to their incompatibility with the mobile phase system used; totally 33 individual phenolic compounds) and only HT, *p*-coumaric acid, pinoresinol, luteolin and apigenin were detected in the extracts. The chromatograms are given in Figure 3. The results clearly showed that the proposed LLE method was more effective for the extraction of HT and *p*-coumaric acid from VOO. On the other hand, the LLE method

failed to extract the pinoresinol, luteolin and apigenin when compared to the UAE method. When considering luteolin and apigenin exhibited considerable absorbance at approximately 400-410 nm wavelength in the spectrophotometric measurements, it was suggested that the LLE method using only ultra-pure water as extractant is more compatible with the proposed analysis method.
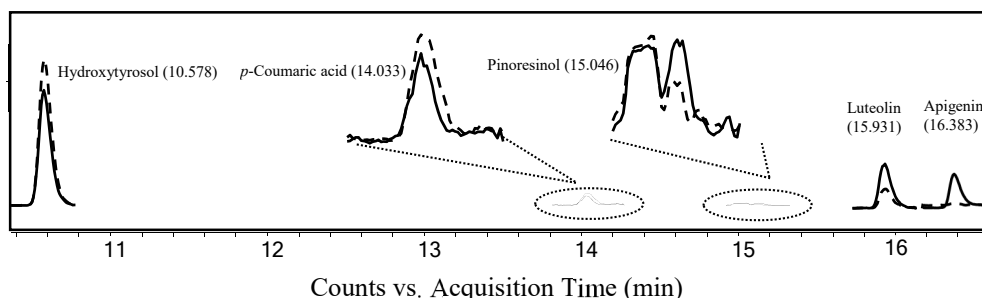


**Figure 3.** LC-ESI-MS/MS MRM chromatograms of the virgin olive oil extracts (ultrasound-assisted extraction using methanol/water mixture as extractant: ———— , ultra-pure water based liquid-liquid extraction: – – – – -).

Furthermore, recovery of the proposed LLE technique was evaluated by spiking 1 mL of VOO sample at 10.0 and 100.0 mg L$^{-1}$ concentration levels of HT standard (three repetitions of each concentration). The spiked samples were extracted via LLE procedure and analyzed (n=3) with LC-ESI-MS/MS. Quantitative recoveries were obtained in all cases, varying from 108 to 117% (Table 2). As a result, the proposed LLE method is not only efficient for HT extraction, but also environmental friendly because of using only ultra-pure water in the extraction step.

**Table 2.** Recovery of the proposed liquid-liquid extraction method for hydroxytyrosol

| Content (mg L$^{-1}$) | Spiked (mg L$^{-1}$) | Found (mg L$^{-1}$) | Recovery (%) | Mean (%) |
|---|---|---|---|---|
| 16.6±0.5 | 10.0 | 28.4 | 118 | 108±9 |
| | | 26.7 | 101 | |
| | | 27.2 | 106 | |
| | 100.0 | 138.0 | 121 | 117±4 |
| | | 131.4 | 115 | |
| | | 130.1 | 114 | |

## Quantitative analysis of virgin olive oil sample

1 mL of VOO samples were extracted simultaneously via LLE and acid hydrolysis procedures to determine the total HT content of the sample by the proposed spectrophotometric and LC-ESI-MS/MS method, respectively. The extracts were analyzed in triplicate using the relevant analysis method to compare the accuracy of the proposed spectrophotometric technique. The aqueous extracts were used as blank in spectrophotometric measurements. Then, appropriate volume of 3 M NaOH was added to each aqueous extract for a final concentration of 0.1 M before measuring absorbance at a wavelength of 530 nm.

A typical calibration curve obtained using a series of standard solutions over the concentration range from 25.0 to 500.0 µg L$^{-1}$ used for total HT determination in VOO sample by the LC-ESI-MS/MS method is shown in Figure 4. On the other hand, Figure 5 shows the standard addition (2.0, 4.0 and 6.0 mg L$^{-1}$ HT) spectrums and calibration curve obtained for the VOO sample. The results were in agreement, 18.0±0.1 mg L$^{-1}$ for the proposed spectrophotometric technique combined with a simple ultra-pure water based LLE and 17.5±0.5 mg L$^{-1}$ for the LC-ESI-MS/MS method following the acid hydrolysis process.
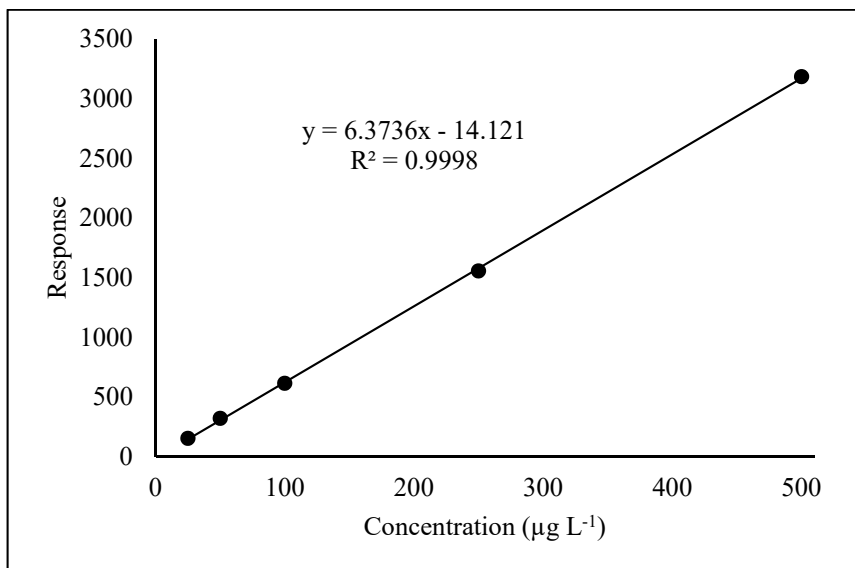


**Figure 4.** Typical calibration curve of hydroxytyrosol in LC-ESI-MS/MS method.
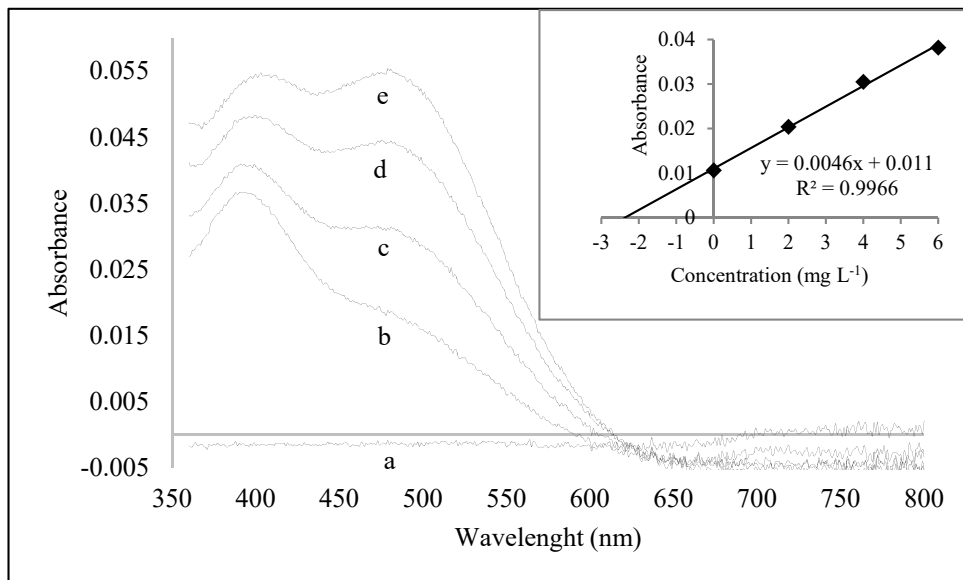
**Figure 5.** Visible absorption spectrums of (a) blank, (b) sample, after addition of (c) 2, (d) 4 and (e) 6 mg L$^{-1}$ hydroxytyrosol standard. The standard addition calibration curve is inset.

## Matrix effect

Matrix effect was evaluated to ensure the bias-free analytical results. Due to absence of blank matrices for VOOs, it was determined at three different concentrations (2.0, 4.0 and 10.0 mg L$^{-1}$) of HT. The matrix effect was calculated relatively by comparing the absorbance measurement of three spectrums [41]. The Eq. (1) is given as:

$$ME(\%) = \left[ \frac{A(\text{matrix} + \text{std}) - A(\text{matrix})}{A(\text{std})} - 1 \right] x\ 100(\%) \tag{1}$$

where A(matrix + std) is the response for the matrix with the addition of standard; A(matrix) is the response for the matrix only; and A(std) is the response for the standard only.

The mean matrix effect was 1.4% with a standard deviation of 1.0%, which suggested that a very slight signal enhancement observed. On the other hand, the matrix effect was also assessed by comparing the slopes of standard calibration curve and standard addition method. Good agreement between the slopes of both curves (Figure 2B and 5) and the calculated matrix effect were proved that there was no significant matrix effect when the sample preparation was carried out by the proposed LLE method.

### Mass spectrometric evaluation of the resulting colored solution

The mass spectrum (Figure 6) of the colored solution formed by the proposed method was evaluated in order to clarify the autopolymerization of the quinones that occurs with the oxidation of diphenols in a basic medium by direct infusion of HT of 50 mg $L^{-1}$ concentration in 0.1 M NaOH in to the mass spectrometer in the 50 to 2200 amu mass range. The ions at m/z 757.7, 929.0, and 1082.1 amu, defined as integer multiples of the HT molecular weight (154.16 g $mol^{-1}$) in the mass spectrum, support the described autopolymerization approach.
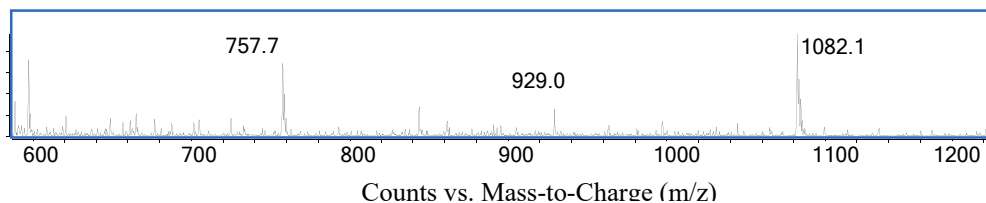


**Figure 6.** Mass spectrum of the resulting colored solution.

### CONCLUSIONS

It is more useful to choose simple and cheap analytical techniques in matrices where the analyte is the main component. In such cases, trace compounds do not interfere significantly with the determination of the major analyte. Thus, the amount of analyte in the matrix can be easily estimated by using simple and cheap analytical techniques as an alternative to existing complicated methods.

HT and Tyr are the main phenolic compounds in VOO. Many beneficial effects of VOO have been attributed to HT and, to a lesser extent, to Tyr. The proposed method in the present study proved to be simple, low-

cost, effective, and suitable for determining total HT in VOOs without the interference of Tyr and its derivatives (the other predominant components of VOOs). The method is also quite important since it determines the total HT as HT equivalent regardless of whether it is free or combined.

The proposed technique was linear in a concentration range of 0.2-15.0 mg L$^{-1}$ with a correlation coefficient of 0.9990. The limit of detection and quantification of the method were obtained as 0.05 and 0.18 mg L$^{-1}$, respectively. The method showed a good overall repeatability (the intra-day RSDs were lower than 2.1% and lower than 13.5% for inter-day assays) when the HT concentration was above 1.0 mg L$^{-1}$. Environmental friendly ultra-pure based LLE of HT and its derivatives had good recovery values between 108 and 117%. No significant matrix effect was observed. Finally, a detailed investigation of the interference effects of the other potential VOO phenolics to the methodology was carried out and it was suggested that the proposed analytical technique is quite reliable and easily applicable for total HT determination when the test matrix is VOO.

## EXPERIMENTAL

### Apparatus

Absorption spectra were recorded in an ultraviolet and visible (UV-Vis) spectrophotometer (Agilent Technologies, Cary 60). An Agilent Technologies 1260 Infinity liquid chromatography system hyphenated to a 6420 Triple Quad mass spectrometer was used for LC analyses. The ultrasound cleaning bath was Daihan, WUC-D10H. A WiseShake SHO-2D digital orbital shaker was used for the agitation in acid hydrolysis process.

### Reagents

All commercial phenolic standards were purchased from Sigma-Aldrich (St. Louis, MO, USA), Fluka (St. Louis, MO, USA) and HWI Analytik (Ruelzheim, Germany). In addition, hydrochloric acid and methanol were purchased from Sigma-Aldrich (St. Louis, MO, USA). Formic acid and sodium hydroxide were obtained from Merck (Darmstadt, Germany). Ultra-pure water (18 mΩ) was obtained from a Milli-Q water purification system (Millipore Co., Ltd.). Stock solutions of the phenolic compounds were prepared in methanol.

### LC-ESI-MS/MS method

Phenolic determination of VOOs was carried out following the procedure described in our previous study by using a Poroshell 120 EC-C18 (100 mm x 4.6 mm I.D., 2.7 μm) column [40].

### Assays for the extraction of phenolic compounds

Extraction of phenolic compounds from VOOs were carried out using (i) a simple, environmental friendly ultra-pure water based LLE procedure that combined with the proposed spectrophotometric method, (ii) an UAE procedure that mentioned as an effective technique in the literature using methanol/water (80:20, v/v) mixture as extractant and, (iii) an acid hydrolysis process of aglycons to determine the total contents of HT described elsewhere [12]. Figure 7 shows the scheme for the three processes of the extraction methods.

| Liquid-liquid extraction (LLE) | Ultrasound-assisted extraction (UAE) | Acid hydrolysis process |
|---|---|---|
| 1 mL sample + 6 mL ultra-pure water in 15 mL centrifuge tube | 1 mL sample + 6 mL methanol 80% in 15 mL centrifuge tube | 1 mL sample + 10 mL 2 M HCl in 50 mL centrifuge tube |
| Shake for 1 min | Apply ultrasound for 15 min | Agitation at 200 rpm for 4 h |
| Centrifuge at 5000 rpm for 5 min | Centrifuge at 5000 rpm for 5 min | Centrifuge at 5000 rpm for 5 min |
| Extract aqueous phase | Extract methanolic phase | Extract aqueous phase |
| Filter through a 04.45 μm syringe filter | Filter through a 0.45 μm syringe filter | Filter through a 0.45 μm syringe filter |
| Analyze | Analyze | Analyze |

**Figure 7.** Scheme of the extraction methods followed in the study.

### Ultra-pure water based liquid-liquid extraction procedure

VOO (1 mL) samples were extracted with 6 mL of ultra-pure water in a polyethylene centrifuge tube (15 mL, conical bottom). The centrifuge tubes were sealed tightly and shaken vigorously for 1 min by hand. The content of the tube was then centrifuged at 3000 rpm for 5 min. Finally, the aqueous phase was filtered through a 0.45 μm syringe filter prior to analysis.

### Ultrasound-assisted extraction procedure

VOO (1 mL) was placed into polyethylene centrifuge tube (15 mL, conical bottom) containing 6 mL of methanol/water mixture (80:20, v/v) and directly sonicated using an ultrasonic bath for 15 min. The content of the tube was then centrifuged at 3000 rpm for 5 min and the extracts were filtered through a 0.45 μm syringe filter prior to analysis.

### Acid hydrolysis process

1 mL of VOO was weighed in in a polyethylene centrifuge tube (50 mL, conical bottom) and 10 mL of 2 M HCl was added. The mixture was vigorously homogenized by agitation at 200 rpm in the orbital shaker for 4 hours. After the centrifugation process at 3000 rpm for 5 min, the aqueous phase was filtered through a 0.22 μm pore size.

### Method validation

A validation procedure was performed in order to establish the analytical performance features of the proposed method, ensuring the successful quantification of total HT in VOOs, evaluating linearity, selectivity, limit of detection and quantification, precision (intra and inter-day), matrix effect and extraction recovery.

## REFERENCES

[1]  E. Couto, P. Boffetta, P. Lagiou, P. Ferrari, G. Buckland, K. Overvad, C. C. Dahm, A. Tjønneland, A. Olsen, F. Clavel-Chapelon et al., *Br. J. Cancer*. **2011**, *104* (9), 1493–1499.
[2]  R. Estruch, M. A. Martínez-González, D. Corella, J. Salas-Salvadó, V. Ruiz-Gutiérrez, M. I. Covas, M. Fiol, E. Gómez-Gracia, M. C. López-Sabater, E. Vinyoles et al., *Ann. Intern. Med.* **2006**, *145* (1), 1–11.
[3]  M. A. Martínez-González, J. Salas-Salvadó, R. Estruch, D. Corella, M. Fitó, E. Ros, *Prog. Cardiovasc. Dis.* **2015**, *58* (1), 50–60.

[4] J. Salas-Salvadó, M. Bulló, R. Estruch, E. Ros, M. I. Covas, N. Ibarrola-Jurado, D. Corella, F. Arós, E. Gómez-Gracia, V. Ruiz-Gutiérrez et al., *Ann. Intern. Med.* **2014**, *160* (1), 1–10.

[5] A. Varela-Lopez, P. Bullon, M. Battino, Mc. Ramirez-Tortosa, J. J. Ochoa, M. D. Cordero, C. L. Ramirez-Tortosa, C. Rubini, A. Zizzi, J. L. Quiles, *Journals Gerontol. - Ser. A Biol. Sci. Med. Sci.* **2016**, *71* (5), 593–600.

[6] M. Robles-Almazan, M. Pulido-Moran, J. Moreno-Fernandez, C. Ramirez-Tortosa, C. Rodriguez-Garcia, J. L. Quiles, Mc. Ramirez-Tortosa, *Food Res. Int.* **2018**, *105*, 654–667.

[7] E. N. Frankel, *J. Agric. Food Chem.* **2010**, *58* (10), 5991–6006.

[8] K. L. Tuck, P. J. Hayball, *J. Nutr. Biochem.* **2002**, *13* (11), 636–644.

[9] V. Lavelli, L. Bondesan, *J. Agric. Food Chem.* **2005**, *53* (4), 1102–1107.

[10] M. Becerra-Herrera, M. Sánchez-Astudillo, R. Beltrán, A. Sayago, *LWT - Food Sci. Technol.* **2014**, *57* (1), 49–57.

[11] M. I. Alarcón Flores, R. Romero-González, A. Garrido Frenich, J. L. Martínez Vidal, *Food Chem.* **2012**, *134* (4), 2465–2472.

[12] C. Romero, M. Brenes, *J. Agric. Food Chem.* **2012**, *60* (36), 9017–9022.

[13] P. Reboredo-Rodríguez, L. Rey-Salgueiro, J. Regueiro, C. González-Barreiro, B. Cancho-Grande, J. Simal-Gándara, *Food Chem.* **2014**, *150*, 128–136.

[14] M. J. Tovar, M. J. Motilva, M. P. Romero, *J. Agric. Food Chem.* **2001**, *49* (11), 5502–5508.

[15] S. Charoenprasert, A. Mitchell, *J. Agric. Food Chem.* **2012**, *60* (29), 7081–7095.

[16] A. Incani, M. Deiana, G. Corona, K. Vafeiadou, D. Vauzour, M. A. Dessì, J. P. E. Spencer, *Mol. Nutr. Food Res.* **2009**, *54* (6), 788–796.

[17] R. Owen, A. Giacosa, W. Hull, R. Haubner, B. Spiegelhalder, H. Bartsch, *Eur. J. Cancer.* **2000**, *36* (10), 1235–1247.

[18] A. Pastor, J. Rodríguez-Morató, E. Olesti, M. Pujadas, C. Pérez-Mañá, O. Khymenets, M. Fitó, M.-I. Covas, R. Solá, M.-J. Motilva et al., *J. Chromatogr. A.* **2016**, *1437*, 183–190.

[19] E. Terzuoli, A. Giachetti, M. Ziche, S. Donnini, *Mol. Nutr. Food Res.* **2016**, *60* (3), 519–529.

[20] S. D'Angelo, D. Ingrosso, V. Migliardi, A. Sorrentino, G. Donnarumma, A. Baroni, L. Masella, M. Antonietta Tufano, M. Zappia, P. Galletti, *Free Radic. Biol. Med.* **2005**, *38* (7), 908–919.

[21] R. Fabiani, A. De Bartolomeo, P. Rosignoli, M. Servili, G. F. Montedoro, G. Morozzi, *Eur. J. Cancer Prev.* **2002**, *11* (4), 351–358.

[22] G. Corona, M. Deiana, A. Incani, D. Vauzour, M. A. Dessì, J. P. E. Spencer, *Mol. Nutr. Food Res.* **2009**, *53* (7), 897–903.

[23] F. M. Pirisi, P. Cabras, C. F. Cao, M. Migliorini, M. Muggelli, *J. Agric. Food Chem.* **2000**, *48* (4), 1191–1196.

[24] R. Mateos, J. L. Espartero, M. Trujillo, J. J. Ríos, M. León-Camacho, F. Alcudia, A. Cert, *J. Agric. Food Chem.* **2001**, *49* (5), 2185–2192.

[25] M. N. Franco, T. Galeano-Díaz, Ó. López, J. G. Fernández-Bolaños, J. Sánchez, C. De Miguel, M. V. Gil, D. Martín-Vertedor, *Food Chem.* **2014**, *163*, 289–298.

[26] M. L. Pizarro, M. Becerra, A. Sayago, M. Beltrán, R. Beltrán, *Food Anal. Methods*. **2013**, *6* (1), 123–132.

[27] A. García, E. Rodríguez-Juan, G. Rodríguez-Gutiérrez, J. J. Rios, J. Fernández-Bolaños, *Food Chem.* **2016**, *197*, 554–561.

[28] M. Tasioula-Margari, O. Okogeri, *Food Chem.* **2001**, *74* (3), 377–383.

[29] M. P. Godoy-Caballero, M. I. Acedo-Valenzuela, T. Galeano-Díaz, *Talanta*. **2012**, *101*, 479–487.

[30] M. Suárez, A. Macià, M.-P. Romero, M.-J. Motilva, *J. Chromatogr. A*. **2008**, *1214* (1–2), 90–99.

[31] M. I. Alarcón Flores, R. Romero-González, A. Garrido Frenich, J. L. Martínez Vidal, *Food Chem.* **2012**, *134* (4), 2465–2472.

[32] M. Tasioula-margari, O. Okogeri, *J. Food Sci.* **2001**, *66* (4), 530–534.

[33] M. Bonoli, M. Montanucci, T. Gallina Toschi, G. Lercker, *J. Chromatogr. A*. **2003**, *1011* (1–2), 163–172.

[34] H. Hotta, M. Ueda, S. Nagano, Y. Tsujino, J. Koyama, T. Osakai, *Anal. Biochem.* **2002**, *303* (1), 66–72.

[35] A. Carrasco Pancorbo, C. Cruces-Blanco, A. Segura Carretero, A. Fernández Gutiérrez, *J. Agric. Food Chem.* **2004**, *52* (22), 6687–6693.

[36] S. Kesen, H. Kelebek, S. Selli, *J. Am. Oil Chem. Soc.* **2014**, *91* (3), 385–394.

[37] F. Priego-Capote, J. Ruiz-Jiménez, M. Luque de Castro, *J. Chromatogr. A*. **2004**, *1045* (1–2), 239–246.

[38] Y.-Q. Ma, J.-C. Chen, D.-H. Liu, X.-Q. Ye, *Ultrason. Sonochem.* **2009**, *16* (1), 57–62.

[39] E. Espada-Bellido, M. Ferreiro-González, C. Carrera, M. Palma, C. G. Barroso, G. F. Barbero, *Food Chem.* **2017**, *219*, 23–32.

[40] M. Cittan, A. Çelik, *J. Chromatogr. Sci.* **2018**, *56* (4), 336–343.

[41] R. Wu, F. Ma, L. Zhang, P. Li, G. Li, Q. Zhang, W. Zhang, X. Wang, *Food Chem.* **2016**, *204*, 334–342.

# OPTIMIZATION, KINETICS AND THERMODYNAMICS OF THE SOLID-LIQUID EXTRACTION PROCESS OF FLAVONOIDS FROM ROSEMARY (*ROSEMARINUS OFFICINALIS*) LEAVES

**MILAN MITIĆ[a], SONJA JANKOVIĆ[a*], JELENA MRMOŠANIN[a], MILAN STOJKOVIĆ[a], DANIJELA KOSTIĆ[a], RUŽICA MICIĆ[b]**

**ABSTRACT.** Solid-liquid extraction of total flavonoids (TF) from rosemary (*Rosemarinus officinalis*) leaves was studied in the present work. The effects of type of solvent and its concentration, temperature and extraction time on amount of flavonoids as well as the effects of these parameters on the kinetics and thermodynamic parameters of extraction process were investigated. The effects of the process factors on the TF were assessed using the full factorial test plan $2^3$. Extraction using 50% ethanol in a 50 °C during 100 min, was the most suitable conditions to produce a extract with high content of flavonoids (32.428 mg catechin equivalents / g rosemary leaves). The following two-parametric models were analyzed: non-stationary diffusion model trough the plant material, model of Ponomarev and parabolic diffusion model. All models gave a good fit to the experimental data (root mean square, RMS<2%, coefficient of determination, $R^2$>93%). The ΔG°, ΔS° and ΔH° values of the flavonoids extraction process were -4.89 – (-7.02) kJ/mol, 23.59 – 25.91 KJ/mol and 0.95 – 9.90 kJ/mol, respectively, indicating spontaneous, irreversible, and endothermic process.

*Keywords: rosemary, flavonoids, kinetic model*

## INTRODUCTION

During the last few decades, consumption of the plants and their products is in constant growth. The continental climate in Serbia favours the growth of a great of number plant species, some of them have various

---

[a] *Faculty of Sciences and Mathematics, Department of Chemistry, University of Niš, Višegradska 33, P.O. Box 224, 18000 Niš, Serbia*
[b] *Faculty of Science and Mathematics, Department of Chemistry, University of Priština*
[*] *Corresponding author: sonjajankovic1991@gmail.com*

MILAN MITIĆ, SONJA JANKOVIĆ, JELENA MRMOŠANIN, MILAN STOJKOVIĆ,
DANIJELA KOSTIĆ, RUŽICA MICIĆ

medicinal and antioxidant properties [1,2]. Health benefits include antimicrobial and antioxidant efficacies, which can be of great significance in therapeutical approaches of many diseases [3].

*Rosemarinus officinalis,* commonly known as rosemary, is an shrub belonging to the *Lamiaceae* family. Native to the Mediterranean region, rosemary is now cultivated around the world due to its use as a natural food preservative and flavouring agent. Rosemary has also been used as a source of traditional medicine for centuries; its applications have ranged from memory enhancement to the treatment of gastrointestinal diseases [4, 5].

Formulations of rosemary include the raw leaves, and extracts of rosemary. Rosemary extract contains different classes of polyphenols including phenolic acids, flavonoids and phenolic terpenes. Phenolic acids include: the hydroxycinnamic acids, hydrobenzoic acids and hydroxyphenylacetic acids. Flavonoids include the flavones and flavonols [6, 7, 8].

Extraction is the first step in the isolation of phenolic compounds from plant materials. Different techniques have been applied to recover antioxidant phenolic compounds from natural sources including solid/liquid extraction with organic solvent, microwave-assisted extraction, ultrasound-assisted extraction and supercritical fluid extraction. However, the efficiency of the extraction process is effected by several factors, such as the type of solvent and its concentration, the solvent/solid ratio, the number of extraction steps, pH, time of contact, temperature and particle size of the solid matrix [9, 10]. Thus, it is very important to optimize the extraction efficiency to each raw material. Also, mathematical modelling of solid-liquid extraction process is on important engineering tool in the design process in order to reduce energy, time and chemical reagents consumption.

The objectives of this study were to (1) evaluate the effect of type of solvent and its concentration, extraction temperature and extraction time on the flavonoids yield from rosemary, and then (2) investigate the kinetics and thermodynamics of the flavonoids extraction.

## RESULTS AND DISCUSSION

### Optimization of extraction process

The type of solvent and its concentration, extraction temperature and extraction time are key factors in extraction process, as they affect both kinetics and the extraction yield. Therefore, this study consisted in evaluating the effect of these variables, namely solvent concentration, extraction temperature and extraction time on the extraction process of flavonoids from rosemary leaves. The results obtained in these experiments shown significant changes in

flavonoids content with different independent variables (supplementary materials Table 1S). By varying the extraction conditions, the flavonoid contents were increased about 5-fold in ethanol and about 3-fold in methanol solution. When comparing the maximum flavonoid content, the extraction in 50% ethanol seem the most successful. The efficiency of different solvents is related to the physicochemical properties of the flavonoid compounds (polarity, stability, solubility). The optimum extraction conditions were as follows: 50% ethanol, extraction temperature 50 °C, and extraction time 100 min.

A mathematical model was proposed for the extraction of flavonoids with ethanol and methanol as extraction solvent, The values of all linear regression coefficients for flavonoids extraction with ethanol and methanol are given in Table 2.

The positive signs of the coefficients for extraction temperature and extraction time indicate a synergistic effect, while the negative sign for solvent concentration indicated an antagonistic effect.

The analysis of variance (ANOVA Test) for the response variables (content of flavonoids in ethanol and methanol solvent) are presented in Table 3S, Supplementary Material. The statistical significance of all three factors and their possible two- and three-way interaction for the flavonoids yields were evaluated for their $F$-and $p$-values. The statistical significance of a factor is greater if its $F$-value is higher. The value of $p<0.05$ indicates the significance of the factors and their interaction. The simplified regression equations are given in Table 6. The predicted values of the flavonoids content are presented in Table 1S, Supplementary Material.

It was clear that the linear and interaction terms were highly significant ($p<0.05$). The $F$-values for $x_1$, $x_2$ and $x_3$ factors are in interval 52.029–1658.4, respectively. The most important factor was the solvent concentration ($x_1$), which was followed by the extraction temperature ($x_2$) in cause extraction with ethanol, but in cause extraction with methanol followed by the extraction time ($x_3$). On the two-ways interaction, it is worth to mention the combination of the solvent concentration and extraction time ($x_1$ $x_3$) affected flavonoids content in both solvents. The three-way interaction ($x_1x_2x_3$) had no significant influence ($p>0.05$) on the extraction yield of flavonoids. It is also necessary that the developed regression models (Table 3) provide an adequate approximation in real system. The regression analysis and ANOVA Test were used for fitting the models. The coefficients of determination ($R^2$), the adjusted $R^2$ ($R^2_{adj}$) and coefficient of variation (CV) were calculated to check the model adequacy (Table 3). Our results showed that the $R^2>98\%$ and $R^2_{adj}>97\%$, indicating that the regression model was suitable for explaining the behavior. Our results showed also that the coefficients of variation were <5% for both the responses, representing a better precision and reliability of the conducted experiments.

MILAN MITIĆ, SONJA JANKOVIĆ, JELENA MRMOŠANIN, MILAN STOJKOVIĆ,
DANIJELA KOSTIĆ, RUŽICA MICIĆ

### Kinetic analysis

Since the data from previous experiment showed the highest influence of the solvent concentration and the temperature on the flavonoids content, different temperature (T=30, 40 and 50 $^{o}$C) at extraction time intervals (t=10, 20, 30, 40, 50, 60, 80 and 100 min) with pure ethanol, 50% ethanol, pure methanol and 50% methanol were used the kinetic study. It is evident from Fig. 1 that flavonoids yield increase with temperature during the extraction process. This was due to increase in diffusion on the flavonoids and decrease in viscosity as the temperature. It is also evident from Fig. 1, the flavonoids content using 50% ethanol was higher when compared to the other solvents under to same conditions.

By analyzing the extraction curves for all extraction solvents used in this study, two periods of extraction were observed. A rapid increase in the content of flavonoids at the early beginning of the process and the slow increase in the content of total flavonoids, likely due to internal diffusion. The rapid extraction process at the beginning was due to free flavonoids on the surface of the plant material that was exposed to fresh solvent. In general, as seen in Fig. 1, most of the flavonoids are released from the rosemary leaves to the solvent during first 20 min of the extraction process.

In this work non-stationary diffusion model through the plant material, model of Ponomarev and parabolic diffusion model were used for description of flavonoids extraction process. The list of estimated kinetic parameters for all extraction solvent and all three analysed temperatures is given in Table 4. Kinetic parameters for non-stationary diffusion model, model of Ponomarev and parabolic diffusion model were obtained by plotting log $q/q_o$ and $(q_o-q)/q_o$ versus t, and $\bar{q}$ versus $t^{1/2}$, respectively.

As it can be seen their values were, more or less, dependent on the extraction conditions. It was observed that for all models, their kinetic parameters increased with increase in temperature. The flavonoids amount increase with temperature was due to the thermodynamic effect of flavonoids solubilization in the solid matrix particles [15]. A similar tendency was observed in previous studies where bioactive compounds were extracted from sage (*Salvia officinalis* L.) and glutinous sage (*Salvia glutinosa* L.) [13], from hop (*Humulus lupulus* L.) [18], and oil was extracted from *Terminalia catappa* [17] and from tabacco (*Nicotiniatabacum* L.) seeds [19].

When the ethanol concentration increased from 50 to 100% by volume, all kinetic parameters decreased, except k, which increased. But, when methanol concentration increased from 50 to 100%, diffusion extraction coefficients decreased, but washing coefficients increased. Also, the parabolic diffusion model predicts the smallest values of washing coefficients, while the same model predicts the highest values of diffusion extraction coefficients.

114

Linear coefficient of determination ($R^2$) and root mean square (RMS) were used to evaluate correlation between the experimental data and selected model. Table 3S, Supplementary Material presented of the $R^2$ and RMS for each kinetic models and for all extraction conditions. From the results in Table 3S, Supplementary Material it was evident that irrespective of type solvent and their concentration, individual values of the RMS were less than ±2% for each of the three models considered. It could be observed from Table 5 that while the average RMS decreased, the best fit of the models increased in the following order:

parabolic diffusion model→non-stationary diffusion model through the plant material→model of Ponomarev.

Similarly, the average linear correlation coefficient $R^2$ value increased in the following order:

parabolic diffusion model→non-stationary diffusion model through the plant material→model of Ponomarev

Based on these results, model of Ponomarev, having the highest value of the linear correlation coefficient $R^2$, and lowest RMS values were chosen as the best extraction kinetics model for flavonoids extraction from rosemary leaves.

**Thermodynamic parameters**

The influence of temperature on extraction rate of flavonoids from rosemary was analysed using the Arrhenius equation (Eq.6). Calculated values of activation energies are given in Table 6. The plot of lnb' (or k') (model of Ponomarev) vs. 1/T were used to determine the value of activation energies.

Calculated activation energies were in the range 2.38-13.22 kJ/mol. These values were in good agreement with literature values reported for other bioactive compounds [20, 21, 22].

These results imply that the washing and diffusion coefficients were the most sensitive to temperature in the case of extraction with 100% methanol, and the least sensitive to temperature in case of extraction with 100% ethanol. Values of the activation energy are greater for the washing process than for the diffusion process, meaning that the former is stronger influenced by both extraction temperature and concentration of solvent than the latter process. The $E_a$-value for the flavonoids washing in 50% ethanol were higher

than those in 100% ethanol, but those for 100% methanol were higher than those for the washing in 50% methanol. The $E_a$-value for the flavonoids' diffusion in 50 and 100% ethanol were similar to each other, and that for diffusion in 100% methanol was higher than those in 50% methanol.

Table 7 shows the values of equilibrium constants and thermodynamic parameters for the flavonoids extraction process from rosemary leaves. The plot of $\ln K_e$ vs. 1/T were used to determined the value of thermodynamic parameters. The values of enthalpy were the range of 1.07-2.26 kJ/mol. They increased with increase in the solvent concentration. Positive enthalpy change indicates the endothermic nature of the extraction process and as such required external energy source during the extraction [17, 23].

The entropy values for the extraction process were in the range of 23.59-25.91 KJ/mol. The positive value of entropy change describes the process is irreversible.

Similar results were obtained for extraction process for other compounds with different solvent [24, 25, 26, 27, 28].

The Gibbs free energy change values lie between -6.25 to -6.93 kJ/mol and -5.12 to -7.02 kJ/mol, respectively for both types of extraction solvents. The Gibbs free energy change values for the extractions were all negative. Thus, indicating that the process was feasible and spontaneous.

The efficiency of the flavonoids extraction was favoured with increasing extraction temperature. A similar tendency was also reported for flavonoids extraction from *Phyllanthus emblica* (-2.65 to 0.15 kJ/mol) [24], total phenolics from hop (-11.99 to -10.78 kJ/mol) [22], coconut oil (-1.16 to -0.12 kJ/mol) [23], olive cake oil (-6.25 to -4.45 kJ/mol)[26], and hempseeds oil (-5.17 to -2.41 kJ/mol) [28].
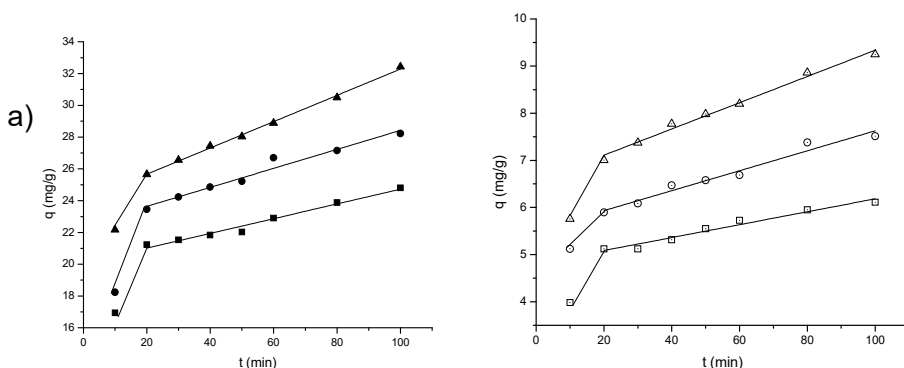


a)

b)
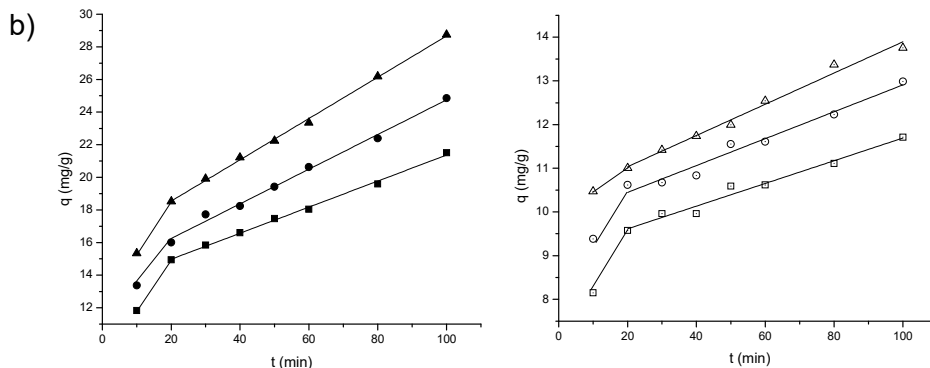


**Figure 1.** Effect of the extraction time on the total flavonoids yield in a) ethanol and
b) methanol extraction solvent at different solvent concentration: 50% at ▲-30 ºC,
●-40 ºC and■-50 ºC; 100% at △-30ºC, ○-40 ºC and □-50 ºC

**Table 1.** Parameters and levels using in the $2^3$ factorial design study

| Parameters | Levels | |
|---|---|---|
| | (-1) | (+1) |
| Solvent concentration[a], % ($x_1$) | 50 | 100 |
| Extraction temperature, ºC ($x_2$) | 30 | 50 |
| Extraction time, min ($x_3$) | 20 | 10 |
| Extraction method | Maceration | |

**Table 2.** Regression coefficient of the predicted linear first-order models

| Model parameters | Regression TF, mg g in ethanol | Coefficients TF, mg g in methanol |
|---|---|---|
| Intercept | 16.451 | 16.221 |
| *Linear* | | |
| $x_1$ – solvent concentration | -9.578 | -4.709 |
| $x_2$ – temperature | 2.133 | 1.788 |
| $x_3$ – time | 1.696 | 2.709 |
| *Interaction* | | |
| $x_1x_2$ | -0.879 | -0.920 |
| $x_1x_3$ | -0.889 | -1.488 |
| $x_2x_3$ | 0.556 | 0.533 |
| $x_1x_2x_3$ | -0.244 | --0.380 |

**Table 3.** Regression equations

| Solvent | | CV(%) | $R_{adj}^2$(%) | $R^2$(%) |
|---|---|---|---|---|
| Ethanol | $y=16.451-9.578x_1+2.133x_2+1.696x_3-0.879x_1x_2-0.889x_1x_3+0.556x_2x_3$ | 4.04 | 99.23 | 99.59 |
| Methanol | $y=16.221-4.709x_1+1.788x_2+2.709x_3-0.920x_1x_2-1.488x_1x_3+0.533x_2x_3$ | 3.99 | 97.85 | 98.85 |

**Table 4.** Values of estimated model parameters for solid/liquid extraction
for total flavonoids from rosemary leaves

| Solvent | T | | Model | A | |
|---|---|---|---|---|---|
| | (ᵒC) | b | k | RMS | $R^2$ |
| 100% ethanol | 30 | 0.741 | $1.038 \cdot 10^{-3}$ | 1.33 | 95.64 |
| | 40 | 0.775 | $1.365 \cdot 10^{-3}$ | 1.56 | 96.11 |
| | 50 | 0.811 | $1.478 \cdot 10^{-3}$ | 1.24 | 98.10 |
| 50% ethanol | 30 | 0.823 | $0.885 \cdot 10^{-3}$ | 0.72 | 98.37 |
| | 40 | 0.842 | $1.013 \cdot 10^{-3}$ | 1.18 | 96.10 |
| | 50 | 0.851 | $1.245 \cdot 10^{-3}$ | 0.32 | 99.83 |
| 100% methanol | 30 | 0.822 | $1.070 \cdot 10^{-3}$ | 1.09 | 97.31 |
| | 40 | 0.835 | $1.148 \cdot 10^{-3}$ | 1.19 | 97.30 |
| | 50 | 0.844 | $1.252 \cdot 10^{-3}$ | 0.93 | 98.31 |
| 50% methanol | 30 | 0.771 | $1.923 \cdot 10^{-3}$ | 0.71 | 99.68 |
| | 40 | 0.786 | $2.276 \cdot 10^{-3}$ | 1.55 | 99.02 |
| | 50 | 0.806 | $2.586 \cdot 10^{-3}$ | 1.78 | 98.66 |

The continuation of Table 4

| 2 | Model | B | | | Model | C | |
|---|---|---|---|---|---|---|---|
| b' | k' | RMS | $R^2$ | $A_o$ | $A_1$ | RMS | $R^2$ |
| 0.382 | $1.095 \cdot 10^{-3}$ | 1.24 | 96.18 | 0.325 | $16.306 \cdot 10^{-3}$ | 1.26 | 96.86 |
| 0.437 | $1.685 \cdot 10^{-3}$ | 1.42 | 96.96 | 0.353 | $24.604 \cdot 10^{-3}$ | 1.43 | 96.87 |
| 0.521 | $2.212 \cdot 10^{-3}$ | 0.94 | 98.94 | 0.409 | $32.363 \cdot 10^{-3}$ | 0.70 | 96.79 |
| 0.562 | $1.296 \cdot 10^{-3}$ | 0.80 | 97.88 | 0.500 | $18.571 \cdot 10^{-3}$ | 1.14 | 94.67 |
| 0.628 | $1.677 \cdot 10^{-3}$ | 1.08 | 96.66 | 0.543 | $24.580 \cdot 10^{-3}$ | 0.93 | 97.56 |
| 0.672 | $2.324 \cdot 10^{-3}$ | 0.37 | 99.75 | 0.557 | $33.640 \cdot 10^{-3}$ | 1.08 | 97.91 |
| 0.557 | $1.597 \cdot 10^{-3}$ | 1.06 | 97.43 | 0.478 | $23.184 \cdot 10^{-3}$ | 1.21 | 96.64 |
| 0.602 | $1.890 \cdot 10^{-3}$ | 1.26 | 96.99 | 0.511 | $27.179 \cdot 10^{-3}$ | 1.75 | 93.83 |
| 0.632 | $2.192 \cdot 10^{-3}$ | 0.77 | 98.75 | 0.523 | $31.920 \cdot 10^{-3}$ | 1.01 | 98.20 |
| 0.423 | $2.520 \cdot 10^{-3}$ | 0.56 | 99.74 | 0.280 | $36.536 \cdot 10^{-3}$ | 1.51 | 98.19 |
| 0.446 | $3.356 \cdot 10^{-3}$ | 1.19 | 99.38 | 0.298 | $28.370 \cdot 10^{-3}$ | 1.78 | 98.14 |
| 0.506 | $3.997 \cdot 10^{-3}$ | 0.57 | 99.85 | 0.309 | $57.860 \cdot 10^{-3}$ | 1.95 | 98.18 |

**Table 5.** Comparison of the average percentage RMS and $R^2$
for different kinetic models

| Kinetic model | 100% RMS | Ethanol $R^2$ | 50% RMS | Ethanol $R^2$ | 100% RMS | Methanol $R^2$ | 50% RMS | Methanol $R^2$ |
|---|---|---|---|---|---|---|---|---|
| Model A | 1.37 | 96.62 | 0.75 | 98.09 | 1.07 | 97.64 | 1.35 | 99.14 |
| Model B | 1.20 | 97.36 | 0.74 | 98.10 | 1.03 | 97.72 | 0.77 | 99.66 |
| Model C | 1.30 | 96.84 | 1.05 | 98.72 | 1.32 | 96.23 | 1.75 | 98.17 |

**Table 6.** Activation energy (kJ/mol) at different extraction solvent

| Process | 100% ethanol | 50% ethanol | 100% methanol | 50%methanol |
|---|---|---|---|---|
| Washing | 5.43 | 9.33 | 13.22 | 8.93 |
| Diffusion | 2.38 | 2.71 | 5.35 | 3.61 |

**Table 7.** Thermodynamic parameters of the flavonoids'
extraction process with different solvents

| Solvent | T (°C) | $K_e$ | $\Delta H^o$ (kJ/mol) | $\Delta S^o$ (JK/mol) | $\Delta G^o$ (kJ/mol) |
|---|---|---|---|---|---|
| 100% ethanol | 30 | 0.945 | 1.601 | 25.906 | -6.248 |
| | 40 | 1.482 | | | -6.507 |
| | 50 | 2.701 | | | -6.766 |
| 50% ethanol | 30 | 2.271 | 1.117 | 24.929 | -6.437 |
| | 40 | 3.764 | | | -6.686 |
| | 50 | 9.841 | | | -6.935 |
| 100% methanol | 30 | 2.543 | 2.259 | 23.588 | -4.888 |
| | 40 | 3.896 | | | -5.124 |
| | 50 | 5.366 | | | -5.360 |
| 50% methanol | 30 | 2.119 | 1.067 | 25.037 | -6.519 |
| | 40 | 3.655 | | | -6.769 |
| | 50 | 9.899 | | | -7.020 |

MILAN MITIĆ, SONJA JANKOVIĆ, JELENA MRMOŠANIN, MILAN STOJKOVIĆ,
DANIJELA KOSTIĆ, RUŽICA MICIĆ

## CONCLUSIONS

A full factorial experiment $2^3$ was used to determine the optimum parameters that gave high extraction yields. The analysis of variance showed that the effects of all variables (solvent concentration, extraction temperature and extraction time) were extremely significant. The linear regression mathematical models had higher correlation and could be employed to optimize the flavonoids extraction from rosemary leaves. Results from this study suggested that 50% ethanol was the best solvent for the extraction of flavonoids from rosemary leaves since it give the highest flavonoids yield compared to the other solvents (pure ethanol, pure methanol, 50% methanol) examined. The three kinetic models describe: non-stationary diffusion model through the plant material, model of Ponomarev and parabolic diffusion model all reasonably described flavonoids extraction from rosemary leaves as indicated by high $R^2$ and low RMS values. Model of Ponomarev gave the best fit followed by non-stationary diffusion model, and then parabolic diffusion model. The $\Delta H^o$, $\Delta S^o$, and $\Delta G^o$ values obtained for the four different extraction solvents indicated that the extraction process was spontaneous, irreversible, and endothermic, respectively.

## EXPERIMENTAL

### Plant materials

Rosemary (*Rosemarinus officinalis*) leaves was collected in B. Palanka area (Republic of Serbia) during the flowering season of 2018 and dried naturally in the shade for one month. Dried plant material was grounded in the blender (average plant particle size: 0.60 mm) and kept the paper bags before its usage.

### Solvent and chemicals

### *Extraction procedure and experimental design*

In the first stage, the extraction experiments were performed using different conditions of solvent concentration (ethanol or methanol), extraction temperature and extraction time. The conditions used in each experiment were settled according to the $2^3$ full factorial design presented in Table 1. The maceration procedure was employed for the extraction of flavonoids from rosemary leaves. Thus, according to the experimental design (Table 1S,

Supplementary Material), plant samples (2g) were extracted by a same volume but different solvent concentration, at a different temperature and a different extraction time. The extraction process was carried out using a bath thermostate. After each extraction, extract filtered on Whatman filter paper (No.1) and evaporated to dryness using a rotary evaporator (BUCHI rotavapor R-200). Dried extract was dissolved in extraction solvent before analysis. For each extraction solvent (experimental design), the response function investigated was $y$ = mg of flavonoid/g of dry plant material (mg/g). Regression analysis was performed based on the experimental data and was fitted into a proposed linear first-order model using the following equation [11]:

$$y = \beta_o + \sum_{i=1}^{k} \beta_i x_i + \sum_{i=1}^{k-1} \sum_{j=2}^{k} \beta_{ij} x_i x_j + \sum_{i=1}^{k-2} \sum_{j=2}^{k-1} \sum_{k=3} \beta_{ijk} x_i x_j x_k \quad (1)$$

Where $y$ is the flavonoids content (response), $x_i$ the independent variables influencing the responses, $\beta_o$, $\beta_i$, $\beta_{ij}$, $\beta_{ijk}$ ($i, j, k = 1,2,3$) are the regression coefficients of variables for intercept, linear and 2- and 3-factor interaction terms, respectively. The quality of the fit of the regression model was expressed by the adjusted R-squared (adjusted $R^2$), coefficient of determination ($R^2$) and coefficient of variation (CV).

### *Initial content of flavonoids*

Macerated plant material (2g) was weighed into a 250 mL Erlenmeyer flask with a ground stopper and covered with 50 ml of the extraction solvent. The extraction was carried out by the maceration method for a period of 100 minutes. The extracts were separated from the residues by filtering through the Whatman No. 1 filter paper. The residues were extracted twice with the same fresh solvent and extracts combined. The combined extracts were concentrated and freed of solvent under reduced pressure at 45 °C, using a rotary evaporator (BUCHI Rotavapor R-200). The dried crude concentrated extracts were dissolved using extraction solvent until used for analysis. The dried extracts were prepared thrice and the results averaged. The values of the initial contents of flavonoids in rosemary were 12.583, 35.723, 16.318 and 31.653 mg/gdw in 100% ethanol, 50% ethanol, 100% methanol and 50% methanol, respectively.

### *Determination of total flavonoids*

Total flavonoids were determined using previously described spectro-photometric method [12]. The results for total flavonoids were expressed as milligrams of catechin equivalents per g of dry rosemary leaves (mg CE/g).

MILAN MITIĆ, SONJA JANKOVIĆ, JELENA MRMOŠANIN, MILAN STOJKOVIĆ,
DANIJELA KOSTIĆ, RUŽICA MICIĆ

### Kinetics of flavonoids extraction

The rosemary leaves (2g) and the extraction solvent (50 mL) were placed in a series of Erlenmayer flasks (250 mL) and the flasks were macerated in 10, 20, 30, 40, 50, 60, 80 and 100 minutes. The temperature was controlled and maintained at 30±0.1°C. After each time interval the liquid extract was separated from the plant material residues by vacuum filtration. Liquid extracts were prepared thrice and the results averaged. The procedure was repeated at 40±0.1°C and 50±0.1°C.

### Modelling of flavonoids extraction kinetics

The extraction kinetics flavonoids from rosemary was modelled by three models (Table 2S, Supplementary Material): non-stationary diffusion model through the plant material, model of Ponomarev [13] and parabolic diffusion model [14].

### Thermodynamic parameters

Influence of temperature on the extraction rate was assessed using Arrhenius equation:

$$k = Ae^{-E_a/RT} \tag{2}$$

where $k$ represent the extraction rate, $A$ is the Arrhenius constant, $E_a$ is the activation energy, $R$ is the universal gas constant, and $T$ is the absolute temperature. A plot of $lnk$ versus $1/T$ gives a straight slope where $-E_a/R$ represents the activation energy of the extraction process [3].

Thermodynamic parameters (ΔG°, ΔH°, ΔS°) were estimated using Eqs.(3)- (5):

$$\Delta G^o = -RTlnK_e \tag{3}$$

$$lnK_e = -\frac{\Delta G^o}{RT} = -\frac{\Delta H^o}{RT} + \frac{\Delta S^o}{R} \tag{4}$$

$$K_e = \frac{q_L}{q_S} \tag{5}$$

where $K_e$ is equilibrium constant, $q_L$ is amount of flavonoids in liquid at equilibrium temperature T, $q_S$ is amount of flavonoids in solid at equilibrium temperature, while $\Delta H^o$ (kJ/mol), $\Delta S^o$ (JK/mol), and $\Delta G^o$ (kJ/mol) are enthalpy change, entropy change and Gibbs free energy change, respectively [15].

### *Statistical analysis*

A full factorial model $2^3$ with replication was used to optimize the flavonoids extraction with respect to type of solvent and its concentration, extraction temperature and extraction time, the factors affecting flavonoids yields. The significance of the factors and their combinations were evaluated by the ANOVA Test using a computer program. The linear first-order regression equations were also developed to show the dependence of flavonoids yields on factors and their interactions.

The best fit among the models was evaluate using coefficient of determination ($R^2$) [16] and root mean square (RMS) [14, 17].

The higher the value of $R^2$ and lower the values of the RMS; the better will be goodness of the fit [14].

**SUPPLEMENTARY MATERIALS** can be obtained by request from the authors.

**REFERENCES**

1. P. Mašković; V. Veličković; S. Đurović; Z. Zeković; M. Radojković; A. Cvetanović; J. Švarc-Gajić; M. Mitić;  J.Vujić; *Phytomedicine,* **2018**, *38*, 118-124.2. A. Žugić; S. Đorđević; I. Arsić; G. Marković; J. Živković; S. Jovanović; V. Tadić; *Ind. Crop Prod.,* **2014**, *52*, 519-527.
3. A. J. Tušek; M. Benković; A. Belščak Cvitanović; D.Valinger; *Ind. Crop Prod.*, **2016**, *91*, 205-214.
4. H. Rafi; H. Soheila; E. Grant; *Herbal Medicine,* **2017**, *3*, 2-8.
5. S. Selmi; K. Rtibi; D. Grami; H. Sebai; L.Marzonki; *Pathophysiology*, **2017**, *24*, 297-303.
6. M. B. Hassain; D. K. Rai; N. P. Brunton; A. B. Maktin-Diana; C. Barry-Ryan; *J. Agric. Food Chem.*, **2010**, *58*, 10576-10581.
7. A. Valverdu-Queralt; J. Regueiro; M. Martinez-Huelamo; J. F. Rinaldi Avarega; L. N. Leal; M. R.Lamuela-Raventos; *Food Chem.*, **2014**, *154*, 299-307.
8. P. Mena; M. Cirtina; K. A. Herrlinger; C. Dall'Asta; D. Del Rio; *Molecules*, **2016**, *21*, 1576.
9. M. T. Escribano-Bailon; C. Santos-Buelga; *Methods in Polyphenol Analysis*; Polyphenol extraction from foods, In: C. Santos-Buelga, G. Williamson (Eds.), The Royal Society of Chemistry: Cambridge, United Kingdom, **2003**; pp. 1-16.

10. S. I. Mussato; L. F. Ballesteros; S. Martins; J. A. *Teixeira; Sep. Sci. Technol.*, **2011**, *83*, 173-179.

11. M. A. Bezerra; R. E. Santelli; E. P. Oliveira; L. S. Villar; L. A. Escaleira; *Talanta*, **2008**, *76*, 965-977.

12. B. T. Stojanović; S. S. Mitić; G. S. Stojanović; M. N. Mitić; D. A. Kostić; D.Đ. Paunović; B. B. Arsić; A. N. Pavlović; *Food Chem.*, **2017**, *232*, 466-475.

13. D. T. Veličković; D. M. Milenović; M. S. Ristić; V. B. Veljković; *Ultrason. Sonochem.*, **2006**, *13*, 150-156.

14. S. Kitanović; D. Milenović; V. Veljković; *Biochem. Eng. J.*, **2008**, *41*, 1-11.

15. M. Y. Liauw; F. A. Natan; F. A. Widiyanti; D. Ikasari; N. Indraswati; F. E. Soetaredjo; *ARPN J. Eng. Appl. Sci.*, **2008**, *3*(3), 1-6.

16. R. C. A. Amarante; P. M. Oliveria; F. K. Schwantes; J. A. Morón-Villareyes; *Ind. Eng. Chem. Res.*, **2014,** *53*, 16, 6824-6829.

17 M. C. Menkiti; C. M. Agu; T. K. Udeigwe; *Ind. Crop Prod.*, **2015**, *77*, 713-723.

18. D. Đ.Paunović; S. S. Mitić; D. A. Kostić; M. N. Mitić; B. T. Stojanović, J. Lj. Pavlović; *Adv. Technol.*, **2014**, *3*, 58-63.

19. I. T. Stanisavljević; M. L. Lazić; V. B. Veljković; *Ultrason.Sonochem.*, **2007**, *14*, 646-652.

20. A. Bucić-Kojić; M. Planinić; S. Tomas; M. Bilić; D. Velić; *J. Food Eng.*, **2007**, *81*, 236-242.

21. V. Sant'Anna; A. Brandelli; L. D. F. Marczak; I. C. Ressaro; *Sep. Pur. Thechnol.*, **2012**, *100*, 82-87.

22. D. Đ.Paunović; S. S. Mitić; G. S. Stojanović; M. N. Mitić; B. T. Stojanović; M. B. Stojković; *Sep. Sci. Technol.*, **2015**, *50*, 1658-1664.

23. S. Sulaiman; A. R. Abdul Aziz; M. K. Aroua; *J. Food Eng.*, **2013**, *114*, 228-234.

24. R. Y. Krishnan; K. S. Rajan; *Braz. J. Chem. Eng.*, **2017**, *34*, 885-899.

25. S. Amin; S. Hawash; G. El Diwani; S. El Rafei; *Am. J. Sci.*, **2010**, *6*, 8.

26. S. Meziane; H. Kadi; *J. Am. Oil Chem. Soc.*, **2008**, *85*, 391-396.

27. H. Topolar; U.Gecgel; Turk. *J. Chem.*, **2000**, *24*, 247-253.

28. M. D. Kostić; N. M. Joković; O. S. Stamenković; K. M. Rajković; P. S. Milić; V. B.Veljković; *Ind. Crop Prod.*, **2014**, *52*, 679-686.

# TRACKING THE GROWING RINGS IN BIOGENIC ARAGONITE FROM FISH OTOLITH USING CONFOCAL RAMAN MICROSPECTROSCOPY AND IMAGING

**GEZA LAZAR[a], CALIN FIRTA[a,b], SANJA MATIĆ-SKOKO[c],
MELITA PEHARDA[c], DARIO VRDOLJAK[c], HANA UVANOVIĆ[c],
FRAN NEKVAPIL[a,b], BRANKO GLAMUZINA[d],
SIMONA CINTA PINZARU[a*]**

**ABSTRACT.** Fish otoliths pose increasing interest due to their potential of rendering information about environmental changes, underlined in their non-linear time-dependent biogenic crystal growth. Otoliths are acellular, metabolically inert and continuously grow in a complex process which still needs to be understood. In the present work confocal Raman micro-spectroscopy (CRM) and imaging is employed to investigate the growth pattern in otoliths from *Sparus aurata* of Mediterranean provenance. CRM signal acquired from otolith sagittal section is exploited to associate it with the periodic growth increments denoted as rings. Raman signal collected from the core to the margins with micrometer spatial resolution invariably revealed characteristic signal of aragonite. Relative intensity variability was observed particularly for the lattice modes, indicating changes in crystalline orientation relative to incident laser. Bands associated with organic fraction were absent in the 90-1840 cm$^{-1}$ spectral range. Daily growth rings were further studied using the Raman mapping of main aragonite bands intensities at 1083, 704 and the lattice modes in the 100-350 cm$^{-1}$ range. The spectral intensity pattern closely follows the daily growth pattern. Traces of toxic or heavy metals incorporated in biogenic carbonate mineral were spuriously detected in the mapped areas, according to the position and width of the Raman bands of witherite ($BaCO_3$), strontianite ($SrCO_3$), along with the main aragonite and trace of its calcite polymorph.

*Keywords*: *Confocal Raman micro-spectroscopy, fish otoliths, Raman mapping, growth rings, aragonite.*

[a] *Babes-Bolyai University, Biomolecular Physics Department, Kogalniceanu 1, RO-400084 Cluj-Napoca, Romania*
[b] *National Institute for Research and Development of Isotopic and Molecular Technologies, 400293 Cluj-Napoca, Romania*
[c] *Institute of Oceanography and Fisheries, Šetalište I. Meštrovića 63, 21000 Split, Croatia*
[d] *University of Dubrovnik, Department for Aquaculture, Ćira Carića 4, 20000 Dubrovnik, Croatia*
\* *Corresponding author simona.cinta@phys.ubbcluj.ro*

GEZA LAZAR, CALIN FIRTA, SANJA MATIĆ-SKOKO, MELITA PEHARDA, DARIO VRDOLJAK, HANA UVANOVIĆ, FRAN NEKVAPIL, BRANKO GLAMUZINA, SIMONA CINTA PINZARU

## INTRODUCTION

Otoliths are crystalline $CaCO_3$ biominerals with a small fraction of organic matrix, located in the inner ear of vertebrates. They serve as a balance organ for equilibrium and contribute to hearing [1], [2]. Fish otoliths are increasingly investigated due to the potential correlation of their lifetime development with the environmental changes they encountered. Defined as opaque zones delimiting the translucent ones, the otoliths growing rings provide valuable tool for the fish age determination. The use of otoliths as chronometric structures to track the recorded environmental conditions along the organism life-time is still in its infancy. However, increasing number of Raman spectroscopy studies already refer to the otolith sclerochronology as valuable tools for tracking environmental changes [3-4], employing the characteristic Raman signature of calcium carbonate polymorphs [5] which could occur in otoliths complex biomineralization process. Their growth pattern is composed of a number of concentric rings with different radii. Depending on the amount of organic material in each shell or zone, its appearance will vary from extremely opaque to complete hyaline (transparent) with the first zone being the nucleus (core) of the otolith. These zones are also called growth rings [4]. Previous Raman studies showed that the characteristic polymorph of calcium carbonate biomatrix, present in otoliths, is aragonite with the typical Raman vibration modes $\nu_1$ (1085 cm$^{-1}$) and $\nu_4$ (701 cm$^{-1}$ and 705 cm$^{-1}$) as well as lattice modes (8 bands between 142 cm$^{-1}$ and 282 cm$^{-1}$) [3, 6]. Moreover, some studies have reported two different $CaCO_3$ crystalline structures, aragonite and vaterite, in the otoliths of different fish species [7] [8] [9], which can differ dramatically in their trace elemental composition [10, 11]. Some of the studies reported the coexistence of three polymorphs of calcium carbonate (calcite, aragonite, vaterite) in the shell of Antarctic bivalves having the same growing pattern (rings) as fish otoliths [12]. Gauldie et al (1997) [13] reported first vaterite polymorph signature in the low wavenumber range of the micro-Raman spectra of otoliths core from the coho salmon *Oncorhynchus kisutch* (Teleostei: Salmonidae) and highlighted the aragonite nature of the otolith first ring.

On the other hand, the polymorphs of calcium carbonate may interfere with other, mixed carbonate minerals, whose Raman analysis relies on correct interpretation of the specific lattice modes [14, 15]. Furthermore, strict similarity of the biogenic with geogenic mineral Raman feature must be treated with caution, since their environment and mechanism of formation is different. Wehrmeister et al (2010) showed that the structure of vaterite contains three crystallographic independent carbonate groups and similar carbonate group layers, and firstly assigned a band at 263 cm$^{-1}$ to vaterite [16].

The aim of the current study is to probe the potential of the confocal Raman micro-spectroscopy (CRM) technique for detailed investigation of otolith morphology and growing pattern in Mediterranean **Sparus aurata** and to probe the versatility of the Raman technique to upscale the study for larger otoliths groups. Optimized conditions for screening would generate robust Raman data which could be further exploited for any correlation with environmental conditions encountered during fish otoliths lifetime period.

## RESULTS AND DISCUSSIONS

From the larger set of otoliths, we randomly selected one as subject for the present detailed study, as a prerequisite for the forthcoming comparative Raman analyses of otolith sets. The investigated otolith fragment is shown in the Figure 1 along with the optical micrographs taken with the Raman microscope in transmission (b) and direct illumination (c) using a 20x objective (NA 0.35).
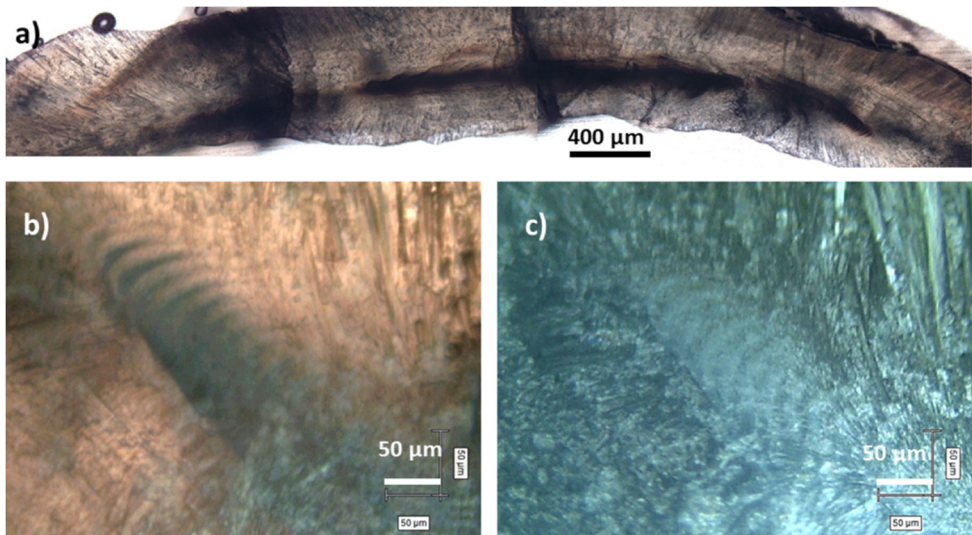


**Figure 1**. Photo-stitch of the otolith fragment in sagittal section (a), together with the light microscopy images taken with the Raman microscope in transmission (b) or direct illumination (c), using a 20x objective. Scale bars: 400 µm (a) and 50 µm (b and c).

A series of CRM spectra presented in the Fig. 2 acquired from otolith along a line starting from core toward edge, with a 50 µm step and corresponding to the growing direction, indicated by the orientation of the

micro-crystallites, clearly depict aragonite as the main mineral component of the otolith across its sagittal section. These spectra were collected using the lowest magnification objective available (5x, NA 0.12). We noted lower background of the recorded signal when higher magnification objectives are employed. However, for gross screening of the whole otolith while preserving the screening line direction, the 5x objective was optimal. Bearing in mind that high background in the Raman spectra could potentially masque additional, low intensity bands from other trace minerals, further analysis is devoted later.
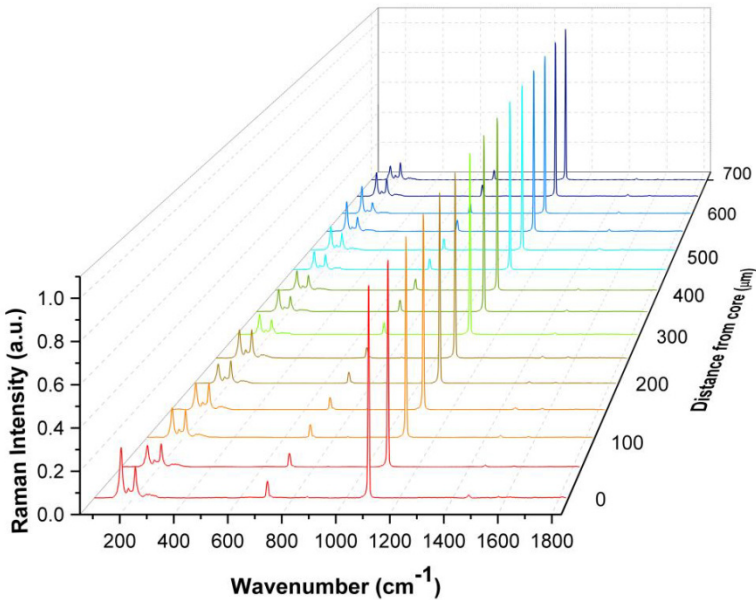


**Figure 2.** 3D display of the normalized, background subtracted CRM spectra collected along a line direction starting from otolith core toward edge with a 50 μm step. Excitation: 532 nm, 5x objective (NA 0.12).

In geogenic aragonite, the unit cell of crystalline orthorhombic aragonite comprises 20 atoms (four fomula units in a crystalline cell). Its 57 vibrational modes are classified [19] according to the irreducible representations of point groups theory, as follows:

$$\Gamma_{total} = 9A_g + 6A_u + 6B_{1g} + 8B_{1u} + 9B_{2g} + 5B_{2u} + 6B_{3g} + 8B_{3u}.$$

The g (*gerade*) modes are all Raman active while u (*ungerade*) modes are IR active, with the exception of Au modes, which are silent [19]. Thus, Raman spectrum of aragonite is expected to show 30 fundamental modes. However, due to the fact that many of the vibrational modes are of very weak intensity, it is

extremely difficult to detect experimentally all the active modes [19], particularly in natural samples. In synthetic aragonite [13] the lattice modes detected in Raman spectra were reported at 113 (w), 142 (s), 153 (s), 180 (w),190(w), 206 (m), 242 (w), 261 (w), 284 cm$^{-1}$ (w), the symmetric stretching mode $\nu_1$ at 1085 cm$^{-1}$ (vs), the $\nu_3$ at 1462 (w) and 1574(w) and the $\nu_4$ at 701(s) and 705 cm$^{-1}$ (m). Table 1 summarized the observed Raman bands in otolith core and first ring, in comparison with the reported Raman data of geogenic aragonite [18, 19] calcite [19], vaterite [17] and two other minerals from the aragonite group, witherite [14] and strontianite [17], along with their assignment.

**Table1.** The Raman bands observed in spectra collected from otolith core and first ring along with the characteristic bands of geogenic aragonite polymorphs (calcite, vaterite) and other carbonate minerals from aragonite group, witherite, (BaCO$_3$) or strontianite (SrCO$_3$)

| Otolith Core | Otolith 1$^{st}$ ring | Aragonite [19] | Aragonite [18] | Calcite [19] | Vaterite [17] | Whiterite [14] | Stronitianite [17] | Assignment (Symmetry) [19] |
|---|---|---|---|---|---|---|---|---|
| 1461 | 1457 1571 | 1462.2 1573.9 | 1463 1576 | 1435.8 | | 1420 | 1445 | $\nu_3$ (B$_{1g}$) |
| 1083 | 1081 | 1085.3 | 1085 | 1086.2 | 1080 1090 | 1059 | 1071 | $\nu_1$ (A$_{1g}$) |
| | | 853.3 | 853 | | | | | $\nu_2$ (A$_g$) |
| 685 | | | | | | 690 | 510 | |
| 690 | | | | | | 699 | 710 | |
| 699 | 700 | 701.8 | 701 | | | | | $\nu_4$ (A$_g$) (B$_{2g}$) |
| 704 | 704 | 706.1 | 705 | | | | | |
| 716 | 714 | 717.1 | 716 | 712.4 | | | | |
| 727 | | | | | 739 | | | |
| 731 | | | | | 749 | | | |
| | | 113.5 | 115 | | | | | |
| | | 125 | 125 | | | | | |
| | | 142.9 | 145 | | | | | |
| 152 | 153 | 153 | 155 | | | | | |
| | | 162.2 | 164 | | | | | |
| 180 | 180 | 180 | 182 | | 106 | 100 | 148 | |
| | | 190.7 | 192 | 154.9 281.2 | 206 265 299 | 135 153 179.67 224.9 | 180 214 236 244 258 | Lattice Modes |
| 206 | 206 | 206.3 | 208 | | | | | |
| | | 214.7 | 216 | | | | | |
| | | 225.5 | | | | | | |
| | 247 | 248.3 | 250 | | | | | |
| | 260 | 260.1 | 263 | | | | | |
| | | 272 | 274 | | | | | |
| | | 283.6 | 285 | | | | | |

GEZA LAZAR, CALIN FIRTA, SANJA MATIĆ-SKOKO, MELITA PEHARDA, DARIO VRDOLJAK, HANA UVANOVIĆ, FRAN NEKVAPIL, BRANKO GLAMUZINA, SIMONA CINTA PINZARU

The strong aragonite signal in the otolith (Fig. 2) was identified by the presence of the symmetric stretching mode of the carbonate $\nu_1$ at 1083 cm$^{-1}$ and the $\nu_4$ vibrational mode at 701 and 704 cm$^{-1}$ as well as lattice modes in the low wavenumbers region: 152, 180 and 206 cm$^{-1}$. The aragonite signal has proved to be the strongest along the entire scan line with apparent traces [14] of other calcium carbonate polymorphs, while the organic matrix was not detectable using the 5x objective (NA 0.12) for excitation and collecting optics in 1 s acquisition.

Taking a closer microscopy look while taking Raman spectra with higher magnification objectives, such as 20x (NA 0.35) or 100x (NA 0.9), respectively, subtle details have been observed on much lower background. The spectral details as showed in the Figure 3. Micro-Raman spectra collected from the first ring of otolith using three different objectives, 5x, 20x and 100x respectively, are showed in the Fig. 3 a) in comparison with the Raman spectra from RRUFF database of geogenic aragonite (RRUFF ID: R080142), calcite (RRUFF ID: R150075) and strontianite (RRUFF ID: R040037). Their spectra showed subtle differences, particularly in the lattice modes range (50-300 cm$^{-1}$), and in the main stretching modes around 1083 and 704 cm$^{-1}$. Spectral details are highlighted in the Fig. 3 b, c and d, which allowed us to argue that trace of calcite, witherite and strontianite could be present [14]. In addition, the main Raman stretching mode at 1083 cm$^{-1}$, which is slightly shifted from those of geogenic aragonite observed at 1085 cm$^{-1}$, showed a narrower band for the otolith core than for the first ring. The shoulder at 1077 cm$^{-1}$ (Fig. 3 b) slightly higher in spectrum from the first ring than that from the core, and further different from that of geogenic aragonite, may suggest the presence of other carbonate mineral, such as strontianite (amorphous calcium carbonate was excluded, due to the clear evidence of the lattice modes). Zoom of the 680-740 cm$^{-1}$ spectral range (Fig. 3 d) revealed aragonite modes at 704 cm$^{-1}$ with additional weak band (shoulder) at 700 cm$^{-1}$, and other weak bands, potentially indicating calcite and witherite traces [14]. In the lattice modes region (Fig. 3 c) subtle differences among biogenic and geogenic aragonite are observed; the band at 180 cm$^{-1}$ could be attributed to either aragonite or to a certain mixture of different carbonates [14]. Strontianite (Sr 0.91 Ca 0.09)CO$_3$ exhibited main Raman band at 1077 cm$^{-1}$ while in the lattice modes range it shows bands at 150 (strong) and 183 cm$^{-1}$ (weak) which are overlapped with the aragonite lattice modes. Therefore, in an aragonite crystalline matrix, trace of Sr to replace Ca ions is difficult to reveal via Raman spectroscopy although the shoulder at 1077 cm$^{-1}$ may suggest strontianite trace presence. Moreover, the 699 cm$^{-1}$ mode of witherite [14] or strontianite [15] could be responsible for the observed shoulder in the $\nu_4$ Raman mode of aragonite centered at 704 cm$^{-1}$ (Fig. 3).
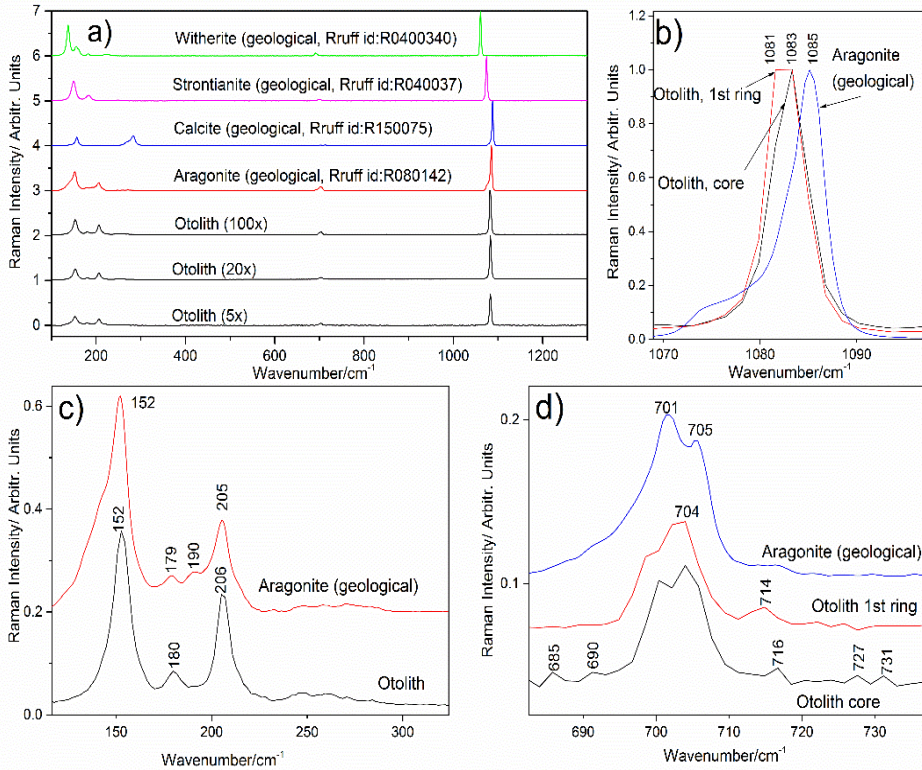
**Figure 3.** Micro-Raman spectra collected from the otolith in the optical region of the first yearly ring, using three different objectives, as indicated (a), in comparison with the geological aragonite (red, RRUFF ID: R080142), calcite (blue, RRUFF ID: R150075), strontianite (magenta, RRUFF ID: R040037) and witherite (green, RRUFF ID: 040040); (b) zoom of the main stretching mode at 1083 cm$^{-1}$ showing narrower band for the otolith core than for the first ring; (c) lattice modes highlighting subtle differences among Raman signal of biogenic and geologic aragonite; (d) spectral zoom of the characteristic mode of aragonite at 704 cm$^{-1}$ with additional weak bands potentially indicating calcite / strontianite trace; Excitation: 532 nm. Otolith spectra from (b, c, d) are collected with 20x objective.

The presence of a weak band at 690 cm$^{-1}$ suggests the presence of barium carbonate (witherite) [14]. The supposition is further sustained by the preliminary scanning electron microscopy and energy dispersive X-Ray analyses (SEM-EDX) preliminary data (not shown here) on the otoliths set (manuscript in preparation), although the Sr trace randomly appeared at 0.2 Wt%, thus, at the

GEZA LAZAR, CALIN FIRTA, SANJA MATIĆ-SKOKO, MELITA PEHARDA, DARIO VRDOLJAK,
HANA UVANOVIĆ, FRAN NEKVAPIL, BRANKO GLAMUZINA, SIMONA CINTA PINZARU

limit of EDX detection. The Raman spectra obtained with higher magnification objectives, describes a smaller area with better focus on the otolith saggital section surface and the presence of the new bands could be attributed to different crystal orientations or to the trace presence of other carbonates in that spot. Potential accumulation of heavy or toxic metals from environment at a certain moment of the fish otolith evolution is random and could result in random deposit of carbonate mineral with replaced calcium by the respective metal. Powdering the whole otolith for X-ray powder difraction (XRPD) would be an alternative solution for analysis, provided that the trace metal form other carbonate minerals is sufficient for the XRPD detection limit. The drawback of such analysis is the complete loss of the spatial location to track the moment (or ring age) the event occurred during the fish lifetime. Another isssue related to the fish age and the counting rings is connected to the non-linear growth and development of the otolith, where plethora of factors can compete.

Choosing appropriate optics, vaterite trace could be presumably detected according to the weak bands observed at 263 cm$^{-1}$ [16], although the main vaterite bands at 740-750 cm$^{-1}$ as well as the split of the main $\nu_1$ mode of carbonate is rather expected for typical vaterite polymorph presence. However, the major bands of vaterite were absent in the recorded spectra, sugesting its absence or trace occurence (vaterite being a metastable polymorph of calcium carbonate) compared to other dminant minerals. Also, the presence of other cations may promote the formation of the aragonite crystals. [17]

The daily rings or increments have been Raman mapped following the fast streamline imaging and signal-to-baseline criteria of the Wire 3.4 software. An area of 260 μm x 96 μm has been selected over the light microscopy image of the otolith viewed with the 20x objective. A scan step of 4 μm was used, resulting 65x24 pixels with distinct spectral information from 1560 spectra. For map analysis, signal-to-baseline criteria for representative modes of aragonite (696-707 cm$^{-1}$, 240-265 cm$^{-1}$), calcite (279-285, 712-716 cm$^{-1}$), strontianite (1073-1079 cm$^{-1}$) distribution have been selected. Further, overlay maps were generated.

Examination of the mapping results (Fig. 4) in terms of Raman intensity distribution over the selected area provides an overview of the chemical and crystalline composition. The intensity distribution over the mapped area showed consistent feature supporting aragonite main component but trace of calcite and strontianite could be detected. Mapping over the main Raman mode at 1083 cm$^{-1}$ resembled similar distribution feature. The fact that the growth rings are visible both in optical microscopy images and in Raman maps is a clear sign that the Raman signal intensity is strongly correlated to certain activity patterns of the daily rings fish development. The maps clearly show an alternation of minima and maxima in all cases which can be linked to the activity of the
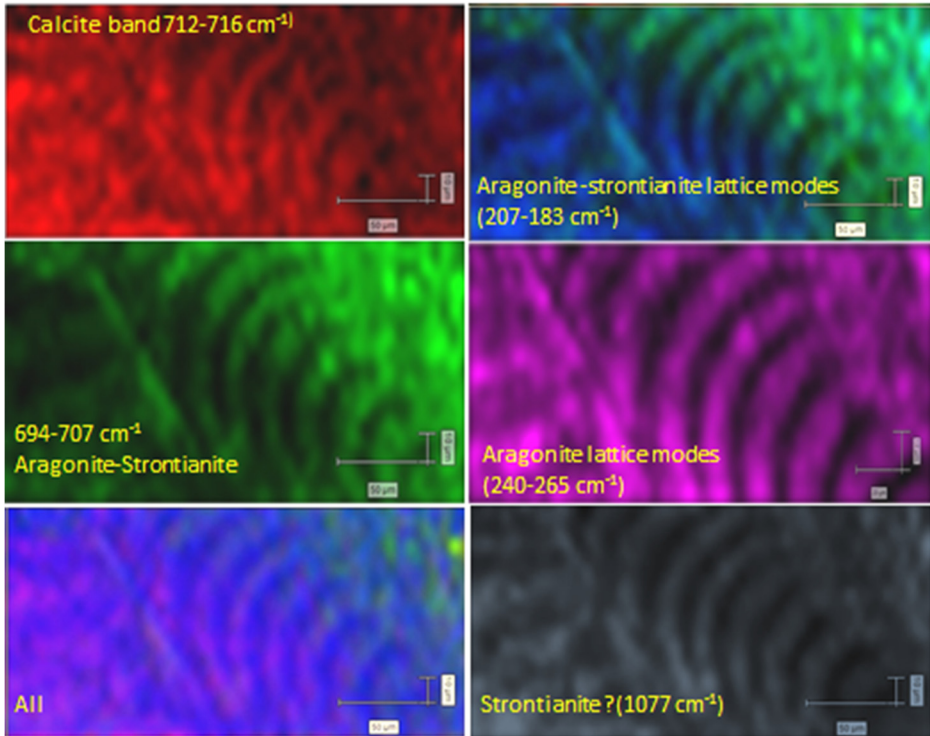
**Figure 4.** Raman mapping of otolith increments or "daily rings" following the signal-to-baseline criteria, as indicated in each map for trace of calcite (weak band between 712-716 cm$^{-1}$, top left), aragonite-strontianite (lattice modes - top right), $v_4$ mode - midde left), aragonite lattice modes (middle, right), trace of strontianite (1077 cm$^{-1}$ bottom right) and all the overlapped images (bottom left).

fish on a daily cycle. The Raman intensity variation patterns follows the opacity patterns from light microscopy. The more intense color zones represeting areas with highest signal-to-baseline, suggest more deposited, highly ordered crystalline material and dark zones areas with less crystalline deposited material. This feature clearly suggests non-uniform otolith crystal growth which may be due to the genetic factors, water chemistry, temperature, migration habits, depth, and other variable conditions occuring in fish environment. Otolith spectroscopic data and their correlation in fish populations still needs to be understood. For such approaches, Raman versatility seems to be optimal for fast tracking information on the otolith gowth patterns.

## CONCLUSIONS AND OUTLOOK

The current study provides additional insight into the Raman spectroscopy of otoliths and the dependencies of the Raman spectral features on the selected optics for otolith screening. Confocal Raman micro-spectroscopy is suitable for tracking the otoliths development and potential heavy or toxic metals intake in chemical composition. Thus, Raman techniques proved to be important tools for tracing biomineralization. An integrated, larger study on otolith sets from similar species and habit could use the present results for comparative Raman analysis. For long term, we aim to probe the correlation of otolith morphology and composition revealed from Raman data with environmental parameters. Further environmental changes could be potentially tracked according to the otoliths spectral characteristics, provided that robust data sets are available. Understanding the effects of environmental factors on the chemical composition and structure of otoliths could be very useful in the field of fisheries science, biomineralization or sclerochronology. Their use in reconstructing fish migratory paths or in analyzing population structure could prove to be very important in future approaches.

## EXPERIMENTAL

### Materials

One otolith was randomly selected from a stock of 16 adults of gilthead sea bream, *Sparus aurata*, collected from four locations in the eastern Adriatic Sea during 2017 (open sea, coastal waters, estuary and aquaculture rearing cages). The studied otolith is from a female captured from estuary area of Novigrad - Karinsko Sea, (Zadar County, Croatia), weighting 274 g and 27 cm in length with an estimated age of 2.5 years. For standardization purposes, the left sagittae were systematically considered. The otoliths were washed in 30% hydrogen peroxide solution for 2-4 minutes and rinsed in distilled water. Samples were then cleaned in an ultrasonic bath (SONOREX SUPER RK 103 H) for 2 minutes and left to air-dry. Epoxy resin (MEGAPOXY H) was prepared by mixing three parts of resin and one part of hardener. These two components were stirred together for 2-3 minutes until the mixture changed color to translucent. The otoliths were embedded in the molds which were lightly coated with Struers Silicone and they were left to dry in the fume cupboard for one day.

Isomet low-speed diamond bladed saw was used for preparing otolith section. Saw was fitted with two blades separated by a spacer (500 μm), producing a 400-500 μm otolith thin section. Each thin section was carefully grounded with Struers Labopol-5 using Struers wetted silicon carbide paper

(4000 grit) at the speed of 50 rpm. Thin sections were then polished using a soft cloth sprayed with diamond paste (3 μm) and washed again in ultrasonic bath for 2 minutes.

Stitched photography of otolith section has been achieved using a series of images taken with a ZEISS microscope equipped with AXIO camera and ZEN 2 (blue edition) program. Stitched image has been obtained with Image-Pro Premier 9.1 software. All sections (core and growth marks) were observed via optical microscopy. Opacity data were acquired on transects from the core to the ventral edge with black areas corresponded to opaque zones.

## Methods

Confocal Raman spectra were acquired using a Renishaw InVia Confocal Raman System and a Cobolt DPSS laser emitting at 532 nm. During Raman microscopy the, 5X (NA 0.12 WD 13.2 mm), 20X (NA 0.35, WD 2 mm) and 100X (NA 0.9, WD 3.4 mm) collecting objectives were used with theoretical spatial resolutions of 2.7 μm, 0.927 μm and 0.36 μm respectively, and for single spectra acquisitions at controlled distances from otolith core, the acquisition parameters were 1 s, 1 acquisition, 200 mw laser power. An edge filter has been employed to record spectra in the 90-1840 $cm^{-1}$ spectral range with 0.5 $cm^{-1}$ resolution. Signal has been detected using a Rencam CCD and data acquisition and processing has been achieved with WIRE 3.4 and Origin 8.1 software. Micrographs of the morphological details have been acquired along with spectral data acquisition using the video image facility of the WIRE software. Yearly growing rings have been observed via optical microscopy before Raman measurements and subtle incremental rings have been observed and mapped using the "signal-to-baseline" or "intensity-at-point" options of the Wire 3.4 mapping software.

## ACKNOWLEDGEMENT

## REFERENCES

1. S. E. Campana, *Mar. Ecol. Prog. Ser.*, **1999**, *188*, 263-297.
2. S. E. Campana, S. R. Thorrold, *Can. J. Fish. Aquat. Sci.*, **2001**, *58(1)*, 30-38.
3. S. Cinta Pinzaru, S. Matić-Skoko, M. Peharda, D. Vrdoljak, H. Uvanović, C. Firta, G. Lazar, F. Nekvapil, L. Barbu-Tudoran, M. Suciu, B. Glamuzina, in Peharda, M., Ezgeta-Balić, D., Uvanović, H. (Eds). "5th Int. Sclerochronology Conf., 16-20th June 2019, Split, Croatia. Book of Abstracts", **2019**, p. 144.

4. R. P. Rodríguez Mendoza, *Croat. J. Fish.,* **2006**, *64* (3), 89- 102.
5. G. Behrens, L.T. Kuhn, R. Ubic, A. H. Heuer, *Spectrosc. Lett.*, **1995**, *28*, 983-995.
6. S. E. Campana, *Comp. Biochem. Physiol.,* **1983**, *75A,* 215‑220.
7. R. W. Gauldie*, J. Mar. Fish. Res.*,**1985**, *20*, 209–217.
8. J. M. Casselman, J. M. Gunn, *Can. J. Fish. Aquat., Sci.,* **1992**, *49(Supp1.1),* 102-111.
9. J. Tomás, A. J. Geffen, *J. Fish Biol.*, **2003**, *63(6),* 1383-1401.
10. R. Brown, K. P. Severin, *Can. J. Fish. Aquat. Sci.*, **1999**, *56*,1898–1903.
11. S. Melancon, B. J. Fryer, J. E Gagnon, S. A. Ludsin, and Z. Yang, *Can. J. Fish. Aquat. Sci.*, **2005**, *62*, 2609-2619.
12. G. Nehrke, H. Poigner, D. Wilhelms-Dick, T. Brey, D. Abele, *Geochem. Geophys. Geosyst.*, **2012**, *13*, Q05014.
13. R. W. Gauldie, S. K. Sharma, E. Volk, *Comp. Biochem. Physiol. A-Physiol.*,**1997**, *118*, 753-757.
14. W. Kaabar, S. Bott, R. Devonshire, *Spectrochim. Acta A Mol. Biomol. Spectrosc.*, **2011**, *78*,136–141.
15. N. Buzgar, Al. Apopei, *An. Stiint Univ. Al. I. Cuza Iasi, Geol.*, **2009***, 55*, 97–112.
16. U. Wehrmeister, A. L Soldati, D. E. Jacob, T. Häger, W. Hofmeister*, J. Raman Spectrosc.*, **2010**, *41,* 193-201.
17. F. C. Donnelly, F. Purcell-Milton, V. Framont, O. Cleary, P. W. Dunne, Y. K. Gun'ko, *Chem. Commun.*, **2017**, *53*, 6657–6660.
18. S. Farsang, S. Béclin, S. Redfern, *Am. Min.,* **2018**, *103*, 1988–1998.
19. M. De La Pierre, C. Carteret, L. Maschio, E. André, R.Orlando, R. Dovesi, *J. Chem. Phys.,* **2014**, *140*, 164509.

# STRUCTURAL, MORPHOLOGICAL AND DISSOLUTION PROPERTIES OF $ZrO_2$-BASED BIOCOMPOSITES FOR DENTAL APPLICATIONS

**LILIANA BIZO[a], KLARA SABO[a], RÉKA BARÁBAS[b], GABRIEL KATONA[b], LUCIAN BARBU-TUDORAN[c,d], ANTONELA BERAR[e,*]**

**ABSTRACT.** In the present work, zirconia-based biocomposites were prepared by adding different amounts of antibacterial magnesium oxide and bioactive and biocompatible hydroxyapatite (HAP). The biocomposites were synthesized by the conventional ceramic processing route. The structure and morphology of the materials were investigated using X-ray powder diffraction (XRPD), scanning and transmission electronic microscopy (SEM and TEM). The stability of the tetragonal structure of $ZrO_2$ was confirmed by XRPD analyses. Moreover, their bioactivity was studied by soaking the samples in artificial saliva (AS) to evaluate the effect of MgO and HAP on the biological performances of the prepared biocomposites. UV-VIS analyses carried out on artificial saliva after immersion of the prepared materials showed that MgO plays an important role in the post-immersion dissolution process.

**Keywords:** *zirconia ($ZrO_2$), magnesium oxide (MgO), hydroxyapatite (HAP), biocomposites.*

[a] *Babeş-Bolyai University, Faculty of Chemistry and Chemical Engineering, Department of Chemical Engineering, 11 Arany Janos str., RO-400028, Cluj-Napoca, Romania*
[b] *Babeş-Bolyai University, Faculty of Chemistry and Chemical Engineering, Department of Chemistry and Chemical Engineering of Hungarian Line of Study, 11 Arany Janos str., RO-400028, Cluj-Napoca, Romania*
[c] *Babeş-Bolyai University, Faculty of Biology and Geology,Department of Molecular Biology and Biotechnology, 1 Mihail Kogălniceanu str., RO-400084, Cluj-Napoca, RO-400015, Romania*
[d] *National Institute for Research and Development of Isotopic and Molecular Technologies, 67-103 Donath Street, RO-400293, Cluj-Napoca, Romania*
[e] *"Iuliu Haţieganu" University of Medicine and Pharmacy, Faculty of Dentistry, Department of Prosthetic Dentistry and Dental Materials, 32 Clinicilor str., RO-400006, Cluj-Napoca, Romania*
* *Corresponding author: berar.antonela@umfcluj.ro*

LILIANA BIZO, KLARA SABO, RÉKA BARÁBAS, GABRIEL KATONA,
LUCIAN BARBU-TUDORAN, ANTONELA BERAR

## INTRODUCTION

Beside many dental ceramic materials, zirconia ($ZrO_2$) has been considered to be of great importance, due to its exceptional physical and biological properties and many researches were published on the synthesis of zirconia-based dental materials for applications in dental implants and prostheses [1-11]. $ZrO_2$ is an oxide which presents three types of crystalline structures at ambient pressure as follow: the monoclinic phase ($m$-$ZrO_2$), which is stable from room temperature up to 1170 °C and exhibits poor mechanical properties, the tetragonal phase ($t$-$ZrO_2$), which is stable in the temperature range 1170–2370 °C and has good mechanical properties, and the cubic phase ($c$-$ZrO_2$), which is stable above 2370 °C and has moderate mechanical properties [12-15].The spontaneous transformation from the $t$-phase to the more stable $m$-phase is associated with a volume increase of 3% to 5%. The tension which occurs inside of the different restorations made of pure $ZrO_2$, during the cooling after sintering, results in numerous microcracks, which could lead to premature failure of the restoration [16]. In order to stabilize the $t$-phase at room temperature, zirconia can be mixed with other metallic oxides, e.g. MgO, $CeO_2$, $La_2O_3$, CaO, $Y_2O_3$, etc. [17-19]. Yttria-doped tetragonal zirconia polycrystal (Y-TZP) has been the most attractive material in terms of toughness and structural properties and has recently been used for prosthetic rehabilitations as restorative materials in the fabrication of single crowns or fixed partial dentures and also in dental implantology. However, leaching of yttria in humid environments and the related degradation in properties have been a major bottleneck for wider applications of Y-TZP. Conversely, it was demonstrated that magnesium stabilized zirconia has several advantages and can be developed with a good combination of mechanical and tribological properties by using the appropriate preparation technique [20]. Moreover, the advantages of MgO as antibacterial material are multiple, as this oxide is an ample raw material, low cost and safe to human beings. [21]. Its mild antibacterial property lies mainly in the basicity and oxygen vacancies of MgO nanopowders [21-23].

Hydroxyapatite (HAP), a calcium phosphate (CaP) bioceramics similar to the human hard tissues in morphology and composition showed good osteoconductivity and bone-bonding ability [24]. Due to its outstanding properties like bioactivity, biocompatibility, non-toxicity, and non-inflammatory nature, HAP attracted great interest as a biomaterial used in different medical applications among orthopedic and dental implant coating, maxillofacial and dental surgery and restoration of periodontal defects, biodegradable scaffolds, and drug delivery systems occupy an important place.

ZrO$_2$-HAP composites are considered to be interesting materials, due to the combination between two bioceramics, the inert ZrO$_2$ and the active HAP, which could increase the bonding ability with natural bone in many medical fields. For these reasons, in the past decade, many ZrO$_2$-HAP composites have been developed as coating or substrate in order to achieve both bone reconstruction and regeneration needed in the treatment of large bone defects [25].

The present work aimed to prepare ZrO$_2$-based biocomposites by using different amounts of antibacterial MgO and bioactive and biocompatible HAP, by ceramic method followed by sintering at high temperature. The obtained biocomposites were further analyzed by X-ray powder diffraction (XRD), scanning electron microscopy (SEM) and transmission electron microscopy (TEM). Moreover, UV-VIS spectroscopy was employed to evaluate the bioactivity and biocompatibility of the prepared composites by *in vitro* preliminary tests, after immersion in artificial saliva (AS).


# RESULTS AND DISCUSSION

## Structural Studies

Structural analyses of the prepared composites were performed by XRPD before and after immersion in AS during 32 days. Figure 1 displays the XRPD patterns of biocomposites following sintering in the air at 1550 °C and before immersion in AS. XRPD analysis of powder samples showed that all patterns display a pure tetragonal phase (S.G. P4$_2$/nmc,) with peaks at 30.5º, 40.3º, 47.1º, 53.1º 68.5º, 72.9º and 78.4º corresponding to the (111), (112), (202), (221), (113), (132), (004) and (114) planes of *t*-ZrO$_2$ (JCPDS card no. 89-7710). By increasing the amount of MgO in the prepared composites, supplementary phase with peaks at 42.98º and 62.49º corresponding to (200) and (220) planes of periclase (MgO) appears, increasing in intensity, as visible from Figure 1. However, no characteristic peaks corresponding to any CaP-compounds, like HAP, TCP (tricalcium phosphate) or TTCP (tetracalcium phosphate) or CaO and CaZrO$_3$ was detected for any of the samples, within the detection limit of XRPD. These crystal structure transformations are the reactions that generally occur when sintering ZrO$_2$ and HAP at a high temperature.

The XRPD patterns after immersion in AS are presented in Figure 2. Examination of XRPD patterns indicates structural stability of the tetragonal phase but always accompanied by the periclase phase, with increasing its amount in the prepared biocomposites. As visible from XRPD patterns for S2 sample, pre- and post-immersion, two small peaks at 2θ = 28.3º and 31.43 belong to (-111) and (111) planes of m-ZrO2 phase, respectively (Figure 1 and Figure 2).
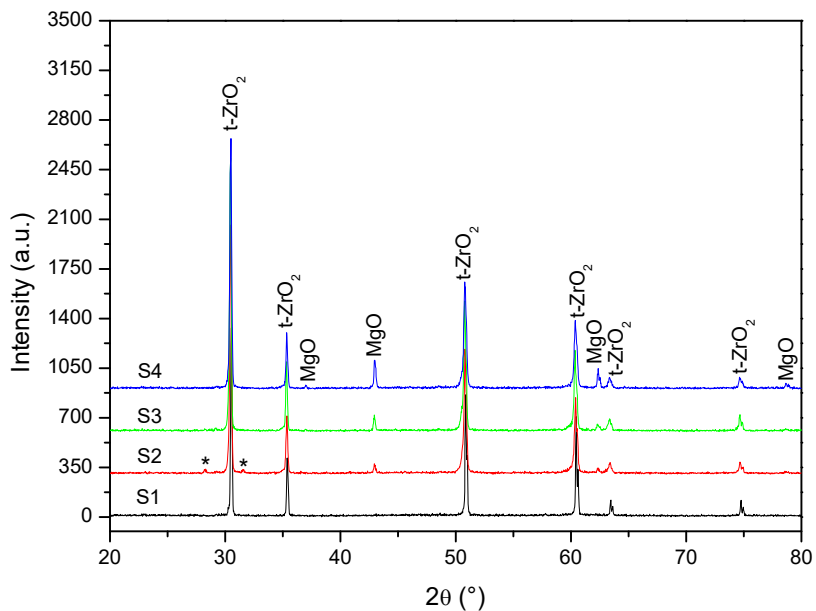
**Figure 1.** XRPD pattern of samples before immersion in AS.
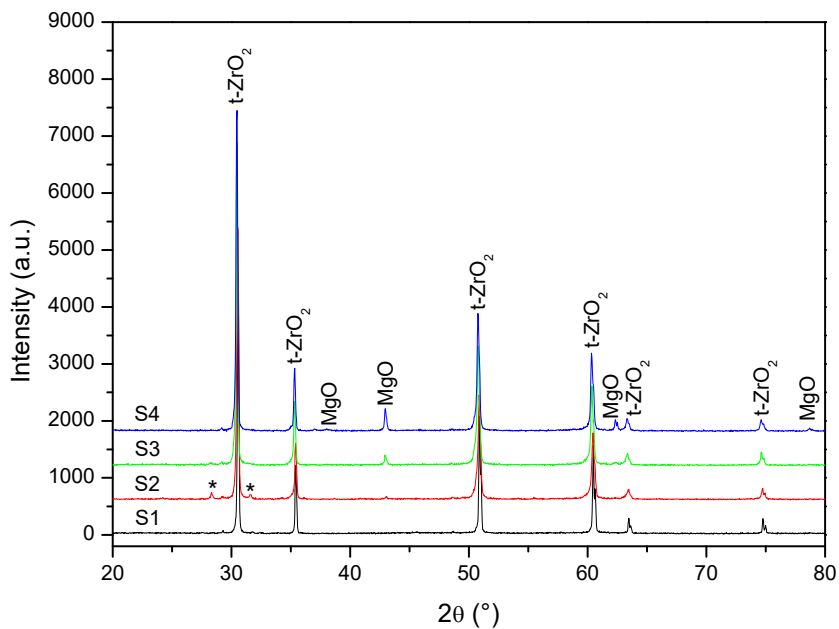


**Figure 2.** XRPD pattern of samples after immersion in AS.

The crystallite sizes (D) of the composites were calculated based upon on the (101) diffraction peak's broadening in the XRD pattern using the Scherrer equation:

$$D_{hkl} = 0.9\lambda/(\beta\cos\theta)$$

where: D - crystallite size along (hkl) direction, β - full width half maximum (FWHM) of the most intense diffraction line, λ - wavelength of X-ray, θ - the Bragg angle [26].

The evolution of the crystallite sizes in the prepared composites pre- and post-immersion is summarized in Table 1. As listed in Table 1, the crystallite sizes estimated using the Scherrer equation are ranged in the nanometric domain, between 51.91 nm to 71.27 nm. The results suggest the stabilization of ZrO$_2$ in the tetragonal phase for all the studied composites, which could be attributed to substitution of Zr$^{4+}$ by Mg$^{2+}$. Due to their ionic radii, Mg$^{2+}$(0.64 Å) should replace Zr$^{4+}$(0.89 Å) in the normal sites of the lattice, but replacing the host cation with a foreign cation of different radius and valence state introduces strain. The appropriate position for Mg$^{2+}$ in the ZrO$_2$ was Zr$^{4+}$ site and the charge difference was compensated by oxygen vacancies [27]. Consequently, substituting the Zr$^{4+}$ with a smaller ion, in this case Mg$^{2+}$, leads to a contraction of the lattice.

**Table 1.** Calculated crystallite sizes of compositespre- and post-immersion in AS.

| Composition | D$_{Scherrer}$ (nm) pre-immersion | D$_{Scherrer}$ (nm) post-immersion |
|---|---|---|
| S1 | 71.27 | 67.03 |
| S2 | 56.11 | 51.91 |
| S3 | 55.56 | 54.11 |
| S4 | 52.13 | 57.68 |

We can conclude that the weak changes noticed in the XRPD patterns prove that the structural units involved in matrix network are quite stable in the AS environment. However, low intensity peaks corresponding to m-ZrO$_2$, are presents only on post-immersed S2 sample and could be attributed to the martensitic transformation of t-ZrO$_2$ to m-ZrO$_2$ during cooling.

## Morphological Studies

The morphology of the composites after immersion in AS was examined by SEM and TEM. Figure 3 shows the morphological details of composites and coral-like interconnection of grains in the sintered ceramics. Figure 3a shows the typical connectivity of grains from which the sintering neck can be easily

observed. Between interconnected grains, uniform 2D rectangular MgO micro-sheets stacked in 3D are observed (Figure 3b-d). These MgO micro-sheets have tiny thickness and irregular shape. This type of interconnected structure in zirconia-based materials was previously observed by Hu et al. for yttria-stabilized zirconia ($ZrO_2$-8 mol% $Y_2O_3$, YSZ) ceramics sintered at 1550 °C [28]. They showed that the strong network provided by the interconnection of grains made it possible for the bodies to obtain high mechanical strength, easy to handle during the fabrication process and more adaptive to the working condition [28].
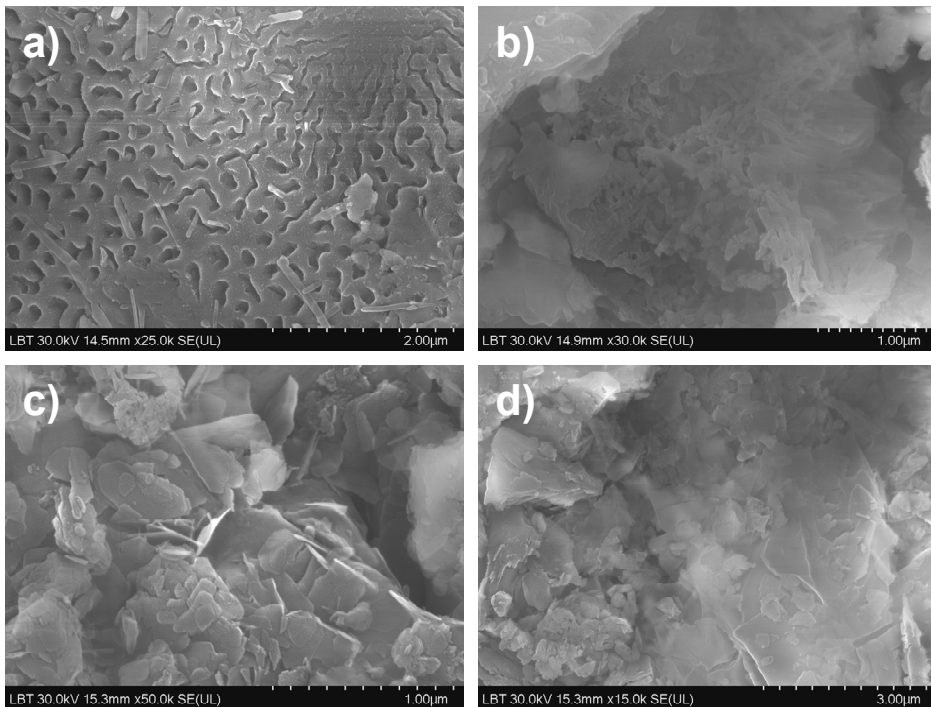


**Figure 3.** SEM images of (a) S1, (b) S2, (c) S3 and (d) S4 biocomposites after immersion in AS.

On the other hand, the microstructural observations reveal the presence of pores as seen in Figure 3a. The presence of such finer pores could favor the initial osteoblast cell attachment by a mechanical anchorage process, even though for an effective osteointegration process large pore sizes are desirable. Once cells are attached at the initial stage of implantation, the attached cell assembly would subsequently favor formation of multiple cells and thereby lead to *in vivo* tissue formation [20, 29]. Therefore, finer pores and less volume

fraction of porosity, as observed in the composites investigated here, should be beneficial from the point of view of both physical properties and biological cell attachment.

TEM images (Figure 4a-d) reveals highly agglomerated particles with size varying in the nanometric domain. These observations are in agreement with the results obtained by XRPD. Although all of the composites produced from the powders consist of fine grains of the ZrO$_2$, MgO and HAP phases, these are clustered into coarse-phase domains that are distributed rather inhomogeneously.
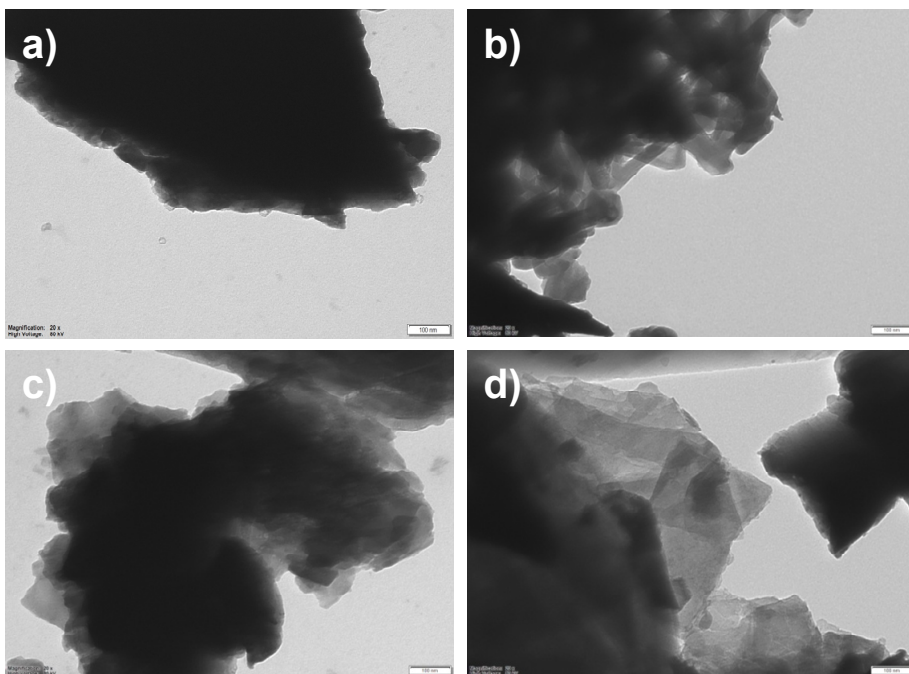


**Figure 4.** TEM images with a 20x magnification (scale bar 100 nm) of (a) S1, (b) S2, (c) S3 and (d) S4 biocomposites after immersion in AS.

### *In vitro* dissolution analysis

Figure 5 presents the UV-Vis absorption spectra for the as-prepared AS (AS before composites immersion) and AS after a 32 day immersion time of different prepared composites, further refer to AS1, AS2, AS3 and AS4, which corresponds to AS after immersion of S1, S2, S3, and S4 composites, respectively.

Absorption bands appear at 224 nm and 270 nm in the case of as-prepared AS. As seen from Figure 5, in the case of AS after immersion of composites, an absorption band appears at 205 nm, which is not evidenced in the as-prepared AS. These observed changes could be caused by the migration of ions between the biocomposites and the AS in which it is immersed. As zirconia has chemical stability under physiological conditions, MgO could have a significant impact on the interactions between the composites and AS in which incubation takes place. Due to the relatively weak ionic divalent metal-oxygen bonds, MgO dissolution could proceed by breaking these bonds, which release the $Mg^{2+}$ ions directly into the solution. The fast dissolution of magnesia contrasts with the behavior of other multi-oxide phases that require the breaking of more than one type of metal-oxygen bond. In these cases, the dissolution mechanism involves the sequential breaking of the bonds, which follows an order according to their reactivity. Taking into account the result obtained by Grima et al. [30] the phenomena which take place can be explained as follow. MgO dissolution is controlled by chemical reactions that involve the dissolution of MgO in a liquid medium to produce $Mg^{2+}$ and $OH^-$. Forwards, due to the water molecules, an intermediate brucite product could be generated and subsequently dissociated into $Mg^{2+}$ and $OH^-$ ions that form water by protonation [30].
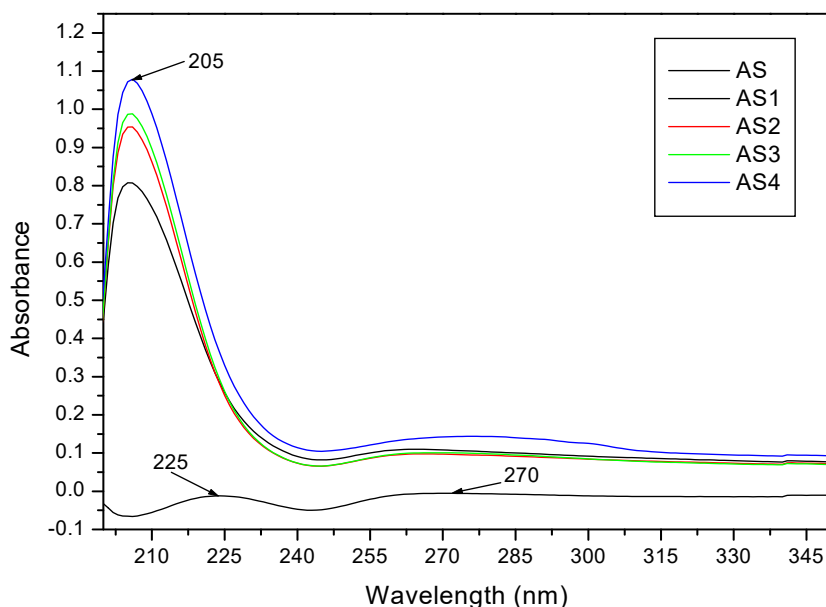


**Figure 5.** UV-VIS absorbance spectra of AS (as–prepared) and AS1, AS2, AS3 and AS4, which corresponds to AS after immersion of S1, S2, S3 and S4 composites, respectively.

One observation should be emphasized. Samples immersed in AS for 32 days did not form the HAP phase and this fact could favor the dissolution of the MgO phase. The release of biocompatible $Mg^{2+}$ ions acted as an inhibitor of HAP crystal growth suppressing unwanted crystallization *in vivo* [30].

In addition, the absorbance at 205 nm is increased with increasing MgO amount on the prepared composites. Further studies need to complete elucidate the *in vitro* complex mechanism which takes place.

## CONCLUSIONS

In order to improve the biological performances of the inert $ZrO_2$, a different amount of antibacterial MgO and bioactive and biocompatible HAP, was added to $ZrO_2$ matrix. $ZrO_2$-based biocomposites were successfully obtained by conventional ceramic method at 1550°C, followed by their characterization using XRPD, SEM and TEM techniques. The analyses indicated the presence of tetragonal $ZrO_2$ phase accompanied by periclase MgO with incresing its amount on the prepared biocomposites. HAP, or other CaP phases were not detected between the whole series of the prepared samples. Moreover, the stability and bioactivity of the prepared materials were tested by simulating the conditions from the oral cavity, by their immersion in artificial saliva (AS) for 32 days. The results suggest that MgO have an important role in the dissolution of biocomposites. Further studies need to understand both the physical and molecular level changes which take place following *in vitro* test of biocomposites.

## EXPERIMENTAL SECTION

### Preparation

#### *Preparation of HAP*

HAP was prepared by the precipitation method described in previous works [31-36] under continuous mechanical stirring. The following materials were used: 0.15 mol $L^{-1}$ solution of calcium nitrate tetrahydrate (Merck, Germany), 0.09 mol $L^{-1}$ solution of diammonium hydrogen phosphate (Merck), and 25 mass % ammonia solution (Posch Basic, Poland). The diammonium hydrogen phosphate and the ammonium solution were slowly added to the calcium nitrate solution. The pH of the reaction mixture was adjusted with ammonia solution to 11, and the reaction temperature was maintained at ambient temperature. The reaction mixture was stirred for 22 h. The Ca/P mole ratio was maintained at 1.67. After the reaction was accomplished, the precipitate was washed with ethanol and filtered. The filtered material was dried at 90 °C for 6 h.

## Biocomposites preparation

$ZrO_2$-based bioceramics were obtained by ceramic processing route which involved mixing, compaction and sintering. Commercial pure $ZrO_2$ (Riedel-de Haën AG, Seelze, Germany, 99%, $d_{50}$=22.842 μm), MgO (Alfa Aesar, Germany, 99.99%, $d_{50}$=1.780 μm) and HAP powders ($d_{50}$=0.015 μm) in different ratio were used as raw materials. The experimented compositions are presented in Table 2. The starting precursor powders were mechanically activated using an agate mortar and pestle. The resulted powders were mixed with 5% PVA and uniaxially cold pressed in a metallic dye into cylindrical pellets of 1 g with 10 mm in diameter at a pressure of 400 kgf using a Carver Inc. hydraulic press (Carver Inc, Wabash, IN, USA). Further, the pellets were sintered at 1550 °C under air atmosphere with a heating and cooling rate of 5 °C/min and dwell time of 12 h at the maximum temperature.

**Table 2.** The nominal composition (wt.%) and notation of the samples.

| Sample ID | ZrO₂ (wt.%) | MgO (wt.%) | HAP (wt.%) |
|-----------|-------------|------------|------------|
| S1 | 94.75 | 5 | 0.25 |
| S2 | 89.5 | 10 | 0.5 |
| S3 | 84 | 15 | 1 |
| S4 | 73.5 | 25 | 1.5 |

## Dissolution analysis in AS

In order to study the dissolution behavior of the heat treated biocomposites in physiological environment, the *in vitro* dissolution study was carried out by immersing the four different composites in artificial saliva (AS) for 32 days.The dissolution and the stability of the prepared pellets were assessed under static conditions in AS prepared by the following formulation [37]: 4200 mg/L $NaHCO_3$ (Merck, Germany), 500 mg/L NaCl (Reactivul, România), 200 mg/L KCl (Reactivul, România) and maintained at 37±0.1 °C by a Memmert incubator. Before the immersion the samples were sonicated for 10 min in acetone to be degreased and then rinsed with ultrapure water. One pellet of each composition was placed in a recipient with 100 mL of AS. The containers were removed from the incubator after 32 days and the solutions were further analyzed by UV-VIS spectroscopy. Finally, the pellets were removed from AS, were washed with ultrapure water and dried in oven at 100 °C for 24 h before XRPD, SEM and TEM analysis.

## Characterization Methods

### *X-ray powder diffraction (XRPD)*

XRPD analysis was performed in order to investigate the structure of the samples using a Shimadzu XRD-6000 diffractometer operating at 40 kV, 30 mA with a monochromator of graphite for CuKα (λ=1.54060 Å). The diffraction patterns were recorded in the 2θ range of 10–80ʻI at a scan speed of 2 °/min.

### *Scanning Electron Microscopy (SEM)*

SEM analysis was performed using a Hitachi SU8230 (Tokyo, Japan) microscope. The electron microscope was coupled with an Aztec X-Max 1160 EDX detector (Oxford Instruments).

### *Transmission Electron Microscopy (TEM)*

The size and shape of biocomposites crystallites were investigated by TEM on Hitachi H-7650 equipment.

### *UV VIS spectroscopy*

Spectrophotometric measurements of AS before and after biocomposites' immersion were performed in 1 cm wide quartz cuvettes on a JASCO V-650 spectrophotometer.

## REFERENCES

1. K. Nakamura; T. Kanno; P. Milleding; U. Ortengren; *Int. J. Prosthodont.,* 2010, *23*, 299-309
2. H. J. Wenz; J. Bartsch; S. Wolfart; M. Kern; *Int. J. Prosthodont.,* **2008,** *21*, 27-36
3. M. Hisbergues; S. Vendeville; P. Vendeville; *J. Biomed. Mater. Res. B Appl. Biomater*., **2009**, *88*(2), 519-529
4. S. D. Heintze; V. Rousson; *Int. J. Prosthodont*., **2010**, *23*, 493-502
5. L. Nistor; M. Grădinaru; R. Rîcă; P. Mărăşescu; M. Stan; H. Manolea; A. Ionescu; I. Moraru; *Curr. Health Sci. J*., **2019**, *45*, 28-35
6. J. S. Schley; N. Heussen; S. Reich; J. Fischer; K. Haselhuhn; S. Wolfart; *Eur. J. Oral Sci*., **2010**, *118*, 443-50
7. A. L. Gomes; J. Montero; *Med Oral Patol Oral Cir Bucal.*, **2011**, *16*(1), e50-e55
8. A. J. Raigrodski; M. B. Hillstead; G. K. Meng; K.-H. Chung; *J. Prosthet Dent*., **2012**, *107*, 170-177
9. P. Triwatana; N. Nagaviroj; C. Tulapornchai; *J. Adv. Prosthodont.,* **2012**, *4*, 76-83
10. E. D. Roumanas; *J. Evid. Based Dent. Pr.*, **2013**, *13*, 14-5

11. R. D. L. Mattiello; T. M. K. Coelho; E. Insaurralde; A. A. K. Coelho; G. P. Terra; A. V. B. Kasuya; I. N. Favarão; L. de S. Gonccalves; R. B. Fonseca; *ISRN Biomater*, **2013**, 1-10

12. R. H. French; S. J. Glass; F. S. Ohuchi; Y.-N. Xu; W. Y. Ching; *Phys. Rev. B.*, **1994**, *49*, 5133-5142

13. J. P. Goff, W. Hayes, S. Hull, M. T. Hutchings; K. N. Clausen; *Phys. Rev. B.*, **1999**, *59*(22), 14202-14219

14. I. Denry; J. R. Kelly; *Dent. Mater.,* **2008,** *24, 3,* 299-307

15. B. Al-Amleh; K. Lyons; M. Swain; *J. Oral Rehabil.,* **2010**, *37*, 641-52

16. J. Chevalier; L. Gremillard; A. V. Virkar; D. R. Clarke; *J. Am. Ceram. Soc.,* **2009**, *92*, 1901–20

17. E. C. Subbarao; Zirconia - an overview, in *Advanced Ceramics,* Science and Technology of Zirconia, A. H. Heurer and L. W. Hobbs Eds.; The American Chemical Society, Columbus, OH, USA, vol. *3*, **1981**, pp.1-24

18. G. Wang; X. Liu; C. Ding; *Surf. Coatings Technol.,* **2008**, *202*, 5824-5831

19. Y.-W. Hsu; K.-H. Yang; K.-M. Chang; S.-W. Yeh; M.-C. Wang; *J. Alloys Compd.*, **2011**, *509*, 6864-6870

20. S. Nath; S. Baja; B. Basu; *Int. J. Appl. Ceram. Technol.*, **2008**, *5*(1), 49-62

21. Y. Rao; W. Wang; F. Tan; Y. Chi; J. Lu; X. Qiao; *Appl. Surf. Sci.*, **2013**, *284*, 726-731

22. K. Krishnamoorthy; G. Manivannan; S. J. Kim; K. Jeyasubramanian; M. Premanathan; *J. Nanopart. Res.*, **2012**, *14*(9), 1063, 1-10

23. S. Makhluf; R. Dror; Y. Nitzan; Y. Abramovich; R. Jelinek; A. Gedanken; *Adv. Funct. Mater.*, **2005**, *15*(10), 1708-1715

24. R. Z. LeGeros; *Clin. Orthop.*, **2002**, *395*, 81–98

25. I. Antoniac; *Bioceramics and Biocomposites: From Research to Clinical Practice*, Wiley-VCH, Weinheim, New York, **2019**, pp. 400

26. A. L. Patterson; *Phys. Rev.*, **1939**, *56*, 978-982

27. L. Renuka; H. P. Nagaswarupa; S. C. Prashantha; K. S. Anantharaju; S. C. Sharma; H. Nagabhushana; Y. S. Vidya, *J. Alloys Compd.*, **2016**, *672*, 609-622

28. L. Hu; C. Wang; Y. Huang; *J. Mater. Sci.,* **2010**, *45*, 3242–3246

29. B. Annaz; K. A. Hing; M. Kayser; T. Buckland; L. Di Silvio; *J. Microsc.*, **2004**, *215*, 100-110

30. L. Grima; M.Díaz-Pérez; J. Gil; D. Sola; J.I. Peña; *Appl. Sci.,* **2020**, *10*(1), 1-15

31. R. Barabás; M. Czikó; I. Dékány; L. Bizo; E. S. Bogya, *Chem. Pap.*, **2013**, *67*(11), 1414–1423

32. R. Barabás; E. de Souza Ávila; L. O. Ladeira; L. Mosqueira Antônio; R. Tötös; D. Simedru; L. Bizo; O. Cadar; *Arab. J. Sci. Eng.*, **2020**, *45*, 219-227

33. R. Barabás; D. Deemter; G. Katona; G. Batin; L. Barabas; L.Bizo; O. Cadar; *Turk. J. Chem.*, **2019**, *43*(3), 809-824

34. R. Barabás; N. Muntean; G. Szabó; K. Maurer; L. Bizo; *Studia UBB Chemia*, **2017**, LXII, *4*(II), 253-268

35. E. S. Bogya, I. Bâldea, R. Barabás, A. Csavdári, G. Turdean, V. R. Dejeu, *Studia UBB Chemia*, **2010**, *2*(2), 363-373

36. R. Barabás, M. Rigó, M. Eniszné-Bódogh, C. Moisa, O. Cadar, *Studia UBB Chemia*, LXIII, **2018**, *3*, 137-154

37. K. Engelhart; A. Popescu; J. Bernhardt; *BMC Ear Nose Throat Disord.,* **2016**, 16(6), 1-7

# SURFACE CHARACTERIZATION AND CYTOTOXICITY ANALYSIS OF THE TITANIUM ALLOYS FOR DENTISTRY

**PAULA ARGENTINA JIMAN[a,b], MARIOARA MOLDOVAN[c],
CODRUTA SAROSI[c*], ALEXANDRINA MUNTEAN[a],
ANDREEA SIMONA POP[a], VIORICA TARMURE[a],
CATALIN POPA[b], AUREL GEORGE MOHAN[d]**

**ABSTRACT.** Three methods of treating the Ti and Ti-6Al-4V alloy surface used as dental implants have been tried both to increase the corrosion resistance and to create diffusion barriers, which prevent the release of toxic ions in the body, at the separation surface, implant living tissue. The anticorrosive performances of the experimental oxide films, realized on the pure Ti and Ti-6Al-4V alloy were evaluated electrochemically by cyclic voltammetry after immersion of samples in Ringer's solution at 37°C. The A2-Ti sample (Ti-6Al-4V alloy anodized with $H_3PO_4$, 1N, and citric acid, 20 g/l electrolyte solution) shows lower viability values, compared to the other samples, with a tendency to decrease after 48h of incubation. The cytotoxic effect is slightly higher in A1-Ti (Ti-6Al-4V alloy anodized with 0.6% $H_3PO_4$ electrolyte solution) compared to Ti over a period. This can be attributed to the presence of aluminium and vanadium. The results revealed that the specific processing of titanium and titanium alloy (Ti-6Al-4V) by obtaining an oxide layer influence the toxicity that is stabilize and decrease with time, which makes to be used in dental implantology.

*Keywords:* Ti-6Al-4V *surface treatment*, *electrochemical processing*, *dental implant, cytotoxicity, SEM.*

---

[a] *Iuliu Hatieganu University of Medicine and Pharmacy, Faculty of Dentistry, 31 A. Iancu Street, RO-400083, Cluj-Napoca, Romania*
[b] *Technical University of Cluj-Napoca, Faculty of Materials Science and Engineering, Cluj-Napoca, Romania*
[c] *Babeş-Bolyai University, Institute of Chemistry Raluca Ripan, 30 Fantanele Str., RO-400294, Cluj-Napoca, Romania*
[d] *University of Oradea, 1 Universitatii Street, RO-410087, Oradea, Romania*
 * *Corresponding author: codruta.sarosi@ubbcluj.ro*

PAULA ARGENTINA JIMAN, MARIOARA MOLDOVAN, CODRUTA SAROSI, ALEXANDRINA MUNTEAN, ANDREEA SIMONA POP, VIORICA TARMURE, CATALIN POPA, AUREL GEORGE MOHAN

## INTRODUCTION

The metallic alloys currently used to manufacture implants for corrective surgery of orofacial deformities and defects, are bioinert materials when in contact with human bone tissue, which can become bioactive by controlling the morphology of the chemical composition of the surface [1,2]. The type of material, method of production, chemical composition and mechanical properties of the material influence the interaction between bone and implant and long-term stability is closely related to its integration into the remnant bone [3-6].

Titanium is used extensively in surgery, due to its good biocompatibility, explained by its physical and mechanical properties and by the fact that the surface of titanium is always covered with an $TiO_2$ layer [6,7]. This nanometric layer is responsible for the materials' resistance to corrosion and its bioinert behavior in vivo, which leads to an acceptable osseointegration. Currently, implants are processed through additve and substractive manufacturing [8,9]. After manufacturing, the surfaces of the implants are modified by: sandblasting, etching, anodizing, depositing of biocomposites or chemical treatments. Each of these methods have been used to improve the stability and facilitate the process of osseointegration [10-12]. Furthermore, it was demonstrated that the implant surface topography can certainly help the cellular and molecular mechanisms [13]. Porous surfaces showed better absorption of biomolecules in biological fluids and in vitro tests indicate that porous surfaces enhance bone cell response [14-16]. Rigidity and crystallization directly affects surface receptors on the cell surface and focal points, triggering a cascade of intracellular signals that determines activation of specific genetics [17]. Basically, by changing longitudinal modulus of elasticity of the implant, cell differentiation can be improved. If the balance of rigidity is achieved both by the metal structure of the implant and the bone tissue, the risk of adverse effects is very small. Several studies present that the functionalisation of the metallic implants surface that are in direct contact with bone with bioceramic is a good solution. Bioceramic presents advantages such as: absence of corrosion, absence of release of metal ions which are very harmful for the organism, more resistance to tearing and greater resistance to fatigue [18, 19]. A major importance is represented by the bonding between the bioceramics and metallic implant structure [20,21,22].

Changes in the titanium surface and titanium alloys used in the medical field can considerably affect the process of osteointegration of dental implants in contact with the organic environment. In particular, the morphology of the surfaces can be a key factor in the colonization and adhesion of osteoblasts to the bone-implant contact surface. Recent world studies have considered the development of functional groups on the surface of titanium and titanium alloys capable of inducing and improving the process of bone tissue formation (osteoblast adhesion, hydroxyapatite crystal nucleation process). It is hoped

that by these treatments the duration of the process of osteointegration will be substantially reduced and the quality of the connections obtained will be substantially improved [23].

The response of cells and tissues to the interface may be affected by the topography or surface geometry at the macro level, as well as its morphology and roughness at the micro level. Also, a particular influence may have the crystalline structure at the atomic level [24,25]. The crystalline structure is the result of numerous treatments either mechanical, chemical, thermal, or combinations thereof. The different forms of the crystalline structure can be a great control to ensure the successful osseointegration of the implants made of titanium and its alloys [26,27].

The purpose of this study is to determine the optimum electrochemical and thermochemical processing of Ti and the Ti-6Al-4V, titanium alloy, in order to obtain surfaces with high inertia and high chemical configurations, capable of creating strong and stable bonds with bone tissues at the implant-bone interface. The newly created surfaces should favor the growth of the osteoblasts and the interaction of the bone tissue with the implanted material.

## RESULTS AND DISCUSSION

### Electrochemical investigations regarding the anticorrosive performances of the experimental oxide layers realized on the Ti-6Al-4V alloy

The anticorrosive performances of the experimental oxide films, realized on the pure Ti and Ti-6Al-4V alloy were evaluated electrochemically. The analysis is a comparative one, the reference being each time, the Ti-6Al-4V alloy, mechanically polished. The results obtained by cyclic voltammetry are presented in table 1.

**Table 1.** Electrochemical characteristics of investigated samples, polished, without anodizing

| Samples | Emc [mVesc] | Ecp1/ Icp1 [mVesc/ uA/cm$^2$] | Ecp2/ Icp2 [mVesc/ uA/cm$^2$] | Ecp3/ Icp3 [mVesc/ uA/cm$^2$] | Ecp4/ Icp4 [mVesc/ uA/cm$^2$] | Ip500 [uA/cm$^2$] | Ip1000 [uA/cm$^2$] | Ip1000 [uA/cm$^2$] | E$_T$ [mVesc] |
|---|---|---|---|---|---|---|---|---|---|
| **A1-Ti** | -505 | -456/14 | - | 1079/235 | 3100/2500 | 39 | 228 | 4125 | 2700 |
|  | 1080 | -682/-711 | -5/-72 | - | - | -9 | -2 |  |  |
| **A2-Ti** | 1500 | - | - | - | - | - | -5 | -3 | 14 |
|  | 1862 | - | - | - | - | - | -7 | -5 |  |
| **Ti** | -510 | -445/22 | 210/64 | 1100/290 | 3100/3330 | 80 | 270 | 5000 | 2400 |
|  | 576 | -680/-770 | 10/-70 | - | - | -10 | 0 |  |  |

\* A1-Ti, A2-Ti, Ti, see in the Table 2.

PAULA ARGENTINA JIMAN, MARIOARA MOLDOVAN, CODRUTA SAROSI, ALEXANDRINA MUNTEAN, ANDREEA SIMONA POP, VIORICA TARMURE, CATALIN POPA, AUREL GEORGE MOHAN

The electrochemical characteristics evaluated are the mixed corrosion potential $E_{mc}$, the critical passivation potentials and currents, $E_{cp}$ respectively $I_{cp}$, the passivity current $I_p$, at 500, 1000 and 4000mVe.s.c. and the potential of $E_T$ transferability. In a separate row (and highlighted by a tint of color), for each sample and the specific values of the return curve were noted. These maxima may indicate the reversibility of oxidative anodic processes. The difference between the mixed corrosion potential and the potential to return to the cathode is a measure of the ennobling due to the anodic polarization and the electrochemical passivization of the investigated surface.

Table 1 shows the behavior of titanium and Ti-6Al-4V alloy in Ringer's solution at 37°C. Besides the oxidation in three or four stages, the specificity of both materials is compared, a decrease in the amplitude and complexity of the anodic process is realized, a single critical potential, Ecp1

The experimental data generally indicate better anticorrosive performances in the case of the alloy than in the case of pure titanium, and the mixed corrosion potential is more noble in the case of the alloy, -505mVe.s.c. the others at – 510mVe.s.c. in the case of the titanium.

Representative samples A1-Ti and A2-Ti show a greater electrochemical inertia and we used for representation a current scale of max. $0,1\mu A/cm^2$. The electrochemical characteristics presented in table 1 lead to the conclusion that these samples have excellent anticorrosive performances. The A1-Ti and A2-Ti samples have excellent performances, do not exhibit electrochemical passivation processes, they do not have a mixed corrosion potential, in a predictable field, considering the chemical composition of the estimated substrate of the oxide film; the samples behave as an ohmic resistance, the current / potential relationship is practically linear, nor can a potential for trans-passivity be estimated [28,7,8]. All samples have significantly lower anodic densities than those recorded for the polished alloy.

## Study of the oxide layers obtained on Ti and Ti-6Al-4V alloy by electrochemical techniques, using scanning electron microscopy

The samples were studied using the Inspect S scanning electron microscope, FEY Company. The morphology of the experimental oxide layers made on titanium and Ti-6Al-4V alloy was followed by electrochemical oxidation techniques.

The oxide layer has a continuous appearance with many excrescences in the form of small islands and has a good adhesion on the support. The images in fig.1 show the most characteristic aspects of the studied layer.
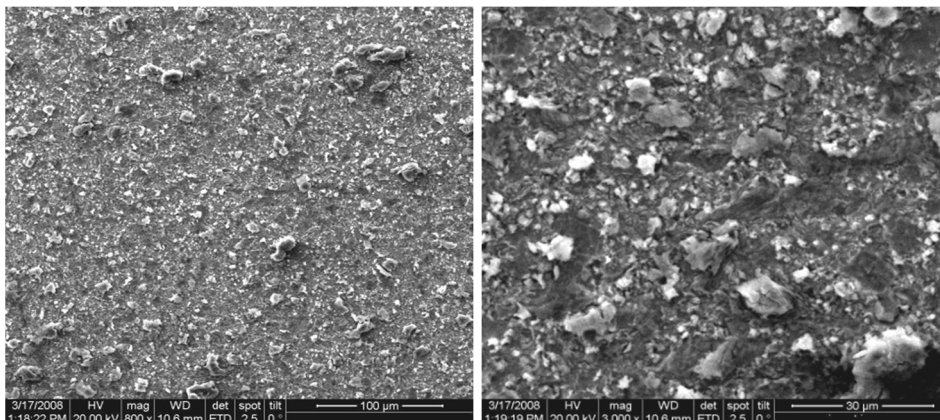
**Figure 1.** SEM images of the surface of A1-Ti sample after the anodizing with H$_3$PO$_4$ electrolyte solution 0,6% and treated at 760°C for 5 min, captured with 800x and 3000x magnification

From the morphological point of view, the layer presents itself as a continuous deposit with a soluble appearance that is easily contaminated in the electron beam. This contamination indicates in this case a poor electrical conductibility of the layer. The images from fig. 2 present the aspects characteristic of this deposit.
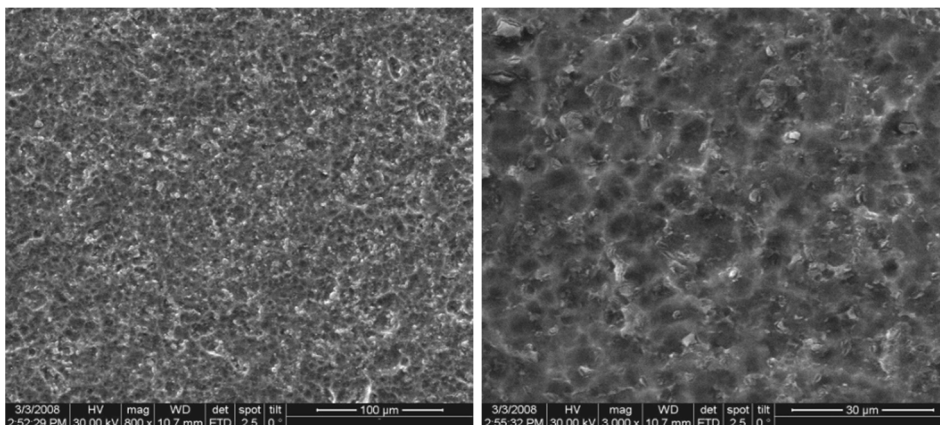


**Figure 2.** SEM images of the surface of A2-Ti sample after the anodizing with H$_3$PO$_4$ 1N + 20 g/l citric acid electrolyte solution and treated at 360°C for 5 min, captured with 800x and 3000x magnification
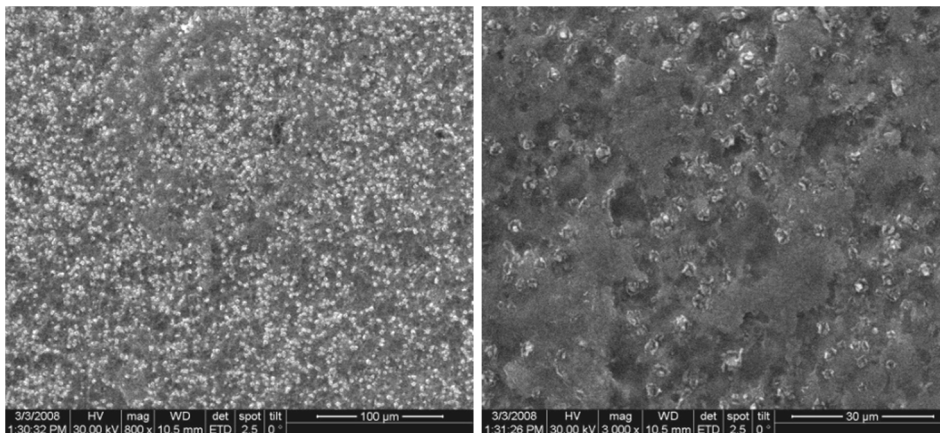
**Figure 3.** SEM images of the surface of Ti sample after the electrolytic oxidation, captured with 800x and 3000x magnification

After immersion in the Ringer solution, the surfaces of the samples are presented in Figure 4, 5 and 6.
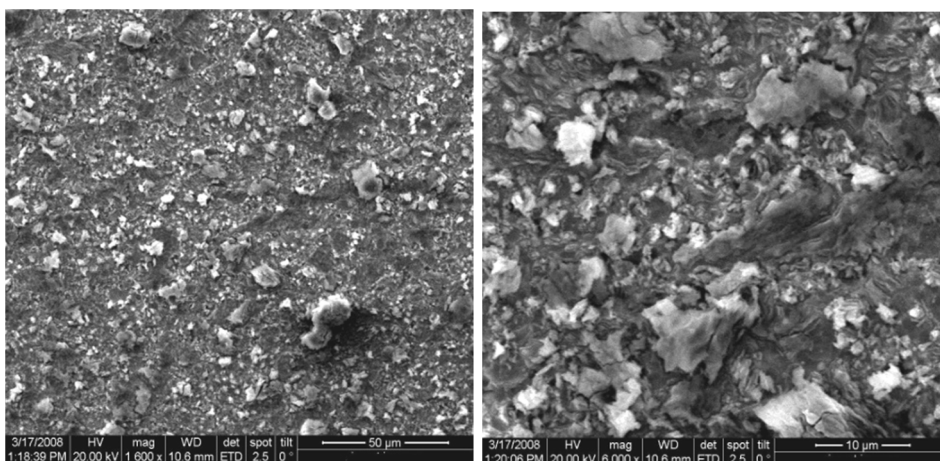


**Figure 4.** SEM images of the surface of A1-Ti sample after electrochemical investigations regarding the anticorrosive performances in Ringer solution, captured with 1600x and 6000x magnification

From the presented research study it results that the samples of titanium alloy Ti-6Al-4V show a high chemical inertia in Ringer synthetic liquid, following the specific electrochemical and thermochemical processes performed at the surface level.
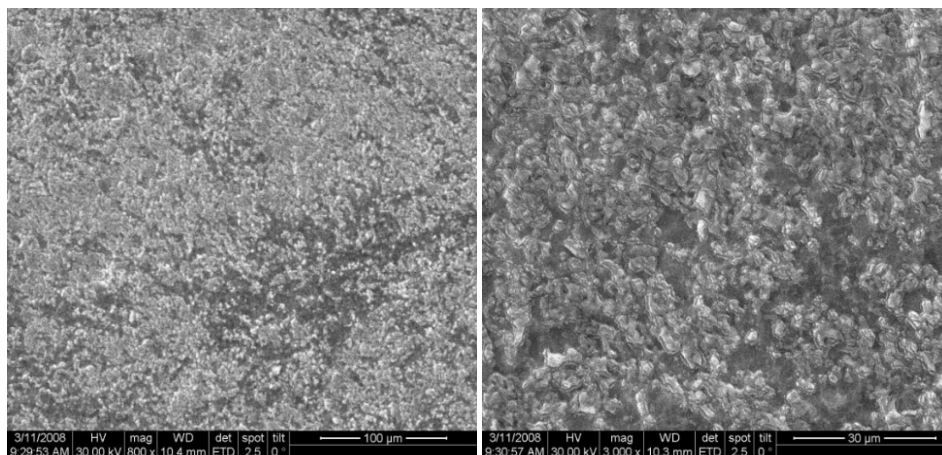
**Figure 5.** SEM images of the surface of A2-Ti sample after electrochemical investigations regarding the anticorrosive performances in Ringer solution, captured with 800x and 3000x magnification
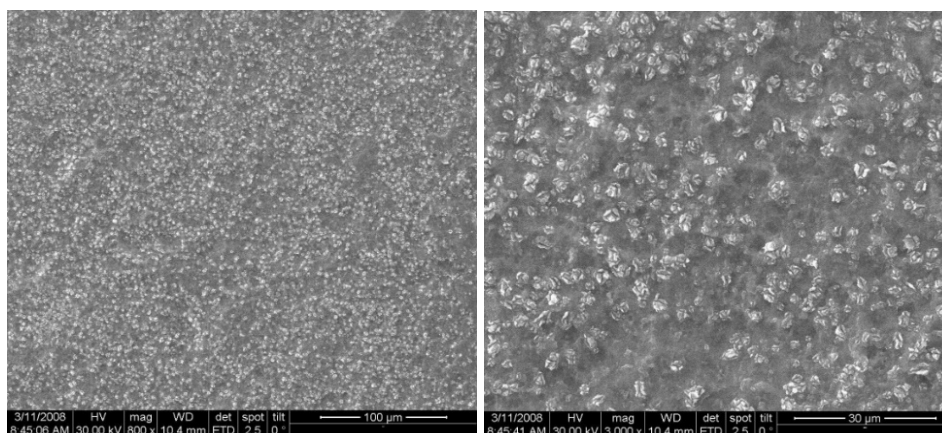


**Figure 6.** SEM images of the surface of Ti sample after electrochemical investigations regarding the anticorrosive performances in Ringer solution, captured with 800x and 3000x magnification

Different types of titanium oxide-based structures with amorphous or crystalline structure such as anatase and rutile have been obtained, doped with phosphorus-based compounds, which can be real diffusion barriers for potential toxic aluminum and vanadium ions at the contact of the implant with the organic environment [23,29-31].

The obtained configurations will have to lead to the growth and adhesion of the osteoblast cells in order to make a solid connection at the implant-bone interface level [10,11,30].

Specific tests of cell growth and implantology will continue to be performed to study the compatibility of the studied alloy with the environment and oral tissues.

**Viability test of normal human fibroblasts treated with fully incubated media with experimental titanium alloy samples for 24 and 48 h**
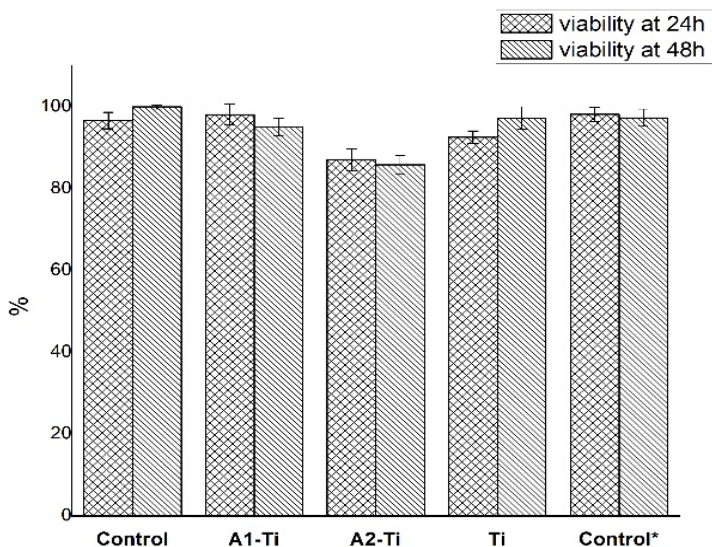


**Figure 7.** Comparison of the viability of fibroblasts exposed to the incubated environment of the studied samples for 24 and 48h. *untreated control is represented only by the complete fibroblast environment (the liquid component represented by the biological environment).

The A2-Ti sample shows lower viability values, compared to the other samples, with a tendency to decrease after 48 h of incubation.

The cytotoxic effect is slightly more in A1-Ti compared to Ti over a period. This can be attributed to the presence of aluminum and vanadium. [7,11,32,33] However, the effect of toxicity was found to stabilize and decrease with time. The increase of $TiO_2$ passivating layer over a period of time, which is formed in contact with tissue cells, moderated the toxicity by curtailing the release of Ti, Al, and V ions from test materials into the tissue cells. [34,35]

## CONCLUSIONS

A research study was conducted on the specific processing of titanium and titanium alloy Ti-6Al-4V for use in dental implantology.

Electrochemical evaluations indicate a good stability of these experimental interfaces in synthetic biological solutions. The morphology of the sample surface, generally alveolar and favorable for cell growth at the interface, represents an interesting premise in the continuation of this research direction.

The electrochemical methods of treating the surface of samples by controlled anodization processes, in electrolytes compatible with its structure and its physico-chemical characteristics, have generated at the surface level oxide layers formed from titanium oxides having the role of diffusion barrier and anticorrosive protection, which can contribute to increasing the biocompatibility of implants in the body and to improving the characteristics of rapid osteointegration. Both the titanium and the Ti-6Al-4V alloy behaved well from the electrochemical point of view in the electrolysis solutions, their behavior being similar.

The chemical surface treatment methods did not lead to obtaining anti-corrosion protection layers on the titanium and Ti-6Al-4V alloy samples. The surface of the samples is active, does not have passivity properties and cannot attribute to the applied chemical treatments any ability to protect the titanium base. To a large extent, these samples behave just like pure titanium.

Surface properties analyzed by scanning electron microscopy revealed the existence of an compact, uniform and adherent titanium oxide layer. The oxide layer had a slim appearance, this contributing to a better growth of the tissue on the implant, and to a better anchorage of the dental implant.

These surface properties justify that the sandblasted implants is able to significantly increase bone contact and bone growth with very good osseointegration results in vivo.

## EXPERIMENTAL

### Sample preparation

Ti and Ti-6Al-4V alloy with the following composition was used (%): Ti=base; N=0,0051; C=0,030; Al=5,53; V=3,90; Fe=0,13; Si=0,05-0,1; Ni=0,01-0,05; Cr=0,005-0,01; Co$<$0,005; Cu$\cong$0,001.

15 samples of Ti-6Al-4V with dimmension 28x20x0.5mm were analysed. The surface of samples were mechanicaly prepared (polishing with metallographic paper 150-400 granulation; washing with usual hot water; washing with distilled water; hot air drying) followed by degreasing with acetone and ethyl alcohol and

finally the pickling treatment (pickling - depasivation with HF (1%; 20%), HF6% + $HNO_3$23%; washing with usual hot water; washing with distilled water; hot air drying).

After the preparation the samples obtained were subjected to electrochemical treatments as are presented in table 2.

The electrolytic oxidation of the titanium, its anodization, is a process of artificial creation, of growth on the surface of the titanium a oxide layers, of course of much greater thicknesses than the natural layer, which is realized spontaneously on the titanium.

In this process, the titanium represents the anode, the cathode being represented by metals such as Pb, Al, chemically stable metals in the electrolytes used. The anodic reaction is an oxidation process that takes place on the surface of the anode (titanium anode): $R_A$:Ti +$2H_2O \rightarrow TiO_2$ + 4H + $4e^-$.

The cathodic reaction is a reduction process that occurs on the cathode surface (Pb, Al): $R_K$ : 4H + $4e^- \rightarrow 2H_{2(g)}$.

**Table 2.** Ti and Ti-6Al-4V alloy samples subjected to electrochemical treatments (controlled anodization in electrolytes compatible with the processed material).

| Sample | Sample preparation | Heat treatment * in air |
|---|---|---|
| Ti-6Al-4V alloy A1-Ti | Anodizing with electrolyte solution 0.6% $H_3PO_4$ U(Vcc)= 30, Is=40(mA), 30 min., 60°C | 760°C, 5 min. |
| Ti-6Al-4V alloy A2-Ti | Anodizing with electrolyte solution $H_3PO_4$ 1N + 20 g/l citric acid solution (ratio 1: 1) U(Vcc)= 50, Is=0.5 (mA), 120 min., 25°C | 350°C, 60 min. 600°C, 60 min. |
| Ti | Purity 99,9% | - |

**Electrochemical investigations regarding the anticorrosive performances of the Ti and TA6V4 alloy**

The experimental technique used is cyclic voltammetry. Sample and storage parameters have been set: the sample time 1000 X 100 $\mu$sec., the scale head for current 0.1, 0.5 or 1mA. The surface investigated of the samples was 0.2 $cm^2$.

The electrolyte used was a synthetic biological solution, the Ringer solution, table 3, a complex solution with a high content of $Cl^-$ ions. pH 2.5 was established by acidification with hydrochloric acid.

**Table 3**. Synthetic biological solutions

| Components [g/l] | Hank Solution | Ringer Solution | Artificial physiological solution | Artificial saliva |
|---|---|---|---|---|
| NaCl | 8 | 8 | 8,44 | - |
| KCl | 0,40 | 0,4 | - | 1,47 |
| $CaCl_2$ | 0,14 | 0,3 | - | - |
| $KH_2PO_4$ | 0,06 | - | - | 0,19 |
| $MgCl_2.6H_2O$ | 0,1 | 0,2 | - | - |
| $MgSO_4.7H_2O$ | 0,1 | - | - | - |
| $NaHCO_3$ | 0,35 | 1,25 | 0,35 | 1,25 |
| $Na_2HPO_4.7H_2O$ | 0,09 | 0,18 | 0,06 | - |
| $NaH_2PO_4$ | - | - | 0,06 | - |
| D-glucose | 1 | 2 | - | - |
| KSCN | - | - | - | 0,52 |

The electrolyte temperature of 37°C, the temperature of the human body, was achieved and maintained by a Potentiostat MLW U15c (Mesu Lab Instruments, Guangzhou, China), which permanently recirculated the heated water through the cell mantle. Thus, the conditions of experimentation simulated with the conditions encountered in the human body were simulated. In the Ringer solution, at 37°C, the titanium undergoes an electrochemical passivation in lower than the anodic current recorded in 1N sulfuric acid, for the same surface, up to only 1000 mVe.sc.

The passivation performances of the titanium in Ringer's solution are relatively good and justify the use of this material as such, without further processing, when performing medical implants. The area of potential investigated was here wider -1000÷4000mVe.s.c.

In this case, the polarization speed was 100mV / sec., at the lower limit of the working speeds in cyclic voltammetry. For all samples, three complete cycles, two polarization cycles, 1 and 3, were recorded and evaluated. The analysis considered both recorded polarization cycles. Prior to polarization, all samples were erased with acetone.

## SEM Microscopy

The surface of the samples electrochemical treated and after immersion in Ringer solution were evaluated by Scanning Electron Microscopy (SEM) using Inspect-S Microscope produced by FEI Company.

### Viability test of the samples

Viability test of normal human fibroblasts treated with fully incubated media with Ti and Ti-6Al-4V alloy samples for 24 and 48 h.

Samples were incubated for 24 and 48h respectively in complete medium for fibroblasts (DMEM, FCS, ATB), at 37°C, 5% $CO_2$. Normal human fibroblasts, in the third passage, were cultured on 24-well plates of $3*10^4$ / well and incubated 24 hours in complete culture medium at 37°C, 5% $CO_2$. The culture medium was removed and the cells were washed twice with PBS. Cells were treated with incubated media at 37°C, 5% $CO_2$ for 24h, then washed twice with PBS, enzymatically removed (trypsin / EDTA) from the culture surface and then performed the viability test with trypan blue. The cells were counted in the improved Neubauer room. Viability is expressed as a percentage and results from the ratio of viable cells (which do not capture the dye) to the total number of cells.

**Viability** = (normal cells / total cells) x 100

### REFERENCES

1. D. Bunea, A. Nocivin, *Materiale biocompatibile*, Ed. BREN, Bucuresti, 1998, pp. 65-74.
2. M. Kulkarni, A. Mazare, P. Schmuki, A. Iglič, Biomaterial surface modification of titanium and titanium alloys for medical applications, in *Nanomedicine*, One Central Press, United Kingdom, **2014,** Chapter 5, pp. 111-136.
3. V. Antoniac, O. Trante, C. Trante, Materiale biocompatibile utilizate la realizarea implanturilor ortopedice, in *Buletin Ştiinţific–Conferinţa Naţională de Ştiinţa şi Ingineria Materialelor, BRAMAT'99*, **1999**, *vol. I*, ISBN 973-98797-0-5, pp.270-273.
4. D. Leordean, S. A. Radu, D. Fratila, P. Berce, *Int. J. Adv. Manuf. Tech.*, **2015**, *79*, 905-920.
5. M. Bruschi, D. Steinmüller-Nethl, W. Goriwoda, M. Rasse, *J. Oral Implantol*, **2015**, 527426, http://dx.doi.org/10.1155/2015/527426.
6. A.V. Burde, S. Cuc, A. Radu, M.A. Rusu, C.S. Cosma, D. Leordean, *Studia UBB Chemia*, **2016**, *61*, 205-214.
7. C. Cosma, N. Balc, M. Moldovan, L. Morovic, P. Gogola, C. Miron-Borzan, *J. Optoelectron. Adv. M.*, **2017**, *19*, 738-747.
8. S. L. Assis, S. Wolynec, I. Costa, *Eletrochim. Acta*, **2006**, *51*, 1815-1819.

9. T. Chaturvedi T. *Indian J. Dent. Res.*, **2009**, *20*, 91-98.
10. M. Nica, B. Cretu, D. Ene, I. Antoniac, D. Gheorghita, R. Ene, *Materials* **2020**, *13*, 1201; doi:10.3390/ma13051201
11. T.D. Morgan, M. Wilson, *J. Appl. Microbiol.,* **2001**, *91,* 47-53.
12. M. Hajisafari. A. Z. Bidaki, S. Yazdani, *Adv. Mater. Process.,* **2017***, 3,* 12-22*.*
13. S. Cavalu, I. V. Antoniac, L. Fritea, I. M. Mates, C. Milea, V. Laslo, S. Vicas, A. Mohan, *J. Adhes. Sci. Technol.,* **2018***, 32,* 2509-2522.
14. O. H. Orasan, A. M. Chisnoiu, M. L. Dascalu (Rusu), O. Pastrav, M. Pastrav, M. Moldovan, R. Chisnoiu, *Studia UBB Chemia,* **2017**, *3*, 215-223.
15. V.A. Barão, M.T. Mathew, W.G. Assunção, J. C. Yuan, M. A. Wimmer, C. Sukotijo, *Clin. Oral Implants Res.,* **2012***, 23,* 1055-1062.
16. D. Sucala, C. Sarosi, C. Popa, I. Cojocaru, M. Moldovan, A. G. Mohan, *Studia UBB Chemia,* **2018**, *63*, 71-81.
17. C. Castellani, R. A. Lindtner, P. Hausbrandt, *Acta Biomater.,* **2011**,*7*, 432-440.
18. I. Antoniac, Fundamental properties of bioceramics and biocomposites*,* in *Handbook of Bioceramics and Biocomposites*, Springer International Publishing, **2016**, Vol. 1-2, Chapter 1, pp.35-58.
19. I. Antoniac, C. Sinescu, A. Antoniac, *J. Adhes. Sci. Technol.*, **2016**, *30*, 1711-1715.
20. I. Karacan, B. Ben-Nissan, H. A. Wang, A. Juritza, M. V. Swain, W. A. Müller, J. Chou, A. Stamboulis, I. J. Macha, V. Taraschi, Mater. *Sci, Eng. C.*, **2019**, *104*, 109757.
21. A. Saplontai-Pop, M. Moldovan, R. Oprean, O. Orasan, S. Saplontai, C. Ionescu, *Studia UBB Chemia,* 2014, 59, 39-46.
22. M. Ahmad, D. Gawronski, J. Blum, J. Goldberg, G. Gronowicz, *J. Biomed. Mater. Res.*, **1999**, *46*, 121-131.
23. X. Liu, S. Chen, J. K. H. Tsoi, J. P. Matinlinna, *Regen. Biomater.,* **2017**, 315. doi: 10.1093/rb/rbx027.
24. J. Curtin, M. Wang, H. Sun, *Int. J. Oral Max. Surg.*, **2017**, *46,* 94-99.
25. A. D. Tinoco, M. Saxena, S. Sharma, *J. Am. Chem. Soc.*, **2016**, *138*, 5659-5665.
*26.* L.Silaghi-Dumitrescu, A. M. Mihailescu, A. Muntean, C. Sarosi, D. Prodan, M. R. Simu, M. Moldovan, A. Kui, M. Pastrav, *Studia UBB Chemia,* **2019***, 4,* 107-119*.*
27. A. Han, J. K. H. Tsoi, F. P. Rodrigues, *Int. J. Adhes. Adhes.*, **2016,** *69*, 58-71.
28. A. Wennerberg, L. M. Svanborg, S. Berner, *Clin. Oral Implants Res.*, **2013**, *24*, 203-209.
29. I. M. Hamouda, E. T. Enan, E. E. Al-Wakeel, *Int. J. Oral Max. Impl.,* **2012**, *27*, 776-784.
30. Y. T. Sul, C. B. Johansson, Y. Kang, *Clin. Implant Dent. R.*, **2002**, *4*, 78-87.
31. H. Tschernitschek, L. Borchers, W. Geurtsen, *Quintessence Int.*, **2005**, *36*, 523-530.
32. N. Sykaras, A.M. Iacopino, V. A. Marker, *Int. J. Oral Max. Impl.,* **2000,** *15,* 675-690.

33. A. D. Tinoco, M. Saxena, S. Sharma, *J. Am. Chem. Soc.*, **2016**, 138, 5659-5665.
34. A. Saplontai-Pop, A.Mot, M. Moldovan, R. Oprean, R. Silaghi-Dumitrescu, O.H. Orasan, S. Saplontai, M.Parvu, G. Emese C. Ionescu, *Open Life Sci.,* **2015**, *10*, 89-98.
35. S. Chandar, R. Kotian, P. Madhyastha, S. P. Kabekkodu, Padmalatha Rao, *J. Indian Prosthodont. Soc.*, **2017**, *17*, 35-40.

# PRINCIPAL COMPONENT ANALYSIS AND THERMOMECHANICAL PREFERENCE OF WHITE Au ALLOYS WITHOUT Ag

## MLADEN MIRIĆ[ab], BILJANA ARSIĆ[c,*], MILOŠ ĐORĐEVIĆ[b], DRAGAN ĐORĐEVIĆ[b], DRAGOSLAV GUSKOVIĆ[a], SVETLANA IVANOV[a]

**ABSTRACT.** Addition of different amounts of Cu and Ag to Au alloys, as well as some new elements (Zn and Cd), gives alloys of the different colour spectrum (from red to yellow) and different technological and metallurgical characteristics. The trend today is the implementation of new alloys not containing Ag, and including new elements, such as Ga and In. Differences in two Au alloys exist: the first alloy contains Ni and Pd, and the second alloy is without them. The values of electrical conductivity and hardness are different, due to the reduction, which was shown using PCA (r=0.985 and the strong positive correlation between hardness and electrical conductivity). Performed tests confirm that those multiphase multi component gold alloys can find their application not only in jewellery making but also in the world of modern electrical engineering. The performed statistical analysis shows strong positive and negative correlations of properties of investigated Au alloys, and it provides significant savings in the design and efficiency of metallurgical processes.

*Keywords: alloy, PCA, metallurgical process.*

# INTRODUCTION

The subject of this work, through the prism of processing metallurgy and legal metrology, was to determine the conditions for obtaining semi-finished products in jewellery with a suitable equivalent axial structure (with

[a] *University of Belgrade, Technical Faculty Bor, Vojske Jugoslavije 12, 19210 Bor, Republic of Serbia*
[b] *Department of Chemistry, University of Niš, Faculty of Sciences and Mathematics, Višegradska 33, 18000 Niš, Republic of Serbia*
[c] *Department of Mathematics, University of Niš, Faculty of Sciences and Mathematics, Višegradska 33, 18000 Niš, Republic of Serbia*
\* *Corresponding author: biljana.arsic@pmf.edu.rs*

MLADEN MIRIĆ, BILJANA ARSIĆ, MILOŠ ĐORĐEVIĆ, DRAGAN ĐORĐEVIĆ,
DRAGOSLAV GUSKOVIĆ, SVETLANA IVANOV

the crystal grains of the same crystallographic orientation, and the grains about the same shape and boundaries), and optimal physico-chemical and mechanical properties. Our first aim, in the framework of this task, was to obtain multi-component alloys of gold and white colours for melting and casting and then investigate their formation in the solid state. The method of cold rolling of the molded pieces in combination with certain annealing processes gives plastic properties for the material that are optimal for cold rolling and drawing, as well as further cold deformations of samples.

The latest medical and technological achievements led us to focus, in this paper, on so far poorly investigated 585 alloys of gold for white jewellery, without Ag, mostly in the form of annealed and cold-deformed sheet, strip, tube and wire [1,2]. The investigated gold alloys are of quantitative composition Au585Cu312Zn40Ga35In28 (white and reddish-gray colour) and Au585Cu233Ni80Zn70Pd32 (white-gray colour).

Regarding applied statistical analysis tool, we used non-parametric analysis - principal component analysis (PCA) in order to obtain the initial solution reducing the original dataset [3-5]. The earliest works in principal component analysis can be found in Karl Pearson (1901) [6]. In chemistry, PCA was firstly introduced by Malinowski in 1960s as a principal factor analysis [7].

In this work, we used microstructural analysis, metallography with optical microscopy and scanning electron microscopy (SEM) with energy-dispersive spectroscopy (EDS) in combination with principal component analysis (PCA), and contributed to better understanding of new Au alloys.


## RESULTS AND DISCUSSION

A cold-rolled sheet of alloy Au585Cu233Ni80Zn70Pd32 (thickness 0.38 mm and hardness HV 155) was examined by straining [8-10]. The obtained value was $R_m$ = 610 MPa, and the relative elongation $A_{100}$ = 35 %. The hardness of samples increases monotonically from 155 HV in a molten state, up to 316 HV after 8 reductions in rolling mills, with the total degree of deformation increasing up to 71.74 % (Table 1). After the first annealing hardness decreases to 183 HV, and with subsequent cold deformation, after 3 reductions in rolling mills, increases monotonically up to 314 HV with the increase of the degree of cold deformation to 91.74 %. After the second annealing, the hardness of the sample decreases to 160 HV with the increase of the degree of cold deformation to 70.70 % [11-13].

PCA performs reductions of data matrix by transforming the data into orthogonal components (F1-F4) that represent a linear combination of the original variables (samples I-XII from Table 1). Before applying PCA analysis, we tested the data matrix in order to detect outliers. Application of Grubb's

test to experimental data resulted in the detection of no outliers in the datasets
(the critical value for $\alpha$=0.05 and n=12 was 2.412). Strong positive correlations
were observed between data of Width (b) and Hardness (HV10) (r=0.833),
Width (b) and Electrical conductivity (MS/m) (r=0.823), and Hardness (HV10)
and Electrical conductivity (MS/m) (r=0.989); and strong negative correlations
between Width (b) and Height (h) (r=-0.980), Height (h) and Hardness (HV10)
(r=-0.887), and Height (h) and Electrical conductivity (MS/m) (r=-0.867) [14,15].
From the shape of the scree plot, shown in Fig. 1a, the number of important
components that will be used in further calculations can be observed.

**Table 1.** The ratio of elongation, hardness and electrical conductivity for the alloy
Au585Cu233Ni80Zn70Pd32, depending on the degree of reduction

| Sample | Width (b) (mm) | Height (h)(mm) | $\varepsilon$ total | $\varepsilon$individually | $F_0/F$ | Hardness (HV 10) | Electrical conductivity (MS/m) |
|--------|------|------|------|------|------|------|------|
| I | 28.3 | 4.6 | | | | 155 | 5.83 |
| II | 28.4 | 4.4 | 4.35% | 4.35% | 1.0454 | 162 | 5.86 |
| III | 28.6 | 4.1 | 10.87% | 6.81% | 1.1219 | 174 | 5.88 |
| IV | 28.7 | 3.6 | 21.74% | 12.19% | 1.2778 | 209 | 5.91 |
| V | 28.8 | 3.1 | 32.61% | 13.89% | 1.4839 | 244 | 5.97 |
| VI | 29.0 | 2.7 | 41.30% | 12.90% | 1.7037 | 263 | 6.00 |
| VII | 29.1 | 2.2 | 52.17% | 18.52% | 2.0909 | 276 | 6.03 |
| VIII | 29.2 | 1.7 | 63.04% | 22.73% | 2.7058 | 298 | 6.08 |
| IX | 29.4 | 1.3 | 71.74%/0% | 23.53% | 3.5385 | 316/183[A] | 6.12/5.89[A] |
| X | 29.6 | 0.86 | 81.30%/33.85% | 33.85% | 5.3489 | 247 [B] | 5.96 |
| XI | 29.9 | 0.58 | 87.39%/55.38% | 32.56% | 7.9310 | 280 | 6.05 |
| XII | 30.1 | 0.38 | 91.74%/70.70% | 34.48% | 12.1053 | 314/160[A] | 6.11/5.85[A] |

[A] values after annealing, T = 650°C, t = 10 min.
[B] sample was taken for wire making.

PCA of dataset revealed the presence of one component with characteristic
value (3.690) exceeding 1, explaining 92.249 % of the variability. Based on
the Kaiser criterion [16], two components (F1 and F2) will be used in further
explanations of variances. This two-component solution explained a total of
99.354 % of the variance, with the contribution of the first component of
92.249 %, and the second component of 7.105 %. Since two-component solution
based on the Kaiser criterion explained 99.354 % of the total variability, this
criterion was accepted. Observation plot based on the contents of components
is represented in Fig. 2a.

**Figure 1.** Scree plots of Eigen values

The high value of Width (b) is present in samples on the right side of the plot and low on the left side of the plot. Also, it can be concluded that high value of Height (h) is present in samples in the upper half of the plot and low on the opposite side of the plot (Fig. 2a).

The hardness of samples increases from 174 HV after forming the tube and welding, to 248 HV after 4 drawings at a tow bench and with increasing of the total coefficient of elongation to 1.1133 (Table 2). After interphase annealing hardness decreases to 181 HV, and with subsequent cold deformation after 3 drawings on the tow bench increases to 241 HV, with the increase of total coefficient of elongation to 1.406612 [11-13,17,18]. The cold-rolled sheet of alloy Au585Cu312Zn40Ga35In28 with the hardness of HV 150 of thickness 0.38 mm was examined by straining [8-10]. The obtained value is $R_m$ = 590 MPa, while the relative elongation is $A_{100}$= 34 %. Before applying PCA analysis on the dataset, we examined the data matrix in order to detect outliers. Application of Grubb's test to experimental data resulted in the detection of no outliers in

**Table 2.** The ratio of elongation and hardness for a tube of alloy
Au585Cu233Ni80Zn70Pd32, depending on the reduction degree

| Sample | Length (l) (mm) | Diameter (Ø) (mm) | λ individually | λ total | Hardness (HV 10) | Electrical conductivity (MS/m) |
|---|---|---|---|---|---|---|
| I | 150 | 6.0 | | | 174 | 5.88 |
| II | 152 | 5.8 | 1.0133 | 1.0133 | 187 | 5.90 |
| III | 157 | 5.6 | 1.0328 | 1.0466 | 208 | 5.92 |
| IV | 163 | 5.2 | 1.0382 | 1.0866 | 230 | 5.94 |
| V | 167 | 4.8 | 1.0245 | 1.1133 | 248/181[A] | 5.96/5.89 |
| VI | 180 | 4.6 | 1.0778 | 1.2000 | 200 | 5.90 |
| VII | 193 | 4.3 | 1.0722 | 1.2866 | 210 | 5.91 |
| VIII | 211 | 3.9 | 1.0932 | 1.4066 | 241 | 5.93 |

[A] *hardness of tubes after annealing*

the datasets (the critical value for $\alpha$=0.05 and n=8 was 2.127). Strong positive correlations were observed between Hardness (HV10) and Electrical conductivity (MS/m) (r=0.947); and strong negative correlations between Length (l) and Diameter (Ø) (r=-0.980) [14,15]. From the shape of the scree plot, shown in Fig. 1b, the number of important components that will be used in further calculations can be observed (F1 and F2). PCA of dataset revealed the presence of two components with characteristic values (2.890 and 1.082) exceeding 1, explaining 99.282 % of variability. Based on the Kaiser criterion [16], two components will be used in further explanations of variances. This two-component solution explained a total of 99.282 % of the variance, with the contribution of the first component of 72.244 %, and the second component of 27.038 %. Since two-component solution based on the Kaiser criterion explained 99.282 % of the total variability, this criterion was accepted. Observation plot based on the contents of com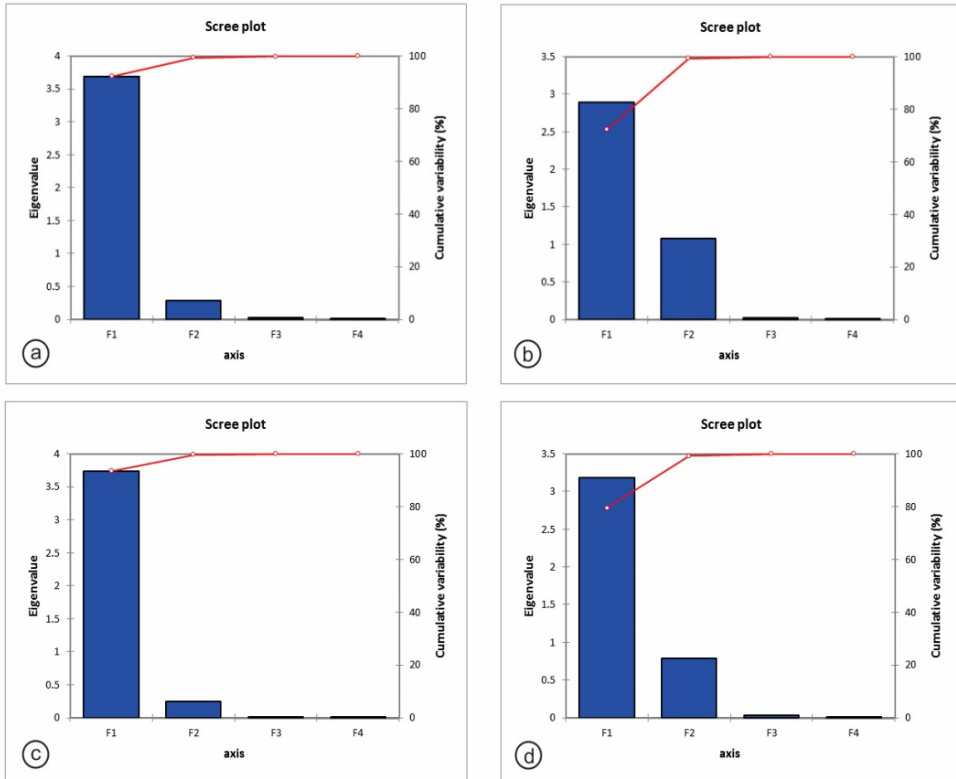ponents is represented in Fig. 2b. The high value of Length (l) is present in samples on the right side of the plot and low on the left side of the plot. Also, it can be concluded that high value of Diameter (Ø) is present in samples in the upper half of the plot and low on the opposite side of the plot (Fig. 2b). The hardness of samples increases from 150 HV in a molten state, up to 310 HV after 7 reductions in rolling mills while the total degree of deformation increased to 73.91% (Table 3).

After the first annealing, hardness decreases to 180 HV, and with subsequent cold deformation, after 3 reductions in rolling mills increases to 305 HV with the degree of cold deformation increasing to 91.74%. After the second annealing, the hardness of samples decreases to 150 HV with increasing degree of cold deformation to 68.33% [8-10]. Application of Grubb's test for

the detection of outliers to experimental data (samples I-XI from Table 3) resulted in the detection of no outliers in the datasets (the critical value for $\alpha=0.05$ and n=11 was 2.355). Strong positive correlations were observed between data of Width (b) and Hardness (HV10) (r=0.891), Width (b) and Electrical conductivity (MS/m) (r=0.843), and Hardness (HV10) and Electrical conductivity (MS/m) (r=0.985); and strong negative correlations between Width (b) and Height (h) (r=-0.994), Height (h) and Hardness (HV10) (r=-0.905), and Height (h) and Electrical conductivity (MS/m) (r=-0.854) [14,15].

**Table 3.** The ratio of elongation, hardness and electrical conductivity of alloy Au585Cu312Zn40Ga35In28, depending on the reduction degree

| Sample | Width (b) (mm) | Height (h) (mm) | $\varepsilon_{total}$ | $\varepsilon_{individually}$ | $F_0/F$ | Hardness (HV 10) | Electrical conductivity (MS/m) |
|---|---|---|---|---|---|---|---|
| I | 28.6 | 4.6 | | | | 150 | 5.80 |
| II | 28.7 | 4.3 | 6.52% | 6.52% | 1.0697 | 156 | 5.82 |
| III | 28.9 | 3.9 | 15.22% | 9.30% | 1.1795 | 172 | 5.87 |
| IV | 29.1 | 3.4 | 26.09% | 12.82% | 1.3529 | 204 | 5.90 |
| V | 29.3 | 2.7 | 41.30% | 20.59% | 1.7037 | 243 | 5.94 |
| VI | 29.6 | 2.1 | 54.35% | 22.22% | 2.1905 | 268 | 6.01 |
| VII | 29.8 | 1.6 | 65.22% | 23.81% | 2.8750 | 290 | 6.06 |
| VIII | 29.9 | 1.2 | 73.91%/0% | 25.00% | 3.8333 | 310/180 [A] | 6.11/5.88 |
| IX | 30.1 | 0.8 | 82.61%/33.33% | 33.33% | 5.7500 | 240 [B] | 5.93 |
| X | 30.3 | 0.5 | 89.13%/58.33% | 37.50% | 9.2000 | 275 | 6.02 |
| XI | 30.5 | 0.38 | 91.74%/68.33% | 24.00% | 12.1052 | 305/150 [A] | 6.07/5.81 [B] |

[A] values after annealing, temperature 650°C, t = 10 min.
[B] sample was taken for wire making.

From the shape of the scree plot, shown in Fig. 1c, the number of important components that will be used in further calculations can be observed (F1 and F2). PCA of dataset revealed the presence of one component with characteristic value (3.736) exceeding 1, explaining 93.4 % of the variability. Based on the Kaiser criterion [16], two components will be used in further explanations of variances. This two-component solution explained a total of 99.619 % of the variance, with the contribution of the first component of 93.4 %, and the second component of 6.218 %. Since two-component solution based on the Kaiser criterion explained 99.619 % of the total variability, this criterion was accepted. Observation plot based on the contents of components is represented in Fig. 2c.
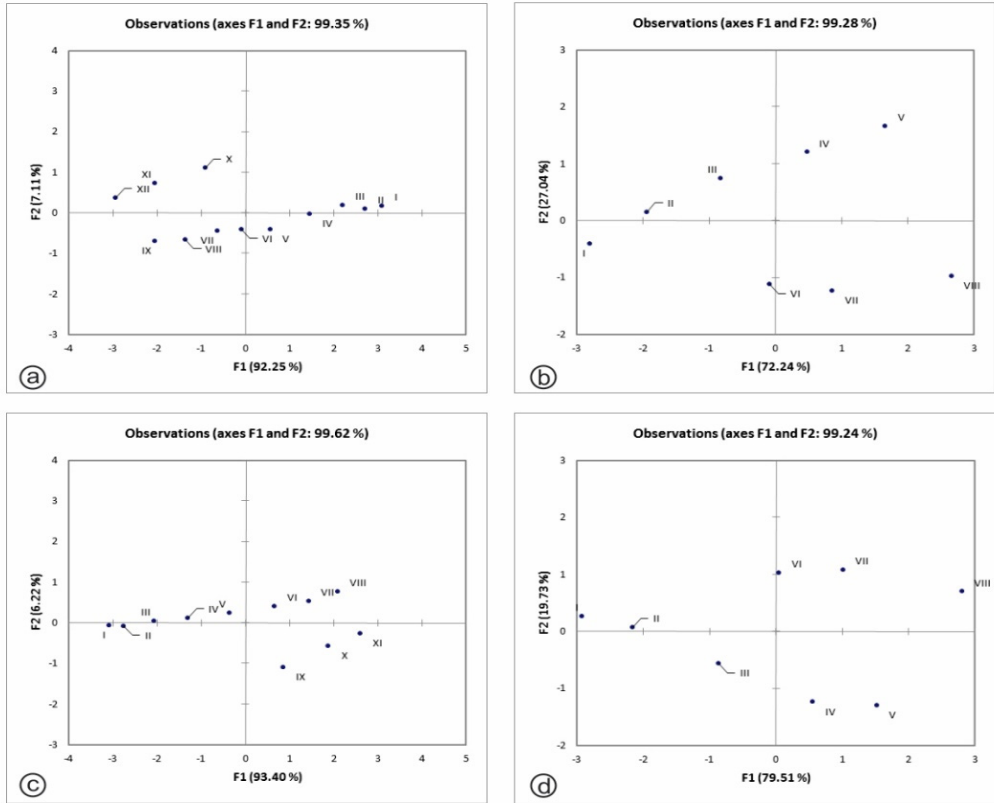
**Figure 2.** Principal component score plots (F1 and F2) of the studied samples

The high value of Width (b) is present in samples on the right side of the plot and low on the left side of the plot (Fig. 2c). Also, it can be concluded that high value of Height (h) is present in samples in the upper half of the plot and low on the opposite side of the plot.

The hardness of samples increases from 170 HV after forming the pipe and welding, up to 240 HV after 4 drawings at a tow bench with the increase of the total coefficient of elongation to 1.1400 (Table 4). After the interphase annealing hardness decreases to 171 HV, and with subsequent cold deformation after 3 drawings on the tow bench increases to 238 HV with the increase of the total coefficient of elongation to 1.4266 [8-10].

Application of Grubb's test to experimental data (samples I-VIII from Table 4) resulted in the detection of no outliers in the datasets (the critical value for $\alpha=0.05$ and n=8 was 2.127). Strong positive correlations were observed

between data of Hardness (HV10) and Electrical conductivity (MS/m) (r=0.988); and strong negative correlations between Length (l) and Diameter (Ø) (r=-0.958), and Hardness (HV10) and Diameter (Ø) (r=-0.715) [14,15].

**Table 4.** The ratio of elongation and hardness of alloy Au585Cu312Zn40Ga35In28 tube depending on the reduction degree

| Sample | Length (l) (mm) | Diameter (Ø) (mm) | λ individually | λ total | Hardness (HV 10) | Electrical conductivity (MS/m) |
|---|---|---|---|---|---|---|
| I | 150 | 6.0 | | | 170 | 5.87 |
| II | 153 | 5.7 | 1.0200 | 1.0200 | 180 | 5.88 |
| III | 158 | 5.4 | 1.0326 | 1.0533 | 202 | 5.90 |
| IV | 164 | 5.1 | 1.0379 | 1.0933 | 228 | 5.92 |
| V | 171 | 4.7 | 1.0426 | 1.1400 | 240/171[A] | 5.93/5.88 |
| VI | 183 | 4.5 | 1.0701 | 1.2200 | 198 | 5.89 |
| VII | 195 | 4.2 | 1.0655 | 1.3000 | 208 | 5.90 |
| VIII | 214 | 3.9 | 1.0974 | 1.4266 | 238 | 5.92 |

[A] *hardness of tubes after annealing*

From the shape of the scree plot, shown in Fig. 1d, the number of important components that will be used in further calculations can be observed (F1 and F2). PCA of dataset revealed the presence of one component with characteristic value (3.181) exceeding 1, explaining 79.513 % of the variability. Based on the Kaiser criterion [16], two components will be used in further explanations of variances. This two-component solution explained a total of 99.244 % of the variance, with the contribution of the first component of 79.513 %, and the second component of 19.731 %. Since two-component solution based on the Kaiser criterion explained 99.244 % of the total variability, this criterion was accepted. Observation plot based on the contents of components is represented in Fig. 2d. The high value of Length (l) is present in samples on the right side of the plot and low on the left side of the plot (Fig. 2d). Also, it can be concluded that high value of Diameter (Ø) is present in samples in the upper half of the plot and low on the opposite side of the plot.

The microstructure of cold-rolled sample of alloy Au585Cu233Ni80Zn70Pd32 (the overall reduction degree 71.74 %, the hardness of HV 316), was etched in the solution 10 % KCN: 10 % $(NH_4)_2S_2O_8$ in the ratio of 1:1 for 2 h at 40 °C, at 200 × magnification. Because of technological and metallurgical characteristics that are reflected in the higher hardness values, this sample is reduced 8 times at the rolling stands. The grains are elongated and oriented in the direction of the deformation (Figure 3a) [8-10,13].
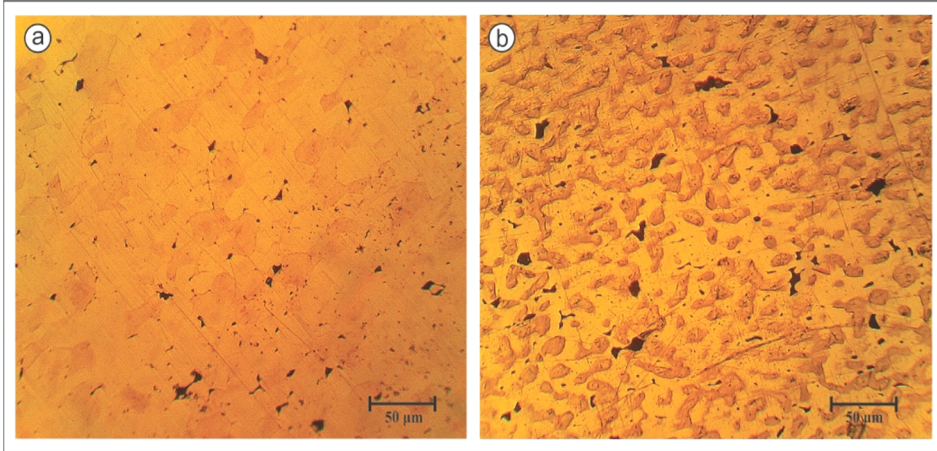
**Figure 3.** The pattern of alloy Au585Cu233Ni80Zn70Pd32 a) after 8 reductions of hardness HV 316, $\varepsilon$=71.74% etched in the solution of 10 % KCN: 10 % $(NH_4)_2S_2O_8$ in the ratio of 1:1 for 2 h at 40 °C, at 200 x magnification, b) etched in the solution of 8 ml of distilled $H_2O$, 3 ml of HCl and $HNO_3$ in 1 ml where 2 g $CrO_2$ was added

The microstructure of annealed samples of white gold with nickel obtained by SEM method, magnified 500 times, where the points 2, 4 and 5, residing in the light phase, have less copper than the points 1 and 3, residing in the darker phase (Figure 4). Two distinct phases coexist, where the lighter contains a higher percentage of gold and a small percentage of copper, while the darker contains a lower percentage of gold and a higher percentage of copper.

Figure 5a shows the microstructure of cold-rolled sample with the overall reduction degree of 74.47%. The sample was reduced 7 times at the rolling stands, and a sample of white gold without nickel shows hardness values lower than the white gold alloy with nickel [8-10,13,19]. The grains are elongated and oriented in the direction of the deformation. There is also the occurrence of twin crystals and phases [12]. Figure 5b shows the sample from Figure 6a, which is annealed at a constant temperature of 923 K (650 °C) for 10 min. It can be observed the recrystallised structure of the multi-component system that is ready for further deformation [12].

| Spectrum | In stats. | Ni | Cu | Zn | Pd | Au | Total |
|---|---|---|---|---|---|---|---|
| Spectrum 1 | Yes | 7.29 | 22.49 | 6.69 | 3.24 | 60.29 | 100.00 |
| Spectrum 2 | Yes | 7.95 | 20.06 | 7.87 | 3.61 | 60.51 | 100.00 |
| Spectrum 3 | Yes | 7.46 | 20.97 | 6.63 | 3.87 | 61.07 | 100.00 |
| Spectrum 4 | Yes | 13.22 | 20.63 | 5.40 | 2.70 | 58.05 | 100.00 |
| Spectrum 5 | Yes | 11.54 | 20.45 | 7.36 | 1.82 | 58.83 | 100.00 |
| Max. | | 13.22 | 22.49 | 7.87 | 3.87 | 61.07 | |
| Min. | | 7.29 | 20.06 | 5.40 | 1.82 | 58.05 | |
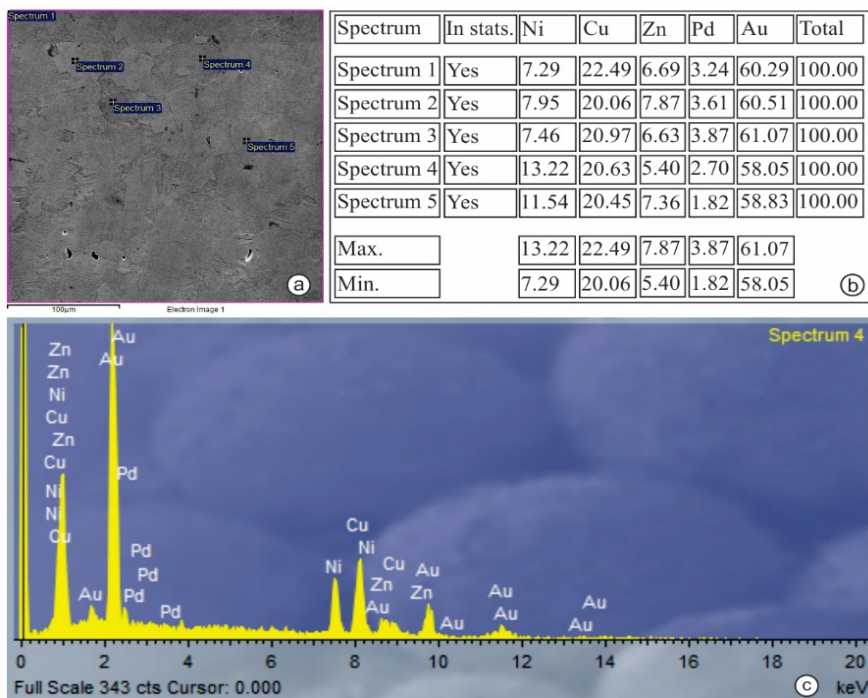
**Figure 4.** The microstructure of annealed samples of white gold with nickel:
a) Overview of points for chemical composition analysis, magnification 500×,
b) the table showing the content of the alloy components in the individual points,
c) EDS spectrum analysis of point 4
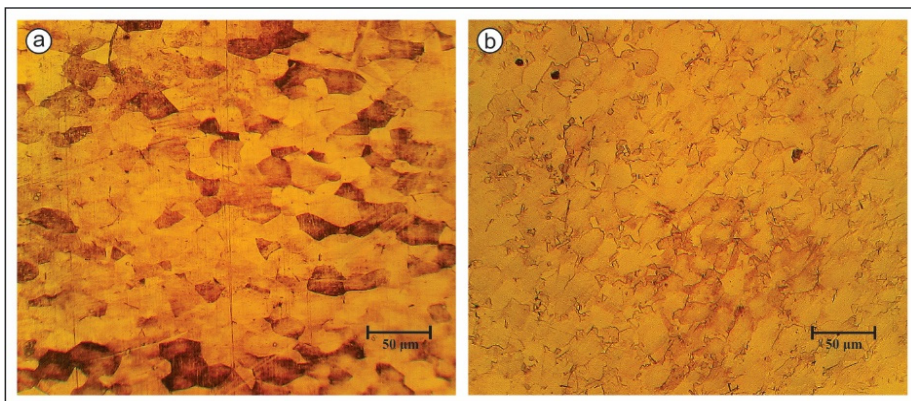


**Figure 5.** Pattern of alloy Au585Cu312Zn40Ga35In28 etched in KCN solution of
10%:10% $(NH_4)_2S_2O_8$ in the ratio of 1:1 for 2 hours at 40 °C, 200x magnification:
a) after 7 reduction of hardness HV 313, $\varepsilon$ = 74.47%, b) after the first annealing
with hardness HV 180

Figure 6 shows the microstructure of annealed recrystallised samples of the Au585Cu312Zn40Ga35In28 alloy obtained by SEM method with a magnification of 500 times, where it can be seen that points 1 and 2, from the lighter phase, have much less copper content than points 3 and 4, from the darker phase. Two different phases coexist, where the lighter one contains greater % of gold and lower % of copper, while the dark has lower % of gold and higher % of copper.



| Spectrum | In stats. | Cu | Zn | Ga | In | Au | Total |
|---|---|---|---|---|---|---|---|
| Spectrum 1 | Yes | 0.72 | 0.93 | 0.81 | 0.69 | 96.85 | 100.00 |
| Spectrum 2 | Yes | 4.43 | 1.00 | 0.93 | 0.60 | 93.05 | 100.00 |
| Spectrum 3 | Yes | 27.80 | 3.71 | 2.18 | 1.81 | 64.50 | 100.00 |
| Spectrum 4 | Yes | 29.92 | 3.28 | 2.44 | 1.53 | 62.83 | 100.00 |
| Spectrum 5 | Yes | | | | | 100.00 | 100.00 |
| | | | | | | | |
| Max. | | 29.92 | 3.71 | 2.44 | 1.81 | 62.83 | |
| Min. | | 0.72 | 0.93 | 0.81 | 0.60 | 100.00 | |
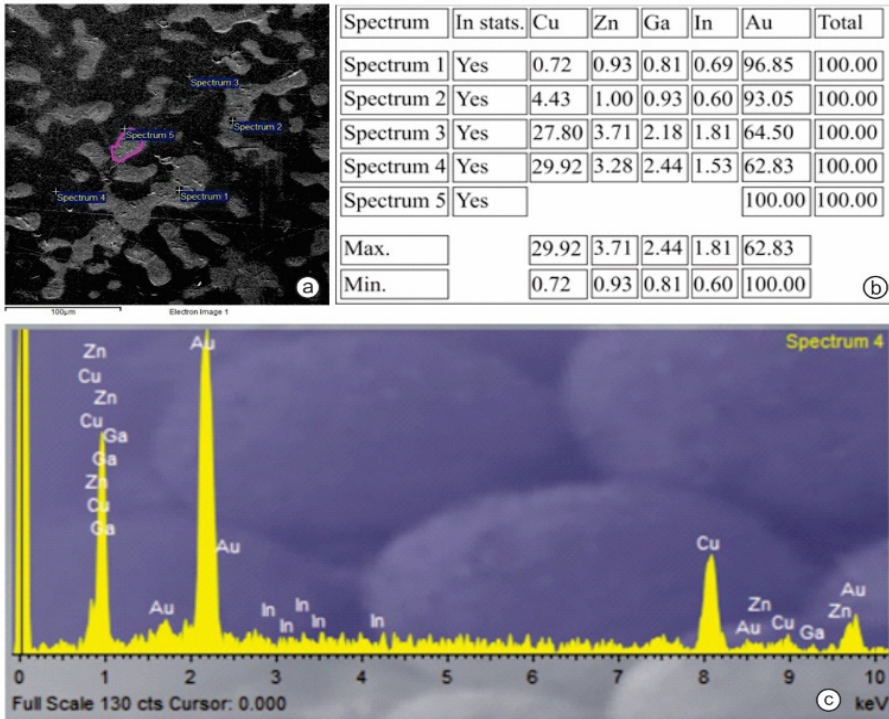
**Figure 6.** The microstructure of annealed recrystallised samples of Au585Cu312Zn40Ga35In28: a) Overview of points for chemical composition analysis, magnification 500×, b) the table shows the content of the alloy components in the individual points, c) EDS spectrum analysis of point 4

## CONCLUSIONS

By rolling cast pieces of the white gold alloy without silver, high-quality rectangular profiles of flat-sheet-strips with smooth edges, without cracks, uniform thickness and width all along the length, were obtained. Using the method of

cold rolling, with the increase in the total strain, the curves for the hardness value show the increase for both types of samples, more for the alloy Au585Cu233Ni80Zn70Pd32 than for the alloy Au585Cu312Zn40Ga35In28. The values obtained for the tensile strength in both tested alloys are at the upper limit of the literature values, while the relative elongation values are in the field of expected values. The values of electrical conductivity and hardness are different, due to the reduction, which was shown using PCA (r=0.985 and the strong positive correlation between hardness and electrical conductivity). Annealing under these conditions does not achieve the desired recrystallised structure. It is concluded that it is necessary for this white gold alloy to be annealed for a longer period or at a higher temperature. The microstructure of this alloy type, analyzed by optical and scanning electron microscopy - SEM, shows that during the metallurgical processes, micro-structural changes of structures happened. The processes of crystal grains fragmentation play an important role in the grain boundary dislocations, impurities, and intermetallic compounds.

## EXPERIMENTAL SECTION

Sample preparation was performed in an induction furnace graphite ladle (the processes of heating, melting, mixing and production). The resulting mixture was discharged into the wax-coated molds and casts of dimensions: 92 mm × 28.6 mm × 4.6 mm (Au585Cu312Zn40Ga35In28) and 92 mm × 28.3 mm × 4.6 mm (Au585Cu233Ni80Zn70Pd32). The resulting cast was several times on rolling stands (after every 5 passes it was annealed-recrystallised at 650 °C for 10 min) to achieve the appropriate sheet thickness-0.38 mm, which was suitable for cutting using circular shears.

Obtained strip (thickness 0.38 mm and a width 18.5 mm) was passed through the device for resistance welding in the presence of argon. The entire scheme of sampling is shown in Figures 7a and 7b.

Qualitative determination of the composition of the examined alloys using XRF device was performed in the Laboratory of the Directorate of Measures and Precious Metals in Belgrade, Republic of Serbia. Several investigations (hardness testing of samples, tensile testing, metallographic investigations, investigations using scanning electron microscopy and energy-dispersive spectroscopy, determination of electrical conductivity and determination of the colour of tested alloys) were conducted in the Laboratories of the Technical Faculty in Bor, Republic of Serbia [20-26].
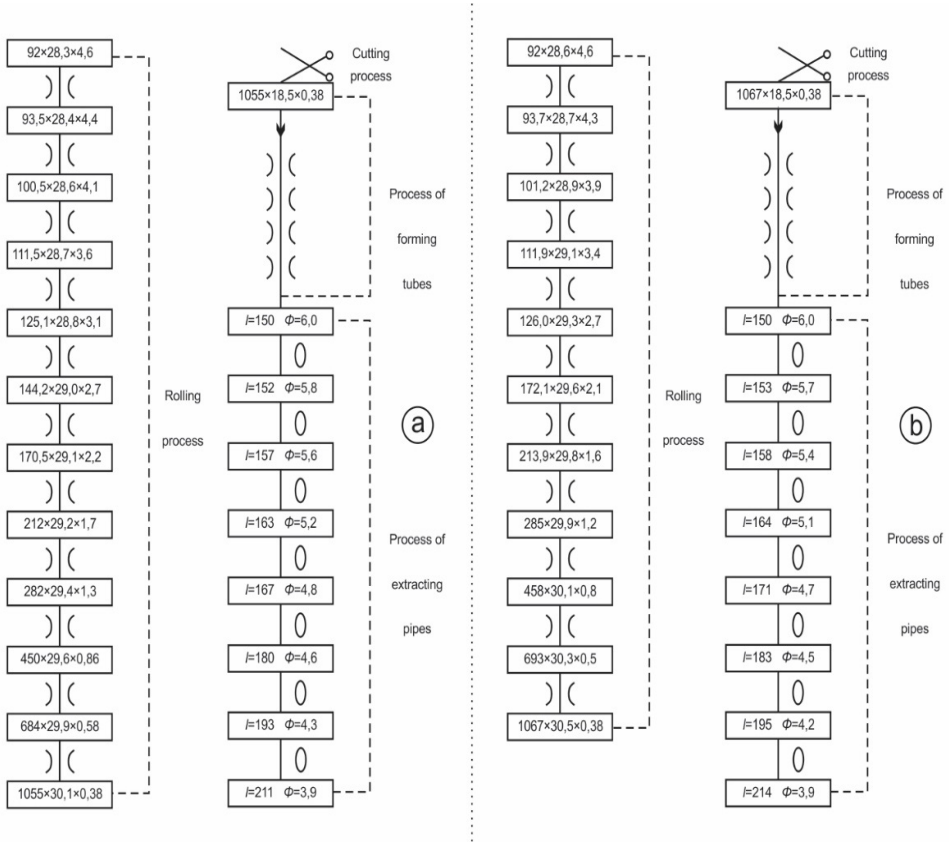
**Figure 7.** a) Pass plan for the alloys Au585Cu233Ni80Zn70Pd32,
b) Au585Cu312Zn40Ga35In28

## Statistical analysis (Principal component analysis)

The principal component analysis was used with the aim to evaluate the dataset, reducing its dimension and conserving most of the statistical information. PCA permits establishing the relationships among variables. The analysis was performed using statistical application available for Microsoft Excel® (XLSTAT 2015.6.01.24412, Addinsoft SARL, Paris, France) [27].

MLADEN MIRIĆ, BILJANA ARSIĆ, MILOŠ ĐORĐEVIĆ, DRAGAN ĐORĐEVIĆ,
DRAGOSLAV GUSKOVIĆ, SVETLANA IVANOV

# REFERENCES

1. Direttiva 2004/96/CE della Commisione, Gazzetta ufficiale dell'Unione europea journal, L 301/51, 27 settembre 2004. http://eur-lex.europa.eu/legal-content/IT/TXT/?uri=CELEX%3A32004L0096

2. Direttiva 2002/96/CE del Parlamento Europeoe del Consiglio, Gazzetta ufficiale dell'Unione europea journal, L 37/24, 27 gennaio 2003. http://eur-lex.europa.eu/legal-content/IT/TXT/?uri=CELEX%3A52003PC0723

3. J. Shlens; *A Tutorial on Principal Component Analysis*, Salk Institute for Biological Studies and Institute for Nonlinear Science: San Diego, USA, **2005**.

4. J. D. Horel; J. M. Wallace; *Mon. Weather Rev.*, **1981**, *109*, 2080-2092.

5. M. C. Janzen; J. B. Ponder; D. P. Bailey; C. K. Ingison; K. S. Suslick; *Anal. Chem.*, **2006**, *78*, 3591-3600.

6. P. Jolicoeur; J. E. Mosimann; *Growth*, **1960**, *24*, 339-354.

7. S. Wold; K. Esbensen; P. Geladi; *Chemometr. Intell. Lab.*, **1987**, *2*, 37-52.

8. M. B. Mirić; R. S. Perić; S. P. Dimitrijević; S. A. Mladenović; S. R. Marjanović; *Bulg. Chem. Commun.*, **2015**, *47*, 161-166.

9. M. Mirić; D. Marković; D. Gusković; 38th International October Conference on Mining and Metallurgy, **2006**, 280-285.

10. M. Mirić; D. Gusković; S. Ivanov; S. Marjanović; S. Mladenović; *Metalurgia Int.*, **2013**, *18*, 47-50.

11. D. Ott; *Gold Bull.*, **2000**, *33*, 25-32.

12. D. Gusković; D. Marković; S. Ivanov; S. Nestorović; M. Mirić; International Research/Expert Conference 15th Trends in the Development of Machinery and Associated Technology", Eds. by S. Ekinović, J. Vivancos Calvet, E. Tacer, TMT, Prague, **2011**, 713-716.

13. J. Fischer-Bühner; A. Basso; M. Poliero; *Gold Bull.*, **2010**, *43*, 11-20.

14. S. Shrestha; F. Kazama; *Environ. Modell. Softw.*, **2007**, *22*, 464-475.

15. M. Varol; B. Gokot; A. Bekleyen; B. Sen; *Catena*, **2012**, *92,* 11-21.

16. H. F. Kaiser; *Educ. Psychol. Meas.*, **1960**, *20*, 141-151.

17. M. Kazemineshad; A. K. Taheri; *Mater. Design*, **2005**, *26*, 99-103.

18. M. Kazemineshad; A. K. Taheri; A. K. Tieu; *J. Mater. Process. Tech.*, **2008**, *200*, 325-330.

19. L. Battezzati; I. Moiraghi; I. Calliari; M. Dabalà; *Intermetallics*, **2004**, *12*, 327-332.

20. http://xrf-spectroscopy.com/

21. B. Hafner; Scanning Electron Microscopy Primer-Characterization Facility, Twin Cities, Minnesota, **2007**.

22. R. A. Schwarzer; D. P. Field; B. L. Adams; M. Kumar; A. J. Schwartz; In *Electron backscatter diffraction in materials science*; A. J. Schwartz, M. Kumar, B. L. Adams, D. P. Field Eds.; Springer: US, 2009, pp. 1-20.

23. http://www.charfac.umn.edu/instruments/eds_on_sem_primer.pdf

24. H. Šuman; *Metalografija*; TMF: Belgrade, **1981**.

25. R. G. Kuehni; *Color Res. Appl.*, **2002**, *27*, 126-127.

26. http://www.foerstergroup.de/SIGMATEST.171.0.html

27. https://www.xlstat.com/en/

# SYNTHESIS AND CHARACTERISATION OF $Fe_3O_4$-$SnO_2$ NANOCOMPOSITES WITH ELECTROCHEMICAL PROPERTIES

**SERGIU MACAVEI[a], MARIA ŞTEFAN[a*], FLORINA POGACEAN[a], OVIDIU PANĂ[a], CRISTIAN LEOSTEAN[a], ADRIANA POPA[a], DANA TOLOMAN[a], LUCIAN BARBU-TUDORAN[a]**

**ABSTRACT.** Composite $Fe_3O_4$-$SnO_2$ nanoparticles were synthesized by growing $SnO_2$ nanoparticles on the surface of previously prepared $Fe_3O_4$ nanoparticles. First, $Fe_3O_4$ nanoparticles were prepared by chemical precipitation of precursors followed by the obtaining of $SnO_2$ nanoparticles by chemical precipitation or sol-gel process. The composite nanoparticle samples were characterized by using X-Ray diffraction (XRD), Transmission Electron Microscopy (TEM) and X-Ray photoelectron Spectroscopy (XPS) techniques. Also, electrochemical behaviour was recorded. The results revealed that by adjusting the composition of components one can control the properties of composite nanoparticles.

*Keywords: $SnO_2$; nanoparticles; photocatalytic properties, electrochemical properties*

## INTRODUCTION

For the past several decades, studies of nanometer-sized materials have attracted a considerable attention due to their unique optical, electrical, physical, chemical, and magnetic properties [1-4]. Since the current investigated materials are limited in terms of properties, price and multifunctionality, the increasing need of new nanostructured composite materials for different applications is become critical due to rapid growing of this market [5-7].

The composite nanostructures with different architecture like core-shell do not simply combine properties of the original components but also possess novel and collective performances which are not seen in the original

[a] *Institute for Research and Development of Isotopic and Molecular Technologies, Donath Str.67-103, RO-400293 Cluj-Napoca, Romania*
* *Corresponding author: mstefan@itim-cj.ro*

constituents. Physical and chemical properties of nanostructured composite materials can be adjusted by controlling the composition and the relative sizes of various components [8-11].

In this regard, combining the properties of $Fe_3O_4$ and $SnO_2$ a novel composite nanostructure with morpho-structural and magnetic properties in one single entity was obtained. These properties of $Fe_3O_4$-$SnO_2$ composite nanostructure would greatly broaden their application in photocatalysis [12,13], Li-ion batteries (LIBs) [14,15], magnetic resonance imaging (MRI) [16], sensors and biosensors [17], etc.

From a large variety of metal oxides, special attention has been paid to oxides of the $Fe_3O_4$, $SnO_2$ and their combinations due to their good electrochemical capacitance low cost and their positive impact on the environment [18,19].

The paper aims to report the synthesis and morpho-structural characterisation of $Fe_3O_4$-$SnO_2$ nanocomposites. The electrochemical properties were also evidenced.

## RESULTS AND DISCUSSION

The X-ray diffraction analysis of the synthesized sample was performed in order to identify the crystal structure and to estimate average crystallite size. In figure 1 are presented the XRD pattern of the samples with different $Fe_3O_4$:$SnO_2$ molar ratio.

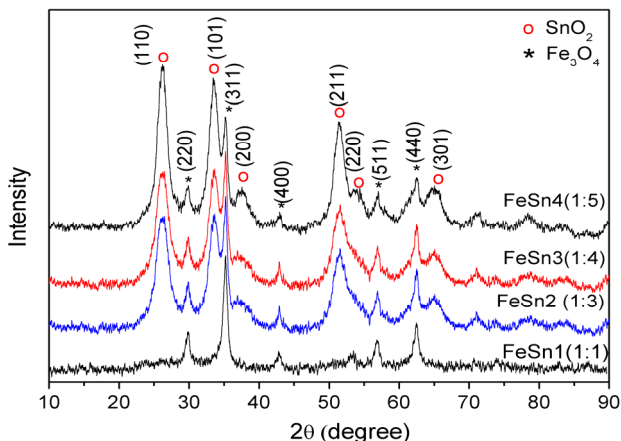The diffraction planes (220), (311), (400), (511), (440) of $Fe_3O_4$ (JCPD 99-100-2343) was identified.



**Figure 1.** XRD diffraction patterns and corresponding indexation of $SnO_2$-$Fe_3O_4$ samples with different molar ration between the two components.

By increasing the $SnO_2$ content diffraction peaks at $2\theta = 26.11$, $33.58$, $37.56$, $51.26$, $52.53$, $64.96$ corresponding to (110), (101), (200), (211), (220), (301) planes for rutile type tetragonal structure of $SnO_2$ can be observed. The intensity of these peaks increases with the increase of $SnO_2$ content.

The average crystallites sizes were calculated with Scherrer equation by using diffraction peaks related to the planes (220) for $Fe_3O_4$ and (110) for $SnO_2$ and a size of 12.5 nm and 5 nm was obtained for $Fe_3O_4$ and $SnO_2$ crystallites, respectively.

The morphology of $Fe_3O_4$-$SnO_2$ nanocomposites was determined by transmission electron microscopy (TEM). As an example, the TEM image for FeSn2 sample with corresponding size distribution is shown in Figure 2. The larger $Fe_3O_4$ cores are embedded in a berry structure of $SnO_2$ smaller nanoparticles. The particle size distribution for FeSn2 sample (inset of figure 2) shows two maxima distribution. The dotted line represents the best fit realized by using a superposition of two lognormal distribution functions. The obtained mean diameters 6.8 and 12.3nm are in agreement with XRD results and are attributed to $SnO_2$ and $Fe_3O_4$.
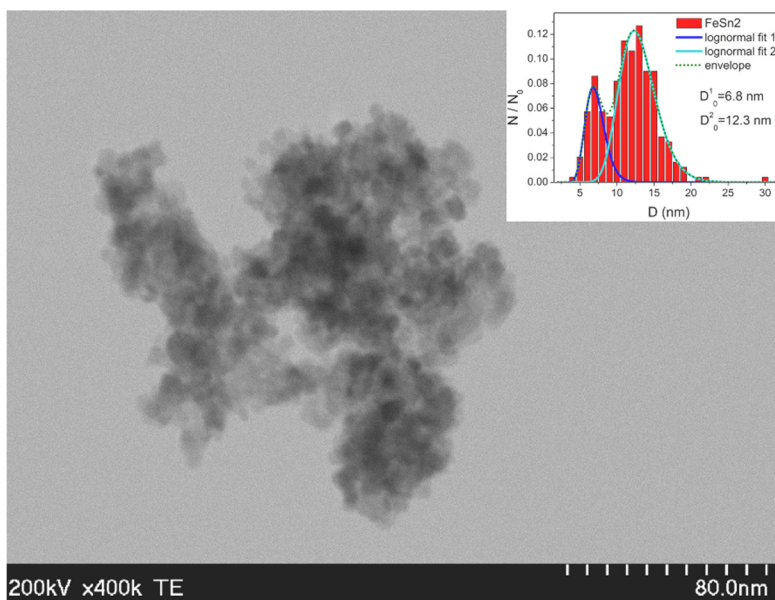


**Figure 2.** TEM image of FeSn2 sample together
with corresponding size distribution

SERGIU MACAVEI, MARIA ŞTEFAN, FLORINA POGACEAN, OVIDIU PANĂ, CRISTIAN LEOSTEAN, ADRIANA POPA, DANA TOLOMAN, LUCIAN BARBU-TUDORAN

The high-resolution TEM (HRTEM) image of $Fe_3O_4$-$SnO_2$ sample is given in figure 3. Lattice fringes are clearly visible in images revealing the crystalline nature of nanoparticles. Based on the Fourier Transform analysis, the interplanar distances were atribued to crystalline phases of $Fe_3O_4$ and $SnO_2$. As one can see in the inset of figure 3, the reciprocal lattice points for $Fe_3O_4$ (111) and $SnO_2$ (301), $SnO_2$ (101), $SnO_2$ (111), $SnO_2$ (110), $SnO_2$ (211) were found in the square marked area.

For quantitative analysis of samples the following XPS core-level lines were recorded: Fe 3$p$, Sn 3$d$, O 1$s$ and C 1$s$. The C 1$s$ line associated to C-C or C-H bindings positioned at 284.6 eV was used for spectra calibration. A Shirley background was used for the deconvolution.
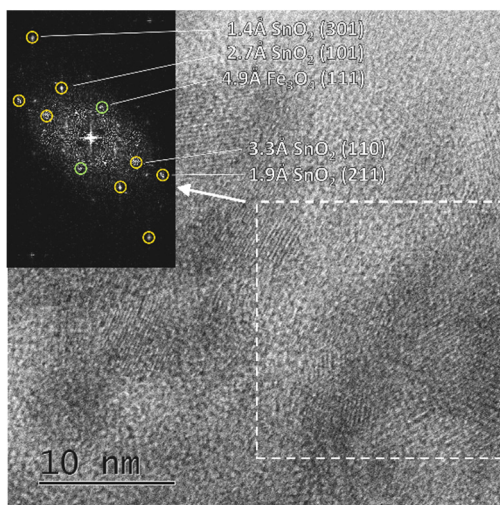


**Figure 3.** HRTEM image corresponding to FeSn1 sample. Fourier transform (inset) of marked square area reveal the presence of $Fe_3O_4$ and $SnO_2$.

For qualitative analysis the XPS survey spectrum of FeSn2 sample is shown in Figure 4a. One can see that only the expected elements are observed: Sn, Fe and O. The small C 1$s$ peak is attributed to adventitious carbon.

The XPS spectrum together with the corresponding deconvolutions of Sn 3$d$ core-level for FeSn2 sample is presented in figure 4b. The deconvoluted features represent the Sn atoms in (4$^+$) oxidation states. Besides the main lines, two sets of satellite peaks are also seen in all spectra.

The XPS Fe 3$p$ core-level spectrum for FeSn2 sample is presented in Figure 4c. The deconvoluted features represent the Fe atoms in (3$^+$) and (2$^+$) oxidation states with the corresponding 2:1 ratio for $Fe_3O_4$.

The core-shell architecture of nanoparticles was investigated by XPS depth profile analysis. It was performed by using Ar ions etching with 1000 V and 10 mA filament current.



**Figure 4.** (a) XPS survey spectrum of FeSn2 sample; XPS spectrum together with the corresponding deconvolutions of (b) Sn 3*d* core-levels;(c) Fe 3*p* core-level.
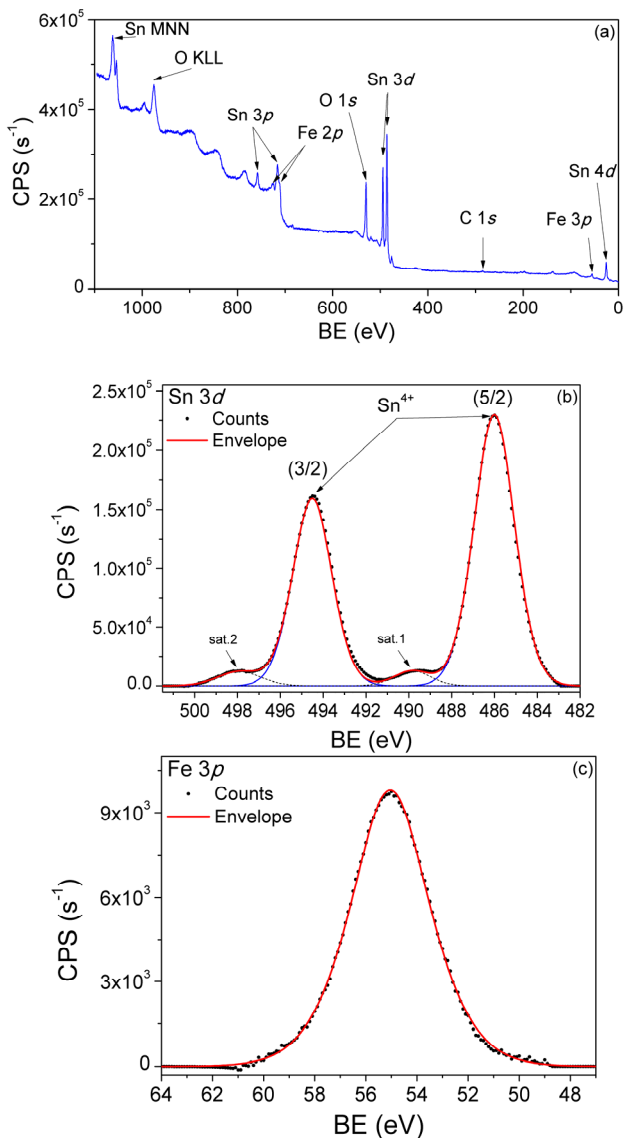
SERGIU MACAVEI, MARIA ŞTEFAN, FLORINA POGACEAN, OVIDIU PANĂ, CRISTIAN LEOSTEAN,
ADRIANA POPA, DANA TOLOMAN, LUCIAN BARBU-TUDORAN

In figure 5 one can see that the intensity of the Sn $3d(5/2)$ line decrease while the intensity Fe $3p$ lines (core) increase. This is an indication of core-shell structure formation.
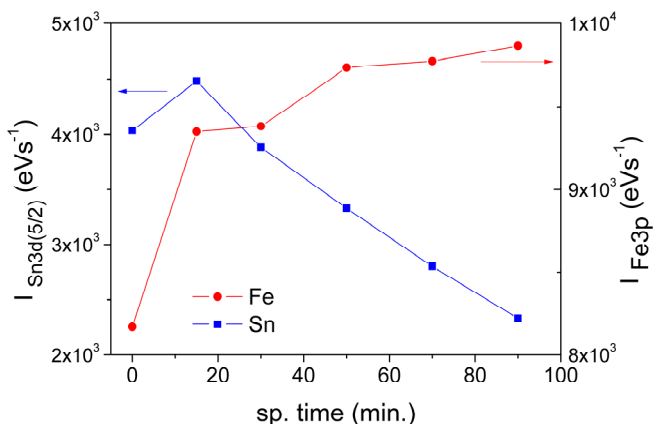


**Figure 5.** Variation of $Sn^{4+}$ 3p(3/2) and Fe 3p core-level lines as a function of sputtering time

The electrochemical behavior of the electrodes containing $Fe_3O_4$-$SnO_2$ nanocomposites has been investigated by using cyclic voltammetry performed at different scan rates and testing their stability at multiple cycling.

Electrochemical response of paste electrodes obtained from FeSn1 sample and graphite using the aqueous solution of LiCl 1M as support electrolyte are shown in figure 6 (a and b).

Cyclic voltammograms reveal the existence of well-defined redox couples corresponding to both $Fe_3O_4$ and $SnO_2$ even at low scan rates. Also, the anodic peaks ($Ep_a$) and the cathodic peak ($Ep_c$) intensity were measured. Thus, for scan rates 2 mV, the oxidation potential is at 0.13V, while higher than 10 mV the potential value is shifted to 0.70V (figure 6b). The intensities of the redox peaks increase with the number of cycles indicating that the presence of the two reactive species in FeSn1 sample improve the electrochemical response of the material. The electrochemical stability FeSn1 is shown in figure 6a. The good stability of $Fe_3O_4$-$SnO_2$ nanocomposites at multiple cycles (50 at high scan speed (100mV) was observed.

Possible electrochemical reactions during the intercalation/extraction process of $Li^+$ ions for FeSn1 nanocomposites can be described by the following reactions.

**Figure 6.** Cyclic voltammograms recorded with FeSn1 paste electrode
in LiCl 1M electrolytes: a) Stability testing (50 cycles, scan rate 100mV/s);
b) variation of scanning rates from 2 -10 mV/s.

$$Fe_3O_4 + 2Li^+ + 2e^- \rightarrow Li_2 (Fe_3O_4) \qquad (1)$$

$$Li_2 (Fe_3O_4) + 6Li^+ + 6e^- \rightarrow 3Fe + 4Li_2O \qquad (2)$$

$$Fe + 4Li_2O \rightarrow Fe_3O_4 + 8Li^+ + 8e^- \qquad (3)$$

Regarding the samples with high content of $SnO_2$, FeSn3 electrochemical stability was tested by cycling electrodes in 1 M LiCl, for 50 cycles at a scanning speed of 100 mV / s (figure 7).

SERGIU MACAVEI, MARIA ŞTEFAN, FLORINA POGACEAN, OVIDIU PANĂ, CRISTIAN LEOSTEAN,
ADRIANA POPA, DANA TOLOMAN, LUCIAN BARBU-TUDORAN

**Figure 7**. Cyclic voltammograms recorded with FeSn3 paste electrode,
in LiCl 1 M electrolytes; Stability testing (50 cycles, scan rate 100mV/s).

The cyclic voltammograms presented show that through repeated cycling in the LiCl 1 M electrolytes, the oxidation and reduction peaks increase due to adsorption on the surface electrode of different electrochemical species.

In the specific case of sample FeSn3, the concentration of $Fe_3O_4$ in the composite being reduced (the molar ratio between $Fe_3O_4$ and $SnO_2$ is 1: 3), the intensity of the oxido-reduction peaks related to the intercalation-de-intercalation of $Li^+$ ions in $Fe_3O_4$ decreases or is even absent at low scanning speeds.

The same behavior is observed for FeSn4 samples. The cyclic voltamograms corresponding to FeSn4 sample in LiCl 1 M aqueous solution as electrolyte support was presented in figure 8.
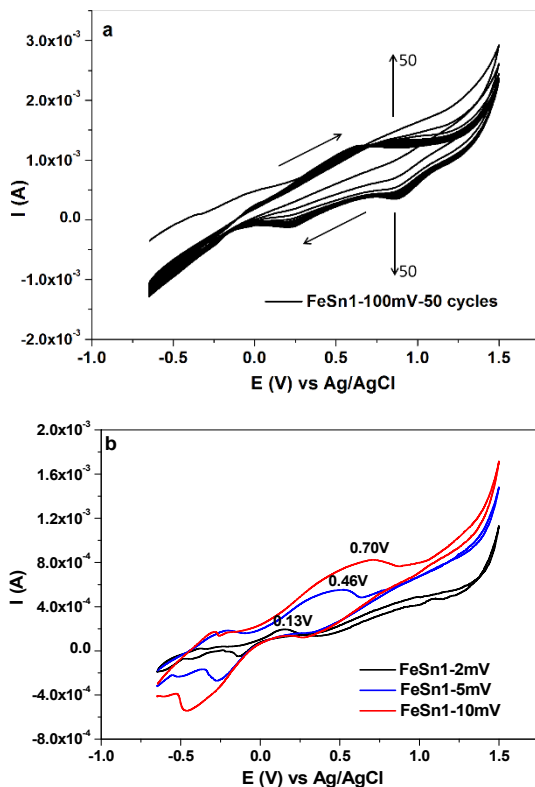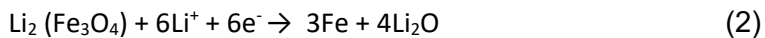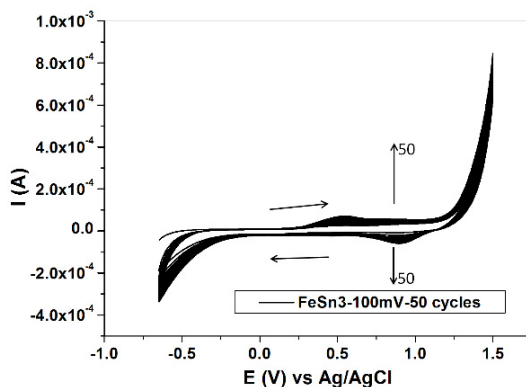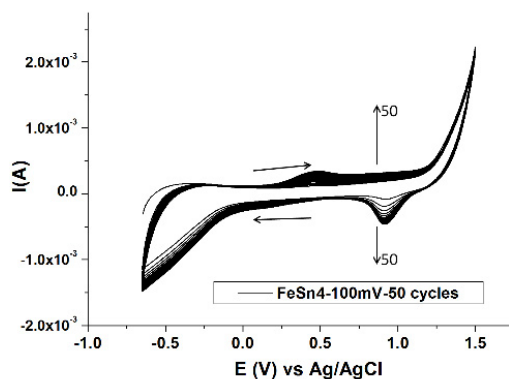


**Figure 8**. Cyclic voltammograms recorded with FeSn4 paste electrode
in LiCl 1 M electrolytes;Stability testing (50 cycles, scan rate 100mV/s).

Cyclic voltammeters occur with increasing oxidation and reduction peaks intensity involved in the reversible processes at electrode. This behavior demonstrates the good electrochemical performance of electrode material based on FeSn1 sample (molar ratio $Fe_3O_4$:$SnO_2$= 1:1). The composition and structure of the investigated electrode materials plays an important role in the oxidation-reduction processes at the electrode. The increasing the quantity of $SnO_2$ in composite samples relative to the amount of $Fe_3O_4$ seems to have no effect on electrochemical response of nanocomposites.

## EXPERIMENTAL SECTION

### Materials

The chemical reagents used for the preparation of $Fe_3O_4$-$SnO_2$ composite nanoparticles are: $FeCl_3$ x $6H_2O$ (98% Alfa Aesar), $FeCl_2$ x $4H_2O$ (98% Alfa Aesar), $NH_3$ (25% Merck), sodium laurylsulphate-SLS (p.a Fluka) tin cloride $SnCl_2$ x $2H_2O$ (for synthesis, Merck), sodium hydroxide (98% Alpha Aesar), graphite powder (99.99%, Sigma-Aldrich). $LiNO_3$ (98% Chemapol), LiCl (for synthesis, Merck), silicone oil (Sigma-Aldrich). All chemicals are analytical grade without further purification and were used as received.

### Sample preparation

The $Fe_3O_4$-$SnO_2$ nanocomposites were prepared by precipitation seed mediated growth onto preformed magnetite nanoparticles [20, 21]. The magnetite nanoparticles were obtained by chemical precipitation. Next, $SnO_2$ nanocrystals were obtained by precipitation method performed by adding the reagents one-into-another via reagent sequential addition technique (S*eqAdd*) to form $Fe_3O_4$-$SnO_2$ nanocomposites. The details of experimental procedure are presented as follows. In the first stage, magnetite nanoparticles were redispersed in bidistilled water 1 h, then in aqueous solution of sodium laurylsulphate (SLS) (0.6 mMol) to prevents the aggregation of $Fe_3O_4$ nanoparticles due to the steric repulsion, under vigorous stirring at room temperature for 12 h. The as treated magnetite particles were separated and then redispersed in 100 ml $SnCl_2x2H_2O$ (0.70÷3.2 mMol) aqueous solution under continuous stirring for 24 h. Further 100 ml NaOH (1.4÷6.4 mMol) aqueous solution was drop wise added to the mixture. After the addition of NaOH was finished, the reaction was kept 4 hours under vigorous stirring. The as prepared $Fe_3O_4$-$SnO_2$ nanocomposite were magnetically collected and washed with water and ethanol (1:1 v/v) for several times to remove the excess of reactants and then dried at 65°C, in air.

SERGIU MACAVEI, MARIA ŞTEFAN, FLORINA POGACEAN, OVIDIU PANĂ, CRISTIAN LEOSTEAN, ADRIANA POPA, DANA TOLOMAN, LUCIAN BARBU-TUDORAN

Finally, the dried and homogenized samples were thermally treated for 2h at 600°C in furnace, at a rate of 5°C/min, in order to get the $Fe_3O_4$-$SnO_2$ composite nanoparticles. In order to evidenced the influence of $SnO_2$ content on the morpho-structural and electrochemical characteristics of $Fe_3O_4$-$SnO_2$ nanocomposites, a series of samples with different $Fe_3O_4$:$SnO_2$ molar ratios were prepared, as following: 1:1 (FeSn1), 1:2 (FeSn2), 1:3 (FeSn3) and 1:4 (FeSn4).

## Samples characterization

The crystalline structure of samples was evidenced by X-ray diffraction (XRD), recorded by using a Bruker D8 Advance X-ray diffractometer set-up, at 40 kV and 40 mA equipped with a germanium monochromator in the incident beam. The X-ray diffraction patterns were collected in a step-scanning mode with steps of $\Delta\theta = 0.02°$ using Cu Kα1 radiation ($\lambda = 1.54056$ Å) in the 2θ range 10°-80°. Pure silicon powder was used as standard for instrument broadening correction.

Transmission electron microscopy (TEM) was carried out to determine morphology of the nanocomposites. The TEM measurements were performed with Hitachi SU8230 Transmission Electron Microscope equipped with a cold field emission gun. The powder were dispersed in ethanol, with a BANDELIN SONOREX homogenizer and deposited on 400 meshes copper grid, which was coated with carbon film. The HRTEM images were collected with Hitachi H9000NAR transmission electron microscope.

The qualitative and quantitative compositions of samples were investigated by using X-Ray Photoelectron Spectroscopy (XPS) assisted by Ar ions etching. The XPS spectra were recorded by using a SPECS spectrometer working with Al anode (1486.6 eV) as X-rays source. XPS depth profile analysis was performed by using Ar ions etching with 1000 V and 10 mA filament current.

The electrochemical measurements (Cyclic Voltammetry-CV) were performed with an Autolab 302N Potentiostat/Galvanostat (Metrohm Autolab B.V., Utrecht, the Netherlands) connected to a three-electrode cell and controlled by Nova1.11 software and a personal computer. A paste electrode with graphite and nanocomposite $Fe_3O_4$-$SnO_2$ was used as working electrode, Pt electrode was employed as counter-electrode, and Ag/AgCl electrode was used as reference.

The electrochemical experiments were carried out in electrolyte solutions of LiCl 1M with different scan rate (2, 5, 10 mV/s) were typically recorded between -0.5 and +1.5 V vs Ag/AgCl.

The paste electrodes were prepared by adding silicon oil into the composite materials containing $Fe_3O_4$-$SnO_2$ and mixing them into an agate mortar, until a uniformly wetted paste was obtained. The obtained paste was

mix with two parts of graphite and then packed in a PVC tube (3 mm internal diameter and 5 cm long). A copper disk inserted into the electrode paste to ensure the electrical contact.

## CONCLUSIONS

$Fe_3O_4$-$SnO_2$ nanocomposites with different ratio of components were prepared in two stages by growing $SnO_2$ onto preformed $Fe_3O_4$ nanoparticles. XRD investigations evidenced the presence of crystalline $Fe_3O_4$ and $SnO_2$. The crystallite size of 12.5 nm and 5 nm was obtained for $Fe_3O_4$ and $SnO_2$ crystallites, respectively.

The TEM/HRTEM investigation shows that the 12.3 nm $Fe_3O_4$ cores are embedded in a berry structure of 6.8 nm $SnO_2$ nanoparticles. XPS investigations show the qualitative compositions of samples and oxidation state $Sn^{4+}$ ($SnO_2$) and $Fe^{2+}$/$Fe^{3+}$ ($Fe_3O_4$) in the samples. The formation of the core shell structure was investigated by depth profile evolution of Sn $3d$ and Fe 3p core-levels XPS lines. The electrochemical behavior was evidenced on paste electrodes containing $Fe_3O_4$-$SnO_2$ nanocomposites. The results indicate the excellent rate capability and a significantly enhanced cyclic performance depending on composition of electrode material. The increasing oxidation and reduction peaks intensity involved in the reversible processes at electrode demonstrates the good capability of samples to be used as anodes in Li-ion batteries. Further researches are needed to establish optimized synthesis parameters for the electrode material and a complex electrochemical characterization.

## ACKNOWLEDGEMENTS

## REFERENCES

1. J. Chang, J. Ma, Q. Ma, D. Zhang, N. Qiao, M. Hu, H. Ma, *Appl. Clay Sci.,* **2016**, *119*, 132-133.
2. R. Li, X. Ren, F. Zhang, C. Du, J. Liu, *Chem. Commun.*, **2012**, *48*, 5010-5012.
3. H. J. Zhang, G. H. Chen, D. W. Bahnemann, *J. Mat. Chem.*, **2009**, *19*, 5089-5121.
4. N. Du, Y. F. Chen, C. X. Zhai, H. Zhang, D. Yang, *Nanoscale*, **2013**, *5*, 4744-4750.

SERGIU MACAVEI, MARIA ŞTEFAN, FLORINA POGACEAN, OVIDIU PANĂ, CRISTIAN LEOSTEAN, ADRIANA POPA, DANA TOLOMAN, LUCIAN BARBU-TUDORAN

5. X. N. Zheng, X. Y. Yin, B. Wang, M. G. Ma, *Sci. Adv. Mat.,* **2020**, *12*, 613-627.

6. R. G. Chaudhuri, S. Paria, *Chem. Rev.,* **2012**, *112*, 2373-2433.

7. C. Song, Z. Ye, G. Wang, J. Yuan, Y. Guan, *ACS Nano,* **2010**, *4*, 5389-5387.

8. W. Wu, S. Zhang, F. Ren, X. Xiao, J. Zhou, C. Jiang, *Nanoscale*, **2011**, *3*, 4676-4684.

9. J. U. Hur, J. S. Han, J. R. Shin, H. Y. Park, S. C. Choi, Y-G. Jung, G. S. An, *Ceram. Int*., **2019**, *45*, 21395-21400.

10. J. Jiang, Y. Y. Li, J. P. Liu, X. T. Huang, C. Z. Yuan, X. W. Lou, *Adv. Mater.,* **2012**, *24*, 5166-5180.

11. C. Karunakaran, S. S. Raadha, P. Gomathisankar, P. Vinayagamoorthy, *Powder Technol*., **2013**, *246*, 635-642.

12. V. M. Vinosel, S. Anand, Y. A. Janifer, S. Pauline, S. Dhanavel, P. Pravvena, A. Stephen, *J. Mat. Sci. Mater. Electron.*, **2019**, *30*, 9663-9677.

13. D. Chu, J. Mo, Q. Peng, Y. P. Zhang, Y. G. Wei, Z. B. Zhuang, Y. D. Li, *Chem. Cat. Chem*., **2011**, *3*, 371-377.

14. R. Li, X. Ren, F. Zhang, *Chem. Com*., **2012**, *48*, 5010-5012.

15. X. Chai, C. Shi, E. Liu, *Appl. Surf. Sci*., **2016**, *361*, 1-10.

16. W. W. Wang, J. L. Yao, *J. Phys. Chem. C*, **2009**, *113*, 3070-3075.

17. H. Bagheri, N. P. Jamali, S. Amidi, A. Hajian, H. Khoshsafar, *Microchem. J.,* **2017***, 131*, 120-129.

18. A. Mehdinia, M. Jebeliyan, T. B. Kayyal, A. Jabbari, *Microchim. Acta,* **2017**, *184*, 707-713.

19. Y. K. Wang, H. Y. Zhang, R. Z. Hu, J. W. Liu, T. van Ree, H. H. Wang, L. C. Yang, M. Zhu, *J. Alloy Compd.,* **2017**, *693*, 1174-1179.

20. C. Leostean, O. Pana, M. Stefan, A. Popa, D. Toloman, M. Senilă, S. Gutoiu, S. Macavei, *Appl. Surf. Sci.,* **2018**, *427,* 192-201.

21. M. Stefan, A. Popa, O. Panā, C. Leostean, D. Toloman, D. Lazar, F. Pogăcean, S. Macavei, S. Gutoiu, *J. Mat. Sci.: Mater. Electron.,* **2018**, *29,* 14132-14143.

188

# MORPHO-TEXTURAL AND FLUORESCENCE STUDIES ON SIO$_2$ AND SIO$_2$@Ce$^{3+}$

**ELENA-MIRELA PICIORUȘ**[a]**, CĂTĂLIN IANĂȘI**[a]**, ROXANA NICOLA**[a]**,
PAULA SFÎRLOAGĂ**[b]**, PAULA SVERA**[b]**, ANA-MARIA PUTZ**[a]

**ABSTRACT.** Spherical silica xerogels were synthesized by Stöber route using tetra-ethyl-orthosilicate (TEOS) in order to obtain good properties for opto-electronic and catalytic applications. The reactants mole ratio was $n$ TEOS: H$_2$O: ETOH: NH$_3$ (where $n$ = 0.098 ÷ 0.26: 0.45: 0.789: 0.06). To study these properties, we know from literature, that nanoparticles under 100 nm show unique electrical, mechanical and optical properties. We have choosen the optimum sample, with the smaller surface area and particles size of 91 nm. To improve the optical properties, this sample was further doped with 0.1% Ce$^{3+}$. The obtained xerogel was thermally treated at 300, 600 and 900 °C. The changes in properties were put in evidence by morpho-textural (N$_2$ adsorption–desorption isotherms and SEM images) and optical measurements (FT-IR, Fluorescence and Raman spectra's).

*Keywords: sol-gel, Ce (III) carbonate hydrate, Stöber, spherical particles*

## INTRODUCTION

SiO$_2$ has been considered a promising material as host matrix for rare earth elements because of its transparence and simplicity in synthesis [1]. Generally, lanthanide ions, such as Ce$^{3+}$ have been incorporated in SiO$_2$ matrix to tune the catalytic and fluorescence properties [2].

High annealing temperature of lanthanide doped nanomaterial's forming lanthanide ion clustering leading to the phase separation and the nanoparticles sintering have a reduction in surface area. As applications of these nanomaterial's, can be listed in optical domains, such as lasers [3] and as activators in SiO$_2$ materials because they allow 4f-5d optical transitions [4]. A. Vedda [5] observed that by increasing the concentration of Ce$^{3+}$ above 0.1%, led to a decrease in fluorescence, due to the formation of aggregates or by valence changes.

---

[a] *"Coriolan Dragulescu" Institute of Chemistry, 24 Mihai Viteazu Bvd., 300223, Timisoara, Romania*
[b] *National Institute for Research and Development in Electrochemistry and Condensed Matter, 144 Prof. Dr. Aurel Paunescu Podeanu Str., Timisoara, Romania*
* *Corresponding author: putzanamaria@yahoo.com*

The sol-gel technique has the advantage over other methods because it yields materials with low density [6] this being an important factor for enhancing the fluorescence. The fluorescence of cerium doped $SiO_2$ may be influenced by multiple factors like modification of the ligand field around the $Ce^{3+}$ ions in silica, presence of hydroxyl ions, energy transfer by cross relaxation and concentration of dopants [7]. Therefore, it is important to distinguish between the fluorescence ascending from $Ce^{3+}$ ions and of that arising from defect centers in the silica matrix. In parallel to optical studies, structural and morphological investigation appeared to be useful, and the present work is specifically aimed at shedding further light on the incorporation of $Ce^{3+}$ ions into the sol-gel silica matrix. The purpose of this study was to investigate the morphological and textural properties and to put in evidence the fluorescence by doping with 0.1% $Ce^{3+}$ concentration and fired at three different temperatures.

## RESULTS AND DISCUSSION

Firstly, the three xerogels obtained were characterized by physicochemical methods to underline the effect of TEOS concentration. In the second step we will effectively choose the optimum sample and we will add cerium as dopant to improve the fluorescent properties.

### Part I

### *FT-IR Spectroscopy*

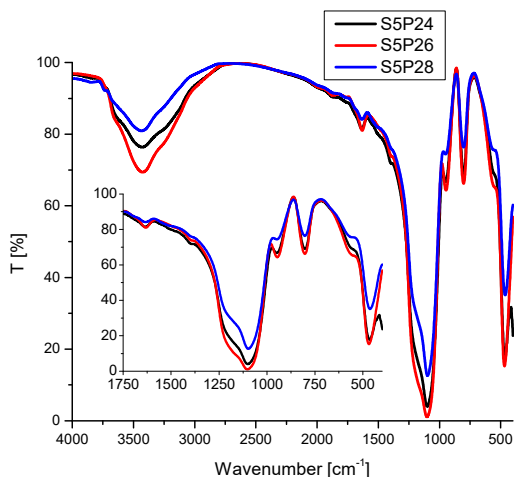Figure 1 shows the infrared transmission spectra of solid silica particles.



**Figure** 1. FT-IR spectra of dried (60 °C) silica xerogels with different [TEOS]

The broad absorption band around 3400-3600 cm$^{-1}$ was assigned to stretching mode of the hydroxyl group and molecular water [8]. The peak at 1635 cm$^{-1}$ can be ascribed to the H-O-H bending vibration of the free water or the physically absorbed water [9]. The absorption bands due to Si-OH stretching and bending vibrations appeared at ~950 cm$^{-1}$ [10]. The spectrum reveals intense bands at 1100 cm$^{-1}$, 804 cm$^{-1}$ and 468 cm$^{-1}$ specific for Si-O-Si stretching, Si-O$^-$ symmetric stretching and Si-O-Si asymmetric bending, respectively [9, 11]. The results indicate that all bands are suggesting the formation of a silica network.

### $N_2$ adsorption - desorption isotherms

The textural parameters of dried silica xerogels, evaluated by $N_2$ adsorption - desorption isotherms are presented in **Figure 2**.
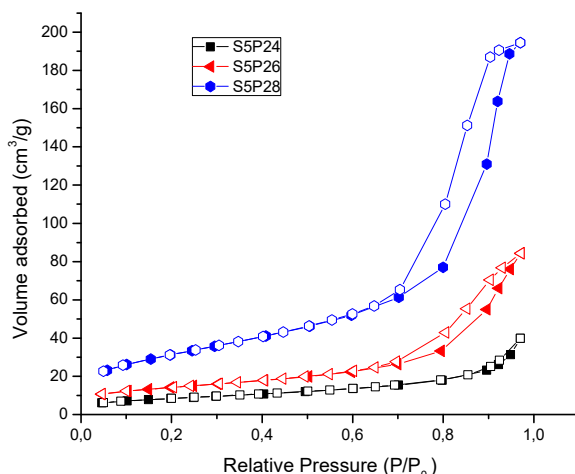


**Figure 2.** $N_2$ adsorption-desorption isotherms of dried xerogels

According to IUPAC classification [12, 13] the $N_2$ adsorption-desorption isotherms indicate for the sample with low TEOS concentration, S5P24, a *type II isotherms*, specific for non-porous materials. Also, this material presents a small percentage a type IVa isotherm with a type H3 hysteresis loop. With the increase of TEOS concentration, the $N_2$ isotherm of sample S5P26 indicate a *type IVa isotherms* which are characteristic for mesoporous materials presenting a H3 hysteresis loop specific for aggregates and slit-shaped pores [12, 13]. For xerogel S5P28, with the highest concentration of TEOS, exhibits a type IVa isotherm with a H1 hysteresis loop, typically characteristic for cylindrical pores [12, 13].

From N$_2$ adsorption-desorption isotherms, the textural parameters were evaluated and presented in Table 1.

**Table 1**. Textural parameters of silica xerogels with different TEOS concentrations

| Xerogels | BJH Adsorption pore diameter [nm] | BJH Desorption pore diameter [nm] | BET surface area [m$^2$/g] | Total pore volume [cm$^3$/g] | Particle diameter* [nm] |
|---|---|---|---|---|---|
| S5P24 | 3.63 | 3.03 | 29.8 | 0.061 | 91 |
| S5P26 | 15.22 | 8.94 | 49.2 | 0.013 | 55 |
| S5P28 | 15.32 | 9.03 | 112.8 | 0.030 | 24 |

*Particle diameter was calculated with the: (D$_{particle}$) = 6/Ssp*d$_{SiO2}$*10$^6$

In Figure 3 *the pore size distribution* was assessed from N$_2$ adsorption-desorption isotherms, using the method proposed by Barrett, Joyner and Halenda (BJH) [14]. The sample S5P26 and S5P28 indicate a wider unimodal pore distribution in the range of 10-20 nm. For xerogel S5P24 the pore size distribution indicates a very small diameter of pore with less than 4 nm.
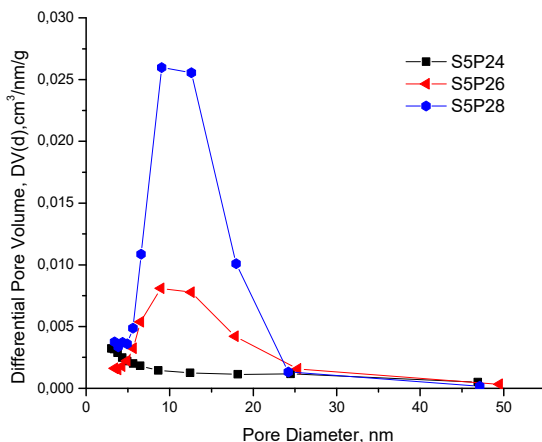


**Figure 3**. Pore size distribution

The particle sizes were calculated with the equation proposed by Sun et al. [15]. It was observed that the size of particles decreases with the increase of TEOS concentration. The decrease of particle size below 100 nm enables good optical transparency, especially for silica [16].

The sample S5P28, with the maximum concentration of TEOS, presented the highest surface area value with a value of ~113 m2/g.

### SEM

The morphology of the silica xerogels was evaluated by Scanning Electron Microscopy (SEM) and the SEM images are shown in Figure 4.
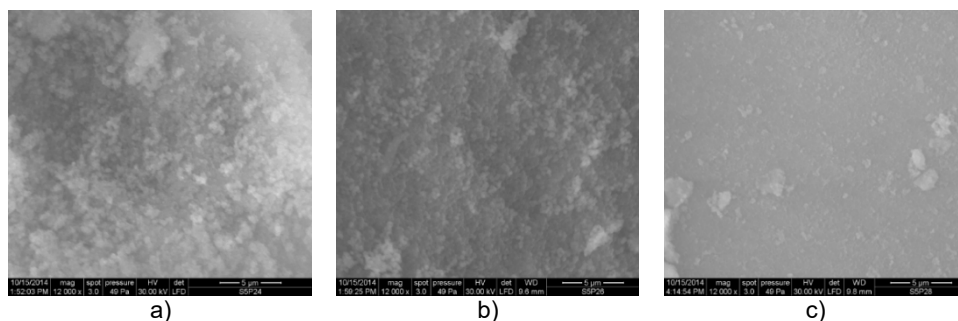


**Figure 4.** SEM image of xerogels: a) S5P24 TEOS 0.098M,
b) S5P26 TEOS 0.179M and c) S5P28 TEOS 0.26M.

From Figure 4 it was observed that the amount of TEOS is very important to control the size of particles and morphology. It can be seen that by varying the TEOS concentration in the range 0.098-0.26M has a major impact on the morphology of silica xerogels. Correlating the data from SEM images with N$_2$ adsorption-desorption isotherms we observed that as the amount of TEOS is increased above 0.098 M TEOS to 0.26M TEOS, the silica nanoparticles decrease in diameter ranging from 91 nm to 24 nm in diameter. The morphology for all samples indicates spherical shape. In case of sample S5P24 more irregular clusters are formed but in case of sample S5P28 the surface is smoother.

### Fluorescence spectra

The Figure 5 a), b) shows the emission spectra in the range of 525-750 nm, at a rate of 100 nm/min, of samples excited at 433 nm and 480 nm with the slit width of 10 nm for excitation and 7.5 nm for emission.
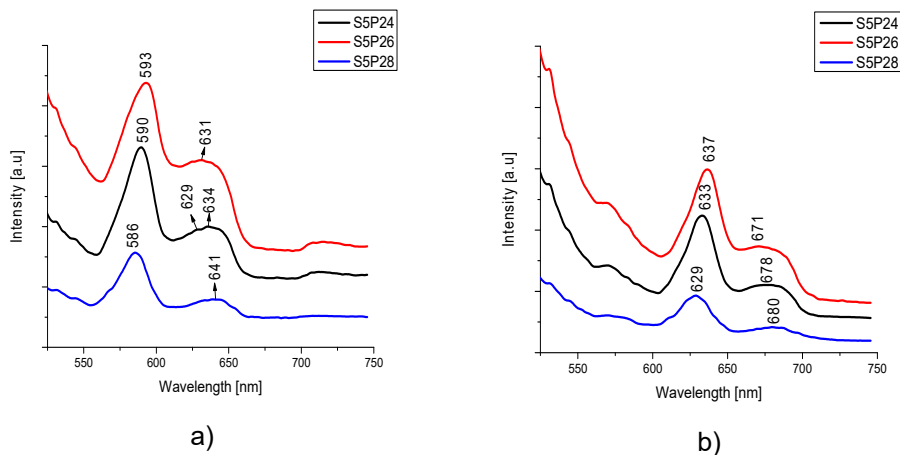
**Figure 5.** Fluorescence image of silica nanoparticles a) excited at 433 nm
b) excited at 480 nm

For sample excited at 433 nm the spectra indicate two main emission peaks at ~590 nm and ~635 nm. For sample excited at 480 nm the spectra present two main peaks at ~630 nm and 680 nm. With the increase of TEOS concentration the spectra reveal a bathochromic effect and by increasing more the quantity of TEOS a hypsochromic effect occurs. The shifts in all samples are almost the same. The sample S5P26 present the best fluorescence properties in both cases. Correlating our results with the literature we observed that all shifts and fluorescence properties of the samples are due to defects in structure formation.

### *Raman spectra*

By using Raman spectroscopy, the three xerogels dried at 60 °C with different TEOS concentration were evaluated and presented in Figure 6.

The results from Raman spectroscopy correlated with FT-IR spectra indicate for all samples a rather weakly developed peak situated at 435 cm^{-1} corresponding to siloxane ring breathing mode (with 3 or 4 SiO[-] units) [17, 18] or to bending vibrations in Si-O-Si bridges [19, 20]. Comparing the data with fluorescence spectra the results showed that the intensity of fluorescence is changing, the most prominent fluorescence is observed in the case of S5P26, followed in decreasing order by S5P28 and S5P24.
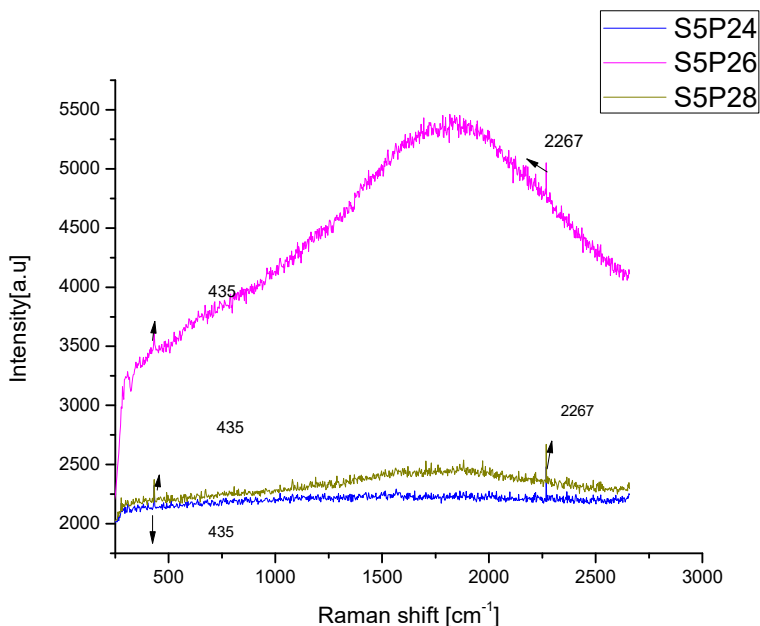
**Figure 6.** Raman spectra of xerogels dried at 60 °C

The material with required properties was further doped with cerium in order to improve the fluorescence. Based on the results, the sample S5P24 was chosen due to small surface area and higher particle size.

**Part II**

In this second part, the selected material, S5P24 was doped with 0.1% $Ce^{3+}$ concentration and thermally threated at 3 different temperatures (300, 600 and 900°C).

***FT-IR Spectroscopy***

The FT-IR spectra of the blank xerogel sample S5P24 with 0.1% Ce concentration dried at 60°C and fired at three different temperatures are shown in Figure 7.
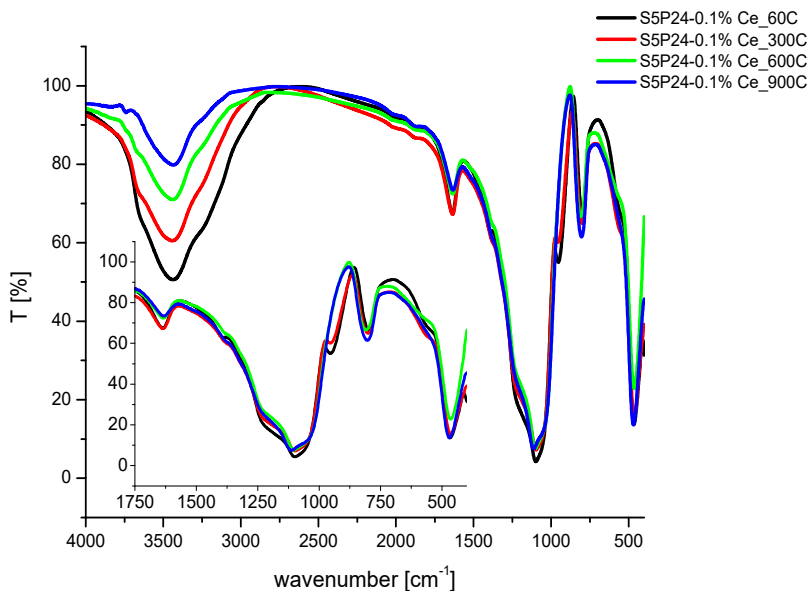
**Figure 7.** FT-IR spectra of xerogel S5P24 with 0.1% $Ce^{3+}$ concentration dried at 60°C and treated at different fired temperature

After the cerium was added, the broad band at ~3440 specific for the –OH symmetric stretching from the surface hydroxyl group was observed [21]. By increasing the temperature, the bands specific to -OH are decreasing in intensity. Similar behavior can be seen for the bands at 1634 $cm^{-1}$, possible due to the existence of residual free water resided in the pores of the xerogel. From Figure 7, the specific bands of silica at ~1100 $cm^{-1}$, ~800 $cm^{-1}$ and ~470 $cm^{-1}$ were observed. With the increase of temperature, the intensity of bands is more increased indicating the formation of $[SiO_4]^{4-}$ tetrahedral units and Si-O-Si bonds [22, 23]. After thermal treatment at 300 °C, the Si-OH bonds observed at ~950 $cm^{-1}$ starts to brake and above 600 °C the bands are disappeared due to decomposition of hydroxyl group. Due to small quantity of cerium introduced in synthesis of 0.1% Ce concentration, the bands specific are overlapped with the silica bands.

### $N_2$ adsorption desorption isotherms

The textural parameters of xerogels with 0.1% Ce concentration dried at 60°C and thermally threated at three temperatures was evaluated by $N_2$ adsorption -desorption isotherms and are presented in Figure 8.
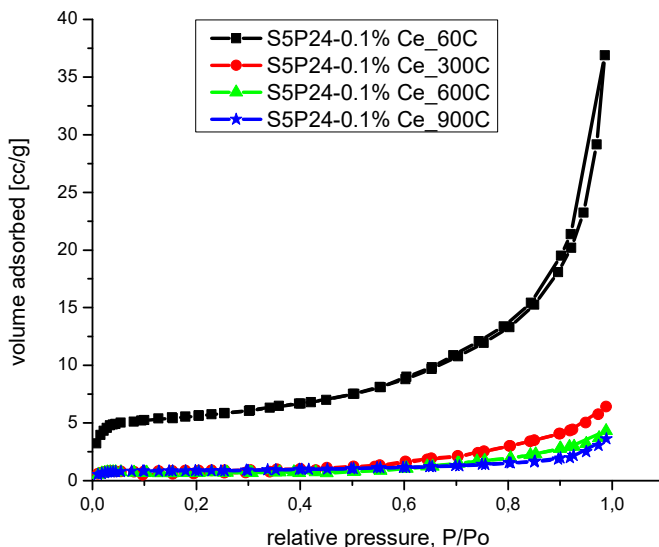
**Figure 8.** N$_2$ adsorption-desorption isotherms of xerogels with 0.1% Ce concentration dried at 60°C and fired at 300, 600 and 900 °C

From Figure 8, according to IUPAC we can assume that sample S5P24-0.1% Ce_60C indicate a type IVa isotherm with a hysteresis of H3 but in case of the fired sample the isotherms are type II isotherms. The textural parameters obtained are presented in Table 2.

**Table 2**. The textural data of sample S5P24 with 0.1% Ce concentration dried at 60 °C and fired at 300, 600, 900 °C

| Xerogels | BJH Adsorption pore diameter [nm] | BJH Desorption pore diameter [nm] | BET surface area [m$^2$/g] | Total pore volume [cm$^3$/g] |
|---|---|---|---|---|
| S5p24-0.1% Ce_60C | 5.670 | 4.965 | 22.6 | 0.057 |
| S5p24-0.1%Ce_ 300C | 4.936 | 4.891 | 4.2 | 0.010 |
| S5p24-0.1%Ce _600C | 4.965 | 4.951 | 4.0 | 0.007 |
| S5P24-0.1%Ce_900C | 3.853 | 3.297 | 3.5 | 0.006 |

In Figure 9 the pore size distribution obtained by BJH method was presented.
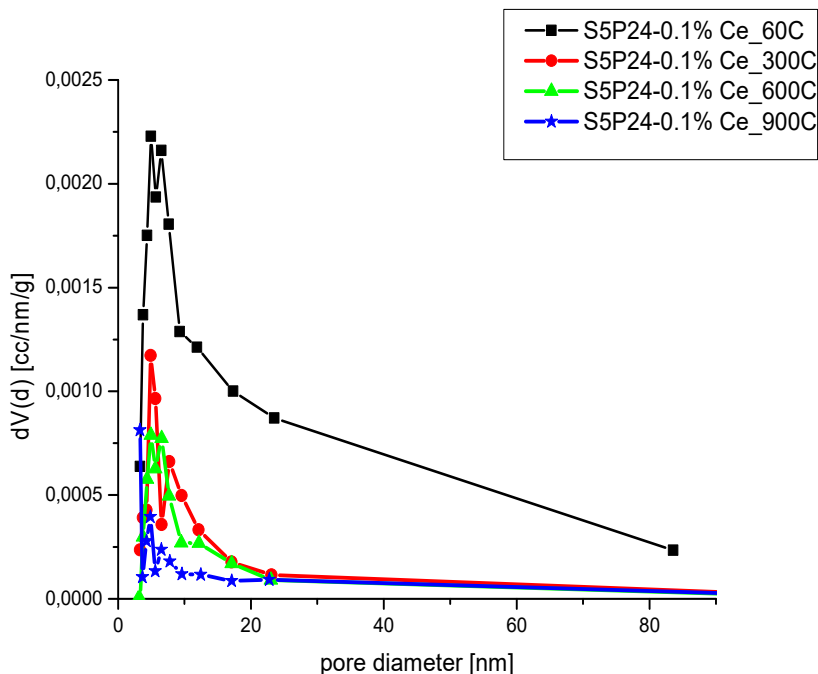


**Figure 9**. Pore size distribution of xerogel sample S5P24 with 0.1% Ce concentration dried at 60°C and fired at 300, 600 and 900 °C

Evaluating the results obtained we can conclude that, with the increase of temperature, the pore size distribution, surface area and total pore volume is decreasing indicating that the skeletal structure of silica shrinks.

### Fluorescence spectra

Figure 10. a), b) shows the emission spectra of nanocomposites with cerium in the range of 525-750 nm, at a rate of 100 nm/min, of samples excited at 433 nm and 480 nm with the slit width of 10 nm for excitation and 7.5 nm for emission.

From Figure 10, by overlapping the emission bands, it has been observed that after fired the sample above 300 °C the intensity decreases because of pore collapsing [24].

a)                                                           b)
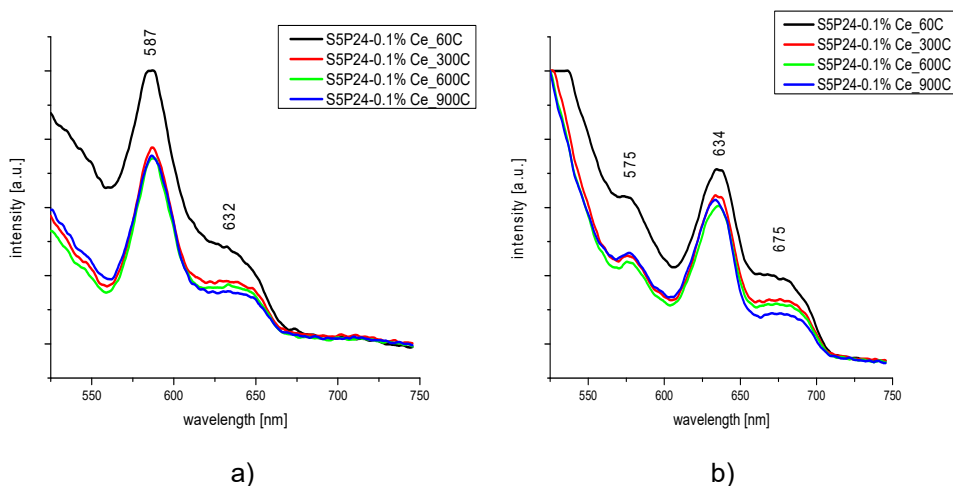
**Figure 10.** The S5P24@0.1%Ce$^{3+}$ dried at 60 °C and S5P24@0.1%Ce$^{3+}$ series of samples fired at 300, 600 and 900 °C, a) Excitation at 433 nm and b) Excitation at 480 nm

For sample excited at 433 nm, the cerium nanocomposites indicate a small hypsochromic effect for the maximum at 593 nm in case of silica doped cerium and dried at 60°C. In case of sample excited at 480 nm, the cerium nanocomposites indicate no shifts in spectra.

## Raman spectra

Figure 11 represent the Raman spectrum of S5P24 sample with 0.1% Ce concentration dried at 60°C and fired at 300, 600 and 900 °C.
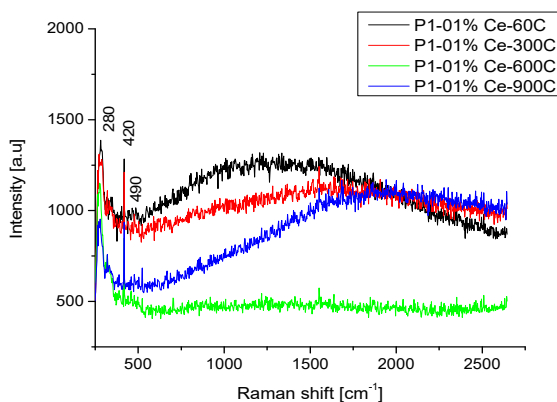


**Figure 11.** RT Raman spectra of S5P24@0.1%Ce$^{3+}$ dried at 60 °C and S5P24@0.1%Ce$^{3+}$ fired at 300, 600 and 900 °C

The $CeO_2$ exhibits a strong band at 462 $cm^{-1}$ due to $F_2g$ Raman active mode. This bands corresponds to the triply degenerate $F_2g$ mode and can be viewed as a symmetric breathing mode of the oxygen atoms around cerium ions [25]. Also, from literature, the Ce-O stretching vibrations at 402 and 490 $cm^{-1}$, were found in cerium (II) oxide-hydroxide [26] In our case, the Raman spectra obtained shown a prominent band at 420 $cm^{-1}$ meaning that cerium is present. Also, the Raman features of $SiO_2$ are observed at 490 $cm^{-1}$ assigned to symmetric stretching modes of four-fold and three-fold rings of $SiO_2$ tetrahedra [27].

Besides, it also exhibits a prominent 280 $cm^{-1}$, which are attributed respectively to the normal Raman inactive (IR active) transverse and longitudinal optical photon modes at the Brillouin zone center (IR active) transverse and longitudinal optical photon modes at the Brillouin zone center [28].


## CONCLUSIONS

Spherical silica particles were synthesized by sol-gel process, Stöber method. In this paper, was investigated how the precursor concentrations (TEOS) from 0.049 to 0.26 M TEOS affected the characteristics of the synthesized silica powders. Also, the fluorescence properties on the sample S5P24, with the lowest degree of fluorescence intensity, doped with 0.1%$Ce^{3+}$ and fired at three different temperatures, were studied. For xerogels samples dried at 60°C, the FT-IR spectra has showed the main specific bands for silica. From morpho-textural properties, for the sample S5P28 (0.26M) the highest pores diameter (9 nm from $N_2$ desorption branch isotherm), and surface area (113 $m^2/g$) were obtained. The spherical shape of the silica particles was due to ammonia, which acts as catalyst in Stöber process. From fluorescence spectra, by exciting the samples at two different wavelengths 433 nm and 480 nm, the best fluorescence properties for sample S5P26 were registered. From Raman spectroscopy, the prominent fluorescence also for sample S5P26, and the lowest intensity of fluorescence for sample S5P24 were showed. To improve the fluorescence, the sample S5P24 was co-doped with 0.1% $Ce^{3+}$ concentration. Sintered at three different temperatures (300, 600, 900°C), the morpho-textural and fluorescence properties were investigated. By increasing the temperature, the surface area, pore size distribution and total pore volume were decreased. From FT-IR spectra, the bands specific for $Ce^{3+}$ are overlapped with the silica bands. The fluorescence spectra exhibited an increase in fluorescence intensity for xerogel sample S5P24 doped with 0.1% $Ce^{3+}$ concentration. The Raman spectra has shown that the band situated at 420 $cm^{-1}$ validated the $Ce^{3+}$ appearance. In

conclusion, the major differences are observed in the obtained intensities of the spectra, in which case the samples doped with cerium have the highest intensity and therefore, superior fluorescence properties.

## EXPERIMENTAL

### Reagents

*Tetra-ethyl-orthosilicate (TEOS, 98% Merck), absolute ethanol (ETOH, 99.8%, Riedel de Haën), ammonia (NH$_3$, 25%, S.C. Silal Trading SRL); Ce$_2$ (CO$_3$)$_2$*xH$_2$O.*

### Synthesis

Three silica xerogels samples were synthesized by sol-gel technique using different molar ratios TEOS as silica precursor and NH$_3$ as alkaline catalyst.

In a 150 mL Berzelius glass, was added 10.5 mL ammonia solution of 12.5% concentration was added in 42 mL ethanol. The solution was mechanically stirred ten minutes at ±50°C and 400 rot/min. After ten minutes, were added different amounts of TEOS (22, 40, 60 mL) and, the solution became opaque and precipitate, being left five hours to be mechanically stirred. The silica particles were centrifuged and washed with water and ethanol four times. The decanted solution was dried at the oven at 60°C for 12 hours. In Table 3 and Table 4 it has presented the mole and amount of each reactants utilized in obtained of spherical silica xerogels.

**Table 3.** Xerogel's synthesis parameters

| Xerogels | TEOS [Mol] | H$_2$O [Mol] | ETOH [Mol] | NH$_3$ [Mol] | NH$_{3solution}$[%] |
|----------|-----------|-------------|------------|-------------|---------------------|
| S5P2-4 | 0.098 | 0.45 | 0.789 | 0.06 | 12.5% |
| S5P2-6 | 0.179 | 0.45 | 0.789 | 0.06 | 12.5% |
| S5P2-8 | 0.260 | 0.45 | 0.789 | 0.06 | 12.5% |

**Table 4**. Amounts of reactants

| | S5P2-4 | S5P2-6 | S5P2-8 |
|-------------------------|--------|--------|--------|
| TEOS [mL] | 22 | 40 | 60 |
| ETOH [mL] | 42 | 42 | 42 |
| NH$_{3solution}$ 12.5%[ml] | 10.5 | 10.5 | 10.5 |

ELENA-MIRELA PICIORUȘ, CĂTĂLIN IANĂȘI, ROXANA NICOLA, PAULA SFÎRLOAGĂ, PAULA SVERA, ANA-MARIA PUTZ

### Synthesis of S5P24@Ce$^{3+}$

Silica doped with Ce$^{3+}$ ions were synthesized by sol-gel technique using TEOS, ETOH, 12.5%NH$_3$ as catalyst, Ce(III) carbonate hydrate 99%, Ce$_2$(CO$_3$)$_{3*}$xH$_2$O as material sources. During the preparation of silica nanocomposite, 42 mL ETOH was mixed in a beaker of 150 mL with 12.5% dilute aqueous NH$_3$ solution (10.5 mL). The solution was mechanically stirred at ±50°C, 400 rpm for 10 min. After that, the 0.009 g of Ce (III) carbonate were added in the solution with 0.1% Ce$^{3+}$ concentration and the solution was stirred 30 minutes. To ensure the hydrolysis and condensation reactions, 22 mL TEOS was added and the mixture was stirred for 5 hours at ±50°C (400 rpm). Then, the gels were washed with distilled H$_2$O and ETOH four times, centrifuged and dried at 60°C (12 hours). Then, the nanocomposite was calcined at 300°C, 600°C and 900°C.

### Characterization

BET (Brunauer-Emmett-Teller) technique was used to determine the surface area; BJH (Barrett-Joyner-Halenda) was used for determining the pore diameter; the both methods were determined from N$_2$ adsorption-desorption isotherm by using a Quantachrome Nova 1200e. Size and morphology of samples were determined by Field Emission Scanning Electron Microscopy, (*SEM*). For SEM an INSPECT S (FEI Company, Holland) instrument has been used. FT-IR spectra were carried out as KBr pellets, in the 4000-400 cm$^{-1}$ range on JASCO 430 apparatus and the fluorescence has been measured with the Perkin Elmer spectrophotometer. Raman spectra was done with Shamrock 500i Spectrograph from Andor United Kingdom.

**ACKNOWLEDGMENTS**

## REFERENCES

1.  O. M. Ntwaeaborwa; P. H. Holloway; *Nanotechnology*, **2005**, *16(6)*, 865–868.
2.  R.S. Ningthoujam; V. Sudarsan; A. Vinu; P. Srinivasu; K. Ariga; S.K. Kulshreshtha; A.K. Tyagi; *J. Nanosci. Nanotechnol.* **2008**, *8(3)*, 1489-1493.
3.  R. Reisfeld; *Opt. Mater.*, **2001**, *16(1-2)*, 1-7.
4.  V. P. Dotsenko; I. V. Berezovskaya; N. P. Efryushina; A.S. Voloshinovskii; P. Dorenbos; C. W. E van Eijk; *J. Lumin.*, **2001**, *93(2)*, 137-145.

5.  A. Vedda; A. Baraldi; C. Canevali; R. Capelletti; N. Chiodini; R. Francini; M. Martini; F. Morazzoni; M. Nikl; R. Scotti; G. Spinolo; *Nucl. Instrum. Methods Phys. Res. A.;* **2002**, *486(1-2)*, 259–263.
6.  W. Stoeber; A. Fink; E. Bohn; *J. Colloid. Interface. Sci.*, **1968**, *26(1)*, 62-69.
7.  A. J. Silversmith; N. T. T. Nguyen; B. W. Sullivan; D. M. Boye; C. Ortiz; K.R. Hoffman; *J. Lumin.*, **2008**, *128*, 931–933.
8.  C. J. Brinker; G. W. Scherer; *Sol-Gel Science, The Physics and Chemistry of Sol-Gel Processing, Academic Press*: New-York, **1990**; pp. 581-585.
9.  A Beganskienė; V. Sirutkaitis; M. Kurtinaitienė; R. Juškėnas; A. Kareiva; *Mater. Sci.*, **2004**, *10(4),* 287-290.
10. C. L. D. Vasconcelos; W. R. Campos; V. Vasconcelos; W. L. Vasconcelos; *Mater. Sci. Eng. A-Struct.*, **2002**, *334(1-2)*, 53-58.
11. A. Bertoluzza; C. Fagnano; M. A. Morelli; V. Gottardi; M. Guglielmi; *J. Non-Cryst. Solids*, **1982**, *48(1)*, 117-128;
12. K. S. W. Sing; D. H. Everett; R. W. Haul; L. Moscou; R. A. Pierotti; J. Rouquerol; T. Siemieniewska; *Pure Appl. Chem., 1984*, *57*, 603–619.
13. M. Thommes; K. Kaneko; A. V. Neimark; J. P. Olivier; F. Rodriguez-Reinoso; J. Rouquerol; K. Sing; *Pure Appl. Chem.*, **2015**, *87(9-10),* 1051-1069.
14. E. P. Barrett; L. G. Joyner; P. P. Halenda; *J. Am. Chem. Soc.*, **1951**, *73(1)*, 373-380.
15. S. Sun; H. Zeng; *J. Am. Chem. Soc.,* **2002**, *124*, 8204–8205.
16. I. A. Rahman; P. Vejayakumaran; C.S. Sipaut; J. Ismail; C.K. Chee; *Mater. Chem. Phys.*, **2009**, *114(1)*, 328–332.
17. H. Zhang; D. R. Dunphy; X. Jiang; H. Meng; B. Sun; D. Tarn; M. Xue; X. Wang; S. Lin; Z. Ji; R. Li; F. L. Garcia; J. Yang; M. L. Kirk; T. Xia; J. I. Zink; A. Nel; C. J. Brinker; *J. Am. Chem. Soc.*, **2012**, *134(38)*, 15790−15804.
18. L. Brentano-Capeletti; J. H. Zimnoch; Fourier Transform Infrared and Raman Characterization of Silica-Based Materials, in *Applications of Molecular Spectroscopy to Current Research in the Chemical and Biological Sciences*, M. Stauffer Eds.; Intech Open, London, UK, **2016**, Chaper 1, pp. 3-21.
19. P. Borowicz; A. Taube; W. Rzodkiewicz; M. Latek; S. Gieraltowska; *Sci. World J.,* **2013**, *2080-2081,* 1-6.
20. K. J. Kingma; R. J. Hemley; *Am. Mineral.* **1994**, *79(3-4),* 269-273.
21. Y. Li; X. Yu; T. Yu; *J. Mater. Chem. C*, **2017**, *5*, 5411-5419.
22. I. Coroiu; E. Culea; A. Darabont; J. *Magn. Magn. Mater.*, **2005**, *290-291*, 997–1000.
23. Y. Yu; D. Chen; Y. Wang; W. Luo; Y. Zheng; Y. Cheng; L. Zhou; **2006**, *Mater. Chem. Phys. 100(2-3),* 241–245.
24. A. Papavasiliou; D. Tsiourvas; E. G. Deze; S. K. Papageorgiou; F. K. Katsaros; E. Poulakis; C. J. Philippopoulos; N. Boukos; Q. Xin; P. Cool; *Chem. Eng. J.* **2016**, *300*, 343–357.
25. X. M. Lin; L. P. Li; G. S. Li; W. H Su; *Mater. Chem. Phys.*, **2001**, *69(1-3)*, 236-240.
26. F. Liu; L. Chen; J. K. Neathery; K. Saito; K. Liu; *Ind. Eng. Chem. Res.* **2014**, *53*,16341-16348.
27. A. Pasquarello; R. Car; *Phys. Rev. Lett.*, **1998**, *80(23)*, 5145-5147.
28. J. Z. Shyu; W. H. Weber; H. S. Gandhi; *J. Phys. Chem.,* **1988**, *92(17)*, 4964-4970.

# PLANTWIDE CONTROL AND DYNAMICS BEHAVIOR OF AN INTEGRATED PLANT COUPLING NITROBENZENE HYDROGENATION AND METHYL-CYCLOHEXANE DEHYDROGENATION

## AHTESHAM JAVAID[a*], COSTIN S. BILDEA[a]

**ABSTRACT.** Coupling of exothermic and endothermic processes is an application of process intensification where two or more processes can be combined in single unit for better utilization of material and energy. Nitrobenzene hydrogenation and dehydrogenation of Methyl cyclohexane in a single adiabatic reactor was investigated and found efficient, stable and economical in the previous study. The scope of this research is to implement plantwide control structure to analyze the dynamics behavior of an integrated system using Aspen Dynamics. Integrated plants where un-reacted reactants are recycled have high sensitivity towards disturbances. The complexity of the plant is reduced by fixing flow rates of reactants at reactor inlet using feedback control strategy. On introduction of individual and combined disturbances in flow rates of reactants ±10%, the system showed robust behavior and achieved stable operation. The system allows production rate changes keeping high purity of products.

*Keywords: Aspen Dynamics; Plantwide Control; Process Intensification; Reaction Coupling.*

## INTRODUCTION

Process integration is a method of combining several processes in one system. This concept of reducing material and energy consumption by intensification started back in 1970's [1, 2]. The possibility of coupling exothermic and endothermic reactions directly in a single unit is studied by several researchers for improved thermal efficiency, which leads to increase equilibrium conversion and reaction rate [3]. Consequently, simpler reduced size reactor and considerable energy savings can be achieved. Practically these energy savings and cheap reactor investment must outweigh the cost of required

---

[a] *University Politehnica of Bucharest, Department of Chemical and Biochemical Engineering, Str. Polizu 1-7, 011061 Bucharest, Romania*

[*] *Corresponding author: ahteshamjavaid@hotmail.com*

additional units for separation [4]. Extensive review of integrating exo-endo reactions system, particularly hydrogenation-dehydrogenation is given elsewhere [5, 6]. Most of the previous work considered stand-alone reactor only, without looking at the economy and controllability of the entire plant. However in some studies coupling behavior of different types of reactions is studied in the entire plant [7-10]. There are number of processes available for coupling but major limitation is the availability of reaction kinetics. This system (methyl-cyclohexane and nitrobenzene) is selected because kinetics parameters are available for both reactions. In our previous study, stand-alone and the integrated processes were compared in a complete plant [11]. Newly proposed coupled process was found economical & stable in steady state. Non-linear analysis of reactor-separation-recycle shows difficulties in controlling integrated plants when un-reacted reactant is recycled. On introduction of process disturbances, the system becomes highly sensitive and non-linear. This non-linearity could lead to phenomena state multiplicity and closed loop instability [12].

The purpose of this research is to select such a plantwide control structure which could handle non-linear phenomena (snowball effect). Feedback control structure is selected for this study in which reactor is decoupled from plant and production rate can be changed indirectly; either by reactor inlet flow or by reactor condition.

## INTEGRATED NITROBENZENE HYDROGENATION - METHYL-CYCLOHEXANE DEHYDROGENATION

On industrial scale, aniline (AN) is produced by hydrogenation of nitrobenzene (NB). The reaction is highly exothermic and requires large excess of hydrogen in addition of using multi-tubular reactor. On the other hand, toluene (TOL) is produced by dehydrogenation of methyl cyclohexane (MCH), an endothermic process which requires large amount of energy. The reactions are given below.

$$C_6H_5 - NO_2 + 3H_2 \rightarrow C_6H_5 - NH_2 + 2H_2O \quad \Delta H = -443.0 \text{ KJ/mole} \quad (1)$$
$$C_6H_{11} - CH_3 \rightarrow C_6H_5 - CH_3 + 3H_2 \qquad\qquad \Delta H = 205.3 \text{ KJ/mole} \quad (2)$$

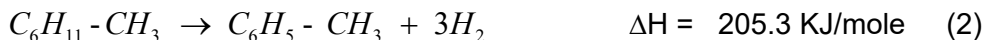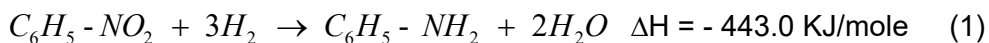Figure 1 presents the schematic diagram for combined hydrogenation-dehydrogenation process. Reactants (MCH, NB and hydrogen) are fed to single tube adiabatic reactor where both reactions take place. Separation is performed; toluene and aniline are taken as products, water as by-product. Hydrogen and un-reacted MCH is recycled to be fed with fresh reactants. Physical properties of chemical species are given in Table 1.
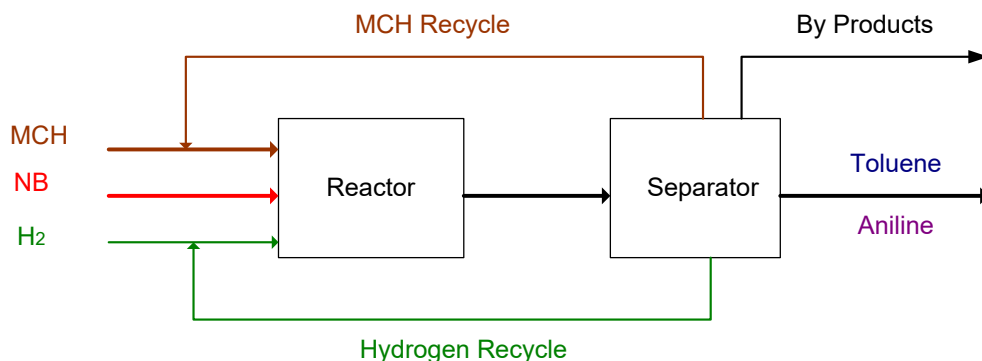
**Figure 1.** Schematic Diagram of MCH Dehydrogenation and NB Hydrogenation

**Table 1**. Physical Properties of Chemicals [11]

| Reactor-outlet species | Boling Point [ºC] | Sol. In Water [g/l] | Destination | Separation |
|---|---|---|---|---|
| Hydrogen, $H_2$ | -253 | - | Recycle | |
| Water, $H_2O$ | 100 | - | By-Product | V-L-L split |
| AN, $C_6H_5NH_2$ | 184 | 36 | Product | Distillation-1 |
| NB, $C_6H_5NO_2$ | 211 | 1.9 | Traces | |
| MCH, $C_7H_{14}$ | 101 | Insoluble | Product/Recycle | Distillation-2 |
| TOL, $C_7H_8$ | 111 | 0.52 | Product | |

### Design Specification

Design of an integrated process was achieved using Aspen Plus [13] and dynamic behavior is studied using Aspen Dynamics [14]. The design starts by specifying the reactor performance as reactant conversion. This allows a preliminary mass balance, which gives the reactor-inlet stream. Then, the reactor diameter can be easily calculated. Finding the reactor length which achieves the specified performance requires knowledge of the reaction kinetics. Distillation columns are designed using DSTWU short-cut model which calculates the minimum number of trays $N_{min}$, and the minimum reflux ratio $R_{min}$ starting from the recovery of light key & heavy key components. The number of trays was set 2 $N_{min}$ and the corresponding reflux ratio (R) was calculated, together with the feed tray and the distillate to feed ratio (D/F). These specifications are then used by rigorous distillation model RADFRAC. By means of the "*Design Specification*" option provided by the simulator, small adjustments of R and D/F are made such that the required distillate and bottoms purities (or recoveries) are achieved. The mixers, vapor-liquid or vapor-liquid-liquid separators

were designed assuming 10 minutes residence time and 2:1 height to diameter ratio. Specified values of the reactor-inlet flow rates are achieved by changing the plant-inlet flows of fresh reactants.

Peng-Robinson EOS is used in this simulation because it provides more accurate value of state variable calculation (P, V, T) for liquid as well as non-polar gases. The following kinetic expressions were used in the simulation:

Nitrobenzene Hydrogenation (Copper-Nickel Catalyst) [15]:

$$r_1 = k.p_{NB}^{0.5}.p_{H_2}^{0.5} \tag{3}$$

$$k = 0.114 \exp\left(-\frac{8323}{T}\right) \qquad \text{kmol} \times \text{m}^{-3} \times \text{s}^{-1} \times \text{Pa}^{-1} \tag{4}$$

MCH dehydrogenation (Platinum on Alumina Catalyst) [16]:

$$r_1 = k_1.p_{MCH} \tag{5}$$

$$k_1 = 3.07 \times 10^{13} \exp\left(\frac{-26539}{T}\right) \qquad \text{kmol} \times \text{m}^{-3} \times \text{s}^{-1} \times \text{Pa}^{-1} \tag{6}$$

To assess the feasibility of performing the MCH dehydrogenation and NB hydrogenation simultaneously, an adiabatic reactor was considered. The reactor is fed with 60 kmol/hr MCH, 20 kmol/hr NB, and 100 kmol/hr H$_2$, at 1.5 bar and 300 °C. The reactants ratio was chosen to approximately match the theoretical value for which the heat of reactions perfectly balances each other. The reacting phase is vapor and all the given values are based on the reactor volume. The length is taken 4 m and the diameter is 0.5 m for proper reaction as it is suitable combination of residence time and conversion of MCH into Toluene. In reactor both catalysts used are mixed in equal proportion. The conversion of nitrobenzene to aniline and MCH to toluene is 97% and 76%, respectively. The reactants & products molar profiles and temperature changes plotted along the reactor length are given in Figure 2. The uniform temperature distribution resists the catalyst deactivation.
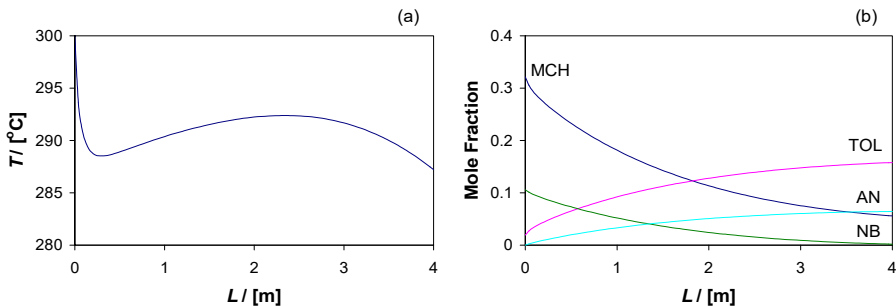


**Figure 2.** Integrated Reactor: Temperature (a) and Mole Fraction (b) Profiles

## PLANT WIDE CONTROL

All control systems must perform three basic operations; measurement, decision and action. On the basis of measurement a decision is made, and on the basis of decision an action is taken. The actions taken must response and effect measurement otherwise it is a key mistake in the design, and control will not be achieved [17]. The coupled system in Aspen plus is exported to Aspen Dynamics as flow driven simulation. The core job of plantwide control system is to regulate or control the inventory of products, reactants and impurities. Inventory of reactants within the plant can be controlled in two ways [18]; i) by estimating, directly or indirectly, the inventory of each reactant and then control it by feedback using the corresponding fresh feed as manipulated variable ii) by fixing the fresh feed rate and using the self-regulation property of the mass balances [19].

We used feedback control inventory strategy because of its important advantage of decoupling reactor from the whole plant. The production rate can be changed indirectly, by changing the reactor-inlet flow. Moreover, it can better handle non-linear phenomena (snowball effect [20] or state multiplicity).

Overview of an integrated plant is shown in Figure 3, where fixing the flow rates of methyl-cyclohexane, hydrogen and nitrobenzene at the reactor inlet by manipulating flow rates of fresh feeds. The amount of reactants in the buffer vessels are used as indirect indication of inventories. Therefore, accumulation or depletion of reactants is avoided by adjusting the fresh reactants feed rate. Control structure and stream table of complete plant is given in Figure 4 and Table 2 respectively**.**
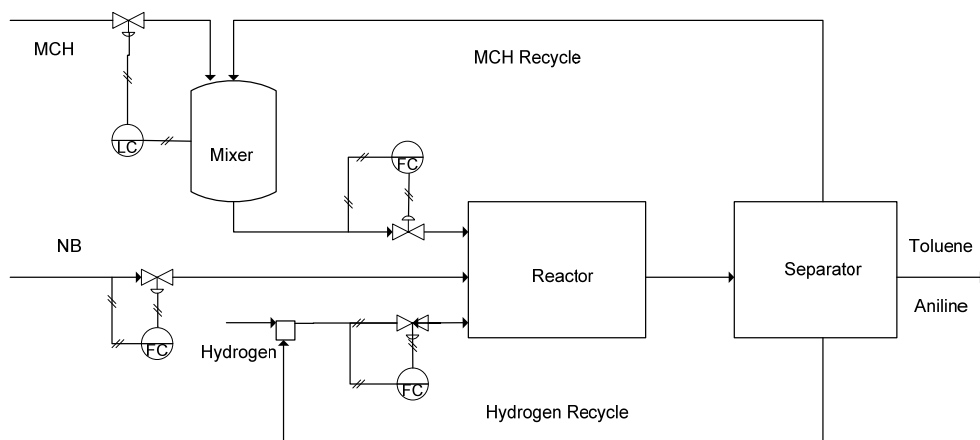


**Figure 3.** Overview of Control Strategy
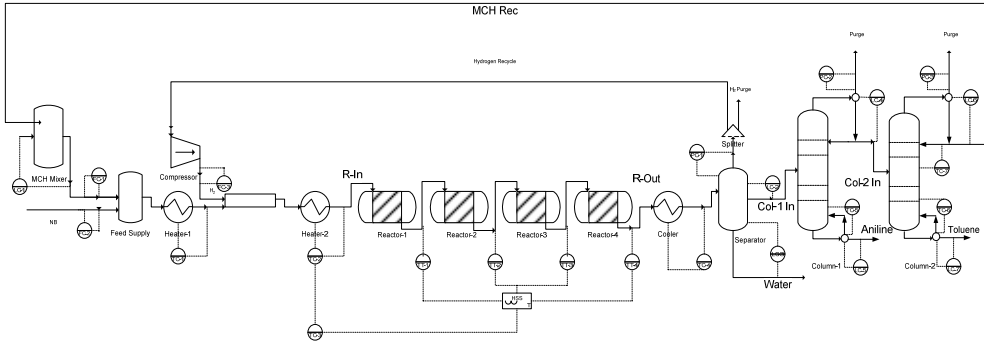
**Figure 4.** Control Structure of an Integrated Plant

**Table 2.** Stream Table

|  | R-In | R-Out | Col-1In | Col-2 In | MCH Rec | Aniline | Toluene | Water |
|---|---|---|---|---|---|---|---|---|
| Temperature / [ºC] | 300 | 287.2 | 20 | 60 | 50.2 | 183.4 | 88.7 | 20 |
| Pressure / [bar] | 1.5 | 1.5 | 1.2 | 1 | 1.5 | 1 | 0.5 | 1.2 |
| Vapor Fraction | 1 | 1 | 0 | 0 | 0 | 0 | 0 | 0 |
| Mole Flow / [kmol/hr] | 189.2 | 301.82 | 83.86 | 63.95 | 20.56 | 19.9 | 43.17 | 37.43 |
| Mole Fraction |  |  |  |  |  |  |  |  |
| Methyl-cyclohexane | 0.321 | 0.056 | 0.183 | 0.24 | 0.733 | 0 | 0.005 | 0 |
| Toluene | 0.019 | 0.158 | 0.538 | 0.706 | 0.109 | 0.001 | 0.993 | 0 |
| Hydrogen | 0.528 | 0.576 | 0 | 0 | 0 | 0 | 0 | 0 |
| Nitrobenzene | 0.106 | 0.002 | 0.007 | 0 | 0 | 0.029 | 0 | 0 |
| Aniline | 0 | 0.064 | 0.231 | 0.002 | 0 | 0.97 | 0.002 | 0 |
| Water | 0.025 | 0.145 | 0.04 | 0.053 | 0.157 | 0 | 0 | 1 |

The control of heater-1, cooler and three phase separator is standard. Heater-1 keeps the temperature of outlet stream at 250 ºC. Temperature controller is added to the heater-2 to keep the temperature of stream entering in to the reactor constant at 300 ºC. Temperature inside the reactor cannot be measured due to limitation of simulation tool, so to monitor temperature after small length; the reactor of 4 meter length is disintegrated into four reactors of 1 meter length each. Temperature from each reactor output stream is transmitted to high selector switch (HSS). This HSS is attached to the temperature controller and this temperature controller is cascaded to the temperature controller responsible for maintaining temperature of reactor inlet feed. The high selector switch takes the highest temperature of reactor output streams as its output process variable. Pressure drop of 0.001 bar is specified in each reactor. The strategy has an advantage that the disturbances

in the inlet feed as well as in the reactor are encountered by the temperature controller, so the system will be less effected by the disturbances and returned to its set point quickly. Temperature control structure for reactor is given in Figure 5, and temperature profiles are shown in Figure 6.
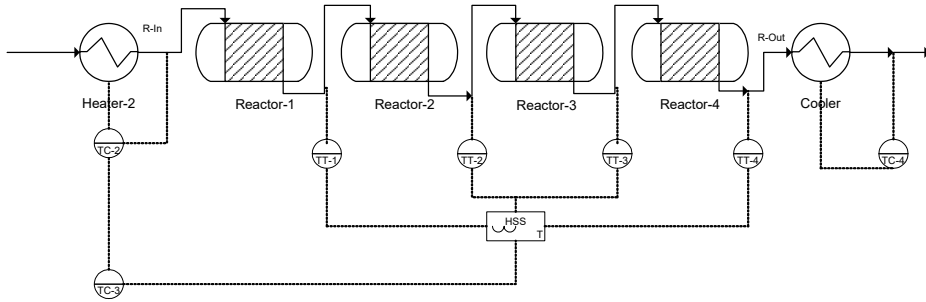


**Figure 5.** Temperature Control Strategy of Reactor
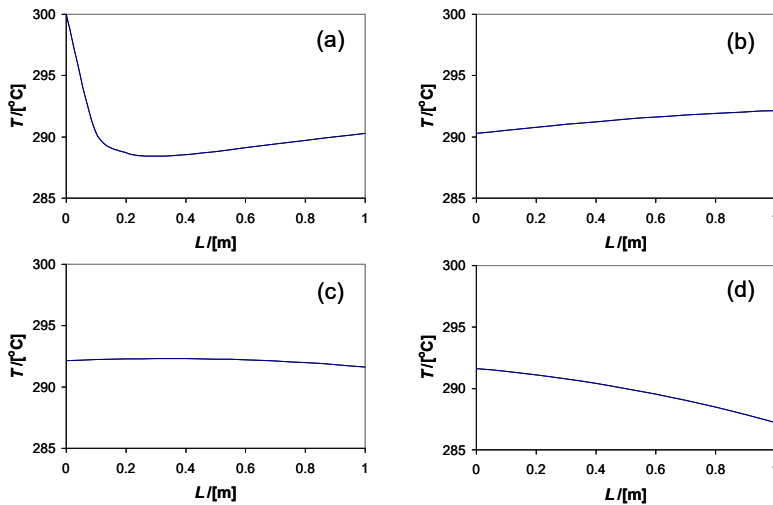


**Figure 6.** Temperature Profiles of Reactors (a-d)

A temperature controller for measuring stream entering in the separator and maintain its temperature at 20 °C by manipulating the duty of the condenser. The level controllers in three phase separator control level for water as well as for the stream entering into the column-1, and pressure controller keeps the pressure stable during operation by manipulating condenser duty. In controlling distillation columns; some additional design information regarding

reflux drum and sump is required by the software. Pressure drop of 0.01 bars is specified along the column and assuming similar geometry of trays throughout the distillation columns. The pressure and condenser drum level are controlled by cooling duty and distillate rate respectively. During dynamic simulation, it is observed that the standard control strategy is not sufficient to control distillation columns. The temperature in the bottom (18th tray) of column-1 is controlled by the reboiler duty. It is observed that single temperature controller in column-2 is not sufficient so we use two temperature controllers in top (2nd tray) and in the bottom (36th tray) and are controlled by reflux and reboiler duty respectively. Control strategy and profiles of distillation columns is shown in Figure 7, 8 and 9 respectively, and their detail data is provided in Table 3.
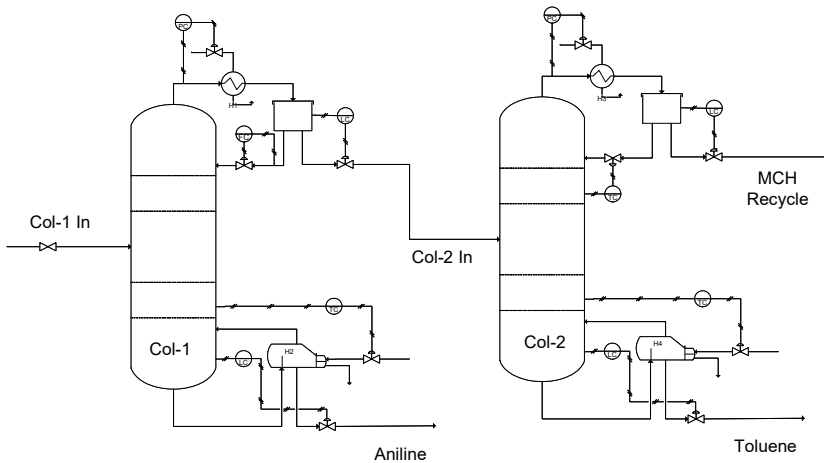


**Figure 7.** Control Strategy of Distillation Columns
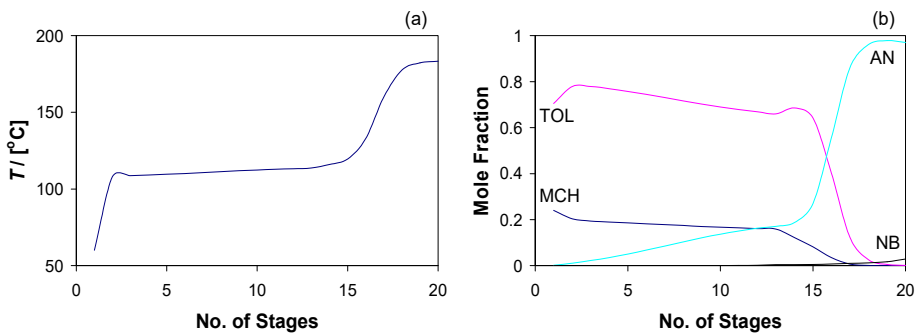


**Figure 8.** Distillation Column-1: Temperature (a), Mole Fractions (b) Profiles
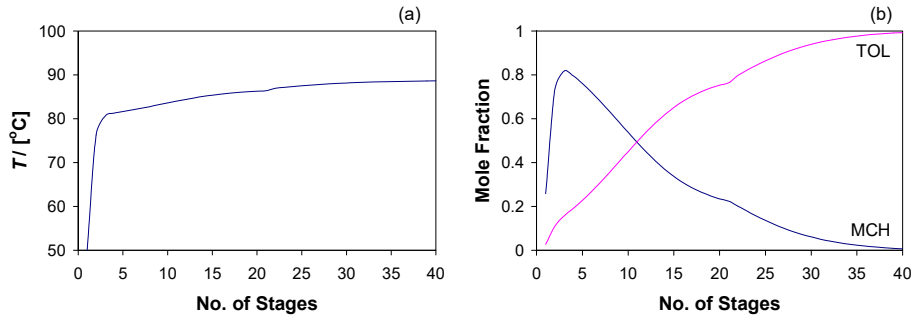
**Figure 9.** Distillation Column-2: Temperature (a), Mole Fractions (b) Profiles

**Table 3.** Data of Distillation Column

|  | Column-1 | Column-2 |
|---|---|---|
| Total Stages | 20 | 40 |
| Feed Stage | 13 | 21 |
| Reflux ratio | 0.204 | 7.178 |
| D/F | 0.7296 | 0.321 |
| Pressure | 1 bar | 0.5 bar |
| Condenser Type | Partial Vapor-liquid | Partial Vapor-liquid |
| Design Specs |  |  |
| Recovery | 99.5 % (AN) | 95 % (TOL) |
| Purity | 97 % (AN) | 99.3 % (TOL) |
| Condenser duty | -0.853 MW | -2.93 MW |
| Reboiler duty | 1.125 MW | 2.98 MW |

The controllers were chosen as PI and were tuned by a simplified version of the direct synthesis method. For each controller, the appropriate range of the controlled and manipulated variables was specified (for example, 30 degrees for temperature measurements, and twice the nominal value for pressure and flow rate manipulations). The controller gain was set to 1%/%. The integral time was set as equal to the time constant of the process, namely 12 min for pressure and 20 min for the temperature control loops. For the level controllers, a large reset time $\tau_i$ = 60 min was chosen as no tight control was required. Table 4 summarize the stream table and controller settings respectively. The advantage of this control structure is to achieve diverse production rates by changing the flow rates and unique steady state exist for different values of inlet flow rates.

**Table 4.** Controller Settings

| Equipment | Controlled Variable, PV | Set Point, PV | Manipulated Variable, OP | OP range | Kc [%/%] | τ [min] |
|---|---|---|---|---|---|---|
| Heater-1 | Tempearture | 250 °C | Heater duty | 220-280 | 1 | 20 |
| Heater-2 | Tempearture | 300 °C | Heater duty | 280-320 | 1 | 20 |
| Reactor | Tempearture | 300 °C | Heater duty | 285-315 | 1 | 20 |
| Separator | Pressure | 1.2 bar | Condenser duty | 0-2.4 | 20 | 12 |
| | Level Liq-1 | 1.25 m | Col-1 in flow | 0-2.5 | 10 | 60 |
| | Level Liq-2 | 0.165 m | Water out flow | 0-0.33 | 10 | 60 |
| Cooler | Tempearture | 20 °C | Condenser duty | 10-30 | 1 | 20 |
| Column-1 | Pressure | 1 bar | Condenser duty | 0-2 | 20 | 12 |
| | Level Reflux Drum | 1.1875 m | Flow top-1 | 0-2.375 | 10 | 60 |
| | Level Sump | 1.375 m | Aniline flow | 0-2.75 | 10 | 60 |
| | Temperature Bottom | 145 °C | Reboiler duty | 120-170 | 1 | 20 |
| Column-2 | Pressure | 0.5 bar | Condenser duty | 0-1 | 20 | 12 |
| | Level Reflux Drum | 1.875 m | MCH recycle flow | 0-3.75 | 10 | 60 |
| | Level Sump | 2 m | Toluene flow | 0-4 | 10 | 60 |
| | Temperature Top | 76 °C | Reflux rate | 50-100 | 1 | 20 |
| | Tempearture Bottom | 105 °C | Reboiler duty | 80-120 | 1 | 20 |

## PLANT DYNAMICS

Performance of process control system can be analyzed conveniently through dynamic simulation. In order to prove the stability of the operating point and the resiliency with respect to disturbances, plant dynamics must be considered. A dynamic model of the plant is built in Aspen Dynamics, and the flexibility in manipulating the inlet flow rates is investigated. Change in flow rates of streams entering into the system is very crucial parameter. As discussed earlier that by changing flow rates, non-linearity occurs in system, so to check the reliability of the integrated system, this variable is chosen. The effect of manipulation in inlet flows are plotted to observe the behavior on product purity, production and recycle rates.

In Figure 10, starting from the steady state, the reactor inlet feed of MCH is increased 10% at $t$ = 1hr and continued simulation for 5 hrs. Similarly in next simulation MCH feed is decreased 10%. The change of the MCH feed
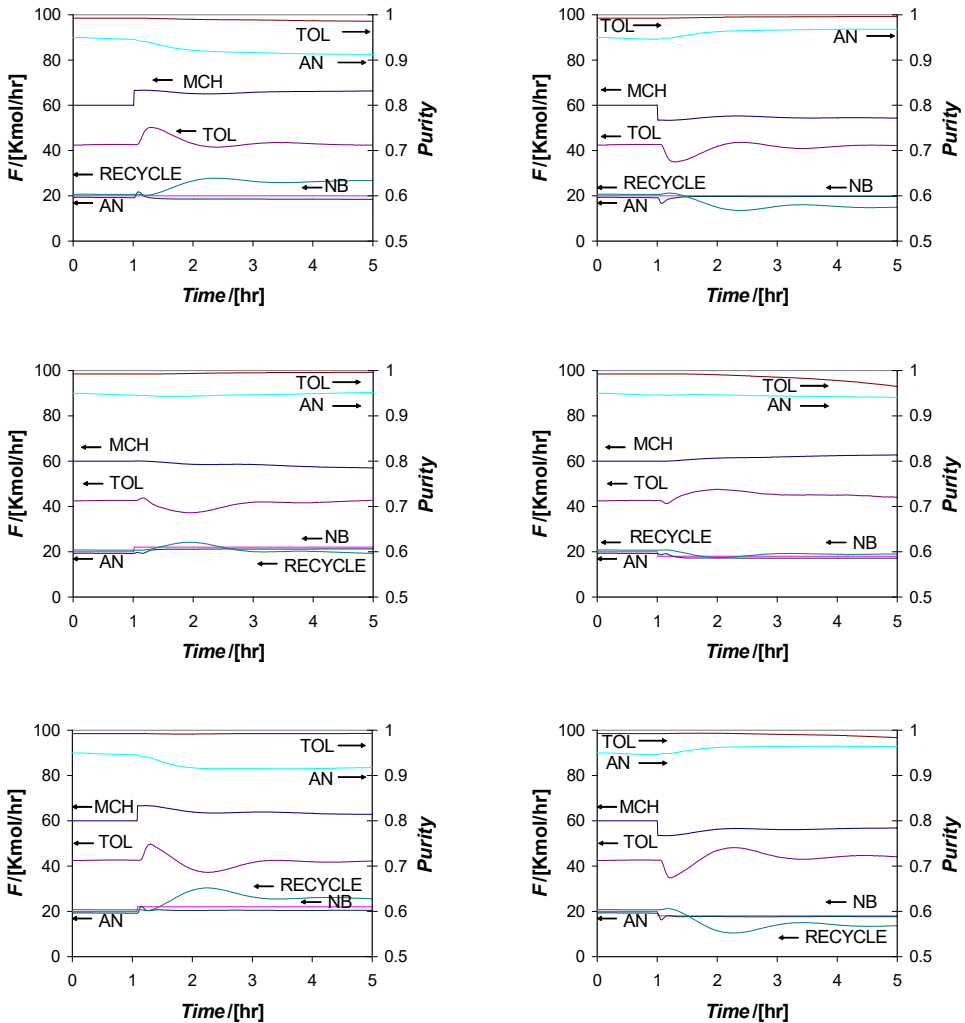
**Figure 10.** Effect of MCH and NB (10% Increase Left, 10% Decrease Right)

rate effect production of toluene, recycle of MCH and purity of aniline but aniline production and toluene purity is less effected. On the same lines, changed the NB feed rate by increasing and decreasing 10%, which effected toluene production rate, MCH recycle and aniline purity. Aniline production and purity of toluene is again less effected by the disturbances. In third simulation, inlet flow rates of both MCH and NB together are changed. This change introduced in the system effect toluene production rate, MCH recycle and aniline purity.

After investigating integrated system with changes (increase and decrease) in inlet flows through separate simulations, the robustness of system is checked by multiple flow disturbances in single simulation. In Fig. 11, the inlet flows of MCH and NB (independently and combined) varied for 10 hr simulation time. They are increased 10% at $t = 1$hr and decreased at $t = 5$ hr. The obtained results are similar and comparable to results achieved in separate simulations. The integrated plant can withstand independent disturbances as well as on combined disturbances. It has been observed that the normal operating point is stable, and if the system is disturbed, it reaches new steady state.
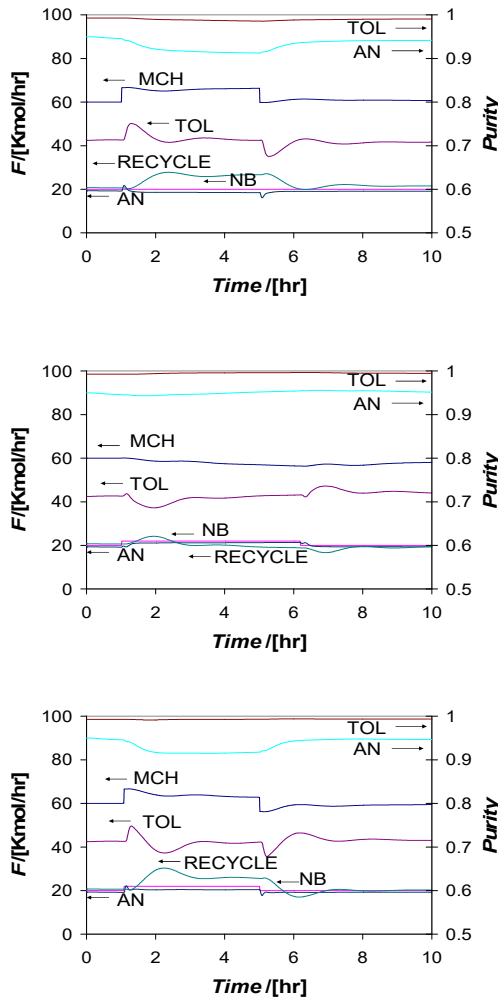


**Figure 11.** Effect of MCH and NB (±10%)

## CONCLUSIONS

On the basis of results achieved in previous study, a plant wide control structure is implemented on the coupled system and stable operation of plant is observed. The complexity of the plant is reduced by fixing the inlet flow of methyl-cyclohexane, nitrobenzene and hydrogen at reactor inlet. The feed rate of NB and MCH is changed (increased and decreased), independently & combined and effect on recycle stream, production rates of products (Toluene and Aniline) and on their purity is observed. The system showed a robust behavior, resiliency with respect to input disturbances (±10%), allowing for production rate changes and maintaining high purity of products. The result achieved in this study is also applicable to processes of practical relevance.

## REFERENCES

1.  F. Friedler, *Appl. Therm. Eng.*, **2010**, *30*, 2270-2280.
2.  R. Smith, *Appl. Therm. Eng.*, **2000**, *20 (15-16)*, 1337-1345.
3.  G. Towler, S. Lynn, *Chem. Eng. Sci.*, **1994**, *49 (16)*, 2585-2591.
4.  P. R. Pujado, M. Moser, Catalytic Reforming, In *Handbook of Petroleum Processing*, D. S. J. S. Jones, P. R. Pujado, Eds., Springer, Dordrecht, **2008**, Chapter 5, pp. 217-237.
5.  M. R Rahimpour, M. R. Dehnavi, F. Allahgholipour, D. Iranshahi, S. M. Jokar, *Appl. Energy*, **2012**, *99*, 496-512.
6.  C. V Pramod, C. Raghavendra, K. Hari Prasad Reddy, G. V Ramesh Babu, K. S. Rama Rao, B. David Raju, *J. Chem. Sci.*, **2014**, *126(2)*, 311-317.
7.  P. Octavian, V. van der Last, C. S. Bildea, P. Altimari, *Chem. Prod. Process Model.*, **2009**, *4 (5)*, Article 19, 1-21.
8.  A. Javaid, C. S. Bildea, *Chem. Eng. Technol.*, **2014**, *37 (9)*, 1515-1524.
9.  A. Javaid, C. S. Bildea, *Period. Polyteh. Chem. Eng.*, **2014**, *58 (2)*, 165-169.
10. A. Javaid, C. S. Bildea, *U.P.B. Sci. Bull.*, Series B, **2014**, *76 (3)*, 33-42.
11. A. Javaid, C. S. Bildea, *Asia-Pac. J. Chem. Eng.*, **2018**, *13 (4)*, 1-12.
12. M. Horvath, A. Szitkai, P. Mizsey, *Period. Polyteh. Chem. Eng.*, **2007**, *51(2)*, 37-44.
13. ASPENTECH, Aspen Plus Getting Started Building and Running a Process Model, ASPEN Technology, Burlington, **2010**.
14. ASPENTECH, Aspen Dynamics User Guide, ASPEN Technology, Burlington, **2009**.
15. D. N. Rihani, T. K. Naraynan, L. K. Doraiswamy, *Ind. Eng. Chem. Process Des. Dev.*, **1965**, *4(4)*, 403-410.
16. G. Maria, A. Marin, C. Wyss, S. Muller, E. Newson, *Chem. Eng. Sci.*, **1996**, *51(11)*, 2891-2896.

17. C. Smith, A. Corripio, Principles and Practice of Automatic Process Control, 3rd ed., John Willey & Sons, USA, **2006**, pp. 415-425.
18. C. S. Bildea, A. C. Dimian, *Ind. Eng. Chem. Res.*, **2003**, *42(20)*, 4578-4585.
19. J. J. Downs, Distillation Control in a Plantwide Control Environment in *Practical Distillation Control*, W. L. Luyben, Eds., Springer, New York, NY, **1992**, Chapter 20, pp. 413-439.
20. W. L. Luyben, *Ind. Eng. Chem. Res.*, **1994**, *33(2)*, 299-305.

# DEMETALLIZATION OF HEAVY VACUUM RESIDUUM BY TITANIUM-VANADIUM ZEOLITE ADSORBENTS

**YERDOS ONGARBAYEV[a,b*], SHYNAR OTEULI[a,b],
YERBOL TILEUBERDI[a,b], GALYMZHAN MALDYBAEV[b],
SAULE NURZHANOVA[b]**

**ABSTRACT.** Demetallization and desulfurization of vacuum residuum from the Pavlodar Petrochemical Plant (Kazakhstan) was carried out by adsorbents based on zeolite modified with titanium compounds and vanadium oxide. The process was carried out at a temperature of 320-360°C for 1 to 3 hours at atmospheric pressure. The results of determining the physico-chemical characteristics of the modified adsorbents showed that, after modification, their specific surface area increases, but the specific pore volume decreases. The maximum degree of demetallization is observed when using an adsorbent based on zeolite modified with titanium oxides and vanadium oxides. The change in the structure of vanadylporphyrins in vacuum residuum composition after the demetallization process is determined. After demetallization etioporphyrins have $C_{27}$-$C_{32}$ with a center of mass at $C_{29}$, phylloporphyrins have $C_{28}$-$C_{34}$, after treatment at 360 °C, the center of mass shifts towards an increase in the number of carbon atoms $C_{31}$.

***Keywords:*** *demetallization, desulfurization, heavy vacuum residuum, adsorbent, zeolite, vanadium oxide, titanium, etioporphyrins, phylloporphyrins.*

## INTRODUCTION

The main difficulty in using heavy oil feedstock in the petrochemical industry is the high content of asphaltenes and metal compounds, leading to accelerated deactivation of catalysts for deep oil refining. Vanadium and other metals, such as nickel and iron, are present in petroleum and its heavy residues in the form of porphyrin and asphaltene complexes. In some oils,

[a] *Al-Farabi Kazakh National University, Faculty of Chemistry and Chemical Technology, Al-Farabi Pr., 71, 050040, Almaty, Kazakhstan*
[b] *Institute of Combustion Problems, Bogenbai batyr Str., 172, Almaty, Kazakhstan*
\* *Corresponding author: Erdos.Ongarbaev@kaznu.kz*

the vanadium content can reach 1200 ppm and the porphyrin vanadium content can vary from 20 to 50% of the total vanadium. Vanadium present in the combustion products of liquid fuels catalyzes the oxidation of sulfur dioxide to sulfur trioxide, leading to corrosion and the formation of acid rain.

For the preparation of heavy oil feedstock for deep processing at refineries, preliminary deasphalting and demetallization processes are used, in which the viscosity, density and coking behavior of oil products decrease, the content of metal compounds in it decreases and clarification occurs. The removal of asphaltenes also results in the removal of complexes of vanadium, nickel and organic compounds with heteroatoms, especially nitrogen and sulfur.

Currently, in the oil industry, the demetallization of heavy oil feedstock is carried out by the processes of solvent extraction, deasphalting, hydrogenation and thermal destruction.

The methods of solvent extraction are quite expensive and complex, require very large quantities of solvent in relation to the feedstock, their efficiency and yield are not completely satisfactory, they give large quantities of asphaltene streams and are not suitable for separating metals, such as porphyrin vanadium and nickel, which are not completely removed with asphaltene fraction. One of the main drawbacks of the process is the high energy consumption for solvent regeneration, associated with the need to evaporate it from the asphalt-free oil solution, as well as condensation and compression after its residues are separated in the stripping columns [1]. It is also worth noting the small outputs of the vacuum residue, while maintaining an acceptable composition and properties, in particular the content of metals, heteroatoms and coke residue.

In recent years, catalytic methods have been considered as effective methods for deasphalting and demetallization.

Solid-acid catalysts for hydrocracking high-boiling mineral oils [2] in the presence of hydrogen using polyvalent metal phosphates - 40-80% $AlPO_4$, 35% $FePO_4$ in the xerogel form with 5-10% sodium fluoride have been proposed. The disadvantage of this method is not only the impossibility of using viscous vacuum residues on stationary catalysts as raw materials, but also deactivation of the catalyst by hetero-organic compounds, and thermal instability of the used catalyst during regeneration after the formation of coke on the surface.

Thermal adsorption (or thermo-contact-adsorption) processing is among the effective processes of deasphalting and demetallization. In the processes of thermo-adsorption refining there is no hardly-utilizable asphaltite formed during solvent deasphalting. In refining, four main processes of thermoadsorption refining of hydrocarbon residues are used: ART (Asphalt Residual Treating) and 3D (discriminatory destructive distillation), developed in the USA, and ACC (adsorption-contact cleaning) and ETCC (express thermal-

contact cracking), created in Russia. The processes of ART and ACO are processes with lift-reactor type adsorbers, and the processes of 3D and ETCC are processes with adsorbing reactors that have an ultrashort contact time of the raw material with the adsorbent.

In the process of thermal contact cracking of heavy oil residues, granular or powdered solid materials are used, the so-called contact adsorbents, on the particles of which physical and chemical processes take place and the transformation of raw materials with the formation of coke and the adsorption of metals from the cracked raw material.

One of the first processes of this variety, mastered in industry, is the ART process, which is a combination of processes of partial evaporation of raw materials and its decarbonization and demetallization in the fluidized bed of the adsorbent. The process pressure is 0.1-0.2 MPa, the temperature is 450-550 °C. As an adsorbent with the trade name Artkat [3], a microspherical inert adsorbent based on kaolin with a low specific surface (about 15 $m^2$/g) is used, which has a good affinity for asphaltenes and metals. However, if oil residues are used in contact cracking processes, it is destroyed due to the deposition of a larger amount of coke and a high burning-out temperature of the latter. In addition, it has a high cost, since it is manufactured in special factories.

The following contact adsorbents for thermal cracking of petroleum residues are known: powdered petroleum coke [4], oxide contact — iron ore pellets [5]. The disadvantages of petroleum coke are low strength and very low porosity, so it quickly collapses and poorly adsorbs metals from raw materials. Pellets of iron ore have a high density and strength, but practically do not possess porosity. When they are used, energy consumption increases for the circulation of the contact adsorbent between the reaction apparatus and for maintaining its fluidized bed. Pellets poorly adsorb metals from raw materials and the resulting coke.

Adsorption-catalytic materials containing rare and rare-earth metals are increasingly used in refining processes. Vanadium-titanium systems are widely used as catalysts for such industrial processes as the partial oxidation of hydrocarbons and the removal of nitrogen oxides from gas mixtures. Therefore, many studies have been devoted to studying the properties of $V_2O_5/TiO_2$ systems using a wide variety of research methods [6].

In recent years, researchers have paid special attention to intercalation compounds based on xerogel vanadium (V) oxide, exhibiting the properties of both the original vanadium-oxygen matrix and the implanted substances. A characteristic feature of such compounds is the quasi-one-dimensional structure of the layers and their turbostratic disordering. Not only cations, but also molecules of organic compounds can be easily incorporated into this structure.

YERDOS ONGARBAYEV, SHYNAR OTEULI, YERBOL TILEUBERDI,
GALYMZHAN MALDYBAEV, SAULE NURZHANOVA

In a previous work [7], we carried out demetallization and desulfurization of vacuum residuum from the Pavlodar petrochemical plant with an adsorbent based on zeolite modified with xerogel vanadium (V) oxide.

In this work, demetallization of vacuum residuum was carried out with a zeolite adsorbent modified with vanadium and titanium oxides at various temperatures and durations of the process.

## RESULTS AND DISCUSSION

To carry out the process of demetallization and desulfurization of vacuum residuum from the Pavlodar Petrochemical Plant, samples of zeolite modified with titanium (IV) compounds and vanadium oxide (V) were prepared as adsorbents.

Table 1 presents the main physico-chemical characteristics of adsorbents based on zeolite modified with titanium compounds and xerogel vanadium (V) oxide obtained by the sol-gel method.

The main carrier of adsorbents is zeolite KN-4 of the Novosibirsk Chemical Concentrates Plant, which has the following characteristics: specific surface area 329 $m^2$/g, mechanical strength 5.9 MPa, granule diameter 3.1-4.0 mm, $Al_2O_3$ mass fraction - 10.13 %. To improve the adsorption characteristics, the zeolite is modified with vanadium oxide (V) and titanium compounds. As can be seen from table 1, when modifying a zeolite with vanadium oxide (V) xerogel, the specific surface area increases from 329 to 376.5 $m^2$/g, but the specific pore volume decreases from 0.173 to 0.161 $cm^3$/g, the average pore size increased slightly. Modifying the zeolite with titanium oxysulfate in an amount of 1% also increases the specific surface of the carrier from 329 to 336.6 $m^2$/g, while the specific pore volume also decreases, the average pore size remains unchanged. Zeolite modified with 1% $TiCl_4$ and 1% $V_2O_5$ showed lower values of specific surface and specific pore volume in comparison with indicators of initial zeolite.

**Table 1.** Physico-chemical characteristics of adsorbents

| Adsorbents | Specific surface, $m^2$/g | Specific pore volume, $cm^3$/g | Average pore size, nm |
|---|---|---|---|
| Zeolite KN-4 | 329,0 | 0,173 | 1,713 |
| Zeolite modified with 1% $V_2O_5$ xerogel | 376,5 | 0,161 | 1,714 |
| Zeolite modified with 1% $TiOSO_4$ and 1% $V_2O_5$ | 336,6 | 0,144 | 1,713 |
| Zeolite modified with 1% $TiCl_4$ and 1% $V_2O_5$ | 312,6 | 0,134 | 1,714 |

The data of Table 2 presents the results of determining the content of sulfur and metals in the vacuum residuum composition after demetallization at temperatures from 320 to 360 °C with an adsorbent - zeolite modified with 1% titanium oxysulfate and 1% vanadium oxide. As can be seen from the tabular data, the sulfur content in the vacuum residuum decreases at 340 °C from 1.72 to 1.28%, which gives a degree of desulfurization of 25.6%. The metal content at all temperatures decreases slightly - vanadium from 0.054 to 0.017%, nickel from 0.0058 to 0.0022%, iron from 0.0033 to 0.0027%.

Table 3 shows the results of determining the elemental composition of vacuum residuum after demetallization with an adsorbent, a zeolite modified with 1% titanium chloride and 1% vanadium oxide at temperatures of 320 and 360 °C. As can be seen from the table, the content of nitrogen, carbon and hydrogen decreases after demetallization. A decrease of the sulfur content is observed at a temperature of 360 °C after demetallization within 2 hours. The content of sulfur is reduced from 1.72 to 0.98%.

**Table 2.** The content of metals and sulfur in the composition of vacuum residuum after demetallization with zeolite modified with 1% $TiOSO_4$ and 1% $V_2O_5$

| Sample | S, % | V, % | Ni, % | Fe, % |
|---|---|---|---|---|
| Vacuum residuum | 1,72 | 0,054 | 0,0058 | 0,0033 |
| Vacuum residuum after demetallization at 320 °C | 1,46 | 0,020 | 0,0023 | 0,0030 |
| Vacuum residuum after demetallization at 340 °C | 1,28 | 0,017 | 0,0022 | 0,0027 |
| Vacuum residuum after demetallization at 360 °C | 1,49 | 0,017 | 0,0023 | 0,0031 |

**Table 3.** Results of the analysis of the elemental composition of the samples

| Sample | N, % | C, % | H, % | S, % |
|---|---|---|---|---|
| Vacuum residuum | 0,51 | 87,04 | 11,512 | 1,720 |
| Vacuum residuum after demetallization at 320 °C | 0,47 | 86,35 | 11,387 | 1,213 |
| Vacuum residuum after demetallization at 360 °C (1 hour) | 0,43 | 86,67 | 11,433 | 1,373 |
| Vacuum residuum after demetallization at 360 °C (2 hour) | 0,48 | 89,96 | 11,113 | 0,987 |
| Zeolite modified with 1% $TiCl_4$ and 1% $V_2O_5$ | - | 0,46 | 0,346 | - |
| Zeolite modified with 1% $TiCl_4$ and 1% $V_2O_5$ after demetallization | 0,06 | 18,95 | 2,555 | 0,008 |

Table 3 also shows the compositions of the adsorbent before and after demetallization. After treatment, the content of the adsorbent increases the carbon content by 18.5%, hydrogen by 2.2% and sulfur by 0.008%, which confirms its desulfurizing adsorption capacity.

Table 4 presents the changes in the content of metals in the composition of vacuum residuum after treatment with zeolite modified with 2% $V_2O_5$ and 10% $TiO_2$ at different temperatures. As can be seen from the tabular data, the maximum decrease in the metal content is observed in the vacuum residuum composition after treatment at 340 °C. The degree of extraction of vanadium was 35.5%, nickel 40.5%, iron 37.3%, copper 56.3%, manganese 46.9%.

The adsorption capacity of the tested adsorbents is due to the fact that the layered structure of the xerogel vanadium (V) oxide is retained when vanadium is replaced by four- and hexavalent ions. It has been established that even small additions of titanium contribute to the polymerization of sols and the production of stable gels. Intercalation compounds based on such complex vanadium and titanium oxides are characterized by high intercalation capacity and thermal stability.

**Table 4.** Metal content in the composition of vacuum residuum before and after demetallization with zeolite modified with 2% $V_2O_5$ and 10% $TiO_2$

| Sample | V,mg/kg | Ni,mg/kg | Fe,mg/kg | Cu,mg/kg | Mn,mg/kg |
|---|---|---|---|---|---|
| Vacuum residuum | 178,7 | 67,00 | 20,63 | 4,856 | 0,2669 |
| Vacuum residuum after treatment at 320 °C | 134,9 | 46,65 | 19,81 | 4,01 | 0,2269 |
| Vacuum residuum after treatment at 340 °C | 115,2 | 39,83 | 12,94 | 2,122 | 0,1416 |
| Vacuum residuum after treatment at 360 °C | 134,4 | 46,94 | 17,15 | 3,49 | 0,2229 |

According to the results of SARA analysis (Table 5), the main components of the original vacuum residuum are aromatic hydrocarbons (45.7%), resins (20.5%) and asphaltenes (27.2%). After demetallization, a decrease in the asphaltene content by 7.5%, a slight change in the vacuum residuum content and an increase in the content of saturated and aromatic hydrocarbons are observed. The resin-asphaltene part of vacuum residuum is adsorbed on the sorbent with partial thermal destruction. The maximum change in the content of components is also observed during demetallization by a sorbent at a temperature of 340 °C.

**Table 5.** Group composition of vacuum residuum before and after demetallization
with zeolite modified with 2% $V_2O_5$ and 10% $TiO_2$

| Sample | Saturated hydrocarbons, % | Aromatic hydrocarbons, % | Resins, % | Asphalte-nes, % |
|---|---|---|---|---|
| Vacuum residuum | 6,6 | 45,7 | 20,5 | 27,2 |
| Vacuum residuum after treatment at 320 °C | 7,2 | 47,4 | 19,9 | 25,5 |
| Vacuum residuum after treatment at 340 °C | 9,1 | 51,7 | 19,5 | 19,7 |
| Vacuum residuum after treatment at 360 °C | 8,8 | 50,4 | 20,4 | 20,4 |

**Table 6**. Elemental composition (%) of adsorbents

| Element | Zeolite | Zeolite with c 1% $V_2O_5$ | Zeolite with 2 % $V_2O_5$ and 10 % $TiO_2$ | Zeolite with 2 % $V_2O_5$ and 10 % $TiO_2$ after process |
|---|---|---|---|---|
| O | 52,289 | 51,983 | 51,314 | 52,375 |
| Si | 40,514 | 39,229 | 37,485 | 39,857 |
| Al | 6,667 | 7,29 | 5,938 | 6,407 |
| Zr | 0,305 | 0,580 | 0,438 | 0,406 |
| Fe | 0,092 | 0,119 | 0,076 | 0,101 |
| Na | 0,032 | 0,034 | 0,437 | 0,048 |
| Nb | 0,025 | 0,081 | 0,035 | 0,034 |
| Mg | 0,020 | 0,028 | - | 0,023 |
| Hf | 0,020 | 0,030 | 0,024 | 0,022 |
| Cl | 0,017 | 0,030 | - | 0,027 |
| S | 0,007 | 0,045 | 0,003 | 0,685 |
| Cr | 0,006 | - | - | - |
| Ni | 0,006 | 0,010 | 0,005 | 0,003 |
| Cu | - | 0,005 | 0,003 | 0,0033 |
| Ir | - | 0,003 | 0,003 | 0,003 |
| Sr | - | 0,003 | 0,002 | - |
| Zn | - | 0,002 | 0,002 | 0,002 |
| Bi | - | 0,001 | - | - |
| As | - | 0,001 | 0,001 | - |
| Pb | - | 0,000 | 0,000 | - |
| V | - | 0,595 | 1,915 | - |
| Ti | - | - | 2,108 | 0,002 |

The elemental composition of the prepared adsorbents before and
after the tests is presented in Table 6. The content of the initial zeolite is
dominated by the content of oxygen, silicon, aluminum. When modifying with

1% vanadium (V) oxide, the content of oxygen and silicon slightly decreases, the content of vanadium is 0.595%. With further modification of 10 % titanium oxide, the content of oxygen, silicon and aluminum also decreases, the content of vanadium is 1.915%, and titanium - 2.108. The elemental composition of the adsorbent after demetallization showed an increase in the iron content by 32.3%, sulfur - from 0.003 to 0.685%. However, there is a decrease in the content of nickel, vanadium and titanium.

Figure 1 shows the positive-ion ESI FT-ICR MS broadband spectra of the initial vacuum residue sample and after demetallization at 320, 340 and 360 °C with zeolite modified with 2% $V_2O_5$ and 10% $TiO_2$. As can be seen from the figure, the spectrum of the vacuum residuum differs from its spectra after demetallization. In the spectra before and after demetallization, peaks with maximum intensity are observed at various values of m/z.



**Figure 1.** ESI FT-ICR MS broadband spectra of initial vacuum residuum (a) and after demetallization at 320 °C (b), 340 °C (c) and 360 °C (d)

Figure 2 shows the iso-abundance plots of DBE as a function of the carbon number for vanadyl porphyrins in the samples, derived from positive-ion ESI FT-ICR mass spectra. The double-bond equivalence (DBE) is defined as the number of double bonds plus rings. The double bond in the vanadyl

group (V=O) is not counted in DBE for which only co-valent double bonds connected with carbon atoms are considered. Only, alkyl porphyrins containing the main structure $N_4VO$ have been discovered. The etio porphyrins (ETIO) ($C_nH_{2n-28}N_4V_1O_1$, corresponding to DBE=17) and deoxophylloerythroetio porphyrins (DPEP) ($C_nH_{2n-30}N_4V_1O_1$, corresponding to DBE=18) were the most abundant vanadium porphyrin detected in these samples. The carbon numbers of ETIO were $C_{27}$-$C_{33}$, with a center of mass at $C_{29}$. The DPEPs had $C_{28}$-$C_{34}$, with a center of mass at $C_{31}$.



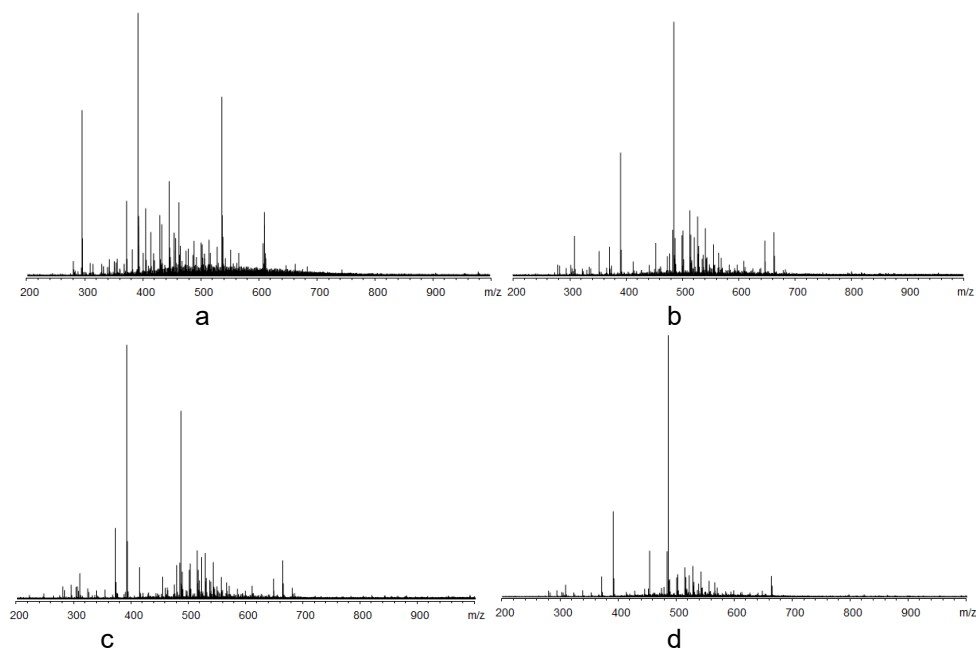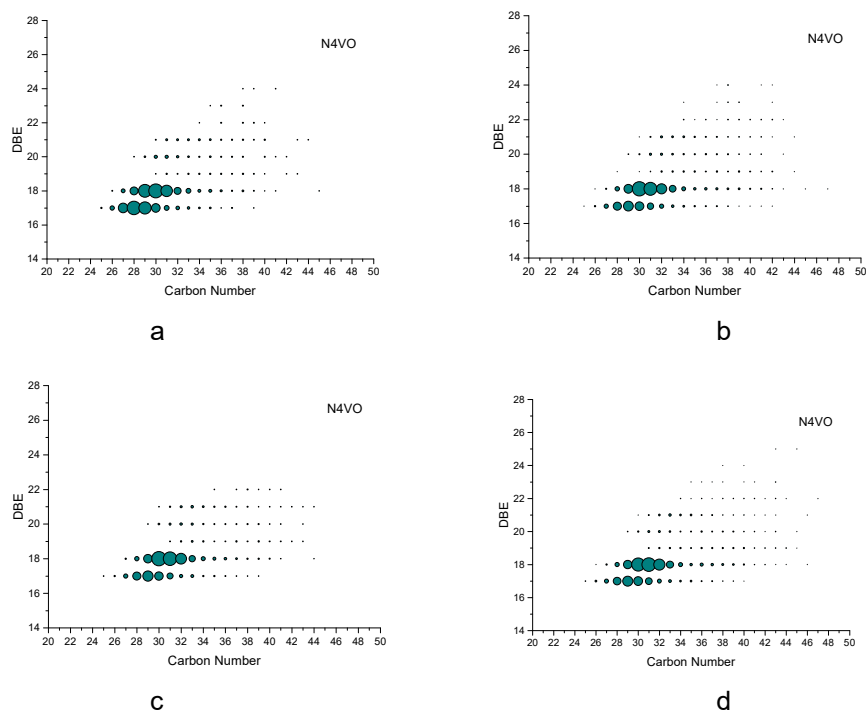**Figure 2.** Iso-abundant plots of DBE as a function of the carbon number for each type of vanadyl porphyrins derived from positive-ion ESI FT-ICR mass spectra of initial vacuum residuum (a) and after demetallization at 320°C (b), 340°C (c) and 360°C (d)

    In the composition of the initial vacuum residuum, etioporphyrins have $C_{26}$-$C_{32}$ with a center of mass at $C_{28}$, which corresponds to the composition of $C_{28}H_{29}N_4VO$. Phylloporphyrins have $C_{27}$-$C_{33}$ with a maximum content at $C_{30}$, this corresponds to the formula $C_{30}H_{31}N_4VO$.

As can be seen from Figure 2, the samples of vacuum residuum after demetallization show the same pattern of petroporphyrins. After processing of vacuum residuum, the content of etioporphyrins decreases and their center of mass shifts. After demetallization at three different temperatures, etioporphyrins have $C_{27}$-$C_{32}$ with a center of mass at $C_{29}$ ($C_{29}H_{31}N_4VO$). The size of the point has decreased compared with the data for the initial vacuum residuum.

In samples of vacuum residuum after demetallization at three temperatures, phylloporphyrins have $C_{28}$-$C_{34}$, however, their maximum content remains unchanged at $C_{30}$ after demetallization of 320 and 340 °C. While after treatment at 360 °C, the center of mass shifts towards an increase in the number of carbon atoms $C_{31}$, which corresponds to the composition of $C_{31}H_{33}N_4VO$.

## EXPERIMENTAL SECTION

As a heavy oil residue used vacuum residuum of the Pavlodar Petrochemical Plant (Kazakhstan). The main carrier of sorbents is the zeolite of the Novosibirsk Chemical Concentrates Plant (Russia), which has the following characteristics: specific surface area 329 $m^2$/g, mechanical strength 5.9 MPa, granule diameter 3.1-4.0 mm, mass fraction of $Al_2O_3$ - 10.13%. For the preparation of the sorbent, the zeolite is modified with vanadium (V) oxide in the amount of 2% and titanium (IV) oxide in the amount of 10%.

The process of demetallization of vacuum residuum was carried out in a steel two-section reactor at temperatures of 320-360 ° C and atmospheric pressure. The duration of the experiment was 3 hours, the consumption of raw materials was 1 l/h.

Metals contents in the samples were detected using an atomic absorption spectrometer.

For SARA analysis the asphaltenes were collected from the samples of vacuum residuum by precipitation in petroleum ether (a boiling range of 30-60 °C), followed by titration. The extracted-asphaltenes fractions were then separated into saturates, aromatics and resins by column chromatography (silica gel:alumina = 4:1), using hexane, benzene and methanol as eluents, respectively.

Fouier transform ion cyclotron resonance mass spectrometry (FT-ICR MS) has been used to quantify the composition of highly complex hydrocarbon mixtures. FT-ICR resolving power has the highest available broadband mass resolution, mass resolving power, and mass accuracy, which enables the assignment of a unique elemental composition to each peak in the mass spectrum [8-10].

For FT-ICR MS analysis 10 mg of asphaltenes was mixed with 1 ml of toluene. A 20 $\mu$l of the toluene solution was diluted with 1 ml of 1:3 toluene:methanol. The toluene and methanol used were analytical reagent grade that were distilled twice and kept in glass bottles with ground glass stoppers. Glassware was used for solvent handling and transfer, except the stell pistons for 10 $\mu$l Hamilton syringes.

The asphaltene sample was analyzed using a Bruker Apex-Ultra FT-ICR MS equipped with a 9.4 T superconducting magnet. The sample solution was infused into an Apollo II electrospray ionization source at 180 $\mu$l/h using a syringe pump. HCOONH$_4$ was added into the solution as ionization promoter to enhance the response of low-polar compounds in positive-ion ESI.

The conditions for positive ion operation were -4.5 kV spray shield voltage, -5.0 kV capillary column front and voltage, and 310 V capillary column end voltage. Ions accumulated for 0.001 s in a hexapole with 2.0 V DC voltage and 500 Vpp RF amplitude. Optimized mass for Q1 was 300 Da. Hexapoles of the Qh-Interface were operated at 5 MHz and 800 Vp-p RF amplitude, in which ions accumulated for 1.2 s. The delay was set to 1.3 ms to transfer the ions to an ICR cell by electrostatic focusing of transfer optics. ICR was operated at 13.84 dB attenuation, 193-1000 Da mass range. The FT-ICR data were acquired in 4M with a transient time about 2.936 s, resulting in a resolving power of roughly 450,000 at m/z 500. Time domain data sets were coadded from 128 acquisitions.

The mass spectral peaks were mass calibrated using a Agilent "Tuning Mix" standard acetonitrile solution with 7 peaks covering a mass range from 118 to 1500 Da. In general, 1 ppm mass accuracy can be achieved with external calibration. Bruker DA molecular formula tool assisted in identifying a major homologous series. Internal calibration was then performed using the identified vanadyl porphyrins series. On average, ~0.4 ppm mass accuracy can be achieved with internal mass calibration. Peaks with relative abundance greater than 5 times the standard deviation of the baseline noise were collected and analyzed using the in-house software. Species with different values of DBE and carbon number along with their isotopes were searched within a tolerance of ±0.001 Kendrick mass defect (KMD) to group into different heteroatom classes.

## CONCLUSION

Thus, the results of studies and analyzes have shown the possibility of extracting metals from heavy petroleum residues by thermo-adsorption treatment with adsorbents based on zeolite modified with vanadium oxide and titanium compounds.

YERDOS ONGARBAYEV, SHYNAR OTEULI, YERBOL TILEUBERDI,
GALYMZHAN MALDYBAEV, SAULE NURZHANOVA

The physico-chemical characteristics of the modified adsorbents based on zeolite were determined. Modifying the zeolite with vanadium oxide (V) xerogel increases the specific surface from 329 to 376.5 $m^2$/g, while the specific pore volume decreases from 0.173 to 0.161 $cm^3$/g. Modifying the zeolite with titanium oxysulfate in an amount of 1% increases the specific surface of the carrier from 329 to 336.6 $m^2$/g, the average pore size remains unchanged. Zeolite modified with 1% $TiCl_4$ and 1% $V_2O_5$ showed lower values of specific surface, specific pore volume in comparison with indicators of initial zeolite.

The content of elements in the composition of adsorbents before and after demetallization and desulfurization was determined. Vanadium-containing compounds have been identified before and after vacuum residuum demetallization. A change in the amount of vanadylporphyrins after the demetallization process has been detected.

The results of the process of demetallization of vacuum residuum on modified adsorbents showed the possibility of extraction of metals and sulfur and the correlation of the values of the specific surface of the adsorbents and the degree of extraction of metals. The maximum degree of iron extraction is provided by the zeolite modified with 1% titanium oxysulfate and 1% vanadium oxide, which has a high specific surface compared with other adsorbents, modified with titanium compounds. The adsorption capacity of the tested adsorbents is due to the fact that the layered structure of the xerogel vanadium oxide (V) is retained when vanadium is replaced by four- and hexavalent ions. It has been established that even small additions of titanium contribute to the polymerization of sols and the production of stable gels. Intercalation compounds based on such complex vanadium and titanium oxides are characterized by high intercalation capacity and thermal stability.

## ACKNOWLEDGMENTS

## REFERENCES

1. J.M. Lee; S. Shin; S. Ahn; J.H. Chun; K.B. Lee; S. Mun; S.G. Jeon; J.G. Na; N.S. Nho; *Fuel Process. Tech.*, **2014**, *119*, 204-210.
2. R.C. Hansford; *Patent of US 3088908*, **1963**.
3. *Patent of US 4435272*, 1984.
4. R. Pfeiffer; D. Borey; C. Jahnig; *Patent of US 2881130,* **1953**.

5.  *Chem. Eng. News*, **1968**, *3*, 46.
6.  L. Bandura; A. Woszuk; D. Kolodynska; W. Franus; *Minerals*, **2017**, *7*, 37-52.
7.  Y. Ongarbayev; Sh. Oteuli; Y. Tileuberdi; G. Maldybaev; S. Nurzhanova; *Petrol. Sci. & Tech.*, **2019**, *37*, 1045-1052.
8.  X. Zhao; Y. Liu; C. Xu; Y. Yan; Y. Zhang; Q. Zhang; S. Zhao; K. Chung; M.R. Gray; Q. Shi; *Energy & Fuels*, **2013**, *27*, 2874-2882.
9.  T. Liu; J. Lu; Y. Zhou; Q. Wei; C. Xu; Y. Zhang; S. Ding; T. Zhang; X. Tao; L. Ju; Q. Shi; *Energy & Fuels*, **2015**, *29*, 2089-2096.
10. F. Zheng; C.S. Hsu; Y. Zhang; Y. Sun; Y. Wu; H. Lu; X. Sun; Q. Shi; *Energy & Fuels*, **2018**, *32*, 10382-10390.

# EXPERIMENTAL STUDY OF STRUCTURAL-MECHANICAL PROPERTIES OF HEAVY OIL

**RYSKOL BAYAMIROVA[a,\*], ALIYA TOGASHEVA[a],
AKSHYRYN ZHOLBASSAROVA[a], ZHARAS ISLAMBERDIYEV[a],
MAX BISSENGALIEV[b], DADEN SUIEROV[b]**

**ABSTRACT.** Structural-mechanical properties of heavy oil from Kazakhstan deposits under the heat treatment were studied in this work. The most important and the least studied issues in the technology for the preparation and collection of oil products is the evaluation of the structural and mechanical properties of heavy oils and emulsions and ways to regulate formation them. A feature of the wells operation of fields with high viscosity oils is a sharp increase in water cut at the initial stage of development, which is associated with an excessively large difference in the rheological characteristics of reservoir oil and water. The formation of stable emulsions does not allow for the effective separation of oil from water and leads to a deterioration in product quality. In this regard, in modern conditions of intensification of hydrocarbon production, consideration of the options for the formation and destruction of complex emulsions is a prerequisite for the effective operation of oilfield treatment facilities. Therefore, the research relevance is of reducing the irretrievable losses of hydrocarbons in production systems and study the physical-chemical, structural-mechanical properties of heavy oils emulsions and to develop methods for their regulation, as well as improving oil treatment devices.

*Keywords: heavy oil, asphaltene, tar, water-oil emulsions, structural-mechanical properties*

## INTRODUCTION

Increasing of viscosity and yield strength of heavy crude oil makes the preparation process for transporting much more complicated, starting pressure of pumps gets higher [1-4].

[a] *Yessenov University, Faculty of Engineering, 32 microdistrict, 130003, Aktau, Kazakhstan*
[b] *Atyrau University of Oil and Gas, Faculty of Oil and Gas, md. Railway station, st. Baimukhanova, 45A, Atyrau, Kazakhstan*
\* *Corresponding author: erzhan-90vko@mail.ru, ryskol.bayamirova@yu.edu.kz*

RYSKOL BAYAMIROVA, ALIYA TOGASHEVA, AKSHYRYN ZHOLBASSAROVA,
ZHARAS ISLAMBERDIYEV, MAX BISSENGALIEV, DADEN SUIEROV

Thermal treatment is the most commonly used way of preparing high-viscous oils for transportation by pipelines [5-8]. Thermal treatment of oils improves rheological properties of oils. Heating the oil to the certain temperature, and then cooling it with constant speed till the temperature of pumping it carried out in static conditions.

Structural-mechanical properties of the paraffin base oil and emulsions thermal treatment study conducted in the laboratory of "Giprovostokneft" [6]. It has been shown that the thermal treatment (50 ºC) strongly improves rheological properties of oil in some deposits in Perm Region. For example, Kozubaev's oils viscosity declined from 122.2 cSt to 16.6 cSt before and after thermal treatment.

Authors of work [8, 9] shows only the oils with abnormal viscosity and plastic properties can be thermally treated. Thermal treatment of Newton oils doesn't give such an effect. Fast cooling paraffin petroleum oils leads to forming of numerous centers of paraffin crystallization, fine-crystalline system, which increases viscosity and yield point.

Experiments of determining dependence of yield point from thermal treated oil of Mangyshlak deposits with the temperature of 50 ºC, 70 ºC and 90 ºC have shown that Mangyshlak's oil, treated with 90 ºC has the least yield point than the untreated one. Moreover, the higher the yield point, the higher the effect of thermal treatment on the oil [25]. With the speed of cooling 10 ºC per 1 hour (after thermal treatment 90 ºC) non-Newton properties of Mangyshlak oil begin to show up while being at lower temperatures (lower than 20-15 ºC). Changing of viscosity with all temperatures of thermal treatment shows that the oil heated up to 50, 80 and 110 ºC cooled down afterwards, has a higher viscosity, than the one that was treated with 90 ºC. The lowest viscosity is seen at the cooling speed of 10 ºC per hour [10]. Thermal treatment till 150 ºC leads decreasing of effective viscosity in all the interval of temperatures for almost 3 times, and absence of yield point at a temperature higher than 65 ºC.

Thermal treatment of Ozen's oil showed, that thermal treated petroleum, cooled down after thermal treatment till 30 ºC with the speed of cooling 20 ºC per hour, with all temperatures of treatment (50 ºC, 80 ºC, 90 ºC, 100 ºC) are Newton liquids. With all other temperatures (lower than 30 ºC) thermal treated Mangyshlak's oil is viscous-plastic liquid, according to the law of Shvedov-Bingham.

Mechanism of decreasing of viscosity during the thermal treatment of paraffin base oils is demonstrated in the following ways: During the heating of oil higher than the temperature of melting point of paraffin, oil becomes a homogenous Newton liquid. Cooling process of oil in static condition crystals of paraffin covered with asphaltene-resin substances. The protective layer of asphaltene-tar substances that forms on the crystals during this process, hinder the forming of other layers of paraffin on the surface of crystals.

It should be mentioned, that current works on thermal treatment of the oil are related to the paraffin based oils. Thermal treatment researches of highly resinous oils are almost absent.

In modern conditions of intensification of the production of hydrocarbon, considering the options for developing the structural-mechanical properties of heavy oils are an essential condition for an effective exploitation of the oil preparing structures. Therefore, the experiments regarding the impact of thermal treatment on the structural-mechanical properties of the highly resinous oils from the West Kazakhstan are interesting not only because of an understanding of their behavior, but also for comparative analysis with the thermal treatment of the paraffin oils.

## RESULTS AND DISCUSSION

It is known that the changing of viscosity of the paraffin based oils after thermal treatment is explained by the ability of paraffin to crystallize in different forms after the heating. During the thermal treatment of highly resinous oils, irreversible processes leading to decreasing of the yield point and partly the structural viscosity take place.

**Table 1.** Rheological parameters of the oil of the North Buzachi before and after the thermal treatment.

| Without thermal treatment at 30 ºC | | Heating temperature at 70 ºC, final cooling temperature is 60 ºC, cooling speed – 12 ºC/hour | | Heating temperature at 85 ºC, final cooling temperature is 70 ºC, cooling temperature until 60 ºC is 50 ºC/hour, until 22 ºC is 10 ºC/hour | |
|---|---|---|---|---|---|
| P, Pa | V, s⁻¹ | P, Pa | V, s⁻¹ | P, Pa | V, s⁻¹ |
| 79.7 | 3.4 | 80.0 | 4.4 | 78.9 | 4.8 |
| 147.9 | 6.9 | 150.3 | 7.6 | 148.8 | 9.2 |
| 219.3 | 11.0 | 233.3 | 13.2 | 218.6 | 13.8 |
| 248.9 | 13.1 | 288.7 | 18.2 | 288.4 | 18.8 |
| 292.2 | 16.3 | 323.6 | 20.6 | 323.3 | 21.3 |
| 355.2 | 21.1 | 358.5 | 23.5 | 358.2 | 24.9 |
| 389.7 | 23.9 | 393.4 | 26.0 | 393.2 | 26.9 |
| 435.4 | 27.4 | 432.8 | 28.7 | 428.1 | 29.4 |
| 463.7 | 30.1 | 468.1 | 31.5 | 463.0 | 32.2 |
| 502.1 | 32.2 | 504.8 | 34.7 | 500.4 | 35.2 |
| 532.8 | 35.7 | 527.4 | 37.7 | 532.8 | 38.2 |

RYSKOL BAYAMIROVA, ALIYA TOGASHEVA, AKSHYRYN ZHOLBASSAROVA,
ZHARAS ISLAMBERDIYEV, MAX BISSENGALIEV, DADEN SUIEROV

In table 2 the results of the experiments on the thermal treatment of some heavy oils from the West Kazakhstan are demonstrated. The thermal treatment of the highly resinous oils does not effect on viscosity so much, but it does strongly effect on the yield point.

**Table 2.** Results of the experimental data of the thermal treatment of the heavy oils of some deposits of the West Kazakhstan.

| Deposit | Condition | Thermal treatment temperature, [ºC] | Cooling speed, [ºC/h] | Yield point at 30 ºC, [Pa] |
|---|---|---|---|---|
| North Buzachi | Before thermal treatment | – | – | 72.5 |
| | After thermal treatment | 70 | 12 | 6.3 |
| | | 85 | 12 | 3.9 |
| Karazhanbas | Before thermal treatment | – | – | 66.8 |
| | After thermal treatment | 70 | 12 | 4.9 |
| | | 85 | 12 | 2.8 |
| Karaturisk | Before thermal treatment | – | – | 69.8 |
| | After thermal treatment | 70 | 12 | 4.9 |
| | | 85 | 12 | 2.8 |
| Kalamkas | Before thermal treatment | – | – | 69.7 |
| | After thermal treatment | 70 | 12 | 6.9 |
| | | 85 | 12 | 5.5 |

In the oil industry the traditional method is deconstruction of emulsions by thermochemical way, which is continuously developing and is used together electrical fields and hydrodynamic characteristics of the flow [11-23, 33]. Heavy hydro-petroleum emulsions water drops of which are surrounded by strong protective shells, consisting of asphaltene-resin substances and mechanical admixtures are stable emulsions. Destruction of these emulsions by simple ways is way more complicated.

An important factor in the process of destruction of the emulsion is a hydrodynamic impact. Intensity of the destruction of emulsions is not affected much by the settling time as a factor of unmixable substances always taken into consideration during an elaboration of the projects of oil treatment plants, but manifesting hydrodynamic demolishing of the water globules at an intensive flow turbulence. Some experimental results showed hydrodynamic demolishing is a more effective way of destruction of the emulsions. Thus hydrodynamic method of destruction of the emulsion can be used as the most effective in the technology of oil treatment and in construction of a heavy-duty continuous emulsion breakers.

The movement of the gases, going into the receptacle with the oil product is usually followed by a formation of bubbles and it pushes the liquid. The layers of the liquid surrounding the stream are moved according to the movement of the stream. Therefore, part of the movement of the liquid is transferred to the surrounding liquid. At the same moment the speed of the liquid captured by the moving stream is less than the speed of the stream which was captured by the liquid.

Each of the layers of the liquid come into motion makes other calm layers in its vicinity which did not before to the movement. The stream has a bigger cut the further it is from the beginning and the less its speed is. When the surrounding liquid is captured by the stream and come to the motion, it creates a rarefaction for some time in the space it covered before. Lowering of the pressure makes surrounding and calm liquids get sucked into that part of the space. Kinetic energy of the stream, which appears in the process of liquid suction from the external environment is dependent to the starting speed of the leaking from nozzle.

The liquids located very close to the surface comes to motion and proceeds towards the surface by the impact of a tangential stress during the rising of bubbles. The rarefaction appears after the rising bubbles which can explain the suction of the liquid from the surrounding volume. The size of the bubbles is defined by the pressure of the gas inside of the bubble and by the outer hydrostatic pressure, which responds to the height of the pillar of the liquid above the bubble. Hydrostatic pressure inside of the liquid is continuously changing towards the surface, so, the size of the bubbles increases. The shape of bubbles is deviated from being a ball, and the way of movement by vertical line, collisions between the bubbles will take place, simultaneously with the bubbles growing of the volume of the them. An increasing of size of the bubble creates an enormous interfacial area between the bubble and the surface, in other words, a free bubbling takes place. The liquid pushed out by the gas leaks towards the periphery of reservoir and goes down to the trough after the gas went to the surface.

If we consider a condition in which the bubble appears inside of the liquid. The pressure of the liquid hampers the creation of the bubble when the gas under pressure goes to the liquid. The pressure of the liquid can be overcome by the pressure of the gas, and also by the surface stress. As soon as the bubble appears. It gets affected by the buoyancy power. The bubble gets of the estuary and rises up at the moment when the buoyancy power overcomes the surface tension.

For the ball shaped bubble with the diameter of d the buoyancy power can be defined by the following formula:

RYSKOL BAYAMIROVA, ALIYA TOGASHEVA, AKSHYRYN ZHOLBASSAROVA,
ZHARAS ISLAMBERDIYEV, MAX BISSENGALIEV, DADEN SUIEROV

$$G_1 = \frac{1}{6}\pi d^3(\gamma_l - \gamma_g) \tag{1}$$

In which $\gamma_l$ – specific weight of the liquid; $\gamma_g$ – specific weight of the gas.

If the specific weight of the liquid is noticeably more than specific weight of the gas, we can neglect the $\gamma_g = 0$.

The speed of the rising of bubbles during its way through the layer of the liquid mainly depends on its viscosity, specific weights of gas and liquid, yield point and the size of the bubble. Temperature effects on viscosity, yield point and specific weigh, and therefore on the speed of rising of bubbles. That is why different formulas related to different hydrodynamic conditions are used for defining the speed of the rising bubble.

The speed of the rising bubble can be approximately found according to the balance with the resistance against the motion of the bubble:

$$v = 2\sqrt{\frac{dg}{3\psi}} \tag{2}$$

Where $\psi$ is a coefficient of resistance, which depends on the motion regime and the Reynold's number:

$$Re = \frac{vd\rho}{\mu} \tag{3}$$

At $Re \leq 2$ laminar-flow conditions take place, and the coefficient of resistance has a value of:

$$\psi = \frac{24}{Re} \tag{4}$$

If we put this value in the equation (2) we get the Stokes formula:

$$v = \frac{d^2(\gamma_l - \gamma_g)}{18\mu} \tag{5}$$

Furthermore, for the speed of rising the coefficient of resistance at the $Re \leq 2$ (laminar flow), and also for the bubble flow will be equal to $\psi=24/Re$, so, the Stokes formula can be used for defining the speed of the motion.

The coefficient of resistance for the turbulent region can be written as $\psi=8/3$ [24]. If it is put in the formula (2), we can get the speed of the rising of the bubble, in cases when we can neglect the specific weight of the gas compared to the specific weight of the liquid.

238

Imagine that during the motion of the bubble inside resistant powers which are conditioned by the viscous and plastic properties are added to each other. Then the formula for the power of resistance can be demonstrated as [26]:

$$\omega_n = \pi d^2 \tau_0 + 3\pi\eta dv \tag{6}$$

Equalizing (10) to the resultant power:

$$v = \frac{d}{3\eta}\left[\frac{(\rho_l - \rho_g)gd_g}{6} - \tau_0\right] \tag{7}$$

For the power law fluid in work, we can use the following formula:

$$v = \frac{1}{3}\left[\frac{d_g(\rho_l - \rho_g)g}{6\kappa} - \tau_0\right]^{\frac{1}{n}} d_g \tag{8}$$

Where n and k – indicators of non-newton behavior (consistency);

$$c_\omega = \frac{8 \cdot 3^n}{Re}, \quad Re = \frac{\rho_l\, v_g^{2-n}\, d_g^2}{\kappa} \tag{9}$$

At n=1 formulas (8) and (9) transit to the formula for the viscous liquid.

It should be mentioned that if the system of nozzles is used for the gas supply the ratio below is not lost in case, that the distance between two centers of the neighbor estuaries is equal to the diameter of bubbles.

The difference between velocities of the gas flow and petroleum product provides the creation of tangential strains lead to deformation of drops, because of the tangential strain, interfacial tension, which makes droplets decrease their surface. Even though the existence of emulsion breakers makes the process of decreasing the toughness of heavy emulsion and destruction of the background shell of the water-oil emulsion much easier.

Singled bubbles do not appear at the high enough speed of the gas in the estuary of the opening, but a gas flow which divides in bubbles leaks.

Liquid droplets deform after getting into the warm air flow and the internal motion appears inside of them. Development of this processes leads to deformation and deconstruction of an armor-plate shell of the emulsion droplets. A type of process of their splitting process according to the speed of the flow and physical parameters of gas and droplets of emulsions can be different. In the work [28] deformations of bubbles and splitting of droplets in gas flows

RYSKOL BAYAMIROVA, ALIYA TOGASHEVA, AKSHYRYN ZHOLBASSAROVA,
ZHARAS ISLAMBERDIYEV, MAX BISSENGALIEV, DADEN SUIEROV

were discussed. It is shown that the process of deconstruction depends on the speed of the gas flow, density and viscosity of liquid and gas environment, surface stress, time of the impact, diameter of globules and acceleration. Splitting of droplets is mainly represented by the Webber number We and Laplace Lp:

$$We = \frac{2a\rho_g gv^2}{\sigma}, \; Lp = \frac{2a\rho_{2l}\sigma}{\mu_l^2} \qquad (10)$$

where a – radius of the droplet; v – speed of the gas flow; $\mu_l$ – dynamic viscosity of the liquid.

The maximal splitting of the droplet comes to reality in some diapason of Weber numbers, limited by some critical numbers, depending on the Laplace liquid.

As it is known in oil industry, the traditional way of destruction of emulsions is by thermochemical way, which is continuously developing and is used with electrochemical fields and hydrodynamic properties of the flow [29-32].

Conditions of the oil preparation process strongly depend on the condensation of natural emulsifiers (asphaltene, paraffin, resin and etc.) which create entrained highly viscous emulsion. Destruction of this emulsion in traditional preparing apparatuses is followed by an enormous wasting of emulsion breakers, heat, electric energy and long settling period. That is why right complex impact on emulsions makes emulsion breaks easier.

A hydro mixing receptacle with the pipes with openings was constructed in the laboratory for researches of the impact of hydrodynamic effect on emulsion breaks. The amount and the diameter of the openings provides the speed of the flow of 1-3.5 m/s, experiments were done on the emulsions of the oil from the deposit of Karazhanbas. Researches were made with 20 % emulsion at the temperature of 20 ºC and 40 ºC. The preparation of the emulsion carried out on the emulsifier.

Results of the laboratory works have shown that hydrodynamic demulsification is more effective than simple thermochemical settling and emulsion breaking. For example, at the thermochemical method during the usage of dissolvan 4411 – 100 g/t, the amount of emitted water at the temperature 40 ºC is 40 %, and the usage of the energy of the flow is 90 %.


**CONCLUSION**

The way of heating by using the energy of the flow is one of the effective ways of intensification of destruction of stable oil-water emulsions. To conclude everything that was written in this work, it can be said, that the research of the

thermal method of developing of structural-mechanical properties of heavy oils shows that the thermal treatment of oils from the deposits of North Buzachi negligibly effects on their viscosity, but hugely on lowering the yield point. By experimental results can be shown the rheological parameters of the North Buzachi oil before and after the thermal treatment at temperature 70 ºC with final cooling temperature 60 ºC viscosity of oils from 4.4 to 37.7 s$^{-1}$. In other case, at temperature 85 ºC with final cooling temperature 70 ºC viscosity of oils increased from 4.8 to 38.2 s$^{-1}$.

According to results of experimental study can be offered an improved oil preparation set for heating heavy oils and oil-water emulsions. This oil preparation set provides a high level of heating and dehydration of heavy oils and emulsions with integrated effect on the process of temperature and hydrodynamic factors.


**EXPERIMENTAL SECTION**

Experiments considering the research of the impact of the thermal treatment on the structural-mechanical properties of the oils from North Buzachi, Karazhanbas and Kalamkas were conducted in the laboratory. The structural-mechanical properties of thermal treated oil were scrutinized with using capillary viscometer. The starting temperature of heating and the speed of cooling affect the effectiveness of thermal treatment, that is experiment oil was heated up to 70 ºC and cooled down to 30 ºC with the speed of 12 ºC per hour (Table 1). The effectiveness of the thermal treatment was defined by comparing of the rheological parameters of the oil before and after heat treatment.

Proposed installation is shown in the Figure 1 [24]. The installation consists of reservoir 1, filled with viscous petroleum product 2, also the air duct 3 with hoses 4, connected to a pipe 5 for a high-pressure heated air on the heating unit by a concentrator or an electric heater. Air extracting from the reservoir 1 is done by the pressure reducing valve 7 adjusted to 1.5-2 atm., through which the exhausted air goes to the heating. There is a pipe 9 in the lowest part of the conical shaped cap of the reservoir for collecting and pulling out condensed water.

Compressed air goes from the compressor to the heating unit 6, heated by the sun concentrator or by the electric heater till 90-100 ºC. The electrical heater is used at the low intensity of the sun flow and an insufficient air heating. Then, the hot pressed air goes through the pipe 5 goes to the air duct 3 of the reservoir 1 to the hoses 4, where the stream of the hot air flows to the petroleum product 2 through the openings in the hoses, and then goes up as a vapor-air foam.

The high intensity is existing due to the transitional behavior of the gas-dynamic impact of the hot compressed air to the changing viscosity of oil products, resisting by the vapor-air foams followed by a breakup. As a result, it condenses on the conical shaped cap of the reservoir 1 from the vapor-air foams, and leaks by an oblique surface to the pipe 9 by the bottom of the cap and disappears. An air withdrawal goes by the reduction valve 7, adjusted to the pressure of 1.5-2 atm. and supplied through the channel 8, to the heating unit 6.

The given construction allows heat the oil product in the reservoir more intensively, dehydrate and save the energy resources during the preparation and transporting.
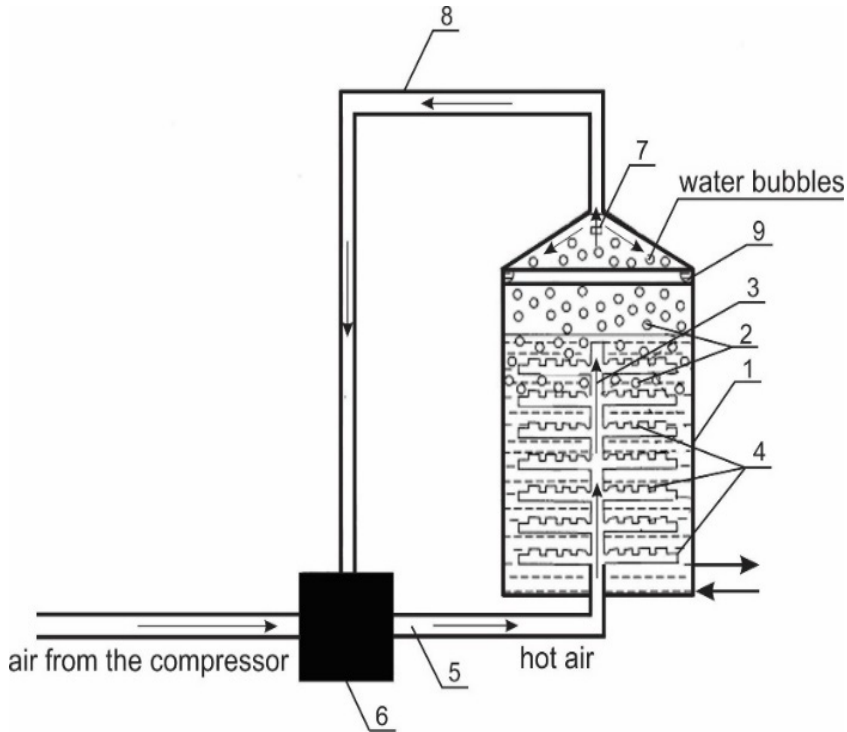


1 – reservoir; 2 – oil product; 3 – air duct; 4 – hoses; 5 – pipeline; 6 – heating unit;
7 – valve; 8 – withdrawing; 9 – channel

**Figure 1.** Scheme of the installation for the heating of the water-oil emulsions

# REFERENCES

1. A. Kh. Mirzadzhanzade; A. K. Gallyamov; B. I. Maron; V. A. Yufin; Hydrodynamics of pipeline transportation of oil and oil products, Nedra, Moscow, **1984**, p. 286. (In Russian)
2. I. N. Evdokimov; N. Yu. Eliseev; D. Yu. Eliseev; *J. Petrol. Sci. Eng.*, **2001**, *30*, 199-211
3. S. O. Ilyin; M. P. Arinina; M. Yu. Polyakova; V. G. Kulichikhin; A. Ya. Malkin; *Fuel,* **2016**, *186*, 157-167
4. K. Moussa; M. Djabourov; J. L. Volle; *Fuel,* **2004**, *83*, 1591-1605
5. R. M. Webber; *J. Rheol.,* **1999**, *43*, 911-931
6. S. W. Hasan; M. T. Ghannam; N. Esmail; *Fuel,* **2010**, *89*, 1095-1100
7. S. Ilyin; M. Arinina; M. Polyakova; G. Bondarenko; I. Konstantinov; V. Kulichikhin; A. Malkin; *J. Petrol. Sci. Eng*. **2016**, *147*, 211-217
8. S. O. Ilyin; M. P. Arinina; Y. S. Mamulat; A. Y. Malkin; V. G. Kulichikhin; *Colloid J.,* **2014**, *76*, 425-435
9. A. M. McKenna; L. J. Donald; J. E. Fitzsimmons; P. Juyal; V. Spicer; K. G. Standing; A. G. Marshall; R. P. Rodgers; *Energ. Fuel.*, **2013**, *27*, 1246-1256
10. B. Sorina; A. Tamas; *Studia UBB Chemia*, **2013,** *58,* 21-30
11. A. Gaspar; E. Zellermann; S. Lababidi; J. Reece; W. Schrader; *Energ. Fuel.*, **2012**, *26*, 3481-3487
12. A. Y. Malkin; S. N. Khadzhiev; *Pet. Chem.*, **2016**, *56*, 541-551
13. A. Tamasa; M. Vincze; *Studia UBB Chemia,* **2011**, *56,* 247-255
14. I. A. Wiehe; *Energ. Fuel.,* **2012**, *26*, 4004-4016
15. E. Rogel; C. Ovalles; J. Vien; M. Moir; *Fuel*, **2016**, *178*, 71-76
16. C. Tudose; L. Patrascu; P. Alexe; *Studia UBB Chemia,* **2014,** 59, 87-102
17. R. Z. Syunyaev; R. Z. Safieva; R. R. Safin; *J. Petrol. Sci. Eng.*, **2000**, *26*, 31-39
18. F. Yziquel; P. J. Carreau; M. Moan; P. A. Tanguy; *J Non-Newton. Fluid,* **1999**, *86*, 133-155
19. J. Zhang; X. Chen; D. Zhang; J. Xu; *J. Petrol. Sci. Eng.*, **2017**, *156*, 563-574
20. W. S. Hasan; M. T. Ghannam; N. Esmail; *Fuel*, **2010**, *89*, 1095-1100
21. C. Chang; Q. D. Nguyen; H. P. Ronningsen; *J. Non-Newton Fluid,* **1999**, *87*, 127-154
22. M. Fingas; B. Fieldhouse; *Mar. Pollut. Bull.*, **2003**, *47*, 369-396
23. Y. Imanbayev; Y. Tileuberdi; Y. Ongarbayev; Z. Mansurov; A. Batyrbayev; Y. Akkazin; E. Krivtsov; A. Golovko; S. Rudyk; *Eurasian Chem. Technol. J.,* **2017**, *19,* 147-154
24. M. D. Bissengaliyev; M. E. Baymirov; *Kazakhstan patent* 20504, 2008. (In Russian)
25. J. A. Boxall; C. A. Koh; E. D. Sloan; A. K. Sum; D. T. Wu; *Ind. Eng. Chem. Res.,* **2010**, *49*, 1412-1418
26. P. Sherman; *Encyclopedia of emulsion technology*, Marcel Dekker, New York, **1983**, p. 725
27. M. R. Khan; *Energ. Source.*, **1995**, *18*, 385-391

28. A. Siavash; S. Mehdi; M. Mohammad; M. S. Mehdi; *Egypt. J. Pet.,* **2017**, *26*, 209-213

29. S. N. Ashrafizadeh; E. Motaee; V. Hoshyargar; *J Pet. Sci. Eng.,* **2012**, *86-87*, 137-143

30. R. Martínez-Palou; M. L. Mosqueira; B. Zapata-Rendón; E. Mar-Juárez; C. Bernal-Huicochea; J. C. Clavel-López; J. Aburto; *J. Pet. Sci. Eng.,* **2011**, *75*, 274-282

31. S. Ashrafizadeh; M. Kamran; *J. Pet. Sci. Eng.*, **2010**, *71*, 205-211

32. Y. Ongarbayev; A. Golovko; E. Krivtsov; E. Tileuberdi; Y. Imanbayev; B. Tuleutayev; Z. Mansurov; *Studia UBB Chemia,* **2014,** 59, 57-64

# MATHEMATICAL APPROACH FOR PILOT-SCALE EXPERIMENT SETUP ON BIOGAS PRODUCTION

## ADRIAN EUGEN CIOABLĂ[a], MĂDĂLINA IVANOVICI[b,c], GABRIELA-ALINA DUMITREL[d,*], LAURENȚIU-VALENTIN ORDODI[d], DELIA-GABRIELA CĂLINOIU[e], GAVRILĂ TRIF-TORDAI[a], VASILE PODE[d]

**ABSTRACT.** In this work, pilot scale experiments were carried to evaluate the biogas production through anaerobic co-digestion for two different mixtures of feedstock based on agricultural biomass and agricultural waste. The first mixture consisted of degraded row barley and wastewater from treatment plant and the second mixture contained wheat, corn grains and shell sunflower seeds with wastewater from treatment plant. The temperature, pH, pressure and the amount of the produced biogas were daily monitored for 26 days and the results of the two experimental charges were assessed and compared using statistical analysis: the box plot method and summary statistics. The latter feedstock mixture showed a better production of biogas for which the mean value of produced biogas amount is 18.43 $m^3$, whereas the mean value of the biogas generated for the former feedstock mixture was 14.95 $m^3$.

*Keywords: biogas production, agricultural biomass, pilot scale, co-digestion, statistics*

## INTRODUCTION

Anaerobic digestion is reported to be one of the most exploited and attractive technologies for renewable energy production by conversion of biomass. Biogas production by anaerobic digestion is a versatile process,

---

[a] *Politehnica University of Timisoara, Faculty of Mechanical Engineering, 1 Mihai Viteazu blvd., RO-300222, Timisoara, Romania*
[b] *Politehnica University of Timisoara, 2 Piata Victoriei, RO-300006, Timisoara, Romania*
[c] *National Institute for Research and Development in Electrochemistry and Condensed Matter, 144 Aurel Paunescu Podeanu str., RO-300569, Timisoara, Romania*
[d] *Politehnica University of Timisoara, Faculty of Industrial Chemistry and Environmental Engineering, 6 Vasile Parvan blvd., RO-300223, Timisoara, Romania*
[e] *Politehnica University of Timisoara, Faculty of Electrical and Power Engineering, 2 Vasile Parvan blvd., RO-300223, Timisoara, Romania*
\* *Corresponding author: alina.dumitrel@upt.ro*

worldwide used at small and large scale for heat and electricity generation and also as a transport fuel [1,2]. It can be applied for a large variety of feedstock: energy crops, organic fraction from municipal solid waste, commercial and industrial sector waste, agricultural waste including animal manure and slurry and crop and forest residue, algae, sewage sludge [2-4]. In European Union, approximately half of the biogas production comes from energy crops (primary maize), followed by landfill, organic waste, sewage sludge and manure [5].

In order to avoid the competition with food chain production, the usage of energy crop as a feedstock for biogas production has been discouraged [6]. As well, due to the environmental and economical reasons, the developments in this field have focused on biogas production from biodegradable waste [7].

The waste generated in the agriculture sector is considered a promising organic matter for biogas production. Different types of waste are produced depending on the agricultural activities, therefore it can be distinguished crop and food processing waste (such as maize, sugarcane bagasse, corn stalks, fruits, vegetables), waste from farm animals (manure, organic residue from slaughterhouse, wastewater containing urine) and also toxic substances coming from crop treatments (pesticides, insecticides, etc.) [8,9]. The interest in energy recovery by exploitation of agricultural waste has led to numerous research activities related to efficiency of biogas generation from crops residues. Hence, among the agro-waste feedstock subjected to anaerobic digestion, there may be mentioned: rice straw, maize straw, barley, wheat, corn silage, meadow grass, ryegrass, switchgrass, rotten fruits and vegetables with a methane yield ranging from 0.122 to 0.388 $m^3$ per kg of volatile solids [10-14].

Still, anaerobic digestion of a single substrate results in low amounts of obtained biogas. In this sense, co-digestion is one of the several approaches for enhancement of biogas production technology. In the anaerobic co-digestion process, two or more organic substrates are used simultaneously as feedstock for biogas generation. The advantages of co-digestion referred in literature are: a better ratio of carbon to nitrogen elements, an improvement of pH values variation during the process, close to the optimal pH range, higher methane yields (up to 200% depending on the process operating parameters) which implies also the increasing of biogas reactors economics, synergetic effect caused by mixture of different substrates involved in the process [8,15-17]. If not chosen properly, due to the diversity and characteristics of feedstock, the combination of various substrates may lead to process instability. Experimental models are frequently used in order to estimates the biogas quality and quantity as a function of process parameters [18,19], while also determining the potential calculus errors due to experimental approach [20]. Pilot-scale plants are required in order to evaluate the feasibility of the co-digestion process for specific substrates [21].

In this study, a pilot scale experimental setup was used for evaluation of biogas production by anaerobic co-digestion of different agricultural biomass (row barley, wheat, corn grains and shell sunflower) with wastewater from treatment plant. The process performances are assessed by statistical interpretation of the data using summary statistics and box plot method.

## RESULTS AND DISCUSSION

The paper focuses on statistical analysis done on the amount of biogas resulted from the anaerobic fermentation. The types of agricultural biomass used, in the biogas pilot plant at Politehnica University Timisoara, are: i) reactor 1 (R1) – degraded two row barley and wastewater from treatment plants, ii) reactor 2 (R2) – 40% wheat and 40% corn grains plus 20% shell sunflower seeds and wastewater from treatment plant.

Fig.1 shows the results of daily biogas production for each reactor, which was taken on a daily, over the course of July. Here are represented the most important parameters characterizing the fermentation process. The variation of biogas production, in $m^3$, can be seen in Fig. 1a.
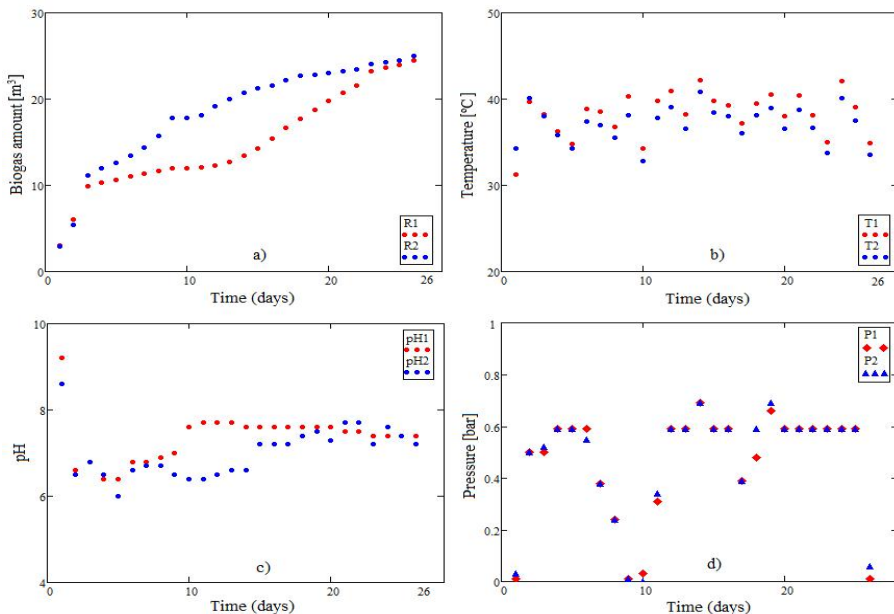


**Figure 1.** The daily biogas production in fermentation process for 26 days, in July. a) biogas production, expressed in $m^3$; b) temperature, in ºC; c) pH; d) pressure, in bar. Parameters that have index 1 are specific for reactor 1, and index 2 for reactor 2.

Also, in Fig.1b and Fig.1c are shown the daily values measured for temperature and pH respectively. It was observed that throughout the duration of the digestion process, the temperature ranges from 31.3 to 42.2 °C in the first reactor and in the second reactor is between 32.8 °C and 40.8 °C respectively. In this study, the variation of temperatures recorded from the two reactors had the same trend.

An important role related to microbial life growth during fermentation is played by the pH, the anaerobes prefer a pH close to optimum values, in the range of 6.6 - 7.3, and the neutral pH is best suitable for biogas production, since most of the methanogens grow at the pH range of 6.5 - 7.5. In the first day the pH values for the both reactor was strongly alkaline, after that the value was adjusted in the range 6 and 7.8 (see Fig.1c).

The pH graphical representation is not similar, after 10 days until the end of the measurement period, in first reactor the values is in range 7.4 and 7.6, while in the second reactor the variation is higher between 6.4 and 7.7.

The $CH_4$ percentage on 3 and 11 days is 23 % for the both reactors and 77 % in R1, and 80% in R2 respectively. Also, the $CO_2$ percentage on 3 and 11 days is 77% for the both reactors and 23 % in R1, and 20% in R2 respectively. Another important parameter in the fermentation process is the pressure, which is represented in Fig. 1d. Note that the points that mark the readings of pressure, expressed in bar, almost coincide.

The box plot from Fig. 2 allows to visualize and compare the distribution of data based on the five numbers summary: minimum, first quartile, median, third quartile, and maximum.
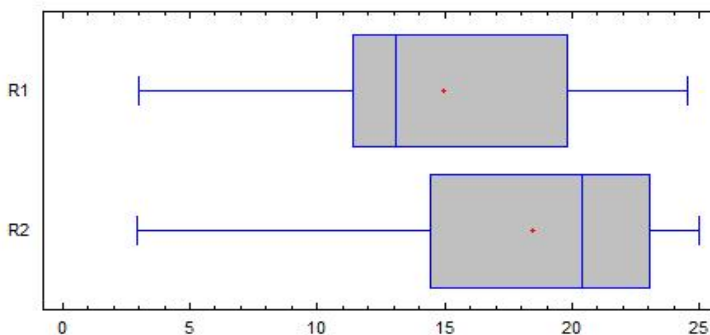


**Figure 2.** Variation of biogas production in anaerobic fermentation - box plot.

The plots show that the distribution between the data points is different. The median of the values is depicted as a line splitting the box in half. Also, the mean is represented by a red plus. In case of R1 the mean is positioned

after median, and before the median for R2, respectively. The interquartile range (IRQ) of a box plot is a visualization of the range from the first quantile to the third quantile, which is 8.41 for R1, and 8.59 for R2, respectively. In IRQ are 50% from measured data of biogas production.

Table 1 and Table 2 show summary statistics of data measured from amount of biogas production, pressure, pH and temperature by the both reactors. The mean of amount of biogas production is 14.95 $m^3$ for R1 and 18.43 $m^3$ for R2. The difference between the amounts of biogas production is given by biomass used for each reactor. Also, the coefficient of variation (defined as the ratio of the standard deviation to the mean) is 1.2 times higher for R1 indicating a larger distribution of values around the mean.

**Table 1.** Summary statistics for amount of biogas production and the most important parameters in fermentation process from R1 reactor. *P* is pressure and *T*– temperature.

|  | R1 [m³] | P [bar] | pH | T [ºC] |
|---|---|---|---|---|
| Mean | 14.947 | 0.457 | 7.361 | 38.235 |
| Standard deviation | 5.691 | 0.218 | 0.564 | 2.583 |
| Coefficient of variation | 38.07% | 47.76% | 7.66% | 6.76% |
| Minimum | 3 | 0.01 | 6.4 | 31.3 |
| Maximum | 24.524 | 0.69 | 9.2 | 42.2 |
| Range | 21.524 | 0.68 | 2.8 | 10.9 |
| Stnd. skewness | 0.266 | -2.673 | 1.786 | -1.740 |
| Stnd. kurtosis | -0.601 | 0.302 | 3.756 | 0.690 |

**Table 2.** Summary statistics for amount of biogas production and the most important parameters in fermentation process from R2 reactor. *P* is pressure and *T*– temperature.

|  | R2 [m³] | P [bar] | pH | T [ºC] |
|---|---|---|---|---|
| Mean | 18.436 | 0.464 | 7.0 | 37.081 |
| Standard deviation | 5.937 | 0.216 | 0.572 | 2.120 |
| Coefficient of variation | 32.20% | 46.63% | 8.17% | 5.72% |
| Minimum | 2.962 | 0.0 | 6.0 | 32.8 |
| Maximum | 24.963 | 0.69 | 8.6 | 40.8 |
| Range | 22.001 | 0.69 | 2.6 | 8.0 |
| Stnd. skewness | -2.368 | -2.723 | 1.510 | -0.728 |
| Stnd. kurtosis | 0.766 | 0.386 | 0.865 | -0.524 |

Of particular interest here are the standardized skewness and standardized kurtosis, which can be used to determine whether the samples come from normal distributions. Values of these statistics outside the range

of -2 to +2 indicate significant departures from normality, which would tend to invalidate the tests which compare the standard deviations. In this case, pressure for R1 and R2 has a standardized skewness value outside the normal range. Also, the biogas production in R2 has standardized skewness - 2.36, which value outside the normal range. On the other hand, standardized kurtosis value of pressure from R1 is outside the normal range. With few exceptions discussed above, both standardized kurtosis values are within the range expected.

## CONCLUSIONS

The present paper underlines the usage of agricultural type biomass in fermentation processes from the point of view of using a renewable energy carrier with impact on local energetic autonomy.

The process was treated from different points: experimental and mathematical in order to determine the possible errors of the developed method of monitoring.

From the obtained data, the batch containing the cereal recipe had the greater biogas production and the mean standard deviation resulted from calculation is acceptable in terms of possible errors that could appear from a measuring stand. Further testing and experimental approach is still needed in order to better determine the process details and to accurately correlate them with the mathematical approach.

## EXPERIMENTAL SECTION

The used materials that were used are: for reactor 1 (R1) – degraded two row barley and wastewater from treatment plant and for reactor 2 (R2) – 40% wheat and 40% corn grains plus 20% shell sunflower seeds and wastewater from treatment plant. The fermentation process was monitored for 26 days, recording the following parameters for the two reactors: pressure (SCP01 pressure sensors with an accuracy of ± 0.1 %), pH (BL931700 pH Mini Controller with an accuracy of ±0.02), temperature (thermocouple K type with an accuracy of ± 0.4%) and biogas production (mechanical gas counter with diaphragms, G1 model, accuracy class 1.5). Also, during the process there were observed the produced biogas quantities and quality in terms of methane and carbon dioxide concentrations in the produced biogas. The results were obtained using a DELTA SIV gas analyzer with data accuracy of ±5 % by volume. The materials were initially prepared by grinding to an average value of 1-2 mm for each chosen type. The pH was initially corrected by using caustic soda in

the first days of the process in order to have an overall value in the domain 6.5 – 7.5. The temperature was kept in the domain of 36 – 39 °C during the entire process. The materials were used in batch type reactors and measurements were taken on daily basis.

# REFERENCES

1. L. C. Grangeiro; S. G. Coêlho de Almeida; B. Sampaio de Mello; L. T. Fuess; A. Sarti; K. J. Dussán; New trends in biogas production and utilization. In *Sustainable Bioenergy: Advances and Impacts*, 1st ed.; M. Rai, A. P. Ingle Eds.; Elsevier, **2019**, Chapter 7, pp. 199-233
2. S. Achinas; V. Achinas; G. J. W. Euverink; *Engineering*, **2017**, *3*, 229-307
3. P. Baltrėnas; A. Misevičius; *J. Environ. Health Sci. Eng.*, **2015**, *13*
4. M. M. Kabir; K. Rajendran; M. J. Taherzadeh; I. Sárvári Horváth; *Bioresour. Technol.*, **2015**, *178*, 201-208
5. B. Kampman; C. Leguijt; T. Scholten; J. Tallat-Kelpsaite; R. Brückmann; G. Maroulis; J. P. Lesschen; K. Meesters; N. Sikirica; B. Elbersen; *Optimal use of biogas from waste streams. An assessment of the potential of biogas from digestion in the EU beyond 2020,* March 2017. Accessed on: June 29, 2019. [Online]. Available at: https://ec.europa.eu/energy/en/studies/optimal-use-biogas-waste-streams-assessment-potential-biogas-digestion-eu-beyond-2020
6. Directive (EU) 2015/1513 of the European Parliament and of the Council Amending Directive 98/70/EC Relating to the Quality of Petrol and Diesel Fuels and Amending Directive 2009/28/EC on the Promotion of the Use of Energy from Renewable Sources (2015), Official Journal of the European Union L239, p. 1-29
7. K. C. Surendra; D. Takara; A. G. Hashimoto; S. K. Khanal; *Renew. Sust. Energ. Rev.*, **2014**, *31*, 846-859
8. G. Merlin; H. Boileau; Anaerobic Digestion of Agricultural Waste: State of the Art and Future Trends. In *Anaerobic Digestion: Types, Processes and Environmental Impact,* A. Torrles Eds.; Nova Science Publishers, New York, USA, **2013**
9. F. O. Obi; B. O. Ugwuishiwu; J. N. Nwakaire; *NIJOTECH,* **2016**, *35*, 957-964
10. G. V. Nallathambi; *Biomass Bioenerg.*, **2004**, *26*, 389–99
11. M. M. Søndergaard; I. A. Fotidis; A. Kovalovszki; I. Angelidaki; *Energ. Fuel.*, **2015**, *29*, 8088–8094
12. R. A. Labatut; L. T. Angenent; N.R. Scott; *Bioresour. Technol.*, **2011**, *102*, 2255–2264
13. P. Tsapekos; P. G. Kougias; I. Angelidaki; *Energ. Fuel.*, **2015**, *29*, 4005–4010
14. Y. Li; R. Zhang; G. Liu; C. Chen; Y. He; X. Liu; *Bioresour. Technol.*, **2013**, *149*, 565–569
15. K. Hagos; J. Zong; D. Li; C. Liu; X. Lu; *Renew. Sust. Energ. Rev.,* **2017**, *76*, 1485-1496
16. T. Dias; R. Fragoso; E. Duarte; *Bioresour. Technol.,* **2014**, *164*, 420-423

17. J. H. Ebner; R. A. Labatut; J. S. Lodge; A. A. Williamsona; T. A. Trabold; *Waste. Manage.*, **2016**, *52*, 286-294

18. A.E. Cioabla; G.-A. Dumitrel; I. Ionel; *Rev. Chim. – Bucharest*, **2017**, *68(11),* 2614-2617

19. G.-A. Dumitrel; A.E. Cioabla; I. Ionel; L.A. Varga; *Rev. Chim. – Bucharest*, **2017**, *68(6),* 1294-1297

20. A.E. Cioablă; G.-A. Dumitrel; A.-M. Pana; F. Popescu; D. Lelea; A. Tenchea; L. I. Dungan; *VIII International Conference Industrial Engineering and Environmental Protection 2018 (IIZS 2018)* October 11-12th, **2018**, Zrenjanin, Serbia, 362-367

21. S. Xie; F. I. Hai; X. Zhan; W. Guo; H. H. Ngo; W. E. Price; L. D. Nghiem; *Bioresour. Technol.,* **2016**, *222*, 498-512

# QUALITATIVE ANALYSIS OF FILTERS FOR THE MECHANICAL NANOFILTRATION OF HOUSEHOLD DRINKING WATER

**OANA-ADRIANA CRIȘAN[a*], MARIUS SORIN PUSTAN[b],
CORINA JULIETA BÎRLEANU[b], ANCUȚA ELENA TIUC[a], IOANA SUR[a],
HOREA-GEORGE CRIȘAN[b], FLORINA MARIA ȘERDEAN[b],
LAZĂR FLĂMÎND[a], TIBERIU RUSU[a]**

**ABSTRACT.** The research carried out in this paper aimed to identify and compare the mechanical filtration capacity of the existing nanoparticles, correlated with the electro-chemical properties of the drinking water provided to the household users through the public network of Cluj-Napoca. The tested filters are available to the general public and the results of the research provide both the certainty of the importance of using drinking water filters, but also the prospect of purchasing an optimal relation quality - price filter based on the needs of the domestic users.

The qualitative analysis of the tested filters was carried out by laboratory testing of a representative sample of drinking water filters that once reached the maximum lifetime, were cut and subjected to microscopic analysis using an Atomic force microscope (AFM). The microscopic analysis aimed to determine the filtration capacity by identifying the size and agglomeration density of the nanoparticles retained by mechanical filtration.

*Keywords: mechanical nanofiltration, atomic force microscopy, nanoindentation, optical microscopy, water filters, drinking water*

## INTRODUCTION

The low presence of eco-innovation in drinking water distribution companies has led, among other things, to the low interest of citizens to consume drinking water from the public network, which has determined the attention of the population towards the use of drinking water packaged in polyethylene terephthalate (PET) bottles [1].

[a] *Technical University of Cluj-Napoca, Faculty of Materials and Environmental Engineering, 103-105 Muncii Ave, Cluj-Napoca, Romania*
[b] *Technical University of Cluj-Napoca, Faculty of Machine Building, 103-105 Muncii Ave, Cluj-Napoca, Romania*
\* *Corresponding author: crisanoanaadriana@yahoo.com*

O.-A. CRIȘAN, M. S. PUSTAN, C. J. BÎRLEANU, A. E. TIUC, I. SUR, H.-G. CRIȘAN,
F. M. ȘERDEAN, L. FLĂMÎND, T. RUSU

Therefore, the importance and necessity of approaching this topic is the continuous decrease of the quality of drinking water as a finite resource, this putting pressure on the researchers to find new approaches to water production and consumption. This is a new type of study that allows us to analyse with the cantilever the agglomeration and maximum dimensions of the remaining particles after testing the water filters in the household regime.

The premise of the research is that 400 billion litres of bottled water are consumed annually. Moreover, for bottling it in PET bottles (polyethylene terephthalate), 30 million barrels of oil and 7 times more water are consumed each year for the production of a single bottle compared to the one that is bottled [2]. In 2012, the global consumption of bottled water was amounted to 288 billion litres and was projected to reach 391 billion litres by 2017. In 2015, there was the highest per capita consumption of bottled water in the world, in the amount of approximately 244,159 litres [3]. Thus, it is observed that the excessive use of bottled water in PET packaging is encouraged rather than its economy. Starting from these aspects, one of the most viable solutions in this regard, is the use of some filtration systems for water provided from the public network, installed at the users' home (at the final point of distribution of drinking water) [4]. Therefore, a major step for the protection of water consumption, possibly in Romania for several years, is the purchase of filters for drinking water, intended for domestic use [5,6].

From a scientific point of view, the research of the efficiency of the drinking water filters intended for the domestic users, wants to contribute to the implementation of methods to increase the quality of the drinking water, by using the filter elements with high efficiency, through the identification of the nanometric dimensions, which contribute to the pollution of it.

From the technological point of view, it is reflected the importance of the use of drinking water filters in the domestic regime in order to increase the quality of life of the household users, to the detriment of the use of bottled drinking water [7]. The main difficulty lies in the policy of marketing strategies that encourage the use of bottled water in PET packaging. It can be concluded that several aspects related to the quality of bottled water in PET packaging, in relation to the drinking water filtered in the domestic regime, remains a topical subject that requires studies, followed by scientific answers [8].

The aim of this article is to:

- Compare the performances of two water filters from different materials (ceramic and polypropylene);
- To identify the possibilities of mechanical filtration of the pollutant particles of nanometric order, in correlation with the electro-chemical parameters of the drinking water;

- To find the optimum filter element from the point of view of the quality-price ratio, which ensures superior properties of drinking water coming from the public network and used in the domestic regime, which leads to the abandonment of the purchase and use of bottled water in PET packaging.

These determinations were made for the drinking water that was initially analysed to correspond to the specific chemical parameters, nanofiltration representing a next but imperative step in increasing the quality of the drinking water and discouraging the consumption of bottled drinking water.


## RESULTS AND DISCUSSION

The first step required before testing the filters for drinking water is to determine the pollution level of the drinking water tested by analysing chemical indicators, for the two test points of the studied water network. The electro-chemical parameters of drinking water can decisively influence the quality of the drinking water, but also the structure and distribution of the polluting mechanical nanoparticles (for example the oxides from the oxidation of the metallic pipes of drinking water distribution). Thus, this first step in performing quality analyses of drinking water, consists in ensuring that the tested drinking water corresponds to the electro-chemical parameters with parameters provided in the legislative norms and thus, the premise from which the testing of the filters for the mechanical retention of nanoparticles starts, to be a correct one. A particularly important group in the chemical analysis of water is the pollution indicators, together with other parameters necessary to establish the quality and purity of drinking water. In order to reveal the quality of the drinking water from the two selected points - Cluj-Napoca and Gilău, an analysis of the main determining parameters was used [9, 10]: turbidity, pH, electrical conductivity, dissolved oxygen in water and temperature. The results of the analyses of the water samples taken from the Iris area (sample 1 a), respectively the Gilău village (sample 1 b) are shown in Table 1.

Compared with the results of the water quality bulletin issued by the Someș Water Company S.A., the values for the two sampling points are not similar. From the Table 1, it can be concluded that the determinant parameters, for both water samples, are in accordance with the limits allowed by the special laws that regulate these aspects [11, 12], as well as with the methods of analysis of the specific standards. Also, it is noted that in the case of the first sample, the water has a higher conductivity and turbidity, whereas in the case of sample 2, we can talk about a pH and a dissolved oxygen concentration also higher than the first sample analysed. So the higher presence of oxygen dissolved in water in the case of sample 2 signifies it has an increased freshness, a fact that benefits the inhabitants of the Gilău village.

O.-A. CRIȘAN, M. S. PUSTAN, C. J. BÎRLEANU, A. E. TIUC, I. SUR, H.-G. CRIȘAN,
F. M. ȘERDEAN, L. FLĂMÎND, T. RUSU

**Table 1.** The value of the water sample analyses for the two sampling points

| Crt. no. | Determined parameters | UM | The value obtained | | Permitted limit * | Analysis method |
|---|---|---|---|---|---|---|
| | | | Sample 1 a | Sample 1 b | | |
| 1. | Turbidity | FTU | 1 | 0,78 | ≤ 5 | SR EN ISO 7027/2001 |
| 2. | pH | pH units | 7,01 | 7,25 | 6,5 - 9,5 | SR ISO 10523/2012 |
| 3. | Electrical conductivity | µS/cm | 99,5 | 83,3 | < 2500 | SR EN 27888/97 |
| 4. | Oxygen dissolved in water | Mbar | 170,2 | 224 | > 6 mg $O_2$/l | SR EN ISO 5814:2013 |
| 5. | Temperature | ℃ | 23,5 | 20 | - | - |

*\* according to Law 458/2002 republished in 2011 and of the Law 311/2004.*

After the first step, we wanted to investigate which is the best type of filter between ceramic and polypropylene one, so that people can buy it and discard the PET type water packaging. For this, using the AFM microscope, a comparative analysis of the two main types of filters was performed.

In this sense, with the help of the XEI Park System software, after the maximum life cycle use, a comparative analysis was made which consisted of: a) the topography of the filters, b) roughness analysis and c) the larger particles size retained by each one. These three analyses represent an effective indicator for those who want to buy the best home water filter.

*Scanning of ceramic and polypropylene cartridge samples.* The microscopic analyses have the role of determining the quality of the drinking water filtration (from the point of view of the topography, roughness, size and density of the impurities deposited in the structure of the filter elements tested experimentally) and these objectives were possible to be achieved with the help of the atomic force microscope (AFM) [13]. From the obtained results it can be said that the efficiency of the filters is directly proportional to the value of the number of microns held by each one, for the capacity of filtration [14]. The maximum allowable surface scanned for the topography of the ceramic sample is 40 x 40 µm, and for the topography of the polypropylene sample, due to the reduced dispersion of the determined particles, it was sufficient to analyse a surface of only 16 X 16 µm. From Figure 1 a) and b) results a high density of particle agglomeration, with approximate heights of 2000 nm, in the case of samples from ceramic material, while Figure 1 c) and d) show a much lower particle density agglomeration, with average heights up to 1000 nm, in the case of polypropylene samples, for both test points [15].
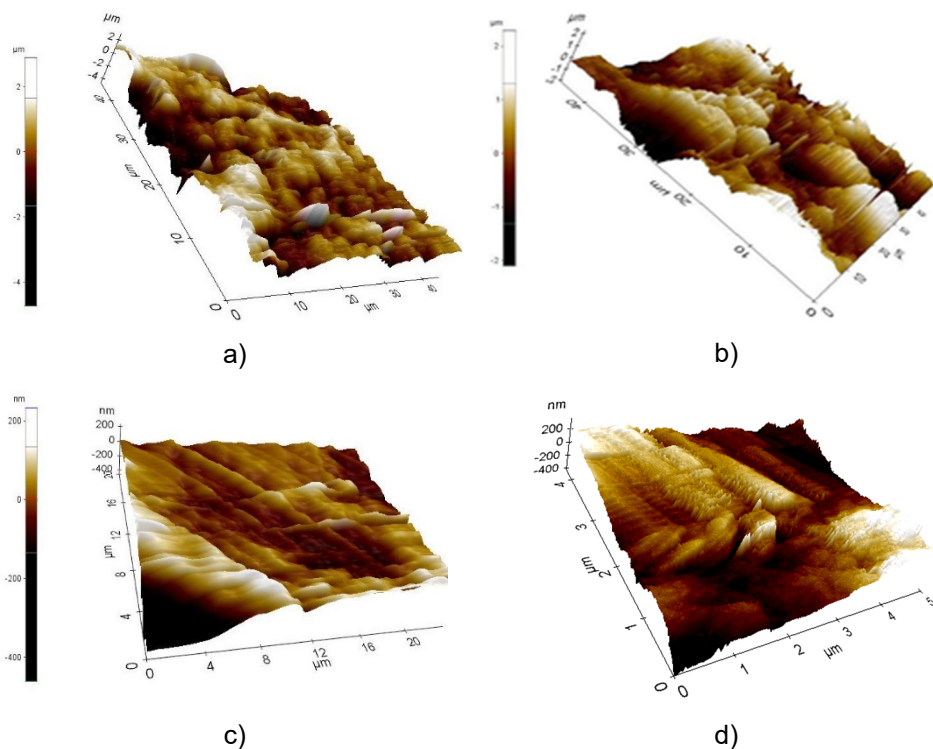
**Figure 1.** Topography of the filter cartridge from: a) ceramic used in Cluj-Napoca;
b) ceramic used in Gilău; c) polypropylene used in Cluj-Napoca;
d) polypropylene used in Gilău

The surface scan of the samples of the analysed sample reflects several roughness parameters, but an important one is the average arithmetic height of the roughness which is called $R_a$. $R_a$ with high values shows the influence of the deposition of polluting particles in relation to the standard filtering surface [16] and also the quality of the filter.

Next, it was compared the most important roughness's recorded on the filter cartridges made of ceramic material, respectively polypropylene. In Figure 2 a), it was observed the surface roughness of the sample of ceramic material, where $R_a$ = 984 nm. In Figure 2 b), also it was observed the roughness of the ceramic surface of the polypropylene filter element, where $R_a$ = 62.239 nm.
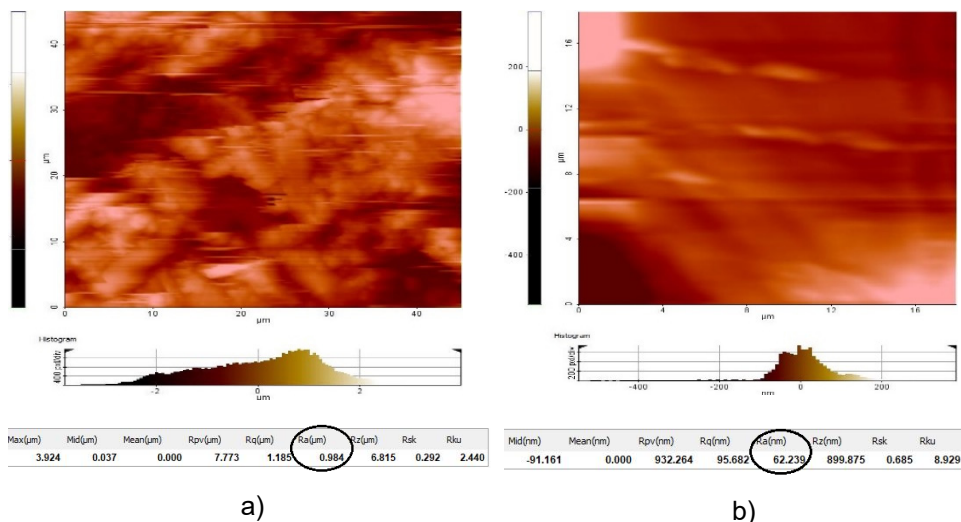
O.-A. CRIȘAN, M. S. PUSTAN, C. J. BÎRLEANU, A. E. TIUC, I. SUR, H.-G. CRIȘAN,
F. M. ȘERDEAN, L. FLĂMÎND, T. RUSU

**Figure 2.** The roughness of the cartridges from Cluj-Napoca:
a) ceramic type; b) polypropylene type

As can be seen from the value of the two roughness of the ceramic cartridges shown in Figure 2 a), respectively polypropylene from Figure 2 b), it can be stated that most deposits are registered on the first type of cartridge, with values of 15 times higher than the last one. On the opposite side, the low roughness of the surface of the polypropylene is reflected by the lower capacity of the filter tested, as can be seen from the particle density agglomeration, highlighted in the topography of Figure 1 c) and d). Due to the net superior roughness of the samples in the ceramic filter cartridge, it was made an individual analysis of the most relevant dimensional particles from analysed samples, deposited on the surfaces of the ceramic samples. For this, the samples taken from the Iris area and Gilău village were analysed. There are several relevant results regarding the efficiency of ceramic filters, so next there are several examples of depositions recorded on the sample probe analysed in Figures 3 a) and b) from the first test point, respectively on the sample probe from figures 4 a) and b) from the second test point.

In the samples shown in Figure 3 a), a particle height dimension of 3969 nm is observed, while the next sample records a particle height dimension about to 2284 nm. The sample from Figure 4 a) has a particle size of 2643 nm, while the sample from Figure 4 b) has a size of 2220 nm.
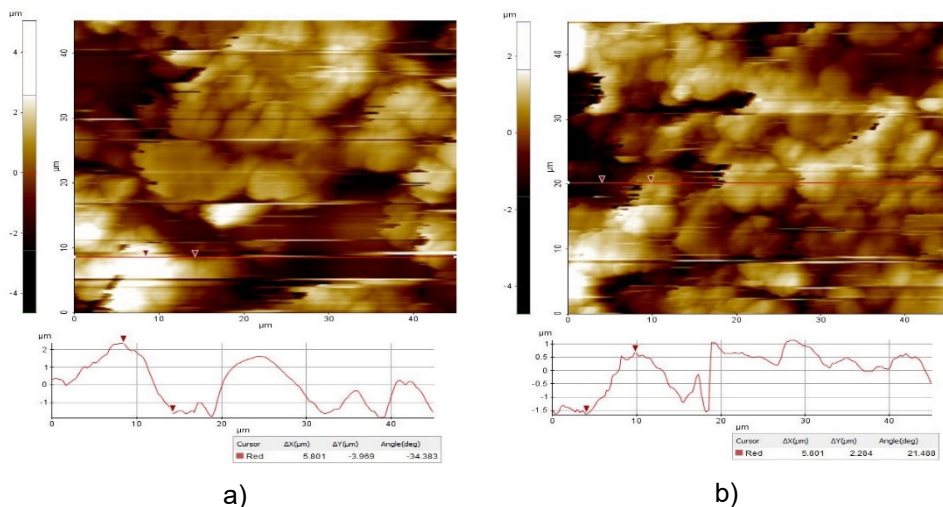
**Figure 3.** The particle size of the ceramic cartridge from the first test point:
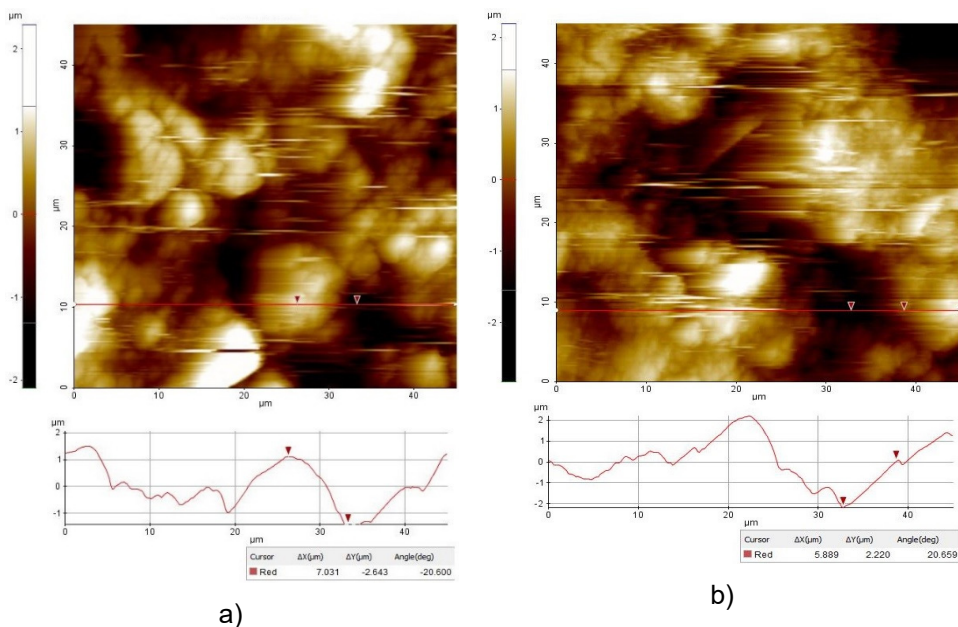a) sample 1; b) sample 2



**Figure 4.** The particle size of the ceramic cartridge from the second Test Point:
a) sample 1; b) sample 2

259

As a result of the tested samples, it can be observed that the largest deposits were registered on the ceramic cartridge from the first test point in Cluj-Napoca, which means that, in conjunction with the laboratory analyses performed for the two mentioned points, the water from the first tested area registered the most particle depositions. This aspect means that it is devoid of purity, which can cause various negative health effects for users. Considering the increased quality parameters of the water specified by the supplier, it can be seen that the increased level of polluting particles with significantly larger dimensions results from an unfavourable technical state of the water transport network from Cluj-Napoca Municipality.

*Discussions.* Corroborating the results of the topographic analyses with those of the roughness of the scanned surfaces, it is observed that the highest density of the particles retained by filtration is found on the ceramic sample. From the dimensional analysis of the relevant particles, it is found that, in the case of the ceramic sample, the structure of the material and its roughness allow the retention of a much larger number of particles, and the characteristics of the polypropylene material, although they allow the retention of a significant number of particles, their number is lower than the ceramic one. Thus, it is noted that the best filtering efficiency is held by the ceramic cartridge, which is one of the best indicators for both manufacturers and consumers who want to purchase a water filter with superior characteristics.

## CONCLUSIONS

Although filters for domestic users have recently appeared on the domestic market, the benefits that it brings, compared to bottled water in PET containers, are much more financially, economic and social beneficial, with direct effects on the environment and population [16]. Providing a drinking water from the public network, with not only chemical parameters but also optimal mechanics, at a lower price than the one generated by the purchase and use of bottled drinking water, represents the objective achieved by the present study. This is one that supports the wise decision of consumers to use the optimum filter for drinking water from the network and thus to obtain drinking water of superior quality, while also avoiding the purchase and use of bottled drinking water in PET-type packaging - that are powerful pollutants on the environment.

## EXPERIMENTAL SECTION

The steps followed for carrying out the experimental tests were the following:

1) Taking water samples from two critical points of the water network;

2) Analysis of the electrochemical parameters of the drinking water taken;

3) Carrying out a classification of the filter elements according to their performance;

4) Performing experimental tests, using a sample of analyzed filters, on a specially developed experimental stand [15];

5) Collection of sections from the middle area of the tested filters (who reached the maximum life);

6) Identification of the filter with optimum nanofiltration capacities, in order to ensure the superior quality of the drinking water and from the perspective of mechanical impurities, not only chemical ones, which at the same time ensure an optimal quality-price ratio, with the purpose of its implementation among the domestic users, to the detriment use of bottled water in PET packaging.

*Identification of the service areas that are subject of drinking water quality tests*. In order to analyse the water samples quality, two diametrically opposed sampling points were chosen, both with the sole supplier, represented by the regional Water Someș Company. Being the water with superior electrochemical properties in the North-West region, an immediate next priority would be to improve its quality from the point of view of mechanical impurities (influenced by the distribution network) in order to be similar to bottled PET, but supplied drinking water at a much lower price. At the same time, a positive side effect is the reduction of the pollution degree of the environment, by the use of fewer and fewer PET-type packaging in which the drinking water is bottled.

Therefore, for the research, the first sampling point was located in the Iris district on the 103-105 Muncii Boulevard in the city of Cluj-Napoca, and the second being located in the village of Gilău, on Braniște street, number 172 in the area of Cluj. The reason for choosing the two areas was primarily that they are located at a considerable distance, more than 21 km from each other, which can lead to different effects of water quality, both before and after the installation of the filter elements.

*Performing preliminary tests of drinking water*. In order to carry out appropriate laboratory tests, using an experimental stand which can test the drinking water filters, it was necessary a primary determination of the quality characteristics, in terms of potability, of the water that will be the object of the experimental test. Thus, the following quality indicators were followed: turbidity, pH, electrical conductivity, oxygen dissolved in water and temperature. With these parameters, it will be possible to determine the quality of the water coming from the SC WATER COMPANY SOMEȘ S.A. treatment plant, from the two collection points, both before using the filters and after mounting them. Even if water from the underground source Florești is delivered into the municipality's

O.-A. CRIȘAN, M. S. PUSTAN, C. J. BÎRLEANU, A. E. TIUC, I. SUR, H.-G. CRIȘAN,
F. M. ȘERDEAN, L. FLĂMÎND, T. RUSU

network, this one, once reached at the pumping station in the Grigorescu district, it is mixed with the water coming from the Gilău Treatment Station, which came from Tarnița lake.

It is worth mentioning that what may differ substantially and may influence the characteristics of the water reached the household user, is the age of the interior water networks of the buildings or the technical state of the regional operator's distribution water network. For this reason, including the taste of water can be changed, which leads to the decision of people to consume packaged water in PET bottles. Therefore, through these analyses, it will be possible to determine precisely the water quality coming from the two diametrically opposed sampling points. Therefore, the quality of the water from the point of view of the electro-chemical parameters, can influence the formation of the type, size and structure of the polluting particles of mechanical order, thus there is a direct correlation between the two aspects (oxidized metallic particles, mineral deposits due to the age of the network, salt possible in agglomeration with other types of particles, etc.). The tested filters have the ability to retain these types of particles up to nanometric dimensions.

The first of the parameters - turbidity, is influenced by the presence in water of very fine suspensions that have the direct effect of water transparency. Its determination was made using the turbidimeter, in accordance with the standard SR EN ISO 7027/2001 [17]. The second determining parameter for the analysed water quality, is the pH. A low pH below 7 indicates an acidic water, in which hydrogen ions are dominant. In contrast, a pH above 7 indicates a basic alkaline water, due to the dominant presence of oxydril ions. The pH determination was performed according to the standard SR EN ISO 10523/2012 [18], which establishes that this method applies to all samples of drinking or waste water, with a pH between 3 and 10 [19]. The third determining parameter for the research carried out, is the degree of electrical conductivity. The conductivity depends first of all by the presence of the salts dissolved in water and by its temperature. This analysis provides information with regard to the presence of salts in water. The instrument used for the measurement was the conductometer. The electrical conductivity of the water was determined according to the standard SR EN 27888/97 [20]. The fourth parameter analysed was the determination of the amount of oxygen dissolved in water. The presence of oxygen in water determines its quality. Absence of oxygen in water can have negative effects, such as, for example, changing the type of decomposing bacteria that lives in the aquatic environment, losing the freshness of the water or increasing the degree of pollution. The instrument used for this parameter was Multi 3430. The presence of oxygen in the water was determined according to the standard SR EN ISO 5814/2013 [21]. The last of the analysed parameters was the water temperature. Depending on its temperature, the maximum oxygen amount that can be dissolved in water, decreases with increasing of the temperature. The surface water temperature in Romania varies between 0 and 27 °C.

*Classifying the used water filter for microscopic analysis*. For microscopic analysis, were tested two types of filters used for household water, which have superior filtration characteristics. Although these filter cartridges have superior filtering characteristics, guaranteed by the manufacturer, the purchase price is accessible to domestic users. For example, the average purchase price values of the 2 filter cartridges are equivalent to the purchase price of a shuttle bottle containing bottled water of 2 PET litre. Regarding the technical-functional characteristics of the filter cartridges, based on the manufacturer's declaration, the 2 filter cartridges tested have the following particularities:

a) Ceramic filter cartridge: used for mechanical filtration of rust particles, sand or other impurities, with dimensions up to 0.03 μ. Its durability is 3 months or maximum use in the amount of 3 m$^3$. The maximum operating temperature is 30 ºC.

b) Polypropylene filter cartridge: obtained by melting and expanding polypropylene, can retain mechanical impurities (sand, rust, etc.) up to 5 μ in size. Its durability is 6 months or 3 m$^3$ of water. The maximum operating temperature is 40 ºC.

*Analysis methods using microscopic infrastructure.* The CAD environment [15] was used to design an experimental stand, which was constructed and used for the purpose of testing the chosen filters, under laboratory conditions. Also, for the analysis of the deposition results, the AFM technology was used, with which the 3D scan of the filter cartridge samples was performed. The samples are shown in figure 5. The samples analysed from the representative sample were taken from the same middle area of the tested filters, as seen in figure 5 a) and b), because the tests were performed on the experimental stand, having the uniform water flow and the thickness on the filter section was constant.
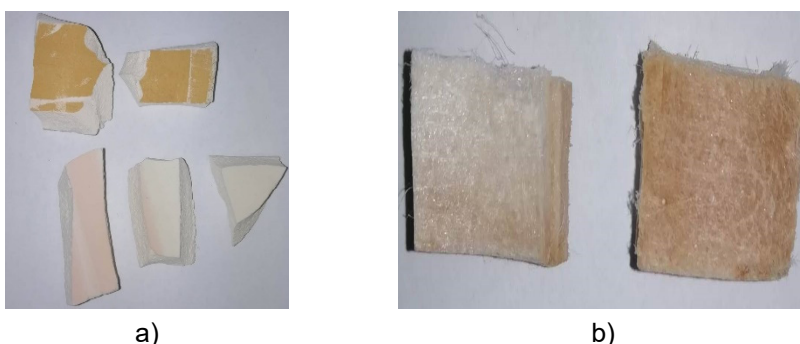


a)                                          b)

**Figure 5.** Sectioned cartridge samples: a) ceramic; b) polypropylene

O.-A. CRIȘAN, M. S. PUSTAN, C. J. BÎRLEANU, A. E. TIUC, I. SUR, H.-G. CRIȘAN,
F. M. ȘERDEAN, L. FLĂMÎND, T. RUSU

At the end of the filter usage cycle, of 3 m³ of water, it was made a topographic analysis of the sample surfaces from the obtained samples and a mechanical nano characterization of the pollutant particle deposition from the Iris area and the Gilău village. Figure 6 shows the process of stand testing of one of the analysed filters.

**Figure 6.** Filter testing on the experimental stand

*Microscopic analysis.* Also, for the analysis of the deposition results, the AFM technology was used, wherewith the 3D scanning of the tested samples was performed. This was made possible using the AFM XE 70 microscope from the MINAS research laboratory, from the Technical University of Cluj-Napoca, together with its software - XEI Park System. The tests were performed in non-contact mode, for a relative humidity of 28% at a room temperature of 23 °C. Topography determination and nano characterization were performed using a PPP-NCHR cantilever defined by: 4 μm thickness, 30 μm width, 125 μm length, 400 kHz resonance frequency and 42 Nm$^{-1}$ constant force; also the peak height is 15 μm and the radius is less than 10 nm [22]. The roughness of the filter surfaces of the analysed samples is directly influenced by the size and distribution of the pollutant particles deposited, closely related to the structure of the material filter elements [23, 24].

## ACKNOWLEDGMENTS

## REFERENCES

1. J.-H Jo; T. Roh; S. Kim; Y.-C. Youn; M.S. Park; K.J. Han; E.K. Jang, *J. Environ Sustain.*, **2015**, *7,* 16820-16835.
2. M. Arfanuzzaman, R. Atiq, *Glob. Ecol. Conserv.*, **2017**, *10*, 9-22.
3. K. Webster, The Circular Economy: A Wealth of Flows - 2nd Edition; Ellen MacArthur Foundation Publishing, Cowes, UK, **2017**, pp. 110-200.
4. S. G. Thornhill, M. Kumar, *Life Sci. Space Res.*, **2018**, *17,*40-43.
5. E. Zanacic, J. Stavrinides, D. W. McMartin, *J. Water Res.*, **2016**, *104,* 397-407.
6. Q. Xiaolei, P. J. J. Alvarez, L. Qilin, *J. Water Res.*, **2013,** *47,* 3931-3946.
7. T. Wang, J. Kim, A. J. Whelton, Resour. Conserv. Recycl., **2019**, *140,* 115-124.
8. K. Pietrucha-Urbanik, B. Tchórzewska-Cieślak, *Adv. Intel. Syst. Comput.* 14th International Conference on Dependability of Computer Systems, DepCoS-RELCOMEX, **2019**, *987*, 411-424.
9. S. Butaciu, M. Ponta, E. Darvasi, M. Frentiu, G. Horvath, T. Frentiu, *Studia UBB Chemia.*, **2016**, *3,* 299-310.
10. E. Radu, R. Balaet, E. Vliegenthart, P. Schipper, *Environm. Eng. Res.*, **2010**, *15,* 085-091.
11. *** Law no. 458/2002 on the quality of drinking water, published in Romanian Official Monitor, part I, 875, 2011.
12. *** Law no. 311/2004 on the quality of drinking water, published in Romanian Official Monitor, part I, 582, 2004.
13. W. G. Morris, Atomic Force Microscopy, in Encyclopedia of Materials: Science and Technology - second Edition; Pergamon, New York, USA, **2003**, *Volume 1*, pp.1-6.
14. G. A. D. Briggs, B. J. Briscoe, Journal of Physics D: Applied Physics, **1959**, *Volume 10*, No. 18, p. 2453.
15. H.G. Crișan, O. A. Crișan, M. S. Pustan, C. J. Bîrleanu, V.V. Merie, Microscopic testing and analysis of drinking water filters after the final life cycle, using an experimental stand, presented at The 14th International Conference on Tribology (ROTRIB'2019), Cluj-Napoca, **2019**.
16. *** Directive (EU) 2019/904 of the European Parliament and of the Council of 5 June 2019 on reducing the impact of certain plastic products on the environment (Text with EEA relevance), published in Official Journal of the European Union, series L 155 of June 5, **2019**.
17. *** SR EN ISO 7027/2001, standard for turbidity determination in water.
18. *** SR EN ISO 10523/2012, standard for measuring the pH value of water.
19. A. T. Rusu, Procedee și echipamente pentru tratarea și epurarea apelor – Îndrumător de laborator, UT Press, Cluj-Napoca, Romania, **2013**, pp.42-44; 49-51.
20. *** SR EN 27888/97, standard for measuring the standard for measuring conductivity in water.
21. *** SR EN ISO 5814/2013, standard which establishes the electrochemical method for determining the dissolved oxygen content in water.

22. C. Bîrleanu, M. Pustan, V. V. Merie, H. G. Crișan, P. Romanian Acad. A, **2019**, *20,* 174–183.
23. V. Bellitto, Atomic Force Microscopy – imaging, measuring and manipulating surfaces at the atomic scale, published online: Intech, **2012**.
24. L. Blunt, X. Jiang, Advanced techniques for assessment surface topography. Development of a basis for 3D surface texture standards "Surfstand", Butterworth-Heinemann Publisher, **2003**.

# AN ECOLOGICAL TREATMENT METHOD FOR IFOSFAMIDE CONTAMINATED WASTE WATER RESULTING FROM ONCOLOGICAL THERAPY

**VALENTIN ORDODI[a,b,*], ANA-MARIA PANĂ[a,*], ALINA DUMITREL[a,#], DANIEL HĂDĂRUGĂ[a], ANDRA TĂMAȘ[a], VASILE PODE[a], ANAMARIA TODEA[a], VIRGIL PĂUNESCU[c], ȘERBAN NEGRU[c]**

**ABSTRACT**. Ifosfamide is a potent alkylating agent used to treat many forms of human cancer. Exposure to this substance for the long term even in small quantities has serious negative effects on human health and the environment. This study presents an ecological method of electrochemical inactivation of ifosfamide in an automatic laboratory installation. The neutralization process consists of ifosfamide electrochemical and chemical oxidation via reactive chlorine species generated in situ at the anode of the electrochemical reactor with asymmetric current densities. The neutralization efficiency of ifosfamide using this method is approximately 99% if the duration of the electrodegradation process under the presented conditions is 30 minutes.

*Keywords*: *electrochemical wastewater treatment, ifosfamide, electrooxidation, asymmetric current density reactor*

## INTRODUCTION

In recent years, the problem of eliminating liquid waste from medical institutions by ecological methods has become increasingly acute. In most cases, incineration is not a viable solution for this category of waste due to the very large volumes, and at the same time, during incineration process a series of chemical compounds harmful to the environment are generated [1,2]. Medical units with an oncological profile generate large amounts of liquid waste

a  *Politehnica University of Timișoara, 2 Victoriei Square, RO-300006, Timișoara, Romania*
b  *SC Natural Ingredients R&D SRL, Tabacari Street, No. 10/1, RO-505200, Făgăraș, Romania*
c  *University of Medicine and Pharmacy "V. Babeș" Timișoara, 2 Eftimie Murgu Square RO-300041, Timișoara, Romania*
*  *These authors Contributed equally to this paper.*
#  *Corresponding author: alina.dumitrel@upt.ro*

VALENTIN ORDODI, ANA-MARIA PANĂ, ALINA DUMITREL, DANIEL HĂDĂRUGĂ, ANDRA TĂMAȘ, VASILE PODE, ANAMARIA TODEA, VIRGIL PĂUNESCU, ȘERBAN NEGRU

(i.e. patients' urine) that often contains significant amounts of cytostatic drugs either unmetabolized or metabolized into other species with cytotoxic, mutagenic, carcinogenic and teratogenic activity. In 1996, the International Agency for Cancer Research (IARC) proposed the use of chemical treatments with oxidizing agents, acids or bases for the neutralization of cytostatic wastewater [3,4].

Nowadays, hematooncology is increasingly using high-dose cytostatic therapies associated with stem cell transplantation in order to save a large proportion of patients who until recently were considered incurable. Ifosfamide is one of the most commonly used cytostatic drugs in these treatments, administrated in high-doses per day from which approximately 50% is excreted unchanged in patients' urine [5,6].

The aim of this current study is the design and testing of an automated laboratory installation that allows inactivation of ifosfamide content from contaminated wastewater by chemical and electrochemical oxidation in a reactor with asymmetric current densities [7,8]. In the literature, electrochemical methods are used relatively frequently to remove hazardous pollutants but ordinary electrochemical reactors are used having electrodes with equal surfaces that can not only promote the oxidation reaction of the pollutants, thus implicitly generating reduced forms of them which themselves constitute potential polluting agents. The major advantage of the installation presented in the paper is the use of the electrochemical reactor with asymmetrical current densities, which is especially favoring the anodic electrooxidation reactions by using an anode with a significantly larger surface area than the cathode. This constructive aspect ensures a high efficiency of inactivation of cytotoxic pollutants compared to a regular electrochemical reactor. Compared to the classical methods, the electrochemical methods are much more eco-friendly [9].

## RESULTS AND DISCUSSIONS

The experimental installation designed by our group, consists of three distinct parts: the electrochemical reactor with asymmetric current densities, hydraulic part and the automation devices [10]. Figure 1 presents the scheme of experimental installation depicted at large in the experimental section. The ifosfamide contaminated wastewater from tank-14 is fed inside the electrochemical reactor-1. The electrochemical reactions takes place for about 30 minutes, during which samples are being collected from time to time and analyzed by HPLC in order to determine ifosfamide contents. After reaction completion, the treated ifosfamide wastewater is placed in tank-17. The experiment involved several runs, using an artificial sample with predefined ifosfamide content (50 mg/dL) and samples of urine from patients under the cytostatic therapy.
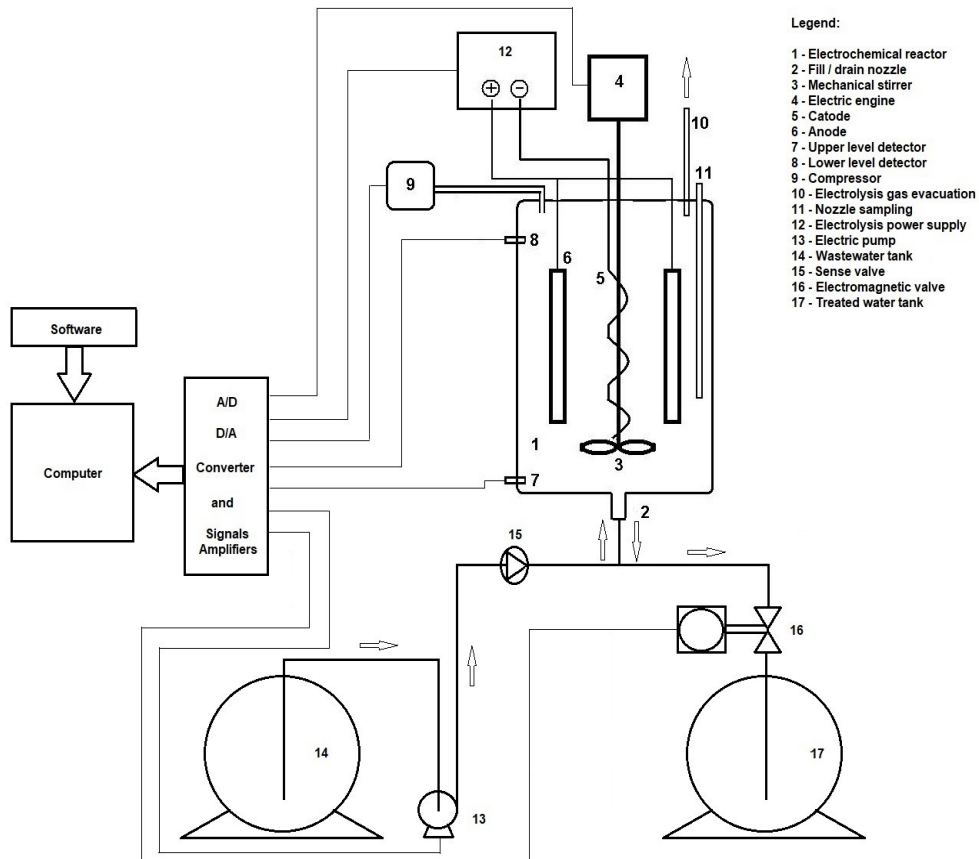
**Figure 1**. The simplified scheme of laboratory-scale ifosfamide
wastewater depuration installation

The evolution of the ifosfamide concentration during treatment of artificial wastewater and the urine samples from the ten patients is presented in Table 1. The ifosfamide concentration is gradually decreasing until dropping below the limit of detection (LOD) of the HPLC detector in about 30 minutes. The calculated values for the detection and quantification limits were: LOD = 0.05 mg ifosfamide/dL, and LOQ = 2.54 mg ifosfamide/dL.

VALENTIN ORDODI, ANA-MARIA PANĂ, ALINA DUMITREL, DANIEL HĂDĂRUGĂ, ANDRA TĂMAȘ,
VASILE PODE, ANAMARIA TODEA, VIRGIL PĂUNESCU, ȘERBAN NEGRU

**Table 1**. Evolution of ifosfamide concentration during electrochemical
treatment for synthetic and urine samples

| Time (min) | 0 | 1 | 2 | 3 | 4 | 5 | 10 | 15 | 30 |
|---|---|---|---|---|---|---|---|---|---|
| Ifosfamide artificial sample [mg/dL] | 50 | 35 | 27 | 20.5 | 14 | 12 | 3 | 0.3 | - |
| Sample 1 [mg/dL] | 32 | 24 | 19 | 14 | 11 | 9 | 0.6 | 0.2 | - |
| Sample 2 [mg/dL] | 43.5 | 33 | 26.5 | 19 | 14.5 | 11.5 | 0.8 | 0.3 | - |
| Sample 3 [mg/dL] | 30 | 22 | 17 | 12.5 | 10 | 8 | 0.6 | 0.2 | - |
| Sample 4 [mg/dL] | 32 | 24 | 18.5 | 13.5 | 10 | 7 | 0.6 | 0.3 | - |
| Sample 5 [mg/dL] | 42 | 31 | 25 | 18 | 14 | 11 | 0.7 | 0.2 | - |
| Sample 6 [mg/dL] | 41 | 31 | 23 | 16.5 | 12 | 10 | 0.7 | 0.4 | - |
| Sample 7 [mg/dL] | 54 | 40 | 32 | 23 | 18 | 14 | 1 | 0.3 | - |
| Sample 8 [mg/dL] | 36 | 27 | 22 | 16 | 12.5 | 9.5 | 0.6 | 0.2 | - |
| Sample 9 [mg/dL] | 24 | 18 | 14 | 10.5 | 8 | 6.5 | 0.4 | 0.1 | - |
| Sample 10 [mg/dL] | 36 | 26 | 21 | 15 | 11.5 | 9 | 0.7 | 0.3 | - |

Figure 2 shows the variation of ifosfamide concentration from artificial sample during electrochemical depuration process obtained by regression curve. From the analysis of the experimental data it is observed that 15 minutes are sufficient for the inactivation of synthetic wastewater and 10 minutes for urine samples (ifosfamide concentration decreases below LOQ in all samples). From the chart, it can be noticed that the decreasing in ifosfamide concentration during electrochemical process follows an exponential equation (1) obtained by regression curve:

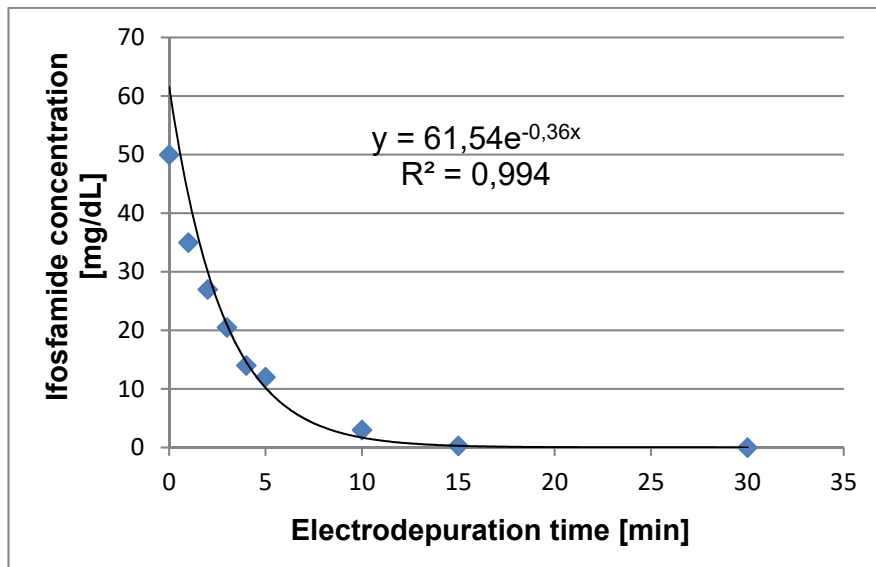$$C_{ifosfamide} = 61,54 \cdot e^{-0,36 \cdot t} \tag{1}$$

**Figure 2.** Variation of ifosfamide concentration from artificial wastewater during electrochemical depuration

The correlation coefficient ($R^2 = 0,994$) indicates that equation (1) fits very well the evolution of ifosfamide concentration from synthetic wastewater during the electrochemical process of treatment [11,12].

Ifosfamide is a cyclophosphamide isomer, having one of the N-chloroethyl substituents moved to the nitrogen atom from the oxazophosphoric ring. The mechanism of action is similar to that of cyclophosphamide. From the pharmacokinetic data it is found that the bioavailability of the product is 100%, the half-life is 5-6 hours, and the renal elimination is 50% unchanged. Ifosfamide is administrated in patients in high doses of 2 - 3 $g/m^2$ body surface area per day in bone marrow transplantation procedure.

Experimental data show that this electrochemical method is efficient for purifying wastewater with ifosfamide content. The operating parameters of the electrochemical treatment device have been optimized through a series of preliminary experiments. The concentration of 5% NaCl solution was optimal in terms of the speed of the electrochemical process, under the conditions in which it was desired to minimize the amount of reagents used. Also the intensity of the electrolysis current of 1 A ensures a reasonable speed of inactivation of the cytotoxic agent, avoiding an excessive heating of the electrolyte that

would generate harmful vapors and would require the existence of a cooling system that would increase the total energy consumption of the installation. The most likely mechanism of this degradation is presented by the sequence of reactions shown in Figure 3.
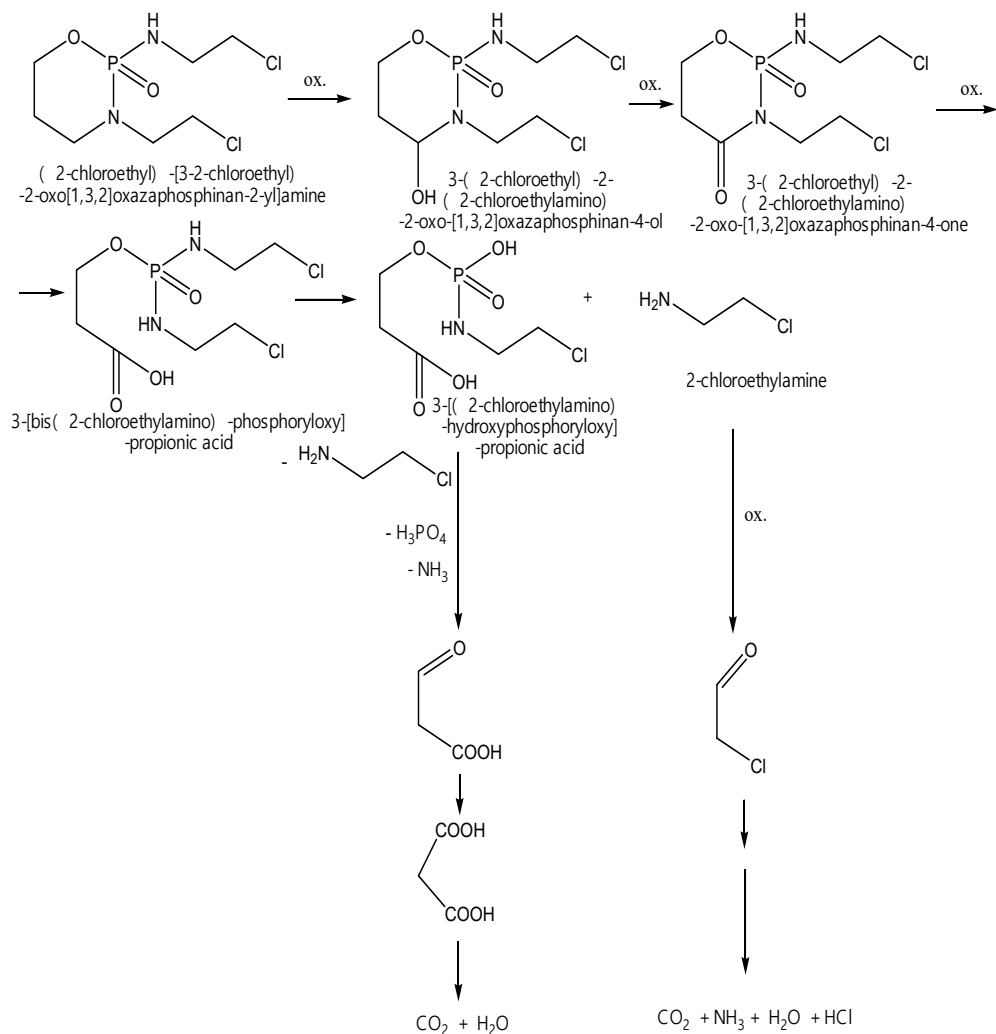


**Figure 3**. Degradation mechanism of ifosfamide
by electrochemical oxidation

From the analysis of the experimental data obtained from the depuration of the urine samples from the 10 patients it is observed that they are very close to the theoretical regression curve calculated using the equation (1) and shown in Figure 4. This confirms that the proposed electrochemical method can be successfully applied to any urine sample containing ifosfamide within the specified concentration range.
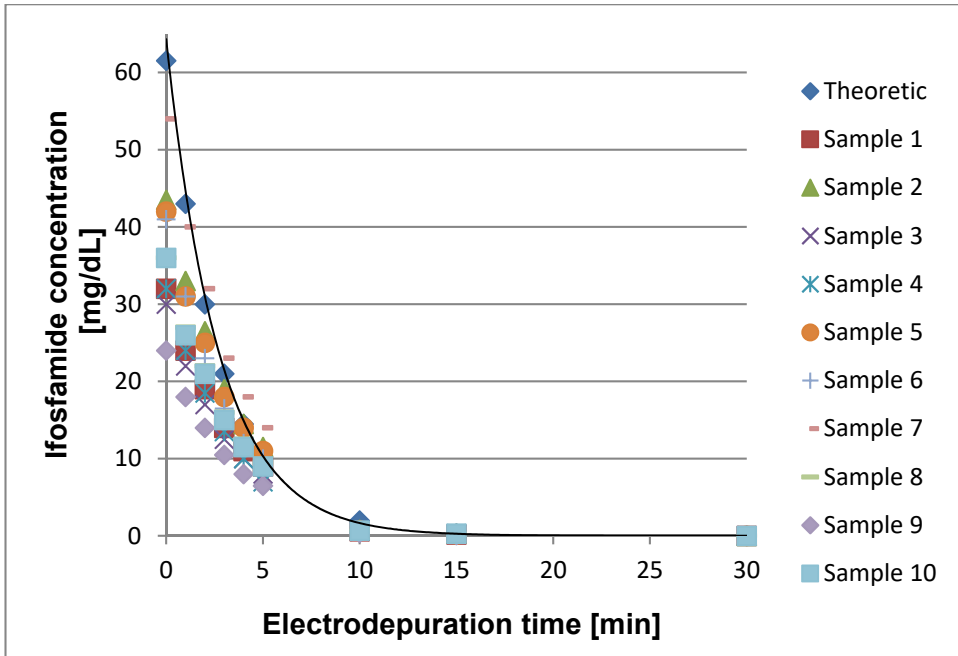


**Figure 4.** Experimental data obtained during electrochemical depuration of ten urine samples vs. theoretical model applied on the synthetic sample.

The yield of the electrochemical degradation (2) was calculated using the initial average concentration ($C_i$) of the ten urine samples before the electrochemical treatment and the final average concentration ($C_f$) after 10 minutes of degradation treatment (value below LOQ), right before the concentrations drops below the limit of detection. Equation (2) displays the average calculated yield for the electrochemical method of ifosfamide wastewater treatment using average concentrations of the real urine samples:

$$\eta_{ifosfamide} = 100 - \frac{C_f}{C_i} * 100 = 99.33\% \tag{2}$$

273

VALENTIN ORDODI, ANA-MARIA PANĂ, ALINA DUMITREL, DANIEL HĂDĂRUGĂ, ANDRA TĂMAȘ, VASILE PODE, ANAMARIA TODEA, VIRGIL PĂUNESCU, ȘERBAN NEGRU

## CONCLUSIONS

The proposed electrochemical method and the experimental installation presented are very well suited for treatment of wastewater with ifosfamide content from medical institutions with an oncological profile. The use of electrochemical reactors with asymmetric current densities represents an ecological method of treatment of these wastewaters, as their products are mostly compounds with reduced impact onto environment in the given concentrations.

## EXPERIMENTAL SECTION

### Description of the experimental installation and the operating mode

The experimental installation consists of: the electrochemical reactor with asymmetric current densities, tanks for sample storage and related pumps and the automation devices [10]. Figure 1 presents the scheme of the laboratory-scale experimental installation.

The most important part of the experimental installation is the electrochemical reactor with asymmetric current densities (fig. 1 - 1), made up of a plexiglass container with a useful volume of 100 cm$^3$, with a filling / draining nozzle at the bottom (fig. 1 - 2), a mechanical stirrer (fig. 1 - 3), operated by an electric micro-motor (fig. 1 - 4). The cathode of the reactor (fig. 1 - 5) is constructed from a stainless steel wire spiraled around the shaft of the mechanical stirrer with a diameter of 1 mm and a length of 115 mm, having a working surface of 3.6 cm$^2$. The anode (fig. 1 - 6) is made of 8 graphite bars connected in parallel from an electrical point of view, with a total usable area of 45.2 cm$^2$. Under the experimental conditions presented in this paper, the anodic current density is 220 A/m$^2$, while the cathodic current is 2700 A/m$^2$. The power supply of the electrochemical reactor (fig. 1 - 12) generates a constant current (1 A) throughout the electrolysis thus maintaining the kinetic constant of the electrochemical process. To remove the gases resulting from the electrochemical process, the reactor is continuously purged with compressed air (100 cm$^3$ / min) generated by a microcompressor (fig. 1 - 9) and discharged out of the laboratory through the corresponding nozzle (fig. 1 - 10). For sampling of the reaction mass for physico-chemical analyses, the reactor is provided with a nozzle valve (fig. 1 - 11). The reactor is provided at the top and bottom respectively with two level sensors (fig.1 - 7,8) through which the electric pump is controlled during the filling of the reactor, respectively the electromechanical valve

for draining [11]. The hydraulic part includes the wastewater tank (fig. 1 - 14) with the volume of 2 L from which the water is fed to the reactor using an electric pump (fig. 1 - 13). In order to avoid water leakage back, a sense valve is mounted on the hydraulic path immediately after the pump. The purified waste water is evacuated from the reactor by means of the electromechanical valve (fig. 1 - 16), in a storage tank of 2 L capacity (fig. 1 - 17).

The automation device includes an acquisition board (LabJak U3) with appropriate amplifiers for all signals, a laptop, and custom made software. This device controls the filling and emptying of the reactor by means of level sensors, the electric pump and the electromechanical valve, as well as the duration of the electrolysis by controlling the power supply of the electrochemical reactor. Additionally, this device controls the operation of the mechanical agitator and the compressor for the exhaust gases resulting during the electrochemical process [14,15].

## Depuration of Ifosfamide contaminated wastewater

For these experiments, urine samples were collected from 10 patients treated for various malignant lymphomas. The administered doses were in the range 3.4 - 5.1 grams ifosfamide in 24 hours. Of this, about 50% is eliminated unchanged by the kidneys and along the urine of the respective patients the environment is contaminated.

The medium concentration of ifosfamide in the analyzed samples was 37 mg/dL in the salefied urine (5% NaCl). An artificial ifosfamide wastewater with a concentration of 50 mg/dL ifosfamide in 5% NaCl solution was also prepared and compared against the real samples. Depuration duration was 30 minutes for all samples including the artificial waste water, at electrolysis constant current 1A [16,17,18].

For the collection of urine samples, each patient completed and signed an informed consent and obtained the approval of the Bioethics Commission of the University of Medicine and Pharmacy "V. Babeș" Timișoara.

Ifosfamide concentrations were measured using a high performance liquid chromatography (HPLC) - Agilent 1100 system equipped with a spectrophotometric detector. The analysis conditions were as follows: mobile phase acetonitrile : water = 20 : 80. The pH of the samples was adjusted to 5 with phosphate buffer. The mobile phase flow rate was constant: 1 mL / min. A 20 μL sample was injected into a C18 Zorbax SB column at $25^0$C temperature. The spectrophotometric detector was set at 373 nm. The acquisition time was 10 minutes for each sample [19,20]. Prior to HPLC analysis, all samples were treated with a 5% sodium thiosulphate solution (100 μL to 900 μL sample) to neutralize traces of free chlorine and kept in the refrigerator until analysis.

VALENTIN ORDODI, ANA-MARIA PANĂ, ALINA DUMITREL, DANIEL HĂDĂRUGĂ, ANDRA TĂMAȘ,
VASILE PODE, ANAMARIA TODEA, VIRGIL PĂUNESCU, ȘERBAN NEGRU

To determine the concentration of ifosfamide in the studied samples, both synthetic residual water with ifosfamide content and urine samples from patients, a calibration curve was constructed using ifosfamide (≥ 98%) purchased from Sigma-Aldrich, in the concentration range 0 , 1 - 50 mg / dl. For all concentrations, three determinations were made. Figure 5 shows graphically the average values of the areas corresponding to the peaks of ifosfamide for each concentration.
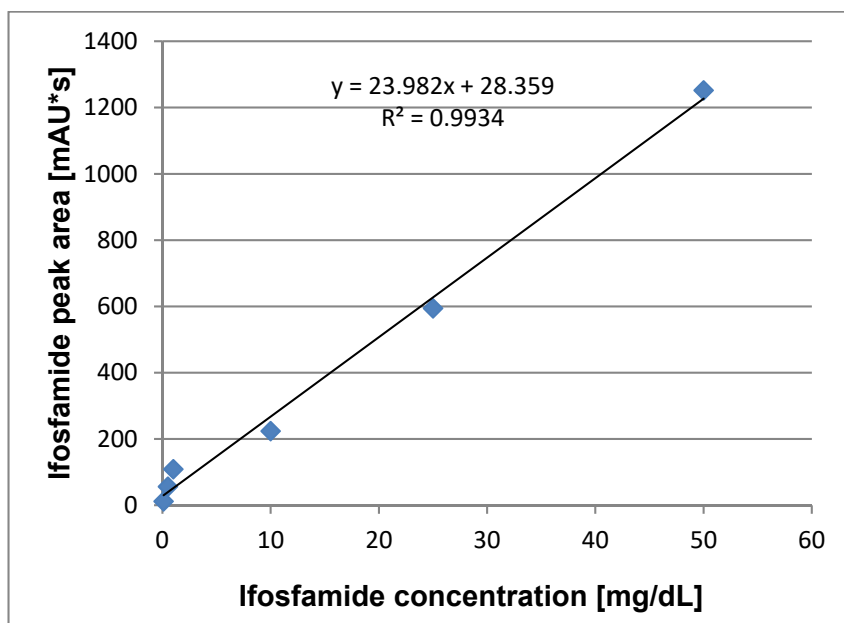


**Figure 5**. Ifosfamide HPLC calibration curve

The limit of detection (LOD) and the limit of quantification (LOQ) were estimated with the following mathematical relations:

$$LOD = \frac{(3{,}3 \cdot SD) - intercept}{slope} \qquad (3)$$

and

$$LOQ = \frac{(10 \cdot SD) - intercept}{slope} \qquad (4)$$

276

# REFERENCES

1. S. Hellweg, B. Thomas, H. K. Hungerbühler, "Modeling waste incineration for life-cycle inventory analysis in Switzerland. Environmental Modeling and Assesment", Kluwer Academic Publishers, **2001**.
2. E. A. Cociş, V. F. Soporan, P. Ilea, F. Imre-Lucaci, B. M. Soporan, P. Bere, O. Nemeş, *Studia UBB Chemia*, **2012**, LVII, 2, 147.
3. International Agency for Research on Cancer, "IARC Monograph on the Evaluation of Carcinogenic Risks to Humans: List of IARC Evaluations" IARC Lyon, France, **1996**.
4. M.Ikematsu, K. Kaneda, M. Iseki, M. Yasuda, *Sci. Total Environm.*, **2007**, *382*, 159-164.
5. F.I Badulescu, V. Voicu, L. Pop, A. Badulescu, "Vademecum de chimioterapie antineoplazica", Editura Medicala, Bucuresti, **1999**.
6. N. Ghilezan, "Oncologie Generala", Editura Medicala, Bucuresti, **1982**.
7. M.C. Mirica, "Reactoare electrochimice cu densităţi de curent asimetrice", Teză de doctorat, Craiova, **2005**.
8. K. Yoshida, "Electrooxidation in Organic Chemistry", Krieger Publishing Company, Malabar Florida **1993**.
9. S. Fogarasi, F. Imre-Lucaci, A. Ghirişan, B. R. H. Mişca, A. Imre-Lucaci, *Studia UBB Chemia*, **2016**, *LXI(3),* 145.
10. D. J. Pickett, "Electrochemical reactor design", Elsevier, Amsterdam, **1979**.
11. A. Nichici, E. Cicală, R. Mee, "Prelucrarea datelor experimentale. Curs şi aplicaţii", Centrul de multiplicare, Timişoara, **1996**.
12. G.A. Brusturean, T. Todinca, D. Perju, J. Carre, *Environm. Technol*, **2007**, *28(10)*, 1153-1162.
13. V. Ordodi, G.A. Dumitrel, A. Gruia, M. Iacob, A. F. Mic, G. Jinescu, D. Perju, *Revista de Chimie (Bucharest)*, **2010**, *61(9),* 857-861.
14. J. Hirose, F. Kondo, T. Nakano, T. Kobayashi, N. Hiro, Y. Ando, H. Takenaka, K. Sano, *Chemosphere,* **2005**, *60*, 1018-1024.
15. M. Ikematsu, K. Kaneda, M. Iseki, M. Yasuda, *Sci. Total Environm.*, **2007**, *382*, 159-164.
16. S. Hansel, M. Castegnaro, M. H. Sportouch, M. De Meo, J. C. Milhavet, M. Laget, G. Dumenil, *Int. Arch. Occup. Environm. Health*, **1997**, *69*, 109-114.
17. A. Oprisoni, S. Arghirescu, C. Jinca, L. Balint-Gib, A. Isac, V. Ordodi, M. Baica, G. Doros, M. Serban. Abstracts of the 36th Annual Meeting of the European Group for Blood and Bone Marrow Transplantation, *Bone Marrow Transplantation*, **2010,** *45*, S78-S327.
18. B. B. Park, W. S. Kim, H. S. Eom, J. S. Kim, Y. Y. Lee, S. J. Oh, D. H. Lee, C. Suh, *Invest New Drugs*, **2011**, *29*, 154-160.
19. R. R. Larson, M. B. Khazaeli, H. K. Dillon, *Applied Occupational and Environmental Hygiene*, **2003**, *18(2)*, 109-119.
20. J.J. Kirkland, L.R.Synder, "Introduction to Modern Liquid Chromatography", 2nd Edition, Jon Wiley and Sons, New York, **1979**.

# ENZYMATIC DEGRADATION OF AZO DYES USING PEROXIDASE IMMOBILIZED ONTO COMMERCIAL CARRIERS WITH EPOXY GROUPS

**PAULA BORZA[a], IOANA CRISTINA BENEA[a], IOAN BÎTCAN[a], ANAMARIA TODEA[a*], SIMONA GABRIELA MUNTEAN[b*], FRANCISC PETER[a]**

**ABSTRACT.** The treatment of colored wastewater has been paid attention in the recent years because of the high amount of dyes, mostly carcinogenic, discharged into the water. Enzymatic degradation shows several advantages such as: shorter processing time, reduction in sludge volume and ease of controlling the process. In this work, seven different industrial dyes were tested as substrates for horseradish peroxidase. The native enzyme was covalently immobilized onto two types of epoxy-supports, different in spacer length. Among the tested dyes the highest substrate conversions were achieved for Amido Black 10 (AB10). The highest recovered activity was obtained when the epoxy-activated support with longer spacer arm was used. After ten reuse cycles for the degradation of AB10, the covalently bound peroxidase preserved about 80% of the initial activity.

*Keywords: horseradish peroxidase, biocatalysis, ReliZyme™ support, covalent immobilization, dye degradation, environment*

## INTRODUCTION

The use of enzymes for treatment of waste waters containing dyes was intensively studied, based on the capacity of enzymes to modify the original structure of dyes and thus obtaining compounds that can be degraded or eliminated more easily [1,2,3]. A wide range of enzymes, mainly oxidoreductases, have been proven to be excellent catalysts in the wastewater purification process, due to the mild reaction conditions, the ability to transform complex substances and higher reaction rates compared to chemical catalysts [2,3,4]. Oxidoreductases are able to catalyze degradation of phenols, anilines, benzidines, chlorophenols and various heterocyclic aromatic substances [5].

[a] *University Politehnica Timisoara, Faculty of Industrial Chemistry and Environmental Engineering, Biocatalysis Group, C. Telbisz 6, 300001 Timisoara, Romania*
[b] *"Coriolan Drăgulescu" Institute of Chemistry, Mihai Viteazul 24, 300223 Timisoara, Romania*
\* *Corresponding authors: anamaria.todea@upt.ro, sgmuntean@acad-icht.tm.edu.ro*

PAULA BORZA, IOANA CRISTINA BENEA, IOAN BÎTCAN, ANAMARIA TODEA,
SIMONA GABRIELA MUNTEAN, FRANCISC PETER

Several factors can influence the degradation of residual dyes, such as the concentration and structure of dye, the presence of other compounds, pH and temperature of the effluent [6]. When enzymes are employed for the elimination of pollutants from waste waters, the properties of the biocatalyst must be properly tuned in order to ensure the highest efficiency, considering all these factors. Plant peroxidases have been extensively studied as a useful tool for bioremediation of industrial waste. Particularly, horseradish peroxidase (HRP) is a widely used catalyst in enzymatic reactions [7]. HRP proved important advantages including high activity and selectivity, high resistance to inhibition by various compounds over a broad concentration range, as well as high operability and reliability in different treatment conditions [5]. Studies have shown that in the presence of H2O2 HRP can effectively precipitate a wide variety of organic compounds, aromatic compounds, and recalcitrant contaminants, such as dyes and phenolic compounds. HRP has been extensively used in wastewater treatments as it offers long lifetime, stability and also retention of the enzymatic activity over a broad range of temperature and pH [8].

Recently it was found that chlorophenols, labeled as "priority pollutants" by the US Environmental Protection Agency, can be removed from contaminated water by HRP. Like other native enzymes, HRP has several drawbacks such as low stability, short lifetime, high susceptibility to inactivation, and difficulty in re-using [9]. Immobilization proved to be a viable solution to overcome these drawbacks, improving the activity, stability, and recovery of the enzyme. Moreover, immobilized enzymes could be broadly applied to various reaction environments and harsh conditions [9].

The immobilization of HRP was carried out using several supports: modified chitosan, polymeric acrylamide matrix, alginate, glycidyl methacrylate copolymers, glutaraldehyde-activated aminopropyl glass beads, magnetite, ion exchange resins, and various polymers [4,11,12,13].

Immobilization by covalent binding is considered appropriate for obtaining solid-phase biocatalysts with high operational stability [14]. Alongside the physical properties of the support, the structure and reactivity of the active group attached to the carrier is essential for a successful immobilization. Epoxy activated supports are very stable, can be stored for a long time and can be applied for immobilization of the enzymes to be used in the laboratory or at industrial scale [15]. Immobilization of enzymes on supports activated with epoxy groups is achieved by covalent bonding, thus increasing the stability of the enzyme, and diminishing the possible adverse effects of organic solvents, formed 9 products or temperature on the activity of the enzyme [16,17]. Covalent bonds are formed between the support and nucleophilic groups from the enzyme structure, such as amino, hydroxy or thiol groups. By covalent immobilization on such supports, the conformational changes are greatly diminished [16].

There are reports of immobilization on epoxy-activated polyacrylamide beads, like as Eupergi C [18]. Another possibility is to use a long-chained cross-linker holding epoxy groups. A ZnO nanowires/macroporous $SiO_2$ nanocomposite was used as support for HRP immobilization by in situ cross-linking, with diethylene glycol diglycidyl ether as cross-linker [19].

Although there are several studies on HRP immobilization, the utilization of commercial epoxy-functionalized methacrylate carriers was not yet reported. Compared to many other support materials, these carriers have the advantage of reproducible properties, large-scale availability, and convenient price. The aim of the present study was to develop a protocol for the covalent immobilization of HRP on epoxy-functionalized beads and to use the obtained biocatalysts for the degradation of industrial azo dyes. The effects of temperature and pH on the enzyme activity, as well as the operational stability have been evaluated for both free and immobilized

HRP, using AB10 dye as model substrate. The influence of hydrogen peroxide concentration was also studied. The results may provide new opportunities for the application of immobilized enzymes in the field of environmental protection, allowing the efficient oxidative degradation of residual dyes.

## RESULTS AND DISCUSSION

### The selectivity of HRP for commercial azo dyes

The selectivity of the HRP was tested using the native enzyme and six substrates, at 25°C and two pH values, 3.5 and 6.0. The chemical structures of the selected dyes are presented in Figure 1S (Supplementary material). The results obtained after 24 h of reaction, shown in Figure 1, indicate that at pH 3.5 the conversions were lower compared to those obtained at pH 6.0, except for the Neutral gray dye. At pH 6, the highest conversions values (up to 80%) were obtained for Amido Black 10 (AB 10) and Acid Orange 7 (AO 7) dyes.

Considering these results, the AB10 dye was used as substrate in the following experiments.

### The effect of hydrogen peroxide concentration

Recent studies have shown that for HRP there is an optimal hydrogen peroxide/dye molar ratio [2]. However, addition of excess hydrogen peroxide, after conversion has reached optimal value, favored the dye degradation process. A possible explanation for this phenomenon might be that addition of excess $H_2O_2$ at the beginning of the process leads to formation of a larger amount of intermediate products which inhibit the peroxidase activity, or even excess hydrogen peroxide can inhibit the activity of the enzyme [2].
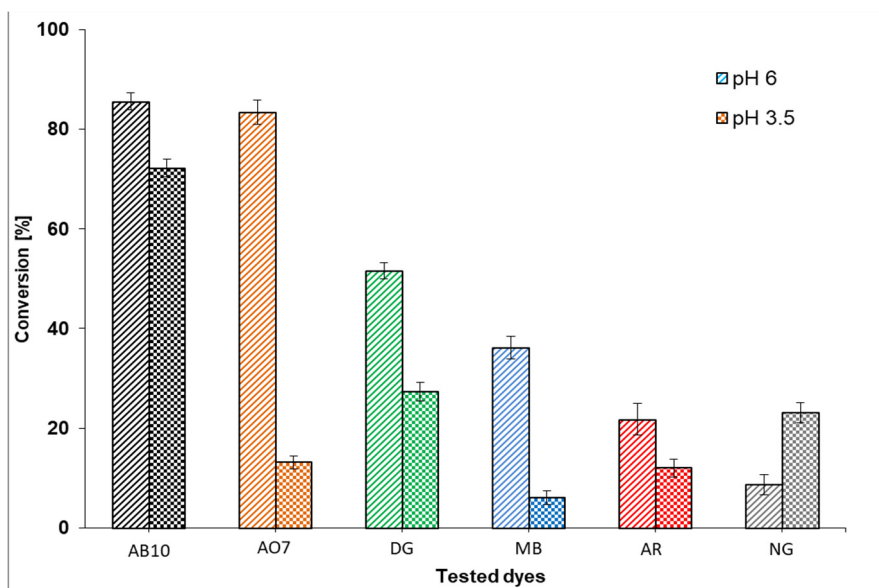
PAULA BORZA, IOANA CRISTINA BENEA, IOAN BÎTCAN, ANAMARIA TODEA,
SIMONA GABRIELA MUNTEAN, FRANCISC PETER

**Figure 1.** Comparative evaluation of the selectivity of HRP for degradation of six
different dyes (AB 10 - Amido Black 10, AO7 - Acid Orange 7, DG - Direct green;
MB - Methylene blue; AR - Acid red; NG - Neutral grey)

As hydrogen peroxide acts as co-substrate, three concentrations
were tested. The results, presented in Figure 2, show that at concentrations higher
than 1.43 mM there were no changes in activity, therefore in the subsequent
studies the $H_2O_2$ concentration was set at 1.43 mM.
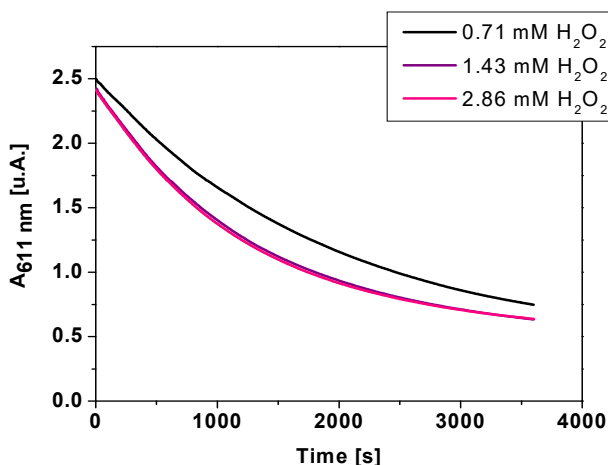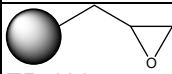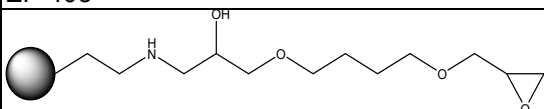


**Figure 2**. The effect of hydrogen peroxide amount on the decrease
of absorbance at 611 nm in time, using AB10 dye as substrate

## Immobilization of HRP onto ReliZyme™ supports

The practical interest on peroxidases, illustrated by the increasing number of publications in the past years, reveals that the research towards stabilization of this enzyme still presents scientific importance. Among the available immobilization methods, a simple and rapid covalent binding was selected. Considering that the biocatalyst was designed to be used in aqueous solutions, the covalent binding could also avoid the leaching of the enzyme from the support.

Two commercial ReliZyme™ supports, with active epoxy groups and different chain length and structure of the spacer arm, were selected (Table 1). The immobilization was performed in a single step, by mixing the enzyme solution with the support for 24 h. The activity of the immobilized HRP was determined by using ABTS as substrate, as described in the experimental part. The results, presented in Table 1, indicate high protein loading values (>90%), for both support types. The specific activity and the reproducibility were higher when the epoxy-amino HFA 403 support was used. Probably, the longer spacer arm favors multipoint covalent attachment of the enzyme to the epoxy groups of the support. However, considering the high immobilization efficiencies, the characterization studies were performed for both biocatalysts and the results were compared to the native enzyme.

**Table 1**. Protein loading and recovered activity of HRP immobilized
onto epoxy- ReliZyme™ supports

| Type of the solid support | Protein loading [%] | Specific activity [U g protein$^{-1}$] |
|---|---|---|
|  EP 403 | 93.5 | 21.24 ± 2.36 |
|  HFA 403 | 99.6 | 37.24 ± 0.78 |

## Comparative characterization of the native and immobilized horseradish peroxidase

### *Modification of the pH profile by immobilization*

pH is one of the most important factors influencing the enzyme activity, because at extreme pH values the activity can be inhibited [20]. Often, for native enzymes the highest activity is in a relatively narrow pH range, and this shortcoming can be overcome by immobilizing the enzyme [20,21]. The reactions

were carried out at 25 °C, in the presence of 1.43 mM $H_2O_2$, for 30 minutes, under stirring at 300 rpm. Compared to the native enzyme that showed the optimal pH at 5, the activity of the immobilized biocatalyst was improved over the whole tested pH range (Figure 3).
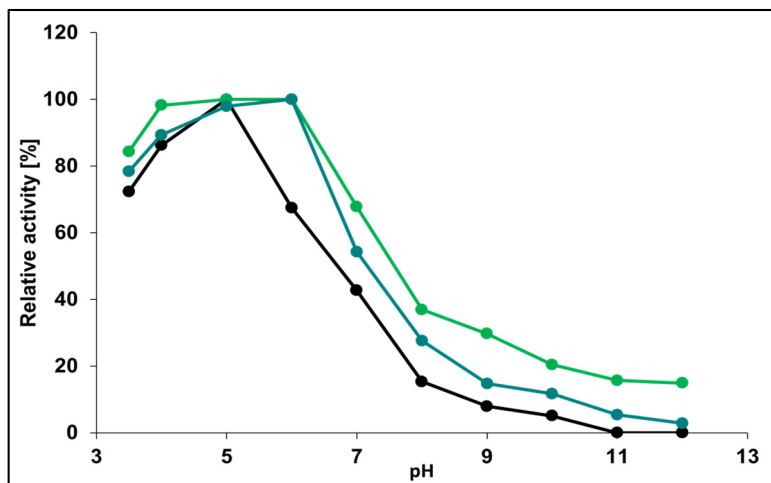


**Figure 3**. Effect of pH on the decolorization of Amido Black 10 dye by native (black color), and immobilized HRP on HFA 403 (green color) and EP 403 (turquoise color) carriers. Reaction conditions: 25°C, 30 min, 1.43 mM $H_2O_2$, 300 rpm

The highest activity was obtained for the HRP-HFA biocatalyst, in the pH range 4-7.

An improvement of the pH stability of HRP by immobilization was also observed by Bilal et al., when calcium alginate was used as support and glutaraldehyde as linker [23]. The activity of the immobilized HRP on calcium alginate was at least 10% higher in the range 7-9 compared to the native enzyme. Mohameda et al. immobilized HRP onto activated wool support and Wool-HRP showed broad optimum pH at 7.0–8.0 [24].

### *Effect of temperature on the stability of immobilized peroxidase*

The stability of the enzymes decreases with increasing temperature, he enzyme becoming inactive at high temperatures, due to the irreversible modification of the tertiary structure. Several studies concluded that thermal inactivation can be limited by enzyme immobilization [20]. To evaluate the effect of temperature on the enzymatic activity, the native and immobilized enzymes were incubated for 1h at 25°C, 35°C, 45°C and 55°C, in buffer solution pH 5.0, then cooled at 25°C when the model substrate (AB10) was added. The assay was carried out in the presence of 1.43 mM $H_2O_2$, for 30 minutes at 300 rpm.
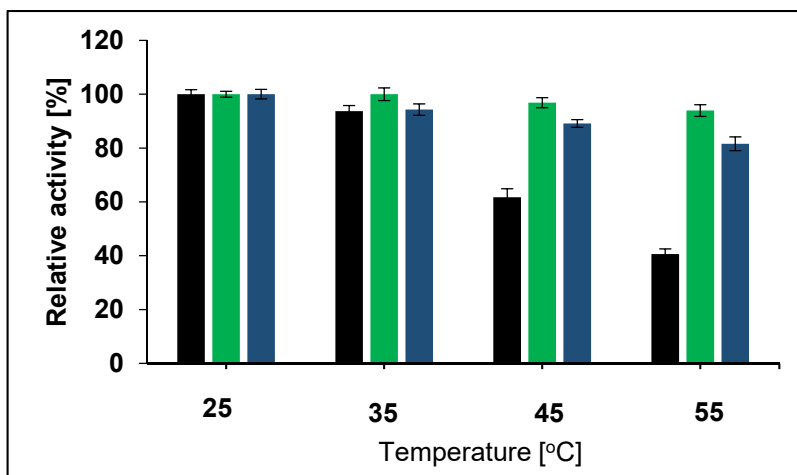
**Figure 4**. Thermal stability of native (black color) and immobilized horseradish peroxidase (on HFA 403, green color; on EP 403, turquoise color). The degradation of Amido Black 10 dye was carried out at 25°C, 30 min, 300 rpm, in presence of 1.43 mM $H_2O_2$

The results (Figure 4) indicate up to 60% activity loss for the native HRP with increasing temperature in the studied range, while the enzyme immobilized on both HFA 403 and EP 403 demonstrated excellent thermostability (only 6.1% and 18.4 % decrease, respectively). Among the two preparations, the HRP immobilized on HFA 403 showed superior thermal stability. Compared to ~84% recovered activity value for decoloring of Acid Black dye after incubation at 55°C, reported by Sun et al. for HRP immobilized onto ZnO nanowires/ macroporous $SiO_2$ and diethylene glycol diglycidyl ether as cross-linker [19], the 93.8% value obtained in this study indicates a higher thermal stability after immobilization, which could be explained by the multipoint attachment of the cross-linked HRP, improving the rigidification of the protein and protect it from denaturation [19].

## Operational stability of the immobilized enzyme

To increase the operational stability of the enzymes, in order to be reused in several production cycles, is one of the main objectives of immobilization. Provided that the immobilized enzyme does not lose its activity even after prolonged operational period, it can be employed in both continuous and discontinuous processes and the costs become lower [22].

The degradation of Amido Black 10 by HRP immobilized on HFA-403 epoxy-activated beads was studied in repeated batch reaction cycles, considering the activity of the first batch as reference. After ten cicles the relative activity

remained about 80% (Figure 5), an excellent value for an enzyme working in aqueous environment. Compared to previous literature reports concerning the reuse of HRP immobilized by different methods (Table 2), the operational stability of our preparate was higher, indicating the efficiency of the selected immobilization support and method.
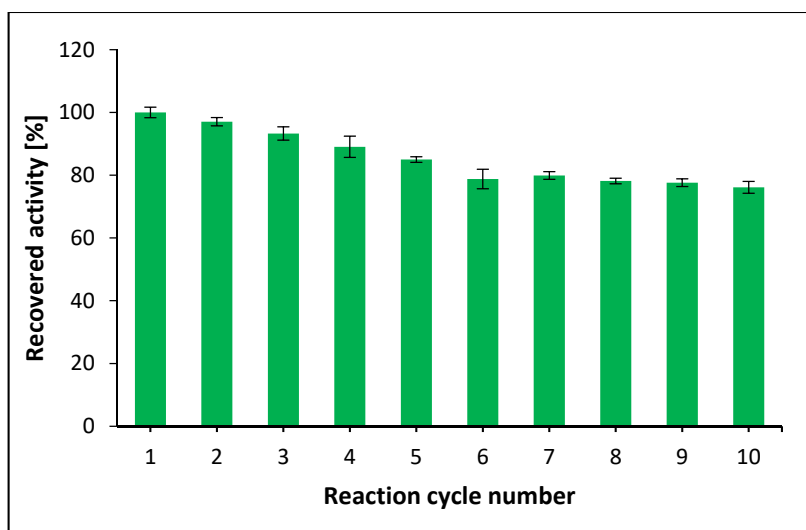


**Figure 5.** Stability of the peroxidase immobilized on HFA 403 epoxy beads, in repeated batches of Amido Black 10 degradation at 35°C, 30 min, 1.43 mM $H_2O_2$, 300 rpm.

**Table 2.** Comparative evaluation of several immobilized horseradish peroxidases, based on the recovered activities after repeated reaction cycles

| Immobilization method | Support | Linker | Reaction cycles | Recovered activity [%] | Ref. |
|---|---|---|---|---|---|
| Encapsulation | chitosan beads | - | 6 | 64.9 | [25] |
| Covalent binding | calcium-alginate | GA* | 7 | 40.0 | [23] |
| Covalent binding | activated wool | | 7 | 50.0 | [24] |
| Covalent binding | chitosan beads | hydrazine hydrate | 6 | 65.8 | [25] |
| Covalent binding | cashew gum polysacch. | GA | 9 | 50.0 | [27] |
| Covalent binding | nano-composite | epoxy cross-linker | 12 | 71.1 | [19] |
| Covalent binding | ReliZyme™ HFA 403 | - | 10 | 76.1 | This study |

*glutaraldehyde

## CONCLUSIONS

Horseradish peroxidase was successfully immobilized by covalent bonding, on two ReliZyme™ supports containing active epoxy groups. The immobilization on the HFA 403 support proved to be more advantageous, allowing probably a multipoint linkage. By immobilization, both the stability and the activity of the enzyme were improved over a wider range of pH, particularly in the pH range 5-6, which represents the typical pH of waters contaminated with dyes. In the basic domain, the enzymatic activity decreased significantly, but even at pH 11 the immobilized enzyme was still active, unlike the native enzyme which was completely inactivated.

The thermostability of the enzyme was considerably enhanced by immobilization. In the case of peroxidase immobilized on HFA 403, 90% of the initial enzymatic activity was recovered after incubation for 30 minutes at 55°C, while the native enzyme lost ~60% activity in the same conditions.

The selected immobilization method and support were also able to provide a stable end robust enzyme, suitable for several utilization cycles at high residual activity. The immobilized enzyme was successfully reused in batch decolorization processes, the activity remaining at 80% of the initial value after 10 cycles of use.

## EXPERIMENTAL SECTION

### Chemicals

Amido Black 10 B (AB10), Acid Orange (AO7), Acid Red (AR), Direct Green (DG), Methylene Blue (MB), Neutral Gray (NG) dyes were purchased from Merck (Germany) and Loba-Feinchemie (Austria). Sodium hydrogen phosphate, sodium dihydrogen phosphate (used to prepare the buffer solutions), hydrogen peroxide 35%, citric acid, boric acid, trisodium phosphate, and 2,2'-azino-di (3-ethylbenzothiazoline-6-sulfonate) (ABTS) were from Sigma-Aldrich Chemie GmbH (Germany). The horseradish peroxidase (HRP) used in the immobilization process and as reference native enzyme was also purchased from Merck. Both commercial supports utilized for covalent immobilization of HRP were products of Resindion S.r.l (Italy), a subsidiary of Mitsubishi Chemical: ReliZyme™ HFA 403 and ReliZyme™ EP 403 (polymethacrylate beads with oxiranyl active groups which differ by the length and structure of the spacer, oxirane content min. 30 µmol/g wet, average pore diameter 40÷60 nm).

## Determination of peroxidase activity using ABTS

The activity of the immobilized HRP was tested using a known method with ABTS as substrate [28]. 20 µL native peroxidase solution of (1 mg/mL), or 10 mg immobilized peroxidase, were added to 100 µL of 3 mM ABTS, followed by addition of 1498 µL citrate-phosphate buffer solution pH 5 and 40 µL $H_2O_2$. The absorbance was measured at 414 nm, after 5 minutes incubation at 25 °C, using a Jasco V-530 UV/vis Spectrophotometer (JASCO, Japan).

## Effect of hydrogen peroxide concentration

The influence of the co-substrate concentration ($H_2O_2$) was studied in the 0.21-2.86 mM range using AB10 as substrate. The decrease of the absorbance at 611 nm was continuously measured for 3500 s at 25 °C, using a Jasco V-530 UV/vis Spectrophotometer.

## Immobilization by covalent binding on epoxy supports

900 µl of peroxidase solution (1.5 mg / mL) in 50 mM phosphate buffer pH 6.5 was added to 100 mg epoxy-activated support. The mixture was incubated for 24 hours at 1000 rpm and 25° C. The immobilized peroxidase was separated by filtration. At the end of the immobilization, the resin was washed 3 times with 20mM phosphate buffer, pH 6.5, and stored at 4°C until subsequent use.

## pH profile of the immobilized peroxidase

The effect of pH on the activity of immobilized HRP (5 mg / mL) was investigated in the range of pH 4.0-12.0, using a wide pH buffer solution containing citric acid, boric acid and trisodium phosphate buffer [29]. The pH profile of native HRP (20 µL,1 mg / mL) was determined in the same conditions, as reference. The activity assay was performed as described in previous section.

## Degradation of azo dyes by immobilized HRP

Six different dyes were used to determine the decolorization percentage subsequent to oxidation with immobilized HRP at two pH values, 3.5 and 6. The dye solutions were at 10 mg/mL concentration, and the experiments were carried out in different pH buffers (1 mL buffer) at room temperature after 3 h, 12 h and 24 h, respectively. The decrease of the absorbance was monitored by using a Jasco V-530 UV/vis Spectrophotometer.

## Effect of temperature on the activity of immobilized HRP

The native (20 µL native enzyme 1 mg / mL)./ immobilized (5 mg / mL) enzyme was incubated for 2 hours in buffer, pH 5.0 in the absence of the substrate at different temperatures, in the range of 25ºC to 55ºC, followed by cooling on ice for 10 minutes and AB10 substrate was added and the decrease of the absorbance was monitored by using a Jasco V-530 UV/vis Spectrophotometer after 30 min.

## Repeated use of the biocatalyst

The immobilized HRP activity was determined after repeated use of the biocatalyst at 30°C for 2 hours buffer, pH 5, with Amido black 10 as substrate. After each cycle, the immobilized enzyme was separated by filtration and washed three times with 50 mM phosphate buffer pH 6.5. A new reaction cycle was performed by adding the same amount of buffer and substrate. The decolorization percentage achieved with the reused biocatalyst was determined as previously described, and the resulting value was compared to the first cycle (set as 100%).

**SUPPLEMENTARY MATERIALS** can be obtained by request from the authors.

# REFERENCES

1. S. Nouren; H.N. Bhatti; *Biochem. Eng. J.,* **2015***, 95*, 9-19.
2. F. Gholami-Borujeni; A. H. Mahvi; S. Naseri; M. A. Faramarzi; R. Nabizadeh; M.Alimohammadi; *Res. J. Chem. Environ.,* **2011**, *15(2)*, 217-220.
3. J. T. Chacko; K. Subramaniam; *Int. J. Environ. Sci.*, **2011**, *1(6),* 1250-1256.
4. M. Monier; D.M. Ayad; Y. SAA Wei; *Int. J. Biol. Macromol.*, **2010**, *46*, 324-330.
5. M. Matto; Q. Husain; *Ecotoxicol. Environ. Saf.,* **2009**, *72*, 965-971.
6. R. G. Saratale; G. D. Saratale; J. S. Chang; S.P. *Gowindvar; J. Taiwan. Inst. Chem. Eng.,* **2011**, *42*, 138-157.
7. G.R. Lopes; D.C.G.A. Pinto; A.M.S. Silva; *RSC Adv.*, **2014**, *4*, 37244-37265.
8. L. Y. Juna; L. S. Yon; N.M. Mubarak; C. H. Bing; S. Pan; M. K. Danquah; E.C. Abdullah; M. Khalid; *J. Environ. Chem. Eng.*, **2019**, 7, 1-14.
9. X. Xie; P. Luo; J. Han; T. Chen; Y. Wang; Y. Cai; Q. Liu; *Enzyme Microb. Technol.*, **2019**, *122*, 26-35
10. B. Yu; H. Cheng; W. Zhuang; C. J. Zhu; J. Wu; H. Niu; D. Liu; Y. Chen; H. Ying; *Process Biochem.*, **2019**, *79*, 40-48.
11. S. Venkata Mohan; K. Krishna Prasad; N. Chandrasekhara Rao; P.N. Sarma; *Chemosphere*, **2005**, *58*, 1097-1100.
12. O. Prodanović; M. Prokopijević; D. Spasojević; Z. Stojanović; K. Radotić; Z.D. Knežević-Jugović; R. Prodanović, *Appl. Biochem. Biotechnol.*, **2012**, *168*, 1288-1301.

13. J. L. Gómez; A. Bódalo; E. Gómez; J. Bastida; A. M. Hidalgo; M. Gómez; *Enzime. Microb. Technol*., **2006**, *39*, 1016-1022.
14. Z. Zhao; M. C. Zhou; R. L. Liu; *Catalysts*, **2019**, *9 (647)*, 1-15.
15. C. Mateo; O. Abian; R. F. Lafuente; J. M. Guisan; *Enzyme Microb. Technol.* **2000**, *26*, 509-515.
16. C. Mateo; V. Grazu; F. Lopez-Gallego; R. Fernandez-Lafuente; *Nat. Protoc*., **2007**, *2(5)*, 1022-1033.
17. C. Mateo; J. M. Palomo; G. Fernandez-Lorente; J. M Guisan; R. Fernandez-Lafuente, *Enzym. Microb. Technol.,* **2007**, *40*, 1451-1463.
18. L. Pramparo; F. Stüber; J. Font; A. Fortuny; A. Fabregat; C. Bengoa; *J. Hazardous Mat.*, **2010**, *177*, 990-1000.
19. H. Sun; X. Jin; N. Long; R. Zhang; *Int. J. Biol. Macromol.*, **2017**, *95*, 1049-1055.
20. E. Biró; D. Budugan; A. Todea; F. Péter; S. Klébert; T. Feczkó; *J. Mol. Catal. B Enzym.*, **2016**, *123*, 81-90.
21. B. Sahoo; S.K. Sahu; P. Pramanik; *J. Mol. Catal. B: Enzym*., **2011**, *69*, 95-102.
22. A. Cimporescu; A. Todea; V. Badea; C. Paul; F. Peter, *Process Biochem.,* **2016**, 51, 2076-2083.
23. M. Bilal; M. N. H. Iqbal; S. Z. H. Shah; H. Hu; W. Wang; X. Zhang; *J. Environ. Manage*., **2016**, *183*, 836-842.
24. S. A. Mohameda; A. A. Darwish, R.M.El-Shishtawy, *Process Biochem*., **2013**, 48, 649–655
25. M. Bilal; H. M. N. Iqbal; H. Hu; W. Wang; X. Zhang; *Sci. Total Environ*., **2017**, *575*, 1352–1360.
26. M. Monier; D. M. Ayad; Y. Wei; A.A. Sarhan; *Int. J. Biol. Macromol.,* **2010**, *46(3)*, 324-330.
27. T. M. Silva, P. O. Santiago; L. L. A. Purcena, K. F. Fernandes, *Mat. Sci. Eng. C- Mater*, **2010,** *30*, 526–530.
28. H. Cai; X. Liu; J. Zou; J. Xiao; B. Yuan; F. Li; Q. Cheng; *Chemosphere*, **2018**, *193,* 833-839.
29. W.R. Carmody, *J. Chem. Educ*., **1961**, *38*, 559-560.

# PRELIMINARY ASSESSMENT OF PARTICULATE CONCENTRATION NEAR COAL FIRED POWER PLANT

## BOGDANA VUJIĆ[a], VASILE PODE[b], JELENA MIĆIĆ[a], FRANCISC POPESCU[c*], UNA MARČETA[a], ADRIAN EUGEN CIOABLA[c]

**ABSTRACT.** This study shows the results of preliminary monitoring of particulate matter (PM10 and PM2.5) at four measurement points, during the three campaigns (spring, autumn, winter) The study was conducted for the first time in residential area near coal-fired power plant, Ugljevik, Bosnia and Herzegovina. The power plant flue gas cleaning equipment in the time of this research was out of the function. Authors investigated seasonal variations of PMs concentration levels, influence of terrain structure and meteorological condition on PMs distribution and identification of PMs origin sources. The results revealed that seasonal variation was more expressed in the case of PM2.5 concentration, while for PM10, occasionally episodic pollution (399µg/m3) was recorded. Also, it was noted that prevailing meteorological conditions and surrounding terrain structure could have limiting effect on PMs dispersion. In order to detect PMs origin, linear regression analysis was applied. Authors revealed that PM2.5 originating from power plant could be prescribed partly for M1 where the greatest correlation was calculated ($R^2$=0,45). Although the measuring sites were set in proper position regarding dominant winds and terrain structure, it was identified that certain measurement sites were affected by the other local particulate matter sources, especially in case of PM10.

**Key words:** *particulate matter, PM2.5, PM10, air quality assessment, large combustion plants*

## INTRODUCTION

Particulate matters (PMs) in ambient air represent one of the most critical pollutants worldwide regardless of whether the area is industrial or urban. PMs are present in the air in various shapes and sizes, ranging from less than 10nm to 10µm in aerodynamic diameter [1].

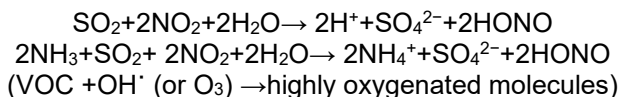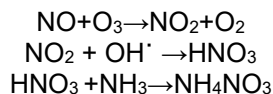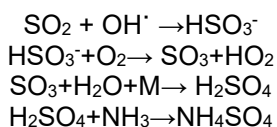[a] *University of Novi Sad, Technical Faculty "Mihajlo Pupin" Zrenjanin, Serbia*
[b] *University Politehnica Timisoara, Faculty of Industrial Chemistry, Timisoara, Romania*
[c] *University Politehnica Timisoara, Faculty of Mechanical Engineering, Environmental Engineering, Timisoara, Romania*
\* *Corresponding author: francisc.popescu@upt.ro*

BOGDANA VUJIĆ, VASILE PODE, JELENA MIĆIĆ, FRANCISC POPESCU,
UNA MARČETA, ADRIAN EUGEN CIOABLA

High PMs concentrations in air, along its negative impact on the environment can also have an impact on human health and could cause chronic respiratory diseases [2]. Health disorder also depends on the size of PMs, exposure time to PMs as well as on population age [3]. Hence, coarse particles (particles with diameter less than 10μm-PM10) affect human health less compared to fine particles (particles with diameter less than 2.5μm-PM2.5). The origin of these two groups of PMs could be different. While PM10 is defined as a primary pollutant, which means that it is emitted directly from natural or anthropogenic source, PM2.5 is defined as a secondary pollutant that occur in complex and uncertain atmospheric processes. In physic-chemical reactions of PM2.5 formations, the main role belongs to the sulfur-dioxide ($SO_2$), nitrous oxides ($NO_x$) and Volatile Organic Compounds (VOC) [4]. Those gasses are responsible for the secondary particle formations in three steps: nucleation, condensation and coagulation [5]. Nucleation is the first step that is the most probable in the presence of the sulfuric acid ($H_2SO_4$) that is prone to form hydrogen bond with other atmospheric compounds (water, ammonia, organic acids, etc.) [6]. In the condensation phase, the most occurring process is merging of gas pollutants with the existing solid particle in the air. The next, and the final phase, is mutual aggregation of previously mentioned forms that leads to the particle size growth.

Since the reactions of particle formation in the atmosphere are very complex there is no universal chemical reaction to describe it. The basic mechanism for forming PM2.5 and other atmospheric aerosols is oxidation of gas phase $SO_2$ or $NO_2$ by hydroxyl radicals ($OH^·$) and formation of sulfur and nitrous acid ($H_2SO_4$ and $HNO_3$) and further interaction of these products [7]:

$$SO_2 + OH^· \rightarrow HSO_3^-$$
$$HSO_3^- + O_2 \rightarrow SO_3 + HO_2$$
$$SO_3 + H_2O + M \rightarrow H_2SO_4$$
$$H_2SO_4 + NH_3 \rightarrow NH_4SO_4$$

$$NO + O_3 \rightarrow NO_2 + O_2$$
$$NO_2 + OH^· \rightarrow HNO_3$$
$$HNO_3 + NH_3 \rightarrow NH_4NO_3$$

$$SO_2 + 2NO_2 + 2H_2O \rightarrow 2H^+ + SO_4^{2-} + 2HONO$$
$$2NH_3 + SO_2 + 2NO_2 + 2H_2O \rightarrow 2NH_4^+ + SO_4^{2-} + 2HONO$$
$$(VOC + OH^· (or\ O_3) \rightarrow highly\ oxygenated\ molecules)$$

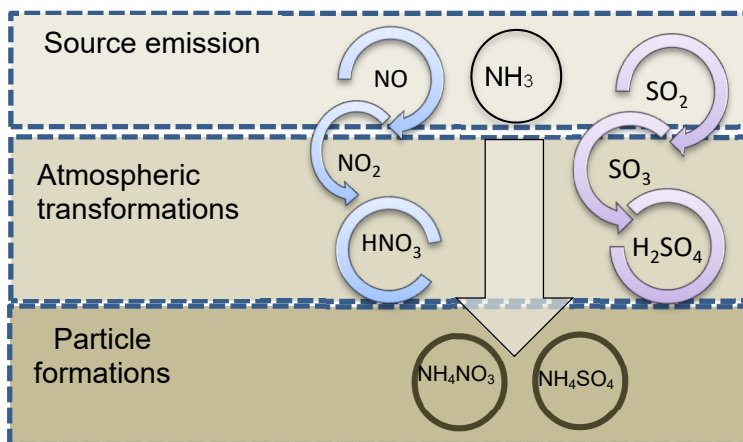A scheme of secondary particle formation in atmosphere is given in Figure 1.

**Figure 1.** Forming of PM2.5 and other atmospheric aerosols is oxidation of gas phase $SO_2$ or $NO_2$ by hydroxyl radicals ($OH^{\cdot}$)

Having in mind that the origins of fine particulates are complex atmospheric processes, it is more likely to happen in the presence of emission sources that discharge precursors of PM2.5 (e.g. combustion processes of fossil fuels) [8]. The occurrence of higher PMs concentration because of Large Combustion Plants (LCP) operation was reported by many studies [9].

There are nine coal fired LCP in the territory of Bosnia and Herzegovina (BiH). Most of the LCPs were built during the seventies in 20th century. In the area of Ugljevik municipality (BiH) there is a coal (with sulfur content 3-6%) fired thermal power plant with one boiler of 350 MW capacity which was constructed in 1983. The average annual electricity production of this LCP is 1560 GWh. The average PM10 emission concentration is 383(mg/Nm³) [10]. The treatment of waste gases is carried out by two Electrostatic Precipitators (EPs), which are in poor condition despite the frequent maintenance. The new electrostatic precipitators reconstruction has begun in 2017 [11]. Hence, LCP Ugljevik generates higher amounts of PM2.5 (373 t) than other plants. For example, LCP "Nikola Tesla" B1/B2 in Serbia generates 290t and LCP Kostolac B1/B2 in Serbia generates 32t.The LCP in Ugljevik is one of the main air pollutants in Bosnia and Herzegovina [12].

The emissions from LCP Ugljevik contribute to the poor air quality within the wider area and constant citizens' complaints. As a first step in improving air quality management as well as enforcement of the national legislation that is harmonized with EU directives [13], the municipality of Ugljevik provided preliminary ambient air quality assessment. For the first time, three monitoring campaigns at four monitoring sites near LCP were conducted. The concentration

of sulfur dioxide (SO2), nitrogen oxides (NOx), fine (PM2.5) and coarse (PM10) particles, carbon monoxide (CO), ozone (O₃) as well as meteorological parameters were measured.

Due to poor condition of EPs at Ugljevik LCP, this study was focused solely on coarse and fine particle monitoring. Thus, according to the obtained monitoring data for the first time, the PMs assessment in LCP surrounding was performed. The assessment was based on detailed data analysis and identifying: 1) the seasonal variations of PMs concentration levels, 2) influence of terrain structure and meteorological condition on PMs distribution and 3) PMs source origin. The results and conclusions obtained within this study is a good starting point in understanding the PMs atmospheric fate in this area which could help decision-makers to undertake necessary control measures for air quality improvement.

## RESULTS AND DISCUSSION

In order to present all data of this extensive PMs monitoring that comprehended three campaigns over large periods of time, at four measurement sites, in this paper, all daily PMs concentrations are presented in the graph form (Figure 2 and Figure 4). Additionally, the statistical data on PMs concentrations are presented in the form of boxplots (Figure 3 and Figure 5.

### Assessment of seasonal variation of PMs concentration levels

Daily PM10 concentration levels during all three campaigns at all sites are presented in Figure 2.
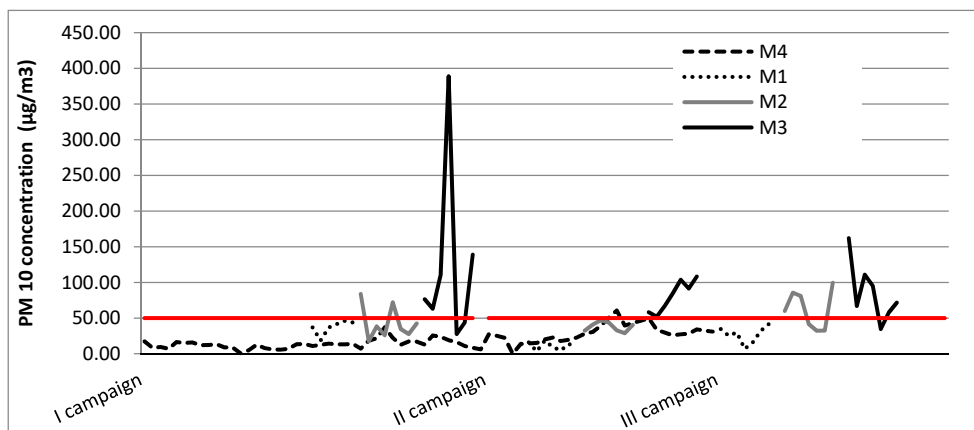


**Figure 2.** Data on PM10 concentration levels on all sites (M1-M4) during three campaigns

The measurement results have shown that daily PM10 concentration levels during all three campaigns at M1 did not exceed the limit value (LV=50μg/m$^3$) [13]. During the II campaign, at M2, there has been an exceedance of the limit value (LV) in 60% of samples (maximum concentration was 99,51μg/m$^3$), as well as in 30% of samples during the III campaign at the same measurement site (maximum concentration was 83,93μg/m$^3$). At M3, higher PM10 concentration levels were noted than at the other sites. Depending on the campaign, the LV exceedance ranged from 71% to 100% of samples at M3. The maximum concentration was measured during the II campaign (399.95 μg/m$^3$). PM10 concentration levels at M4 were significantly lower during the I campaign compared to the II campaign when three exceedances of the mean daily values were noted. During the III campaign, data coverage of PM10 concentration at M4 was less than 90%, so it was not considered in this paper. For each campaign, the highest PM10 concentrations were measured at M2 and M3 (Figure 3).

Figure 3 presents statistical data on PM10 concentration during the monitoring campaigns. The boxes represent 1st and 3rd quartile, the whiskers represent minimum and maximum values, the asterix represents outlier values and the red line represents the daily limit value (50μg/m$^3$).
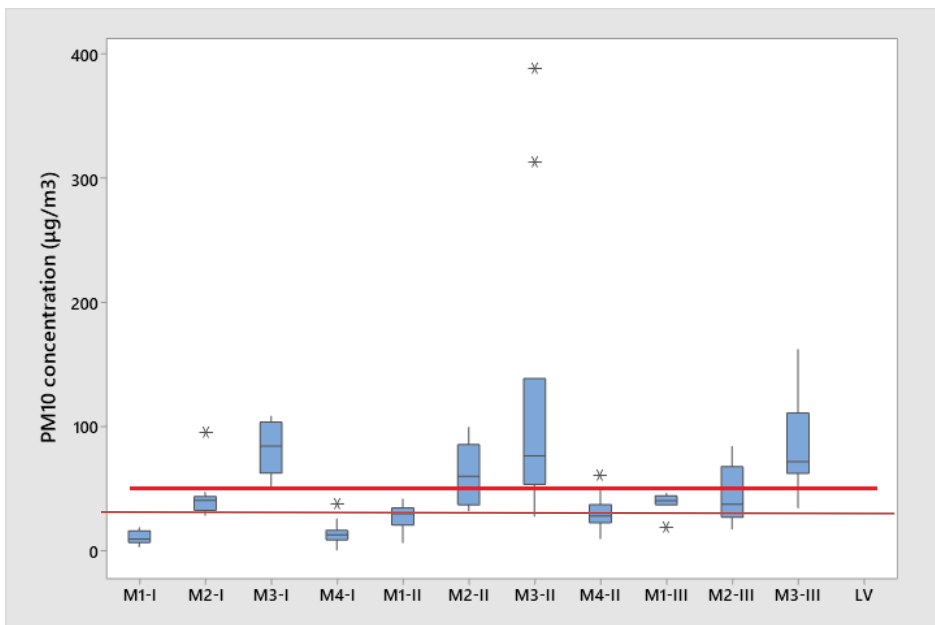


**Figure 3.** Box plot showing the PM10 distribution during the measuring campaign for all three measurement seasons (I, II and II season).

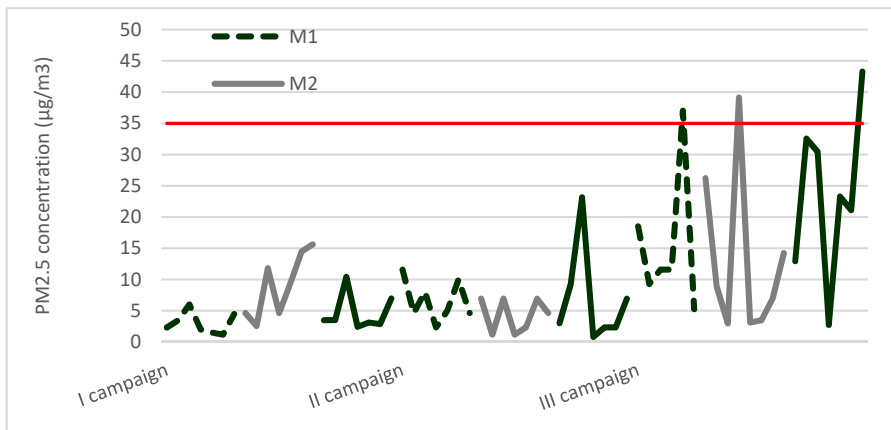Daily PM2.5 concentration levels during all three campaigns at M1-M3 are presented in Figure 4.



**Figure 4**. Data on PM2.5 concentration levels on sites M1-M3
during three campaigns

The statistical data of the measured PM2.5 concentrations for all measuring sites during the three campaigns are given in the form of box plots (Figure 5). During the III campaign, PM2.5 concentrations exceeded the LV of 35 µg/m$^3$ [13] at all measuring sites (M1, M2 and M4). The maximum concentration of 43.3 µg/m$^3$ was noted at M4 during the III campaign. In general, PM2.5 concentrations at all three sites were higher in the III campaign when compared to the I and the II campaign.

Figure 5 presents statistical data on PM2.5 concentration during the three monitoring campaigns. The boxes represent 1st and 3rd quartile, the whiskers represent the minimum and maximum values; The asterix represents outlier values; The Red line represents daily limit value (35 µg/m3).

Regarding seasonal variation of PMs concentration, it could be concluded that PM2.5 concentration showed significantly higher fluctuation during campaigns. Hence, during the winter PM2.5 concentration is much higher in comparison to the spring and autumn season which supports the conclusion that PM2.5 originates from LCP that was operating harder during the colder seasons. PM10 concentration fluctuation was not expressed to ahigh extent during the seasons. However, occasionally episodic pollution by PM10 was recorded.
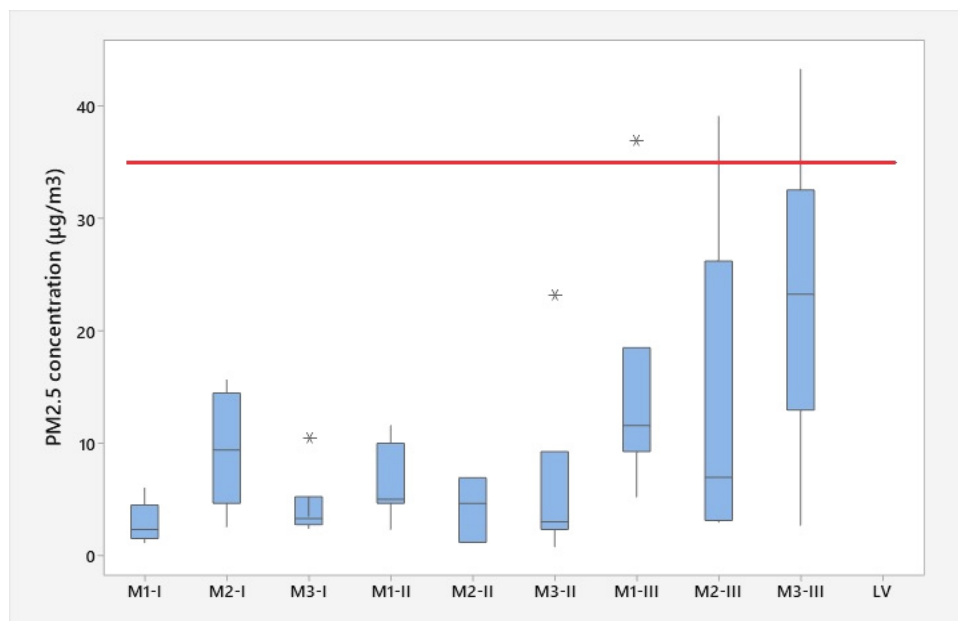
**Figure 5.** Box plot showing the PM2.5 distribution during the measuring campaign
for all three measurement seasons (I, II and II season).

## Influence of topography and meteorological parameters on PMs distribution

The fate of atmospheric pollutants is affected by numerous factors such as emission source properties, pollutant and environmental characteristics where it is being released (topography, meteorological conditions etc.). All abovementioned factors are correlated and cannot be observed separately. Thus, taking into account the topography of Ugljevik environment which is a hilly landscape with slight elevations and valleys in the range of 150 - 400m above the sea level on one hand and the height of the LCP emission source (300m) on the other, undoubtedly leads to the conclusion that this area structure can have some limiting effect on the free pollutant distribution over long distances.

Considering the dominant winds, this area is characterized by winds of an average speed of up to 2 m/s. Calm periods are frequent (308‰) [14, 15].

According to the data on wind speed (WS) and wind direction (WD) measured at M4 it is evident that the potential impact of the LCP on the environment is changeable. During the I and the II campaign, the most potentially impacted areas could be at north-west (NW), south-west (SW) and north-east (NE) from the LCP, while during the III campaign it could be areas at the north-west (NW) direction of the LCP (Figure 6).
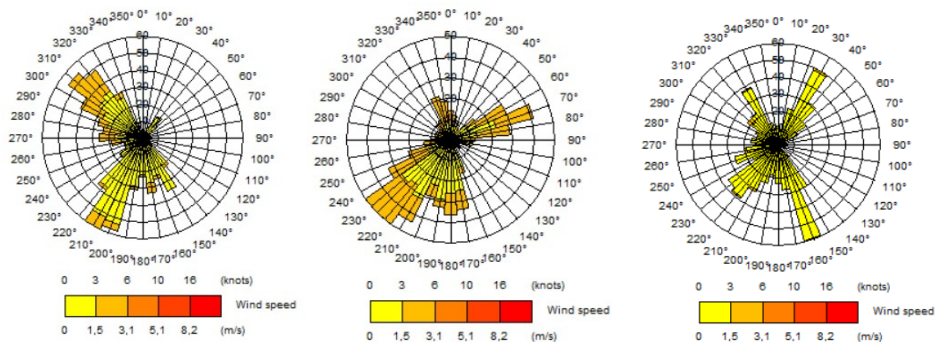
**Figure 6.** Wind Roses for spring (left), autumn (middle) and winter (right) campaign

On the other hand, wind speed during all campaigns was relatively low (maximum speed was lower than 2.5 m/s). By analyzing the relation of PM10 concentration and wind speeds, it was concluded that the maximum PM10 concentrations were measured at low wind speed (less than 1 m/s). Figure 7 represents the relation between wind speed and PM10 at M4 during the I campaign.
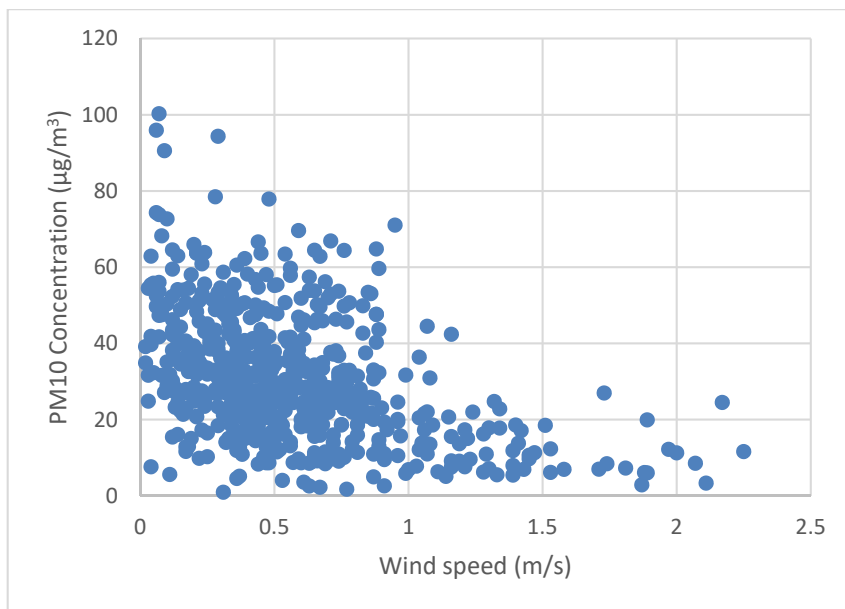


**Figure 7.** Relation between the wind speed and PM10 at M3 during the I campaign

Regarding dominant winds and terrain structure, all measuring sites were placed at locations which are potentially mostly influenced by the emission.

**The origin of the particulates**

In order to derive greater conclusions based on PMs monitoring data, authors decided to use linear regression analysis (LRA). In recent studies, researchers reported that LRA could give crucial information relating to the particle origin [16]. Hence, the relation between PM2.5 and PM10 mass concentration indicated that higher relation coefficient is attributed to anthropogenic particle sources and the higher share of fine particles, while the smaller ratios indicate the higher share of coarse particles, which might be related to natural sources [17].

In order to understand relations between PM2.5 and PM10 and their origin in this area, LRA for each measuring site by seasons was performed. The relations are determined by correlation coefficients ($R^2$) that are calculated in Microsoft Excel software [18].

The results showed very different, but still very low correlation between PM2.5 and PM10 for all sites during all seasons. The highest correlation coefficient ($R^2=0,45$) was calculated for M1 measuring site (Figure 8). On the other hand, at M3, where the highest PM10 concentration and the largest number of LV exceedance were measured, the lowest correlation was noted ($R^2<0,02$). This can lead to the conclusion that there is a low probability that LCP had an influence on the measuring sites M2, M3 and M4, regarding fine particles, but the highest influence of LCP could be noted for M1.
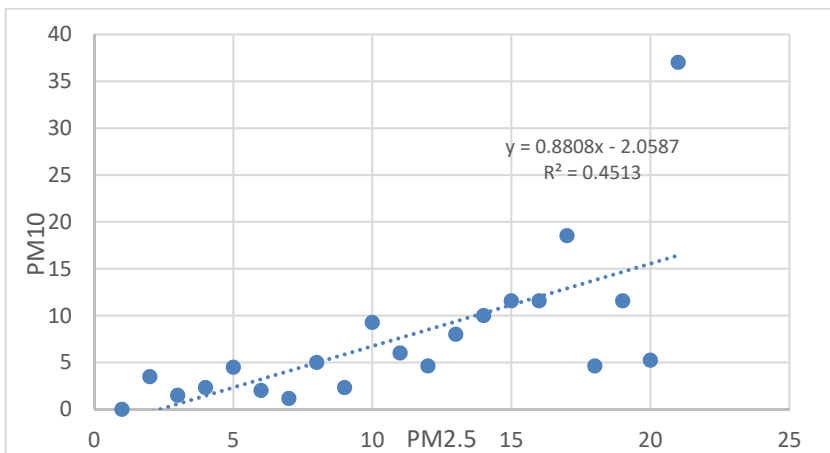


**Figure 8**. Linear regression analysis between PM2.5 and PM10 for M1

Since the measuring points were set relatively close to the point source and considering the source height this could be expected [19]. The relatively weak correlation between concentrations during the seasons could also indicate the possible changes in emission rate due to overhaul, unexpected malfunctions or reduced production capacity (http://riteugljevik.com).

## CONCLUSION

The air pollution represents a major problem in the vicinity of the LCP Ugljevik, BiH. Although the authorities have harmonized legislation with the high EU air quality standards, for LCP operator it is impossible to manage all technical issues within the defined deadlines because the outdated equipment and financial restrictions for new investments. In order to access air quality in populated area around LCP, measurement of PMs concentrations at three sites during three campaigns has been conducted for the first time.

The assessment included detailed analysis of PMs concentrations, their seasonal fluctuation, the indication of possible distribution pattern and PMs source identification as well.

The results indicated that PM2.5 concentration showed intensive seasonal fluctuation, especially during the winter season. However, PM10 seasonal fluctuations were not expressed to that extent. A very high and episodic pollution (399µg/m3) was recorded, regardless of the measuring season

Concerning the distribution pattern due to prevailing meteorological conditions and terrain structure, all measuring sites were placed at locations which could potentially be mostly influenced by the emission. Still, according to the results of LRA, where PM2.5/PM10 relation was calculated, it was noted that the PM2.5 originating from LCP had the most influence on the measuring site M1 with the correlation coefficient of 0,45. Although the authorities requested the air quality assessment for the populated area, it was noted that the measurement sites (M2 - M4) were not set at proper distances from LCP. Thus, it could be said that the impact of other sources (house heating, soil resuspension etc.) was dominant at those monitoring sites. In general, it can be concluded that the seasonal variations in concentration levels were noticeable to a certain extent.

However, this research has some limitations including a short period of time over which the trends were analyzed. Therefore, further investigation should be focused on qualitative and quantitative PMs analysis coupled with modelling of PMs dispersion into the surrounding environment. This approach could be useful as a basis for detailed air quality assessment, improvement plans, pollution control strategies, establishing representative monitoring network and a framework of health impact assessment in accordance with the WHO and EU recommendations.

## EXPERIMENTAL

### Monitoring domain

The city of Ugljevik, with 15710 inhabitants [20] is in the eastern part of Bosnia and Herzegovina. The thermal power plant complex is in the vicinity of a populated place while the closest residential buildings are situated at a distance of only 200 m. The plant is supplied with coal from its own mine located on the south of "Bogutovo Selo" complex (Figure 9) with an annual capacity of 1.75 million tons of coal [21].
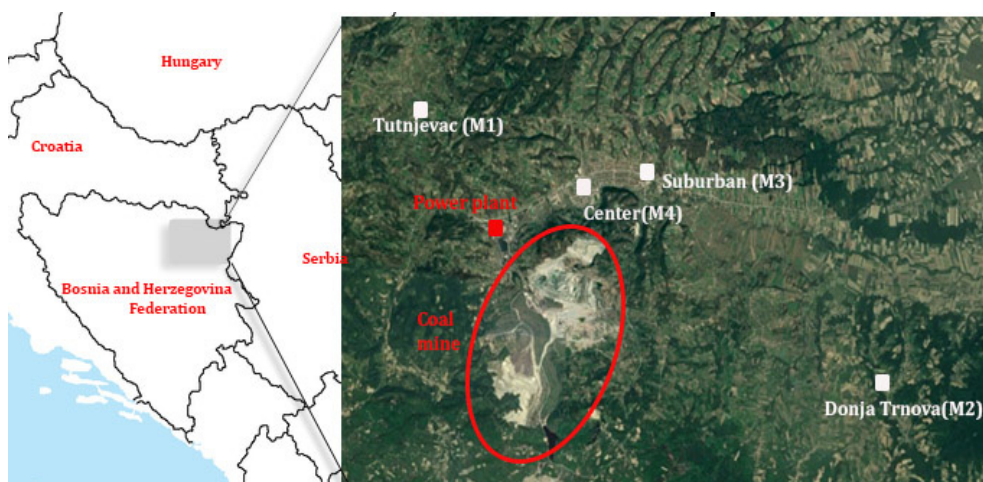


**Figure 9.** Analyzed site domain and position of measurement sites

### Measurement sites

The In-situ measurements of concentration levels of the relevant parameters were carried out at four locations. Indicative measurements of ambient air quality were carried out at four measuring points [13]. Monitoring was conducted during the thirty days in each of the three campaigns: I - spring, II - autumn and III - winter. At automatic station located at city center (M3), the hourly values of meteorological parameters and pollutants during each campaign were conducted. At the remaining three sites (M1, M2 and M3) the measurement of daily particulate concentration was being carried out successively for seven days during each campaign.

The position and distance from the locations and the analyzed pollution source are shown in Figure 9 and Table 1.

BOGDANA VUJIĆ, VASILE PODE, JELENA MIĆIĆ, FRANCISC POPESCU,
UNA MARČETA, ADRIAN EUGEN CIOABLA

## Measurement methods

Measurement of air pollutants, as well as weather conditions, were provided by two types of instruments (Table 1).

**Table 1.** Specification of methods, monitoring sites and parameters

| Equipment | Measurement site abb. | Measurement site location | Distance from point source (km) | Parameters |
|---|---|---|---|---|
| Baghirra instrument for PM sampling | M1 | N44.717353, E18.930450 | 4.9 | PM 2.5 PM10 |
| | M2 | N44.664258, E19.084668 | 9.6 | |
| | M3 | N44.694987, E19.012171 | 3.6 | |
| Air Pointer Instrument (RECORDUM) | M4 | N 44 41.496' E 18 59.783' | 2.5 | wind speed (WS), wind direction (WD), atmospheric pressure (P), relative humidity (RH) and dew point (Dew), PM10 |

Air-pointer, located at M4, has a PM10 analyzer that works based on nephelometry optical technique that uses a light-scattering photometer with a silicon detector hybrid preamplifier and a source reference detector. The light scattered is proportional to the particle concentration. This is the fastest particle concentration measurement with high precision and very low detection limit.

At other measuring sites (M1-M3), after passive sampling, the content of PM10 and PM2.5 was determined in a laboratory using gravimetric method (SRPS EN 12341).

## ACKNOWLEDGMENTS

# REFERENCES

1. World Health Organization, *Health Effects of Particulate Matter*, **2013**.
2. I.P.S. Araujo; D.B. Costa; R.J.B. De Moraes; *Sustainability,* **2014**, *6*, 7666-7688.
3. S.A. Mohd Din; N.N.H. Nik Yahya; A. Abdullah; *Procedia – Social Behavioral Sci.,* **2013**. *85*, 92 – 99.
4. Z. Wang; C. Zhang; G. Lv; X. Sun; N. Wang; Z. Li; *Int. J. Mol. Sci.* **2019**, *20*, 3746.
5. B. Jiang; D.Xia; X. Zhang; *Sci Total Environ.* **2018**, *616-617*, 1414-1422.
6. S. Hu Lee; H. Gordon; H. Yu; K. Lehtipalo; R. Haley; Y. Li; R. Zhang; *J Geograph. Res.: Atmosph.*, **2019**, *124*, 7098-7146.
7. S. Mohankumara, P. Senthilkumarb; *Renew. Sus. Energ. Rev.,* **2017**, *80*, 1227–1238.
8. I.A. Chereches; I. Petean; G.A. Paltinean; A. Mocanu; L. Muresan; G.Arghir; M. Tomoaia-Cotisel; *Studia UBB Chemia*, **2018**, *63*, 159-166.
9. Z. Ma; Z. Li; J. Jiang; J. Deng; Z. Yu; S. Wang; L. Duan; *Aerosol Air Qual. Res.*, **2017**, *17*, 636–643.
10. EIA, *Institute for construction*, Banja Luka, **2016**.
11. B. Stojanović; *S.Đukić; Međunarodna konferencija "Elektrane 2014",* Zlatibor, **2014**.
12. M. Holland; Technical report on goal fired power plants impact on health in West Balcan, Health and Environmental Alliance, Brussels, Belgium; **2016**, pp 16-23 (in Serbian).
13. Directive 2008/50/EC, *Official Journal of the European Union*, **2008**.
14. FHMS Jugoslavije, *Meteorološki godišnjaci I*, **1961-1985**.
15. RHMS RS, FHMI FBiH. Dokumentacija **1986-1990**.
16. G. Xu; L. Jiao; B. Yhang; S. Yhao; M. Yuan; Y. Gu; J. Liu; X. Tang; *Aerosol Air Qual. Res.*, **2017**, *17*, 741–751
17. N. Sugimoto; A. Shimizu; I. Matsui; M. Nishikawa; *Particuology*, **2016**, *28*, 114–120.
18. B. Vujić; A. Pavlović; G. Vujić; D. Jevtić; *Rev.Chim.,* **2010**, *61*, 991-997.
19. V. Valverde; M.T. Pay; J.M. Baldasano; *Sci. Total Environ.,* **2016**, *541*, 701–713.
20. BHAS 2013 - *Agency for Statistics of Bosnia and Herzegovina*, **2013**.
21. Z. Milovanović; V. Sijacki- Zeravcic; D. Milanovic; S. Borojevic; In book: *Prijedlog mjera i aktivnosti na uvođenju optimalnog upravljanja pokazateljima konkurentnosti energetskih I procesnih postrojenja (uvođenje ASSET MANAGEMENT-a na najvišem nivou) - faza I*, Edition: I, Chapter: IV Modul I, **2009**, Publisher: Univerzitet u Banjoj Luci, Mašinski fakultet, Banja Luka, Bosnia and Herzegovina.

# INFLUENCE OF LANDFILL METHANE EMISSIONS ON ENVIRONMENT – DISTRIBUTION MODELLING AND ASSESSMENT

**BOGDANA VUJIĆ[a], NEMANJA STANISAVLJEVIC[b],
FRANCISC POPESCU[c], NIKOLINA TOSIC[b], UNA MARČETA[a],
MARJANA PARDANJAC[a], VASILE PODE[d]**

**ABSTRACT.** Landfilling practice in countries with waste management in transition is associated with non-controlled landfill gas and leachate emission. This practice requires sanitary landfill operations and remediation of unsanitary landfills as a prerequisite to join European Union. In order to get first insights on methane distributions for subsequent risk assessment model, this research, assess methane behavior patterns after emissions in the ambient air on environment from the controlled landfill site in Novi Sad, Republic of Serbia. Methane emission rate was assessed and crosschecked using landfill gas emissions model (LandGEM). The ADMS Mapper was used for the 3D simulation of the real environment of research field, including the complex structure of the landfill body and surrounding area. For simulation of methane dispersion into atmosphere, advanced Gaussian dispersion model ADMS Urban was applied. After processing and synthesis of the meteorological data, and defining the emission potential, simulations of the methane dispersion under different meteorological conditions (wind speed and direction, atmospheric temperature, humidity, pressure and cloud cover) were performed. As a result, methane distribution pattern was noted, several most unfavorable meteorological conditions and scenarios of methane distribution were assessed, and most vulnerable zones and locations influenced by the landfill methane emissions were identified.

*Keywords*: Methane emission, Air dispersion, Modelling, LandGem, ADMS urban, Serbia

---

[a] *University of Novi Sad, Technical Faculty „Mihajlo Pupin ", Zrenjanin, Serbia*
[b] *University of Novi Sad, Faculty of Technical Sciences, Department of Environmental Engineering, Novi Sad, Serbia*
[c] *University Politehnica Timisoara, Faculty of Mechanical Engineering, Environmental Engineering, Timisoara, Romania*
[d] *University Politehnica Timisoara, Faculty of Industrial Chemistry and Environmental Engineering, Timisoara, Romania*
* *Corresponding author: bogdana.vujic@tfzr.rs*

BOGDANA VUJIĆ, NEMANJA STANISAVLJEVIC, FRANCISC POPESCU, NIKOLINA TOSIC,
UNA MARČETA, MARJANA PARDANJAC, VASILE PODE

## INTRODUCTION

The Republic of Serbia is a European Union (EU) candidate country which needs to fulfill the requirements of the EU waste management directives, as a prerequisite for EU membership. One of the most important tasks is to eliminate non-compliant landfilling and to minimize and control emissions from existing waste disposal sites. There are 160 controlled and 3500 uncontrolled waste disposal sites in Serbia [1,2]. Controlled waste disposal sites do not meet sanitary-technical and technological standards (no liner systems, leachate and landfill gas collection). The Latest data indicates that only 30% of totally generated municipal solid waste (MSW) in Serbia is landfilled on sanitary landfills [2].

Uncontrolled landfilling has a huge impact on environment due to the complex chemical reactions during the waste decomposition process that yield in landfill gas (LFG) production. One of the basic problems is LFG which is dominantly composed out of methane ($CH_4$: 55–60% v/v) and carbon dioxide ($CO_2$: 40–45% v/v) that are identified as greenhouse gases (GHG). Representative chemical processes of waste degradation in landfills could be described as follows:

a) Acetogenesis: $C_6H_{12}O_6 \rightarrow 2C_2H_5OH + 2CO_2$

b) Methanogenesis: $CH_3COOH \rightarrow CH_4 + CO$

$$CO_2 + 4H_2 \rightarrow CH_4 + 2H_2O$$

However, quantitative data on LFG emissions from landfills in Serbia are scarce. There have been several attempts to quantify emissions [1,3,4] but no specific reliable data exist for majority of location. Particularly, methane distribution in the ambient air has never been modelled neither quantified although it has 28 times greater global warming potential than $CO_2$.

Where long-term landfill emission data are not available, different estimation models are used [5]. Intergovernmental Panel on Climate Change (IPCC) [6] model is commonly used for assessment of statewide emissions and United States Environmental Protection Agency's, LandGEM is used for specific sites and statewide. Both models are widespread models for prediction and estimation of methane production from landfills. For distribution in the environment, mathematical models are used for calculating the concentration of pollutants in the atmosphere [7,8]. Due to the uncertainties and complexities associated with the methane production and transport process, there are various researches based on methane emission assessment using mathematical models [9-10].

After being emitted into the atmosphere from the landfill, methane becomes the subject of numerous complex atmospheric chemical reactions which eventually produce ozone (Figure 1) [11].

However, in the lowest troposphere meteorological conditions can have diverse influence on methane distribution in the ambient air before its transformations [12]. Understanding distribution and influence of meteorological parameters on methane in ambient air can significantly contribute to human health risk avoidance and environmental quality due to uncontrolled methane emissions [13,14].

The aim of this paper is to generate the preliminary data on influence of different meteorological conditions on methane distribution in the ambient air for controlled municipal landfill in Novi Sad, the Republic of Serbia. In lack of appropriate data this research could be the starting point for risk assessment and landfill remediation prioritization models in the developing and transition countries. Hence, the accent was not on the approach for estimating landfill gas emissions, but on the evaluation of the methane dispersion from a single local source in the atmosphere/ambient air under different meteorological parameters.
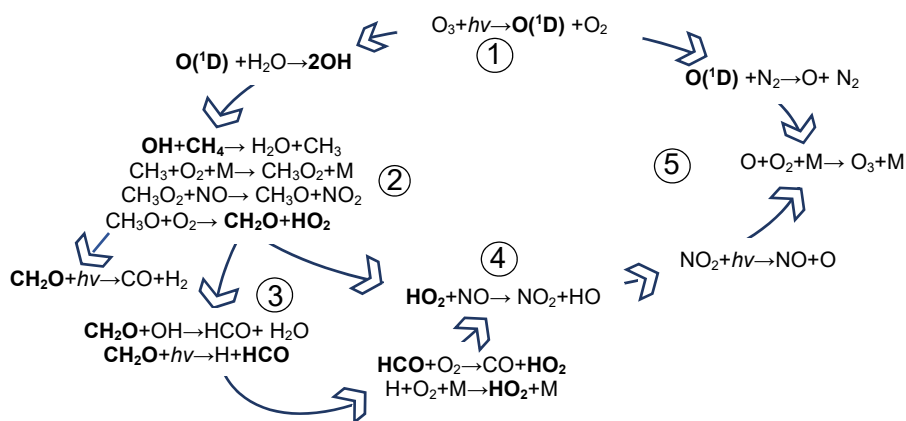


**Figure 1.** Atmospheric methane transformation. Methane transformations happen in presence of hydroxyl radicals (OH) which stem from ozone ($O_3$) and UV light (*hv*) (1). Acetaldehyde ($CH_2O$) (3) and hydroxyl radical ($HO_2$) (4) are formed in the reactions of OH radicals and $CH_4$ (2) in presence of NO (4) which lead to the final product- ozone (5). (M could be $N_2$, $O_2$ or any other molecule which by collision stabilizes $O_3$).

## RESULTS AND DISCUSSION

Results indicate that in 2017. 300 and 274 $gs^{-1}$ of methane were emitted from the landfill in Novi Sad for 1960 and 1970 respectively.

The emission factors (EF) with higher value which refer to 1960 are adopted as an input for distribution modelling (Table 1).

Since the modelling using EF1 0.1 indicated the highest level of concentrations, this emission factor was used for further simulations.

**Table 1.** Potential methane flux from the landfill in Novi Sad

| Initial year of waste disposal/landfill operation | Unit | Oxidation factors | | |
|---|---|---|---|---|
| | | 0.1 | 0.2 | 0.5 |
| 1960 (EF1) | g s$^{-1}$ | 300 | 234 | 167 |
| 1970 (EF2) | | 274 | 213 | 152 |

### Modelling results for the summer

The long-term (LT) modelling using hourly meteorological data for the summer with vertical intersections at 7 points as well as spatial distribution in several receptors was performed. Methane concentrations were modelled using both emission factors (EF1 and EF2) with oxidation factors of 0.1, 0.2 and 0.5. Depending on the emission and oxidation factors, methane concentrations ranged from 62 to 1989 µgm$^{-3}$ at the landfill ground level. The highest methane concentration in ambient air was modelled using EF1 with oxidation factor 0.1 (EF1 0.1) (see Table 2). Concerning the vertical distribution, modelled concentration levels slightly decreased with higher altitudes (up to 25 m). However, modelled concentrations rapidly decreased above 25 m. For instance, for EF1 0.1 at 33 m altitude methane concentration was 1141 µg m$^{-3}$ while at altitudes above 50 m concentration was 159 µgm$^{-3}$ (Table 2).

**Table 2.** Modelled methane concentration (µg m$^{-3}$) with emission factors
EF1 and EF2 at different atmospheric height (H in meters)

| C$_{metahne}$ (µgm$^{-3}$) | H (m) | | | | | | |
|---|---|---|---|---|---|---|---|
| | 0 | 8 | 17 | 25 | 33 | 42 | 50 |
| EF1  0.1 | 1989 | 1933 | 1876 | 1738 | 1141 | 291 | 159 |
| EF1 0.2 | 1119 | 1087 | 1055 | 977 | 642 | 163 | 89 |
| EF1 0.5 | 62 | 60 | 59 | 54 | 36 | 9 | 5 |
| EF2 0.1 | 1269 | 1232 | 1195 | 1106 | 727 | 191 | 106 |
| EF2 0.2 | 1022 | 993 | 964 | 893 | 586 | 149 | 81 |
| EF2 0.5 | 567 | 551 | 535 | 495 | 325 | 83 | 45 |

The spatial methane distribution indicated that the most vulnerable areas were located in the northwest (Industry 1), east (Road 1) and northeast from the landfill (Village 1 and Village 2). In this modelling iteration, methane dispersion was not recorded at ground level in the direction of populated area (Houses 1 and Houses 2), and shopping mall (Figure 2). The zone of spatial methane dispersion was determined by modelling through additional receptors: Industry 2, Village 11 and Road 2 (Table 3). In the dominant wind direction, modelled concentrations at additional receptors show the tendency of gradual decrease at the ground level. The zone of maximum methane concentration on the ground level is located at distances of up to 300 m from the landfill in the dominant wind directions.

This modelling iteration has identified several key patterns in methane distribution according to the prevailing meteorological conditions. Firstly, methane distribution is favorable at higher atmospheric layers. This fact is confirmed by the modelled concentrations in previously identified zones without significant methane impact on the ground level. However, in the zones Shopping mall, Houses 1 and Houses 2, at the altitude of 0 m these zones were not affected (Figure 2), while at 25 m, modelled methane concentrations varied from 46 $\mu gm^{-3}$ to 131 $\mu gm^{-3}$. Similar patterns of increased methane dispersion in higher atmospheric layers were also reported by Soporanet al. [11].

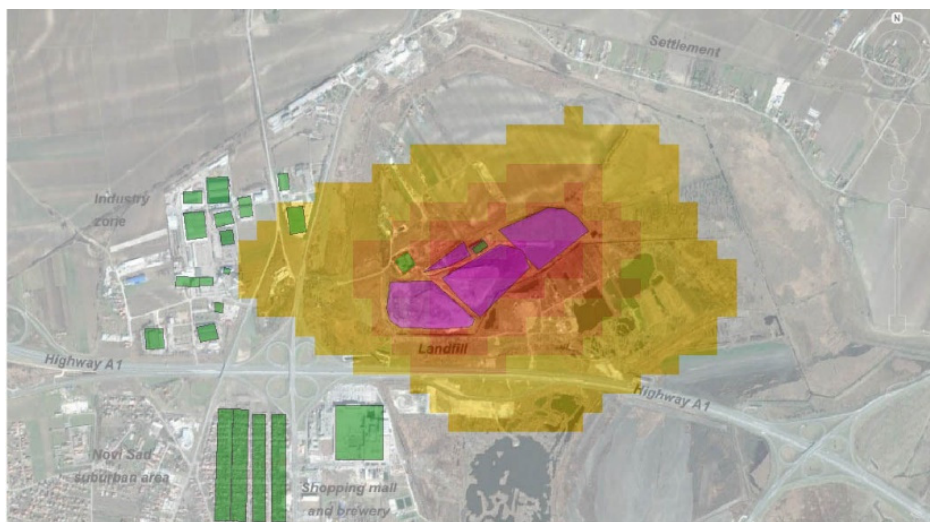Distribution of methane at different altitudes are presented in Figure 2 and Figure 3.



**Figure 2.** Modelled methane concentration H = 0 m
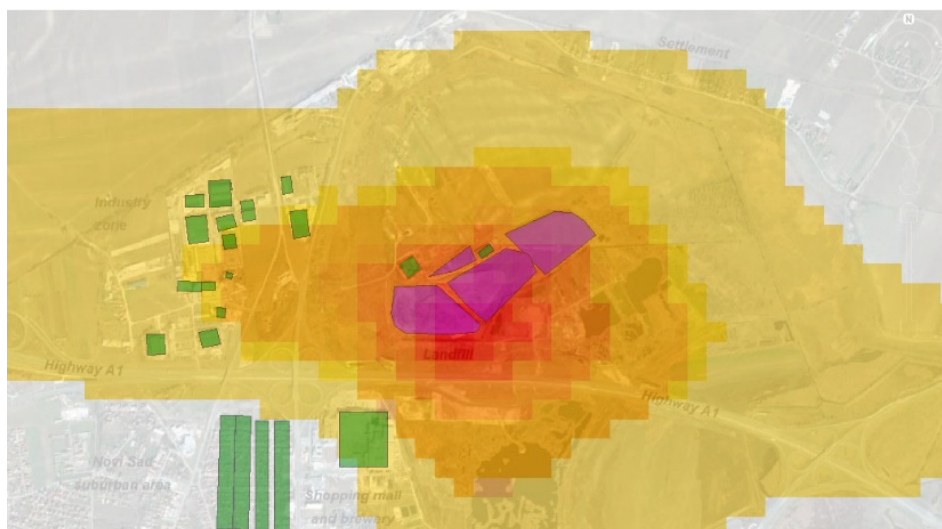
**Figure 3.** Modelled methane concentration at H = 25 m

Although the methane concentration contour plot showed that methane distribution improved on higher altitudes, numerical output confirmed that the modelled methane concentrations at distances larger than 400m from the landfill were relatively constant and below $100\,\mu gm^{-3}$ at all modeling altitudes. Even though vertical methane distribution has improved to the certain height, the maximum concentrations were still calculated at the distances less than 300 m from the landfill.

### Modelling results for different scenarios

To identify the most critical meteorological conditions that are favorable for improved methane dispersion, long-term modelling for specific scenarios (S1-S3) was performed. Methane concentrations in different meteorological scenarios indicated the same pattern as patterns modelled with hourly meteorological data for the whole summer. For all three scenarios the maximum methane concentrations were observed for EF1 0.1 as well. However, compared to modelling of S3, in S1 and S2, higher methane concentrations were observed. The methane dispersion on the ground level (H=0) for S1 and S3 is shown in the Figure 4 and Figure 5.

The maximum methane concentrations of 2686 $\mu gm^{-3}$ were modelled in S1 just above the ground level of the landfill. Lower concentrations of 2358 $\mu gm^{-3}$ were obtained in scenario S2, while the lowest concentration was generated for S3 (1082 $\mu gm^{-3}$).

The first scenario (S1) vulnerable area is relatively small and limited to two receptors: Road 1 (868 $\mu gm^{-3}$) and Road 2 (148 $\mu gm^{-3}$) (Figure 4). Methane distribution in S1 is similar to S2, but modelled concentrations in S2 were lower: in Road 1 modelled concentration was 357$\mu gm^{-3}$, while in Road 2 was 132 $\mu gm^{-3}$. Opposite of S1 and S2, in S3, affected area included west oriented receptors, Industry 1 and Industry 2, where modelled methane concentrations were 78 $\mu gm^{-3}$ and 56 $\mu gm^{-3}$, respectively (Figure 5). Difference in modelled concentration levels between scenarios revealed the meteoritical conditions were favorable for methane distribution. Meteorological conditions, in S1 and S2, which contribute to higher methane concentration were characterized by relatively low wind speed (up to 2.4 m) and high cloudiness (5-8 octas). The same patterns were observed by Garcia et al. [15].
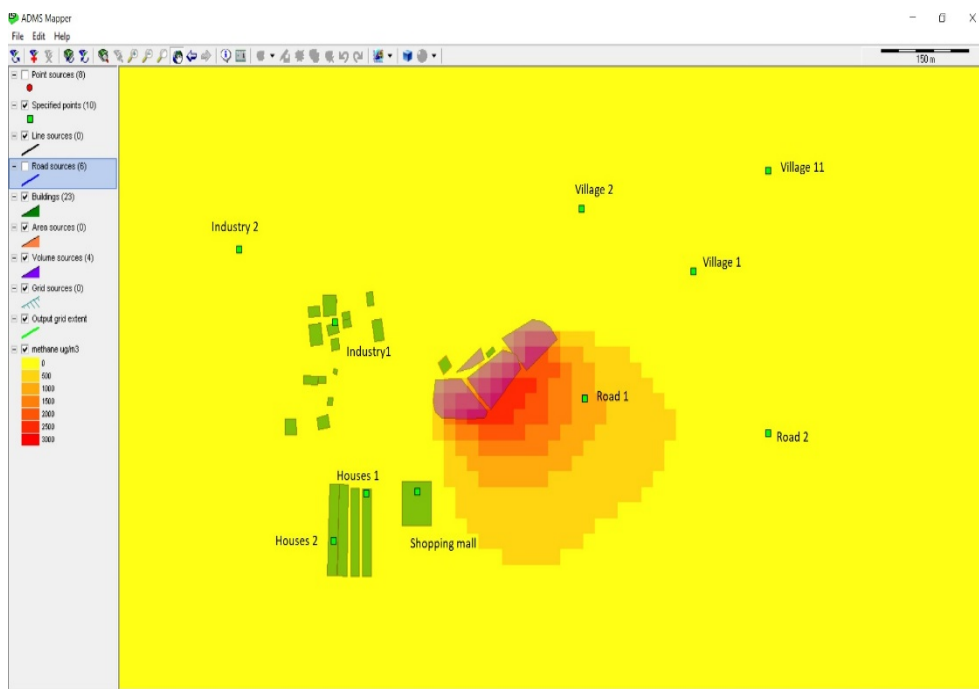


**Figure 4.** Methane dispersion at H = 0 m (simulation for S1 using EF1 0.1)

The spatial methane distribution identified through specific receptors indicated that the maximum methane concentrations at ground level were present at distances of up to 150 m from the landfill in the direction of the dominant air currents (obtained with hourly meteorological data). This is how concentrations in the range from 154 $\mu g\ m^{-3}$ to 440 $\mu g\ m^{-3}$ were modelled at the distance less than 300 m from the landfill depending on the location of the receptors.
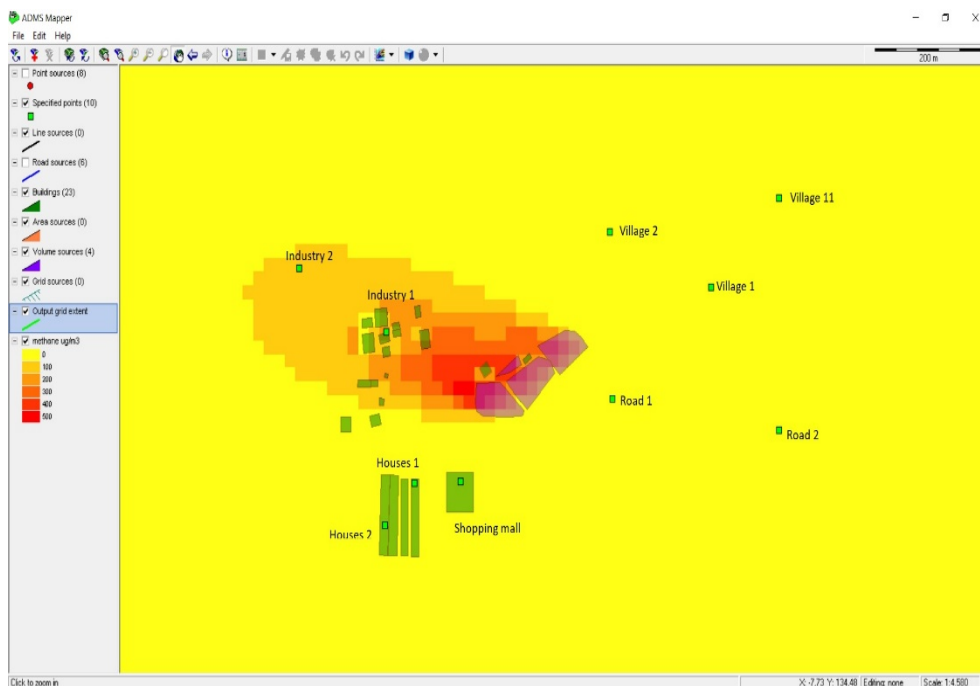
**Figure 5.** Methane dispersion at H =0 m (simulation for S3 using EF1 0.1)

When it comes to different meteorological scenarios, the spatial methane distribution at ground level indicated that the maximum concentrations were found at the distances less than 200 m from the landfill. However, at 500 m distance, the concentrations modelled in scenarios were higher compared to the modelling for the entire summer. The highest modelled concentrations of 194 $\mu gm^{-3}$ were obtained in S1, at 550 m from the landfill in the direction of the dominant winds (Figure 6).

There is no defined limit value for methane in ambient air. Exemption is very high concentration of 500 000 ppm that can cause asphyxiation. Hence, the modelled concentrations were compared to the concentration in recently published studies. Using different mathematical models some authors reported the modelled concentration of methane in ambient air in the range from 12 - 4259 ppm [11,16]. However, the measurement conducted in the three cities of Romania, recorded concentration of ambient methane ranging from 2 to 11. 5ppm [17,18]. In the large urban areas these concentrations could be much higher [19,20]. Since the wide range of modelled and measured methane concentrations were reported, modelled concentrations obtained within this study were in the magnitude of reported values.
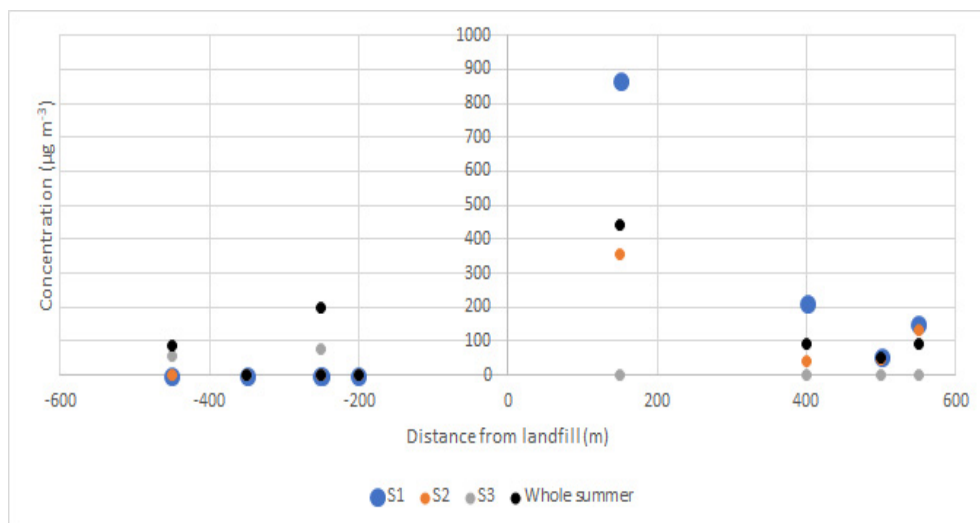
**Figure 6.** Spatial methane concentration for all scenarios (H = 0 m). Landfill location is represented at the beginning of the coordinate system (0); Receptor located west and south-west (Industry 1, Industry 2, Houses 1, Houses 2 and Shopping mall) are represented in the left part of chart (negative axis); Receptor located north-east and east form the landfill are located on the right part of the chart (positive axis).

## CONCLUSION

Landfilling is the dominant waste disposal method and there are numerous controlled and uncontrolled waste landfilling activities. In order to minimize human health and environmental risks, these locations require closure and remediation prior to European Union accession. Currently in the Republic of Serbia only methane potential is considered as one of the risk assessments factors prior to landfill closure and remediation. Since the practice of daily covering with soil layer is not well established and the methane generation potential is different at each landfill, the potential risk of the landfill itself is unique too.

This study implies the need of inclusion of methane distribution patterns after emission in the ambient air in the overall landfill closure risk assessment model. Methane fate in the atmosphere is subject of complex processes and depends on physical properties of the environment as well as of the ambience monitoring of methane at certain distances from the source of emission. In combination with the distribution modelling is important for identification of vulnerable area potentially influenced by emitted methane and risk prioritization of specific locations.

BOGDANA VUJIĆ, NEMANJA STANISAVLJEVIC, FRANCISC POPESCU, NIKOLINA TOSIC,
UNA MARČETA, MARJANA PARDANJAC, VASILE PODE

Determination of methane distribution patterns after emissions from the controlled landfill in Novi Sad was carried out in three phases. Since no reliable and measured data on methane emission are available, methane flux was assessed using LandGEM model for methane generation. Representative meteorological data were collected and processed, and three meteorological scenarios were developed to understand and assess the potential influence of methane distribution after its emission in the atmosphere. The modelling of methane distribution in the ambient air was performed using ADMS Urban software. Modelled methane concentration showed different dispersion patterns. Since the entire landfill body is elevated, modelling of methane dispersion did not indicate significant concentrations at the lower atmospheric levels. Methane dispersion improved in higher altitudes due to methane's buoyancy and increasing of the air volume in the mixing layer. Hence, high concentration of methane could not be expected in identified vulnerable areas of Novi Sad. In addition, modelling indicated the potentially unfavorable meteorological conditions which contribute to methane distribution into the air. The risk for population could exist in scenarios with dominant low speed north-east (NE) or east-north-east (ENE) wind, in which the methane dispersion could be expected in directions towards the settlement. However, that is very rare occurrence concerning the dominant wind directions. Maximal concentrations in all investigated scenarios were reached at less than 300 m from the landfill in direction of the dominant winds.

Models which can generate initial information on methane distribution in the absence of measured data are important to understand and should be included in the overall risk assessment models prior to landfill closure. This research indicates how methane distribution patterns can be assessed if there is no available data and highlights that the methane distribution depending on the terrain and meteorological factors can be important and it should be included as one of the factors in landfill risk assessment models.

## EXPERIMENTAL

Methodological steps presented here provide a roadmap for researchers and waste management stakeholders to develop thorough, data-driven representations of their own case studies.

### Landfill description

Landfill in Novi Sad is controlled, fenced with weigh bridge, daily covered with soil and operated by local municipal waste management company. No bottom liner and no leachate and gas collection system exists. Passive gas

venting system is constructed to prevent methane accumulation in the landfill body. There are no precise historical data on the first year of its operation. The estimation indicates that landfill started operating between 1960 and 1970. Today landfill body covers 22 ha and contains approximately 2,000,000 m$^3$. The distance from residential area is 700 m. Landfill depth varies from 3 to 25 m. For modelling, an average landfill height of 17 m was adopted (personal communications, 2018). The landfill will have been closed by 2025, when a new sanitary landfill will start operating. The location is presented in Figure 7.
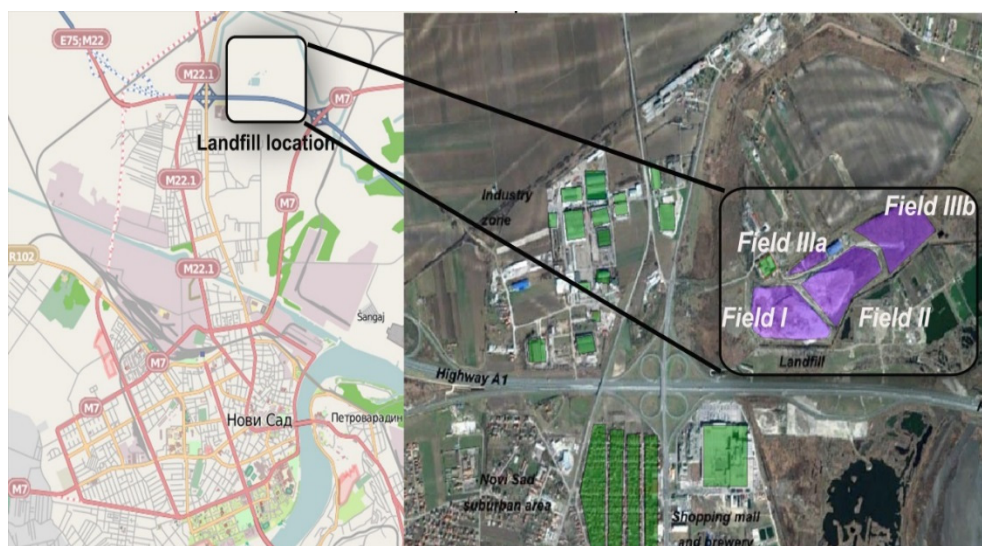


**Figure 7.** Location of the landfill

### Determination of methane distribution in the ambient air

Simulation of methane distribution in the ambient air was performed by ADMS software. The ADMS is widely used dispersion model which simulates a wide range of pollution from various sources based on Gaussian distribution [14, 21-23]. As an output, ADMS generates short-term, ST (daily and monthly) and long-term, LT (annual) propagation scenarios.
The following data are used as an input for modelling in ADMS:

**1. Emission related parameters -** Methane emissions are estimated using LandGEM model. This model is a function of two model parameters, methane production potential and first-order decay rate which is associated with waste decomposition (yr$^{-1}$) [24]. The LanGEM is represented by the following equation:

BOGDANA VUJIĆ, NEMANJA STANISAVLJEVIC, FRANCISC POPESCU, NIKOLINA TOSIC,
UNA MARČETA, MARJANA PARDANJAC, VASILE PODE

$$Q_n = kL_0 \sum_{i=0}^{n} \sum_{j=0.0}^{0.9} \frac{M_i}{10} e^{-kt_{ij}}$$

where $Q_n$ is $CH_4$ generation rate ($m^3 yr^{-1}$) in year n; *k* is first-order waste decay rate ($yr^{-1}$); $L_0$ is the $CH_4$ generation potential ($m^3 Mg^{-1}$ wet waste); $M_i$ is the waste mass placement per year *i* (Mg); j is and intra-annual time increment used to calculate $CH_4$ generation; and *t* is time (yr).

Since no gas collection system existed from the initial year of operation, the landfill gas collection efficiency was set to zero. The following values are used for running the LandGem model: K = 0.040 year$^{-1}$, Lo = 100 $m^3 Mg^{-1}$, Methane Content = 50 % by volume. Because the landfill in Novi Sad is daily covered with the soil layer, methane oxidation factor in landfill cover soil is estimated and included in the model. Various $CH_4$ oxidation rates for different cover materials have been reported [25]. For different soil covers, oxidation factors can vary between 0.1 and 0.81 [26], while for compost oxidation in compost reported rates reported are in the range of 0.16 to 0.98 [27,28]. Considering that Novi Sad the landfill in Novi Sad uses daily soil cover, with no data about its performance and efficiency, oxidation factor of 0.1 is applied. Sensitivity analysis is performed with 0.2 and 0.5 oxidation factors as alternate values to assess influence of methane oxidation variation in soil cover.

Waste generation data was developed based on the International Management Group (IMG) [29]. According to the available data Novi Sad generates 120,000 tons of MSW year$^{-1}$. The landfill started receiving waste between 1960 and 1970. Since no data on MSW generation existed at that time, waste generation rate kg capita$^{-1}$yr$^{-1}$ was used as a constant in order to estimate waste delivery rate from 1960 to 1970. Methane generation modelling is performed using 1960 and 1970 as initial years of waste disposal. The landfill model is set as a volume source of fugitive emissions that are constantly emitted with no significant emission velocity. An average adopted temperature of emitted methane was set up to 30 °C [30].

**2. Meteorological parameters** - Methane emissions from the landfill in Novi Sad are negligible during winter period [3]. In order to simulate and assess the most unfavorable scenario, methane distribution is modelled for the summer season when emissions are the most intensive. Hence, meteorological data for summer 2016 were used. Data were analyzed and processed to identify critical meteorological conditions that contributes methane dispersion in the ambient air.

Accordingly, three metrological scenarios were developed:

- Scenario I (S1) representative for rainy summer period in August: relative low summer temperature (21.4 °C), high relative humidity (98 %), high cloud cover (8 oktas) and dominant NW wind direction with low speed (2.4 ms$^{-1}$).

- Scenario II (S2), representative for warm and cloudy period in July: elevated temperature (29.8°C), low relative humidity (70%), high cloud cover (5 oktas) and, dominant NNW wind direction with relative low wind speed (2.4 ms$^{-1}$).

- Scenario III (S3), representative for hot and windy period in June: elevated temperature (31.8°C), low relative humidity (60%), clear weather (0 oktas), dominant ESE wind speed with high wind speed (9.4 ms$^{-1}$).

**3. Ambient related parameters** - In order to simulate vertical and horizontal $CH_4$ dispersion, modelling domain was defined as an area of 1000 x 1000 m (X, Y), with the resolution of 31 points in each direction. The altitude of 50 m (Z) with 7 output points for concentrations calculation (at 0, 8, 17, 25, 33, 42 and 50 m) have been applied. The simulation of real environment is presented in Figure 8.
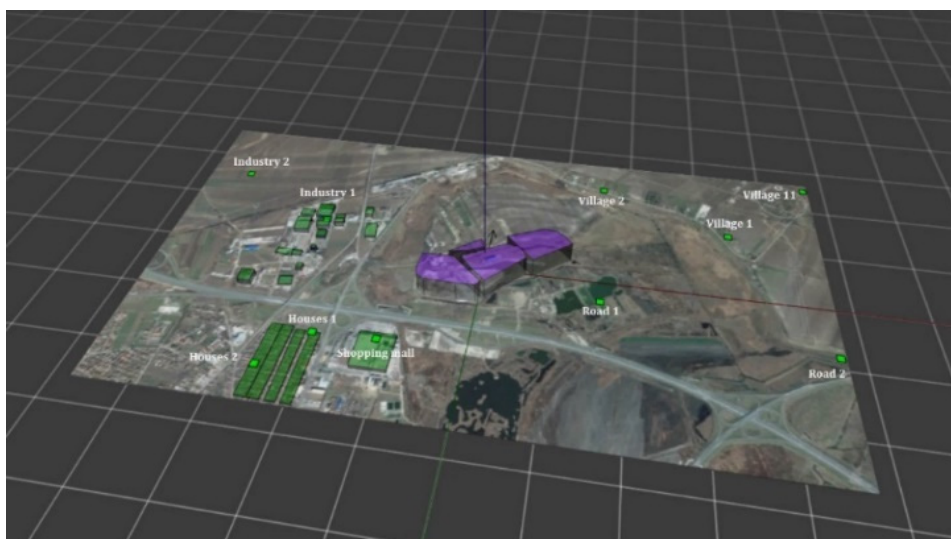


**Figure 8.** Simulation of the real environment

The specific points (receptors) were defined to quantify spatial methane dispersion from landfill in dominant air flows. Disposition of the receptors are given in Figure 8. Distances from receptors are given in Table 3.

**Table 3.** Specified points description

| Specified Points | Distance from the landfill (m) | Description |
|---|---|---|
| Houses 1 | 250 | Suburban area of Novi Sad |
| Houses 2 | 350 | |
| Shopping mall | 200 | Shopping mall (hypermarket) with brewery |
| Road 1 | 170 | Near road receptor, pasture area |
| Village 1 | 380 | Small settlement, mostly old houses |
| Village 2 | 280 | |
| Industry 1 | 270 | Commercial entities |
| Industry 2 | 470 | Additional receptor points at the dominant directions of the methane distribution |
| Road 2 | 470 | |
| Village 11 | 530 | |

The modelling was performed in two iterations with previously described meteorological data sets for the entire testing domain, as well as for specified vulnerable points.

## ACKNOWLEDGEMENTS

## REFERENCES

1. N. Stanisavljević; D. Ubavin; B. Batinić; J. Fellner; G. Vujić; *Waste Management and Research*, **2012**, *30*(10), 1095–1103.
2. SEPA; Serbian Agency for Environmental Protection, **2017**, available at: www.sepa.gov.rs, (accessed 16 November 2017).
3. G. Vujic; N. Jovičić; M. Petrović-Djurović; D. Ubavin; B. Nakomčić; G. Jovičić; D. Gordić; *Therm. Sci.*, **2010**, *14*(2), 555-564.
4. E. Mihajlović; L. Milošević; J. Radosavljević; A. Djordjević; I. Krstić; *Therm. Sci.*, **2016**, *20*(4), 1295-1305.
5. R. V. Karanjekar; A. Bhatt; S. Altouqui; N. Jangikhatoonabad; V. Durai; M. L. Sattler; M. D. Sahadat Hossain; V. Chen; *J. Waste Manag.*, **2015**, 46, 389–398.
6. IPCC, Guidelines for National Greenhouse Gas Inventories, **2006**, Volume 5 - Waste ISBN 4-88788-032-4.

7.  A. Leelossy; Jr. Ferenc Molnár; F. Izsák; A. Havasi; I. Lagzi; R. Mészáros; *Centr. Eur. J. Geosci.*, **2014**, *6*(3), 257-278.

8.  N. S. Holmes; L. Morawska; *Atmos. Environ.*, **2006**, *40*(30), 5902–5928.

9.  D. M. Taylor; F. K. Chow; M. Delkash; P. T. Imhoff; J. *Waste Manag.*, **2018**, 73, 197–209.

10. J. G. Mønster; J. Samuelsson; P. Kjeldsen; C. W. Rella; C. Scheutz; J. *Waste Manag.*, **2014**, *34*(8), 1416–1428.

11. R.J. Cicerone, R.S Oremland; *Global Biogeochem. cycles*, **1988**, *2*(4), 299-327.

12. C. G. Nolte; T. L. Spero; J. H. Bowden; M. S. Mallard; P. D. Dolwick; *Atmosph. Chem. Phys.*, **2018**, *18*(20), 15471–15489.

13. I. Paraskaki; M. Lazaridis; *Waste Manag. Res.*, **2005**, *23*(3), 199–208.

14. Z. Torok, N. Ajtai, A. Ozunu; *Studia UBB Chemia*, **2009,** LIV*1, 49-58*

15. M. Á. García; M. L. Sánchez; I. A. Pérez; M. I. Ozores; N.  Pardo; *Sci.Tot. Environ.*, **2016**, *550*, 157–166.

16. A. T. Lando; H. Nakayama; T. Shimaoka; J. *Waste Manag.*, **2017**, *59*, 255–266.

17. I. Haiduc; M.S. Beldean–Galea; *Air Quality – Models and Applications*, **2011**, INTech, UK, 289–318.

18. C. Cuna; P. Ardelean; S. Cuna; *Studia UBB Physica* XLVIII, **2003**, 565–567.

19. M. Aikawa; T. Hiraki; J. Eiho; *Atmos. Environ.*, **2006**, *40*(23), 4308–4315.

20. E. Ahmed; K. H. Kim; E. C. Jeon; R. J. C; *Sci. Total Environ.*, **2015**, 518–519, 595–604.

21. CERC; ADMS-Urban: Urban Air Quality Management System. User Guide. Version 3.1. 2001, CERC Limited, Cambridge, available at: www.cerc.co.uk, (accessed 14 September 2017).

22. S. E. Belcher; O. Coceal; J. C. R. Hunt; D. J. Carruthers; A. G. Robins; Atmospheric Dispersion Modelling Liaison Committee, ADMLC-R7, **2013**.

23. B. Vujic; U. Marceta; V. Mihajlovic; A. Djuric; *Reciklaza i Odrzivi Razvoj*, **2018**, *10*(1), 9–14.

24. U.S. Environmental Protection Agency: Washington, D.C., Landfill Gas Emissions Model (LandGEM), Version 3.02 User's Guide, **2005**, available at: http://www.epa.gov/ ttncatc1/dir1/landgem-v302-guide.pdf, accessed (03 Jun 2018).

25. C. Scheutz; P. Kjeldsen; J. E. Bogner; A. De Visscher; J. Gebert; H. A. Hilger; K. Spokas; *Waste Manag. Res.*, **2009**, *27*(5), 409–455.

26. R. He; A. Ruan; C. Jiang; D. Shen; *Bioresource Technol.*, **2008**, *99*(15), 7192–7199.

27. J. Berger; L. V. Fornés; C. Ott; J. Jager; B. Wawra; U. Zanke; *Waste Manag.*, **2005**, *25*(4 SPEC. ISS.), 369–373.

28. R. H. Kettunen; J. K. M. Einola; J. A. Rintala; *Water, Air, Soil Pol.*, **2006**, *177*(1–4), 313–334.

29. IMG; International Management Group, Saint-Gilles, Belgium: IMG. **2014**, available at: www.img-int.org/Central/Public08/, (accessed 17 December 2017).

30. C. Frola; D. De Roze; Solid Waste Association of North America, Sylver Spring, SAD, **1997**.